

Lecture Notes on Numerical Methods  
in Engineering and Sciences

Arkadiusz Żak


# A Finite Element Approach for Wave Propagation in Elastic Solids

**CIMNE<sup>B</sup>**

 Springer

# Lecture Notes on Numerical Methods in Engineering and Sciences

## Series Editor

Eugenio Oñate , Jordi Girona, 1, Edifici C1 - UPC, Universitat Politècnica de Catalunya, Barcelona, Spain

## Editorial Board

Charbel Farhat, Department of Mechanical Engineering, Stanford University, Stanford, CA, USA

C. A. Felippa, Department of Aerospace Engineering Science, University of Colorado, College of Engineering and Applied Science, Boulder, CO, USA

Antonio Huerta, Universitat Politècnica de Catalunya, Barcelona, Spain

Thomas J. R. Hughes, Institute for Computational Engineering, University of Texas at Austin, Austin, TX, USA

Sergio Idelsohn, CIMNE - UPC, Barcelona, Spain

Pierre Ladevèze, Ecole Normale Supérieure de Cachan, Cachan Cedex, France

Wing Kam Liu, Evanston, IL, USA

Xavier Oliver, Campus Nord UPC, International Center of Numerical Methods, Barcelona, Spain

Manolis Papadrakakis, National Technical University of Athens, Athens, Greece

Jacques Périaux, CIMNE - UPC, Barcelona, Spain

Bernhard Schrefler, Mechanical Sciences, CISM - International Centre for Mechanical Sciences, Padua, Italy

Genki Yagawa, School of Engineering, University of Tokyo, Tokyo, Japan

Mingwu Yuan, Beijing, China

Francisco Chinesta, Ecole Centrale de Nantes, Nantes Cedex 3, France

This series publishes text books on topics of general interest in the field of computational engineering sciences.

The books will focus on subjects in which numerical methods play a fundamental role for solving problems in engineering and applied sciences. Advances in finite element, finite volume, finite differences, discrete and particle methods and their applications to classical single discipline fields and new multidisciplinary domains are examples of the topics covered by the series.

The main intended audience is the first year graduate student. Some books define the current state of a field to a highly specialised readership; others are accessible to final year undergraduates, but essentially the emphasis is on accessibility and clarity.

The books will be also useful for practising engineers and scientists interested in state of the art information on the theory and application of numerical methods.

Arkadiusz Żak

# A Finite Element Approach for Wave Propagation in Elastic Solids

 Springer

Arkadiusz Żak  
Gdańsk University of Technology  
Gdańsk, Poland

ISSN 1877-7341                      ISSN 1877-735X (electronic)  
Lecture Notes on Numerical Methods in Engineering and Sciences  
ISBN 978-3-031-56835-0              ISBN 978-3-031-56836-7 (eBook)  
<https://doi.org/10.1007/978-3-031-56836-7>

© The Editor(s) (if applicable) and The Author(s), under exclusive license to Springer Nature Switzerland AG 2024

This work is subject to copyright. All rights are solely and exclusively licensed by the Publisher, whether the whole or part of the material is concerned, specifically the rights of translation, reprinting, reuse of illustrations, recitation, broadcasting, reproduction on microfilms or in any other physical way, and transmission or information storage and retrieval, electronic adaptation, computer software, or by similar or dissimilar methodology now known or hereafter developed.

The use of general descriptive names, registered names, trademarks, service marks, etc. in this publication does not imply, even in the absence of a specific statement, that such names are exempt from the relevant protective laws and regulations and therefore free for general use.

The publisher, the authors, and the editors are safe to assume that the advice and information in this book are believed to be true and accurate at the date of publication. Neither the publisher nor the authors or the editors give a warranty, expressed or implied, with respect to the material contained herein or for any errors or omissions that may have been made. The publisher remains neutral with regard to jurisdictional claims in published maps and institutional affiliations.

This Springer imprint is published by the registered company Springer Nature Switzerland AG  
The registered company address is: Gewerbestrasse 11, 6330 Cham, Switzerland

Paper in this product is recyclable.

*This book of mine I dedicate to my beloved wife Małgosia and our children. I would also like to dedicate it to my dear friend Eamon, for his invaluable and unconditional assistance, as well as my colleagues and friends from the department.*

# Preface

*Science is a tool for peace—Pope Francis, 10/09/2022*

This book is intended as a textbook for undergraduate, postgraduate as well as doctoral students, which offers an extended introduction to the problems associated with wave propagation in elastic solids solved by the use of the Finite Element Method (FEM). In a unique way, it guides the reader through the history of the physics of acoustics, computers and numerical analysis software, to end up with a bit more advanced topics related to the specific language of FEM, which is explained to my best intentions in a manner as simple and accessible as possible in the case of such topics.

This book is a summary of my scientific work, which I have been carrying out over the past 10 years. However, my adventure with science dates back to the times of my childhood and the inspiration I had from my father to investigate and learn about the surrounding world, how it works and why so. Following this path of questioning things and trying to understand the relations and mechanisms ruling the world, I was attracted towards physics and mechanics. This is the main reason why my steps led me to the Gdańsk University of Technology, where I studied Applied Mechanics at the Faculty of Applied Physics and Mathematics and where I received my master's degree in 1994.

Yet in 1993, as a junior research assistant, I started my scientific career at the Polish Academy of Sciences in Gdańsk. My interest in modelling physical phenomena, especially by the use of FEM, dates back to the beginning of this career, which is placed some 25 years back. Since that time my scientific work has been gradually more and more focused on FEM as a numerical technique, rather than its simple application to solve more or less complex scientific or engineering problems, mostly in dynamics. In 2012, I left the Polish Academy of Sciences to join a research group at the Gdańsk University of Technology, where I have been continuing my scientific research ever since in the Department of Biomechanics.

At this point, I would like to mention two kinds of research problems that kept my scientific attention for a little bit longer. Firstly, these were problems related to

damage detection in composite structures, which was the subject of my Ph.D. thesis prepared under the supervision of Prof. Wiesław Ostachowicz, which I defended in 1998. Secondly, these were problems related to the modelling and application of intelligent materials for dynamic control, which was the subject of my D.Sc. thesis, which I defended 11 years later in 2009. This latter could never have happened without meeting Professor Matthew Cartmell from the University of Glasgow in Scotland, who was my scientific guide there for several years from 2000 and who remains my friend to this day. I should say, however, that my scientific work at that time had one thing in common, which was the application of FEM. Gradually, my scientific work moved a little bit to high-frequency, non-stationary dynamic problems, which are best represented by problems related to the phenomena associated with the propagation of elastic waves.

My deep interest in modelling various scientific and engineering problems, especially by the use of FEM, resulted in the development of new types of finite elements, especially useful for damage modelling in composite materials. This phase of my research activities is quite well documented by numerous scientific research papers I co-authored, which were published with the great help and support of Prof. Marek Krawczuk, another friend of mine, as well as Prof. Wiesław Ostachowicz. Precise modelling of wave propagation phenomena in elastic solids required, however, the employment of a new class of finite elements, which were developed based on numerical techniques employed in fluid mechanics. In this respect, I also received a lot of help and inspiration from yet another colleague of mine, Prof. Grzegorz Zboiński, who should be mentioned here. All of this led to the formulation of the Time-domain Spectral Finite Element Method (TD-SFEM) in the realm of elastic solids, in contrast to the Frequency-domain Spectral Finite Element Method (FD-SFEM) existing at that time, which is based on the application of the fast Fourier transform (FFT). The results of this work are also well documented not only by many research papers published together with my colleagues from the Polish Academy of Sciences, but also by a common monograph entitled *Guided waves in structures for SHM. The Time-domain Spectral Element Method*, which I had the privilege and honour to be one of the authors.

In the following years, my scientific work concentrated on further development of TD-SFEM and resulted in the formulation of new interesting theories enabling one for more precise modelling of the wave propagation phenomena in various engineering structures, especially for damage detection purposes. On the other hand that led me to many interesting observations related to the numerical properties of TD-SFEM itself, as a more and more popular computational tool amongst scientists, researchers and engineers. As a consequence of that, a new numerical approach was proposed, based on the application of cubic splines, the idea of which dates back to the inspiration I received from the lectures given by Prof. Zbigniew Kosma, which I attended when I was still a student. This novel numerical approach, still under development, combines the superior properties of the cubic spline approximation with the excellent flexibility of FEM. Nowadays this area of research remains the main subject of my interests and is also mentioned in this book.



Finally, I would like to say that to a great extent this book is for me a kind of nostalgic journey through all these years of my scientific work until the present day. I hope very much that it will be the same fascinating journey for every reader as it was for me as the writer.

Gdańsk, Poland

Arkadiusz Żak

# Contents

<b>1</b>	<b>Introduction</b> .....	1
	References .....	16
<b>2</b>	<b>Wave Essentials</b> .....	21
2.1	Wave Motion .....	21
2.2	Wave Relations .....	22
2.3	Simple Wave Equations .....	26
2.3.1	1-D Elastic Rod .....	26
2.3.2	1-D Elastic Beam .....	30
2.4	Fourier Method .....	32
2.5	Wave Dispersion .....	34
2.6	Standing Waves and Normal Modes .....	41
	References .....	48
<b>3</b>	<b>Waves in a 3-D Elastic Space</b> .....	49
3.1	Navier-Cauchy Equation .....	49
3.2	Helmholtz Decomposition .....	53
3.3	Christoffel Equation .....	60
	References .....	64
<b>4</b>	<b>Surface Waves</b> .....	65
4.1	Rayleigh Waves .....	65
4.2	Love Waves .....	73
4.3	Stoneley Waves .....	78
	References .....	82
<b>5</b>	<b>Waves in a 2-D Elastic Space</b> .....	83
5.1	SH-Waves in an Elastic Layer .....	83
5.2	Lamb Waves in an Elastic Layer .....	87
	References .....	96

- 6 Waves in a 1-D Elastic Space** ..... 97
  - 6.1 Longitudinal Waves ..... 97
  - 6.2 Flexural Waves ..... 106
  - 6.3 Torsional Waves ..... 116
  - References ..... 120
- 7 A Step Towards FE Modelling** ..... 123
  - 7.1 Modelling Errors ..... 123
  - 7.2 Some Thoughts About Simplified Theories ..... 126
  - 7.3 Dispersion Curves ..... 131
  - References ..... 136
- 8 Simplified Theories of 2-D Structural Elements** ..... 137
  - 8.1 Symmetric Behaviour of Plates ..... 137
  - 8.2 Antisymmetric Behaviour of Plates ..... 147
  - 8.3 Coupled Behaviour of Shells ..... 158
  - References ..... 163
- 9 Simplified Theories of 1-D Structural Elements** ..... 165
  - 9.1 Longitudinal Behaviour of Rods ..... 165
  - 9.2 Flexural Behaviour of Beams ..... 175
  - 9.3 Torsional Behaviour of Shafts ..... 186
  - References ..... 195
- 10 FEM Essentials** ..... 197
  - 10.1 What Is FEM? ..... 197
  - 10.2 Weak Formulation ..... 198
  - 10.3 Equations of Motion ..... 200
  - 10.4 Shape Functions ..... 202
  - 10.5 Numerical Integration ..... 206
  - 10.6 Division into FEs ..... 208
  - 10.7 Solving Equations of Motion ..... 212
  - References ..... 217
- 11 Waves in Unbounded Structures** ..... 219
  - 11.1 Infinite Versus Finite ..... 219
  - 11.2 Treatment of Unwanted Boundary Reflections ..... 220
  - 11.3 Absorbing Layer with Increasing Damping ..... 223
  - References ..... 227
- 12 Numerical Case Studies** ..... 229
  - 12.1 Wave Propagation in a Stepped Bar ..... 229
    - 12.1.1 Problem Definition ..... 229
    - 12.1.2 Dispersion Curves and Theory Selection ..... 230
    - 12.1.3 ALID Parameters and Numerical Discretisation ..... 233
    - 12.1.4 Numerical Computations and Result Discussion ..... 234

- 12.2 Wave Propagation in a Strip with a Side Cut-Out ..... 238
  - 12.2.1 Problem Definition ..... 238
  - 12.2.2 Dispersion Curves and Theory Selection ..... 239
  - 12.2.3 ALID Parameters and Numerical Discretisation ..... 241
  - 12.2.4 Numerical Computations and Result Discussion ..... 243
- 12.3 Wave Propagation in a Flanged Pipe with a Circumferential Crack ..... 248
  - 12.3.1 Problem Definition ..... 248
  - 12.3.2 Dispersion Curves and Theory Selection ..... 250
  - 12.3.3 ALID Parameters and Numerical Discretisation ..... 253
  - 12.3.4 Numerical Computations and Result Discussion ..... 255
- References ..... 263
- 13 Periodic Properties of FE Discrete Numerical Models ..... 265**
  - 13.1 Bloch’s Theorem ..... 265
  - 13.2 Bloch Reduction ..... 270
  - 13.3 Numerical Dispersion ..... 273
  - 13.4 Numerical Anisotropy ..... 280
- References ..... 287
- 14 Spline-Based FEM Approach ..... 289**
  - 14.1 Some General Considerations ..... 289
  - 14.2 1-D Spline-Based Shape Functions ..... 291
  - 14.3 Wave Propagation Problems by spFEM ..... 295
- References ..... 306
- Afterword ..... 307**
- Appendix A: Material Constants ..... 309**
- Appendix B: Solving for  $c(\omega)$  ..... 313**
- Appendix C: Coordinate Systems ..... 315**
- Appendix D: Transformation of Mid-plane Displacement Fields ..... 319**
- Appendix E: FEM Aggregation/Assembly in MATLAB ..... 323**

# Chapter 1

## Introduction



People have been investigating and trying to explore the world around them since the most ancient times. In their early attempts to understand and to systematise the phenomena they encountered every day, the observations they made, together with their reflections on those observations led centuries ago to the emergence of philosophy in ancient Greece. This was a spark igniting human minds that later, over the upcoming centuries, had disciplined the human way of thinking and reasoning forging that which nowadays we call science.

Ancient Greek philosophers suspected that music results from a mysterious connection between various waves and sounds, behind which lay hidden air vibrations or disturbances—see Fig. 1.1. It was Pythagoras, a great Greek philosopher and mathematician, who said that “... *there is geometry in the humming of the strings, there is music in the spacing of the spheres ...*”. Since music was a particularly beloved and omnipresent field of art for ancient Greeks, accompanying their marriages, funerals, religious ceremonies as well as poetry recitation in theatres, it simply had to have a great and prominent impact on their lives. Perhaps this was a direct reason why ancient Greeks started to study various phenomena, which nowadays we can so easily place within the fields of mathematics (harmonics), physics (sound propagation) or architecture (outdoor theatres), and which could be thought of as the foundations of modern acoustics.

With no doubt Pythagoras (c. 570–c. 495) should be mentioned as the first great Greek philosopher, whose efforts to understand the universe left deep imprints on music and mathematics as well as astronomy. In the field of music Pythagoras, using the monochord, investigated vibrating strings producing harmonious tones in order to determine mathematical formulae describing relations between the lengths of these strings and the tones they produced. By dividing the strings into ratios of halves, thirds, quarters or fifths Pythagoras created music intervals of an octave, a perfect fifth, a second octave, and a major third, respectively. Thanks to these investigations he discovered what we now call the first five overtones, and which create the common intervals being the primary building blocks of modern musical

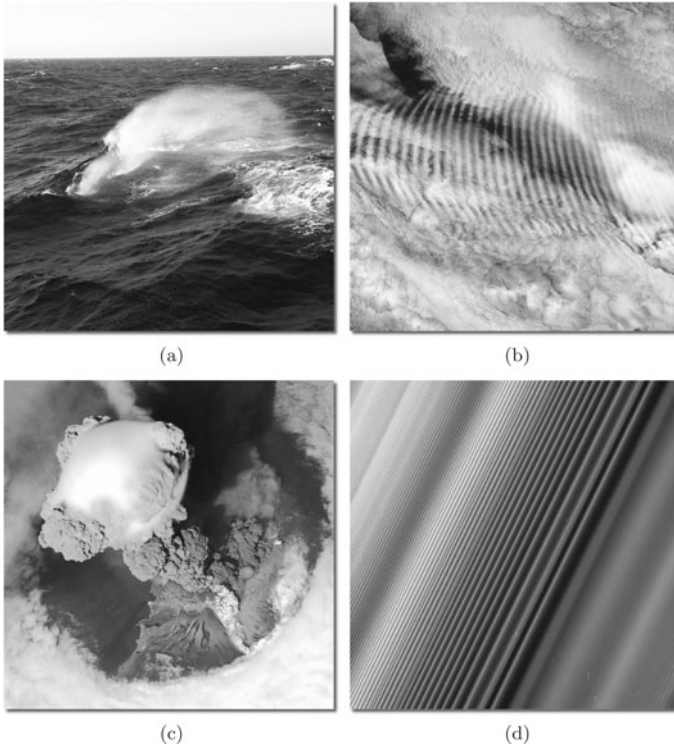


**Fig. 1.1** Waves are inherently a part of the surrounding world as: **a** sea waves resulting from the interaction of the wind blowing over the free surface of the sea [2], **b** atmospheric gravity (internal) waves resulting from the interaction of the rapidly rising air through convection and the wind blowing over the ocean [3], **c** shock waves in the atmosphere resulting from the eruptions of volcanoes [4], **d** wave structure in Saturn’s rings known as the Janus 2:1 spiral density wave, resulting from the same process as this responsible for the creation of spiral galaxies [5]

harmony—see Fig. 1.2. For many centuries this idea of Pythagoras had been the foundation of all music theory, having its roots in antiquity but lasting up to modern times [1].

Another great Greek philosopher Aristotle (384–322 BC), whose interests spanned nearly all fields of ancient science, also studied sounds and investigated the phenomenon of their propagation. He rightly found out that sound propagation in the air results from compressive air movements, but he was wrong to think that the speed of sound is proportional to the sound pitch, greater for sounds of higher frequencies and smaller for sounds of lower frequencies.

It should be noted that in the Middle Ages and the Renaissance it was music which directly stimulated investigations in the field of acoustics as well as other fields of science. An English philosopher John Blund (c. 1175–1248), who studied Aristotle’s works, established frameworks for future acoustics theories by studying generation

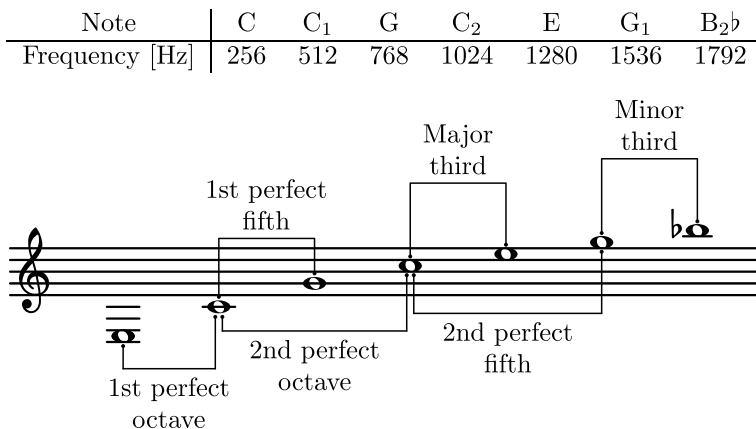


Fig. 1.2 A concept of Pythagorean music intervals based on the note C

of sound and its reception, its medium, etc. Another English music theorist Walter Odington (c. 1260–1346) gathered together all knowledge of music at that time, which he supplemented with his own theoretical considerations about the consonance of the minor and major thirds. A music theorist, Iacobus de Ispania (d.c. 1330), was the author of the longest work on music of the Middle Ages. In contrast to that Thomas Bradwardine (c. 1300–1349), an English scholar, mathematician and physicist together with Johannes Boen (d.c. 1367), a Dutch music theorist, held the position that separation between the theory of music and acoustics was at least questionable [6]. However, over the forthcoming centuries the leading role of music would be gradually fading. Music evolved to become a separate field of art, while those branches of science that were initially serving to music as tools to explain music rules and complexity, now released from this dependence, evolved to become individual science disciplines such as: acoustics, astronomy, chemistry, mathematics, mechanics, physics, etc. However, musical sounds continued to be a very important subject of then research.

From one angle the primary subject of investigation was the air or water and their properties as the media within which sounds can propagate. An Anglo-Irish philosopher, chemist and physicist Robert Boyle (1627–1691), investigating properties of various gasses, proved experimentally that sound cannot propagate through the vacuum. Sir Isaac Newton (1642–1726), an English mathematician, astronomer, theologian and physicist was the first who tried to establish a formula for the speed of sound in air. Assuming harmonic motion of adjacent air particles, Newton expected the speed of sound in air to be equal to the square root of the ratio of the air pressure and density. This problem was also studied by Joseph Louis Lagrange (1736–1813), an Italian astronomer and mathematician, who corrected Newton’s calculations by formulating general equations of air motion and by their subsequent integration along the direction of their propagation. However, it was Pierre Simon Laplace (1749–1827), a French mathematician, physicist and astronomer, who further corrected

both previous formulae by pointing out that elastic properties of the air should take into account the air heat capacity due to adiabatic compression. In turn, a Swiss physicist Daniel Colladon (1802–1893) determined the speed of sound in water. He also measured the compressibility of other principal liquids, thereby winning the prize of the Academy of Sciences in Paris. Another French physicist, astronomer and mathematician Jean Baptiste Biot (1774–1862), carried out measurements on the propagation of sounds in pipes noting that the speed of sound in the pipes themselves is much higher than in the air. Propagation of sound in gasses other than the air was the area of interest of a German physicist and musician Ernst Florence Friedrich Chladni (1756–1827).

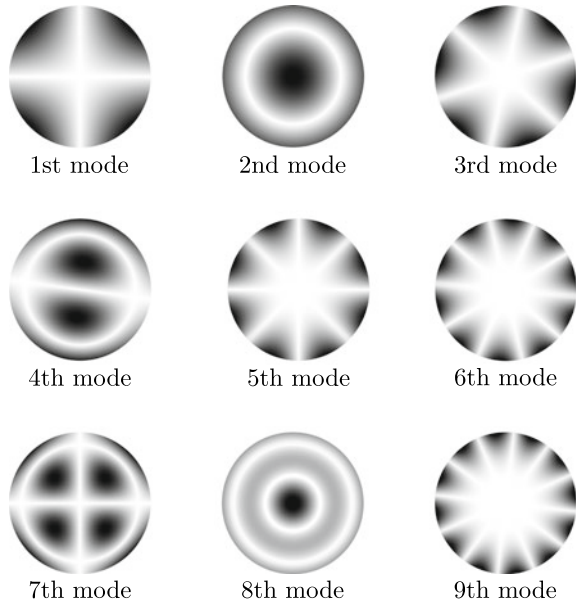
Approaching from the opposite angle, the subjects of investigation were various instruments in the form of strings, plates, membranes, etc. that were responsible for sound generation. Many great names can be mentioned here as well. An ingenious Italian polymath, Galileo Galilei (1564–1642), who worked as an astronomer, physicist, philosopher and mathematician, tried to establish a link between the pitch and frequency of sounds produced by vibrating monochord strings of different lengths. This was also a research subject of a French mathematician and physicist Joseph Sauveur (1653–1716), who investigated this link in great detail, and who is also credited with coining the term *acoustique* [7].

An English mathematician Brook Taylor (1685–1731), thanks to the application of a mathematical tool sophisticated for its time, now known as the *calculus of finite differences*, determined the fundamental form of vibrating strings. In the following years Daniel Bernoulli (1700–1782), a famous Swiss mathematician and physicist, managed to formulate and solve partial differential equations describing the motion of vibrating strings. This was possible thanks to the application of d’Alembert’s formula, which nowadays is broadly used in mechanics. The solution to the equation of motion obtained by Bernoulli was interpreted by Jean le Rond d’Alembert (1717–1783), a French mathematician, mechanician, physicist, philosopher as well as music theorist, as two independent waves travelling in opposite directions along the strings [8]. Transverse vibrations of strings were also studied by Lagrange, who disputed in his works the lack of generality in earlier works of Brook Taylor, d’Alembert or Euler, suggesting a new, general solution form.

A Swiss mathematician, physicist, astronomer, logician and engineer Leonhard Euler (1707–1783) helped to formulate the Euler-Bernoulli equations for transverse vibrations of beams, which today is one of the most common analytical tools of classical mechanics. His studies included fluid dynamics too. In this field Euler is responsible for the formulation of a very important set of equations of fluid dynamics for inviscid fluids, known as the Euler equations. The work of Jean-Baptiste Joseph Fourier (1768–1830), a French mathematician and physicist, well-known for the Fourier theorem, should also be mentioned here. The impact of the Fourier theorem turned out to have very deep implications also in the field of acoustics. His theorem about representing periodic functions by an infinite series of sines and cosines, proved in fact the principle of superposition, which is one of the fundamentals of every linear analysis, including the analysis of sound propagation.



**Fig. 1.3** First nine Chladni patterns of a free aluminium disc. Results of numerical computations by TD-SFEM



Based on the research that had been carried out in the previous decades as well as many indisputable milestones in various field of science, also driven by the demand of the Industrial Revolution, the 18th and 19th century appear as the period of great progress in the field of theoretical and experimental acoustics.

Simeon Denis Poisson (1781–1840), a French mathematician, engineer, and physicist was the first to presented a solution to the problem of vibrating circular and rectangular membranes, which was also studied by a German mathematician Rudolf Friedrich Alfred Clebsch (1833–1872). A simple method to visualise nodal lines of vibrating plates was proposed by Chladni, who for that purpose used sand sprinkled onto their surfaces—see Fig. 1.3. After his name the patterns produced by this technique are known as Chladni figures. In the opinion of Michael Faraday (1791–1867), a famous British scientist, it was the process of acoustic streaming which was responsible for the appearance of Chladni figures. The relationship between vibration frequencies and corresponding modes of vibrations for flat circular surfaces was given the name of Chladni’s law by Lord Rayleigh. Lord Rayleigh, in full John William Strutt, 3rd Baron Rayleigh (1842–1919), a Nobel prize winning British physicist, in his textbook *Theory of Sound* [9] presented a holistic and scientific approach to the most urgent problems of acoustics at that time. A solution to the problem of vibrating plates was given by Marie Sophie Germain (1776–1831), a French mathematician, physicist, and philosopher, who received for her work a prestigious grand prize from the Paris Academy of Sciences. However, it was Gustav Robert Kirchhoff (1824–1887), a German physicist, who corrected her results by presenting a more accurate approach to treat plate boundary conditions. John Tyndall (1820–1893) was a prominent Irish physicist. The results of his scientific investigations on vibrations

of rods, plates and bells were published in his book on sound [10]. Tyndall was also an experimentalist, whose works in the field of acoustics focused on sound transmission in the air, especially on differences in sound propagation at particular locations, resulting from temperature differences of air masses. Hermann Ludwig Ferdinand von Helmholtz (1821–1894) was a German physician and physicist, not only to be remembered for his famous theorem, named after him as Helmholtz's theorem. His works in the field of acoustics were mainly focused on sound perception. As he was also educated in medicine, in his book [11] he combined his knowledge of physics, physiology and music to show that the human sense of hearing is able to differentiate even very complex tones.

The following decades are a time of a great progress and rapid development primarily in mathematics, and consequently in other fields of science, including acoustics and mechanics, which very eagerly took advantage of the achievements of contemporary mathematics. Wave motion stayed at the very centre of scientific interest of then research. A simple classification in the case of various types of waves, as well as in the case of mechanical waves, are presented in Figs. 1.4 and 1.5.

In the field of acoustics the classical theory of longitudinal behaviour of rods is well established, which can be attributed together to d'Alembert, Bernoulli, Euler and Lagrange. The same can be said about the theory of flexural behaviour of beams, which we owe to the works of Bernoulli and Euler. Nowadays it is best known as the classical theory of flexural behaviour, or simply the classical beam theory. On the other hand the theory of torsional vibration can be attributed to Adhemar Jean Claude Barre de Saint-Venant (1797–1886), a French mechanician and mathematician, whose works concentrated on stress analysis and hydraulics. The equations developed by Saint-Venant for unsteady flows in shallow waters through open channels, also known as the Saint-Venant equations, are fundamental in modern hydraulic engineering. Two-dimensional structures such as membranes and plates were also a common subject of research.

In 1888 Augustus Edward Hough Love (1863–1940), an English mathematician famous for his works on mathematical theories of elasticity, developed a theory for flexural behaviour of plates. The theory was a two-dimensional extension of the classical theory of beams by Bernoulli and Euler, and was taking advantage of the same assumptions earlier formulated by Kirchhoff. Love is also known for his works on propagation of horizontally polarised seismic surface waves, which are called Love waves. It should be added that another type of seismic surface waves, which are polarised vertically, as opposed to horizontally polarised Love waves, takes its name from Lord Rayleigh, who predicted their existence. The problem of flexural behaviour of plates was also studied by Poisson and Cauchy, who based their approach on the general theory of elasticity. Baron Augustin-Louis Cauchy (1789–1857) was a famous French mathematician, engineer and physicist. His pioneering works contributed to several branches of mathematics, including mathematical analysis as well as continuum mechanics. The theory of bending was a field of specialisation of another great scientist at that time, Stephan Prokopovych Timoshenko (1878–1972). This Russian born, and since 1922 also an American engineer and academic, is recognised by many as the father of modern engineering mechanics.

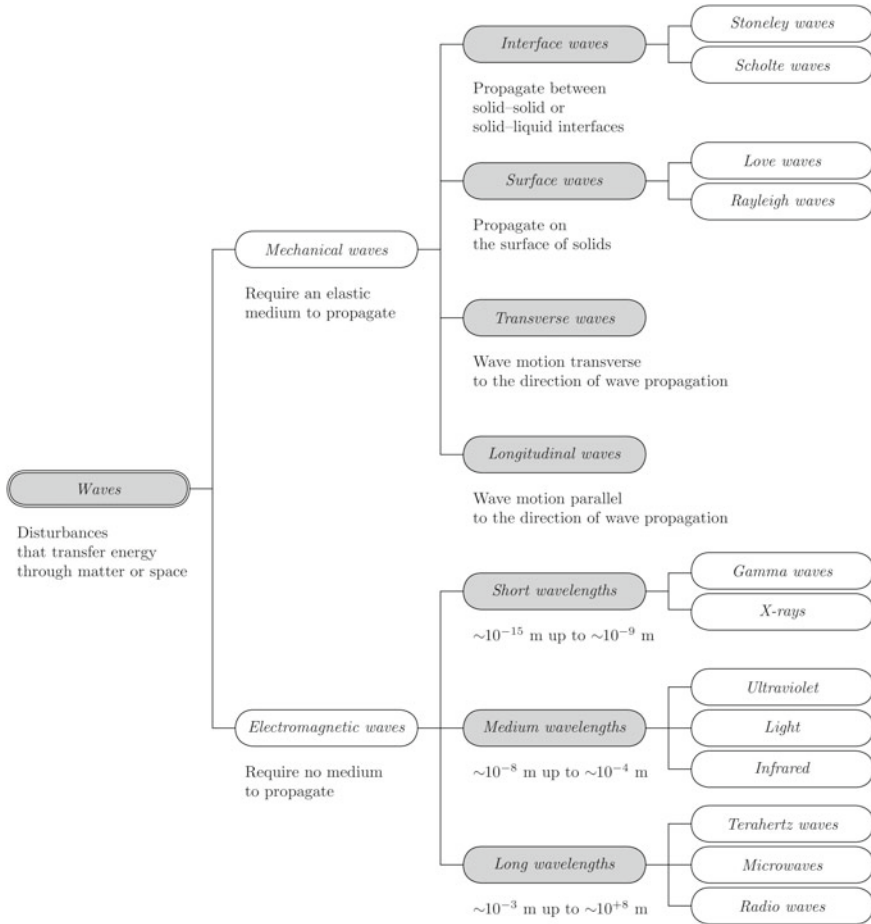
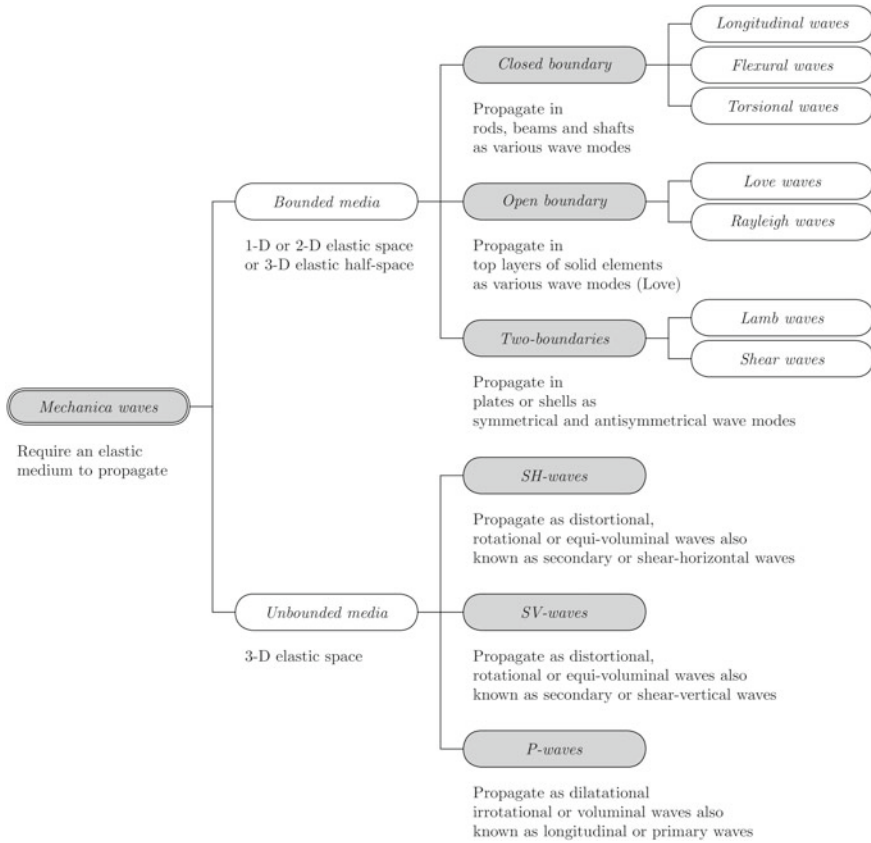


Fig. 1.4 Simple classification of various types of waves

As shown above the tremendous progress in science during these times included not only physics and mathematics, but also acoustics and mechanics. Very often theoretical investigations were driven directly by luck and experiments. Based on the foundations laid by many great scientists and researchers from the previous centuries many new or refined theories, explaining better the observed phenomena or offering a deeper insight into the physics behind them were proposed during this *Golden Age* of acoustics and mechanics. Many well-known names contributing to these fields can be listed here including Pochhammer, Chree, Lamb, Reisner, Mindlin, Herrmann, Reddy, etc. to mention only a few.

Leo August Pochhammer (1841–1920) was a Prussian mathematician, who is mostly known for his works on special functions, but who had a great interest in the theory of elasticity [12]. At the same time as Pochhammer [13], Charles Chree



**Fig. 1.5** Simple classification of mechanical waves in various types elastic media

(1860–1928), a Scottish born British physicist, also worked on elasticity problems, which concerned the longitudinal dynamic behaviour of elastic bars [14]. The result of their parallel work was greatly recognised by the scientific community, and nowadays this result is known as the Pochhammer-Chree equation. The phenomenon of sound propagation in the form of multi-mode flexural and in-plane elastic waves in infinite plates was studied by Sir Horace Lamb (1849–1934) [15]. Lamb was an English applied mathematician, who authored several influential textbooks on classical physics, mechanics and acoustics [16], as well as who contributed to hydrodynamics. Lamb coined the term *vorticity*, which since 1916 remains in use in fluid-dynamics.

Eric Reissner (1913–1996) was a German born, American civil engineer and mathematician, whose works in applied mechanics is fundamental to the theoretical understanding of the behaviour of elastic solids. Reissner [17] is recognised as a co-author of the most commonly used plate theory, which is known to the scientific community as the Mindlin-Reissner theory of plates, since the theory was devel-

oped in parallel and independently by Raymond David Mindlin (1906–1987), an American mechanical engineer [18]. George Herrmann (1921–2007) was a Russia born American scientist working in the field of mechanical and civil engineering. Together with Mindlin he co-authored a theory describing longitudinal behaviour of rods, known in the literature as the Mindlin-Herrman theory of rods [19]. Finally, Junuthula Narasimha Reddy (1945–present) is an Indian born, American civil engineer, scientist and researcher, who significantly contributed to the field of solid and fracture mechanics as well as mechanics of composite materials, who is also responsible for the development of a higher-order theory of plate flexural behaviour, known as the Reddy plate theory [20].

It may be interesting to note that the tremendous progress in many branches of science sometimes led to unusual situations. New theories were formulated, but the ability of the mathematics of the time to show practical solutions for these theories was insufficient. For example, the characteristic equation derived by Pochhammer and Chree had to wait nearly 65 years to get solved. However, its solution was obtained not thanks to the traditional analytical approach of mathematics, but thanks to numerical computations. A new era of numerical computations was about to come and brought to existence a powerful computational tool, which nowadays we call the computer. Together with computers new algorithms and methods were developed to offer computational abilities, which we know from the present day.

The first steps on the path leading to the emergence of modern computers can be attributed to Joseph Marie Jacquard (1752–1834), a French weaver and merchant, who is the inventor of the earliest programmable machine known as the Jacquard loom. The Jacquard loom invented in 1801 used punched wooden cards to weave fabric designs in exactly the same manner as an early version of IBM digital compiler. Based on the idea of Jacquard, an American engineer and inventor Herman Hollerith (1860–1929) developed in 1890 an electromechanical punched card tabulator for the purpose of the 1890 census in the United States. His invention led to the beginning of the Tabulating Machine Company, which in 1911 joined with three other companies to become the Computing-Tabulating-Recording Company, which since 1924 has been known just as IBM. In 1936 Alan Mathison Turing (1912–1954), an English mathematician, computer scientist, logician and cryptanalyst came up with the idea of a universal machine, better known as the Turing machine, being a true and real ancestor of modern computers. Turing is considered as the father of theoretical computer science and artificial intelligence, the originator of the so-called *Turing test* from 1950 measuring the ability of a computing machine to mimic the behaviour of a human being in an intelligent and indistinguishable manner. In 1948 Turing developed and presented the algorithm of the LU decomposition method, which since that time remains in use for solving matrix equations.

A breakthrough was made by two American engineers John Presper Eckert (1919–1995) and John William Mauchly (1907–1980), who built between 1943–1945 the earliest and the most famous electronic computer named ENIAC (Electronic Numerical Integrator and Computer). However, it should be said that the title of the first computer is also claimed by Colossus, built in 1943 under the supervision of a British mathematician and codebreaker Maxwell Herman Alexander Newman (1897–1984)

and an English engineer Tommy Flowers (1905–1998), as well as Alan Turing himself. Additionally, a computational machine Z3 designed in 1943 by a German civil engineer, inventor and computer pioneer Konrad Zuse (1910–1995) must be mentioned here together with the ABC computer (Atanasoff-Berry Computer) built between 1937–1942 by two American engineers John Vincent Atanasoff (1903–1995) and Clifford Edward Berry (1918–1963).

A great leap forward in the development of computers, as we understand this term today, was made in 1947 by William Bradford Shockley (1910–1989), an American physicist and inventor, John Bardeen (1908–1991), an American physicist and electrical engineer, as well as Walter Houser Brattain (1902–1987), an American physicist, who in Bell Laboratories invented the transistor, which today is the most essential and fundamental building block of modern electronic devices. For their joined invention they were awarded the Nobel Prize in Physics in 1956. However, the concept of the transistor undoubtedly belongs to Julius Edgar Lilienfeld (1882–1963), an American physicist and electronic engineer, who presented it more than two decades earlier, in 1926. In 1958 the first integrated circuit (microchip) was built, which is considered the key element of modern computers, and which spurred the revolution in the field of personal computers. The invention of the integrated circuit should be attributed independently to an American inventor and engineer Jack St. Clair Kilby (1923–2005), who for his invention was awarded the Nobel Prize in physics in 2000, and an American physicist Robert Noyce (1927–1990), a co-founder of Fairchild Semiconductor in 1957 and Intel Corporation in 1968.

The inventions of the transistor and the integrated circuit denote a symbolic beginning of the era of personal computers. Altair 8800 is considered by many as the first personal computer. It was built in 1974 by Micro Instrumentation and Telemetry Systems (MITS) founded by an American engineer Ed Roberts (1941–2010), who is recognised as *the father of the personal computer*. In 1976 Apple Computer, Inc. was established by Stephen Gary Wozniak (1950–present), an American inventor, electronics engineer, programmer, and Steven Paul Jobs (1955–2011), which produced one of the first commercially successful and mass-produced home computers, Apple II. Apple II was the successor to a short-series of 200 hand-built Apple I computers. The first personal computer produced by Hewlett-Packard Company HP-85 enters the market in 1980. Only one year later, in 1981 the first personal computer produced by IBM named *Acorn* appears. The number of computers used for various purposes grows tremendously and new companies producing computers for everyday home use appear, including such brands as: ZX series, Commodore, Amiga or Atari. Today the total number of personal computers sold worldwide every year exceeds 250 million. Personal computers, as well as computers in general, assist every day life in every possible aspect of human activity. This also includes science and research.

From the very beginning of their history computers were found by scientists and researchers to be very helpful tools offering enormous speed of computations, which otherwise had to be carried out by many people over long hours or even days, and being so much prone to human error or mistake. Computer programming became practically a separate branch of science giving birth to new, more efficient and more intuitive programming languages, programming packages or environments such as:

computer aided designing (CAD) or computer aided engineering (CAE). Among them, in the realm of scientific research and its needs, numerical computational methods and tools played the most important role. However, before this could have happened it is necessary to travel back in time to much earlier years and such great names as: Navier, Stokes, Ritz or Galerkin.

Claude-Louis Navier (1785–1836), was a famous French engineer and physicist, who is mostly known for his contribution to continuum mechanics. In 1821 Navier presented, formulated by himself, the general theory of elasticity using the language of contemporary mathematics. The input of Navier into the field of continuum mechanics allows him to be considered as the founder of modern structural analysis. The system of partial differential equations describing the behaviour of the elastic continuum under the influence of forces is known in mechanics as the Navier or Navier-Cauchy equations. However, the major contribution of Navier stays at the centre of fluid dynamics. Together with Sir George Gabriel Stokes (1819–1903), an Anglo-Irish physicist and mathematician, Navier is recognised as a co-author of the famous Navier-Stokes equations. Walther Ritz (1878–1909) was a Swiss theoretical physicist, famous for the formulation of a general method for finding approximate solutions of partial differential equations accompanied with sets of boundary conditions, known as boundary value problems. A special variant of the method proposed by Ritz was developed by Boris Grigoryevich Galerkin (1871–1945), who was a Russian mathematician and engineer. In his article from 1915 Galerkin proposed an idea for a new approach that could be effectively used for approximate solutions to partial differential equations. Nowadays the Ritz and Galerkin methods are considered as the foundation of many effective solution algorithms in the fields of mechanics, thermodynamics, electromagnetism, hydrodynamics and many others. One such a method is the Finite Element Method (FEM).

It should be said, however, that the mathematical origins of FEM were not only firmly embedded in the earlier works of Bernoulli, Euler, Lagrange, Legendre, Gauss, Cauchy and many more, considered as the fathers of the calculus of variations, but also in the contemporary works of Rayleigh, Ritz and Galerkin. Its principal idea, as well as the most important feature and advantage, is the subdivision of the computational domain into smaller sub-domains of simpler geometry, which are called finite elements (FEs). Based on numerical properties of FEs the solution of a given problem, through a simple element aggregation procedure, can be presented at the level of the entire domain and solved algebraically.

No precise date can be proposed as the date of birth of FEM, which undoubtedly is one of the most popular and efficient computational tools available these days. However, the beginnings of FEM can be dated back to the 1940s and the names of Hrennikoff and Courant, when the idea of FEs was crystallised [21–24]. Alexander Pavlovich Hrennikoff (1896–1984) was a Russian born, Canadian structural engineer, who is considered as the originator of FEM. The unique approach of Hrennikoff employed to solve a boundary value problem was based on a lattice analogy [21, 22] used for subdivision of the computational domain. The approach presented by Richard Courant (1888–1972), a German born, American mathematician, was different. Courant suggested the subdivision of the computational domain

into a regular mesh of triangular sub-domains [23, 24], in a manner more typical of the current approach of FEM. At first FEM was mostly used as a numerical technique by mechanical engineers in order to solve boundary value problems associated with various types of partial differential equations. In 1973 a fundamental book dealing with mathematical aspects of FEM was published [25]. Since then, FEM has been gradually reinforcing its mathematical foundations gaining its current strength as a tool used for numerical modelling of physical phenomena in a wide range of engineering disciplines.

However, the method had to wait until the 1960 and 1970s, when it achieved its current, great level of interest among engineers and researchers all around the world thanks to the works of such pioneers of FEM as: John Hadji Argyris (1913–2004) [26–28], a Greek born engineer, academic and professor of aerospace engineering at the University of Stuttgart; Ray William Clough (1920–2016) [29–31], an American engineer, academic and professor of structural engineering at the University of California, Berkeley; Olgierd Cecil Zienkiewicz (1921–2009) [32–34], a British engineer and academic of Polish descent, professor at Swansea University; Philippe Gaston Ciarlet (1938–present) [35–37], a French mathematician, professor at Pierre and Marie Curie University in Paris as well as Richard Hugo Gallagher (1927–1997) [38–40], an American engineer and academic, a professor of civil engineering at Cornell University, to name only a few.

Nowadays, FEM is very well-established as a numerical tool as well as a mathematical computational method, which is still improving its capabilities and efficiency. A strong proof of this is perhaps the total number of scientific and research papers published every year, which directly refer to FEM in their titles. Figure 1.6 suggest that not only is the total number of papers published every year vast, but that this number is constantly growing. Despite the fact that the results presented in Fig. 1.6 only concern the Web of Science database, which is one out of many similar databases providing this kind of information, it should be emphasised that the expected number of papers, which will be published within the years 2021–2025 may far exceed 8,000, which is more than 1,600 papers per year. At the same time the total number of papers related to wave propagation problems, so relevant to this monograph, also stays on a high level and within the same years 2021–2025 should reach 5,000, which is 1,000 papers per year.

The growing popularity of FEM is no coincidence. The strength of the method comes from its constant theoretical development, behind which many names of great scientists and researchers can be found. Among many such names, the following may be mentioned: Oden, Babuška, Doyle, Gopa-lakrishnan or Patera.

Ivo Milan Babuška (1926–present) [41–43] is a Czech born, American mathematician, well-known for his studies of FEM as well as the error estimation associated with this numerical technique. John Tinsley Oden (1936–present) [44–46], is an American mathematician and academic, whose works in the field of FEM not only concern problems related to error estimation, but also non-linear mechanics and computation mechanics in general. James Francis Doyle (1951–present) [47–49] is an Irish born, American mechanical engineer and academic, and an expert in the field of computational mechanics. He is one of the fathers of the Frequency-domain



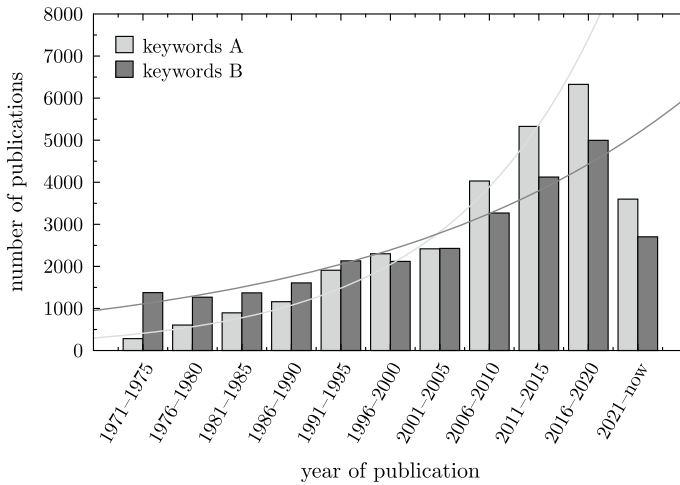


**Fig. 1.6** Number of publications published according to the Web of Science database related to two different topic search keywords: A—*finite* and *element* and *method*, B—*wave* and *propagation*

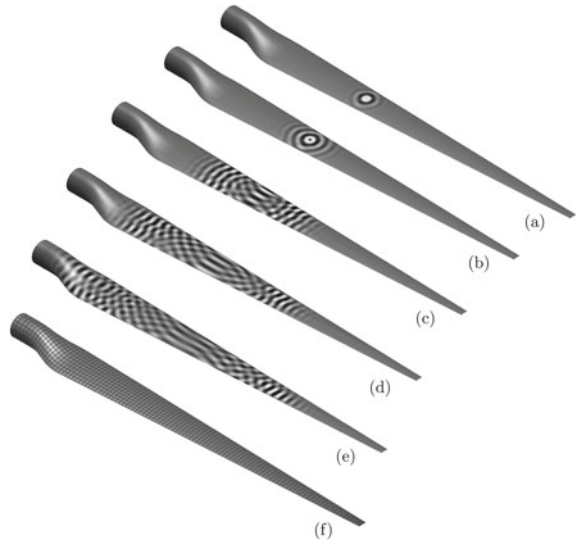
Spectral Finite Element Method (FD-SFEM), an extremely efficient and powerful FEM clone, which is based on the application of the fast Fourier transform (FFT) together with analytical shape functions to built finite elements. An adopter of the idea of FD-SFEM and its further development is Srinivasan Gopalakrishnan (1960–present) [49–51], an Indian aerospace engineer and academic. Another clone of FEM is the Time-domain Spectral Finite Element Method (TD-SFEM), which has been originally proposed and developed by Anthony Tyr Patera (1959–present) [52–54] an American mathematician, academic and professor of mechanical and computational engineering. This specialised variant of FEM, based on the application of special, orthogonal approximation polynomials of higher orders in comparison with the classical FEM, is a particularity efficient computational tool in solving fluid-mechanics problems as well as wave propagation problems—see Fig. 1.7.

However, the popularity of FEM also results from its general availability as an easy-to-use computational tool, which is offered to and used worldwide by engineers, scientists and researchers. This is mostly thanks to many FEM software packages guiding their users through all required steps of FEM analysis including pre- and post-processing of all resulting computational data.

With no doubt NASTRAN [55] (from NASA<sup>1</sup> STRucture ANalysis) developed in late 1960s, thanks to the financial support of the US government, was one of the first FEM packages used to help engineers in complex structural dynamic analysis. Its evolution over the following years changed its original purpose to a multi-physics

<sup>1</sup> NASA, National Aeronautics and Space Administration—an independent agency of the US Federal Government established in 1958, which is responsible for American civilian space programmes, aeronautics and aerospace research. NASA is the successor of NACA, the National Advisory Committee for Aeronautics, founded in 1915.

**Fig. 1.7** Patterns of elastic waves propagating in a laminated wind turbine rotor blade in consecutive moments in time: **a** 112.5  $\mu\text{s}$ , **b** 187.5  $\mu\text{s}$ , **c** 375.0  $\mu\text{s}$ , **d** 562.5  $\mu\text{s}$ , **e** 750.0  $\mu\text{s}$  and **f** the mesh of SFEs. Results of numerical computations by TD-SFEM



computational tool that allows engineers to carry on structural analysis computations of any type. Since that time its source code has been integrated into many different FEM software packages that are available, including such ones as: MSC<sup>2</sup> Software (MSC NASTRAN), NEi<sup>3</sup> Software (NEi NASTRAN) or Siemens PLM Software (NX NASTRAN).

On the same list of early FEM software packages available nowadays is ANSYS [56] (from ANalysis SYStems). ANSYS was originally developed in 1970 by John Arthur Swanson (1940–present), founder of Swanson Analysis Systems Inc. Swanson is an American engineer and entrepreneur who, according to many experts in computational methods, is regarded as a pioneer in the application of FEM in numerous fields of engineering. Since its début ANSYS has been gradually taking over the market of FEM software packages and nowadays the company is one of the biggest producer of computer simulation engineering software in the world. It is the holder of such brand names as FLUENT, ICEM CFD,<sup>4</sup> Reaction Design and many more.

Finite element analysis software ABAQUS [57] (probably derived from the word *abacus*) was originated in 1978 as a computational product based on the application of FEM. It was developed by the team of three scientists Dr Hugh David Hibbitt (1944–present), Dr Bengt Karlsson (1944–present) and dr Paul Sorensen (1959–present), who established Hibbitt, Karlsson and Sorensen, Inc. that later on changed its name

<sup>2</sup> MSC—a software company formed in 1963 by dr Richard MacNeal (1924–2018) and Robert Schwendler (1930–1979) under the name of MacNeal-Swendler Corporation, which specialises in FEM simulation.

<sup>3</sup> NEi—a company that develops engineering FEM software, started in 1991 as Noran Engineering Inc.

<sup>4</sup> CFD—computational fluid dynamics.

to ABAQUS Inc. Since that time ABAQUS has established a firm position in the market of computational tools amongst engineers and researchers all over the world. ABAQUS offers a number of core products addressed to structural engineers, especially those seeking solutions to linear and non-linear structural dynamics problems, as well as problems of computational fluid dynamics and also electromagnetism. ABAQUS remains a highly regarded tool for its multi-physics computational capabilities including various problems of coupled fields, for example acoustic-structural, thermo- and electromechanical, and more.

In 1986 a company was founded by Klass-Jürgen Bathe (1943–present) under the name of ADINA [58] R&D Inc. It is the producer and developer of a FEM computational tool, called ADINA (from **A**utomatic **D**ynamic **I**ncremental **N**on-linear **A**nalysis), which is addressed to academics as well as industry. In a similar way to other FEM commercial packages ADINA offers a complex computational environment to solve problems of fluid dynamics, heat transfer, electromagnetism and more, but primarily ADINA is highly regarded as a numerical computational tool for structural analysis, especially its non-linear analysis capabilities. As a result of this its non-linear solver is also employed by other FEM packages, such as NASTRAN, for example.

In the same year 1986 COMSOL [59] (probably from **C**OMputer **S**OLution) was founded in Sweden, at the Royal Institute of Technology in Stockholm, by Svante Littmarck (1954–present) and Farhad Saeidi (1962–present). Since the time of its emergence COMSOL FEM software has developed its reputation as a multi-platform and multi-physics computational tool offering scientists and researchers an integrated environment to carry on numerical computations in the case of electrical, mechanical and chemical engineering problems as well as fluid dynamics.

It should be emphasised at this point that the list of FEM software that is available nowadays is much longer and the names already mentioned are meant to represent only historical beginnings of FEM software development. The rapid development of numerical computation techniques together with a tremendous increase in the computational power of modern computers is directly responsible for the boom that can be observed in the field of numerical computational tools available to both academia and industry. Another interesting aspect of it comes from the fact that now an increasing number of such computational tools is made available to scientists and researchers as free, very often customised and optimised, computational tools. It is worth mentioning here such FEM packages as: Z88, Code\_Aster, Elmer, CalculiX or SimScale.

Z88 [60] is a free FEM software package, which was developed in 1985 at the University of Bayreuth, in Germany, by a team led by Frank Rieg (1955–present), who is a German academic and professor of mechanical engineering at the same university. Since its development Z88 has been adopted by many universities and small-sized enterprises as a tool offering a three-dimensional analysis of structural problems as well as topology optimisation.

Code\_Aster [61] (from **A**nalyses des **S**tructures et **T**hermomécanique pour des **É**tudes et des **R**echerches in French, which can be translated to Structural and Thermomechanical Analysis for Study and Research in English) appeared in 1989 as a

response to the demand of the French Department of Energy seeking a computational tool, which could allow for structural and thermal analysis of nuclear facilities in France. Since that time the program is maintained and developed to serve as a numerical solver for both academics and engineers. Code\_Aster is freely distributed as open-source FEM software together with Salomé [62], which is a generic software platform for pre- and post-processing.

The origins of Elmer [63] date back to 1995. This FEM software package was developed under support of the Finnish Funding Agency for Technology and Innovation, named Tekes, with help from Finnish universities, research laboratories and industry. Its development was a part of a national CFD technology programme. Nowadays Elmer is a free and open-source FEM-based computational tool for multi-physics problems including fluid and structural mechanics, electromagnetism and acoustics.

CalculiX [64], as open-source and free FEM software, emerged in 1998. Since that time it has been developed by its authors Dr Guido Dhondt (1961–present), who is responsible for the development of the solver, as well as Klaus Wittig (1961–present), who is the author of the pre- and post-processing software. It is interesting to note that CalculiX is compatible, in terms of input data, with a number of commercial FEM software packages such as: NASTRAN, ANSYS or ABAQUS. Additionally, CalculiX offers its users generation of input data for other open-source solvers.

Another free FEM software package is SimScale [65]. It is interesting to note that SimScale is a fully web-based FEM solution for computer aided engineering (CAE) available as a free tool for non-commercial use. It is well integrated with another web-based solution for computer aided design (CAD) named Onshape [66]. Both of them, integrated together, represent a powerful cloud-based computation tool for scientists and engineers employing FEM for solving scientific and/or engineering problems from various fields.

It should be mentioned here once more that the constant development of FEM, as well as many similar numerical techniques based of FEM, comes from the fact that the number of software packages for more general purposes or very specialised ones, changes very rapidly due to the constant demand of engineers and academia. Many specialised and customised solutions are reported in the available literature devoted to the subject of FEM. What is more interesting, many such solutions are successfully adopted by commercial FEM software developers, which can be clearly seen over all these years that have passed since the beginning of FEM.

## References

1. F. V. Hunt. *Origins in acoustics: The science of sound from antiquity to the age of Newton*. Yale University Press, New Haven and London, 1978.
2. A. Kinsella. *Finding nature at sea during NASA's S-MODE field campaign*. <https://blogs.nasa.gov/earthexpeditions/2022/11/03/finding-nature-at-sea-during-nasas-s-mode-field-campaign>, 2022. Visited on 09/12/2023.

3. MISR Team NASA/GSFC/LaRC/JPL. *Gravity waves ripple over marine Stratocumulus clouds*. <https://earthobservatory.nasa.gov/images/4117/gravity-waves-ripple-over-marine-stratocumulus-clouds>, 2003. Visited on 09/12/2023.
4. NASA Earth Observatory. *Volcanic shockwave captured by ISS imagery*. <https://www.universetoday.com/33431/volcanic-shockwave-captured-by-iss-imagery>, 2009. Visited on 09/12/2023.
5. NASA/JPL-Caltech/Space Science Institute. *Staggering structure*. <https://science.nasa.gov/resource/staggering-structure>, 2017. Visited on 09/12/2023.
6. T. F. Glick, S. Livesey, and F. Wallis. *Medieval science, technology, and medicine: An encyclopedia*. Routledge, Taylor & Francis Group, London, 2005.
7. R. B. Lindsay. *Acoustics: Historical and philosophical development*. Dowden, Hutchinson & Ross, Stroudsburg, 1973.
8. R. B. Lindsay. The story of acoustics. *The Journal of the Acoustical Society of America*, 39:629–644, 1966.
9. J. W. S. Rayleigh. *The theory of sound*. Dover Publications, Inc., New York, 1945.
10. J. Tyndall. *Sound. A Course of eight lectures*. Greenwood Press, New York, 1969.
11. H. L. F. Helmholtz. *On sensations of tone*. Greenwood Press, New York, 1862.
12. D. L. Pochhammer. *Gleichgewicht des elastischen Stabes*. Universitäts-Buchhandlung, Kiel, 1879.
13. D. L. Pochhammer. Über die Fortpflanzung Geschwindigkeiten kleiner Schwingungen in einem unbegrenzten isotropen Kreiszyylinder. *Journal für die Reine und Angewandte Mathematik*, 81:324–336, 1876.
14. C. Chree. Longitudinal vibrations of a circular bar. *Quarterly Journal of Mathematics*, 21:287–288, 1886.
15. H. Lamb. On waves in an elastic plate. *Proceedings of the Royal Society A*, 93:114–128, 1917.
16. H. Lamb. *The dynamical theory of sound*. Edward Arnold, London, 1910.
17. E. Reissner. The effect of transverse shear deformation on the bending of elastic plates. *ASME Journal of Applied Mechanics*, 12:68–77, 1945.
18. R. D. Mindlin. Influence of rotatory inertia and shear on flexural motions of isotropic, elastic plates. *ASME Journal of Applied Mechanics*, 18:31–38, 1951.
19. R. D. Mindlin and G. Herrmann. A one dimensional theory of compressional waves in an elastic rod. *Proceedings of the First U.S. National Congress on Applied Mechanics, Chicago, Illinois*, 1:187–191, 11-16 June 1951.
20. J. N. Reddy. A simple higher-order theory for laminated composite plates. *ASME Journal of Applied Mechanics*, 51:745–752, 1984.
21. A. Hrennikoff. Solution of problems of elasticity by the framework method. *Journal of Applied Mechanics*, 8:169–175, 1941.
22. A. Hrennikoff. Framework method and its technique for solving plane stress problems. *International Association for Bridge and Structural Engineering Publications*, 9:217–248, 1949.
23. R. Courant. *On a method for the solution of boundary-value problems*. in: Theodore von Kármán Anniversary Volume. University of Michigan, 1941.
24. R. Courant. Variational methods for the solution of problems of equilibrium and vibrations. *Bulletin of the American Mathematical Society*, 49:1–23, 1943.
25. G. Strang and G. J. Fix. *An analysis of the finite element method*. Prentice Hall, New Jersey, 1973.
26. J. H. Argyris and D. W. Scharpf. Finite elements in time and space. *Nuclear Engineering and Design*, 10:456–464, 1969.
27. J. H. Argyris, P. C. Dunne, and T. Angelopoulos. Non-linear oscillations using the finite element technique. *Computer Methods in Applied Mechanics and Engineering*, 2:203–250, 1973.
28. J. H. Argyris, H. Balmer, J. S. Doltsinis, P. C. Dunne, M. Haase, M. Kleiber, G. A. Melejannakis, H. P. Mlejnek, M. Müller, and D. W. Scharpf. Finite element method – natural approach. *Computer Methods in Applied Mechanics and Engineering*, 17:1–106, 1979.
29. G. Cantin and R. W. Clough. A curved cylindrical shell finite element. *AIAA Journal*, 6:1057–1062, 1968.

30. S. F. Pawsey and R. W. Clough. Improved numerical integration of thick shell finite elements. *International Journal for Numerical Methods in Engineering*, 3:575–586, 1971.
31. G. A. Fonder and R. W. Clough. Explicit addition of rigid body motions in curved finite elements. *AIAA Journal*, 11:305–317, 1973.
32. O. C. Zienkiewicz, D. W. Kelly, and P. Bettess. Reduced integration technique in general analysis of plates and shells. *International Journal for Numerical Methods in Engineering*, 3:275–290, 1971.
33. I. Christie, D. F. Griffiths, A. R. Mitchell, and O. C. Zienkiewicz. Finite element methods for second order differential equations with significant first derivatives. *International Journal for Numerical Methods in Engineering*, 10:1389–1396, 1976.
34. O. C. Zienkiewicz, D. W. Kelly, and P. Bettess. Coupling of finite element method and boundary solution procedures. *International Journal for Numerical Methods in Engineering*, 11:355–375, 1977.
35. P. G. Ciarlet and C. Wagschal. Multipoint Taylor formulas and applications to the finite element method. *Numerische Mathematik*, 17:84–100, 1971.
36. P. G. Ciarlet and P. A. Raviart. General Lagrange and Hermite interpolation in  $R^n$  with applications to finite element methods. *Archive for Rational Mechanics and Analysis*, 46:178–198, 1972.
37. P. G. Ciarlet and R. Glowinski. Dual iterative techniques for solving a finite element approximation of the biharmonic equation. *Computer Methods in Applied Mathematics and Engineering*, 5:277–295, 1975.
38. R. H. Gallagher and R. H. Mallett. Efficient solution processes for finite element analysis of transient heat conduction. *Journal of Heat Transfer*, 93:257–263, 1971.
39. R. H. Gallagher. The finite element method in shell stability analysis. *Computers & Structures*, 3:543–557, 1973.
40. K. Loganathan, S. C. Chang, and R. H. Gallagher. Finite element representation and pressure stiffness in shell stability analysis. *International Journal for Numerical Methods in Engineering*, 14:1413–1420, 1979.
41. I. Babuška and M. Suri. Locking effects in the finite element approximation of elasticity problems. *Numerische Mathematik*, 62:439–463, 1992.
42. I. Babuška and M. Suri. The  $p$  and  $h$ - $p$  versions of the finite element method, basic principles and properties. *SIAM Review*, 36:578–632, 1994.
43. I. Babuška, J. R. Whiteman, and T. Strouboulis. *Finite elements: An introduction to the method of error estimation*. Oxford University Press, Oxford, 2011.
44. J. T. Oden and J. N. Reddy. *An introduction to the mathematical theory of finite elements*. Wiley, New York, 1976.
45. C. E. Baumann and J. D. Oden. A discontinuous  $hp$  finite element method for the Euler and Navier–Stokes equations. *International Journal for Numerical Methods in Fluids*, 31:79–95, 1999.
46. M. Ainsworth and J. T. Oden. *A posteriori error estimation in finite element analysis*. John Wiley & Sons, Ltd., New York, 2011.
47. J. F. Doyle. *Wave propagation in structures*. Springer-Verlag, Inc., New York, 1997.
48. S. A. Rizzi and J. F. Doyle. A spectral element approach to wave motion in layered solids. *Journal of Vibration and Acoustics*, 114:569–577, 1992.
49. S. Gopalakrishnan and J. F. Doyle. Spectral super-elements for wave-propagation in structures with local nonuniformities. *Computer Methods in Applied Mechanics and Engineering*, 121:79–90, 1995.
50. D. R. Mahapatra and S. Gopalakrishnan. A spectral finite element model for analysis of axial-flexural-shear coupled wave propagation in laminated composite beams. *Composite Structures*, 59:67–88, 2003.
51. S. Gopalakrishnan, A. Chakraborty, and D. R. Mahapatra. *Spectral finite element method: Wave propagation, diagnostics and control in anisotropic and inhomogeneous structures*. Springer-Verlag London, London, 2008.

52. A. T. Patera. A spectral element method for fluid dynamics: Laminar flow in a channel expansion. *Journal of Computational Physics*, 54:468–488, 1984.
53. K. Z. Korczyk and A. T. Patera. An isoparametric spectral element method for solution of the Navier-Stokes equations in complex-geometry. *Journal of Computational Physics*, 62:361–382, 1986.
54. Y. Maday, D. Meiron, A. T. Patera, and E. M. Ronquist. Analysis of iterative methods for the steady and unsteady Stokes problems – Application to spectral element discretizations. *SIAM Journal of Scientific Computing*, 14:310–337, 1993.
55. <http://www.mscsoftware.com>. Visited on 23/08/2019.
56. <http://www.ansys.com>. Visited on 23/08/2019.
57. <http://www.simula.com>. Visited on 23/08/2019.
58. <http://www.adina.com>. Visited on 23/08/2019.
59. <http://www.comsol.com>. Visited on 23/08/2019.
60. <http://www.en.z88.de>. Visited on 27/08/2019.
61. <http://www.code-aster.org>. Visited on 27/08/2019.
62. <http://www.salome-platform.org>. Visited on 28/08/2019.
63. <http://www.elmerfem.org>. Visited on 27/08/2019.
64. <http://www.calculix.de>. Visited on 27/08/2019.
65. <http://www.simscale.com>. Visited on 23/08/2019.
66. <http://www.onshape.com>. Visited on 23/08/2019.

# Chapter 2

## Wave Essentials



### 2.1 Wave Motion

Elastic waves or waves in elastic media have exactly the same nature when they propagate in various elements of engineering structures. Their motion can be fully characterised by the language of modern mathematics, as presented in the following sections of this chapter. However, before studying propagation of elastic waves in complex engineering structures, it is necessary to introduce some basic definitions commonly used to describe wave motion, which are very helpful to fully understand and reveal the true nature of elastic waves.

Firstly, it is helpful to clarify what in fact are waves, or what is wave motion in elastic media? It was already mentioned that waves are a kind of disturbance that can transfer energy from one point in space to another, as presented in Fig. 2.1. In the case of elastic media this transfer of energy is achieved thanks to the existence of elastic forces in these media.

The fundamental property of elastic media is that elastic forces are recoverable, or in other words, that no energy is lost during the process of elastic deformation of the media, which can be true only under an assumption of small deformations. Wave motion is associated with elastic forces acting and varying in time. These forces are directly responsible for the existence of waves, as they lead to the transfer of the resulting deformation from one point in space to another, and further on. This can be observed from the outside as the phenomenon known as propagation of elastic waves. The type of elastic deformation can be of two distinctive natures. It can have the nature of either voluminal deformation, due to compression or tension forces acting, or shape deformation, due to shear forces acting.

Particular types of elastic waves, which can propagate in various elements of engineering structures, as a results of the coupled interaction between these two fundamental wave types (voluminal and shear, as presented in Fig. 1.5), as well as the interaction of these waves with structural boundaries, give rise to new types of waves such as, for example, Love and Rayleigh waves in solids or Lamb waves in plates. These are discussed in more detail in the following sections of this book.



**Fig. 2.1** A wave pattern on the surface of water as a results of falling drops [1]



## 2.2 Wave Relations

Harmonic oscillations, as presented in Fig. 2.2, are a type of oscillation that vary sinusoidally in space  $x$  and time  $t$  with some constant frequency  $\omega$  and wave number  $k$ . They play a very important role in many fields of science. It will be shown later that their applicability extends not only to basic or simple cases, but they can be successfully used to study and investigate elastic waves of any type.

Harmonic oscillations, or harmonic waves, in a 1-D elastic medium, can be expressed mathematically in various alternative forms:

$$\begin{aligned}
 u(x, t) &= A \sin(kx - \omega t - \psi) \\
 &= A \cos(kx - \omega t - \theta) \\
 &= A_1 \cos(kx - \omega t) + A_2 \sin(kx - \omega t)
 \end{aligned} \tag{2.1}$$

where  $u(x, t)$  denotes a response of the medium being a function of space  $x$  and time  $t$ . The meaning of physical quantities associated with harmonic waves, as well as Eq. (2.1), are shown in the following list:

- $\omega$ —angular frequency in radians per second (rad/s), where  $\omega = 2\pi f$ ,
- $f$ —cyclic frequency in cycles per second or hertz (c/s, Hz), where  $f = 1/T$ ,
- $T$ —period in seconds (s),
- $k$ —wave number in radians per meter (rad/m), where  $k = 2\pi/\lambda$ ,
- $\lambda$ —wavelength in meters (m),
- $\phi$ —wave phase in radians (rad), where  $\phi = kx - \omega t$ ,
- $\psi$ —initial phase in radians (rad),
- $\theta$ —initial phase in radians (rad), where  $\theta = \psi - \pi/2$ ,
- $c_p$ —phase velocity in meters per second (m/s), where  $c_p = \omega/k$ ,

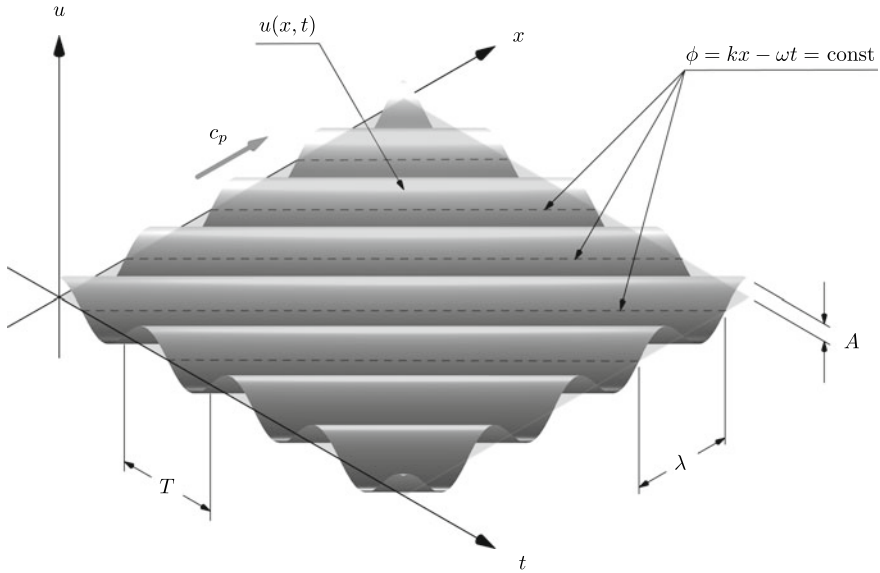


**Fig. 2.2** A harmonic wave propagating in a 1-D elastic medium

$c_g$ —group velocity in meters per second (m/s), where  $c_g = d\omega/dk$ ,

$A$ —amplitude in meters (m), where  $A = \sqrt{A_1^2 + A_2^2}$ ,

$A_1$ —amplitude in meters (m), where  $A_1 = -A \sin \psi = A \cos \theta$ ,

$A_2$ —amplitude in meters (m), where  $A_2 = A \cos \psi = A \sin \theta$ .

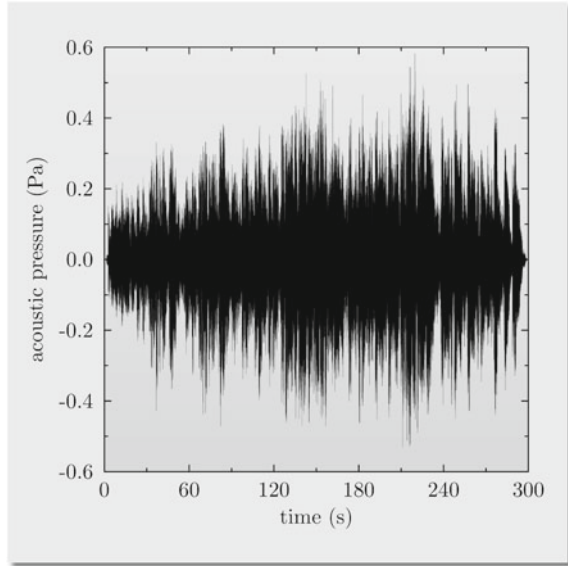
A very important feature of a harmonic wave is the speed of its propagation, which is known as the phase velocity  $c_p$ . The phase velocity  $c_p$  provides information on how fast a wave of constant angular frequency  $\omega$ , or constant wave number  $k$ , propagates in space. Such harmonic waves are also known in the literature as monochromatic waves [2].

Alternatively, it can be said that the phase velocity  $c_p$  is the rate at which the phase  $\phi$  of a harmonic wave propagates in space. This can be easily calculated by considering the phase differential  $d\phi$  as:

$$\begin{aligned}
 \phi = \text{const} &\Rightarrow kx - \omega t - \psi = \text{const} \\
 d\phi = d(kx - \omega t - \psi) &= k dx - \omega dt = 0 \\
 k dx = \omega dt &\Rightarrow \frac{dx}{dt} = \frac{\omega}{k} = c_p
 \end{aligned}
 \tag{2.2}$$

It should be said that the majority of signals propagating in nature are localised in space, travelling as wave packets, as can be seen in Fig. 2.3. This is in contrast to harmonic waves, which are represented by infinite sinusoids travelling throughout

**Fig. 2.3** An example of a sound signal, which represents a song. This signal is formed by many wave packets placed at various moments in time  $t$  along the time axis



space, and which cannot be localised. However, wave packets can be thought of as represented by or composed of many harmonic waves of various frequencies, wave numbers and amplitudes, which propagate at various phase velocities. This is thanks to the famous Fourier theorem and the superposition principle. In such a case the speed at which wave packets propagate in space can be associated with a new velocity, called the group velocity  $c_g$ , rather than the phase velocity  $c_p$  of its components, as these two velocities can be significantly different.

The concept of the group velocity  $c_g$  can be easily explained by considering two harmonic waves  $u_1(x, t)$  and  $u_2(x, t)$  of the same amplitudes, which differ slightly in their angular frequencies  $\omega_1$  and  $\omega_2$  as well as wave numbers  $k_1$  and  $k_2$ :

$$\begin{cases} u_1(x, t) = A_1 \cos(k_1 x - \omega_1 t) + A_2 \sin(k_1 x - \omega_1 t) \\ u_2(x, t) = A_1 \cos(k_2 x - \omega_2 t) + A_2 \sin(k_2 x - \omega_2 t) \end{cases} \quad (2.3)$$

where  $k_1 = \bar{k} + dk$  and  $k_2 = \bar{k} - dk$ , while  $\omega_1 = \bar{\omega} + d\omega$  and  $\omega_2 = \bar{\omega} - d\omega$ .

The sum of the waves  $u_1(x, t)$  and  $u_2(x, t)$ , after simple trigonometric manipulations, takes the following form:

$$u(x, t) = u_1(x, t) + u_2(x, t) = B_1 \cos(\bar{k}x - \bar{\omega}t) + B_2 \sin(\bar{k}x - \bar{\omega}t) \quad (2.4)$$

where now the amplitudes  $B_1$  and  $B_2$  can be expressed in the following manner:

$$B_1 = 2A_1 \cos(dk x - d\omega t), \quad B_2 = 2A_2 \cos(dk x - d\omega t) \quad (2.5)$$

Now, it can be seen from Eqs. (2.4) and (2.5) that the resulting sum of the two harmonic waves  $u_1(x, t)$  and  $u_2(x, t)$  is a new harmonic wave  $u(x, t)$ . This wave can be characterised by the average carrier frequency  $\bar{\omega}$  and the average wave number  $\bar{k}$ , the amplitude of which is modulated rather than being constant. The phase velocity of this modulation, enveloping the carrier wave, can be evaluated as before:

$$\begin{aligned} \phi = \text{const} &\Rightarrow dkx - d\omega t = \text{const} \\ &\downarrow \\ d\phi = d(dkx - d\omega t) &= dk dx - d\omega dt = 0 \\ &\downarrow \\ dk dx = d\omega dt &\Rightarrow \frac{dx}{dt} = \frac{d\omega}{dk} = c_g \end{aligned} \quad (2.6)$$

which in fact is the speed of a group of internal waves enveloped within one modulation cycle. This group travels with the group velocity  $c_g$ .

It can be expected that the difference between the values of the phase velocity  $c_p$  and the group velocity  $c_g$  can lead to interesting behaviour. Such behaviour is commonly known as dispersion and is a direct consequence of different values of the phase velocities  $c_p$  of particular harmonic components of a wave packet. This is explained in detail in Sect. 2.5.

In general, the phase velocity  $c_p$  and the group velocity  $c_g$  can be certain functions of the wave number  $k$  or the angular frequency  $\omega$ . Therefore it can be formally written that  $c_p = c_p(k)$  and  $c_p = c_p(\omega)$ , as well as  $c_g = c_g(k)$  and  $c_g = c_g(\omega)$ .

Now, it is worth looking at a direct link between these two velocities, which can be expressed in the flowing manner:

$$c_g = \frac{d\omega}{dk} = \frac{d}{dk}(kc_p) = c_p + k \frac{dc_p}{dk} \quad (2.7)$$

or alternatively as<sup>1</sup>:

$$c_g = \frac{d\omega}{dk} = \frac{d\omega}{d\left(\frac{\omega}{c_p}\right)} = \frac{d\omega}{\frac{d\omega}{c_p} - \omega \frac{dc_p}{c_p^2}} = \frac{c_p^2}{c_p - \omega \frac{dc_p}{d\omega}} \quad (2.8)$$

which relations will come in useful in the following sections of this book. It should be said here that with no difficulty the formulae given by Eqs. (2.7) and (2.8) can be expressed as functions of the wavelength  $\lambda$  or the cyclic frequency  $f$ , by the use of the relations presented at the beginning of this section.

---

<sup>1</sup> It may be useful to note from Eq. (2.8) that when  $dc_p/d\omega \rightarrow 0$  then  $c_g \rightarrow c_p$ . On the other hand when  $dc_p/d\omega \rightarrow \infty$  then  $c_g \rightarrow 0$ .

## 2.3 Simple Wave Equations

### 2.3.1 1-D Elastic Rod

Investigation of wave propagation in elastic media can be started from a simple case of a stress pulse propagating in a 1-D isotropic elastic rod, as presented in Fig. 2.4.

The resulting wave equation can be straightforwardly obtained by the application of d'Alembert's principle. It should be noticed that the axial force  $N(x, t)$  acting within the rod, varying in time  $t$  and space  $x$ , is responsible for local deformation of the rod material. This deformation can be expressed in terms of the strain  $\epsilon_{xx}(x, t)$ , which links together the local displacement  $u(x, t)$  with the local strain  $\epsilon_{xx}(x, t)$  and the stress  $\sigma_{xx}(x, t)$ , by the very well-known Hooke's law. It can be written that:

$$\sigma_{xx}(x, t) = E\epsilon_{xx}(x, t), \quad \epsilon_{xx}(x, t) = \frac{\partial u(x, t)}{\partial x} \quad (2.9)$$

where  $E$  is Young's modulus of the rod material.

The axial force  $N(x, t)$  can be expressed in terms of the local stress  $\sigma_{xx}(x, t)$ , or in terms of the local displacement  $u(x, t)$  by the application of Eq. (2.9):

$$N(x, t) = \int_S \sigma_{xx}(x, t) dS = S\sigma_{xx}(x, t) = SE \frac{\partial u(x, t)}{\partial x} \quad (2.10)$$

where  $S$  is the cross-sectional area of the rod.

The local nature of rod deformation allows one to expand locally the axial force  $N(x, t)$  into a Taylor series as:

$$N(x + dx, t) = N(x, t) + \frac{\partial N(x, t)}{\partial x} dx + \frac{1}{2} \frac{\partial^2 N(x, t)}{\partial x^2} dx^2 + \dots \quad (2.11)$$

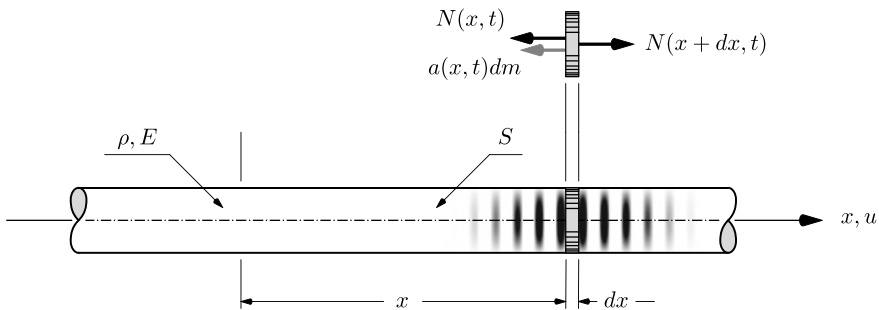


Fig. 2.4 A concept of a 1-D isotropic elastic rod

Considering a thin section of the rod  $dx$ , as presented in Fig. 2.4, it can be found that the rod longitudinal motion is driven by the axial forces acting on the right and left-hand side of the section  $dx$ . Application of d'Alembert's principle leads to the following equation:

$$N(x + dx, t) - N(x, t) = a(x, t)dm \quad (2.12)$$

where  $dm$  is the mass of the section  $dx$ , while  $a(x, t)$  represents its axial acceleration. The mass  $dm$  of the section  $dx$  can be expressed in terms of its material density  $\rho$  and volume  $V$ , which is equal to  $\rho S dx$ .

Knowing that the axial acceleration  $a(x, t)$  is equal to the second time derivative of the axial displacement  $u(x, t)$  with respect to time  $t$ , and that higher-order terms of the Taylor series given by Eq. (2.11) can be neglected due to local nature of the rod deformation  $\epsilon_{xx}(x, t)$ , it can be written that:

$$\frac{\partial N(x, t)}{\partial x} dx = \frac{\partial}{\partial x} \left[ SE \frac{\partial u(x, t)}{\partial x} \right] dx = \rho S dx \frac{\partial^2 u(x, t)}{\partial t^2} \quad (2.13)$$

This equation can be further simplified, assuming the independence of the rod cross-sectional area  $S$  and Young's modulus  $E$  of the spatial coordinate  $x$ , to form the wave equation of the following form:

$$SE \frac{\partial^2 u(x, t)}{\partial x^2} = \rho S \frac{\partial^2 u(x, t)}{\partial t^2} \quad (2.14)$$

Alternatively, the wave equation can be presented in its most well-known form as:

$$\frac{\partial^2 u(x, t)}{\partial x^2} = \frac{1}{\beta^2} \frac{\partial^2 u(x, t)}{\partial t^2}, \quad \beta = \sqrt{\frac{E}{\rho}} \quad (2.15)$$

where  $\beta$  is a certain constant expressed in meters per second (m/s).

It should be emphasised here that its value turns out to be equal to the phase velocity  $c_p$  of longitudinal waves, which can propagate in the rod:

$$\beta = c_p = \sqrt{\frac{E}{\rho}} \quad (2.16)$$

It was found by Jean le Rond d'Alembert that a general solution to the 1-D wave equation (2.15) can be obtained by a simple substitution:

$$\begin{cases} \xi(x, t) = x - c_p t \\ \eta(x, t) = x + c_p t \end{cases} \quad (2.17)$$

which reduces the wave equation (2.15) to:

$$\frac{\partial^2 u(\xi, \eta)}{\partial \xi \partial \eta} = 0 \quad (2.18)$$

This equation has a general solution in the following form:

$$u(\xi, \eta) = F(\xi) + G(\eta) \quad \text{or} \quad u(x, t) = F(x - c_p t) + G(x + c_p t) \quad (2.19)$$

where arbitrary functions  $F(x - c_p t)$  and  $G(x + c_p t)$  represent two waves travelling within the rod in opposite directions.

In the case of an initial value problem, the wave equation (2.15) must be supplemented by certain initial and boundary conditions. These conditions restrict the arbitrariness of the functions  $F(x - c_p t)$  and  $G(x + c_p t)$  and can be presented as:

$$\begin{cases} u(x, 0) = f(x) \\ \frac{\partial u(x, 0)}{\partial t} = g(x) \end{cases} \quad (2.20)$$

where functions  $f(x)$  and  $g(x)$  describe initial displacements and initial velocities within the rod, respectively.

A solution to the initial value problem defined in this way was also studied and found by d'Alembert. It can be presented in the following manner:

$$u(x, t) = \frac{f(x - c_p t) + f(x + c_p t)}{2} + \frac{1}{2c_p} \int_{x - c_p t}^{x + c_p t} g(\tau) d\tau \quad (2.21)$$

It can be clearly seen that in the case of the function  $g(x)$  being equal to zero, the solution given by Eq. (2.21) simplifies to:

$$u(x, t) = \frac{f(x - c_p t) + f(x + c_p t)}{2} \quad (2.22)$$

This allows one to state that the initial displacement, described by the function  $f(x)$ , travels within the rod in opposite directions as two independent wave pulses. Their amplitudes are reduced by half during their propagation, as is shown in Fig. 2.5.

Additionally, it can be clearly seen from Fig. 2.5 that the initial axial displacement  $u(x, 0) = f(x)$  travels within the rod with the phase velocity  $c_p$  as two independent longitudinal waves, exactly as prescribed by Eq. (2.22). Their locations within the rod at particular moments in time  $t$  are precisely described by two sets of characteristics:

$$\begin{cases} x - c_p t - \frac{1}{2} \Delta x = 0 \\ x - c_p t + \frac{1}{2} \Delta x = 0 \end{cases} \quad (2.23)$$

$$\begin{cases} x + c_p t - \frac{1}{2} \Delta x = 0 \\ x + c_p t + \frac{1}{2} \Delta x = 0 \end{cases} \quad (2.24)$$

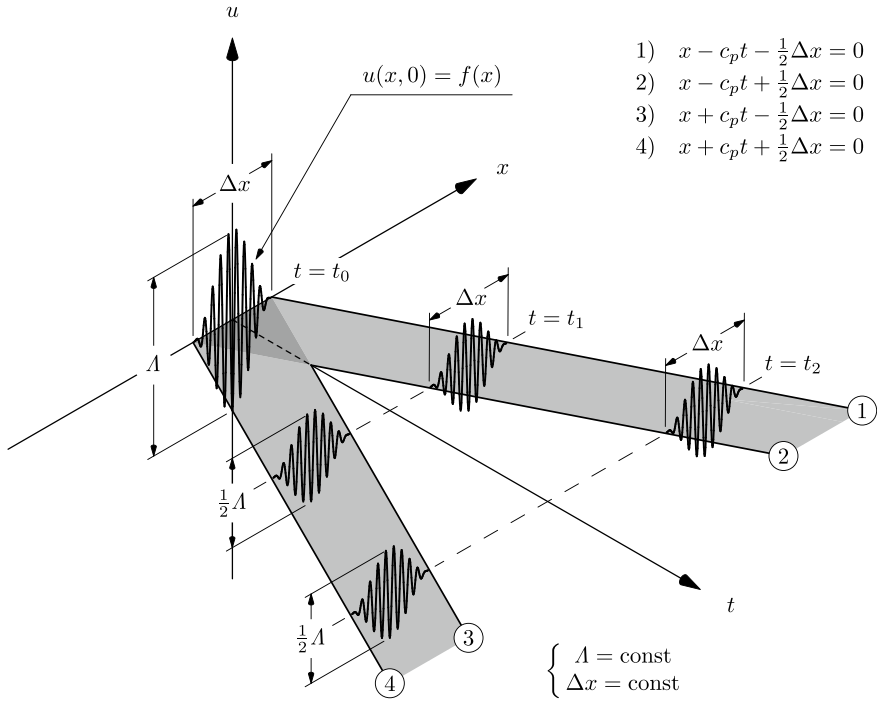


**Fig. 2.5** Propagation of an initial condition in the form of an axial displacement pulse in a 1-D isotropic elastic rod

where  $\Delta x$  denotes the spatial width of the initial displacement in Fig. 2.5. The two sets of characteristics determine the position of the waves travelling in the direction of the  $x$  axis, in the case of Eq. (2.23), and in the opposite direction, in the case of Eq. (2.24).

Moreover, it should be emphasised here that the resulting wave equation (2.15) is a linear partial differential equation and as such it has a very well-known and profound property of superposition. This property allows one to search for a solution to this equation in the form of combined solutions to individual initial value problems instead of a solution to a combined initial value problem.

Alternatively, it can be said that the analysis of wave propagation, determined by the wave equation (2.15), can be carried out by breaking up the initial wave into a number of linearly dependent components. For example, this takes place in the case of a Fourier series introduced by Jean-Baptiste Joseph Fourier, which allows one to represent a given periodic function as a combination of sinusoidal functions of various amplitudes and frequencies.



### 2.3.2 1-D Elastic Beam

In the case of wave propagation in a 1-D isotropic elastic beam, as presented in Fig. 2.6, a stress pulse propagating within the beam also results from the local deformation of the beam material.

However, in the case of flexural waves propagating within the beam, their presence is the effect of the shear force  $Q(x, t)$  and the bending moment acting within the beam  $M(x, t)$ , which varies in time  $t$  and space  $x$ . Once again the use of very well-known Hooke’s law allows one to write the relations between the local strain  $\epsilon_{xx}(x, z, t)$  and the stress  $\sigma_{xx}(x, z, t)$  in the following form:

$$\sigma_{xx}(x, z, t) = E\epsilon_{xx}(x, z, t), \quad \epsilon_{xx}(x, z, t) = -z \frac{\partial^2 w(x, t)}{\partial x^2} \tag{2.25}$$

Additionally, the bending moment  $M(x, t)$  can be obtained in a straightforward manner as a function of the local stress  $\sigma_{xx}(x, z, t)$ :

$$M(x, t) = \int_S z\sigma_{xx}(x, z, t)dS \tag{2.26}$$

which leads, after substitution of Eq. (2.25) to Eq. (2.26), to a well-known relationship:

$$M(x, t) = -E \frac{\partial^2 w(x, t)}{\partial x^2} \int_S z^2 dS = -EI \frac{\partial^2 w(x, t)}{\partial x^2} \tag{2.27}$$

where  $I$  is the the area moment of inertia of the beam cross-section  $S$ .

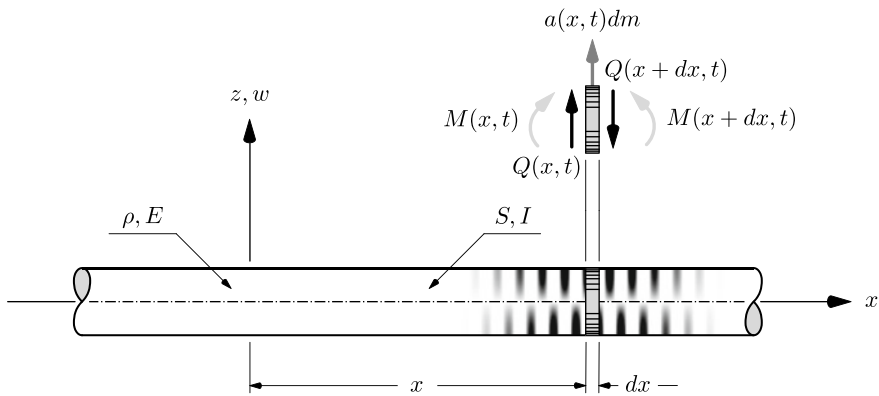


Fig. 2.6 A concept of a 1-D isotropic elastic beam

In a similar manner as in the case of the 1-D elastic rod, it can be stated that the beam deformation allows one to expand locally the shear force  $Q(x, t)$  into a Taylor series as:

$$Q(x + dx, t) = Q(x, t) + \frac{\partial Q(x, t)}{\partial x} dx + \frac{1}{2} \frac{\partial^2 Q(x, t)}{\partial x^2} dx^2 + \dots \quad (2.28)$$

Once again, by considering a thin section of the beam  $dx$ , as presented in Fig. 2.6, it can be found that the beam transverse motion is driven by the shear forces acting on the right and left-hand side of the section  $dx$ . A relationship binding together the shear force  $Q(x, t)$  with the bending moment  $M$  comes from the theory of elasticity as:

$$Q(x, t) = \frac{\partial M(x, t)}{\partial x} \quad (2.29)$$

Application of d'Alembert's principle to the section of the beam  $dx$  leads to the following equation:

$$Q(x + dx, t) - Q(x, t) = a(x, t) dm \quad (2.30)$$

where  $dm$  is the mass of the section  $dx$  of the beam, while now  $a(x, t)$  represents its transverse acceleration. Again, the mass  $dm$  of the section  $dx$  can be expressed in terms of its material density  $\rho$  and its volume  $V$ , which is equal to  $\rho S dx$ , exactly as in the case of the rod.

Now, expressing the transverse acceleration  $a(x, t)$  as equal to the second derivative of the transverse displacement  $w(x, t)$  with respect to time  $t$  leads to:

$$\frac{\partial Q(x, t)}{\partial x} dx = -\frac{\partial^2}{\partial x^2} \left[ EI \frac{\partial^2 w(x, t)}{\partial x^2} \right] = \rho S dx \frac{\partial^2 w(x, t)}{\partial t^2} \quad (2.31)$$

after neglecting higher-order terms of the Taylor series from Eq. (2.28), subsequent substitution of Eq. (2.28) into Eq. (2.30), and the use of Eq. (2.29).

Yet again, the resulting wave equation can be further simplified. This can be done under the assumption of the independence of the beam cross-sectional area  $S$  and the area moment of inertia  $I$ , as well as Young's modulus  $E$ , of the spatial coordinate  $x$ . As a result the wave equation for propagation of flexural waves in the beam can be written in the following form:

$$-\frac{\partial^4 w(x, t)}{\partial x^4} = \frac{1}{\beta^4} \frac{\partial^2 w(x, t)}{\partial t^2}, \quad \beta = \sqrt[4]{\frac{EI}{\rho S}} \quad (2.32)$$

where now  $\beta$  is a different constant, which cannot represent the speed of flexural waves in the beam. It should be noted that  $\beta$  is expressed in metres per square root of a second ( $\text{m}/\sqrt{\text{s}}$ ) rather than in meters per second ( $\text{m/s}$ ).

## 2.4 Fourier Method

A very effective and simple analytical method used to study and analyse wave equations is the Fourier method, also known as the method of separation of variables. In this method an unknown function  $u(x, t)$  of space  $x$  and time  $t$  variables is assumed to have a representation, which can be expressed as a product to two independent functions, a space function  $X(x)$  and a time function  $T(t)$ :

$$u(x, t) = X(x)T(t) \quad (2.33)$$

In the case of the 1-D isotropic elastic rod, the form of Eq. (2.33) allows on to replace the partial derivatives in the wave equation (2.15) by ordinary derivatives, according to the following formulae:

$$u(x, t) = X(x)T(t) \rightarrow \begin{cases} \frac{\partial^2 u(x, t)}{\partial x^2} = T(t) \frac{d^2 X(x)}{dx^2} \\ \frac{\partial^2 u(x, t)}{\partial t^2} = X(x) \frac{d^2 T(t)}{dt^2} \end{cases} \quad (2.34)$$

In this manner a simple substitution of Eq. (2.34) into the wave equation (2.15) leads, after necessary rearrangements, to a set of new ordinary differential equations:

$$\frac{1}{X(x)} \frac{d^2 X(x)}{dx^2} = \frac{1}{\beta^2 T(t)} \frac{d^2 T(t)}{dt^2} \quad (2.35)$$

Since the left-hand side of Eq. (2.35) depends only on the spatial coordinate  $x$ , and the right-hand side only on time  $t$ , this equation can be satisfied only if its both sides are equal to one common constant, which can be conveniently assumed to equal to  $-k^2$ . In this way two separated ordinary equations are formed:

$$\frac{d^2 X(x)}{dx^2} + k^2 X(x) = 0, \quad \frac{d^2 T(t)}{dt^2} + \omega^2 T(t) = 0 \quad (2.36)$$

where  $\omega = k\beta$  denotes the angular frequency and  $k$  is the wave number.

These ordinary differential equations have well-known solutions:

$$X(x) = A_1 \cos kx + A_2 \sin kx, \quad T(t) = A_3 \cos \omega t + A_4 \sin \omega t \quad (2.37)$$

where  $A_1, A_2, A_3$  and  $A_4$  are real constants, which values depend on initial and boundary conditions.

Based on the obtained solutions to the ordinary differential equations given by Eq. (2.37) the unknown function  $u(x, t)$  can be expressed as follows:

$$\begin{aligned} u(x, t) &= X(x)T(t) \\ &= (A_1 \cos kx + A_2 \sin kx)(A_3 \cos \omega t + A_4 \sin \omega t) \end{aligned} \quad (2.38)$$

or alternatively, after simple mathematical manipulations and trigonometric reduction, in a form which clearly indicates particular waves, being solutions to the wave equation (2.15):

$$u(x, t) = B_1 \cos(kx - \omega t) + B_2 \sin(kx - \omega t) + B_3 \cos(kx + \omega t) + B_4 \sin(kx + \omega t) \quad (2.39)$$

where new real constants  $B_1$ ,  $B_2$ ,  $B_3$  and  $B_4$  are introduced, and which result from the rearrangement of appropriate terms in Eq. (2.38).

At this point it is convenient to note that the real solution given by Eq. (2.39) can be expressed by the complex exponential function using Euler's formula:

$$\begin{aligned} \mathcal{A} \cos \phi + \mathcal{B} \sin \phi &= \text{Re}[(\mathcal{A} + i\mathcal{B}) \cos \phi - i(\mathcal{A} + i\mathcal{B}) \sin \phi] \\ &= \text{Re}[(\mathcal{A} + i\mathcal{B})(\cos \phi - i \sin \phi)] \\ &= \text{Re}[(\mathcal{A} + i\mathcal{B})e^{-i\phi}] \\ &= \text{Re}[\mathcal{C}e^{-i\phi}] \end{aligned} \quad (2.40)$$

or alternatively:

$$\begin{aligned} \mathcal{A} \cos \phi + \mathcal{B} \sin \phi &= \text{Re}[(\mathcal{A} - i\mathcal{B}) \cos \phi + i(\mathcal{A} - i\mathcal{B}) \sin \phi] \\ &= \text{Re}[(\mathcal{A} - i\mathcal{B})(\cos \phi + i \sin \phi)] \\ &= \text{Re}[(\mathcal{A} - i\mathcal{B})e^{i\phi}] \\ &= \text{Re}[\bar{\mathcal{C}}e^{i\phi}] \end{aligned} \quad (2.41)$$

where  $i$  is the imaginary unit, i.e.  $i^2 = -1$ , the constants  $\mathcal{C} = \mathcal{A} + i\mathcal{B}$  and  $\bar{\mathcal{C}} = \mathcal{A} - i\mathcal{B}$  are complex conjugate numbers, while the phase  $\phi$  can take the form of either  $kx - \omega t$  or  $kx + \omega t$ .

Based on the complex representation given by Eq. (2.41) the solution to the wave equation (2.15) can be presented in a much simpler form as:

$$u(x, t) = C_1 e^{i(kx - \omega t)} + C_2 e^{i(kx + \omega t)} \quad (2.42)$$

where new complex constants  $C_1$  and  $C_2$  are introduced as  $C_1 = B_1 - iB_2$  and  $C_2 = B_3 - iB_4$ . However, one must remember that the resulting solution is complex in this case and only its real part represents the solution to Eq. (2.36). In order to simplify the notation the symbol  $\text{Re}[\bullet]$ , denoting the real part of a complex expression  $[\bullet]$ , is omitted in Eq. (2.42) and from this point on.

It can be clearly seen that the form of the solution given by Eq. (2.42) fully conforms with the solution given by Eq. (2.19). Moreover, it will be shown later that particular wave solutions to Eq. (2.42) indeed represents waves propagating either in positive or negative direction of the  $x$  axis.

The general solution to the wave equation (2.15) can be presented in an equivalent form, as a combination of two independent spatial solutions multiplied by a time harmonic factor. This can be obtained by the simultaneous use of the complex representations given by Eqs. (2.40) and (2.41) to the phase  $\phi$  equal to  $kx + \omega t$  or  $kx - \omega t$ , respectively. This leads to the following form of the general solution:

$$u(x, t) = (C_1 e^{ikx} + C_2 e^{-ikx}) e^{-i\omega t} \quad (2.43)$$

where now the complex constants  $C_1$  and  $C_2$  are equal to  $C_1 = B_1 - iB_2$  and  $C_2 = B_3 + iB_4$ , respectively.

The form of the general solution obtained fully corresponds to the initial assumption (2.33) of the Fourier method about the representation of the unknown function  $u(x, t)$  as a product of two independent space and time functions, while the latter can be expressed as a time harmonic function:

$$u(x, t) = X(x) e^{-i\omega t} \quad (2.44)$$

and as such, this property will be used later in the following sections of this book.

## 2.5 Wave Dispersion

Dispersion is a very important aspect of the wave propagation phenomena. Due to dispersion different frequency components of elastic waves travel at different speeds. It will be shown that the shape of non-dispersive waves remains unchanged during their propagation as long as they propagate in a non-dissipative medium and their energy is conserved. In contrast to this the shape of dispersive waves evolves during their propagation and the changes in their shapes that can be observed are stronger the longer the distance the waves travel, as presented in Fig. 2.7.

Since wave equations appear in many scientific and engineering problems, their accurate solution is a very important aspect of research practice. In each case dispersion, or dispersion relations, must be very carefully taken into account. There are many methods that can be potentially applied in order to solve a wave equation and their success is directly dependent on the type of problem. In general, they can be divided into analytical and numerical methods, despite the fact that there exist a range of other approximate methods such as, for example, a graphical method of characteristics. In the present era of modern supercomputers and fast parallel computations various numerical methods are successfully adopted for this purpose.

It should be noted that in the case of simple problems, such as the 1-D problems described in the preceding paragraphs, analytical methods are preferable for giving a great insight into the problem, as well as helping to understand the influence of various factors associated with solutions obtained for the wave equation.

It was shown in the previous paragraphs that a very effective and simple analytical method used to examine wave equations is the Fourier method. The effectiveness

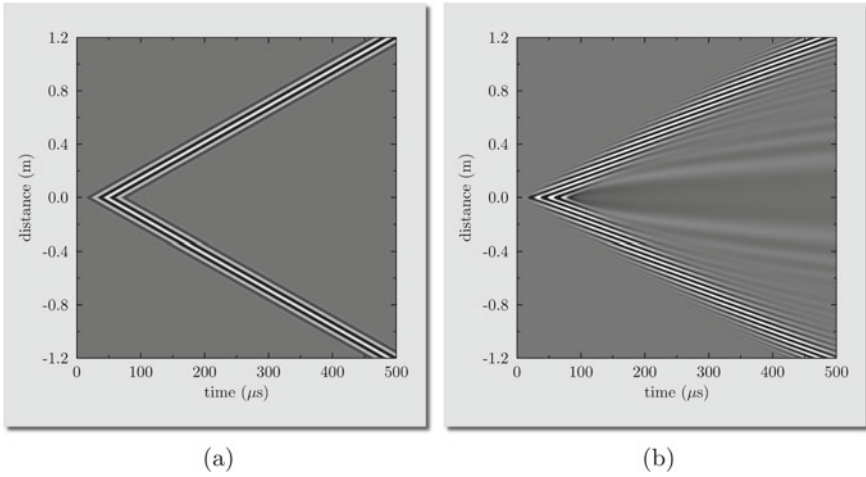


**Fig. 2.7** Wave propagation patterns for: **a** non-dispersive, **b** dispersive, waves in an isotropic elastic medium. Results of numerical computations by FEM

and usefulness of this particular analytical approach in the case of wave propagation can be demonstrated for the wave equations given by Eq. (2.15) and Eq. (2.32).

Taking into account the wave equation given by Eq. (2.15), describing propagation of elastic waves in a 1-D isotropic elastic rod from Sect. 2.3.1, it can be written that:

$$\frac{\partial^2 u(x, t)}{\partial x^2} - \frac{1}{\beta^2} \frac{\partial^2 u(x, t)}{\partial t^2} = 0$$

$$\downarrow u(x, t) = X(x)e^{-i\omega t} \tag{2.45}$$

$$\left[ \frac{d^2 X(x)}{dx^2} + \frac{\omega^2}{\beta^2} X(x) \right] e^{-i\omega t} = 0$$

which is satisfied for any moment in time  $t$  only if the expression within the brackets is satisfied:

$$\frac{d^2 X(x)}{dx^2} + \frac{\omega^2}{\beta^2} X(x) = 0 \tag{2.46}$$

Expected solutions to Eq. (2.46) can be assumed to be in the exponential form  $e^{ikx}$ , and their substitution into Eq. (2.46) leads to the characteristic equation:

$$-k^2 + \frac{\omega^2}{\beta^2} = 0 \tag{2.47}$$

which has two different roots:

$$k = \pm \frac{\omega}{\beta} \quad \text{or} \quad \omega = \pm k\beta \quad (2.48)$$

and which can be associated with two elastic waves propagating within the rod in opposite directions.

Now, the phase velocity  $c_p$  and the group velocity  $c_g$  of these two waves can be evaluated based on the relations given by Eq. (2.2) and Eq. (2.7), or by Eq. (2.8), to obtain:

$$\begin{cases} c_p = \frac{\omega}{k} = \beta = \sqrt{\frac{E}{\rho}} \\ c_g = \frac{d\omega}{dk} = \beta = \sqrt{\frac{E}{\rho}} = c_p \end{cases} \quad (2.49)$$

where for simplicity only the positive root was taken into account out of the two existing roots, as the one associated with the wave travelling in the positive direction of the  $x$  axis.

It can be noted straight away that since the values of the two velocities are the same and  $c_p = c_g$ , regardless the angular frequency  $\omega$ , all wave components within a wave packet/stress pulse must travel at the same speed. As a result of this, the shape of a wave packet propagating within the rod remains unchanged over the distance  $x$ , and in time  $t$ , as already presented in Fig. 2.5.

However, in the case of the wave equation given by Eq. (2.32), describing propagation of elastic waves in a 1-D isotropic elastic beam from Sect. 2.3.2, observations are different. It can be written that:

$$\begin{aligned} \frac{\partial^4 w(x, t)}{\partial x^4} + \frac{1}{\beta^4} \frac{\partial^2 w(x, t)}{\partial t^2} &= 0 \\ \downarrow u(x, t) = X(x)e^{-i\omega t} & \\ \left[ \frac{d^4 X(x)}{dx^4} - \frac{\omega^2}{\beta^4} X(x) \right] e^{-i\omega t} &= 0 \end{aligned} \quad (2.50)$$

which again can be satisfied at any moment in time  $t$  only if the expression within the brackets is satisfied:

$$\frac{d^4 X(x)}{dx^4} - \frac{\omega^2}{\beta^4} X(x) = 0 \quad (2.51)$$

As before, assuming expected solutions to Eq. (2.51) to be in the exponential form  $e^{ikx}$ , their subsequent substitution to Eq. (2.51) leads to the characteristic equation:

$$k^4 - \frac{\omega^2}{\beta^4} = 0 \quad (2.52)$$

which now has four different roots, which can be associated with two different wave propagation modes. The first mode represents solutions being elastic waves travelling within the beam, which are related to the two roots:

$$k = \pm \frac{\sqrt{\omega}}{\beta} \quad \text{or} \quad \omega = \beta^2 k^2 \quad (2.53)$$

while the second mode represents evanescent waves, which are spatially damped wave solutions obtained in the case of the two remaining roots:

$$k = \pm i \frac{\sqrt{\omega}}{\beta} \quad \text{or} \quad \omega = -\beta^2 k^2 \quad (2.54)$$

The phase velocity  $c_p$  and the group velocity  $c_g$  of the two waves, corresponding to the first wave propagation mode, can easily be evaluated from the same relationships as before, which are given by Eq. (2.2) and Eq. (2.7), or Eq. (2.8), as:

$$\begin{cases} c_p = \frac{\omega}{k} = \beta \sqrt{\omega} = \sqrt[4]{\frac{EI}{\rho S}} \sqrt{\omega} \\ c_g = \frac{d\omega}{dk} = 2\beta \sqrt{\omega} = 2 \sqrt[4]{\frac{EI}{\rho S}} \sqrt{\omega} = 2c_p \end{cases} \quad (2.55)$$

where again only the positive root was taken into account.

In the case of waves propagating in the 1-D isotropic elastic beam, in contrast to the case of the 1-D isotropic elastic rod, the phase velocity  $c_p$  and the group velocity  $c_g$  are different, therefore  $c_p \neq c_g$  for all angular frequencies  $\omega$ . The intensity of dispersion, understood as the difference between the value of the group velocity  $c_g$  and the phase velocity  $c_p$  for a given wave number  $k$ , strongly influences and controls the amount by which these amplitudes are reduced, and the way the shapes of the wave packet/stress pulses are distorted. Based on Eq. (2.7) this intensity can be simply expressed as directly dependent on the local derivative of the phase velocity  $c_p$  with respect to the wave number  $k$  and equal to  $k \cdot dc_p/dk$ .

In general, it can be stated that wave packets, understood as groups of waves well localised in space and time, and characterised by finite dimensions, propagate with the group velocity  $c_g$ , while harmonic waves, infinite in space and time, propagate with the phase velocity  $c_p$ . When no dispersion is observed, these two velocities are equal, i.e.  $c_p = c_g$ , exactly as in the case of the 1-D isotropic elastic rod. As a result of this, wave packets propagate within the rod with no changes in their shapes, as clearly seen in Fig. 2.5, as long as the rod material remains elastic.

On the other hand, when dispersion is observed these two velocities are different, i.e.  $c_p \neq c_g$ . However, as presented in Fig. 2.8 also in this case two sets of characteristics can be found, which determine the position of the waves travelling in the direction of the  $x$  axis, in the case of Eq. (2.56), and in the opposite direction, in the



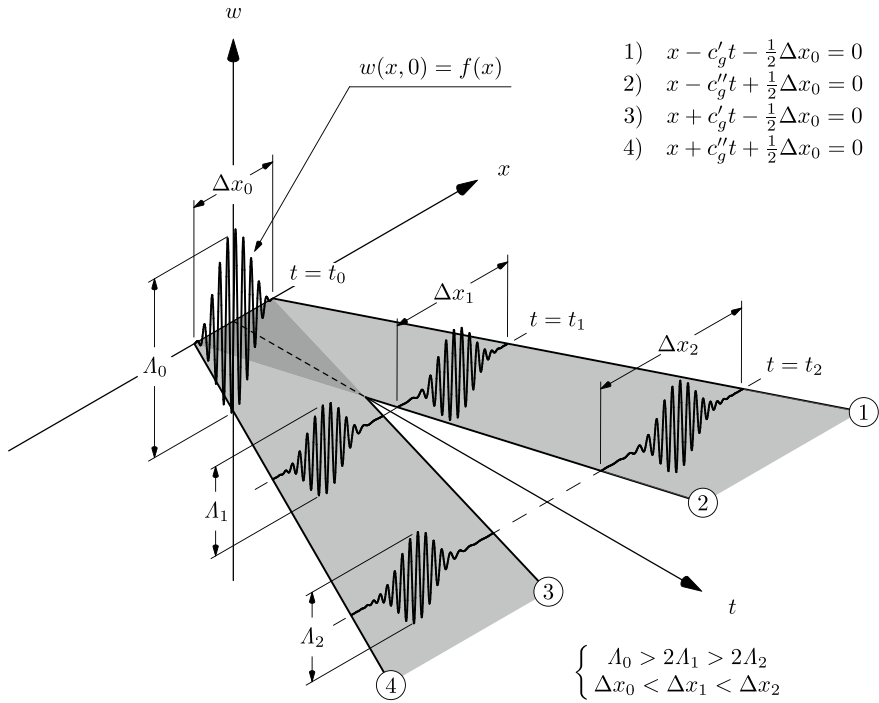


**Fig. 2.8** Propagation of an initial condition in the form of a transverse displacement pulse in a 1-D isotropic elastic beam

case of Eq. (2.57). This time it can be clearly seen from Fig. 2.8 that the initial transverse displacement  $w(x, 0) = f(x)$  travels within the beam with the group velocity  $c_g$  rather than the phase velocity  $c_p$ , as two independent flexural waves, exactly as prescribed by Eq. (2.32). Their locations within the beam in particular moments in time  $t$  are precisely described by two sets of characteristics:

$$\begin{cases} x - c'_g t - \frac{1}{2} \Delta x_0 = 0 \\ x - c''_g t + \frac{1}{2} \Delta x_0 = 0 \end{cases} \quad (2.56)$$

$$\begin{cases} x + c'_g t - \frac{1}{2} \Delta x_0 = 0 \\ x + c''_g t + \frac{1}{2} \Delta x_0 = 0 \end{cases} \quad (2.57)$$

where  $\Delta x_0$  denotes the spatial width of the initial displacement in Fig. 2.8, while  $c'_g$  and  $c''_g$  denote two group velocities associated with the width of the initial displacement in the frequency domain.

At this point it is convenient to assume that the time and frequency representations of a typical excitation signal can have the form of a wave packet. Such a wave packet may consist of a number of higher frequency harmonic oscillations modulated

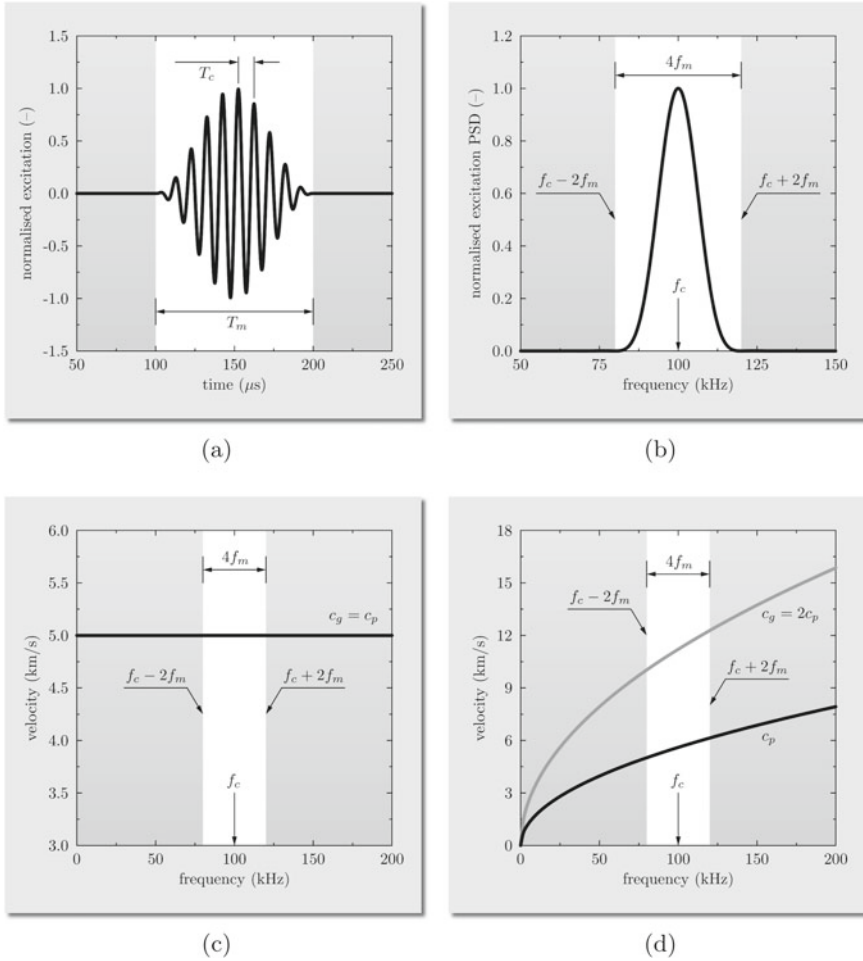


**Fig. 2.9** An example of a normalised excitation signal in the form of a wave packet represented in: **a** the time domain, **b** the frequency domain, as well as dispersion curves for the phase velocity  $c_p$  and the group velocity  $c_g$  obtained in the case of a 1-D isotropic elastic: **c** rod, **d** beam, with corresponding ranges of excited frequencies

by a lower frequency envelope. In the time domain it can be characterised by its total duration or modulation time  $T_m$ , as well as the time corresponding to each particular oscillation  $T_c$  of the carrier wave, or alternatively by the period of the modulation  $T_m$  and the period of the carrier wave  $T_c$ , as presented in Fig. 2.9a. In the frequency domain such a wave packet is represented by a pulse of a certain amplitude and frequency width, which can be easily obtained by the application of the Fourier transform, as presented in Fig. 2.9b. The centre of the pulse is located at the frequency corresponding to the carrier frequency  $f_c = 1/T_c$ , while its total

frequency width depends not only on the modulation frequency  $f_m = 1/T_m$ , but also on the assumed accuracy of its representation. For the majority of practical problems it can be assumed that more than 97% of the signal energy is stored in the range of frequencies starting from  $f_c - 2f_m$  to  $f_c + 2f_m$ , however for higher accuracy, exceeding 99%, this range must expand to cover frequencies from  $f_c - 4f_m$  to  $f_c + 4f_m$  or even more.

Now it can be clearly seen from Fig. 2.9c and d that the frequency representation of the excitation signal can be very helpful in order to determine the values of the group velocities  $c'_g$  and  $c''_g$  describing the set of characteristics given by Eqs. (2.56) and (2.57). Bearing in mind the accuracy of the frequency representation of the excitation signal, it can be immediately seen that these two group velocities are equal to:

$$\begin{cases} c'_g = c_g(f_c - 2f_m) \\ c''_g = c_g(f_c + 2f_m) \end{cases} \quad (2.58)$$

In general, it is observed that the group velocity  $c_g$  is smaller than the phase velocity  $c_p$ , i.e. when  $c_g < c_p$  or  $dc_p/dk < 0$ . This fact leads to the behaviour whereby wave components characterised by longer wavelengths  $\lambda$  (smaller wave numbers  $k$ ), being faster than the wave components characterised by shorter wavelengths  $\lambda$

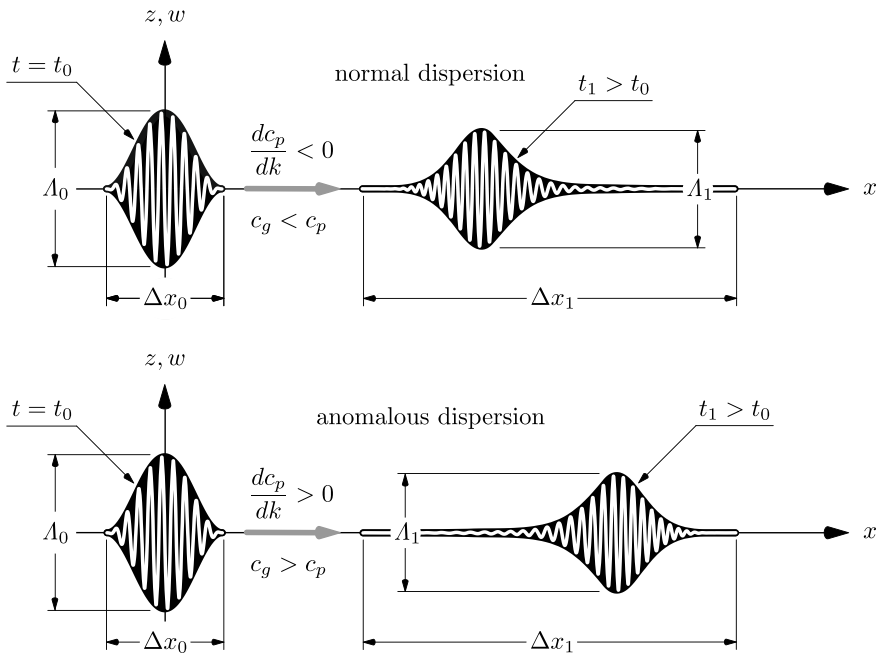


Fig. 2.10 An example of a wave packet characterised by normal or anomalous dispersion

(greater wave numbers  $k$ ), gradually travel through a wave packet to its beginning, substantially elongating the packet at its front. This type of behaviour corresponds to so-called *normal dispersion*.

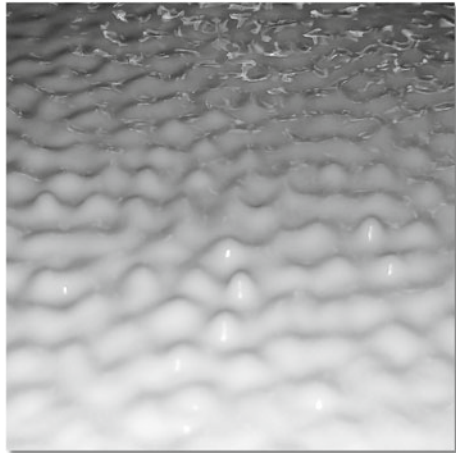
In contrast to this, when the group velocity  $c_g$  is greater than the phase velocity  $c_p$ , i.e. when  $c_g > c_p$  or  $dc_p/dk > 0$ , the observed behaviour corresponds to so-called *anomalous dispersion*. In such a case wave components characterised by longer wavelengths  $\lambda$  (smaller wave numbers  $k$ ), being slower than the wave components characterised by shorter wavelengths  $\lambda$  (greater wave numbers  $k$ ), gradually travel through a wave packet to its end, substantially elongating the packet at its back. Both of these behaviours are illustrated in Fig. 2.10.

## 2.6 Standing Waves and Normal Modes

Standing waves, also known in the literature as stationary waves, result from the superposition (interference) of two harmonic waves of the same wave number  $k$  and angular frequency  $\omega$ , but travelling in opposite directions, as presented in Fig. 2.11.

It should be recalled that the particular form of the general solution to the wave equation (2.15), given by Eq. (2.43) in Sect. 2.4, represents in fact two waves propagating in either positive or negative direction of the  $x$  axis. For this reason it can be written that:

**Fig. 2.11** A standing wave on the free surface of liquid



$$\begin{aligned}
 u(x, t) &= (C_1 e^{ikx} + C_2 e^{-ikx}) e^{-i\omega t} \\
 &\quad \downarrow C_1 = C_2 = A \\
 u(x, t) &= 2A e^{-i\omega t} \cos kx
 \end{aligned} \tag{2.59}$$

under an additional assumption of equal and real amplitudes of the superposing waves, denoted as  $A$ .

Bearing in mind that only the real part of the complex solution given by Eq. (2.59) should be taken into account, it can be immediately noted that:

$$u(x, t) = 2A \cos \omega t \cos kx \tag{2.60}$$

It can be clearly seen that the resulting wave  $u(x, t)$  has interesting properties. First of all it can be seen that now the shape of the wave  $u(x, t)$ , defined by the term  $\cos kx$ , does not travel and is stationary, while its amplitude equal to  $2A \cos \omega t$  varies in time periodically with the angular frequency  $\omega$ , as presented in Fig. 2.12. These points in space, for which the amplitude of the wave is always zero regardless of time  $t$ , are called *nodal points* or *nodes*. Their coordinates on the  $x$  axis correspond to the solution to a simple equation:

$$\cos kx = 0 \rightarrow x = \frac{\pi}{2k} + \frac{n\pi}{k} = \frac{\lambda}{4} + \frac{n\lambda}{2}, \quad n = 0, \pm 1, \pm 2, \dots \tag{2.61}$$

On the other hand those points in space, for which the amplitude takes its extreme values, are called *anti-nodal points* or *anti-nodes*. Their coordinates on the  $x$  axis correspond to the solution to a similar simple equation:

$$\cos kx = \pm 1 \rightarrow x = \frac{n\pi}{k} = \frac{n\lambda}{2}, \quad n = 0, \pm 1, \pm 2, \dots \tag{2.62}$$

Additionally it can be seen that the shape of the resulting standing wave  $u(x, t)$  is independent of time  $t$ , however, a standing wave can be formed at any angular frequency  $\omega$ . The distance between consecutive *nodes* or *anti-nodes* of a standing wave is fixed and equal to  $\lambda/2$ , while between consecutive *nodes* and *anti-nodes* is equal to  $\lambda/4$ .

Standing waves resulting from the interaction of propagating harmonic waves with structural boundaries present another interesting case. Their multiple reflections and superposition give rise to so-called *normal modes* or modes of free vibrations, which are also referred to as modes of natural vibrations. It should be emphasised that this kind of elastic vibration always concerns perfect recovery forces and as such never involves damping, either internal or external. Moreover, in the case of structures representing smooth, simply or multi connected, regions, normal modes may appear as a multiple self-superposition of propagating waves, as is presented in Fig. 2.13 in the case of a spherical shell.

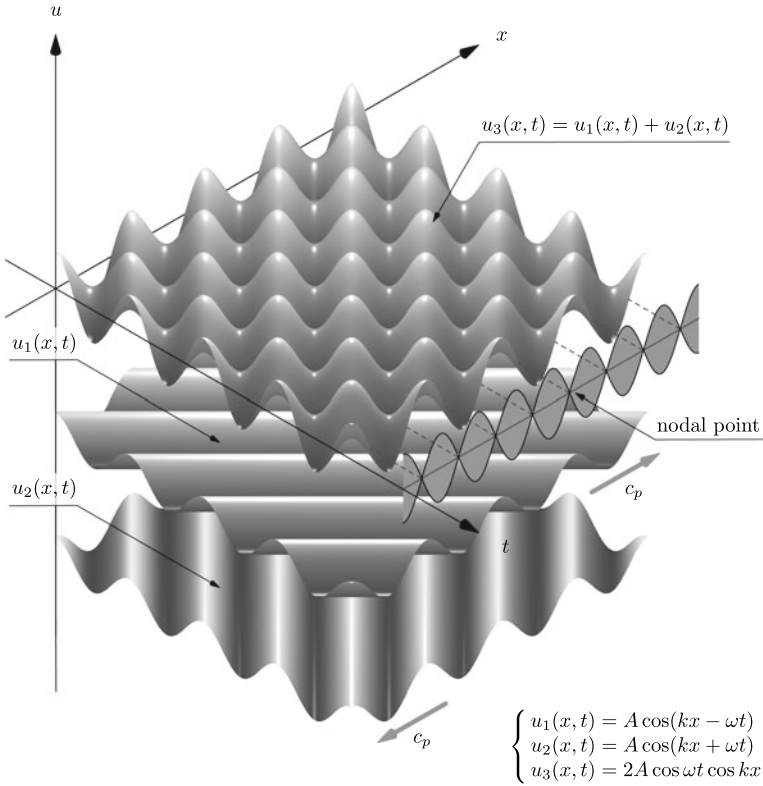


**Fig. 2.12** A standing wave as a superposition of two identical, harmonic waves propagating in opposite directions

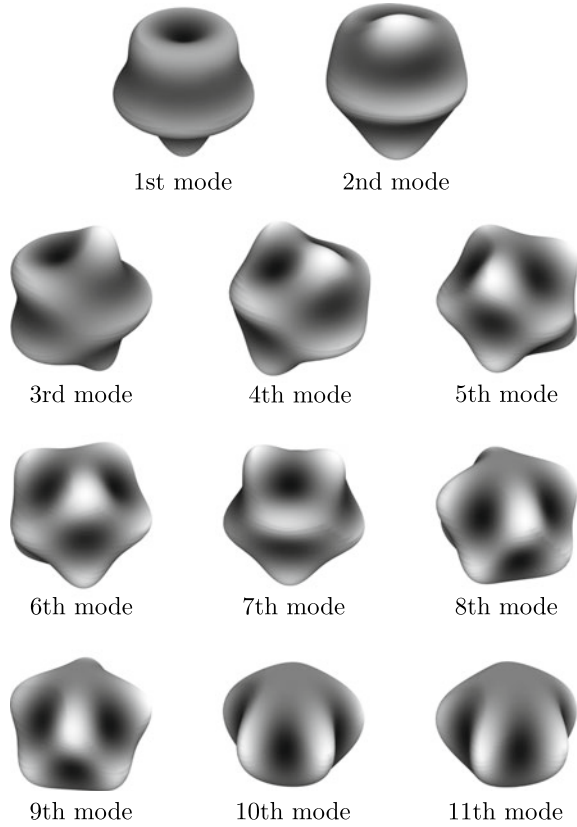
It can be immediately found that finite dimensions of typical engineering structures, which lead to multiple reflections and superposition of the waves that can propagate within them, have a direct impact on the forms of generated solutions to associated equations of motion. Imposing specific conditions on these equations, resulting from various types of physical constraints placed on propagating waves at structural boundaries, limits the characteristic equations to discrete sets of the wave number  $k$  and the angular velocity  $\omega$ , typically denoted as  $k_n$  and  $\omega_n$ .

In the case of the equation of motion (2.15) and the bar of finite length  $l$ , the solution to the resulting Eq. (2.46) must be accompanied by two general, structural boundary conditions, which must be satisfied at any moment in time  $t$ . There are two possible states of the bar ends, which can be described as:

- fixed end, when the axial displacements  $u(x, t)$  must vanish,
- free end, when the axial force  $N(x, t)$  must vanish.

at either end of the bar, i.e. for  $x = 0$  or  $x = l$ .

**Fig. 2.13** Multiple (degenerated) normal modes belonging to the 5th frequency of free vibrations of a thin-walled isotropic elastic spherical shell. Results of numerical computations by TD-SFEM



These two boundary conditions can be expressed in terms of the unknown function  $X(x)$  from Eq. (2.46) as a set of two equations:

$$\begin{cases} X(x) = 0 \\ \frac{dX(x, t)}{dx} = 0 \end{cases} \quad (2.63)$$

which must be satisfied at the selected end of the bar, i.e. for  $x = 0$  or  $x = l$ .

In the next step, bearing in mind the form of Eq. (2.46) as well as Eq. (2.47), one can immediately write the general form of the solution to Eq. (2.46) as:

$$X(x) = C_1 e^{ikx} + C_2 e^{-ikx} \quad (2.64)$$

with  $C_1$  and  $C_2$  being complex constants, or alternatively by the use of real functions:

$$X(x) = B_1 \sin kx + B_2 \cos kx \quad (2.65)$$

where the two real constants  $B_1$  and  $B_2$  must be found based on Eq. (2.63). This leads to the following set of equations:

$$\begin{cases} B_1 \sin kx + B_2 \cos kx = 0 \\ B_1 k \cos kx - B_2 k \sin kx = 0 \end{cases} \quad (2.66)$$

which must be satisfied at the previously selected end of the bar, i.e. for  $x = 0$  or  $x = l$ .

For example, assuming that the bar is fixed at one end, at  $x = 0$ , while the other end of the bar remains free, at  $x = l$ , it can be seen straight away that the first equation leads to  $B_2 = 0$  for  $x = 0$ . However, the second equation leads to non-trivial solutions for  $x = l$ , i.e. when  $B_1 \neq 0$  and  $k \neq 0$ , only if:

$$\cos kl = 0 \rightarrow k_n = \frac{\pi}{2l} + \frac{(n-1)\pi}{l} = \frac{(2n-1)\pi}{2l}, \quad n = 1, 2, 3, \dots \quad (2.67)$$

The non-trivial solutions expressed in terms of the discrete wave number  $k_n$  are more often expressed in terms of the discrete angular frequencies  $\omega_n$ , which by the use of the characteristic equation (2.47) as well as Eq. (2.49), can be written in the following form:

$$\omega_n = \frac{(2n-1)\pi}{2l} \sqrt{\frac{E}{\rho}}, \quad n = 1, 2, 3, \dots \quad (2.68)$$

where now the discrete angular frequencies  $\omega_n$  are known as frequencies of normal modes, frequencies of free vibrations or frequencies of natural vibrations of the bar.

In a similar manner, in the case of equation of motion (2.32) and the beam of finite length  $l$ , the solution to the resulting Eq. (2.51) must be supplemented by four general, structural boundary conditions, which must be satisfied at any moments in time  $t$ . This time, however, there are three possible states of the beam ends, which can be described as:

- fixed end, when the transverse displacement  $w(x, t)$  and the slope  $w'(x, t)$  must vanish,
- simply supported, when transverse displacement  $w(x, t)$  and the bending moment  $M(x, t)$  must vanish,
- free end, when the bending moment  $M(x, t)$  and the shear force  $Q(x, t)$  must vanish,

at either the end of the beam, i.e. for  $x = 0$  or  $x = l$ .

These two boundary conditions can be expressed in terms of the unknown function  $X(x)$  from Eq. (2.51) as a set of four equations:



$$\begin{cases} X(x) = 0, & \frac{d^2 X(x, t)}{dx^2} = 0 \\ \frac{dX(x, t)}{dx} = 0, & \frac{d^3 X(x, t)}{dx^3} = 0 \end{cases} \quad (2.69)$$

which must be satisfied at the same ends of the beam, i.e. for  $x = 0$  or  $x = l$ .

The general form of the solution to Eq. (2.51) can be expressed in similar manner as before, which is:

$$X(x) = C_1 e^{kx} + C_2 e^{-kx} + C_3 e^{ikx} + C_4 e^{-ikx} \quad (2.70)$$

with  $C_1, C_2, C_3$  and  $C_4$  being complex constants, or alternatively by the use of real functions:

$$X(x) = B_1 \sinh kx + B_2 \cosh kx + B_3 \sin kx + B_4 \cos kx \quad (2.71)$$

where the four real constants  $B_1, B_2, B_3$  and  $B_4$  must be found based on Eq. (2.69). This leads to the following set of equations:

$$\begin{cases} B_1 \sinh kx + B_2 \cosh kx + B_3 \sin kx + B_4 \cos kx = 0 \\ B_1 k \cosh kx + B_2 k \sinh kx + B_3 k \cos kx - B_4 k \sin kx = 0 \\ B_1 k^2 \sinh kx + B_2 k^2 \cosh kx - B_3 k^2 \sin kx - B_4 k^2 \cos kx = 0 \\ B_1 k^3 \cosh kx + B_2 k^3 \sinh kx - B_3 k^3 \cos kx + B_4 k^3 \sin kx = 0 \end{cases} \quad (2.72)$$

This time, for example, assuming that the beam is simply supported at both ends, at  $x = 0$  and  $x = l$ , it can be easily seen that for  $x = 0$  the first equation leads to  $B_2 = -B_4$ , while the third equation leads to  $B_2 = B_4$ . These conditions are satisfied only if both these constants vanish, i.e. when  $B_2 = B_4 = 0$ .

By looking at the remaining simply supported end of the beam at  $x = l$  the remaining constants  $B_1$  and  $B_3$  can be easily evaluated from Eq. (2.72), which forms a set of two equations:

$$\begin{cases} B_1 \sinh kl + B_3 \sin kl = 0 \\ B_1 \sinh kl - B_3 \sin kl = 0 \end{cases} \quad (2.73)$$

which has non-trivial solutions only if its determinant vanishes. This leads to the following characteristic equation:

$$\sinh kl \sin kl = 0 \quad (2.74)$$

and which has non-trivial solutions for  $k \neq 0$  only if:

$$\sin kl = 0 \rightarrow k_n = \frac{n\pi}{l}, \quad n = 1, 2, 3, \dots \quad (2.75)$$

Again, the non-trivial solutions expressed in terms of the discrete wave number  $k_n$  are more commonly expressed in terms of the discrete angular frequencies  $\omega_n$ ,

which by means of the characteristic equation (2.52) as well as Eq. (2.55), can be written in the following form:

$$\omega_n = \left(\frac{n\pi}{l}\right)^2 \sqrt{\frac{EI}{\rho S}}, \quad n = 1, 2, 3, \dots \tag{2.76}$$

where now the discrete angular frequencies  $\omega_n$  are known as frequencies of normal modes, frequencies of free vibrations or frequencies of natural vibrations of the beam.

In general, the lowest frequency of free vibrations, which corresponds to  $n = 1$  in Eq. (2.68) or Eq. (2.76), is called *the fundamental frequency*, while the corresponding normal mode is called *the fundamental mode*.

It should be noted that dispersion curves discussed in Sect. 2.5 are inextricably linked with frequencies of free vibrations, which have to follow their changes regardless of the type of structural boundary conditions for a given type of problem, as presented in Fig. 2.14. For this reason dispersion curves remain a very important source of information on dynamic properties of structures, in a similar manner to normal modes and frequencies of free vibrations. However, computation of normal modes and frequencies of free vibrations is nowadays a task, which is relatively simple, even in the case of huge numerical models, thanks to the availability of modern supercomputers and fast parallel computations. On the other hand numerical calculation of dispersion curves presents a much more difficult problem, especially when more advanced theories of structural behaviour are considered than the two simple theories discussed in this chapter. These modelling aspects will be discussed in the following chapters of this book.

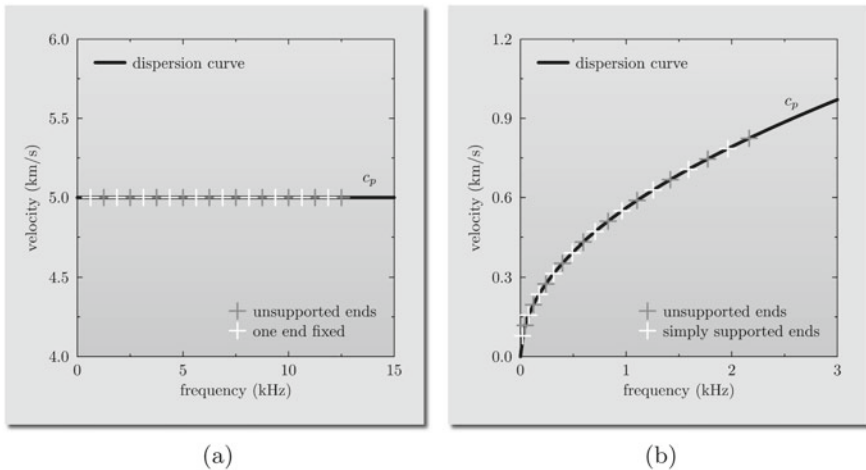


**Fig. 2.14** Dispersion curves for the phase velocity  $c_p$  obtained in the case of a 1-D isotropic elastic: **a** rod, **b** beam. Discrete points on the curves correspond to the first 10 frequencies of free vibrations for various types of structural boundary conditions

## References

1. <https://pixabay.com/pl/photos/woda-upuszczac-plusniecie-1761027>, 2016. Visited on 09/12/2023.
2. J. D. Achenbach. *Wave propagation in elastic solids*. North-Holland Publishing Company, Amsterdam, 1973.

# Chapter 3

## Waves in a 3-D Elastic Space



### 3.1 Navier-Cauchy Equation

Wave motion in a 3-D elastic medium can be expressed in a very elegant way by the use of tensor notation and differential operators. Because of this the resulting form of the equations of motion becomes independent of the selection of the coordinate system. This makes such a form of the equations of motion universal and more suitable for further studies. Under the assumption of small strains and homogeneity of the elastic medium, starting from Newton's second law of motion, it may be written that:

$$\nabla \cdot \boldsymbol{\sigma} + \mathbf{F} = \rho \ddot{\mathbf{u}} \tag{3.1}$$

where the symbol  $\nabla$  denotes the nabla operator of differentiation,  $\boldsymbol{\sigma}$  is the Cauchy stress tensor,  $\mathbf{F}$  is the vector of body forces,  $\rho$  is the material density,  $\mathbf{u}$  is the vector of displacements being a function of space variables  $x$ ,  $y$  and  $z$  as well as time  $t$ , while the symbol  $\ddot{(\bullet)}$  represents the second derivative with respect to time  $t$ .

Equation (3.1) must be supplemented with two additional equations: one being the so-called strain-displacement relationship and the other being the constitutive equation, known as Hooke's law, linking together strains and stresses:

$$\boldsymbol{\epsilon} = \frac{1}{2}[\nabla \mathbf{u} + (\nabla \mathbf{u})^T], \boldsymbol{\sigma} = \mathbf{C} : \boldsymbol{\epsilon} \tag{3.2}$$

where  $\boldsymbol{\epsilon}$  is the strain tensor and  $\mathbf{C}$  is the fourth-order stiffness tensor, while the symbol  $(\bullet)^T$  denotes transposition.

In the case of an isotropic elastic medium the stiffness tensor can be expressed in terms of two independent material constants  $\lambda$  and  $\mu$ , known as the Lamé parameters or constants. These parameters are closely correlated with elastic properties of the medium by the following relationships:

$$\lambda = \frac{\nu E}{(1 + \nu)(1 - 2\nu)}, \quad \mu = \frac{E}{2(1 + \nu)} \quad (3.3)$$

where  $E$  is material Young's modulus and  $\nu$  denotes Poisson's ratio.

It seems reasonable to assume that body forces in Eq. (3.1) can be neglected since wave motion in elastic media is entirely driven by recoverable elastic forces. As a result of this the equation of motion can be expressed in the following manner:

$$\mu \nabla^2 \mathbf{u} + (\lambda + \mu) \nabla (\nabla \cdot \mathbf{u}) = \rho \ddot{\mathbf{u}} \quad (3.4)$$

It should be noted that this neat form of the equation of motion represents in fact three coupled partial differential equations, which can be written independently for each component of the displacement vector  $\mathbf{u} = [u_x, u_y, u_z]^T$  as:

$$\begin{cases} \mu \nabla^2 u_x + (\lambda + \mu) \frac{\partial}{\partial x} (\nabla \cdot \mathbf{u}) = \rho \frac{\partial^2 u_x}{\partial t^2} \\ \mu \nabla^2 u_y + (\lambda + \mu) \frac{\partial}{\partial y} (\nabla \cdot \mathbf{u}) = \rho \frac{\partial^2 u_y}{\partial t^2} \\ \mu \nabla^2 u_z + (\lambda + \mu) \frac{\partial}{\partial z} (\nabla \cdot \mathbf{u}) = \rho \frac{\partial^2 u_z}{\partial t^2} \end{cases} \quad (3.5)$$

where  $u_x = u_x(x, y, z, t)$ ,  $u_y = u_y(x, y, z, t)$  and  $u_z = u_z(x, y, z, t)$  are the displacement components in the direction of the  $x$ ,  $y$  and  $z$  axes, respectively.

It can be shown that Eqs. (3.5) describe the behaviour of three independent wave modes in a 3-D elastic space. In order to see this, one can consider in this space propagation of a plane harmonic wave  $\mathbf{u}$ , which can be assumed to have the following form:

$$\mathbf{u} = \hat{\mathbf{u}} e^{i(\mathbf{k} \cdot \mathbf{r} - \omega t)} = \begin{bmatrix} \hat{u}_x \\ \hat{u}_y \\ \hat{u}_z \end{bmatrix} e^{i(k_x x + k_y y + k_z z)} e^{-i\omega t} \quad (3.6)$$

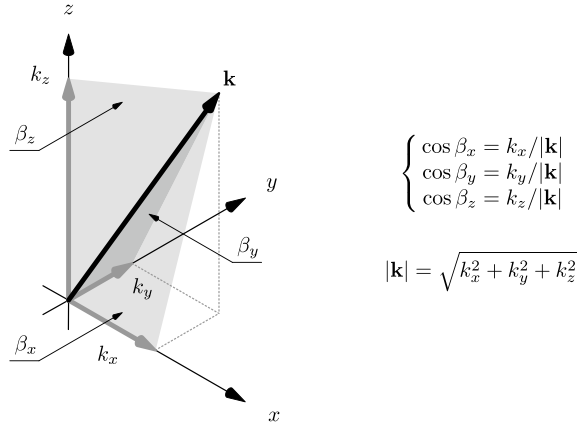
where  $\hat{\mathbf{u}} = [\hat{u}_x, \hat{u}_y, \hat{u}_z]^T$  and  $\mathbf{k} = [k_x, k_y, k_z]^T$  are the vectors of amplitude components and wave numbers, while  $\mathbf{r} = [x, y, z]^T$  denotes the position vector, all in 3-D space, as presented in Fig. 3.1.

Alternatively, as shown in Fig. 3.1, the wave number vector  $\mathbf{k}$  can be conveniently expressed by the use of the direction cosines as:

$$\mathbf{k} = \begin{bmatrix} k_x \\ k_y \\ k_z \end{bmatrix} = |\mathbf{k}| \begin{bmatrix} \cos \beta_x \\ \cos \beta_y \\ \cos \beta_z \end{bmatrix} \quad (3.7)$$

where  $|\mathbf{k}|$  denotes the length of the wave number vector  $\mathbf{k}$  and where the cosines of particular angles  $\beta_x$ ,  $\beta_y$  and  $\beta_z$  can be calculated using the following formulae:

**Fig. 3.1** A wave number vector  $\mathbf{k}$  in the Cartesian coordinate system  $(x, y, z)$  in relation to the the direction cosines



$$\begin{cases} \cos \beta_x = \frac{k_x}{|\mathbf{k}|} \\ \cos \beta_y = \frac{k_y}{|\mathbf{k}|} \\ \cos \beta_z = \frac{k_z}{|\mathbf{k}|} \end{cases}, \quad |\mathbf{k}| = \sqrt{k_x^2 + k_y^2 + k_z^2} \quad (3.8)$$

At this point it is convenient to express the plane harmonic wave  $\mathbf{u}$ , given by Eq. (3.6) in a slightly modified form, by the use of directional cosines as:

$$\mathbf{u} = \hat{\mathbf{u}} e^{i(\mathbf{k} \cdot \mathbf{r} - \omega t)} = \begin{bmatrix} \hat{u}_x \\ \hat{u}_y \\ \hat{u}_z \end{bmatrix} e^{i|\mathbf{k}|(\cos \beta_x x + \cos \beta_y y + \cos \beta_z z)} e^{-i\omega t} \quad (3.9)$$

A simple substitution of Eq. (3.9) into Eqs. (3.5), after necessary mathematical operations and rearrangement of terms, leads to a set of three homogeneous equations:

$$\begin{cases} (\mu|\mathbf{k}|^2 - \rho\omega^2)\hat{u}_x + (\lambda + \mu)|\mathbf{k}|^2 \cos \beta_x \cdot \Delta = 0 \\ (\mu|\mathbf{k}|^2 - \rho\omega^2)\hat{u}_y + (\lambda + \mu)|\mathbf{k}|^2 \cos \beta_y \cdot \Delta = 0 \\ (\mu|\mathbf{k}|^2 - \rho\omega^2)\hat{u}_z + (\lambda + \mu)|\mathbf{k}|^2 \cos \beta_z \cdot \Delta = 0 \end{cases} \quad (3.10)$$

where  $\Delta = \hat{u}_x \cos \beta_x + \hat{u}_y \cos \beta_y + \hat{u}_z \cos \beta_z$ .

It is well-known that non-trivial solutions to the set of three homogeneous equations, given by Eqs. (3.10), can be obtained only if its determinant vanishes, i.e. when:

$$[(\lambda + 2\mu)|\mathbf{k}|^2 - \rho\omega^2](\mu|\mathbf{k}|^2 - \rho\omega^2)^2 = 0 \quad (3.11)$$

which leads straight away to two independent characteristic equations:

$$(\lambda + 2\mu)|\mathbf{k}|^2 - \rho\omega^2 = 0, \quad \mu|\mathbf{k}|^2 - \rho\omega^2 = 0 \tag{3.12}$$

which determine two independent wave propagation velocities.

It is interesting to check which displacement components can be assigned to particular solutions represented by these two characteristic equations. In order to do this without any loss of generality, it can be conveniently assumed that the plane harmonic wave  $\mathbf{u}$  propagates in the direction of the  $x$  axis, thus  $\cos \beta_x = 1$  and  $\cos \beta_y = \cos \beta_z = 0$ . Moreover, in this case  $|\mathbf{k}| = k_x$ , so it can be conveniently noted that  $k_x \equiv k$ . This helps to simplify the set of homogeneous equations, given by Eqs. (3.10), to a much simpler form, which fully reveals the nature of the solutions sought:

$$\begin{cases} [(\lambda + 2\mu)k^2 - \rho\omega^2]\hat{u}_x = 0 \\ (\mu k^2 - \rho\omega^2)\hat{u}_y = 0 \\ (\mu k^2 - \rho\omega^2)\hat{u}_z = 0 \end{cases} \tag{3.13}$$

Now, it can be clearly seen that there are three distinctive and independent wave modes, which can propagate in a 3-D elastic space:

- the primary wave, as presented in Fig. 3.2, also known as the dilatational, irrotational, *longitudinal*, voluminal or P-wave of the form:

$$u_x(x, t) = \hat{u}_x e^{ik(x - c_p t)} \tag{3.14}$$

which propagates with the phase and group velocity:

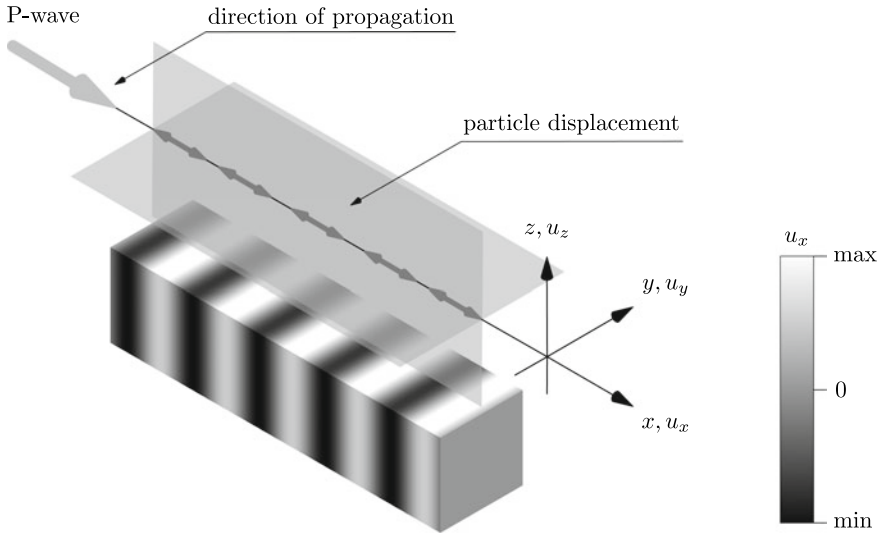


**Fig. 3.2** A schematic representation of a P-wave propagating in a 3-D elastic space

$$c_p = \sqrt{\frac{\lambda + 2\mu}{\rho}} \quad (3.15)$$

- two secondary waves, also known as the equivoluminal, distortional, rotational, *shear* or S-waves of the forms:

$$\begin{cases} u_y(x, t) = \hat{u}_y e^{ik(x-c_s t)} \\ u_z(x, t) = \hat{u}_z e^{ik(x-c_s t)} \end{cases} \quad (3.16)$$

which propagate with the phase and group velocity:

$$c_s = \sqrt{\frac{\mu}{\rho}} \quad (3.17)$$

The type of S-wave that propagates along the  $x$  axis with the non-zero displacement component  $u_y(x, t)$  is called the *shear horizontal* or SH-wave. In contrast to this, the type of S-wave that propagates along the  $x$  axis with the non-zero displacement component  $u_z(x, t)$  is called the *shear vertical* or SV-wave.

It is evident that both types of S-wave represent transverse waves, which are characterised by displacements of particles transverse to the direction of wave propagation, in a 3-D elastic medium, as clearly seen in Figs. 3.3 and 3.4. However, in the case of the P-wave these displacements remain parallel to the direction of wave propagation, thus the P-wave represents a longitudinal wave, as it can be observed in Fig. 3.2.

It should be emphasised that the three wave modes are non-dispersive, as the phase velocities  $c_l$  and  $c_s$  depend only on mechanical properties of the 3-D elastic space, but remain independent of the angular frequency  $\omega$ .

## 3.2 Helmholtz Decomposition

Helmholtz's theorem is a very powerful mathematical tool, which helpful in the study of various problems related to wave propagation. It takes its name from a famous German physician and physicist Hermann Ludwig Ferdinand Helmholtz. This theorem, also known as the fundamental theorem of vector calculus, states that under appropriate conditions<sup>1</sup> a three-dimensional vector field  $\mathbf{u}$  can be represented as a sum of irrotational (conservative or curl-free) and solenoidal (incompressible or divergence-free) vector fields.

The irrotational part of this vector field can be expressed by the gradient of a scalar potential  $\phi$ , since the curl of any scalar field always vanishes, i.e.  $\nabla \times (\nabla\phi) = \mathbf{0}$ . On the other hand the solenoidal part of the vector field  $\mathbf{u}$  can be expressed by the curl

---

<sup>1</sup> These conditions concern the smoothness of the vector field under consideration as well as its fast decay at infinity.



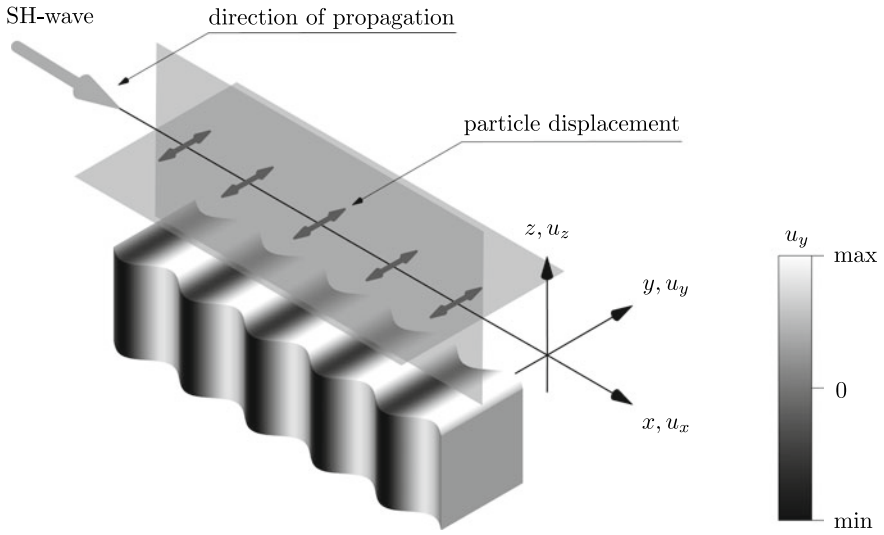


**Fig. 3.3** A schematic representation of a SH-wave propagating in a 3-D elastic space

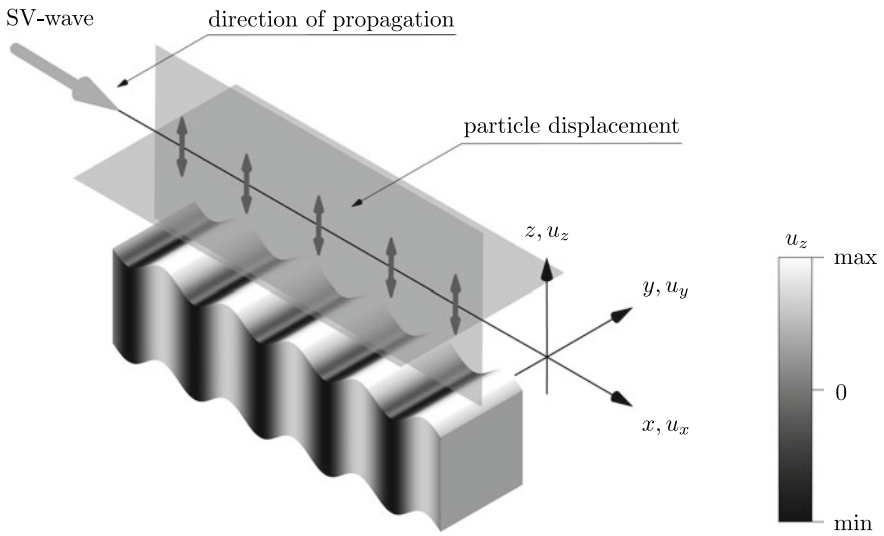


**Fig. 3.4** A schematic representation of a SV-wave propagating in a 3-D elastic space

of a vector potential  $\Psi$ , since the divergence of the curl of any vector field always vanishes, i.e.  $\nabla \cdot (\nabla \times \Psi) = 0$ .

As a result of this it can be written:

$$\mathbf{u} = \nabla\phi + \nabla \times \Psi, \quad \nabla \cdot \Psi = 0 \quad (3.18)$$

where the additional condition  $\nabla \cdot \Psi = 0$  guarantees the uniqueness of the solution.

Next, Eq. (3.18) can be simply substituted into the subsequent parts of the equation of motion, given by Eq. (3.4), in the following manner:

$$\left\{ \begin{array}{l} \nabla^2 \mathbf{u} \rightarrow \nabla^2(\nabla\phi + \nabla \times \Psi) = \nabla^2(\nabla\phi) + \nabla^2(\nabla \times \Psi) \\ \nabla \cdot \mathbf{u} \rightarrow \nabla \cdot (\nabla\phi + \nabla \times \Psi) = \nabla \cdot \nabla\phi + \underbrace{\nabla \cdot (\nabla \times \Psi)}_{=0} = \nabla^2\phi \\ \ddot{\mathbf{u}} \rightarrow \frac{\partial^2}{\partial t^2}(\nabla\phi + \nabla \times \Psi) = \nabla\ddot{\phi} + \nabla \times \ddot{\Psi} \end{array} \right. \quad (3.19)$$

Finally, by the use of the above relationships the equation of motion can be presented as:

$$\begin{aligned} \mu[\nabla^2(\nabla\phi) + \nabla^2(\nabla \times \Psi)] + (\lambda + \mu)\nabla(\nabla^2\phi) &= \rho(\nabla\ddot{\phi} + \nabla \times \ddot{\Psi}) \\ &\quad \left\{ \begin{array}{l} \nabla^2(\nabla\phi) = \nabla(\nabla^2\phi) \\ \nabla^2(\nabla \times \Psi) = \nabla \times (\nabla^2\Psi) \end{array} \right. \\ \mu[\nabla(\nabla^2\phi) + \nabla \times (\nabla^2\Psi)] + (\lambda + \mu)\nabla(\nabla^2\phi) &= \rho(\nabla\ddot{\phi} + \nabla \times \ddot{\Psi}) \quad (3.20) \\ &\quad \downarrow \text{grouping of terms} \\ \nabla[(\lambda + 2\mu)\nabla^2\phi - \rho\ddot{\phi}] + \nabla \times (\mu\nabla^2\Psi - \rho\ddot{\Psi}) &= 0 \end{aligned}$$

The resulting equation can be satisfied only if both scalar and vector equations of motion are simultaneously equal to zero. This leads to two independent wave equations. The first wave equation is a wave equation for the scalar potential  $\phi$  and describes propagation of P-waves:

$$(\lambda + 2\mu)\nabla^2\phi = \rho\ddot{\phi} \quad \text{or} \quad c_p^2\nabla^2\phi = \ddot{\phi} \quad (3.21)$$

while the second wave equation is a wave equation for the vector potential  $\Psi$  and describes propagation of S-waves:

$$\mu\nabla^2\Psi = \rho\ddot{\Psi} \quad \text{or} \quad c_s^2\nabla^2\Psi = \ddot{\Psi} \quad (3.22)$$

Indeed, it can be easily checked that if the solenoidal part of the vector field  $\mathbf{u}$  vanishes, i.e. when  $\nabla \times \boldsymbol{\Psi} = \mathbf{0}$ , the resulting Eq. (3.20) can be written as:

$$\begin{aligned}
 \nabla[(\lambda + 2\mu)\nabla^2\phi - \rho\ddot{\phi}] &= 0 \\
 \downarrow \nabla(\nabla^2\phi) &= \nabla^2(\nabla\phi) \\
 (\lambda + 2\mu)\nabla^2(\nabla\phi) - \rho(\nabla\ddot{\phi}) &= 0 \tag{3.23} \\
 \downarrow \mathbf{u} &= \nabla\phi \\
 (\lambda + 2\mu)\nabla^2\mathbf{u} - \rho\ddot{\mathbf{u}} &= 0 \quad \text{or} \quad c_p^2\nabla^2\mathbf{u} = \ddot{\mathbf{u}}
 \end{aligned}$$

In a similar manner if the irrotational part of the vector field  $\mathbf{u}$  vanishes, i.e. when  $\nabla\phi = \mathbf{0}$ , the resulting Eq. (3.21) can be written as:

$$\begin{aligned}
 \nabla \times (\mu\nabla^2\boldsymbol{\Psi} - \rho\ddot{\boldsymbol{\Psi}}) &= 0 \\
 \downarrow \nabla \times (\nabla^2\boldsymbol{\Psi}) &= \nabla^2(\nabla \times \boldsymbol{\Psi}) \\
 \mu\nabla^2(\nabla \times \boldsymbol{\Psi}) - \rho(\nabla \times \ddot{\boldsymbol{\Psi}}) &= 0 \tag{3.24} \\
 \downarrow \mathbf{u} &= \nabla \times \boldsymbol{\Psi} \\
 \mu\nabla^2\mathbf{u} - \rho\ddot{\mathbf{u}} &= 0 \quad \text{or} \quad c_s^2\nabla^2\mathbf{u} = \ddot{\mathbf{u}}
 \end{aligned}$$

The resulting equations, Eqs. (3.23) and (3.24), are two wave equations, which govern the behaviour of P-waves and S-waves. It is clear that these two types of wave are not coupled and can propagate in a 3-D elastic medium independently with no interaction.

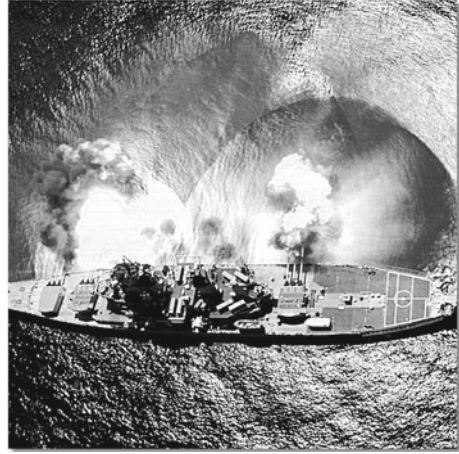
It should be emphasised that in a general case the displacement vector  $\mathbf{u}$  can be expressed by the use of the scalar potential  $\phi$  and the vector potential  $\boldsymbol{\Psi}$  in the following way<sup>2</sup>:

$$\begin{cases} u_x = \frac{\partial\phi}{\partial x} + \frac{\partial\psi_z}{\partial y} - \frac{\partial\psi_y}{\partial z} \\ u_y = \frac{\partial\phi}{\partial y} + \frac{\partial\psi_x}{\partial z} - \frac{\partial\psi_z}{\partial x} \\ u_z = \frac{\partial\phi}{\partial z} + \frac{\partial\psi_y}{\partial x} - \frac{\partial\psi_x}{\partial y} \end{cases} \tag{3.25}$$

---

<sup>2</sup> In a coordinate system different from the Cartesian coordinate system, i.e. cylindrical, spherical or others, different formulae must be used to calculate the components of the displacement vector  $\mathbf{u}$ .

**Fig. 3.5** Spherical atmospheric shock waves visible above the surface of water resulting from the USS Iowa battleship gun firing [1]



where  $\phi = \phi(x, y, z, t)$  and where  $\psi_x = \psi_x(x, y, z, t)$ ,  $\psi_y = \psi_y(x, y, z, t)$  and  $\psi_z = \psi_z(x, y, z, t)$  are appropriate components of the vector potential  $\Psi$ . The general form of the displacement vector  $\mathbf{u}$  can be simplified according to the case under consideration, as will be shown in the following paragraphs.

An interesting case represents spherical P-waves, whose propagation in a 3-D elastic medium is govern by the resulting wave equation (3.23). This kind of wave can be generated by a point source as a rapidly changing pressure or temperature, as presented in Fig. 3.5.

Since the nabla operator of differentiation is independent of the choice of the coordinate system the resulting wave equation (3.23) can be formally written in the spherical coordinate system as:

$$c_p^2 \nabla^2 u_r(r, t) = \ddot{u}_r(r, t) \tag{3.26}$$

when now the only remaining displacement component of the displacement vector  $\mathbf{u}$  is the radial displacement  $u_r$ . The radial displacement  $u_r = u_r(r, t)$  must be a function of one spatial coordinate  $r$  and time  $t$ , since the waves are purely spherical, thus independent of the polar and azimuthal angles, which is clearly seen in Fig. 3.6.

Following the solution procedure presented in Sect. 2.4 it can be written that:

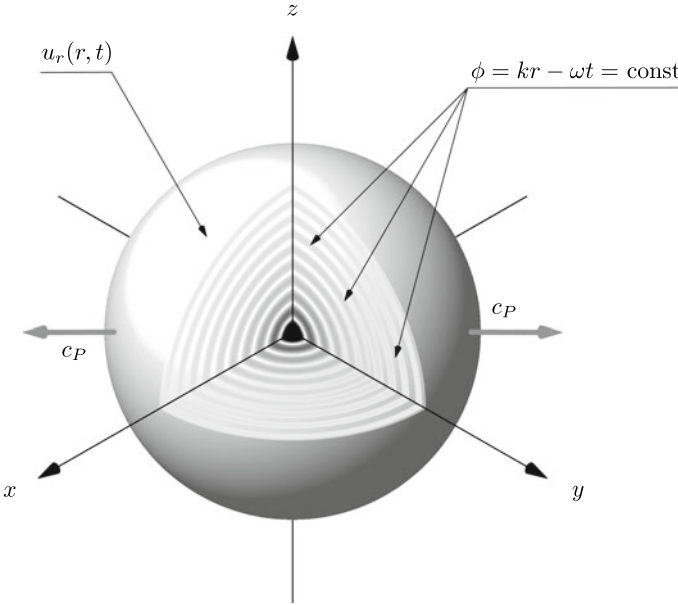


**Fig. 3.6** A schematic representation of a harmonic spherical P-wave propagating in a 3-D elastic space

$$\begin{aligned}
 c_p^2 \nabla^2 u_r(r, t) - \ddot{u}_r(r, t) &= 0 \\
 \downarrow u_r(r, t) &= R(r)e^{-i\omega t} \\
 \left[ \nabla^2 R(r) + \frac{\omega^2}{c_p^2} R(r) \right] e^{-i\omega t} &= 0 \tag{3.27} \\
 \downarrow \nabla^2 R(r) &= \frac{1}{r^2} \frac{d}{dr} \left[ r^2 \frac{dR(r)}{dr} \right] \\
 \left[ r^2 \frac{d^2 R(r)}{dr^2} + 2r \frac{dR(r)}{dr} + (kr)^2 R(r) \right] e^{-i\omega t} &= 0
 \end{aligned}$$

which is satisfied for any moment in time  $t$  only if the expression within the brackets is satisfied:

$$r^2 \frac{d^2 R(r)}{dr^2} + 2r \frac{dR(r)}{dr} + (kr)^2 R(r) = 0 \tag{3.28}$$

and where  $k = \omega/c_p$  is the wave number.

Equation (3.28) represents in fact the radial part of the Helmholtz equation<sup>3</sup> in spherical coordinates. This equation has the following general form:

$$x^2 \frac{d^2 y(x)}{dx^2} + 2x \frac{dy(x)}{dx} + [x^2 - n(n+1)]y(x) = 0 \quad (3.29)$$

which has two linearly independent solutions known as the spherical Bessel functions  $j_n(x)$  and  $y_n(x)$ .

By the use of Rayleigh's formulae the spherical Bessel functions  $j_n(x)$  and  $y_n(x)$  can be presented as:

$$\begin{cases} j_n(x) = (-1)^n x^n \left( \frac{1}{x} \frac{d}{dx} \right)^n \frac{\sin x}{x} \\ y_n(x) = (-1)^{n+1} x^n \left( \frac{1}{x} \frac{d}{dx} \right)^n \frac{\cos x}{x} \end{cases}, \quad n = 0, 1, 2, \dots \quad (3.30)$$

It can be clearly seen that the wave equation given by Eq. (3.28) is identical to Eq. (3.29) when  $n = 0$  and  $x = kr$ . However, since the spherical Bessel function  $y_0(kr)$  is singular at the origin at  $r = 0$ , this particular solution must be disregarded. This leads to a solution to the equation of motion in the following two simple steps.

First of all it can be noted that now:

$$R(r) = A j_0(kr) = A \frac{\sin kr}{kr} = \text{Im} \left[ A \frac{e^{ikr}}{kr} \right] \quad (3.31)$$

where  $\mathcal{A}$  is a certain constant.

Next, the spatial solution  $R(r)$  must be combined with the harmonic factor to produce:

$$u_r(r, t) = R(r)e^{-i\omega t} = A \frac{e^{i(kr - \omega t)}}{kr} = A \frac{e^{ik(r - ct)}}{kr} \quad (3.32)$$

where the symbol  $\text{Im}[\bullet]$ , denoting the imaginary part of a complex expression  $[\bullet]$ , is omitted in Eq. (3.32) in order to simplify the notation.

The solution obtained, in the form of Eq. (3.32), provides some interesting information about the behaviour of spherical P-waves in a 3-D elastic space. Firstly, it should be noted that the amplitudes of P-waves decrease with the distance travelled and they are proportional to the inverse of the distance, i.e.  $\propto 1/r$ . Secondly, since the energy carried by these waves is proportional to the square of their amplitudes, this energy also decreases with the distance, but this decrease is proportional to the inverse of the square of the distance, i.e.  $\propto 1/r^2$ . Thus in a distance far away from

---

<sup>3</sup> The Helmholtz equation, which describes the process of diffusion or wave propagation, presents the eigenvalue problem for the Laplace operator, i.e.  $\nabla^2 \phi = -k^2 \phi$ , and is an important equation in many fields of science.

a source the amplitude and energy carried by spherical P-waves must tend to zero. This conforms with *the Sommerfeld radiation condition* [2].

### 3.3 Christoffel Equation

A very important aspect of wave motion in a 3-D elastic medium is wave propagation in an anisotropic material. Many engineering materials exhibit material properties that depend on the direction of observation, which is just anisotropy, as can be seen in Figs. 3.7 and 3.8. This kind of behaviour is typical for crystals, but is not limited to crystalline materials. Such modern materials as composites and laminates also exhibit similar properties. An increasing interest in the investigation of their properties results in the fact that composites and laminates are more and more often used as structural materials in many fields of modern mechanical and civil engineering. However, their application is not strictly limited to these two branches of engineering.

It can be noted that waves propagating in a 3-D anisotropic elastic medium can also be described by the same Newton's law, as given by Eq. (3.1). However, in the case of anisotropy, it can be conveniently presented using tensor index notation:

$$\sigma_{ij,j} + f_i = \rho \ddot{u}_i, \quad i, j = 1, 2, 3 \quad (3.33)$$

where the symbol  $(\bullet)_{,i}$  represents differentiation  $\partial(\bullet)/\partial x_i$  with respect to spatial coordinates, which now are represented by  $x_1, x_2$  and  $x_3$ .

Also in this case Eq.(3.33) must be supplemented with the same strain-displacement relationship and the constitutive equation. In contrast to isotropy, this time the fourth-order stiffness tensor  $\mathbf{C}$  must have a different form. Using the same

**Fig. 3.7** The most common natural anisotropic (orthotropic) engineering material used nowadays still remains wood [3]



**Fig. 3.8** Anisotropy is naturally observed in crystalline solids like pyrites [4]



tensor index notation the strain-displacement relationship, together with the stress-strain relationship governed by Hooke's law, can be written as:

$$\begin{cases} \sigma_{ij} = C_{ijrs}\epsilon_{rs}, & i, j, r, s = 1, 2, 3 \\ \epsilon_{rs} = \frac{1}{2}(u_{r,s} + u_{s,r}), & r, s = 1, 2, 3 \end{cases} \quad (3.34)$$

The stress-strain relationship represents equations linking together six stress components with six strain components. The symmetry of the stress tensor  $\sigma_{ij} = \sigma_{ji}$ , as well as the symmetry of the strain tensors  $\epsilon_{rs} = \epsilon_{rs}$ , called the minor symmetries, plus the major symmetry resulting from the uniqueness of the strain energy and its differentiation, require that the stiffness tensor  $C_{ijrs}$  is also symmetric, i.e. that:

$$C_{ijrs} = C_{jirs} = C_{ijsr} = C_{rsij}, \quad i, j, r, s = 1, 2, 3 \quad (3.35)$$

which effectively reduces the number of independent elastic constants of the stiffness tensor  $C_{ijrs}$  from 81 down to 21.

Under the assumption of material orthotropy this number can be further reduced—see Appendix A. In the case of material orthotropy there are 9 independent elastic constants in the stiffness tensor  $C_{ijrs}$ , while for materials exhibiting transverse isotropy this number drops down to 5.

Exactly as in Eq. (3.1), also in this case acting body forces  $f_i$  can be formally neglected, since wave motion in elastic media is driven by recoverable elastic forces. Thus, the resulting equation of motion takes the following form:

$$\frac{1}{2}C_{ijrs}\epsilon_{rs,j} = \rho\ddot{u}_i, \quad i, j, r, s = 1, 2, 3 \quad (3.36)$$



or after using the definition of strains  $\epsilon_{rs}$  from Eq. (3.34) as:

$$\frac{1}{2}C_{ijrs}(u_{r,j_s} + u_{s,j_r}) = \rho\ddot{u}_i, \quad i, j, r, s = 1, 2, 3 \quad (3.37)$$

Now, it is convenient to consider propagation of a plane harmonic wave  $\mathbf{u}$  in 3-D space, which can be assumed to have the same form as in Eq. (3.6), but expressed using index notation as:

$$u_i = \hat{u}_i e^{k_j x_j - \omega t} \quad i, j = 1, 2, 3 \quad (3.38)$$

which after substitution to Eq. (3.37) and necessary differentiation leads to:

$$C_{ijrs}k_j k_r u_s - \rho\omega^2 u_i = 0, \quad i, j, r, s = 1, 2, 3 \quad (3.39)$$

It should be noted that by the use of the Kronecker delta the displacement  $u_i$  can be expressed as  $u_i = \delta_{is}u_s$ . This helps to rewrite Eq. (3.39) in a modified form:

$$(C_{ijrs}k_j k_r - \rho\omega^2 \delta_{is})u_s = 0, \quad i, j, r, s = 1, 2, 3 \quad (3.40)$$

which now represents the famous Christoffel equation for a 3-D anisotropic medium.

Moreover, the Christoffel acoustic tensor  $\Gamma_{is}$  can be defined based on the following simple relationship:

$$\Gamma_{is} = C_{ijrs}n_j n_r, \quad i, j, r, s = 1, 2, 3 \quad (3.41)$$

where  $n_j$  denotes the direction cosines, i.e.  $n_j = \cos \beta_j$ , which allows one to express the wave vector components as  $k_j = |\mathbf{k}|n_j$ . This leads to the following equation:

$$(\Gamma_{is}|\mathbf{k}|^2 - \rho\omega^2 \delta_{is})u_s = 0 \quad \text{or} \quad (\Gamma_{is} - \rho c^2 \delta_{is})u_s = 0, \quad i, s = 1, 2, 3 \quad (3.42)$$

which in fact is a set of three homogeneous equations.

As before, non-trivial solutions to Eq. (3.42) can be obtained only if its determinant vanishes, i.e. when:

$$|\Gamma_{is} - \rho c^2 \delta_{is}| = 0, \quad i, s = 1, 2, 3 \quad (3.43)$$

which results in three different wave propagation velocities.

This time, however, their values are dependent on the directions of observation due to the definition of the acoustic tensor  $\Gamma_{is} = C_{ijrs}n_j n_r$ , with  $n_j$  defining these directions. Different observation directions may be associated with different values of the direction cosines  $n_j$ . In each such case the acoustic tensor  $\Gamma_{is}$  must be evaluated. For example, in the case of the element  $\Gamma_{11}$  we can write that:

$$\Gamma_{11} = C_{1jr1}, \quad j, r = 1, 2, 3 \quad (3.44)$$

**Table 3.1** Index conversion from tensor to Voigt notation

$ij$ or $rs$	11	22	33	23, 32	31, 13	12, 21
↓	↓	↓	↓	↓	↓	↓
$p$ or $q$	1	2	3	4	5	6

which after necessary expansion takes the following form:

$$\begin{aligned}
 \Gamma_{11} = & C_{1111}n_1n_1 + C_{1211}n_2n_1 + C_{1311}n_3n_1 \\
 & + C_{1121}n_1n_2 + C_{1221}n_2n_2 + C_{1321}n_3n_2 \\
 & + C_{1131}n_1n_3 + C_{1231}n_2n_3 + C_{1331}n_3n_3
 \end{aligned} \tag{3.45}$$

It turns out that in many practical applications the use of the stiffness tensor  $C_{ijrs}$ , expressed by tensor index notation, in which  $i, j, r, s = 1, 2, 3$ , is very complicated. In order to simplify this Voigt matrix notation can be used instead, in which  $ij$  and  $rs$  indexes are replaced by two independent indexes  $p$  and  $q$ , and where  $p, q = 1, \dots, 6$ , as shown in [5]. Such index transformation, from tensor to Voigt notation, is presented in Table 3.1.

The Voigt notation helps to present the original stiffness tensor  $C_{ijrs}$ , defined as:

$$\mathbf{C} = \begin{bmatrix} C_{1111} & C_{1122} & C_{1133} & C_{1123} & C_{1131} & C_{1112} \\ & C_{2222} & C_{2233} & C_{2223} & C_{2231} & C_{2212} \\ & & C_{3333} & C_{3323} & C_{3331} & C_{3312} \\ & & & C_{2323} & C_{2331} & C_{2312} \\ & & & & C_{3131} & C_{3112} \\ \text{symm.} & & & & & C_{1212} \end{bmatrix} \tag{3.46}$$

in a much simplified manner. Now a new stiffness tensor  $C_{pq}$  has the following general form:

$$\mathbf{C} = \begin{bmatrix} C_{11} & C_{12} & C_{13} & C_{14} & C_{15} & C_{16} \\ & C_{22} & C_{23} & C_{24} & C_{25} & C_{26} \\ & & C_{33} & C_{34} & C_{35} & C_{36} \\ & & & C_{44} & C_{45} & C_{46} \\ & & & & C_{55} & C_{56} \\ \text{symm.} & & & & & C_{66} \end{bmatrix} \tag{3.47}$$

which is much more preferred computationally.

As a result of this the element  $\Gamma_{11}$ , previously expressed by Eq. (3.45), now can be presented as:

$$\begin{aligned}
 \Gamma_{11} = & C_{11}n_1^2 + C_{16}n_2n_1 + C_{15}n_3n_1 \\
 & + C_{16}n_1n_2 + C_{66}n_2^2 + C_{56}n_3n_2 \\
 & + C_{15}n_1n_3 + C_{65}n_2n_3 + C_{55}n_3^2
 \end{aligned} \tag{3.48}$$

In specific cases, when particular directions of observation are not coupled in the acoustic tensor  $\Gamma_{is}$ , as is in the case of full material isotropy, pure and fully decoupled P-waves and S-waves can be obtained. In other cases quasi P-waves and quasi S-waves [6] are obtained. Nevertheless, full information about the dependence of the phase velocities of particular wave modes on the directions of observations, calculated based on the characteristic equation (3.43), requires complex and repeated computations.

## References

1. P. J. A. Elliot. *Shock wave*. [http://www.wikiwand.com/en/shock\\_wave](http://www.wikiwand.com/en/shock_wave), 1984. Visited on 09/12/2023.
2. A. Sommerfeld. *Partial differential equations in physics*. Academic Press, New York, 1949.
3. <http://pixabay.com/pl/photos/sloje-drzewo-drewno-tekstura-tlo-3212803>, 2018. Visited on 09/12/2023.
4. <http://pixabay.com/pl/photos/piryt-krysztal-natura-173716>, 2013. Visited on 09/12/2023.
5. V. Giurgiutiu. *Structural health monitoring of aerospace composites*. Academic Press, Oxford, 2016.
6. J. L. Rose. *Ultrasonic waves in solid media*. Cambridge University Press, Cambridge, 1999.

# Chapter 4

## Surface Waves



### 4.1 Rayleigh Waves

Rayleigh surface waves take their name after Lord Rayleigh, who in 1885 predicted their existence. Rayleigh waves belong to the class of elastic waves, as shown in Fig. 1.5 in *Introduction*, which can propagate near the surface of elastic solids, and having the property that their amplitudes decrease gradually with the depth. In nature Rayleigh surface waves accompany earthquakes, which in geology are very frequent events<sup>1</sup> and their destructive power comes from high amplitudes of ground movements measured even in meters [1], as seen in Fig. 4.1.

Rayleigh surface waves can be studied mathematically starting from the equation of motion, given by Eqs. (3.5), under an additional assumption about the form of the displacement components  $u_x$ ,  $u_y$  and  $u_z$ , which are assumed to be functions of the spatial coordinates  $x$ ,  $z$  and time  $t$ . The form of the displacement field, as proposed by Rayleigh, requires that the displacement components of a plane harmonic wave  $\mathbf{u}$  propagating in a 3-D elastic half-space must vanish asymptotically with  $z$ . In the current case, for  $z \leq 0$ , it can be written that:

$$\begin{cases} u_x(x, z, t) = \hat{u}_x e^{\alpha z} e^{ik(x-ct)} \\ u_y(x, z, t) = \hat{u}_y e^{\alpha z} e^{ik(x-ct)} \\ u_z(x, z, t) = \hat{u}_z e^{\alpha z} e^{ik(x-ct)} \end{cases} \quad (4.1)$$

---

<sup>1</sup> It is estimated by the National Earthquake Information Center (NEIC) that the number of earthquakes recorded every year around the world is near 20,000. The total number of earthquakes, including not recordable events, can be much higher reaching millions.

**Fig. 4.1** The effect of earthquake on house buildings after the San Francisco earthquake of 1906 [2]



where  $\alpha$  is a certain positive constant,  $k$  is the wave number, while  $c$  denotes the phase velocity<sup>2</sup> of a Rayleigh surface wave propagating in the direction of the  $x$  axis.

It is clearly seen from Eqs. (4.1) that indeed all displacement components  $u_x$ ,  $u_y$  and  $u_z$  vanish with  $z \rightarrow -\infty$ . Substitution of Eqs. (4.1) into Eqs. (3.5) leads to a system of three homogeneous equations:

$$\begin{cases} [\alpha^2 c_s^2 + k^2(c^2 - c_p^2)]\hat{u}_x + i\alpha k(c_p^2 - c_s^2)\hat{u}_z = 0 \\ [\alpha^2 c_s^2 + k^2(c^2 - c_s^2)]\hat{u}_y = 0 \\ i\alpha k(c_p^2 - c_s^2)\hat{u}_x + [\alpha^2 c_p^2 + k^2(c^2 - c_s^2)]\hat{u}_z = 0 \end{cases} \quad (4.2)$$

It can be noted from Eqs. (4.2) that the amplitude  $\hat{u}_y$  is equal to zero. Thus, the displacement component  $u_y$  is also equal to zero. The remaining system of two homogeneous equations has non-trivial solutions only if its determinant vanishes. This leads to the following characteristic equation:

$$[\alpha^2 c_p^2 + k^2(c^2 - c_p^2)][\alpha^2 c_s^2 + k^2(c^2 - c_s^2)] = 0 \quad (4.3)$$

The characteristic equation, given by Eq. (4.3), has two independent solutions  $\alpha_1$  and  $\alpha_2$ , which can be presented in the following manner:

---

<sup>2</sup> In order to avoid unnecessary confusion from this point on, wherever it is necessary, the phase velocity  $c_p$  is simply noted as  $c$  to distinguish it clearly from the velocity of primary waves  $c_p$ .

$$\alpha_1 = k\sqrt{1 - \frac{c^2}{c_p^2}}, \quad \alpha_2 = k\sqrt{1 - \frac{c^2}{c_s^2}} \quad (4.4)$$

bearing in mind that  $\alpha$  must be positive, i.e.  $\alpha \geq 0$ . This conditions holds only if  $c \leq c_s \leq c_p$ .

Substitution of  $\alpha = \alpha_1$  or  $\alpha = \alpha_2$  into the first or last equation in Eqs. (4.2) leads to the following relationships between the amplitudes of the non-zero displacement components  $\hat{u}_x$  and  $\hat{u}_z$ :

$$\left. \frac{\hat{u}_z}{\hat{u}_x} \right|_{\alpha_1} = \frac{\alpha_1}{ik} \quad \text{or} \quad \left. \frac{\hat{u}_z}{\hat{u}_x} \right|_{\alpha_2} = \frac{k}{i\alpha_2} \quad (4.5)$$

This allows one to express the solution to the equation of motion, given by Eqs. (3.5), as a linear combination of two particular solutions associated with each of the roots  $\alpha_1$  or  $\alpha_2$  as:

$$\begin{cases} u_x(x, z, t) = (\hat{u}_x|_{\alpha_1} e^{\alpha_1 z} + \hat{u}_x|_{\alpha_2} e^{\alpha_2 z}) e^{ik(x-ct)} \\ u_z(x, z, t) = (\hat{u}_z|_{\alpha_1} e^{\alpha_1 z} + \hat{u}_z|_{\alpha_2} e^{\alpha_2 z}) e^{ik(x-ct)} \end{cases}$$

$$\left\{ \begin{array}{l} \hat{u}_z|_{\alpha_1} = \frac{\alpha_1}{ik} \hat{u}_x|_{\alpha_1}, \quad \hat{u}_z|_{\alpha_2} = \frac{k}{i\alpha_2} \hat{u}_x|_{\alpha_2} \end{array} \right. \quad (4.6)$$

$$\begin{cases} u_x(x, z, t) = (\hat{u}_x|_{\alpha_1} e^{\alpha_1 z} + \hat{u}_x|_{\alpha_2} e^{\alpha_2 z}) e^{ik(x-ct)} \\ u_z(x, z, t) = \left( \frac{\alpha_1}{ik} \hat{u}_x|_{\alpha_1} e^{\alpha_1 z} + \frac{k}{i\alpha_2} \hat{u}_x|_{\alpha_2} e^{\alpha_2 z} \right) e^{ik(x-ct)} \end{cases}$$

Expressing the amplitudes  $\hat{u}_x|_{\alpha_1}$  and  $\hat{u}_x|_{\alpha_2}$  by certain new constants  $A_1$  and  $A_2$ , defined as  $\hat{u}_x|_{\alpha_1} = ikA_1$  and  $\hat{u}_x|_{\alpha_2} = i\alpha_2 A_2$ , enables one to present the final solution to the equation of motion, governing the propagation of Rayleigh surface waves in a 3-D elastic half-space, in the following manner:

$$\begin{cases} u_x(x, z, t) = i(A_1 k e^{\alpha_1 z} + A_2 \alpha_2 e^{\alpha_2 z}) e^{ik(x-ct)} \\ u_z(x, z, t) = (A_1 \alpha_1 e^{\alpha_1 z} + A_2 k e^{\alpha_2 z}) e^{ik(x-ct)} \end{cases} \quad (4.7)$$

The dispersion relation for Rayleigh surface waves can be easily obtained by the use of Eqs. (4.7) assuming that the free surface of a 3-D elastic half-space remains free of stresses. This is expressed by the traction-free boundary conditions,<sup>3</sup> which leads to the following conditions for particular stress components at the free surface, i.e. at  $z = 0$ :

<sup>3</sup> The traction-free boundary conditions states that the traction vector  $\mathbf{T}$  vanishes on the free surface of an elastic body, i.e.  $\mathbf{T} = \boldsymbol{\sigma} \cdot \mathbf{n}$  is equal to  $\mathbf{0}$ , where  $\mathbf{n}$  is the normal vector to the free surface of the body.

$$\sigma_{zz}(x, z, t) = \tau_{xz}(x, z, t) = \tau_{yz}(x, z, t) = 0, \quad \text{for } z = 0 \quad (4.8)$$

The stress component  $\tau_{yz}$  is always equal to zero, as seen from Eqs. (4.7), while the remaining stress components  $\sigma_{zz}$  and  $\tau_{xz}$  can be expressed by the use of Hooke's law as:

$$\begin{cases} \sigma_{zz} = 2\mu\epsilon_{zz} + \lambda(\epsilon_{xx} + \epsilon_{zz}) \\ \tau_{xz} = \mu\gamma_{xz} \end{cases} \quad (4.9)$$

knowing that the strain components  $\epsilon_{xx}$ ,  $\epsilon_{zz}$  and  $\gamma_{xz}$  can be easily expressed by the use of Eqs. (4.7) as follows:

$$\begin{cases} \epsilon_{xx} = \frac{\partial u_x}{\partial x} = -k(A_1k + A_2\alpha_2)e^{ik(x-ct)} \\ \epsilon_{zz} = \frac{\partial u_z}{\partial z} = (A_1\alpha_1^2 + A_2k\alpha_2)e^{ik(x-ct)} \\ \gamma_{xz} = \frac{\partial u_x}{\partial z} + \frac{\partial u_z}{\partial x} = i[2A_1k\alpha_1 + A_2(k^2 + \alpha_2^2)]e^{ik(x-ct)} \end{cases} \quad (4.10)$$

Again, this leads to a system of two homogeneous equations, which after necessary simplifications take the form:

$$\begin{cases} [(\lambda + 2\mu)\alpha_1^2 - \lambda k^2]A_1 + 2\mu k\alpha_2 A_2 = 0 \\ 2\mu k\alpha_1 A_1 + \mu(k^2 + \alpha_2^2)A_2 = 0 \end{cases} \quad (4.11)$$

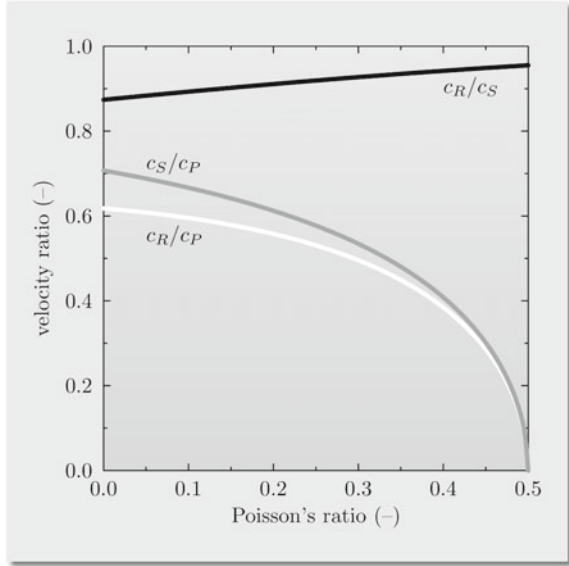
where the factor  $e^{ik(x-ct)}$  is not present, as the system of homogeneous equations Eqs. (4.11) must be satisfied for propagating Rayleigh surface waves independently of the spatial coordinate  $x$  and time  $t$ .

As before, the system of homogeneous equations Eqs. (4.11) has non-trivial solutions only if its determinant vanishes. This leads to the characteristic equation for the phase velocity  $c$  of Rayleigh surface waves, which after necessary simplifications and rearrangements of terms can be presented simply as:

$$\left(2 - \frac{c^2}{c_s^2}\right)^2 - 4\sqrt{1 - \frac{c^2}{c_p^2}}\sqrt{1 - \frac{c^2}{c_s^2}} = 0 \quad (4.12)$$

It should be mentioned that this characteristic equation is dependent only on material properties of a 3-D elastic half-space, through the phase velocities  $c_p$  and  $c_s$ , of longitudinal P-waves and shear S-waves, respectively. On the other hand it remains independent of the wave number  $k$  and/or angular velocity  $\omega$ . As a result of this Rayleigh surface waves are non-dispersive, so their shape remains unchanged during their propagation.

**Fig. 4.2** The effect of Poisson’s ratio on the phase velocity of Rayleigh surface waves in relation to the phase velocities of S-waves and P-waves. A curve for the phase velocity of S-waves in relation to the phase velocity of P-waves is also presented [3]



The characteristic equation (4.12) can be easily solved numerically. It is convenient to introduce a new variable  $\zeta = c/c_S$  and to express the phase velocities  $c_P$  and  $c_S$  directly by Young’s modulus  $E$ , Poisson’s ratio  $\nu$  and material density  $\rho$ . Then it can be found that the characteristic equation (4.12), after necessary mathematical manipulations, can be presented as:

$$\zeta^4 - 4\zeta^2 + 4 - 4\sqrt{1 - \zeta^2}\sqrt{1 - \beta\zeta^2}, \quad \beta = \frac{1 - 2\nu}{2 - 2\nu} \tag{4.13}$$

A solution to Eq. (4.13) is shown in Fig. 4.2 as a function of Poisson’s ratio  $\nu$ . It is expressed as the ratio  $c_R/c_S$ , where now  $c_R$  denotes the phase velocity of Rayleigh surface waves. Additionally, in this graph results corresponding to the ratios  $c_R/c_P$  and  $c_S/c_P$  are presented.

In the case of Rayleigh surface waves it is interesting to observe the wave motion associated with their propagation. Based on the second equation from Eqs. (4.11) it can be found that the amplitude ratio  $A_1/A_2$  can be conveniently presented as:

$$\frac{A_2}{A_1} = -\frac{2k\alpha_1}{k^2 + \alpha_2^2} \tag{4.14}$$

which helps to express the solution to the equation of motion given by Eqs. (4.7) in a modified form:



$$\begin{cases} u_x(x, z, t) = ikA_1 \left( e^{\alpha_1 z} - \frac{\alpha_1 \alpha_2}{k^2 + \alpha_2^2} e^{\alpha_2 z} \right) e^{ik(x-ct)} \\ u_z(x, z, t) = \alpha_1 A_1 \left( e^{\alpha_1 z} - \frac{k^2}{k^2 + \alpha_2^2} e^{\alpha_2 z} \right) e^{ik(x-ct)} \end{cases} \quad (4.15)$$

Bearing in mind that the physical meaning has only the real part of the solution to the equation of motion, Eqs. (4.15) can be formally rewritten in the following manner:

$$\begin{cases} u_x(x, z, t) = -kA_1 \left( e^{\alpha_1 z} - \frac{\alpha_1 \alpha_2}{k^2 + \alpha_2^2} e^{\alpha_2 z} \right) \sin[k(x-ct)] \\ u_z(x, z, t) = \alpha_1 A_1 \left( e^{\alpha_1 z} - \frac{k^2}{k^2 + \alpha_2^2} e^{\alpha_2 z} \right) \cos[k(x-ct)] \end{cases} \quad (4.16)$$

Application of the well-known trigonometric identity to the non-zero components of the displacements  $u_x$  and  $u_z$  allows one to find that:

$$\frac{u_x^2(x, z, t)}{A^2(z)} + \frac{u_z^2(x, z, t)}{B^2(z)} = 1 \quad (4.17)$$

which indicates that the displacement vector  $\mathbf{u} = [u_x, 0, u_z]$  moves along a certain ellipse, which exponentially decreases its dimensions with the depth  $z$  and where:

$$\begin{cases} A(z) = kA_1 \left( e^{\alpha_1 z} - \frac{\alpha_1 \alpha_2}{k^2 + \alpha_2^2} e^{\alpha_2 z} \right) \\ B(z) = \alpha_1 A_1 \left( e^{\alpha_1 z} - \frac{k^2}{k^2 + \alpha_2^2} e^{\alpha_2 z} \right) \end{cases} \quad (4.18)$$

Based on Eqs. (4.16) it is noteworthy that Rayleigh surface waves, which are schematically presented in Fig.4.3, can be understood as a superposition of two independent waves: one being a longitudinal wave propagating along the  $x$  axis, the other being a transverse wave propagating along the  $z$  axis.

The amplitudes of these waves are characterised by exponential attenuation with the depth  $z$ , as clearly seen from Eqs. (4.18) and shown in Fig.4.4. It is obvious that although Rayleigh surface waves are non-dispersive and propagate with a constant velocity  $c_R$ , the amplitudes of their components  $u_x$  and  $u_z$  must be frequency/wavelength dependent through  $\alpha_1$  and  $\alpha_2$ .

The depth of full attenuation of Rayleigh surfaces waves is linearly dependent on the wavelength  $\lambda$ , thus longer waves are characterised by slower attenuation and deeper penetration of the medium than shorter waves. The dependence on the frequency  $f$  is inverse and waves of higher frequencies are characterised by faster attenuation and shallower penetration of the medium than waves of lower frequencies.

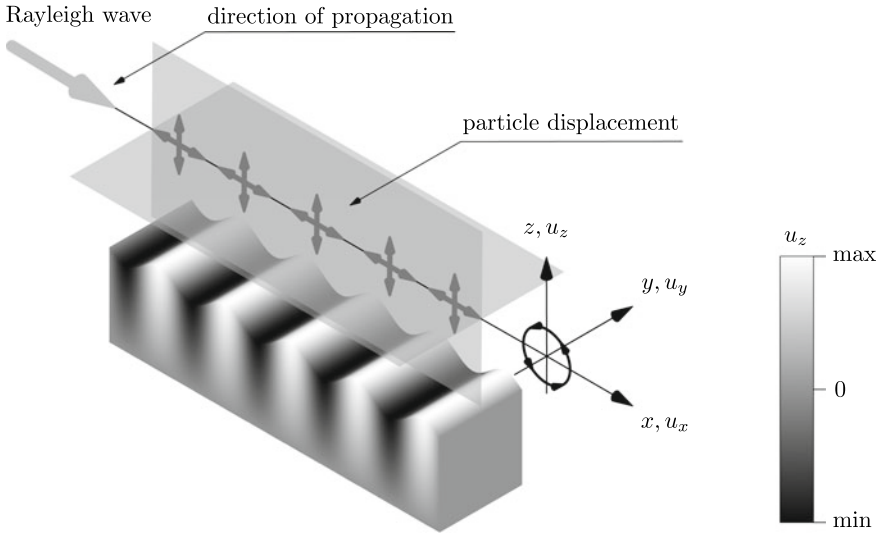


**Fig. 4.3** A schematic representation of a Rayleigh surface wave propagating in a 3-D elastic half-space

**Fig. 4.4** Relative displacement amplitudes of Rayleigh surface waves propagating in aluminium as a function of depth  $z$ , for various frequencies  $f$  of the waves

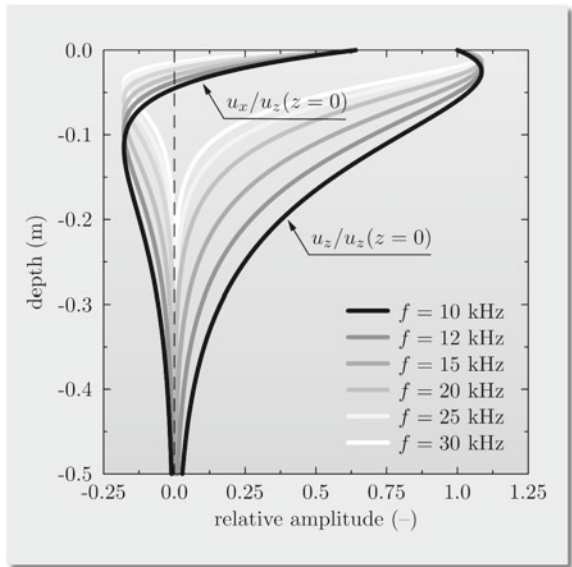
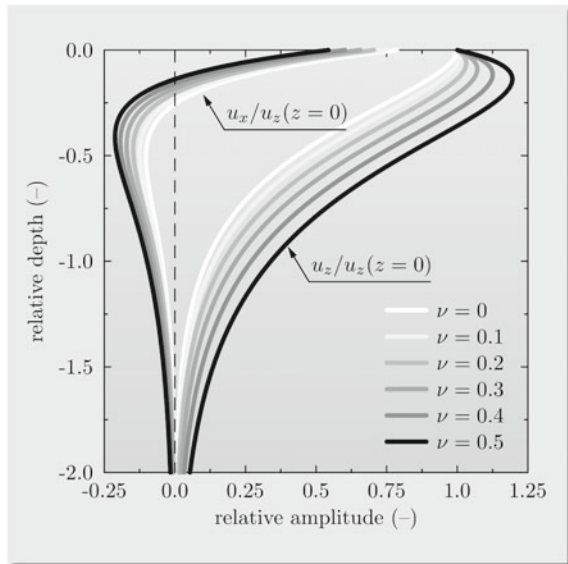


**Table 4.1** Relative displacement amplitudes of Rayleigh surface waves propagating in a 3-D elastic half-space at selected relative depths  $z/\lambda$ , for various materials

Relative depth/material	Aluminium		Steel		Tungsten	
$z/\lambda$ (-)	$\hat{u}_x$ (-)	$\hat{u}_z$ (-)	$\hat{u}_x$ (-)	$\hat{u}_z$ (-)	$\hat{u}_x$ (-)	$\hat{u}_z$ (-)
0	0.640	1.000	0.700	1.000	0.670	1.000
-1	-0.080	0.231	-0.066	0.177	-0.074	0.207
-2	-0.009	0.024	-0.006	0.014	-0.007	0.019
-3	-0.001	0.002	0.000	0.001	-0.001	0.002

$$\hat{u}_x = u_x(z)/u_x(z=0), \hat{u}_z = u_z(z)/u_z(z=0)$$

**Fig. 4.5** Relative displacement amplitudes of Rayleigh surface waves propagating in a 3-D elastic half-space as a function of the relative depth  $z/\lambda$ , for various values of Poisson’s ratio



The linear dependence of the attenuation of Rayleigh surface waves on the wavelength  $\lambda$  allows one to conveniently present their distribution along the  $z$  axis as relative to the wavelength  $\lambda$ , i.e. as  $z/\lambda$ , as shown in Table 4.1. The amplitude profiles obtained in this manner become frequency independent, as presented in Fig. 4.5.

Moreover, it is clearly seen from Table 4.1 and Fig. 4.5 that the amplitude profiles of Rayleigh surface waves propagating within 3-D elastic half-space are well confined to the near surface of the medium and practically their depth of penetration does not exceed twice their wavelengths. It is also evident that their depth of full attenuation remains independent of Poisson’s ratio.

## 4.2 Love Waves

Another type of surface waves is Love waves. They are named after Augustus Edward Hough Love, who mathematically proved their existence in 1911. Together with Rayleigh surface waves, Love waves represent surface elastic waves, as shown in Fig. 1.5 in *Chap. 1*. In a similar manner to the case of Rayleigh waves, their amplitudes also decrease gradually with the depth, however unlike Rayleigh surface waves, Love waves are polarised horizontally. In nature they too accompany earthquakes leading to relative horizontal movements of earth masses, which very often have devastating consequences, as presented in Fig. 4.6.

The mathematical description of Love surface waves may start at the very same point as the description of Rayleigh surface waves, which is the equation of motion given by Eqs. (3.5). However, in the current case, due to the horizontal polarization of Rayleigh surface waves, it must be assumed that the form of the displacement components  $u_x$ ,  $u_y$  and  $u_z$  is different. The nature of these waves requires that the displacement components  $u_x$  and  $u_z$  must vanish, i.e.  $u_x = u_z = 0$ , and the only non-zero displacement component is  $u_y$ , which remains only a function of the spatial coordinate  $x$  and time  $t$ . Also in this case the form of the displacement field requires that the displacement component  $u_y$ , representing a plane harmonic wave  $\mathbf{u}$  propagating in a 3-D elastic half-space, must vanish asymptotically with  $z$ , as seen in Fig. 4.7. For  $z \leq 0$  it can be written that:

$$u_y(x, z, t) = \hat{u}_y e^{\alpha z} e^{ik(x-ct)} \quad (4.19)$$

**Fig. 4.6** Twisted rails near Whittier as a result earth movements during the Alaska earthquake of 1964 [4]



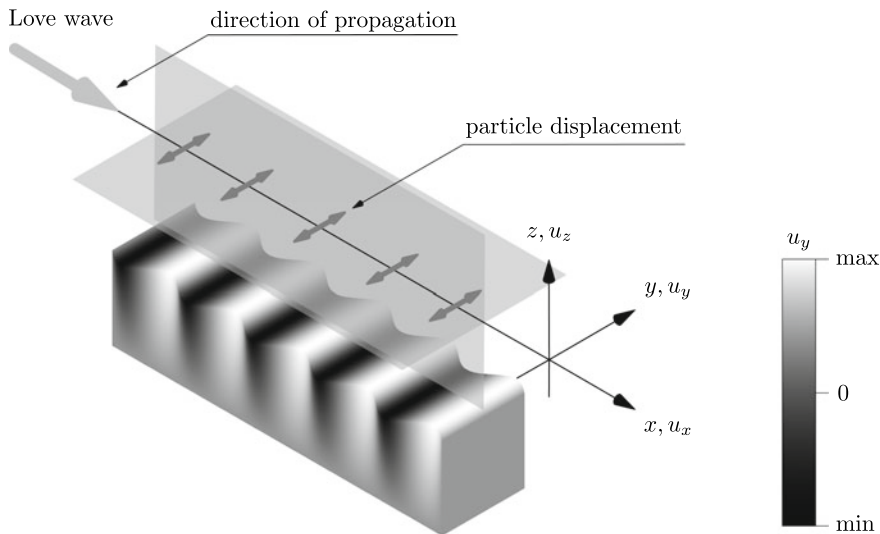


**Fig. 4.7** A schematic representation of a Love surface wave propagating in a 3-D elastic half-space

where  $\alpha$  is a certain positive constant,  $k$  is the wave number, while  $c$  denotes the phase velocity of the Love surface wave propagating in the direction of the  $x$  axis.

Substitution of Eqs. (4.19) into Eqs. (3.5), or even better to the resulting equation from Eqs. (3.24), leads to a simple relationship:

$$[\alpha^2 c_s^2 + k^2(c^2 - c_s^2)]\hat{u}_y = 0 \quad (4.20)$$

This relationship will be satisfied for non-zero amplitudes  $\hat{u}_y$  of the displacement component  $u_y$  only if the characteristic equation is always equal to zero, i.e. when:

$$\alpha^2 c_s^2 + k^2(c^2 - c_s^2) = 0 \quad (4.21)$$

which, under assumptions made, has only one solution in the following form:

$$\alpha = k \sqrt{1 - \frac{c^2}{c_s^2}} \quad (4.22)$$

It can be immediately found that the traction-free boundary conditions for Love surface waves, expressed by the only stress component  $\tau_{yz}$  at the free surface, i.e. at  $z = 0$ , requires that either the amplitude  $\hat{u}_y$  or  $\alpha$  must vanish, since:

$$\tau_{yz}(x, z, t) = \mu \frac{\partial u_y}{\partial z} = \mu \alpha \hat{u}_y e^{ik(x-ct)} \quad (4.23)$$

None of these cases lead to the propagation of Love surface waves. This suggests that in contrast to Rayleigh surface waves Love surface waves cannot propagate in a 3-D elastic half-space as long as the elastic space remains homogeneous.

This problem, as suggested by Love, can be overcome by an additional assumption. Under this assumption the 3-D elastic half-space is covered by an additional material layer of different properties from the properties of the 3-D elastic half-space. Thus, initially a problem of the propagation of horizontal SH-waves within the additional layer of elastic material must be analysed. For the sake of this analysis it may be assumed that the displacement field associated with propagation of a plane harmonic wave  $\mathbf{u}$  propagating within the layer of thickness  $h$  has the form:

$$u_y(x, z, t) = f(z)e^{ik(x-ct)} \quad (4.24)$$

when now  $c$  denotes the phase velocity of the waves resulting from the coupled interaction of the incident SH-waves and their reflections from the layer boundaries.

Again, substitution of Eqs. (4.24) into Eqs. (3.5), or even simpler to the resulting equation from Eqs. (3.24), leads to a simple relationship:

$$\left[ \frac{d^2 f(z)}{dz^2} + k^2 \left( \frac{c^2}{c_s^2} - 1 \right) f(z) \right] \hat{u}_y e^{ik(x-ct)} = 0 \quad (4.25)$$

which has non-zero solutions only if the expression within the square brackets equals to zero, which can be rewritten as:

$$\frac{d^2 f(z)}{dz^2} + \beta^2 f(z) = 0, \quad \beta = k \sqrt{\frac{c^2}{c_s^2} - 1} \quad (4.26)$$

Equation (4.26) has a very well-known general solution<sup>4</sup>:

$$f(z) = A_1 \sin \beta z + A_2 \cos \beta z \quad (4.27)$$

which allows one to present the general form of the displacement field associated with propagation of Love surface waves in the following manner:

- within the covering elastic layer of thickness  $h$ , for  $0 \leq z \leq h$ :

$$u_y(x, z, t) = (A_1 \sin \beta z + A_2 \cos \beta z) e^{ik(x-ct)} \quad (4.28)$$

- within the 3-D elastic half-space, for  $z \leq 0$ :

$$u_y(x, z, t) = \hat{u}_y e^{\alpha z} e^{ik(x-ct)} \quad (4.29)$$

---

<sup>4</sup> The case of an isolated elastic layer is discussed in detail in *Sect. 5.1*.

The application of the traction-free boundary conditions for the stress component  $\tau_{yz}$  at the free surface of the elastic layer, i.e. for  $z = h$ , and the use of the compatibility conditions for the same stress components  $\tau_{yz}$  as well as the displacement  $u_y$  at the interface, i.e. at  $z = 0$ , allows one to obtain the dispersion relation for Love surface waves straight from Eqs. (4.28) and (4.29). It can be written that:

$$\begin{cases} \tau_{yz}|_h = 0 & \rightarrow A_1 \cos \beta h - A_2 \sin \beta h = 0 \\ \tau_{yz}|_{0^+} = \tau_{yz}|_{0^-} & \rightarrow A_1 \beta \mu_1 - \hat{u}_y \alpha \mu_2 = 0 \\ u_y|_{0^+} = u_y|_{0^-} & \rightarrow A_2 - \hat{u}_y = 0 \end{cases} \quad (4.30)$$

where  $\mu_1$  describes material properties within the covering elastic layer of thickness  $h$ , while  $\mu_2$  describes those in the 3-D elastic half-space.

As before the factor  $e^{ik(x-ct)}$  is not present, as the conditions expressed by Eqs. (4.30) must be satisfied for propagating Love surface waves independently of the spatial coordinate  $x$  and time  $t$ .

The conditions given by Eqs. (4.30) form a system of three homogeneous equations, which has non-trivial solutions only if its determinant vanishes, i.e. when:

$$\beta \mu_1 \sin \beta h - \alpha \mu_2 \cos \beta h = 0 \quad (4.31)$$

which can be also expressed in the following well-known form:

$$\tan \left( kh \sqrt{\frac{c^2}{c_{s1}^2} - 1} \right) - \frac{\mu_2 \sqrt{1 - \frac{c^2}{c_{s2}^2}}}{\mu_1 \sqrt{\frac{c^2}{c_{s1}^2} - 1}} = 0 \quad (4.32)$$

It can be immediately seen that the dispersion relation for Love surface waves, expressed by Eq. (4.32), is dependent on the wave number  $k$  and the thickness  $h$  of the covering elastic layer. It can easily be solved numerically—see *Appendix B*. For this reason Love surface waves, unlike Rayleigh surface waves, are dispersive in nature. Moreover, it can be noted that real roots of the dispersion relation correspond to the phase velocity  $c$  of Love surface waves, which stays within the range of velocities  $c_{s1} \leq c \leq c_{s2}$ . In the case when  $c_{s2} \leq c_{s1}$  the characteristic equation has no real roots, thus propagation of Love surface waves is prohibited.

Additionally, it should be realised that unlike the Rayleigh surface waves, the Love surface waves propagating within the covering elastic layer are either partially reflected from the layer boundaries or partially transmitted into the 3-D elastic half-space. These multiple reflections and their subsequent interference [5] lead to the formation of multiple modes of Love surface waves, the existence of which is correctly predicted by solutions to the characteristic equation, as presented in Fig. 4.8. In most cases, however, the most important modes are the fundamental ( $n = 0$ ) mode

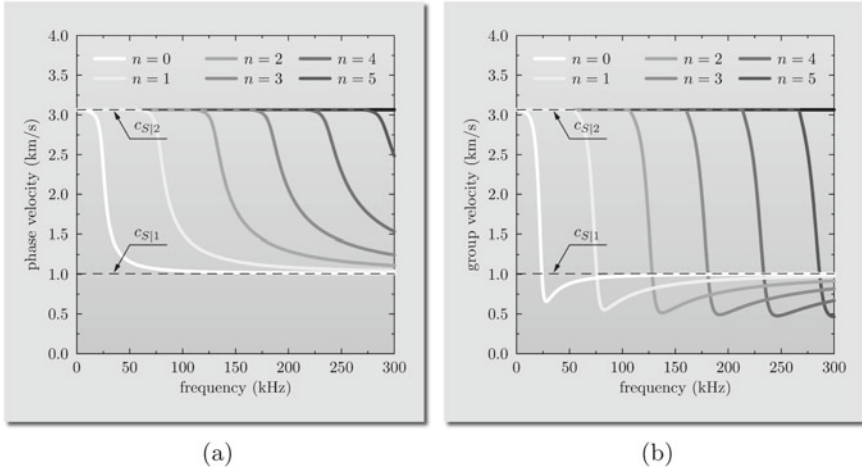


**Fig. 4.8** Dispersion curves for: **a** the phase velocity, **b** the group velocity, for modes of Love surface waves ( $n = 0, 1, 2, \dots$ ) propagating in a 10 mm thick epoxy layer covering an aluminium half-space

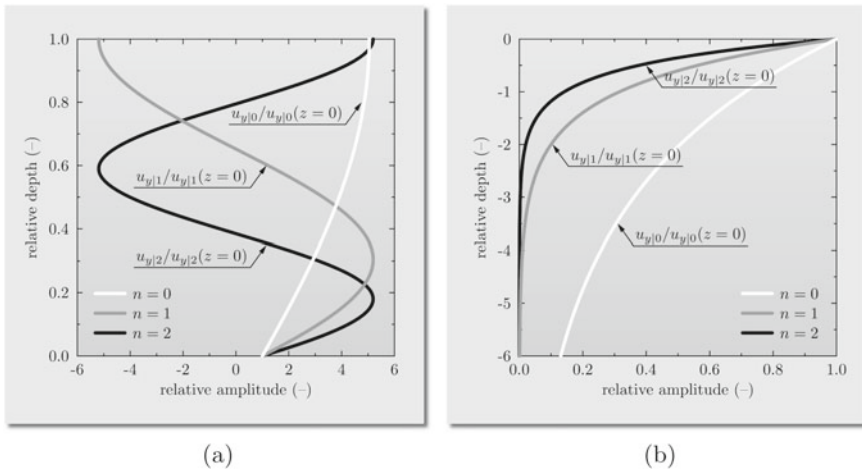


**Fig. 4.9** Relative displacement amplitudes within: **a** covering layer, **b** aluminium half-space, as a function of the relative depth  $z/h$ , for the first three modes of Love surface waves propagating in a 10 mm thick epoxy layer covering an aluminium half-space, for the phase velocity equal to 2.5 km/s

and subsequent modes. It should be also emphasised that due to the multi-mode nature of Love surface waves, within a given frequency range, a number of wave modes can propagate simultaneously.

The profile of the displacement amplitudes associated with Love surface waves is also different from the profile observed for Rayleigh surface waves. This is because it must reflect not only the multi-mode nature of Love surface waves, but also the



existence of the covering elastic layer, as shown in Fig. 4.9. In this case the displacement component  $u_y$  is normalised with respect to the displacement  $u_{y|n}$  associated with the  $n$ -mode of Love surface waves, measured on the surface of the 3-D elastic half-space, i.e. for  $z = 0$ . Additionally its variation is presented not as a function of  $z/\lambda$ , as the wavelength  $\lambda$  is a function of material properties as well as the frequency  $f$ , but rather as a function of the relative depth  $z/h$ , where  $h$  is the thickness of the covering elastic layer. It is interesting to observe that these displacement amplitudes remain continuous but are not smooth, which is a direct consequence of different material properties of the covering elastic layer and the 3-D elastic half-space.

### 4.3 Stoneley Waves

Stoneley waves can be considered as a special case of surface waves, as they propagate in material layers close to the interface between two solids, as presented in Fig. 4.10.<sup>5</sup>

They are also known as boundary or interface waves and were discovered in 1924 by Robert Stoneley (1894–1976), a British seismologist and professor at the University of Cambridge. In practice Stoneley waves are typically associated with seismic investigations of the properties of deep rock formations, which can be carried out through a borehole by sonic logging or vertical seismic profiling. Stoneley waves are also referred to as Scholte waves, when the interface along which they propagate is a solid-liquid interface.

The mathematical description of Stoneley waves is similar to that presented in the case of Rayleigh surface waves, in Sect. 4.1. In this case, however, the displacement field used to define the wave motion in a 3-D elastic half-space, for  $z \leq 0$ , and given by the final set of Eqs. (4.6), must be modified. This modification reflects the existence of the second material, in order to form the interface.

Without any loss of generality it can be conveniently assumed that the interface between two solids, which are represented by two 3-D elastic half-spaces of different material properties, can be defined by a plane  $z = 0$ .

For this reason the displacement field, representing a plane harmonic wave  $\mathbf{u}$ , propagating within material layers close to the interface between two 3-D elastic half-spaces, can be presented in the following manner:

- within the upper 3-D elastic half-space, characterised by material constants  $\lambda_1, \mu_1$  and  $\rho_1$ , for  $z \geq 0$ :

---

<sup>5</sup> The term *von Schmidt waves* or *Schmidt head waves* (SHW) is related to a pseudo-supersonic phenomenon of wave propagation in solids at or near their interface. This type of wave takes its name after a German physicist Oswald von Schmidt (1889–1945), who extensively studied wave propagation at media boundaries, which are characterised by different speeds of wave propagation.

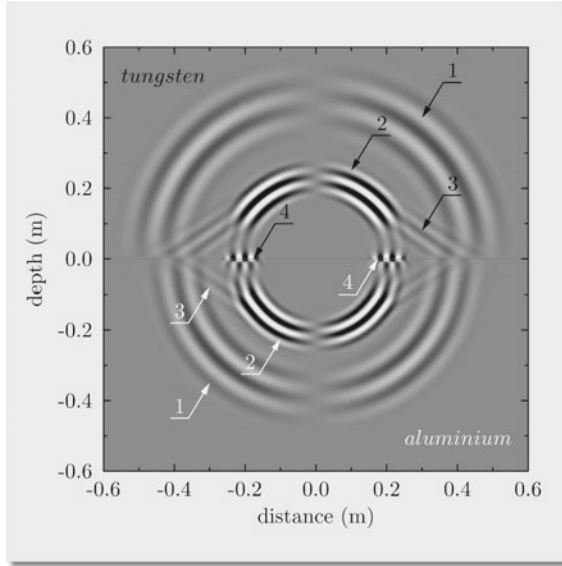


**Fig. 4.10** Wave propagation patterns at the interface between tungsten and aluminium (1—P-waves, 2—SV-waves, 3—von Schmidt waves, 4—Stoneley waves). Results of numerical computations by TD-SFEM

$$\begin{cases} u_x(x, z, t) = (A_1 e^{\alpha_{11}z} + A_2 e^{\alpha_{21}z}) e^{ik(x-ct)} \\ u_z(x, z, t) = \left( \frac{\alpha_{11}}{ik} A_1 e^{\alpha_{11}z} + \frac{k}{i\alpha_{21}} A_2 e^{\alpha_{21}z} \right) e^{ik(x-ct)} \end{cases} \quad (4.33)$$

and where:

$$\alpha_{11} = -k \sqrt{1 - \frac{c^2}{c_{p1}^2}}, \quad \alpha_{21} = -k \sqrt{1 - \frac{c^2}{c_{s1}^2}} \quad (4.34)$$

- within the lower 3-D elastic half-space, characterised by material constants  $\lambda_2, \mu_2$  and  $\rho_2$ , for  $z \leq 0$ :

$$\begin{cases} u_x(x, z, t) = (A_3 e^{\alpha_{12}z} + A_4 e^{\alpha_{22}z}) e^{ik(x-ct)} \\ u_z(x, z, t) = \left( \frac{\alpha_{12}}{ik} A_3 e^{\alpha_{12}z} + \frac{k}{i\alpha_{22}} A_4 e^{\alpha_{22}z} \right) e^{ik(x-ct)} \end{cases} \quad (4.35)$$

and where:

$$\alpha_{12} = +k \sqrt{1 - \frac{c^2}{c_{p2}^2}}, \quad \alpha_{22} = +k \sqrt{1 - \frac{c^2}{c_{s2}^2}} \quad (4.36)$$

Now,  $c_{P|1}$  and  $c_{S|1}$  denote the phase velocities of the P-wave and S-wave within the upper 3-D half-space, i.e. for  $z \geq 0$ , while  $c_{P|2}$  and  $c_{S|2}$  the same velocities within the lower 3-D half-space, i.e. for  $z \leq 0$ .

In the case of Stoneley waves the dispersion relation can be obtained by the use of Eqs. (4.33)–(4.36) under the assumption that both displacement components  $u_x$  and  $u_z$ , as well as the non-zero stress components  $\sigma_{xx}$  and  $\tau_{xz}$ , remain continuous at the interface  $z = 0$ . Yet again the stress components  $\sigma_{xx}$  and  $\tau_{xz}$  can be easily evaluated by the use of Hooke's law, as presented by Eq. (4.9), while the non-zero strain components  $\epsilon_{xx}$ ,  $\epsilon_{zz}$  and  $\gamma_{xz}$  can be presented in the following form:

- within the upper 3-D elastic half-space, for  $z \geq 0$ :

$$\begin{cases} \epsilon_{xx} = \frac{\partial u_x}{\partial x} = -k(A_1 k + A_2 \alpha_{2|1}) e^{ik(x-ct)} \\ \epsilon_{zz} = \frac{\partial u_z}{\partial z} = (A_1 \alpha_{1|1}^2 + A_2 k \alpha_{2|1}) e^{ik(x-ct)} \\ \gamma_{xz} = \frac{\partial u_x}{\partial z} + \frac{\partial u_z}{\partial x} = i[2A_1 k \alpha_{1|1} + A_2 (k^2 + \alpha_{2|1}^2)] e^{ik(x-ct)} \end{cases} \quad (4.37)$$

- within the lower 3-D elastic half-space, for  $z \leq 0$ :

$$\begin{cases} \epsilon_{xx} = \frac{\partial u_x}{\partial x} = -k(A_3 k + A_4 \alpha_{2|2}) e^{ik(x-ct)} \\ \epsilon_{zz} = \frac{\partial u_z}{\partial z} = (A_3 \alpha_{1|2}^2 + A_4 k \alpha_{2|2}) e^{ik(x-ct)} \\ \gamma_{xz} = \frac{\partial u_x}{\partial z} + \frac{\partial u_z}{\partial x} = i[2A_3 k \alpha_{1|2} + A_4 (k^2 + \alpha_{2|2}^2)] e^{ik(x-ct)} \end{cases} \quad (4.38)$$

These continuity conditions lead to a set of four homogeneous equations for the unknown constants  $A_1$ ,  $A_2$ ,  $A_3$  and  $A_4$ , which after necessary mathematical manipulations can be presented as:

$$\begin{cases} A_1 + A_2 - A_3 - A_4 = 0 \\ \frac{\alpha_{1|1}}{k} A_1 + \frac{k}{\alpha_{2|1}} A_2 - \frac{\alpha_{1|2}}{k} A_3 - \frac{k}{\alpha_{2|2}} A_4 = 0 \\ \beta_1 A_1 + 2A_2 - \frac{\beta_2 \mu_2}{\mu_1} A_3 - \frac{2\mu_2}{\mu_1} A_4 = 0 \\ \frac{2\alpha_{1|1}}{k} A_1 + \frac{\beta_1 k}{\alpha_{2|1}} A_2 - \frac{2\alpha_{1|2}}{k} \frac{\mu_2}{\mu_1} A_3 - \frac{\beta_2 k}{\alpha_{2|2}} \frac{\mu_2}{\mu_1} A_4 = 0 \end{cases} \quad (4.39)$$

where  $\beta_1$  and  $\beta_2$  are respectively:

$$\beta_1 = \sqrt{2 - \frac{c^2}{c_{s1}^2}}, \quad \beta_2 = \sqrt{2 - \frac{c^2}{c_{s2}^2}} \tag{4.40}$$

As before the system of homogeneous equations, given by Eqs. (4.39), has non-trivial solutions only if its determinant vanishes. This condition leads straight to the characteristic equation, which in the current case after simplifications and rearrangements of terms can be expressed as:

$$\begin{aligned} &c^4[(\vartheta_2 - 1)\mu_1^2 c_{s2}^4 + (2 + \vartheta_3 + \vartheta_4)\mu_1\mu_2 c_{s1}^2 c_{s2}^2 + (\vartheta_1 - 1)\mu_2^2 c_{s1}^4] \\ &\quad - 4c^2 c_{s1}^2 c_{s2}^2 (\mu_1 - \mu_2)[(\vartheta_2 - 1)\mu_1 c_{s2}^2 - (\vartheta_1 - 1)\mu_2 c_{s1}^2] \\ &\quad - 4c^4 c_{s1}^4 c_{s2}^4 (\vartheta_1 - 1)(\vartheta_2 - 1)(\mu_1 - \mu_2)^2 = 0 \end{aligned} \tag{4.41}$$

where symbols  $\vartheta_i (i = 1, \dots, 4)$  are defined as follows:

$$\begin{cases} \vartheta_1 = \frac{\alpha_{11}\alpha_{21}}{k^2}, & \vartheta_2 = \frac{\alpha_{12}\alpha_{22}}{k^2} \\ \vartheta_3 = \frac{\alpha_{11}\alpha_{22}}{k^2}, & \vartheta_4 = \frac{\alpha_{21}\alpha_{12}}{k^2} \end{cases} \tag{4.42}$$

It may be noted that the characteristic equation (4.41) is independent of the wave number  $k$  and/or angular frequency  $\omega$ . As a result of this Stoneley waves must be non-dispersive, in a similar manner to that observed in the case of Rayleigh surface waves. However, in the case of Stoneley waves the depth of their full attenuation

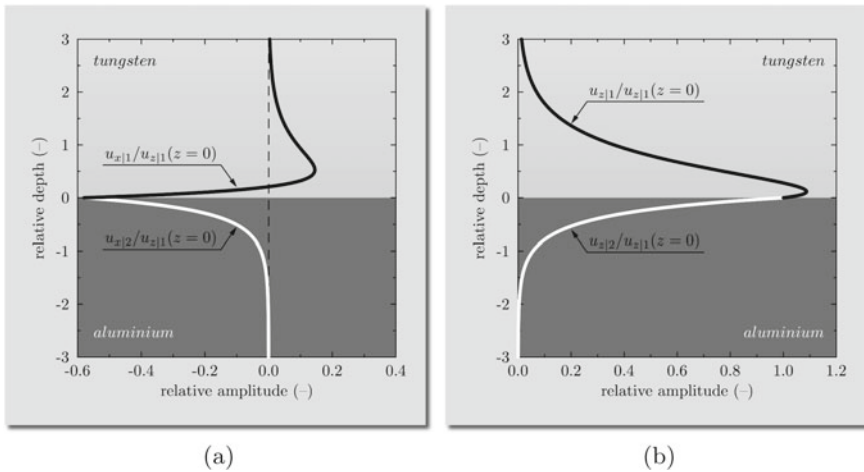


**Fig. 4.11** Relative displacement amplitudes: **a** horizontal, **b** transverse, as a function of the relative depth  $z/\lambda$ , for Stoneley waves propagating in 3-D elastic half-spaces, at the interface between tungsten and aluminium

**Table 4.2** Selected material properties and the calculated speeds of P-, SV-, Rayleigh and Stoneley waves for tungsten and aluminium

Property/material	Aluminium	Tungsten
Poisson's ratio, $\nu$ (-)	0.33	0.28
Density, $\rho$ (kg/m <sup>3</sup> )	2700	19300
Young's modulus, $E$ (GPa)	67.5	411.0
1st Lamé constant, $\lambda$ (GPa)	49.3	204.3
2nd Lamé constant, $\mu$ (GPa)	25.4	160.5
Speed of P-waves, $c_p$ (km/s)	6.09	5.22
Speed of SV-waves, $c_s$ (km/s)	3.07	2.88
Speed of Rayleigh waves, $c_R$ (km/s)	2.86	2.67
Speed of Stoneley waves, $c$ (km/s)	2.78	2.78

generally exceeds twice their wavelength and is dependent on elastic properties of constituent materials, and thus may be different on both sides of the interface, as shown in Fig. 4.11.

Moreover, this characteristic equation is bi-quadratic with respect to the phase velocity  $c$ . It can be found that the number and nature of the roots of this bi-quadratic equation depend not only on the phase velocities of SV-waves  $c_{s1}$  and  $c_{s2}$ , but also depend on the elastic properties of the two 3-D elastic half-spaces, defined by  $\mu_1$  and  $\mu_2$ .

Alternatively, it can be stated that the presence of positive roots of the characteristic equation (4.41) is a certain function of the material densities  $\rho_1$  and  $\rho_2$ , as well as the shear moduli  $\mu_1$  and  $\mu_2$  of both adjacent 3-D elastic half-spaces [5]. Its roots can be easily found numerically. A typical case of materials at whose interface Stoneley waves may propagate is given by tungsten and aluminium. Their selected material properties and the calculated speeds of P-, SV-, Rayleigh and Stoneley waves, are presented in Table 4.2.

## References

1. A. Howell, E. Nissen, T. Stahl, K. Clark, J. Kearse, R. Van Dissen, P. Villamor, R. Langridge, and K. Jones. Three-dimensional surface displacements during the 2016 MW 7.8 Kaikōura earthquake (New Zealand) from photogrammetry-derived point clouds. *Journal of Geophysical Research: Solid Earth*, 125:e2019JB018739:1–46, 2020.
2. National Archives. *San Francisco earthquake, 1906*. <https://www.archives.gov/legislative/features/sf>, 1906. Visited on 09/12/2023.
3. L. Knopoff. On Rayleigh wave velocities. *Bulletin of the Seismological Society of America*, 42:307–308, 1952.
4. National Archives. *Earth movement twisted rails near Whittier. Railroad en route to Whittier*. <https://catalog.archives.gov/id/25342787>, 1964. Visited on 28/01/2021.
5. J. D. Achenbach. *Wave propagation in elastic solids*. North-Holland Publishing Company, Amsterdam, 1973.

# Chapter 5

## Waves in a 2-D Elastic Space



### 5.1 SH-Waves in an Elastic Layer

An elastic layer can be understood as two parallel surfaces bounding a 3-D elastic space. In such circumstances the presence of the bounding surfaces limits potential directions of propagation of elastic waves, so it can be said that an elastic layer is a case of a 2-D elastic space. Although two parallel surfaces represent a every specific example of 2-D space, it significantly helps to simplify not only the analysis but also the mathematical description of the wave phenomenon, as well as to formulate some general conclusions.

Propagation of SH-waves in a thin elastic layer was briefly discussed on the occasion of the analysis of Love surface waves in Sect. 4.2. In the current section this analysis is presented in more detail. First of all it should be observed that the presence of a bounding surface in a 3-D elastic space results in wave reflection and subsequent interaction of the reflected waves with the incident waves. At certain conditions these reflected and incident waves are able to form specific wave patterns, which are called wave modes. Such wave modes could be observed in the case of Love surface waves and because of their dispersive nature they were strongly frequency dependent, as presented in Fig. 4.8. However, such wave modes were not observed in the case of Rayleigh or Stoneley surface waves.

The presence of two surfaces parallel to the  $xy$  plane, bounding a 3-D elastic space, leads to the entrapment of the propagating waves within the elastic layer as well as the formation of various wave modes, as presented in Fig. 5.1. Following the considerations presented in Sect. 4.2 it can be repeated that the displacement field associated with the propagation of a plane harmonic wave  $\mathbf{u}$  within a layer of thickness  $h$  has the already known form. As before the nature of this wave requires that the displacement components  $u_x$  and  $u_z$  must vanish, i.e.  $u_x = u_z = 0$ , and the only non-zero displacement component is  $u_y$ , which remains a function of the spatial coordinates  $x$ ,  $z$  and time  $t$ :

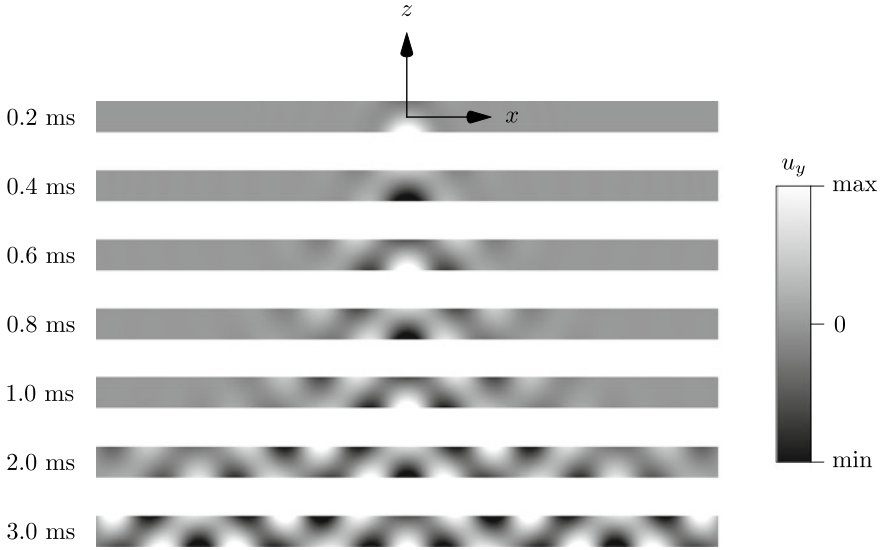


**Fig. 5.1** Formation of the pattern of elastic SH-waves propagating in an aluminium layer, in consecutive moments in time. Results of numerical computations by TD-SFEM

$$u_y(x, z, t) = \hat{u}_y(z)e^{ik(x-ct)} \quad (5.1)$$

where now  $c$  denotes the phase velocity of the wave propagating in the direction of the  $x$  axis and resulting from a coupled interaction of the incident SH-waves and their reflections from the layer boundaries. This interaction leads to the creation of a standing wave in the direction perpendicular to the  $xy$  plane, which is the direction of the  $z$  axis.

As before a simple substitution of Eq. (5.1) into the governing equations of motion (3.5), or simply into the resulting equation from Eq. (3.24), leads to a well-known ordinary differential equation given by Eq. (4.25):

$$\frac{d^2\hat{u}_y(z)}{dz^2} + \beta^2\hat{u}_y(z) = 0, \quad \beta = k\sqrt{\frac{c^2}{c_s^2} - 1} \quad (5.2)$$

which is formally rewritten here for the sake of completeness, where  $|z| \leq a$ , with  $2a = h$  and  $h$  denoting the thickness of the elastic layer.

This equation has a solution composed of two independent harmonic functions: one being the symmetric cosine function and the other the antisymmetric sine function:

$$\hat{u}_y(z) = A_1 \sin \beta z + A_2 \cos \beta z \quad (5.3)$$

Now, the application of the traction-free boundary conditions for the stress component  $\tau_{yz}$  at the free surface of the elastic layer, i.e. for  $z = \pm a$ , allows one to obtain

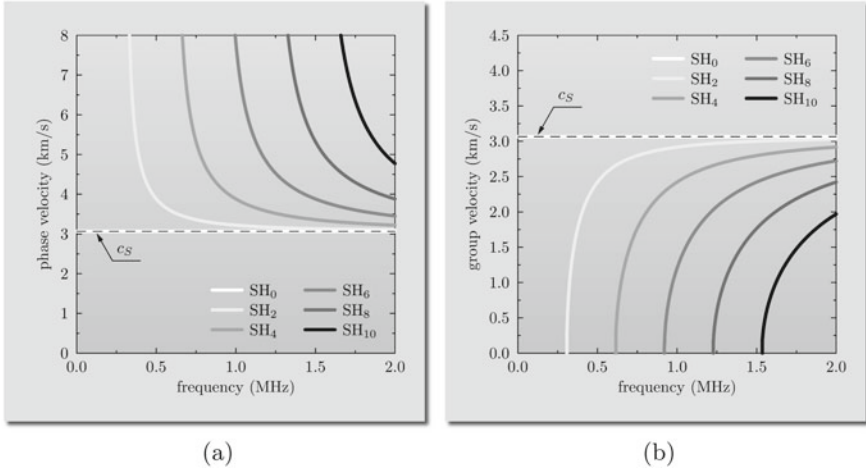


**Fig. 5.2** Dispersion curves for: **a** the phase velocity, **b** the group velocity, for symmetric modes of SH-waves  $SH_n (n = 0, 2, 4, \dots)$  propagating in a 10 mm thick aluminium layer

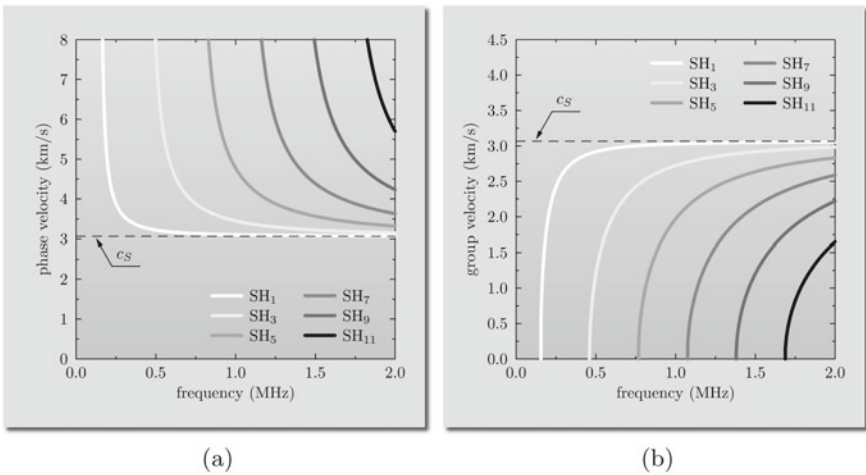


**Fig. 5.3** Dispersion curves for: **a** the phase velocity, **b** the group velocity, for antisymmetric modes of SH-waves  $SH_n (n = 1, 3, 5, \dots)$  propagating in a 10 mm thick aluminium layer

the dispersion relation for SH-waves propagating in the elastic layer, as illustrated in Figs. 5.2 and 5.3.

This condition can be formally presented in the following form:

$$\tau_{yz}|_{\pm a} = 0 \rightarrow A_1 \cos \beta a \pm A_2 \sin \beta a = 0 \tag{5.4}$$



Indeed, it can be found that Eq. (5.4) is satisfied in two cases [1]:

- when  $A_1 = 0$  and  $\hat{u}_y(z) = A_2 \cos \beta z$  then:

$$A_2 \sin \beta a = 0 \rightarrow \beta_n a = n\pi, \quad n = 0, 1, 2, \dots$$

or alternatively:

$$\beta_n a = \frac{n\pi}{2} \rightarrow \beta_n h = n\pi, \quad n = 0, 2, 4, \dots \quad (5.5)$$

- when  $A_2 = 0$  and  $\hat{u}_y(z) = A_1 \sin \beta z$  then:

$$A_1 \cos \beta a = 0 \rightarrow \beta_n a = \frac{(2n-1)\pi}{2}, \quad n = 1, 2, 3, \dots$$

or alternatively:

$$\beta_n a = \frac{n\pi}{2} \rightarrow \beta_n h = n\pi, \quad n = 1, 3, 5, \dots \quad (5.6)$$

It is interesting to note that the case of  $n = 0, 2, 4, \dots$  corresponds to the infinite number of *symmetric modes* of SH-waves propagating within the elastic layer and standing waves described by the symmetric (even) cosine function, while the case of  $n = 1, 3, 5, \dots$  corresponds to the infinite number of *antisymmetric modes* of SH-waves propagating within the elastic layer and standing waves described by the antisymmetric (odd) sine function. In the literature [1–3] modes of SH-waves are very often noted  $\text{SH}_n$  ( $n = 0, 1, 2, \dots$ ) and their associated displacement amplitude profiles are presented in Fig. 5.4.

It should be stressed that the displacement amplitude profiles of both symmetric and antisymmetric modes of SH-waves remain independent of the wave number  $k$  and the angular frequency  $\omega$ .

Finally, by using the definition of the parameter  $\beta$  in Eq. (5.2) as well as the resulting relations from Eq. (5.5) and Eq. (5.6), the dispersion relation for SH-waves propagating within an elastic layer of thickness  $h$ , for symmetric and antisymmetric modes, can be expressed as a function of the wave number  $k$  in the following way:

$$c(k) = c_s \sqrt{1 + \left(\frac{n\pi}{kh}\right)^2}, \quad n = 0, 1, 2, \dots \quad (5.7)$$

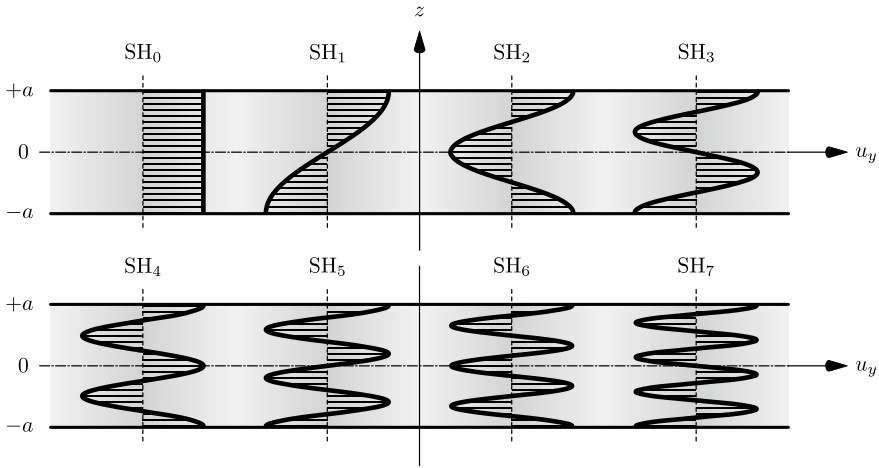


**Fig. 5.4** Relative displacement amplitudes of the transverse displacement  $u_y$  for modes of SH-waves propagating in an elastic layer: symmetric  $SH_n$  ( $n = 0, 2, 4, \dots$ ) and antisymmetric  $SH_n$  ( $n = 1, 3, 5, \dots$ )

or alternatively as a function of the angular frequency  $\omega$ <sup>1</sup> as:

$$c(\omega) = \frac{c_s}{\sqrt{1 - \left(\frac{n\pi c_s}{\omega h}\right)^2}}, \quad n = 0, 1, 2, \dots \tag{5.8}$$

It can be also noted from Figs. 5.2 and 5.3 that SH-waves propagating within an elastic layer are dispersive except for the fundamental mode, i.e. for  $n = 0$ , which is a non-dispersive fundamental symmetric mode  $SH_0$ . Moreover, it can be also seen that in the case of the fundamental mode the phase velocity of the SH-waves propagating in such a layer is equal to the phase velocity of SH-waves propagating in a 3-D elastic space.

## 5.2 Lamb Waves in an Elastic Layer

In a similar manner to SH-waves propagating in an elastic layer discussed previously in Sect. 5.1 the presence of two surfaces parallel to the  $xy$  plane bounding a 3-D elastic space leads to the entrapment of the propagating waves within the elastic layer, as presented in Fig. 5.5. As a result of this, it also leads to the formation of various wave modes, known as symmetric and antisymmetric modes of Lamb waves.

<sup>1</sup> Since the phase velocity  $c$  is simultaneously dependent on the angular frequency  $\omega$  and the thickness of the elastic layer  $h$  this dependence can be also conveniently presented as a function of their product, i.e. as  $c = c(\omega \cdot h)$  or  $c = c(f \cdot h)$ .

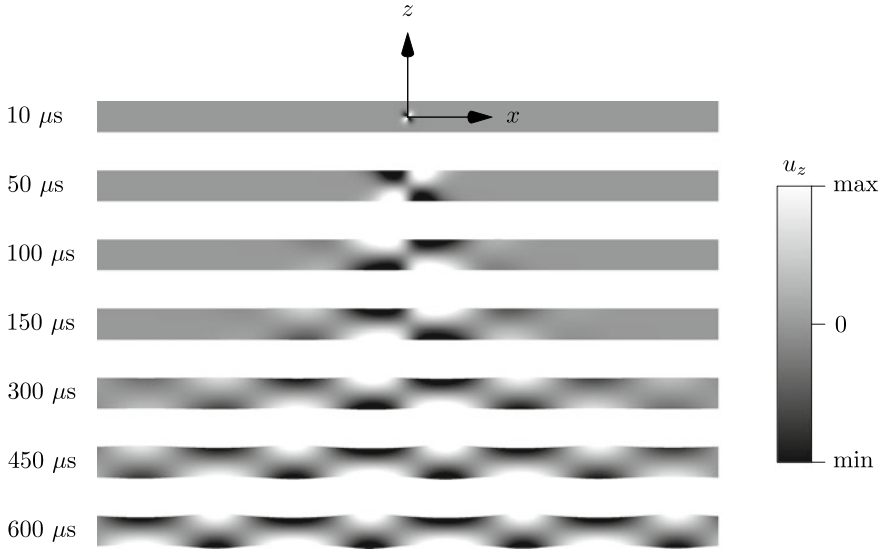


**Fig. 5.5** Formation of the fundamental symmetric Lamb wave mode  $S_0$  propagating in an aluminium layer in consecutive moments in time. Results of numerical computations by TD-SFEM

Lamb waves, very often referred to as Rayleigh-Lamb waves, are a different type of wave from SH-waves, which can also propagate in an elastic layer. Their propagation in an elastic layer is very similar to the propagation of Rayleigh waves discussed in Sect. 4.1. There a detailed discussion examined the formation of Rayleigh waves as a direct consequence of the presence of a free surface bounding a 3-D elastic space, where two types of waves can propagate freely as P-waves and S-waves. The presence of that free surface results in a coupled interaction between P-waves and S-waves, which required a complex mathematical description.

In the case Lamb waves the nature of the wave motion requires that the displacement component  $u_y$  must vanish, i.e.  $u_y = 0$ , while the other two displacement components  $u_x$  and  $u_z$  are retained, remaining only a function of the spatial coordinates  $x$  and  $z$  as well as of time  $t$ . Thus the wave motion stays fully independent of the spatial coordinate  $y$ . As before it is assumed that  $|z| < a$ , with  $2a = h$  where  $h$  denotes the thickness of the layer.

The investigation of Lamb waves benefits a lot from the decomposition of the displacement field, according to Eq. (3.25) from Sect. 3.2, into the scalar potential  $\phi$  and the vector potential  $\Psi$ . Bearing in mind the assumptions made about the nature of the wave motion it can be noted in the case of Lamb waves that Eq. (3.25) reduces to the following form:

$$\begin{cases} u_x(x, z, t) = \frac{\partial \phi}{\partial x} - \frac{\partial \psi_z}{\partial z} \\ u_z(x, z, t) = \frac{\partial \phi}{\partial z} + \frac{\partial \psi_z}{\partial x} \end{cases} \quad (5.9)$$

where now  $\phi = \phi(x, z, t)$  and  $\psi_z = \psi_z(x, z, t)$  represent two scalar potentials.

Both scalar potentials  $\phi$  and  $\psi_z$  must satisfy appropriate wave equations given by Eq. (3.21) and Eq. (3.22). For this reason it can be formally written that:

$$\begin{cases} c_p^2 \nabla^2 \phi = \ddot{\phi} & \text{or} & \frac{\partial^2 \phi}{\partial x^2} + \frac{\partial^2 \phi}{\partial z^2} = \frac{1}{c_p^2} \frac{\partial^2 \phi}{\partial t^2} \\ c_s^2 \nabla^2 \psi_z = \ddot{\psi}_z & \text{or} & \frac{\partial^2 \psi_y}{\partial x^2} + \frac{\partial^2 \psi_y}{\partial z^2} = \frac{1}{c_s^2} \frac{\partial^2 \psi_y}{\partial t^2} \end{cases} \quad (5.10)$$

Solutions to these wave equations (5.10) can be assumed to have well-known forms:

$$\begin{cases} \phi(x, z, t) = \Phi(z)e^{ik(x-ct)} \\ \psi_z(x, z, t) = \Psi(z)e^{ik(x-ct)} \end{cases} \quad (5.11)$$

where  $\Phi$  and  $\Psi$  represent unknown functions dependent only on the spatial coordinate  $z$  and where  $c$  is the phase velocity of Lamb waves propagating in the direction of the  $x$  axis.

A simple substitution of Eq. (5.11) into the appropriate wave equations, expressed by Eq. (5.10), leads to two ordinary differential equations:

$$\begin{cases} \frac{d^2 \Phi(z)}{dz^2} + p^2 \Phi(z) = 0 \\ \frac{d^2 \Psi(z)}{dz^2} + q^2 \Psi(z) = 0 \end{cases} \quad (5.12)$$

with:

$$\begin{cases} p = k \sqrt{\frac{c^2}{c_p^2} - 1} = \sqrt{\frac{\omega^2}{c_p^2} - k^2} \\ q = k \sqrt{\frac{c^2}{c_s^2} - 1} = \sqrt{\frac{\omega^2}{c_s^2} - k^2} \end{cases} \quad (5.13)$$

where  $p$  and  $q$  are certain constants dependent on the angular frequency  $\omega$ , the wave number  $k$  as well as the velocities of P-waves and SH-waves propagating in a 3-D elastic medium.

The displacement field associated with propagation of Lamb waves in an elastic layer, thanks to Eq. (5.11), can be expressed as:

$$\begin{cases} u_x(x, z, t) = \left[ ik\Phi(z) - \frac{d\Psi(z)}{dz} \right] e^{ik(x-ct)} \\ u_z(x, z, t) = \left[ \frac{d\Phi(z)}{dz} + ik\Psi(z) \right] e^{ik(x-ct)} \end{cases} \quad (5.14)$$

which helps to express the strain field in the elastic layer directly as dependent on the unknown functions  $\Phi$  and  $\Psi$ :

$$\begin{cases} \epsilon_{xx} = \frac{\partial u_x}{\partial x} = - \left[ k^2 \Phi(z) + ik \frac{d\Psi(z)}{dz} \right] e^{ik(x-ct)} \\ \epsilon_{zz} = \frac{\partial u_z}{\partial z} = \left[ \frac{d^2 \Phi(z)}{dz^2} + ik \frac{d\Psi(z)}{dz} \right] e^{ik(x-ct)} \\ \gamma_{xz} = \frac{\partial u_x}{\partial z} + \frac{\partial u_z}{\partial x} = \left[ 2ik \frac{d\Phi(z)}{dz} - k^2 \Psi(z) - \frac{d^2 \Psi(z)}{dz^2} \right] e^{ik(x-ct)} \end{cases} \quad (5.15)$$

Since solutions to the ordinary differential equations given by Eq. (5.12) are also well-known:

$$\begin{cases} \Phi(z) = A_1 \sin pz + A_2 \cos pz \\ \Psi(z) = B_1 \sin qz + B_2 \cos qz \end{cases} \quad (5.16)$$

the application of the traction-free boundary conditions for the stress components  $\sigma_{zz}$  and  $\tau_{xz}$  at the free surface of the elastic layer, i.e. for  $z = \pm a$ :

$$\sigma_{zz}(x, z, t) = \tau_{xz}(x, z, t) = 0, \quad \text{for } z = \pm a \quad (5.17)$$

allows one to obtain the dispersion relations for Lamb waves propagating in the elastic layer.

The stress components  $\sigma_{zz}$  and  $\tau_{xz}$  can be expressed by the use of Hooke's law, as was presented in Eq. (4.9) in Sect. 4.1, which results in the following two equations:

$$\begin{cases} \sigma_{zz}|_{\pm a} = 0 \rightarrow k^2 \lambda \Phi(\pm a) - (\lambda + 2\mu) \frac{d^2 \Phi(\pm a)}{dz^2} \\ \qquad \qquad \qquad - 2ik\mu \frac{d\Psi(\pm a)}{dz} = 0 \\ \tau_{xz}|_{\pm a} = 0 \rightarrow \mu \left[ 2ik \frac{d\Phi(\pm a)}{dz} - k^2 \Psi(\pm a) - \frac{d^2 \Psi(\pm a)}{dz^2} \right] = 0 \end{cases} \quad (5.18)$$

where as before the factor  $e^{ik(x-ct)}$  is not present, since the traction-free boundary conditions must be satisfied for propagating Lamb waves independently of the spatial coordinate  $x$  and time  $t$ .

It can be immediately seen that the system of two equations, resulting from the traction-free boundary conditions is dependent on four unknown constants:  $A_1$ ,  $A_2$ ,  $B_1$  and  $B_2$ . However, its solution is possible thanks to the fact that the wave motion associated with propagation of Lamb waves can be split into two independent types of wave modes, i.e. *symmetric modes* and *antisymmetric modes*, in a very similar manner as it was in the case of SH-waves propagating in an elastic layer.

The modes of Lamb waves are noted in the literature [1–3] as  $S_n$  ( $n = 0, 1, 2, \dots$ ) for symmetric modes and  $A_n$  ( $n = 0, 1, 2, \dots$ ) for antisymmetric modes. In contrast

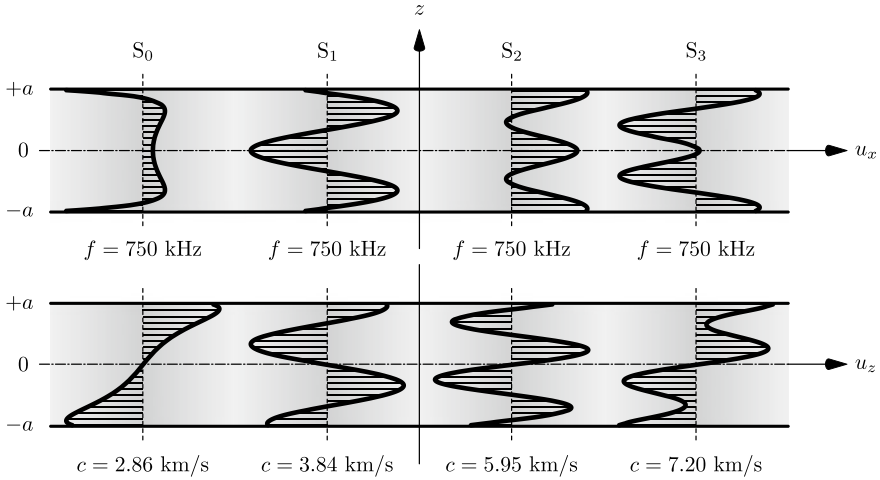


**Fig. 5.6** Relative displacement amplitudes for symmetric modes of Lamb waves  $S_n$  ( $n = 0, 1, 2, \dots$ ) propagating in a 10mm thick aluminium layer, at the frequency  $f = 750$  kHz

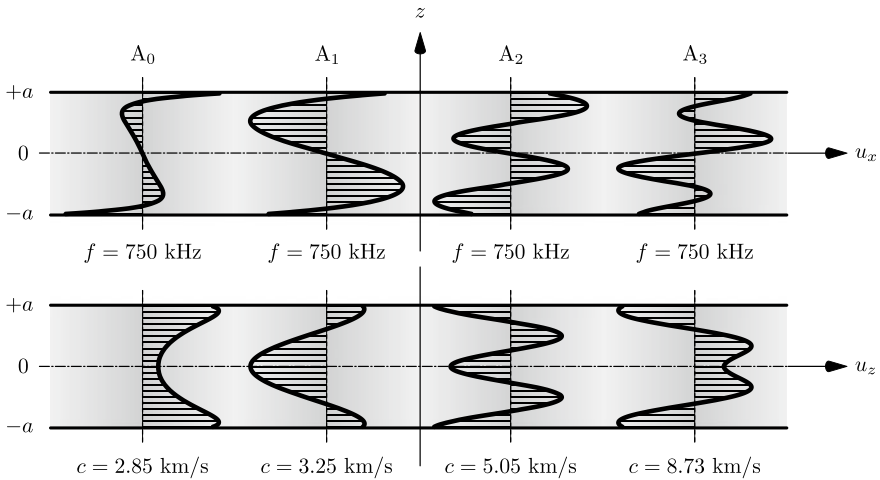


**Fig. 5.7** Relative displacement amplitudes for antisymmetric modes of Lamb waves  $A_n$  ( $n = 0, 1, 2, \dots$ ) propagating in a 10mm thick aluminium layer, at the frequency  $f = 750$  kHz

to SH-waves propagating in an elastic layer, this time the associated displacement amplitudes of Lamb waves concern two components, i.e. the longitudinal displacement component  $u_x$  and the transverse displacement component  $u_z$ , as presented Figs. 5.6 and 5.7.

Moreover, a closer examination of the displacement field expressed by Eq. (5.14) allows one to conclude that in the case of wave motion in the direction of the  $x$  axis (i.e. longitudinal displacement component  $u_x$ ) symmetric modes must be associated

with cosine functions in Eq. (5.16), while antisymmetric modes must be associated with sine functions, as clearly seen in Fig. 5.6. It is opposite in the case of wave motion in the direction of the  $z$  axis (i.e. transverse displacement component  $u_z$ ), when symmetric modes must be associated with sine functions in Eq. (5.16), while antisymmetric modes must be associated with cosine functions, as presented in Fig. 5.7.

Following the notation used in Eq. (5.11) the displacement and stress fields can formally be expressed as plane harmonic waves [1]:

$$\begin{cases} u_x(x, z, t) = \hat{u}_x(z)e^{ik(x-ct)}, & \sigma_{zz}(x, z, t) = \hat{\sigma}_{zz}(z)e^{ik(x-ct)} \\ u_z(x, z, t) = \hat{u}_z(z)e^{ik(x-ct)}, & \tau_{xz}(x, z, t) = \hat{\tau}_{xz}(z)e^{ik(x-ct)} \end{cases} \quad (5.19)$$

which together with all above considerations allows one to present the unknown functions of the spatial coordinate  $z$  in the case of *symmetric modes* of Lamb waves as:

$$\begin{cases} \Phi(z) = A_2 \cos pz \\ \Psi(z) = B_1 \sin qz \\ \hat{u}_x(z) = ikA_2 \cos pz - qB_1 \cos qz \\ \hat{u}_z(z) = -pA_2 \sin pz + ikB_1 \sin qz \\ \hat{\sigma}_{zz}(z) = -[k^2 + p^2(\lambda + 2\mu)]A_2 \cos pz + 2\mu ikqB_1 \cos qz \\ \hat{\tau}_{xz}(z) = -2\mu ikpA_2 \sin pz + \mu(q^2 - k^2)B_1 \sin qz \end{cases} \quad (5.20)$$

while in the case of *antisymmetric modes* of Lamb waves as:

$$\begin{cases} \Phi(z) = A_1 \sin pz \\ \Psi(z) = B_2 \cos qz \\ \hat{u}_x(z) = ikA_1 \sin pz + qB_2 \sin qz \\ \hat{u}_z(z) = pA_1 \cos pz + ikB_2 \cos qz \\ \hat{\sigma}_{zz}(z) = -[k^2 + p^2(\lambda + 2\mu)]A_1 \sin pz - 2\mu ikqB_2 \sin qz \\ \hat{\tau}_{xz}(z) = 2\mu ikpA_1 \cos pz + \mu(q^2 - k^2)B_2 \cos qz \end{cases} \quad (5.21)$$

In such a way the resulting the system of two homogeneous equations leading to the dispersion relations for Lamb waves propagating in an elastic layer are always dependent on two unknown constants:  $A_2$  and  $B_1$  in the case of symmetric modes of Lamb waves and  $A_1$  and  $B_2$  in the case of antisymmetric Lamb waves.

In a similar manner as before the two system of homogeneous equations resulting from the traction-free boundary conditions at the free surface of the elastic layer, i.e. for  $z = \pm a$ , for either symmetric or antisymmetric mode of Lamb waves, have non-trivial solutions only if their determinant vanishes. These conditions lead to the two characteristic equations.

In the case of *symmetric modes* of Lamb waves this characteristic equation can be expressed as:

$$(k^2 - q^2)[\lambda k^2 + (\lambda + 2\mu)p^2] \sin qa \cos pa = 4\mu k^2 pq \sin pa \cos qa \quad (5.22)$$

which can be simplified after necessary mathematical manipulations and rearrangements of terms<sup>2</sup> to its well-know form:

$$\frac{\tan qa}{\tan pa} = -\frac{4k^2 pq}{(k^2 - q^2)^2}, \quad \text{for } \textit{symmetric modes} \quad (5.23)$$

In the case of *antisymmetric modes* of Lamb waves the corresponding characteristic equation can be expressed as:

$$(k^2 - q^2)[\lambda k^2 + (\lambda + 2\mu)p^2] \sin pa \cos qa = 4\mu k^2 pq \sin qa \cos pa \quad (5.24)$$

which can be simplified after the same mathematical manipulations and rearrangements to its well-know form:

$$\frac{\tan qa}{\tan pa} = -\frac{(k^2 - q^2)^2}{4k^2 pq}, \quad \text{for } \textit{antisymmetric modes} \quad (5.25)$$

The characteristic equations for symmetric and antisymmetric modes of Lamb waves, given by Eqs. (5.23) and (5.25), represent transcendental equations, which cannot be solved analytically. Instead, they can be effectively solved numerically leading to desired dispersion curves for Lamb waves propagating in an elastic layer—see Appendix B. Such dispersion curves obtained numerically are presented in Figs. 5.8 and 5.9 for symmetric and antisymmetric modes of Lamb waves.

It is interesting to note that the dispersion curves obtained for the fundamental symmetric  $S_0$  and antisymmetric  $A_0$  modes of Lamb waves are strongly correlated with Rayleigh surface waves, as the speed of Rayleigh waves  $c_R$  is their high frequency limit.

Moreover, it can also be seen from Eqs. (5.20) and (5.20) that displacement amplitude profiles of symmetric and antisymmetric modes of Lamb waves are directly dependent on the wave number  $k$ , hence they are dispersive and as such must be also dependent on the angular frequency  $\omega$ . For this reason these displacement amplitude profiles evolve with changes in the wave number  $k$  or the angular frequency  $\omega$ , which is not observed in the case of SH-waves discussed in Sect. 5.1. This variation is also clearly observed in Figs. 5.10 and 5.11 as a function of the frequency  $f$ , due to the well-known relationship between the angular and cyclic frequencies  $\omega = 2\pi f$ .

---

<sup>2</sup> It can be checked that  $\lambda k^2 + (\lambda + 2\mu)p^2 = (\rho c_p^2 - 2\mu)k^2 + \rho c_p^2 p^2$  since  $\lambda + 2\mu = \rho c_p^2$ , which can be easily rearranged to  $\lambda k^2 + (\lambda + 2\mu)p^2 = \rho c_p^2(k^2 + p^2) - 2\mu k^2$ . Next, from the definition of  $p$  and  $q$  it can be found that  $(k^2 + p^2)c_p^2 = (k^2 + q^2)c_s^2$ , which leads to  $\rho c_p^2(k^2 + p^2) - 2\mu k^2 = \rho c_s^2(k^2 + q^2) - 2\mu k^2 = \mu(k^2 + q^2) - 2\mu k^2$  since  $\mu = \rho c_s^2$ . Finally, after a simple rearrangement one obtains that  $\lambda k^2 + (\lambda + 2\mu)p^2 = -\mu(k^2 - q^2)$ .



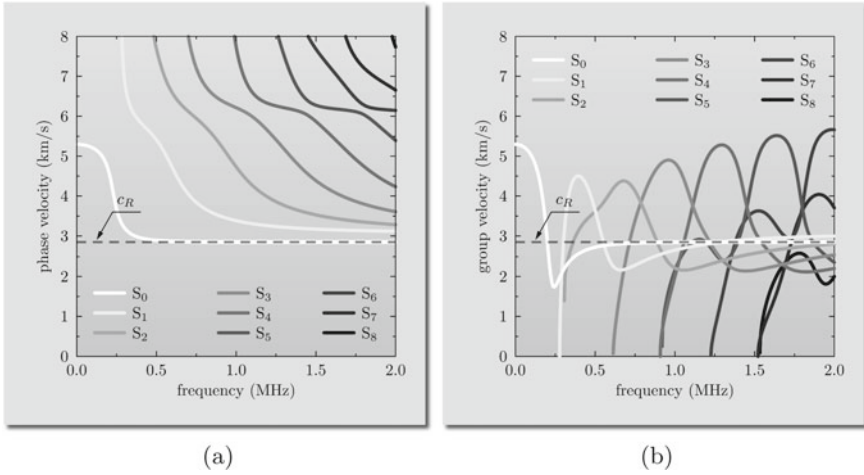


**Fig. 5.8** Dispersion curves for: **a** the phase velocity, **b** the group velocity, for symmetric modes of Lamb waves  $S_n$  ( $n = 0, 1, 2, \dots$ ) propagating in a 10 mm thick aluminium layer

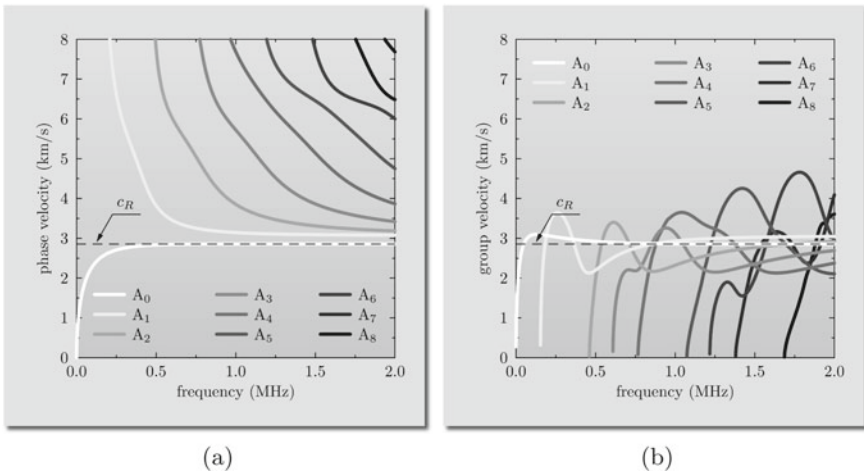


**Fig. 5.9** Dispersion curves for: **a** the phase velocity, **b** the group velocity, for antisymmetric modes of Lamb waves  $A_n$  ( $n = 0, 1, 2, \dots$ ) propagating in a 10 mm thick aluminium layer

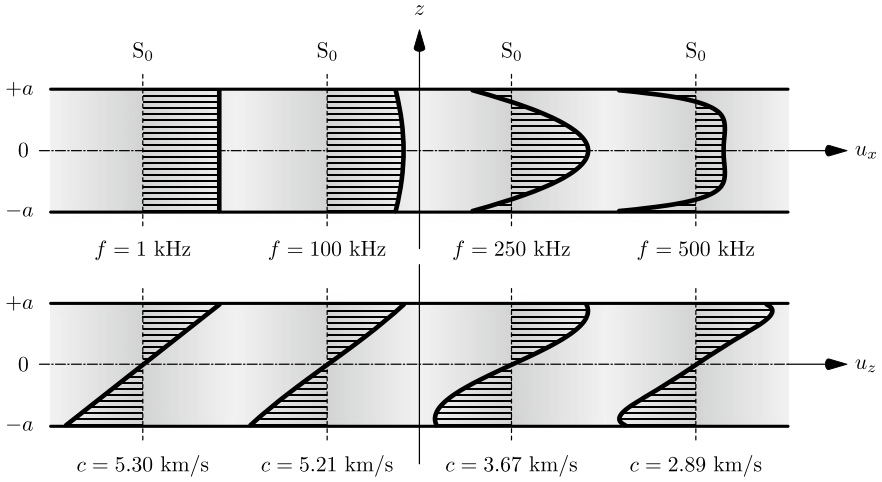


**Fig. 5.10** Relative displacement amplitudes as a function of the frequency  $f$  for the fundamental symmetric mode of Lamb waves  $S_0$  propagating in a 10mm thick aluminium layer

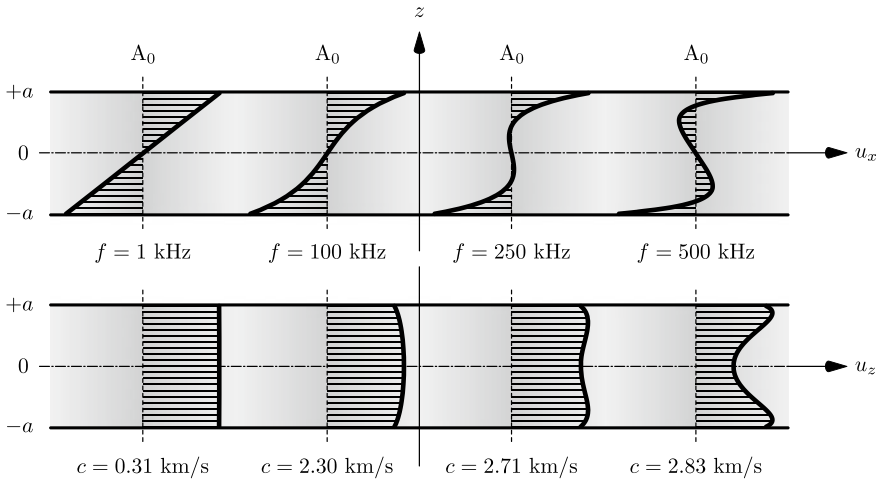


**Fig. 5.11** Relative displacement amplitudes as a function of the frequency  $f$  for the fundamental antisymmetric mode of Lamb waves  $A_0$  propagating in a 10mm thick aluminium layer

## References

1. J. D. Achenbach. *Wave propagation in elastic solids*. North-Holland Publishing Company, Amsterdam, 1973.
2. W. Ostachowicz, P. Kudela, M. Krawczuk, and A. Żak. *Guided waves in structures for SHM. The time-domain spectral element method*. John Wiley & Sons Ltd., Singapore, 2012.
3. J. L. Rose. *Ultrasonic waves in solid media*. Cambridge University Press, Cambridge, 1999.

# Chapter 6

## Waves in a 1-D Elastic Space



### 6.1 Longitudinal Waves

Longitudinal waves in a 1-D elastic space, likewise Rayleigh waves in a 2-D elastic space, also result from a simultaneous reflection and interaction of propagating P-waves and S-waves with the existing boundary. However, due to the closed form of the boundary<sup>1</sup> the observed behaviour is different.

It is most convenient to analyse longitudinal waves in a 1-D elastic space using the cylindrical  $(x, r, \theta)$  rather than the Cartesian  $(x, y, z)$  coordinate system—see Appendix C. Moreover, they can be assumed as propagating in a 1-D infinite elastic bar of circular cross-section presented in Fig. 6.1.

In Sect. 3.1 it was discussed that the equation of motion, given by Eq. (3.4), describing the wave phenomena in elastic media is independent of the selection of the coordinate system. For the sake of clarity and completeness this equation is presented below once more:

$$\mu \nabla^2 \mathbf{u} + (\lambda + \mu) \nabla (\nabla \cdot \mathbf{u}) = \rho \ddot{\mathbf{u}} \quad (6.1)$$

where  $\mathbf{u}$  is the vector of displacements, now dependent on the spatial coordinates  $x$ ,  $r$  and  $\theta$  as well as on time  $t$ .

The investigation of longitudinal waves also benefits from the application of Helmholtz's theorem and decomposition of the displacement field, according to Eq. (3.18) from Sect. 3.2, into a scalar potential  $\phi$  and a vector potential  $\Psi$ . Both potentials  $\psi$  and  $\Psi$  satisfy appropriate wave equations, i.e. Eqs. (3.21) and (3.22), which are also presented below:

---

<sup>1</sup> A closed boundary is the type of boundary, which surrounds the domain of interest confining it to a finite surface or volume. This is contrary to an open boundary, which has no such property, allowing the domain of interest to extend to infinity in one or more directions.

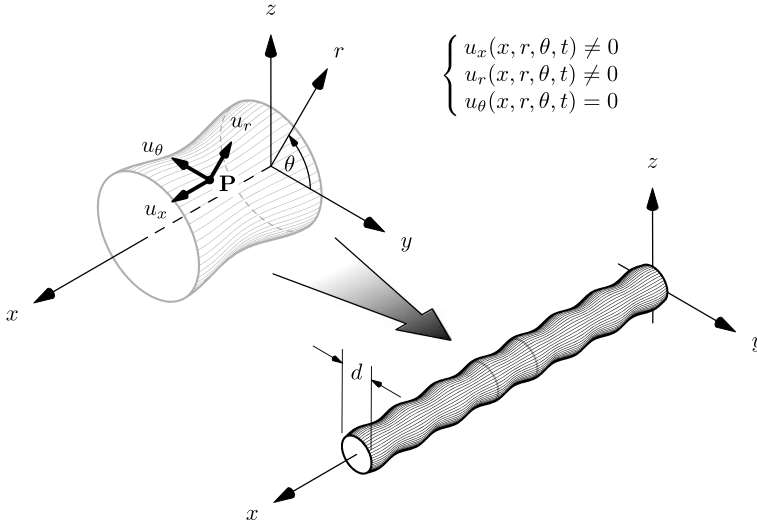


**Fig. 6.1** A schematic representation of a longitudinal wave propagating in a 1-D infinite elastic bar

$$\begin{cases} c_p^2 \nabla^2 \phi = \ddot{\phi} \\ c_s^2 \nabla^2 \Psi = \ddot{\Psi} \end{cases} \quad (6.2)$$

In the most general case particular components of the displacement vector  $\mathbf{u} = [u_x, u_r, u_\theta]^T$  in the cylindrical coordinate system  $(x, r, \theta)$  are defined as follows:

$$\begin{cases} u_x = \frac{\partial \phi}{\partial x} - \frac{1}{r} \frac{\partial \psi_r}{\partial \theta} + \frac{1}{r} \frac{\partial (r \psi_\theta)}{\partial r} \\ u_r = \frac{\partial \phi}{\partial r} + \frac{1}{r} \frac{\partial \psi_x}{\partial \theta} - \frac{\partial \psi_\theta}{\partial x} \\ u_\theta = \frac{1}{r} \frac{\partial \phi}{\partial \theta} + \frac{\partial \psi_r}{\partial x} - \frac{\partial \psi_x}{\partial r} \end{cases} \quad (6.3)$$

where  $\phi$  is the scalar potential,  $\psi_x$ ,  $\psi_r$  and  $\psi_\theta$  are the components of the vector potential  $\Psi = [\psi_x, \psi_r, \psi_\theta]^T$ , which in the most general case all remain dependent on the spatial coordinates  $x, r$  and  $\theta$  as well as on time  $t$ .

It can be noted that in the current case the nature of propagating longitudinal waves requires the vanishing of the tangential displacement component  $u_\theta$ , i.e.  $u_\theta = 0$ , the presence of which is typically associated with propagation of flexural or torsional waves. Additionally, the independence of the longitudinal and radial displacement components  $u_x$  and  $u_r$  of the angle  $\theta$  is implied, which results in the vanishing of two components of the vector potential  $\Psi$ , i.e.  $\psi_x = \psi_r = 0$ . As a consequence also two strain components  $\gamma_{x\theta}$  and  $\gamma_{r\theta}$  must vanish, i.e.  $\gamma_{x\theta} = \gamma_{r\theta} = 0$ .

Finally, the displacement vector  $\mathbf{u}$  can be expressed in the following way:

$$\begin{cases} u_x = \frac{\partial \phi}{\partial x} + \frac{1}{r} \frac{\partial(r\psi_\theta)}{\partial r} \\ u_r = \frac{\partial \phi}{\partial r} - \frac{\partial \psi_\theta}{\partial x} \end{cases} \quad (6.4)$$

where now  $u_x = u_x(x, r, t)$  and  $u_r = u_r(x, r, t)$  depend only on the spatial coordinates  $x$  and  $r$  as well as on time  $t$ .

After substitution of the displacement vector  $\mathbf{u}$ , given by Eq. (6.4), into the equation of motion (6.1) and after necessary mathematical manipulations and rearrangements, it can be checked that the equation of motion reduces to a set of two independent equations of motion expressed in terms of the scalar potentials  $\phi$  and  $\psi_\theta$ . This can be presented as:

$$\begin{cases} c_p^2 \nabla^2 \phi = \ddot{\phi} \\ c_s^2 \left( \nabla^2 \psi_\theta - \frac{\psi_\theta}{r^2} \right) = \ddot{\psi}_\theta \end{cases} \quad (6.5)$$

The second equation of motion can be further simplified<sup>2</sup> by the substitution  $\psi_\theta = -\frac{\partial \psi}{\partial r}$ , which helps to express Eq. (6.5) in the following way:

$$\begin{cases} c_p^2 \nabla^2 \phi = \ddot{\phi} & \text{or} & \frac{\partial^2 \phi}{\partial x^2} + \frac{\partial^2 \phi}{\partial r^2} + \frac{1}{r} \frac{\partial \phi}{\partial r} = \frac{1}{c_p^2} \frac{\partial^2 \phi}{\partial t^2} \\ c_s^2 \nabla^2 \psi = \ddot{\psi} & \text{or} & \frac{\partial^2 \psi}{\partial x^2} + \frac{\partial^2 \psi}{\partial r^2} + \frac{1}{r} \frac{\partial \psi}{\partial r} = \frac{1}{c_s^2} \frac{\partial^2 \psi}{\partial t^2} \end{cases} \quad (6.6)$$

where now  $\psi = \psi(x, r, t)$  is a new scalar potential dependent on the same spatial coordinates  $x$  and  $r$  as well as on time  $t$ .

Consequently, the displacement vector  $\mathbf{u}$  takes the following form:

$$\begin{cases} u_x = \frac{\partial \phi}{\partial x} - \frac{\partial^2 \psi}{\partial r^2} - \frac{1}{r} \frac{\partial \psi}{\partial r} \\ u_r = \frac{\partial \phi}{\partial r} + \frac{\partial^2 \psi}{\partial x \partial r} \end{cases} \quad (6.7)$$

<sup>2</sup> It can be checked that in the current case  $\nabla^2 \frac{\partial}{\partial r} = \frac{\partial}{\partial r} \frac{\partial^2}{\partial x^2} + \frac{\partial}{\partial r} \frac{\partial^2}{\partial r^2} + \frac{1}{r} \frac{\partial}{\partial r} \frac{\partial}{\partial r}$  since  $\nabla^2 = \frac{\partial^2}{\partial x^2} + \frac{\partial^2}{\partial r^2} + \frac{1}{r} \frac{\partial}{\partial r}$ . Noting that  $\frac{\partial}{\partial r} \left( \frac{1}{r} \frac{\partial}{\partial r} \right) = \frac{1}{r} \frac{\partial^2}{\partial r^2} - \frac{1}{r^2} \frac{\partial}{\partial r}$  it can be found that  $\nabla^2 \frac{\partial}{\partial r} = \frac{\partial}{\partial r} \frac{\partial^2}{\partial x^2} + \frac{\partial}{\partial r} \frac{\partial^2}{\partial r^2} + \frac{\partial}{\partial r} \left( \frac{1}{r} \frac{\partial}{\partial r} \right) + \frac{1}{r^2} \frac{\partial}{\partial r} = \frac{\partial}{\partial r} \nabla^2 + \frac{1}{r^2} \frac{\partial}{\partial r}$ . As a result, if  $\psi_\theta = -\frac{\partial \psi}{\partial r}$  then  $-c_s^2 \left( \nabla^2 \frac{\partial \psi}{\partial r} - \frac{1}{r^2} \frac{\partial \psi}{\partial r} \right) = -\frac{\partial \ddot{\psi}}{\partial r}$ , which leads to  $-c_s^2 \left[ \left( \frac{\partial}{\partial r} \nabla^2 \psi + \frac{1}{r^2} \frac{\partial \psi}{\partial r} \right) - \frac{1}{r^2} \frac{\partial \psi}{\partial r} \right] = -\frac{\partial \ddot{\psi}}{\partial r}$ . This reduces to  $\frac{\partial}{\partial r} (c_s^2 \nabla^2 \psi) = \frac{\partial}{\partial r} \ddot{\psi}$ , which has to be satisfied independently of  $r$ , thus  $c_s^2 \nabla^2 \psi = \ddot{\psi}$ .

Following the procedure already known from previous sections, solutions to the wave equations given by Eq. (6.6) can be assumed yet again as two independent harmonic functions:

$$\begin{cases} \phi(x, r, t) = \Phi(r)e^{ik(x-ct)} \\ \psi(x, r, t) = \Psi(r)e^{ik(x-ct)} \end{cases} \quad (6.8)$$

where  $\Phi(r)$  and  $\Psi(r)$  represent unknown functions dependent only on the spatial coordinate  $r$ .

Substitution of Eq. (5.8) into the appropriate wave equations, expressed by Eq. (6.6), leads this time to two Bessel differential equations:

$$\begin{cases} \frac{d^2\Phi(r)}{dr^2} + \frac{1}{r} \frac{d\Phi(r)}{dr} + \alpha^2\Phi(r) = 0 \\ \frac{d^2\Psi(r)}{dr^2} + \frac{1}{r} \frac{d\Psi(r)}{dr} + \beta^2\Psi(r) = 0 \end{cases} \quad (6.9)$$

with:

$$\begin{cases} \alpha = k\sqrt{\frac{c^2}{c_p^2} - 1} = \sqrt{\frac{\omega^2}{c_p^2} - k^2} \\ \beta = k\sqrt{\frac{c^2}{c_s^2} - 1} = \sqrt{\frac{\omega^2}{c_s^2} - k^2} \end{cases} \quad (6.10)$$

where  $\alpha$  and  $\beta$  denote the same constants as in Eq. (5.13) in Sect. 5.2 in the case of Lamb waves. They remain dependent on the angular frequency  $\omega$ , the wave number  $k$  as well as the velocities of P-waves and S-waves propagating in a 3-D elastic medium.

Next, the displacement field associated with propagation of longitudinal waves in the 1-D infinite elastic bar under consideration, thanks to Eq. (6.8), can be easily written as:

$$\begin{cases} u_x(x, r, t) = \hat{u}_x(r)e^{ik(x-ct)} \\ u_r(x, r, t) = \hat{u}_r(r)e^{ik(x-ct)} \end{cases} \quad (6.11)$$

where the amplitudes of particular plane harmonic waves are:

$$\begin{cases} \hat{u}_x(r) = ik\Phi(r) - \frac{1}{r} \frac{d\Psi(r)}{dr} - \frac{d^2\Psi(r)}{dr^2} \\ \hat{u}_r(r) = \frac{d\Phi(r)}{dr} + ik\frac{d\Psi(r)}{dr} \end{cases} \quad (6.12)$$

The strain components, which result from the propagation of longitudinal waves within the bar, can be presented in an analogous way:

$$\begin{cases} \epsilon_{xx} = \frac{\partial u_x}{\partial x} = \hat{\epsilon}_{xx}(r)e^{ik(x-ct)} \\ \epsilon_{rr} = \frac{\partial u_r}{\partial r} = \hat{\epsilon}_{rr}(r)e^{ik(x-ct)} \\ \epsilon_{\theta\theta} = \frac{u_r}{r} = \hat{\epsilon}_{\theta\theta}(r)e^{ik(x-ct)} \\ \gamma_{xr} = \frac{\partial u_x}{\partial r} + \frac{\partial u_r}{\partial x} = \hat{\gamma}_{xr}(r)e^{ik(x-ct)} \end{cases} \quad (6.13)$$

which leads to the following expressions for the amplitudes of the strain field components dependent on the two unknown functions  $\Phi$  and  $\Psi$ :

$$\begin{cases} \hat{\epsilon}_{xx}(r) = -k^2\Phi(r) - \frac{ik}{r}\frac{d\Psi(r)}{dr} - ik\frac{d^2\Psi(r)}{dr^2} \\ \hat{\epsilon}_{rr}(r) = \frac{d^2\Phi(r)}{dr^2} + ik\frac{d^2\Psi(r)}{dr^2} \\ \hat{\epsilon}_{\theta\theta}(r) = \frac{1}{r}\frac{d\Phi(r)}{dr} + \frac{ik}{r}\frac{d\Psi(r)}{dr} \\ \hat{\gamma}_{xr}(r) = 2ik\frac{d\Phi(r)}{dr} - k^2\frac{d\Psi(r)}{dr} + \frac{1}{r^2}\frac{d\Psi(r)}{dr} \\ \quad - \frac{1}{r}\frac{d^2\Psi(r)}{dr^2} - \frac{d^3\Psi(r)}{dr^3} \end{cases} \quad (6.14)$$

At this point it is worth noting that solutions to Eq. (6.9) can be expressed by Bessel functions of the first kind  $J_0(\alpha r)$  and  $J_0(\beta r)$ , as well as Bessel functions of the second kind  $Y_0(\alpha r)$  and  $Y_0(\beta r)$ .

Bearing in mind the fact that the Bessel functions of the second kind  $Y_0(\alpha r)$  and  $Y_0(\beta r)$  are singular at  $r = 0$  these solutions should be disregarded in the case of the bar under investigation. Consequently the unknown functions  $\Phi$  and  $\Psi$  can be presented in the following straightforward manner:

$$\begin{cases} \Phi(r) = A_1 J_0(\alpha r) \\ \Psi(r) = A_2 J_0(\beta r) \end{cases} \quad (6.15)$$

where  $A_1$  and  $A_2$  are certain constants, which help to express the potentials  $\phi$  and  $\psi$  as:

$$\begin{cases} \phi(x, r, t) = A_1 J_0(\alpha r)e^{ik(x-ct)} \\ \psi(x, r, t) = A_2 J_0(\beta r)e^{ik(x-ct)} \end{cases} \quad (6.16)$$

where  $c$  is the phase velocity of longitudinal waves propagating in the direction of the  $x$  axis.



As before, the application of the traction-free boundary conditions for the stress components  $\sigma_{rr}$  and  $\tau_{xr}$  at the free surface of the bar, i.e. for  $r = a$ :

$$\sigma_{rr}(x, r, t) = \tau_{xr}(x, r, t) = 0, \quad \text{for } r = a \quad (6.17)$$

with  $2a = d$ , where  $d$  denotes the diameter of the bar, allows one to obtain the dispersion relations for longitudinal waves propagating in the 1-D isotropic elastic bar under consideration.

According to the standard procedure, well-known from the previous sections, the stress components  $\sigma_{rr}$  and  $\tau_{xr}$  can be expressed by the use of Hooke's law. Thanks to this the following two equations are obtained:

$$\left\{ \begin{array}{l} \sigma_{rr}|_a = 0 \rightarrow \lambda \left[ k^2 \Phi(a) - \frac{1}{a} \frac{d\Phi(a)}{dr} \right] - (\lambda + 2\mu) \frac{d^2\Phi(a)}{dr^2} \\ \quad - 2ik\mu \frac{d^2\Psi(a)}{dr^2} = 0 \\ \tau_{xr}|_a = 0 \rightarrow \mu \left[ 2ik \frac{d\Phi(a)}{dr} - k^2 \frac{d\Psi(a)}{dr} + \frac{1}{a^2} \frac{d^2\Psi(a)}{dr^2} \right. \\ \quad \left. - \frac{d^3\Psi(a)}{dr^3} \right] = 0 \end{array} \right. \quad (6.18)$$

where as previously the factor  $e^{ik(x-ct)}$  is not present since the traction-free boundary conditions must be satisfied for propagating longitudinal waves independently of the spatial coordinate  $x$  and time  $t$ .

Now, the system of two equations resulting from the traction-free boundary conditions can be expressed by the potentials  $\phi$  and  $\psi$ , as presented by Eq. (6.16). This results in a set of two homogeneous equations with two unknown constants  $A_1$  and  $A_2$ . The system has non-trivial solutions only if its determinant vanishes, which leads to the characteristic equation known in the literature as the Pochhammer frequency equation for longitudinal modes propagating in circular rods. The Pochhammer equation can be presented as:

$$\begin{aligned} \frac{2\alpha}{a}(\beta^2 + k^2)J_1(\alpha a)J_1(\beta a) - (\beta^2 - k^2)J_0(\alpha a)J_1(\beta a) \\ - 4k^2\alpha\beta J_1(\alpha a)J_0(\beta a) = 0 \end{aligned} \quad (6.19)$$

It is noteworthy that the Pochhammer equation was studied over the years by many researchers [1–5]. However, due to its mathematical complexity no roots of this equation were known for many years. Nowadays these roots can be effectively found only numerically—see Appendix B. Since the roots are dependent on the wave number  $k$  the longitudinal waves propagating in circular rods must be dispersive in nature. Resulting dispersion curves for the phase and group velocities as a function of the cyclic frequency  $f$  are shown in Fig. 6.2.

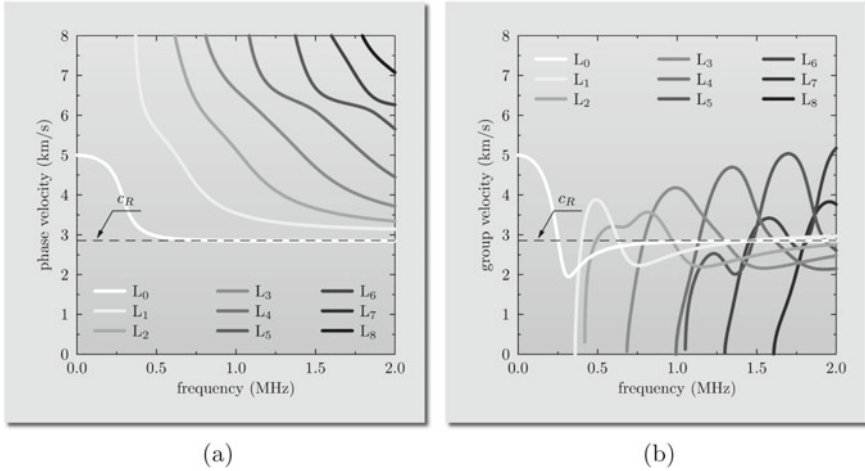
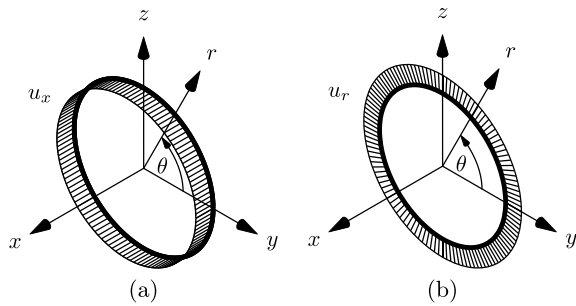


**Fig. 6.2** Dispersion curves for: **a** the phase velocity, **b** the group velocity, for modes of longitudinal waves  $L_n (n = 0, 1, 2, \dots)$  propagating in a 10 mm diameter aluminium bar

**Fig. 6.3** Distribution of displacement components: **a** longitudinal  $u_x$ , **b** radial  $u_r$ , on the bar circumference, for the fundamental mode of longitudinal waves  $L_0$  propagating in a 10 mm diameter aluminium bar, at the frequency  $f = 1$  kHz



The modes of longitudinal waves are very often noted in the literature [6, 7] as  $L_n (n = 0, 1, 2, \dots)$ . Their behaviour is very similar to the behaviour of symmetric modes of Lamb waves propagating in an elastic layer and discussed in Sect. 5.2, however, they originate from very different characteristic equations. This can be clearly seen in Fig. 6.2, when compared with the results presented in Fig. 5.9. This similarity concerns not only the frequency behaviour of modes propagating within the 1-D infinite elastic bar under consideration, but also extends onto the displacement amplitude profiles presented in Figs. 6.4 and 6.5.

As before, the knowledge of the dispersion curves from Fig. 6.2 associated with the propagation of longitudinal waves within the bar, together with the use of Eqs. (6.10), (6.12) and (6.15), enables one to establish the displacement amplitude profiles for required values of the angular frequency  $\omega$  or the cyclic frequency  $f$ , as shown in Fig. 6.3. This can be done based on the following simple relations:

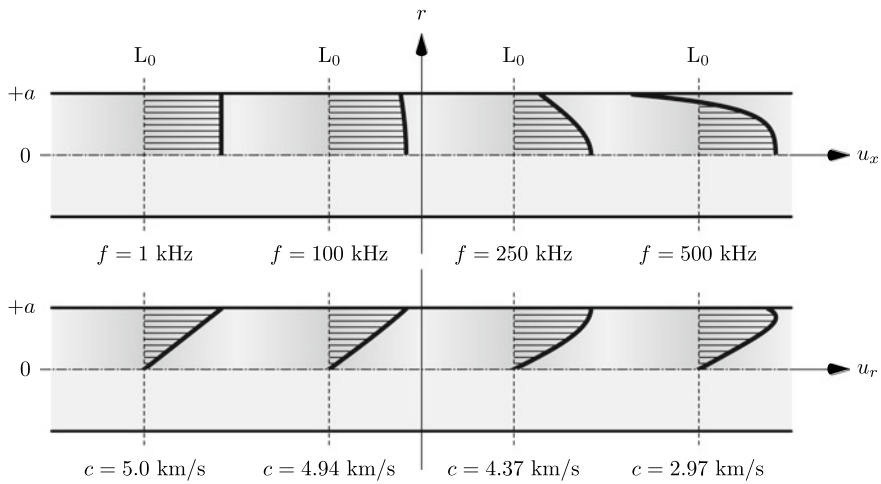


**Fig. 6.4** Relative displacement amplitudes as a function of the frequency  $f$  for the fundamental mode of longitudinal waves  $L_0$  propagating in a 10 mm diameter aluminium bar

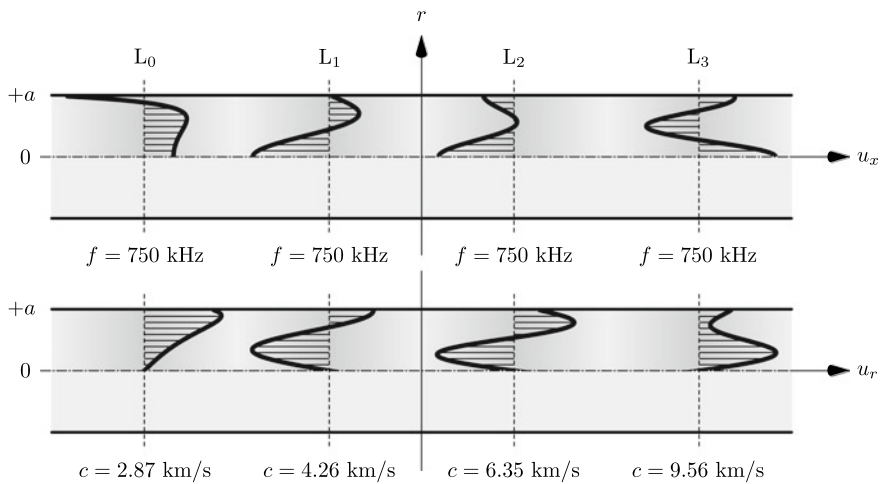


**Fig. 6.5** Relative displacement amplitudes for modes of longitudinal waves  $L_n (n = 0, 1, 2, \dots)$  propagating in a 10 mm diameter aluminium bar, at the frequency  $f = 750$  kHz

$$\begin{cases} \hat{u}_x(r) = A_1 ik J_0(\alpha r) + A_2 \beta^2 J_0(\beta r) \\ \hat{u}_r(r) = -A_1 \alpha J_1(\alpha r) - A_2 ik \beta J_1(\beta r) \end{cases} \quad (6.20)$$

It should strongly emphasised though that in the current case of longitudinal waves propagating in the bar the displacement amplitude profiles concern the longitudinal and radial displacement components  $u_x$  and  $u_r$ , while in the case of symmetric modes of Lamb waves propagating in an elastic layer they represented the longitudinal and

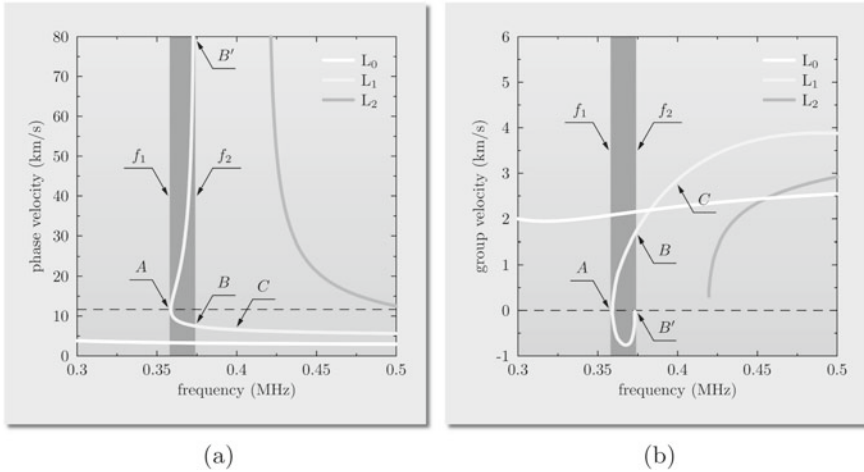


**Fig. 6.6** Detailed view of the dispersion curve for the second mode of longitudinal waves  $L_1$  propagating in a 10 mm diameter aluminium bar: **a** the phase velocity, **b** the group velocity, exhibiting unusual behaviour leading to negative values of the group velocity

transverse displacement components  $u_x$  and  $u_z$ . Here it can be also noted that the dispersion curve obtained for the fundamental mode  $L_0$ , in a similar manner as in the case of the fundamental mode of Lamb waves  $S_0$ , is also correlated with Rayleigh surface waves, as the speed of Rayleigh waves  $c_R$  is its high frequency limit.

In the case of the longitudinal waves propagating within the 1-D infinite elastic bar the frequency dependence of the second mode  $L_1$  exhibits some unusual behaviour. This is when the analysis of the phase velocity  $c$  for this mode is extended onto a wider range of phase velocities, reaching or even exceeding 100 km/s, as presented in Fig. 6.6. Then it can be observed that within a relatively narrow frequency band of 14 kHz, starting from the frequency  $f_1 = 356.8$  kHz up to the frequency  $f_2 = 372.8$  kHz, the dispersion curve for the second mode  $L_1$  is double-valued. This is clearly seen along the dispersion curve for this mode between points  $B'$ ,  $A$  and  $B$ . As a consequence the group velocity within this frequency band exhibits simultaneously positive and negative values, as presented in Fig. 6.6, leading to the phenomenon known in the literature as the so-called *backward wave propagation* [8, 9].

Although individual monochromatic waves within this frequency band have different and always positive values of their phase velocities, simultaneously travelling wave packets are characterised by group velocities of different signs, as shown in Fig. 6.6. Point  $A$  appears as a very specific point on the dispersion curve for mode  $L_1$ . It represents the so-called *zero-group-velocity* resonance [10, 11], where the group velocity drops to zero for a non-zero value of the phase velocity. Such points are typical for most isotropic materials and concern the first order modes, i.e. longitudinal modes in the case of elastic bars or symmetric modes in the case of Lamb waves propagating within elastic layers. At the same time it should be noted that

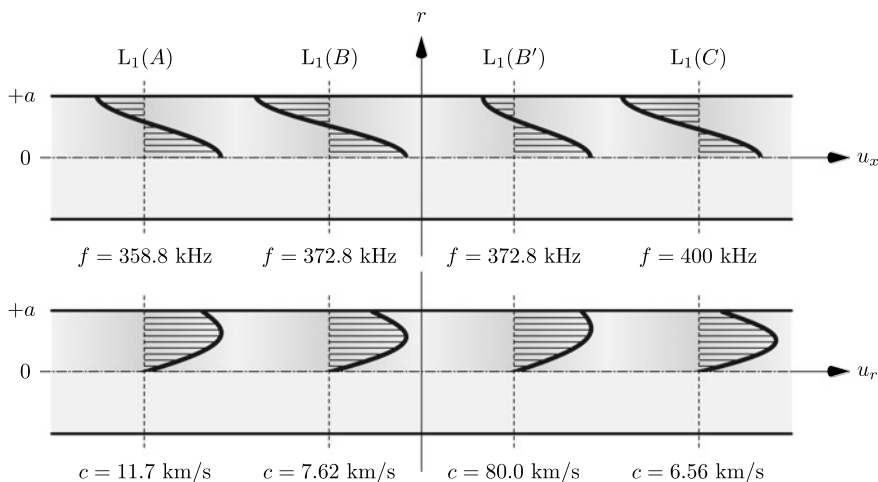


**Fig. 6.7** Relative displacement amplitudes for the second mode of longitudinal waves  $L_1$  propagating in a 10 mm diameter aluminium bar, near the critical point of the mode

the displacement amplitude profiles within this frequency band remain practically unchanged, as illustrated in Fig. 6.7.

Additionally, it should be also strongly emphasised that this kind of phenomenon is not limited to the behaviour of longitudinal modes discussed in the case of the bar under consideration. This kind of behaviour can also be observed in the case of numerous symmetric modes of Lamb waves, and was extensively investigated not only theoretically but also experimentally, by many researchers [12–16].

## 6.2 Flexural Waves

In a similar manner to longitudinal waves, flexural waves also originate from a simultaneous reflection and interaction of propagating P-waves and S-waves with the existing boundary, but their presence results from a different type of excitation, which has no axial symmetry. Consequently, their mathematical description must be similar to that presented in Sect. 4.1 concerning Rayleigh waves in 2-D elastic space.

A starting point in the analysis of propagation of flexural waves in a 1-D infinite elastic bar of circular cross-section, shown in Fig. 6.8, can be the same equation of motion as in the case of longitudinal waves:

$$\mu \nabla^2 \mathbf{u} + (\lambda + \mu) \nabla (\nabla \cdot \mathbf{u}) = \rho \ddot{\mathbf{u}} \tag{6.21}$$

This time, however, the same vector of displacement  $\mathbf{u}$  has three non-vanishing displacement components in the cylindrical coordinate system  $(x, r, \theta)$ —see

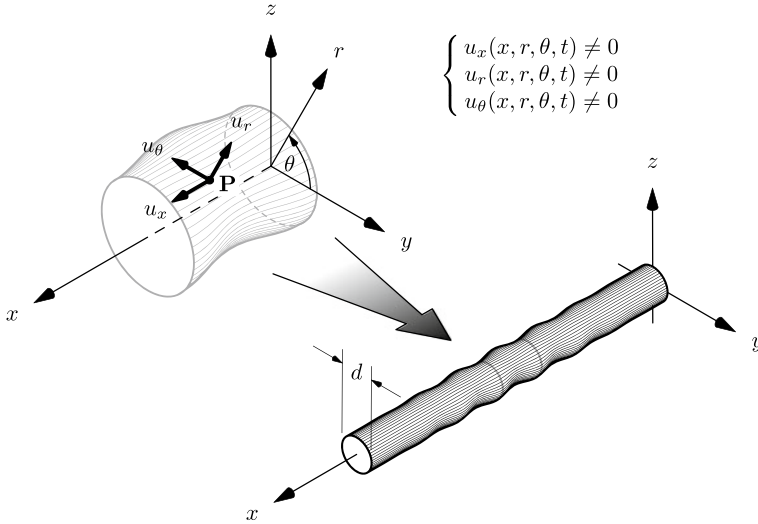


**Fig. 6.8** A schematic representation of a flexural wave propagating in a 1-D infinite elastic bar

Appendix C. They are dependent on the spatial coordinates  $x$ ,  $r$  and  $\theta$  as well as on time and represent longitudinal  $u_x = u_x(x, r, \theta, t)$ , radial  $u_r = u_r(x, r, \theta, t)$  and tangential  $u_\theta = u_\theta(x, r, \theta, t)$  displacements.

Again, it is very convenient to begin with the application of Helmholtz’s theorem and the decomposition of the displacement field into a scalar potential  $\phi$  and a vector potential  $\Psi$  according to Eq. (3.18) from Sect.n 3.2. As a result the potentials  $\psi$  and  $\Psi$  satisfy appropriate wave equations, i.e. Eqs. (3.21) and (3.22), which are also presented below:

$$\begin{cases} c_p^2 \nabla^2 \phi = \ddot{\phi} \\ c_s^2 \nabla^2 \Psi = \ddot{\Psi} \end{cases} \quad (6.22)$$

while particular components of the displacement vector  $\mathbf{u} = [u_x, u_r, u_\theta]^T$  can be expressed in the cylindrical coordinate system  $(x, r, \theta)$  by the same set of relations:

$$\begin{cases} u_x = \frac{\partial \phi}{\partial x} - \frac{1}{r} \frac{\partial \psi_r}{\partial \theta} + \frac{1}{r} \frac{\partial (r \psi_\theta)}{\partial r} \\ u_r = \frac{\partial \phi}{\partial r} + \frac{1}{r} \frac{\partial \psi_x}{\partial \theta} - \frac{\partial \psi_\theta}{\partial x} \\ u_\theta = \frac{1}{r} \frac{\partial \phi}{\partial \theta} + \frac{\partial \psi_r}{\partial x} - \frac{\partial \psi_x}{\partial r} \end{cases} \quad (6.23)$$

where  $\phi$  is the scalar potential,  $\psi_x$ ,  $\psi_r$  and  $\psi_\theta$  are all non-vanishing components of the vector potential  $\Psi = [\psi_x, \psi_r, \psi_\theta]^T$  dependent on the spatial coordinates  $x$ ,  $r$  and  $\theta$  as well as on time  $t$ .

Substitution of Eq. (6.23) into the wave equations given by Eq. (6.22) and some necessary mathematical manipulations and rearrangements leads this time to a set of four independent wave equations expressed in terms of the scalar potential  $\phi$  as well as the scalar potentials  $\psi_x$ ,  $\psi_r$  and  $\psi_\theta$ , being the components of the vector potential  $\Psi$ :

$$\begin{cases} c_p^2 \nabla^2 \phi = \ddot{\phi}, & c_s^2 \nabla^2 \psi_x = \ddot{\psi}_x \\ c_s^2 \left( \nabla^2 \psi_r - \frac{\psi_r}{r^2} - \frac{2}{r^2} \frac{\partial \psi_\theta}{\partial \theta} \right) = \ddot{\psi}_r \\ c_s^2 \left( \nabla^2 \psi_\theta - \frac{\psi_\theta}{r^2} + \frac{2}{r^2} \frac{\partial \psi_r}{\partial \theta} \right) = \ddot{\psi}_\theta \end{cases} \quad (6.24)$$

Solutions to Eq. (6.2) can be represented this time by four independent functions<sup>3</sup>:

$$\begin{cases} \phi(x, r, \theta, t) = \Phi(r) e^{ik(x-ct)} \cos \theta \\ \psi_x(x, r, \theta, t) = \Psi_x(r) e^{ik(x-ct)} \sin \theta \\ \psi_r(x, r, \theta, t) = \Psi_r(r) e^{ik(x-ct)} \sin \theta \\ \psi_\theta(x, r, \theta, t) = \Psi_\theta(r) e^{ik(x-ct)} \cos \theta \end{cases} \quad (6.25)$$

where  $\Phi(r)$  and  $\Psi_x(r)$ ,  $\Psi_r(r)$  and  $\Psi_\theta(r)$  represent four new unknown functions dependent only on the spatial coordinate  $r$ .

A simple substitution of Eq. (6.25) into Eq. (6.24) results in a set of four differential equations for the unknown functions  $\Phi$ ,  $\Psi_x$ ,  $\Psi_r$  and  $\Psi_\theta$ . It can be noted that the last two equations are coupled and as such cannot be solved. However, they can be easily decoupled by producing two new equations representing their sum and difference, i.e. for  $\Psi_r + \Psi_\theta$  and  $\Psi_r - \Psi_\theta$ . In such a manner the complete set of four equations leads to Bessel's differential equations of very well-known solutions.

$$\begin{cases} \frac{d^2 \Phi(r)}{dr^2} + \frac{1}{r} \frac{d\Phi(r)}{dr} - \frac{\Phi(r)}{r^2} + \alpha^2 \Phi(r) = 0 \\ \frac{d^2 \Psi_x(r)}{dr^2} + \frac{1}{r} \frac{d\Psi_x(r)}{dr} - \frac{\Psi_x(r)}{r^2} + \beta^2 \Psi_x(r) = 0 \\ \frac{d^2 \Psi_r(r)}{dr^2} + \frac{1}{r} \frac{d\Psi_r(r)}{dr} - \frac{2\Psi_r(r)}{r^2} + \beta^2 \Psi_r(r) + \frac{2\Psi_\theta(r)}{r^2} = 0 \\ \frac{d^2 \Psi_\theta(r)}{dr^2} + \frac{1}{r} \frac{d\Psi_\theta(r)}{dr} - \frac{2\Psi_\theta(r)}{r^2} + \beta^2 \Psi_\theta(r) + \frac{2\Psi_r(r)}{r^2} = 0 \end{cases} \quad (6.26)$$

<sup>3</sup> In the case of a hollow cylindrical bar the dependence of the scalar potentials  $\phi$  as well as  $\psi_x$ ,  $\psi_r$  and  $\psi_\theta$  on the angle  $\theta$  involves harmonic functions  $\sin m\theta$  and  $\cos m\theta$  where  $m = 0, 1, 2, \dots$ , which lead to an infinite set of circumferential solutions [17, 18]. In the case of a full cylindrical bar the most important family of these solutions, however, is the case of  $m = 1$ .

with:

$$\begin{cases} \alpha = k\sqrt{\frac{c^2}{c_p^2} - 1} = \sqrt{\frac{\omega^2}{c_p^2} - k^2} \\ \beta = k\sqrt{\frac{c^2}{c_s^2} - 1} = \sqrt{\frac{\omega^2}{c_s^2} - k^2} \end{cases} \quad (6.27)$$

where  $\alpha$  and  $\beta$  denote the same constants as in Eq. (5.13) in Sect. 5.2 in the case of Lamb waves. They remain dependent on the angular frequency  $\omega$ , the wave number  $k$  as well as the velocities of P-waves and S-waves propagating in a 3-D elastic medium.

The displacement components associated with propagation of flexural waves in the 1-D infinite elastic bar can be easily expressed by the use of the unknown functions  $\Phi$ ,  $\Psi_x$ ,  $\Psi_r$  and  $\Psi_\theta$  by a simple substitution of Eq. (6.25) into Eq. (6.23) and some rearrangements of terms. Taking into account the considerations from previous sections they can be conveniently expressed as plane harmonic waves of amplitude profiles dependent on the radial coordinate  $r$  additionally multiplied by appropriate factors dependent on the angle  $\theta$ . This can be presented as:

$$\begin{cases} u_x(x, r, \theta, t) = \hat{u}_x(r)e^{ik(x-ct)} \cos \theta \\ u_r(x, r, \theta, t) = \hat{u}_r(r)e^{ik(x-ct)} \cos \theta \\ u_\theta(x, r, \theta, t) = \hat{u}_\theta(r)e^{ik(x-ct)} \sin \theta \end{cases} \quad (6.28)$$

where particular amplitude profiles have the forms:

$$\begin{cases} \hat{u}_x(r) = ik\Phi(r) - \frac{\Psi_r(r)}{r} + \frac{\Psi_\theta(r)}{r} + \frac{d\Psi_\theta(r)}{dr} \\ \hat{u}_r(r) = \frac{d\Phi(r)}{dr} - ik\Psi_\theta(r) + \frac{\Psi_x(r)}{r} \\ \hat{u}_\theta(r) = -\frac{\Phi(r)}{r} + ik\Psi_r(r) - \frac{d\Psi_x(r)}{dr} \end{cases} \quad (6.29)$$

The strain components associated with the propagation of flexural waves in the bar can be expressed in a similar manner thanks to the following relations:



$$\left\{ \begin{array}{l} \epsilon_{xx} = \frac{\partial u_x}{\partial x} = \hat{\epsilon}_{xx}(r)e^{ik(x-ct)} \cos \theta \\ \epsilon_{rr} = \frac{\partial u_r}{\partial r} = \hat{\epsilon}_{rr}(r)e^{ik(x-ct)} \cos \theta \\ \epsilon_{\theta\theta} = \frac{u_r}{r} + \frac{1}{r} \frac{\partial \Psi_\theta(r)}{\partial \theta} = \hat{\epsilon}_{\theta\theta}(r)e^{ik(x-ct)} \cos \theta \\ \gamma_{xr} = \frac{\partial u_r}{\partial x} + \frac{\partial u_x}{\partial r} = \hat{\gamma}_{xr}(r)e^{ik(x-ct)} \cos \theta \\ \gamma_{r\theta} = \frac{\partial u_\theta}{\partial r} - \frac{u_\theta}{r} + \frac{1}{r} \frac{\partial u_r}{\partial \theta} = \hat{\gamma}_{r\theta}(r)e^{ik(x-ct)} \sin \theta \\ \gamma_{x\theta} = \frac{1}{r} \frac{\partial \Psi_x(r)}{\partial \theta} + \frac{\partial \Psi_\theta(r)}{\partial x} = \hat{\gamma}_{x\theta}(r)e^{ik(x-ct)} \sin \theta \end{array} \right. \quad (6.30)$$

This leads to the expressions for amplitude profiles associated with the components of the strain field as dependent on all unknown functions  $\Phi$ ,  $\Psi_x$ ,  $\Psi_r$  and  $\Psi_\theta$ :

$$\left\{ \begin{array}{l} \hat{\epsilon}_{xx}(r) = -k^2\Phi(r) - \frac{ik\Psi_r(r)}{r} + \frac{ik\Psi_\theta(r)}{r} + ik \frac{d\Psi_\theta(r)}{dr} \\ \hat{\epsilon}_{rr}(r) = -\frac{\Psi_x(r)}{r^2} - ik \frac{d\Psi_\theta(r)}{dr} + \frac{1}{r} \frac{d\Psi_x(r)}{dr} + \frac{d^2\Phi(r)}{dr^2} \\ \hat{\epsilon}_{\theta\theta}(r) = -\frac{\Phi(r)}{r^2} + \frac{ik\Psi_r(r)}{r} - \frac{ik\Psi_\theta(r)}{r} + \frac{\Psi_x(r)}{r^2} \\ \quad + \frac{1}{r} \frac{d\Phi(r)}{dr} - \frac{1}{r} \frac{d\Psi_x(r)}{dr} \\ \hat{\gamma}_{xr}(r) = \frac{\Psi_r(r)}{r^2} + k^2\Psi_\theta(r) - \frac{\Psi_\theta(r)}{r^2} + \frac{ik\Psi_x(r)}{r} + 2ik \frac{d\Phi(r)}{dr} \\ \quad - \frac{1}{r} \frac{d\Psi_r(r)}{dr} + \frac{1}{r} \frac{d\Psi_\theta(r)}{dr} + \frac{d^2\Psi_\theta(r)}{dr^2} \\ \hat{\gamma}_{r\theta}(r) = \frac{2\Phi(r)}{r^2} - \frac{ik\Psi_r(r)}{r} + \frac{ik\Psi_\theta(r)}{r} - \frac{\Psi_x(r)}{r} - \frac{2}{r} \frac{d\Phi(r)}{dr} \\ \quad + ik \frac{d\Psi_r(r)}{dr} + \frac{1}{r} \frac{d\Psi_x}{dr} - \frac{d^2\Psi_x(r)}{dr^2} \\ \hat{\gamma}_{x\theta}(r) = -\frac{2ik\Phi(r)}{r} - k^2\Psi_r(r) + \frac{\Psi_r(r)}{r^2} - \frac{\Psi_\theta(r)}{r^2} \\ \quad - \frac{1}{r} \frac{d\Psi_\theta(r)}{dr} - ik \frac{d\Psi_x(r)}{dr} \end{array} \right. \quad (6.31)$$

Following the same solution procedure as in the case of longitudinal waves discussed in previous Sect. 6.1, it can be found that solutions to Eq. (6.26) can be expressed by two Bessel functions of the first kind  $J_i(\alpha r)$  and  $J_i(\beta r)$  as well as two Bessel functions of the second kind  $Y_i(\alpha r)$  and  $Y_i(\beta r)$ , where  $i = 0, 1, 2$ .

As before the singular behaviour of the Bessel function of the second kind  $Y_i(\alpha r)$  and  $Y_i(\beta r)$  at  $r = 0$  leads to the results that this branch of solutions should be

disregarded. Consequently the unknown functions  $\Phi(r)$  and  $\Psi_x(r)$ ,  $\Psi_r(r)$  and  $\Psi_\theta(r)$  take the following forms:

$$\begin{cases} \Phi(r) = AJ_1(\alpha r) \\ \Psi_x(r) = BJ_1(\beta r) \\ \Psi_r(r) = CJ_0(\beta r) + DJ_2(\beta r) \\ \Psi_\theta(r) = CJ_0(\beta r) - DJ_2(\beta r) \end{cases} \quad (6.32)$$

where  $A$ ,  $B$ ,  $C$  and  $D$  are certain constants, which leads to the potentials  $\phi$ ,  $\psi_x$ ,  $\psi_r$  and  $\psi_\theta$  presented in the following manner:

$$\begin{cases} \phi(x, r, \theta, t) = AJ_1(\alpha r)e^{ik(x-ct)} \cos \theta \\ \psi_x(x, r, \theta, t) = BJ_1(\beta r)e^{ik(x-ct)} \sin \theta \\ \psi_r(x, r, \theta, t) = [CJ_0(\beta r) + DJ_2(\beta r)]e^{ik(x-ct)} \sin \theta \\ \psi_\theta(x, r, \theta, t) = [CJ_0(\beta r) - DJ_2(\beta r)]e^{ik(x-ct)} \cos \theta \end{cases} \quad (6.33)$$

At this point it should be noted that the displacement vector  $\mathbf{u}$ , expressed by the potentials  $\phi$ ,  $\psi_x$ ,  $\psi_r$  and  $\psi_\theta$ , is specified in terms of four constants:  $A$ ,  $B$ ,  $C$  and  $D$ , whereas there are only three traction-free boundary conditions for the stress components:  $\sigma_{rr}$ ,  $\tau_{xr}$  and  $\tau_{r\theta}$  at the free surface of the bar.

The fourth condition that could help to determine these potentials can be the already known condition about the solenoidal character of the potential vector  $\Psi$ , i.e.  $\nabla \cdot \Psi = 0$ . This is a sufficient condition for the existence of solutions in the form assumed by Helmholtz's theorem and given by Eq. (3.18), but it is not a necessary condition [8]. Additionally, its application leads to unnecessary mathematical complications [17].

The fourth condition is somehow arbitrary and in the current case can result from the assumption of the vanishing of the potential vector  $\Psi$  when  $r \rightarrow 0$ , which yields  $C = 0$  and  $\psi_r = -\psi_\theta$ . Thus, the potentials  $\phi$ ,  $\psi_x$ ,  $\psi_r$  and  $\psi_\theta$  can be presented as:

$$\begin{cases} \phi(x, r, \theta, t) = AJ_1(\alpha r)e^{ik(x-ct)} \cos \theta \\ \psi_x(x, r, \theta, t) = BJ_1(\beta r)e^{ik(x-ct)} \sin \theta \\ \psi_r(x, r, \theta, t) = DJ_2(\beta r)e^{ik(x-ct)} \sin \theta \\ \psi_\theta(x, r, \theta, t) = -DJ_2(\beta r)e^{ik(x-ct)} \cos \theta \end{cases} \quad (6.34)$$

Now, the application of the traction-free boundary conditions for the stress components:  $\sigma_{rr}$ ,  $\tau_{xr}$  and  $\tau_{r\theta}$  at the free surface of the bar, i.e. for  $r = a$ :

$$\sigma_{rr}(x, r, \theta, t) = \tau_{xr}(x, r, \theta, t) = \tau_{r\theta}(x, r, \theta, t) = 0, \quad \text{for } r = a \quad (6.35)$$

with  $2a = d$ , where  $d$  denotes the diameter of the bar, allows one to obtain the dispersion relations for flexural waves propagating in the 1-D infinite elastic bar under consideration.

All required stress components:  $\sigma_{rr}$ ,  $\tau_{xr}$  and  $\tau_{r\theta}$  can be easily expressed by the use of Hooke's law together with Eq. (6.31), in a similar manner as it was done before. This leads to the following three equations:

$$\left\{ \begin{array}{l} \sigma_{rr}|_a = 0 \rightarrow \lambda \left[ k^2 \Phi(a) + \frac{\Phi(a)}{a^2} - \frac{1}{a} \frac{d\Phi(a)}{dr} \right] \\ \quad - (\lambda + 2\mu) \frac{d^2\Phi(a)}{dr^2} + 2\mu \left[ \frac{\Psi_x(a)}{a^2} \right. \\ \quad \left. - \frac{1}{a} \frac{d\Psi_x(a)}{dr} + ik \frac{d\Psi_\theta(a)}{dr} \right] = 0 \\ \tau_{xr}|_a = 0 \rightarrow \mu \left[ k^2 \Psi_\theta(a) + \frac{ik\Psi_x(a)}{a} + \frac{\Psi_r(a)}{a^2} - \frac{\Psi_\theta(a)}{a^2} \right. \\ \quad \left. + 2ik \frac{d\Phi(a)}{dr} - \frac{1}{a} \frac{d\Psi_r(a)}{dr} \right. \\ \quad \left. + \frac{1}{a} \frac{d\Psi_\theta(a)}{dr} + \frac{d^2\Psi_\theta(a)}{dr^2} \right] = 0 \\ \tau_{r\theta}|_a = 0 \rightarrow \mu \left[ \frac{2\Phi(a)}{a^2} - \frac{ik\Psi_r(a)}{a} + \frac{ik\Psi_\theta(a)}{a} - \frac{\Psi_x(a)}{a^2} \right. \\ \quad \left. - \frac{2}{a} \frac{d\Phi(a)}{dr} + ik \frac{d\Psi_r(a)}{dr} \right. \\ \quad \left. + \frac{1}{a} \frac{d\Psi_x(a)}{dr} - \frac{d^2\Psi_x(a)}{dr^2} \right] = 0 \end{array} \right. \quad (6.36)$$

where the factors:  $e^{ik(x-ct)}$ ,  $\cos(\theta)$  and  $\sin(\theta)$  are not present since the traction-free boundary conditions must be satisfied for propagating flexural waves independently of the spatial coordinates  $x$ ,  $\theta$  and time  $t$ .

The traction-free boundary conditions given explicitly by Eq. (6.36) represent a system of three homogeneous equations dependent on the potentials  $\phi$ ,  $\psi_x$ ,  $\psi_r$  and  $\psi_\theta$ . These potentials can be further expressed by the solutions presented in Eq. (6.33). In this way the system of the homogeneous equations with three unknown constants:  $A$ ,  $B$  and  $D$  is formed, which has non-trivial solutions only if its determinant vanishes. This determinant defines the characteristic equation for flexural modes propagating in circular bars and can be presented in the following form [19]:

$$\begin{aligned} c_1 J_1(\alpha a) J_0^2(\beta a) + J_0(\beta a) J_1(\beta a) [c_2 J_0(\alpha a) + c_3 J_1(\alpha a)] \\ - J_1^2(\beta a) [c_4 J_0(\alpha a) + c_5 J_1(\alpha a)] = 0 \end{aligned} \quad (6.37)$$

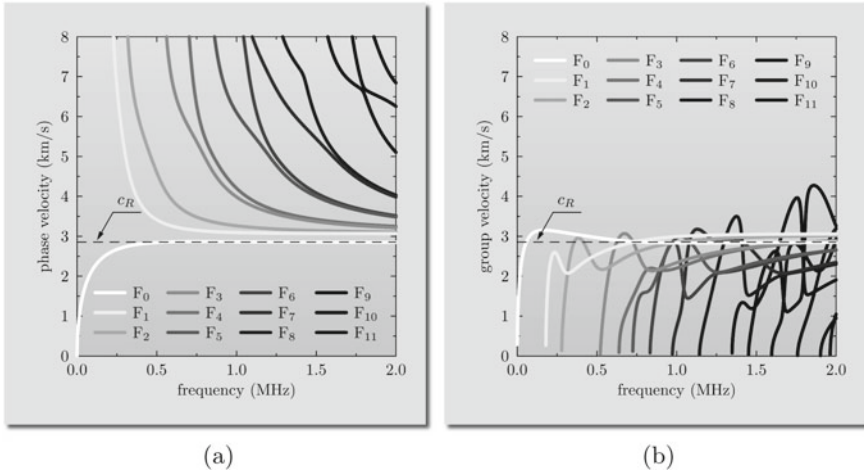


**Fig. 6.9** Dispersion curves for: (a) the phase velocity, (b) the group velocity, for modes of flexural waves  $F_n (n = 0, 1, 2, \dots)$  propagating in a 10 mm diameter aluminium bar

where the coefficients  $c_n (n = 1, 2, \dots, 5)$  are given as:

$$\begin{cases} c_1 = 2\beta a^2(\beta^2 - k^2)^2 \\ c_2 = 2\alpha\beta^2 a^2(\beta^2 + 5k^2) \\ c_3 = a[k^2\beta^2(2 + k^2 a^2) - 2\beta^4(5 + k^2 a^2) + \beta^6 a^2 - 4k^4] \\ c_4 = 2\alpha\beta a[\beta^2 + k^2(9 - 2a^2\beta^2)] \\ c_5 = \beta(k^2 + \beta^2)[a^2(k^2 + \beta^2) - 8] \end{cases} \quad (6.38)$$

Since the characteristic equation, given by Eq. (6.37), is dependent on the wave number  $k$  through the coefficients  $c_n (n = 1, 2, \dots, 5)$  as well as  $\alpha$  and  $\beta$  the flexural waves propagating in a 1-D infinite elastic bar must be dispersive in nature. Roots of this characteristic equation can effectively be found numerically—see Appendix B. These roots represent dispersion curves, which are presented in Fig. 6.9, for the phase and group velocities as a function of the cyclic frequency  $f$ .

The modes of flexural waves<sup>4</sup> are very often noted in the literature [6, 7] as  $F_n (n = 0, 1, 2, \dots)$ . Their behaviour, however, is very similar to the behaviour of antisymmetric modes of Lamb waves propagating in an elastic layer and discussed in Sect. 5.2 and results from very distinct characteristic equations.

<sup>4</sup> Modes of flexural waves are also noted as  $L_{m,n} (m, n = 1, 2, 3, \dots)$ , with  $m$  being the so-called circumferential order of the wave mode number  $n$  associated with harmonic functions  $\sin m\theta$  and  $\cos m\theta$  used in the potentials  $\phi$  as well as  $\psi_x, \psi_r$  and  $\psi_\theta$  [18]. The case of  $m = 0$  corresponds to axisymmetric modes of longitudinal waves noted as  $L_{0,n} (n = 1, 2, 3, \dots)$ . In the same manner modes of torsional waves are very often noted as axisymmetric modes  $T_{0,n} (n = 1, 2, 3, \dots)$  and modes  $T_{m,n} (m, n = 1, 2, 3, \dots)$ .

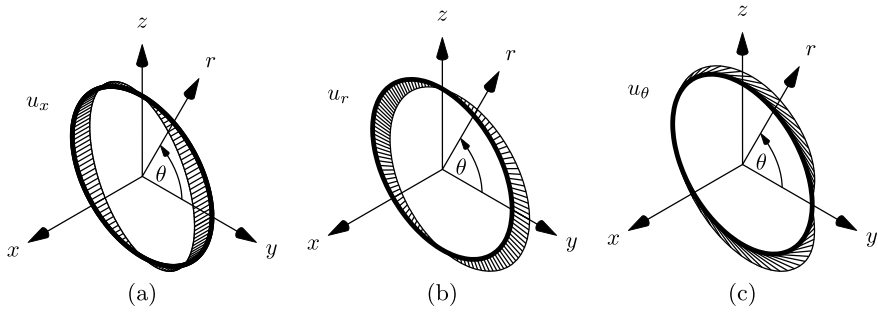


**Fig. 6.10** Distribution of displacement components: **a** longitudinal  $u_x$ , **b** radial  $u_r$  and **c** tangential  $u_\theta$ , on the bar circumference, for the fundamental mode of flexural waves  $F_0$  propagating in a 10 mm diameter aluminium bar, at the frequency  $f = 1$  kHz

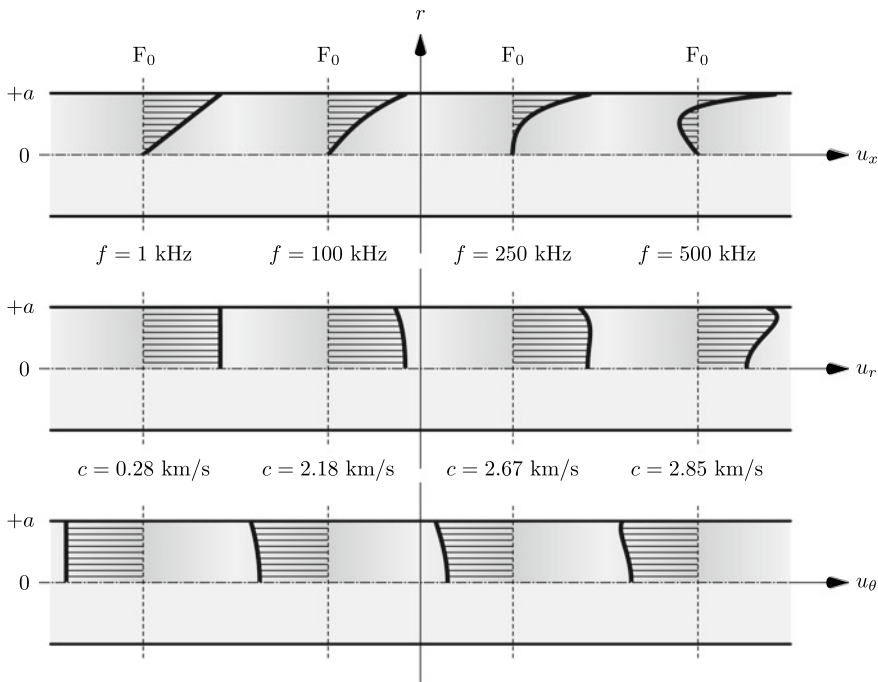


**Fig. 6.11** Relative displacement amplitudes as a function of the frequency  $f$  for the fundamental mode of flexural waves  $F_0$  propagating in a 10 mm diameter aluminium bar

This is easily seen in Fig. 6.9, when compared with the results presented in Fig. 5.9. This similarity concerns not only the frequency behaviour of modes propagating within the 1-D infinite elastic bar under consideration, but also extends onto the displacement amplitude profiles presented in Figs. 6.11 and 6.12.

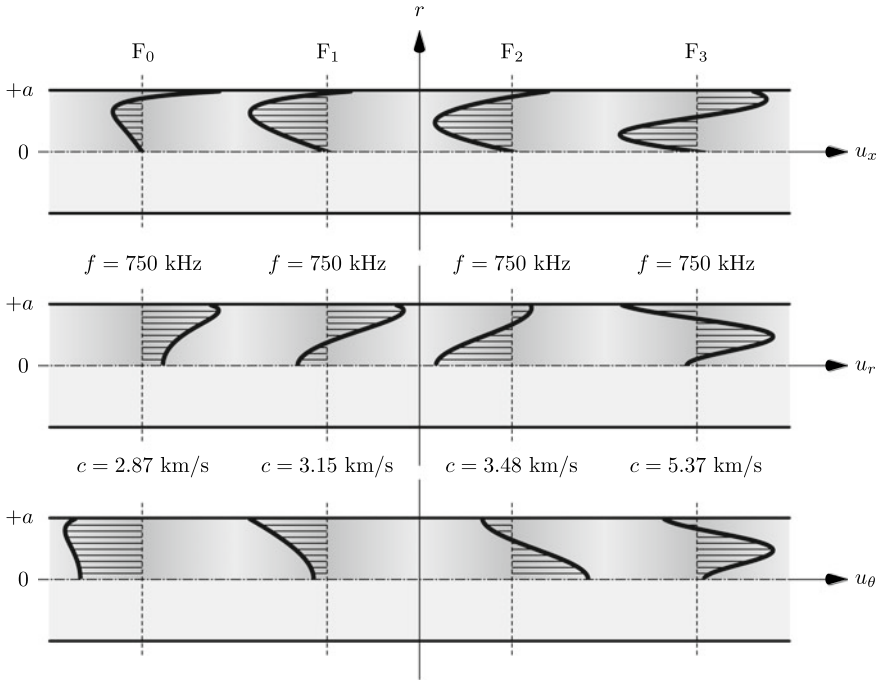


**Fig. 6.12** Relative displacement amplitudes for modes of flexural waves  $F_n$  ( $n = 0, 1, 2, \dots$ ) propagating in a 10 mm diameter aluminium bar, at the frequency  $f = 750$  kHz

Following the same procedure as in the case of modes of longitudinal waves, the use of the dispersion curves from Fig. 6.9 associated with the propagation of flexural waves within the bar, together with the use of Eqs. (6.27), (6.29) and (6.34), enables one to establish the displacement amplitude profiles for required values of the angular frequency  $\omega$  or the cyclic frequency  $f$ , as illustrated in Fig. 6.10. This can be done based on the the following simple relations:

$$\begin{cases} \hat{u}_x(r) = AikJ_1(\alpha r) - B\beta J_1(\beta r) \\ \hat{u}_r(r) = A\frac{dJ_1(\alpha r)}{dr} + BikJ_2(\beta r) + \frac{D}{r}J_1(\beta r) \\ \hat{u}_\theta(r) = -\frac{A}{r}J_1(\alpha r) + BkikJ_2(\beta r) - D\frac{dJ_1(\beta r)}{dr} \end{cases} \quad (6.39)$$

It should be noted that in the current case of flexural waves propagating in the bar the displacement amplitude profiles concern the longitudinal, radial and angular displacement components  $u_x$ ,  $u_r$  and  $u_\theta$ , while in the case of antisymmetric modes of Lamb waves propagating in an elastic layer they represent the longitudinal and transverse displacement components  $u_x$  and  $u_z$ . Again it can be also noted that the dispersion curve obtained for the fundamental mode  $F_0$ , in a similar manner as in

the case of the fundamental mode of Lamb waves  $A_0$ , is correlated with Rayleigh surface waves as the speed of Rayleigh waves  $c_R$  is its high frequency limit.

### 6.3 Torsional Waves

The analysis of propagation of torsional waves in a 1-D infinite elastic bar of circular cross-section, shown in Fig. 6.13, is very similar to the analysis of SH-waves in a 2-D elastic space.

As a starting point the same wave equation can be considered as in the case of SH-waves and given by Eq. (3.24) in Sect. 3.1:

$$c_s^2 \nabla^2 \mathbf{u} = \ddot{\mathbf{u}} \tag{6.40}$$

This wave equation, however, is now reduced to a single equation due to certain additional assumptions. It is assumed that torsional waves propagate in a 1-D elastic bar as shear waves with no longitudinal and radial displacement components, i.e. that  $u_x = 0$  and  $u_r = 0$ . As a result the only non-vanishing component of the displacement vector  $\mathbf{u}$  is the tangential component  $u_\theta$ , which remains dependent only on the spatial coordinates  $x, r$  as well as on time, i.e.  $u_\theta = u_\theta(x, r, t)$ .

Under the above assumptions the wave equation governing the behaviour of torsional waves propagating in a 1-D infinite elastic bar can be written in the cylindrical coordinate system  $(x, r, \theta)$  as:

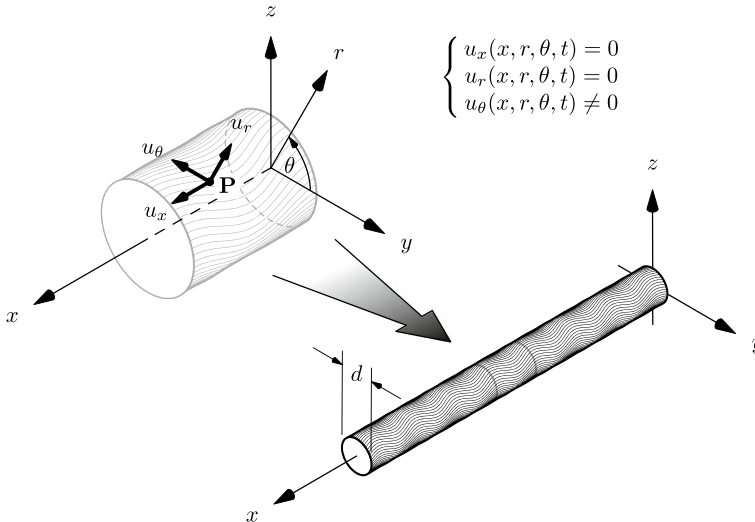


**Fig. 6.13** A schematic representation of a torsional wave propagating in a 1-D infinite elastic bar

$$c_s^2 \left( \nabla^2 u_\theta - \frac{u_\theta}{r^2} \right) = \ddot{u}_\theta \quad (6.41)$$

or presented in its full form as:

$$\frac{\partial^2 u_\theta}{\partial x^2} + \frac{\partial^2 u_\theta}{\partial r^2} + \frac{1}{r} \frac{\partial u_\theta}{\partial r} - \frac{u_\theta}{r^2} = \frac{1}{c_s^2} \frac{\partial^2 u_\theta}{\partial t^2} \quad (6.42)$$

Following the same procedure as in the case of SH-waves, as a solution to Eq. (6.41) a plane harmonic wave can be considered, having the well-known form:

$$u_\theta(x, r, t) = \hat{u}_\theta(r) e^{ik(x-ct)} \quad (6.43)$$

where  $\hat{u}_\theta$  is an unknown function representing the amplitude profile of torsional waves propagating in the bar, which is only dependent on the spatial coordinate  $r$ .

Substitution of the assumed solution into the wave equation (6.41) results in the already known Bessel's differential equation, which now governs the behaviour of the amplitude profile  $\hat{u}_\theta$ :

$$\frac{d^2 \hat{u}_\theta(r)}{dr^2} + \frac{1}{r} \frac{d\hat{u}_\theta(r)}{dr} + \beta^2 \hat{u}_\theta(r) - \frac{\hat{u}_\theta(r)}{r^2} = 0 \quad (6.44)$$

with:

$$\beta = k \sqrt{\frac{c^2}{c_s^2} - 1} = \sqrt{\frac{\omega^2}{c_s^2} - k^2} \quad (6.45)$$

where  $\beta$  is exactly the same constant as used Eq. (5.13) from Sect. 5.2, where Lamb waves were discussed. It remains dependent on the angular frequency  $\omega$ , the wave number  $k$  as well as the velocity of S-waves propagating in a 3-D elastic medium.

As before the solution to Eq. (6.44) can be expressed by the Bessel function of the first  $J_0(\beta r)$  as well as the Bessel function of the second kind  $Y_0(\beta r)$ . Since the Bessel function of the second kind  $Y_0(\beta r)$  is singular at  $r = 0$  this branch of solutions should be disregarded. Additionally, it should be noted that the case of  $\beta a = 0$  should also represent a non-trivial solution, in a similar manner to that observed for SH-waves propagating in an elastic layer. As a consequence the unknown function describing the amplitude profile  $\hat{u}_\theta$  can be assumed to have the form:

$$\hat{u}_\theta(r) = \frac{A}{\beta} J_1(\beta r) \quad (6.46)$$

where  $A$  is a certain constant. This helps to express the tangential displacement component  $u_\theta$  in the following way:

$$u_\theta(x, r, t) = \frac{A}{\beta} J_1(\beta r) e^{ik(x-ct)} \quad (6.47)$$



where  $c$  is the phase velocity of torsional waves propagating within the bar under consideration in the direction of the  $x$  axis.

The only strain component that leads to non-trivial solution is  $\gamma_{r\theta}$ . It can be expressed by the following simple relationship:

$$\gamma_{r\theta} = \frac{\partial u_\theta}{\partial r} - \frac{u_\theta}{r} = r \frac{\partial}{\partial r} \left( \frac{u_\theta}{r} \right) \quad (6.48)$$

which allows one to present the only non-zero stress component  $\tau_{r\theta}$  as:

$$\tau_{r\theta} = \mu \gamma_{r\theta} \rightarrow \tau_{r\theta} = \mu \frac{Ar}{\beta} \frac{\partial}{\partial r} \left[ \frac{J_1(r\beta)}{r} \right] e^{ik(x-ct)} \quad (6.49)$$

Now, the application of the traction-free boundary condition for the stress component  $\tau_{r\theta}$  at the free surface of the bar, i.e. for  $r = a$ , allows one to obtain the characteristic equation for torsional waves propagating in the 1-D infinite elastic bar under consideration.

After necessary mathematical simplifications and manipulations this relationship takes the following simple form:

$$\tau_{r\theta}|_a = 0 \rightarrow J_2(\beta a) = 0 \text{ or } (\beta a)J_0(\beta a) - 2J_1(\beta a) = 0 \quad (6.50)$$

with  $2a = d$ , where  $d$  denotes the diameter of the bar.

The roots of the Bessel function  $J_2(x)$  are well known and tabulated, or alternatively can be easily calculated to any required precision by using modern computation packages [20, 21]. The first five roots obtained in such a manner are:  $r_1 = \beta_1 a = 5.1356$ ,  $r_2 = \beta_2 a = 8.4172$ ,  $r_3 = \beta_3 a = 11.6198$ ,  $r_4 = \beta_4 a = 14.7960$  and  $r_5 = \beta_5 a = 17.9598$  plus the additional zero-root  $r_0 = \beta_0 a = 0$ .

In a similar manner to the case of SH-waves propagating in an elastic layer, the use of the definition of the parameter  $\beta$  in Eq. (6.45), as well as the knowledge of the roots of the characteristic equation  $r_n$  ( $n = 1, 2, 3, \dots$ ) given by Eq. (6.50), leads to the dispersion relation for torsional waves propagating within a 1-D infinite elastic bar. This dispersion relation can be expressed as a function of the wave number  $k$  in the following way:

$$c(k) = c_s \sqrt{1 + \left( \frac{r_n}{ka} \right)^2}, \quad n = 0, 1, 2, \dots \quad (6.51)$$

or alternatively as a function of the angular frequency  $\omega$  as:

$$c(\omega) = \frac{c_s}{\sqrt{1 - \left( \frac{r_n c_s}{\omega a} \right)^2}}, \quad n = 0, 1, 2, \dots \quad (6.52)$$

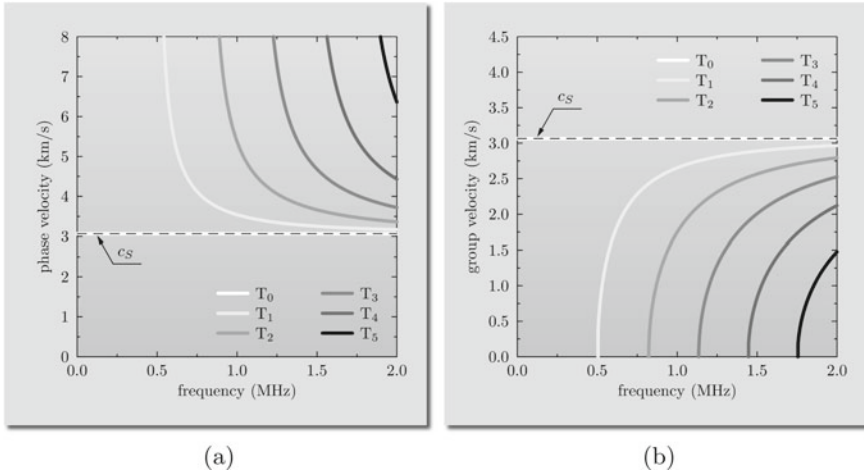


**Fig. 6.14** Dispersion curves for: **a** the phase velocity, **b** the group velocity, for modes of torsional waves  $T_n$  ( $n = 0, 1, 2, \dots$ ) propagating in a 10 mm diameter aluminium bar

Based on the dispersion relation given by Eq. (6.51) it can be seen that modes of torsional waves  $T_n$  ( $n = 0, 1, 2, \dots$ ) propagating in a 1-D infinite elastic bar of circular cross-section are dispersive except for the fundamental mode  $T_0$ , i.e. for  $n = 0$ , which is a non-dispersive mode, as presented in Fig. 6.14 as a function of the cyclic frequency  $f$ .

Moreover, it can be also seen that in the case of the fundamental mode  $T_0$  the phase velocity of the torsional waves propagating in the bar under consideration is equal to the phase velocity of SH-waves propagating in a 3-D elastic space. This also fully corresponds to the case of SH-waves propagating in a 2-D elastic layer.

Additionally, it can be easily checked that for the fundamental mode  $T_0$  distribution of the angular displacement  $u_\theta$  within the cross-sectional area of the bar is purely radial, as presented in Fig. 6.15, since:

$$\lim_{\beta \rightarrow 0} \hat{u}_\theta(r) = \lim_{\beta \rightarrow 0} \frac{A}{\beta} J_1(\beta r) = \frac{Ar}{2} \quad (6.53)$$

which leads to a very simple expression describing the distribution of the angular displacement  $u_\theta$ :

$$u_\theta(x, r, t) = \frac{Ar}{2} J_1(\beta r) e^{ik(x-ct)} \quad (6.54)$$

This is the lowest torsional mode well-known from the literature [17], which is characterised by a bulk rotation of the entire cross-section of the bar around its longitudinal axis.

Moreover, the displacement amplitude profiles shown in Fig. 6.15 are very similar to the displacement amplitude profiles obtained in the case of SH-waves propagat-

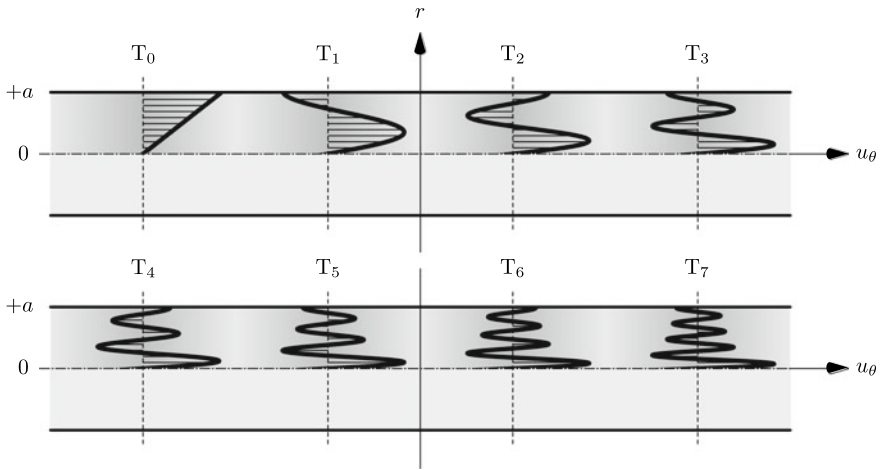


**Fig. 6.15** Relative displacement amplitudes of the transverse displacement  $u_\theta$  for modes of torsional waves  $T_n$  ( $n = 0, 1, 2, \dots$ ) propagating in a 10 mm diameter aluminium bar

ing in an elastic layer. It can be easily noticed that the modes of torsional waves  $T_n$  ( $n = 0, 1, 2, \dots$ ) propagating in the 1-D bar under consideration fully correspond to consecutive antisymmetric modes  $SH_n$  ( $n = 1, 3, 5, \dots$ ) presented in Fig. 5.4. Slight variations in the shapes of the amplitude profiles are entirely due to different geometrical conditions in both cases, i.e. 1-D geometry in the case of the bar and 2-D geometry in the case of the elastic layer.

## References

1. C. Chree. The equations of an isotropic elastic solid in polar and cylindrical coordinates, their solutions and applications. *Proceedings of the Cambridge Philosophical Society. Mathematical and Physical Science*, 14:250–369, 1889.
2. A. E. Love. *A treatise on the mathematical theory of elasticity*. Cambridge: at the University Press, Cambridge, 1892.
3. R. M. Davis. A critical study of the hopkinson pressure bar. *Philosophical Transactions of the Royal Society of London. Series A, Mathematical and Physical Sciences*, 240:375–457, 1948.
4. Y. H. Pao and R. D. Mindlin. Dispersion of flexural waves in an elastic, circular cylinder. *Journal of Applied Mechanics*, 27:513–520, 1960.
5. K. F. Graff. *Wave motion in elastic solids*. Dover Publications, New York, Dover, 1991.
6. W. Ostachowicz, P. Kudela, M. Krawczuk, and A. Żak. *Guided waves in structures for SHM. The time-domain spectral element method*. John Wiley & Sons Ltd., Singapore, 2012.
7. A. Żak and M. Krawczuk. Assessment of rod behaviour theories used in spectral finite element modelling. *Journal of Sound and Vibration*, 329:2099–2113, 2010.
8. T. R. Meeker and A. H. Meitzler. Guided wave propagation in elongated cylinders and plates. In *Physical Acoustics: Principles and Methods*, pages 111–167. Academic Press, 1964.
9. A. H. Meitzler. Backward wave transmission of stress pulses in elastic cylinders and plates. *The Journal of Acoustical Society of America*, 38:835–842, 1965.

10. T. W. Murray, O. Balogun, C. Prada, D. Clorennec, and D. Royer. Theory and application of laser generated zero-group velocity Lamb mode resonance. *API Conference Proceedings: Review of Progress in Quantitative Nondestructive Evaluation*, 975:255–262, 2008.
11. Q. Xie, S. Mezil, P. H. Otsuka, M. Tomoda, J. Laurent, O. Matusuda, Z. Shen, and O. B. Wright. Imaging gigahertz zero-group-velocity Lamb waves. *Nature Communications*, 10:1–7, 2019.
12. G. Kaduchak, D. H. Hughes, and P. L. Marston. Enhancement of the backscattering of high-frequency tone bursts by thin spherical shells associated with a backward wave: Observations and ray approximation. *The Journal of the Acoustical Society of America*, 96:3704–3714, 1994.
13. A. Alippi, A. Bettucci, and M. Germano. Anomalous propagation characteristics of evanescent waves. *Ultrasonics*, 38:817–820, 2000.
14. P. L. Marston. Negative group velocity Lamb waves on plates and applications to the scattering of sound by shells. *The Journal of the Acoustical Society of America*, 113:2659–2662, 2003.
15. K. Negishi. Existence of negative group velocities in Lamb waves. *Japanese Journal of Applied Physics*, 26:171–173, 1987.
16. K. Negishi and H. U. Li. Strobe-photoelastic visualization of Lamb waves with negative group velocity propagating on a glass plate. *Japanese Journal of Applied Physics*, 35:3175–3176, 1996.
17. J. D. Achenbach. *Wave propagation in elastic solids*. North-Holland Publishing Company, Amsterdam, 1973.
18. J. L. Rose. *Ultrasonic waves in solid media*. Cambridge University Press, Cambridge, 1999.
19. A. Żak and M. Krawczuk. Assessment of flexural beam behaviour theories used for dynamics and wave propagation problems. *Journal of Sound and Vibration*, 331:5715–5731, 2012.
20. <http://www.mathworks.com>.
21. <http://www.wolfram.com>.

# Chapter 7

## A Step Towards FE Modelling



### 7.1 Modelling Errors

FE numerical models as such represent the final stage of a very complex and important part of scientific activity, which is known as numerical modelling. As every type of scientific activity, numerical modelling by FEs, or modelling in general, is also prone to errors [1]. These errors appear at every stage of this process and may have a more or less significant impact on the final results. Although the process of numerical modelling may be represented or understood in many ways, some general remarks about particular stages of such a process can be easily made, as presented in Table 7.1. These stages are meant not only to illustrate the importance of particular assumptions, which lead to reliable numerical models, but also to indicate some important aspects and profound consequences related to these assumptions.

As proposed in Table 7.1 a modelling process can be divided into a number of specific levels, which start at *level 0* to end at *level 4*. By no means should the number of these levels be considered as fixed. They may include many other less or more specific steps of modelling process, which under certain circumstances can be of very great importance to a modeller. In order to illustrate particular steps of the modelling process, which formally ends when an FE numerical model is built, the problem of propagation of flexural/bending waves in an aluminium bar is considered below in detail.

- In fact modelling *leve 0* is not related to mathematical modelling, but it rather corresponds to a real physical object and its properties, which in the case under consideration is the aluminium bar. At this stage technically all possible kinds of data can be extracted upon appropriately designed experiments, so no modelling errors are associated with it. If any, some discrepancies may result from finite resolution of experimental techniques and equipment, but not mathematical modelling itself. The latter is not present in modelling *level 0*. As a consequence modelling *level 0* requires no assumptions in this respect.

**Table 7.1** Proposed stages of modelling errors associated with wave propagation problems

<i>Level 0</i>	→	Real object
Typical assumptions	→	None
Available data	→	All
Typical errors	→	None
<i>Level 1</i>	→	Physical model
Typical assumptions	→	Uncoupled physical fields, <sup>1</sup> Linearised behaviour, <sup>2</sup> Homogenised material properties, <sup>3</sup> etc.
Available data	→	None
Typical errors	→	Decoupled and/or restricted responses, No energy transfer, etc.
<i>Level 2</i>	→	Mathematical model
Typical assumptions	→	Reduced dimensionality, <sup>4</sup> Idealised boundary conditions, Or loads, <sup>5</sup> Specific representation, <sup>6</sup> etc.
Available data	→	Analytical responses, Analytical strain/stress fields, Analytical dispersion curves, etc.
Typical errors	→	Under or overestimated responses, Truncation errors, Non-physical solutions, etc.
<i>Level 3</i>	→	Simplified mathematical model
Typical assumptions	→	simplified kinematics, <sup>7</sup> Idealised strain/stress fields, <sup>8</sup> Reduction of specific terms, <sup>9</sup> etc.
Available data	→	Simplified responses, Simplified strain/stress fields, Reduced dispersion curves, etc.
Typical errors	→	Under or overestimated responses, Smaller range of applicability, Non-physical solutions, etc.
<i>Level 4</i>	→	Discrete mathematical model
Typical assumptions	→	Finite number of degrees of freedom, Discrete space/time representation, Reduced resolution, <sup>10</sup> etc.
Available data	→	Discrete responses, Discrete strain/stress fields, Discrete dispersion curves, etc.
Typical errors	→	Under or overestimated responses, Reduced range of applicability, numerical anisotropy, etc.

<sup>1</sup> Independent physical fields and/or displacement/strain/stress components, etc.<sup>2</sup> Neglect of large deformations/strains, neglect of non-linear material behaviour, etc.<sup>3</sup> Neglect of material directionality in all or specific directions, etc.<sup>4</sup> Plane stress or plane stress condition, wave fronts represented as plane waves, etc.<sup>5</sup> Pinned/simply-supported/sliding boundary conditions, point forces/moments, etc.<sup>6</sup> Solutions by means of truncated/infinite series, neglect of damping, etc.<sup>7</sup> Reduced number of displacement/strain/stress components, etc.<sup>8</sup> 3-D displacement/strain/stress fields reduced to 2-D plane or 1-D fields, etc.<sup>9</sup> Neglect of local behaviour strain/stress fields, etc.<sup>10</sup> Result of the Nyquist-Shannon theorem, result of Bloch's theorem, etc.

- Modelling *level 1* is the most general stage of modelling and helps to narrow the observation space to the most important aspects of real physical phenomena related to the behaviour of the object being modelled. Modelling *level 1*, representing a physical model, is an abstract, which helps to identify and take into account the most important features of these phenomena. For this reason no data are generated at this modelling stage and consequently there are no errors associated with these data. In the case of the aluminium bar the observation space can be narrowed to displacements or strains only, which when considered in the linear regime allow one to take full advantage of the properties of elastic waves, such as superposition. Heat transfer, if necessary, may be a part of the analysis or may be neglected, as long as the displacement and temperature fields remain decoupled. An additional assumption of aluminium isotropy decouples particular displacement components making analysis even simpler as long as some further assumptions about the rod symmetry are made.
- Modelling *level 2* is also an abstract, which concerns attempts to express in the language of mathematics the results of the previous modelling level. Despite the fact that modelling *level 2* employs some specific mathematical operators and similar concepts such as, for example, differential operators or specific boundary conditions that do not always having physical representation, modelling *level 2* offers the most general mathematical description. It should be emphasised here that the use of sophisticated mathematical tools leads to formulation of some general governing equations, which very often allow one to search for some first order solutions. In the case of the aluminium bar under consideration these can have the form of analytical dispersion curves resulting from the most general form of the characteristic equation. This is, however, achievable only under additional specific assumptions, such as the assumptions about the circular cross-section of the bar and the angular dependence of the scalar potentials  $\phi$  as well as  $\psi_x$ ,  $\psi_r$  and  $\psi_\theta$  on the angle  $\theta$ , as was demonstrated in Sect. 6.2.
- Modelling *level 3* further simplifies the outcome of modelling *level 2*. Very often such an approach is demanded and it results directly from the complexity of the mathematical description offered by *modelling level 2*. The most typical assumptions made at modelling *level 3* are those regarding kinematics, which lead to simplified forms of displacement/strain fields. As a consequence the resulting governing equations are also simplified, which helps to make subsequent analyses much easier and faster. However, it should be noted that this is possible at some additional cost, namely the reduced range of applicability of such simplified mathematical models. In the case of the aluminium bar discussed here this reduced range of applicability manifests itself as a gradual divergence of calculated dispersion curves based on a simplified mathematical model of modelling *level 3* from its more general counterpart offered by modelling *level 2*. Consequently, mathematical models developed at modelling *level 3* should be carefully examined for their ranges of applicability in order to avoid confusion and some obvious mistakes. On the other hand it should be said that very often typical simplifications at modelling *level 3* lead to better understanding of the physical phenomena related to the behaviour of the object being modelled.

- Modelling *level 4* can be considered as the final stage of the modelling process, when the mathematical description obtained at modelling *level 3* is expressed in a manner which enables one to transform the continuous mathematical model to a discrete numerical model. Amongst many numerical techniques used for this purpose the most popular technique appears to be FEM. The discretisation process itself is a demanding and complex process during which the unknown functions/quantities resulting from modelling *level 3* are expressed by certain discrete functions of some special properties. This is yet another simplification, which consequently reduces the range of applicability of discrete models in comparison to the mathematical models obtained at modelling *level 3*. Moreover, the discrete nature of the resulting models has some extra and profound consequences resulting from the Nyquist-Shannon sampling theorem or Bloch's theorem. Once again the ease and speed of the modelling process at modelling *level 4* is obtained at the additional cost of a further reduced range of applicability in comparison to modelling *level 3*. This can be understood as a direct effect of the substitution of the unknown functions/quantities of predefined mathematical properties with regard to their continuity, smoothness, differentiability, etc. from modelling *level 3* by finite series of much simpler approximation functions. Again, discrete numerical models developed at modelling *level 4* should be even more carefully examined for their ranges of applicability in order to avoid problems emerging, for example, from numerical anisotropy, appearance of frequency band gaps in discrete dispersion curves or instability of numerical solution schemes used.

At this point it should be strongly emphasised once more that Table 7.1 by no means represents any closed and fixed concept of modelling stages and errors associated with them. Its illustrative nature is rather meant to indicate that some important aspects of the modelling process may vary in terms of typical assumptions or errors, as well as the necessary number of modelling levels, in the case of propagation of flexural/bending waves in an aluminium bar and can be different in more specific cases than discussed here. Moreover, very often such errors and assumptions may appear interchangeably at various stages of the modelling process or can be even fully replaced by some others, depending on the specific case.

## 7.2 Some Thoughts About Simplified Theories

Displacement fields of 1-D or 2-D structural elements can be thought of as Maclaurin series expansions of the corresponding displacement fields of 3-D structural elements. If only the characteristic longitudinal dimensions (length, width, radius of curvature, etc.) of these elements are dominant over their characteristic transverse



dimension (thickness) then such series expansions can be considered as mathematically correct.<sup>1</sup>

Consequently, a Maclaurin series expansion of the displacement field of a 3-D structural element may effectively reduce the dimensionality of the static or dynamic behaviour investigated, from 3-D to either the mid-plane behaviour in 2-D or even to the mid-axis behaviour in 1-D. In such a case each displacement component of the displacement field under consideration, only if all required conditions for series expansion are fulfilled,<sup>2</sup> can be expanded and presented as a Maclaurin series.

For the displacement component  $u_x$  in the direction of the  $x$  axis it can be formally written that:

$$u_x(x, y, z, t) = u_x(x, y, 0, t) + \sum_{n=1}^{\infty} \frac{z^n}{n!} \frac{\partial^n u_x(x, y, 0, t)}{\partial z^n} \quad (7.1)$$

which is a step towards FE representation since Eq. (7.1) can be rewritten and presented in the following form:

$$u_x(x, y, z, t) = \sum_{n=0}^m z^n \phi_n(x, y, t) + O(z^{m+1}) \quad (7.2)$$

where  $m$  is the number of terms kept in the truncated Maclaurin series. This is directly associated with the degree of approximation in the traverse directions, i.e. in the direction of the  $z$  axis. Apart from this  $\phi_n$  may be thought of as denoting degrees of freedom (DOF) of a certain FE associated with the Maclaurin expansion of the displacement component  $u_x$ .

Moreover, it should be noted that the above series representation of the displacement component  $u_x$  is not exact due to the truncation of the series and the resulting error  $O(z^{m+1})$ . However, in the case of the majority of engineering problems related to statics or low frequency dynamic problems such series representation is sufficient and can be based only on one or two terms of the corresponding Maclaurin series.

For example, for  $m = 3$  the corresponding Maclaurin series expansion of the displacement component  $u_x$  leads to:

$$u_x(x, y, z, t) \cong \phi_0(x, y, t) + z\phi_1(x, y, t) + z^2\phi_2(x, y, t) + z^3\phi_3(x, y, t) \quad (7.3)$$

---

<sup>1</sup> In the literature the ratio of the thickness  $h$  to the length  $L$  plays an important role in differentiation between various theories and their ranges of applicability. Structural elements of  $h/L \lesssim 0.01$  are considered as very thin and typically exhibit geometrically non-linear behaviour. On the other hand structural elements of  $0.01 \lesssim h/L \lesssim 0.1$  are considered as thin and are typically characterised by negligible transverse shear deformations. Finally, structural elements of  $0.1 \lesssim h/L \lesssim 0.2$  are considered as thick and are typically characterised by non-zero transverse shear deformations.

<sup>2</sup> Mathematically, these conditions require the existence off all the required partial derivatives for a given series-expanded function.

where the functions  $\phi_n$  ( $n = 0, 1, 2, 3$ ) may be considered as representing mid-plane DOFs of a certain 2-D FE, which can be associated with the given Maclaurin series expansion. It can also be noted that:

$$\begin{cases} \phi_0(x, y, t) = u_x(x, y, 0, t), & \phi_2(x, y, t) = \frac{1}{2} \frac{\partial^2 u_x(x, y, 0, t)}{\partial z^2} \\ \phi_1(x, y, t) = \frac{\partial u_x(x, y, 0, t)}{\partial z}, & \phi_3(x, y, t) = \frac{1}{6} \frac{\partial^3 u_x(x, y, 0, t)}{\partial z^3} \end{cases} \quad (7.4)$$

In contrast to this the investigation of problems involving propagation of elastic waves in 1-D or 2-D structural elements requires much more accurate representation of the dynamic behaviour of a 3-D structural element. This is directly linked to the necessity for mathematical modelling of different modes of Lamb waves or SH-waves, as discussed and presented in Chap. 5 as well as modes of longitudinal, flexural or torsional waves, as presented and discussed in Chap. 6.

As explained earlier the phenomena of wave propagation in 1-D or 2-D structural elements is always related to coupled interaction of P-waves and S-waves with existing structural boundaries. As a result of this coupled interaction propagation of various modes of elastic waves can be observed. An appropriate representation of these wave modes in a broad range of frequencies, in order to capture the complexity of the phenomena under investigation, usually requires a greater number of terms of the corresponding Maclaurin series than two. In general, it can be observed that the number of independent terms kept in the Maclaurin series expansion is equal to the number of wave propagation modes based on the theory under consideration, or alternatively it can be understood as the number of DOFs.

In the case of the displacement field of a 2-D shell element based on its representation by the Maclaurin series expansion, the particular displacement components  $u_x$ ,  $u_y$  and  $u_z$  can be presented in the following way:

$$\begin{cases} u_x(x, y, z, t) = \sum_{n=0}^m z^n \phi_n(x, y, t) \\ u_y(x, y, z, t) = \sum_{n=0}^m z^n \psi_n(x, y, t) \\ u_z(x, y, z, t) = \sum_{n=0}^m z^n \theta_n(x, y, t) \end{cases} \quad (7.5)$$

where all mid-plane defined functions  $\phi_n$ ,  $\psi_n$  and  $\theta_n$ , denote the element independent variables, i.e. DOFs.

It can be seen that in the current case the 2-D shell element under consideration has as many as  $3m$  independent variables. This great number of independent variables may be reduced by taking into account the traction-free boundary conditions<sup>3</sup> at the element lateral boundaries for the stress components  $\sigma_{zz}$  as well as  $\tau_{yz}$  and  $\tau_{xz}$ :

---

<sup>3</sup> In this way various higher-order theories of fewer modes can be formulated, which take advantage of the traction-free boundary conditions and the fact that certain higher-order terms of the displacement fields can be expressed by the use of the remaining lower order terms. In contrast, these

$$\sigma_{zz}(x, y, z, t) = \tau_{yz}(x, y, z, t) = \tau_{xz}(x, y, z, t) = 0, \quad \text{for } z = \pm a \quad (7.6)$$

with  $2a = h$ , where  $h$  denotes the thickness of the shell element under consideration.

Because the first traction-free boundary condition for  $\sigma_{zz}$  links together the strain components  $\epsilon_{xx}$ ,  $\epsilon_{yy}$  and  $\epsilon_{zz}$  through Hooke's law,<sup>4</sup> its direct use is difficult and leads to a partial differential equation, which in most cases is too complicated to be solved analytically. However, this problem can be overcome by a simple mathematical substitution and introduction of new mid-plane defined functions  $\bar{\phi}_n$ ,  $\bar{\psi}_n$  and  $\bar{\theta}_n$ , as presented in [2] or Appendix C. In this case the mid-plane functions  $\bar{\phi}_n$  can be presented as:

$$\begin{cases} \bar{\phi}_0(x, y, t) = \phi_0(x, y, t) - \sum_{n=1}^p \bar{\phi}_{2n}(x, y, t) \\ \bar{\phi}_{2n}(x, y, t) = -a^{2n} \phi_{2n}(x, y, t), \quad n = 1, 2, \dots, p \\ \bar{\phi}_1(x, y, t) = \phi_1(x, y, t) - \sum_{n=1}^p \bar{\phi}_{2n+1}(x, y, t) \\ \bar{\phi}_{2n+1}(x, y, t) = -a^{2n} \phi_{2n+1}(x, y, t), \quad n = 1, 2, \dots, p \end{cases} \quad (7.7)$$

where  $m = 2p + 1$ . It should be noted that the equivalent relationships exist for the remaining two mid-plane functions  $\bar{\psi}_n$  and  $\bar{\theta}_n$ .

As a result the displacement components  $u_x$ ,  $u_y$  and  $u_z$ , in the case of  $m = 3$ , can be expressed in the following new form [3]:

$$\begin{cases} u_x(x, y, \zeta, t) = \phi_0(x, y, t) + a\zeta \phi_1(x, y, t) \\ \quad + (1 - \zeta^2) \phi_2(x, y, t) + a\zeta(1 - \zeta^2) \phi_3(x, y, t) \\ u_y(x, y, \zeta, t) = \psi_0(x, y, t) + a\zeta \psi_1(x, y, t) \\ \quad + (1 - \zeta^2) \psi_2(x, y, t) + a\zeta(1 - \zeta^2) \psi_3(x, y, t) \\ u_z(x, y, \zeta, t) = \theta_0(x, y, t) + a\zeta \theta_1(x, y, t) \\ \quad + (1 - \zeta^2) \theta_2(x, y, t) + a\zeta(1 - \zeta^2) \theta_3(x, y, t) \end{cases} \quad (7.8)$$

where a new variable  $\zeta$  is introduced with  $z = a\zeta$  and where the symbol ( $\bar{\bullet}$ ) is omitted for clarity.

At this point it should be emphasised that according to earlier considerations the mid-plane defined functions  $\phi_n$ ,  $\psi_n$  and  $\theta_n$  must be associated either with the

---

theories, which take advantage of some other properties of the strain/stress fields are considered as modified or improved theories.

<sup>4</sup> The theories, for which all 3 normal strain/stress components are non-zero may be thought of as 3-D theories. Otherwise, depending on the number of non-zero strain/stress components, which can be 2 or less, they may be thought of as 2-D or 1-D theories.

symmetric or antisymmetric dynamic behaviour.<sup>5</sup> As a result it can be easily checked that the symmetric modes must be described by the mid-plane functions  $\phi_n$  ( $n = 0, 2$ ),  $\psi_n$  ( $n = 0, 2$ ) and  $\theta_n$  ( $n = 1, 3$ ), and the antisymmetric modes by the mid-plane functions  $\phi_n$  ( $n = 1, 3$ ),  $\psi_n$  ( $n = 1, 3$ ) and  $\theta_n$  ( $n = 0, 2$ ).

For this reason the use of Eqs. (7.6) and (7.7) helps to reduce the total number of independent variables, i.e. DOFs, from 12 down to 6, since the same traction-free boundary conditions can be applied independently either to the mid-plane functions describing the symmetric modes or antisymmetric modes. This leads to the following relationships:

- for the mid-plane functions  $\phi_2$ ,  $\psi_2$  and  $\theta_3$  in the case of symmetric behaviour:

$$\begin{cases} 2\phi_2(x, y, t) = a^2 \frac{\partial \theta_1(x, y, t)}{\partial x} \\ 2\psi_2(x, y, t) = a^2 \frac{\partial \theta_1(x, y, t)}{\partial y} \\ 2\theta_3(x, y, t) = \theta_1(x, y, t) \\ \quad + \frac{\lambda}{\lambda + 2\mu} \left[ \frac{\partial \phi_0(x, y, t)}{\partial x} + \frac{\partial \psi_0(x, y, t)}{\partial y} \right] \end{cases} \quad (7.9)$$

- and for the mid-plane functions  $\phi_3$ ,  $\psi_3$  and  $\theta_2$  in the case of antisymmetric behaviour:

$$\begin{cases} 2\phi_3(x, y, t) = \phi_1(x, y, t) + \frac{\partial \theta_0(x, y, t)}{\partial x} \\ 2\psi_3(x, y, t) = \psi_1(x, y, t) + \frac{\partial \theta_0(x, y, t)}{\partial y} \\ 2\theta_2(x, y, t) = a^2 \frac{\lambda}{\lambda + 2\mu} \left[ \frac{\partial \phi_1(x, y, t)}{\partial x} + \frac{\partial \psi_1(x, y, t)}{\partial y} \right] \end{cases} \quad (7.10)$$

where  $\lambda$  and  $\mu$  are the Lamé constants.

Finally, the displacement field of the 2-D shell element under consideration, initially expressed by Eq. (7.5) and later by Eq. (7.8), can be split up and presented in simpler forms, independently for the symmetric and anti-symmetric behaviour, associated with propagation of Lamb waves and SH-waves. It should be noted that thanks to such an approach two independent higher-order 3-mode 3-D theories of the symmetric and antisymmetric behaviour are established.

By taking into account Eq. (7.9) and Eq. (7.10), resulting from the application of the traction-free boundary conditions, the following relationships are obtained:

- in the case of the symmetric behaviour for the displacement components  $u_x$ ,  $u_y$  and  $u_z$ :

---

<sup>5</sup> The symmetric behaviour requires the in-plane displacements and the transverse strain to be even functions, while the antisymmetric behaviour requires these functions to be odd, with respect to the  $z$  coordinate.

$$\left\{ \begin{array}{l} u_x(x, y, \zeta, t) = \phi_0(x, y, t) + \frac{a^2(1 - \zeta^2)}{2} \frac{\partial \theta_1(x, y, t)}{\partial x} \\ u_y(x, y, \zeta, t) = \psi_0(x, y, t) + \frac{a^2(1 - \zeta^2)}{2} \frac{\partial \theta_1(x, y, t)}{\partial y} \\ u_z(x, y, \zeta, t) = \frac{a\zeta(3 - \zeta^2)}{2} \theta_1(x, y, t) \\ \quad + \frac{a\zeta(1 - \zeta^2)}{2} \frac{\lambda}{\lambda + 2\mu} \left[ \frac{\partial \phi_0(x, y, t)}{\partial x} + \frac{\partial \psi_0(x, y, t)}{\partial y} \right] \end{array} \right. \quad (7.11)$$

- in the case of the antisymmetric behaviour for the displacement components  $u_x$ ,  $u_y$  and  $u_z$ :

$$\left\{ \begin{array}{l} u_x(x, y, \zeta, t) = \frac{a\zeta(3 - \zeta^2)}{2} \phi_1(x, y, t) \\ \quad + \frac{a\zeta(1 - \zeta^2)}{2} \frac{\partial \theta_0(x, y, t)}{\partial x} \\ u_y(x, y, \zeta, t) = \frac{a\zeta(3 - \zeta^2)}{2} \psi_1(x, y, t) \\ \quad + \frac{a\zeta(1 - \zeta^2)}{2} \frac{\partial \theta_0(x, y, t)}{\partial y} \\ u_z(x, y, \zeta, t) = \theta_0(x, y, t) \\ \quad + \frac{a^2(1 - \zeta^2)}{2} \frac{\lambda}{\lambda + 2\mu} \left[ \frac{\partial \phi_1(x, y, t)}{\partial x} + \frac{\partial \psi_1(x, y, t)}{\partial y} \right] \end{array} \right. \quad (7.12)$$

The methodology presented above leading to the formulation of the displacement fields for the higher-order 6-mode 3-D theory of shells, independently for symmetric and antisymmetric behaviour, may be considered as a general procedure. It may also be applied, after appropriate adjustments resulting from the problem dimensionality or the use of specific coordinate systems, in order to build the displacement fields of various 1-D structural elements. This approach can be successfully employed not only in the case of simple one-mode or multi-mode theories of their behaviour, but also higher-order multi-mode theories, which take advantage of the traction-free boundary conditions, as presented above.

### 7.3 Dispersion Curves

Dispersion curves provide very important information about wave propagation properties of a physical medium. This corresponds to modelling *level 1* discussed in Sect. 7.1. In the same manner analytical dispersion curves may be associated with a given mathematical model of the wave propagation phenomena in structural elements, typically at modelling *level 2*. Simplifications of the process of mathematical modelling, which very often results in the simplifications of kinematics and the

reduction of terms in the corresponding Maclaurin series expansions, take place at modelling *level 3*. It should be emphasised that these simplifications usually have an additional influence on dispersion curves, which manifests in the loss of accuracy in a specific range of frequencies. This loss can be measured, however, in a very straightforward manner as a difference between the dispersion curves observed and provided by physical or analytical models and the dispersion curves obtained from simplified mathematical models.

A very effective tool that can be used to obtain dispersion curves for simplified mathematical models, typically associated with modelling *level 3*, is Hamilton's principle.<sup>6</sup> Hamilton's principle allows one to determine the dynamic behaviour of an elastic structure by the use of a single function, which contains all necessary information about the kinetic energy  $\mathcal{K}$  and the strain energy  $\mathcal{U}$  of this structure.

The kinetic energy  $\mathcal{K}$  of a structure associated with its wave motion can be expressed by the use of the following formula:

$$\mathcal{K} = \frac{1}{2} \int_{-a}^a \rho \dot{u}_j \dot{u}_j dz, \quad j = 1, 2, 3 \quad (7.13)$$

where  $\rho$  is the material density and  $\dot{u}_j \dot{u}_j$  is understood as:

$$\dot{u}_j \dot{u}_j = \dot{u}_x(x, y, z, t)^2 + \dot{u}_y(x, y, z, t)^2 + \dot{u}_z(x, y, z, t)^2 \quad (7.14)$$

where the symbol  $(\dot{\bullet})$  represents the first derivative with respect to time  $t$ .

In a similar manner the strain energy  $\mathcal{U}$  of a structure associated with its elastic deformation can be expressed by the following formula:

$$\mathcal{U} = \frac{1}{2} \int_{-a}^a \sigma_{ij} \epsilon_{ij} dz, \quad i, j = 1, 2, 3 \quad (7.15)$$

where  $\sigma_{ij} \epsilon_{ij}$  is understood as:

$$\begin{aligned} \sigma_{ij} \epsilon_{ij} &= \sigma_{xx}(x, y, z, t) \epsilon_{xx}(x, y, z, t) + \sigma_{yy}(x, y, z, t) \epsilon_{yy}(x, y, z, t) \\ &+ \sigma_{zz}(x, y, z, t) \epsilon_{zz}(x, y, z, t) + \tau_{xy}(x, y, z, t) \gamma_{xy}(x, y, z, t) \\ &+ \tau_{yz}(x, y, z, t) \gamma_{yz}(x, y, z, t) + \tau_{zx}(x, y, z, t) \gamma_{zx}(x, y, z, t) \end{aligned} \quad (7.16)$$

In general, Hamilton's principle states that out of all possible evolution paths between the initial and the final state of the structure, described by times  $t_1$  and  $t_2$

---

<sup>6</sup> Hamilton's principle, being one of the most fundamental principles in vibration analysis, takes its name after an Irish mathematician, astronomer and physicist Sir William Rowan Hamilton (1805–1865), whose works concerned algebra, theoretical mechanics and optics. His input into classical mechanics and variational calculus made him the father of Hamiltonian mechanics, which formed the basis for quantum mechanics nowadays.

and resulting from its deformation and motion, those actually realised are on the evolution paths for which the following relationship is true:

$$\delta \int_{t_1}^{t_2} \mathcal{L} dt = \delta \int_{t_1}^{t_2} (\mathcal{K} - \mathcal{U}) dt = 0 \quad (7.17)$$

where the symbol  $\mathcal{L}$  denotes the Lagrangian, with  $\mathcal{L} = \mathcal{T} - \mathcal{U}$ .

The above relationship is satisfied only if:

$$\frac{\partial}{\partial t} \left[ \frac{\partial \mathcal{L}}{\partial \left( \frac{\partial q_n}{\partial t} \right)} \right] + \sum_{j=1}^3 \frac{\partial}{\partial x_j} \left[ \frac{\partial \mathcal{L}}{\partial \left( \frac{\partial q_n}{\partial x_j} \right)} \right] - \frac{\partial \mathcal{L}}{\partial q_n} = 0 \quad (7.18)$$

where  $q_n(t)$  ( $i = 1, 2, \dots, m$ ) denote time dependent components of a so-called general coordinate vector  $\mathbf{q}(t) = [q_1, q_2, \dots, q_m]^T$ , which describes the state of the structure, and where the Lagrangian  $\mathcal{L}$  is a function dependant not only on the particular components  $q_n$  of the vector  $\mathbf{q}(t)$ , but also on their space and time derivatives, i.e. where  $\mathcal{L} = \mathcal{L}(q_n, \frac{\partial q_n}{\partial t}, \frac{\partial q_n}{\partial x_j})$ .

It should be noted that Eq. (7.18), known in the literature as the Euler-Lagrange equations of the variational problem, can be used directly in order to obtain a system of  $m$  equations of motion for the general coordinates  $q_n$ , having determined the kinetic energy  $\mathcal{K}$  and the strain energy  $\mathcal{U}$  associated with the structure deformation and motion [4]. Moreover, nowadays the process of the generation of equations of motion can be fully automated by the use of modern mathematical packages suitable for symbolic computations [5, 6], which were also used here.

Application of this methodology is presented below in the case of the higher-order 6-mode 3-D theory obtained for the shell element from the previous section, for which the displacement field was defined by Eq. (7.8) as well as the additional conditions given by Eqs. (7.9) and (7.10), independently for the symmetric and anti-symmetric behaviour. In this case the use of Hamilton's principle leads to the set of six equations of motion describing the wave motion, according to the assumed kinematics. Because of the great complexity of the final results it is convenient to introduce the following differential operators in order to simplify the notation:

$$\begin{cases} L_1 \equiv \frac{\partial^2}{\partial r^2} - c_p^2 \frac{\partial^2}{\partial x^2} - c_s^2 \frac{\partial^2}{\partial y^2} \\ L_2 \equiv \frac{\partial^2}{\partial r^2} - c_p^2 \frac{\partial^2}{\partial y^2} - c_s^2 \frac{\partial^2}{\partial x^2} \\ L_3 \equiv \frac{\partial^2}{\partial r^2} - c_s^2 \left( \frac{\partial^2}{\partial x^2} + \frac{\partial^2}{\partial y^2} \right) \end{cases} \quad (7.19)$$

Then, thanks to simple mathematical manipulations, equations of motion can be presented in the following manner:

- for symmetric behaviour:

$$\left\{ \begin{array}{l} L_1 s_1(x, y, t) - (c_p^2 - c_s^2) \frac{\partial^2 s_2(x, y, t)}{\partial x \partial y} \\ \quad - (c_p^2 - 2c_s^2) \frac{\partial \theta_1(x, y, t)}{\partial x} = 0 \\ L_2 s_2(x, y, t) - (c_p^2 - c_s^2) \frac{\partial^2 s_1(x, y, t)}{\partial x \partial y} \\ \quad - (c_p^2 - 2c_s^2) \frac{\partial \theta_1(x, y, t)}{\partial y} = 0 \\ L_3 s_3(x, y, t) + c_p^2 \theta_1(x, y, t) \\ \quad - c_s^2 \left[ \frac{\partial \phi_0(x, y, t)}{\partial x} - \frac{\partial \psi_0(x, y, t)}{\partial y} \right] \\ \quad - (c_p^2 - c_s^2) \left[ \frac{\partial s_1(x, y, t)}{\partial x} + \frac{\partial s_2(x, y, t)}{\partial y} \right] = 0 \end{array} \right. \quad (7.20)$$

- for antisymmetric behaviour:

$$\left\{ \begin{array}{l} L_1 s_4(x, y, t) - (c_p^2 - c_s^2) \frac{\partial^2 s_5(x, y, t)}{\partial x \partial y} \\ \quad - \frac{2}{3}(c_p^2 - 2c_s^2) \frac{\partial \theta_2(x, y, t)}{\partial x} - c_s^2 \phi_1(x, y, t) = 0 \\ L_2 s_5(x, y, t) - (c_p^2 - c_s^2) \frac{\partial^2 s_4(x, y, t)}{\partial x \partial y} \\ \quad - \frac{2}{3}(c_p^2 - 2c_s^2) \frac{\partial \theta_2(x, y, t)}{\partial y} - c_s^2 \psi_1(x, y, t) = 0 \\ L_3 s_6(x, y, t) - c_s^2 \left[ \frac{\partial \phi_1(x, y, t)}{\partial x} - \frac{\partial \psi_1(x, y, t)}{\partial y} \right] = 0 \end{array} \right. \quad (7.21)$$

where six auxiliary variables  $s_n$  ( $n = 1, 2, \dots, 6$ ) are introduced and defined as follows:

$$\left\{ \begin{array}{l} s_1(x, y, t) = \phi_0(x, y, t) + \frac{2}{3}\phi_2(x, y, t) \\ s_2(x, y, t) = \psi_0(x, y, t) + \frac{2}{3}\psi_2(x, y, t) \\ s_3(x, y, t) = \frac{1}{3}a^2 \left[ \theta_1(x, y, t) + \frac{2}{5}\theta_3(x, y, t) \right] \end{array} \right. \quad (7.22)$$

$$\left\{ \begin{array}{l} s_4(x, y, t) = \frac{1}{3}a^2 \left[ \phi_1(x, y, t) + \frac{2}{5}\phi_3(x, y, t) \right] \\ s_5(x, y, t) = \frac{1}{3}a^2 \left[ \psi_1(x, y, t) + \frac{2}{5}\psi_3(x, y, t) \right] \\ s_6(x, y, t) = \theta_0(x, y, t) + \frac{2}{3}\theta_2(x, y, t) \end{array} \right. \quad (7.23)$$



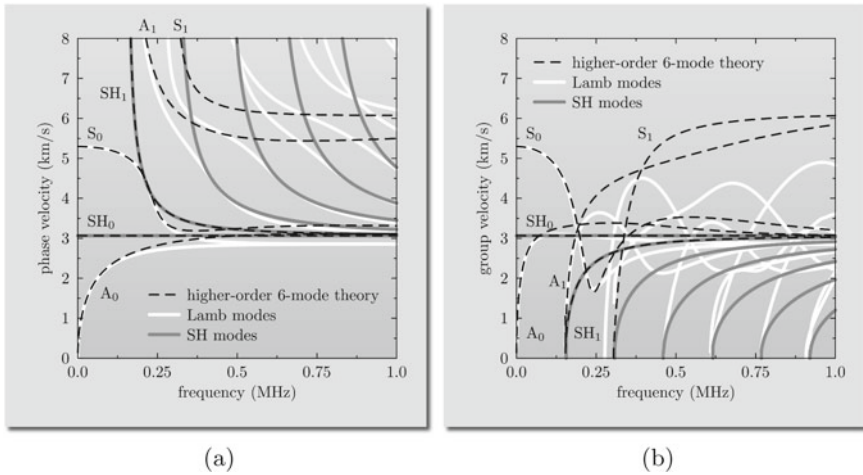


**Fig. 7.1** Dispersion curves for: **a** the phase velocity, **b** the group velocity, for modes of Lamb waves and SH-waves propagating in a 10 mm thick aluminium layer, according to the higher-order 6-mode 3-D theory of shells

The dispersion curves associated with the equations of motion obtained, given by Eqs. (7.20) and (7.21), can be easily obtained by assuming solutions in the form of plane harmonic waves [4] for each independent variable, i.e. DOF,  $\phi_n$ ,  $\psi_n$  and  $\theta_n$  as:

$$\begin{cases} \phi_n(x, y) = \hat{\phi}_n e^{i(k_x x + k_y y)} e^{-i\omega t} \\ \psi_n(x, y) = \hat{\psi}_n e^{i(k_x x + k_y y)} e^{-i\omega t} \\ \theta_n(x, y) = \hat{\theta}_n e^{i(k_x x + k_y y)} e^{-i\omega t} \end{cases}, \quad n = 1, 2 \quad (7.24)$$

where  $\hat{\phi}_n$ ,  $\hat{\psi}_n$  and  $\hat{\theta}_n$  denote the amplitudes of these waves, while  $k_x$  and  $k_y$  associated wave numbers in the directions of the  $x$  axis and the  $y$  axis.

A simple substitution of the assumed form of solutions expressed by Eq. (7.24) to the equations of motion given by Eqs. (7.20) and (7.21) leads to two independent sets of three homogeneous equations, one for the symmetric and one for the antisymmetric behaviour. As before these systems have non-trivial solutions only if their determinants vanish. Bearing in mind that in the current case the following relationship holds:  $|\mathbf{k}|^2 = k_x^2 + k_y^2 = k$ , two independent characteristic equations are obtained, each of them being a 10th degree polynomial with respect to the wave number  $k$ . These characteristic equations are very complex and difficult to handle analytically. However, they can be effectively solved first symbolically and next numerically by the use of modern mathematical packages suitable for such computations [5, 6], which were already mentioned. The result of such computations are presented in Fig. 7.1 as a function of the cyclic frequency  $f$ , for symmetric and antisymmetric modes of Lamb

waves and SH-waves, obtained in the case of elastic waves propagating in a 10 mm thick aluminium layer.<sup>7</sup>

It can be seen that the dispersion curves obtained concerning the symmetric and antisymmetric behaviour are characterised by great complexity and are very difficult to analyse. For this reason, in the following sections it is shown that without any loss of generality dispersion curves associated with the displacement fields of shell structural elements can be viewed and analysed separately, as dispersion curves related to either symmetric or antisymmetric behaviour of plates.

## References

1. W. L. Oberkampf, S. M. DeLand, B. M. Rutherford, K. V. Diegert, and K. F. Alvin. Error and uncertainty in modelling and simulation. *Reliability Engineering and System Safety*, 75:333–357, 2002.
2. A. Žak and M. Krawczuk. Assessment of rod behaviour theories used in spectral finite element modelling. *Journal of Sound and Vibration*, 329:2099–2113, 2010.
3. A. Žak and M. Krawczuk. A higher order transversely deformable shell-type spectral finite element for dynamic analysis of isotropic structures. *Finite Elements in Analysis and Design*, 141:17–29, 2018.
4. J. D. Achenbach. *Wave propagation in elastic solids*. North-Holland Publishing Company, Amsterdam, 1973.
5. <http://www.mathworks.com>.
6. <http://www.wolfram.com>.

---

<sup>7</sup> In the literature dispersion curves are very often presented in a non-dimensional manner as the curves representing the ratio of the phase velocity to the group velocity, i.e.  $c_p/c_g$ . Such a representation can, however, mask some important features of their frequency dependence, which otherwise could be observed separately for either the phase velocity or the group velocity.

# Chapter 8

## Simplified Theories of 2-D Structural Elements



### 8.1 Symmetric Behaviour of Plates

The general form of the displacement field associated with the symmetric behaviour of plates results directly from the same considerations as presented in Sect. 7.2, in the case of the 2-D shell<sup>1</sup> and expressed by Eq. (7.8). The symmetry of the plate behaviour requires that:

$$\begin{cases} u_x(x, y, \zeta, t) = \phi_0(x, y, t) + \sum_{n=1}^p (1 - \zeta^{2n})\phi_{2n}(x, y, t) \\ u_y(x, y, \zeta, t) = \psi_0(x, y, t) + \sum_{n=1}^p (1 - \zeta^{2n})\psi_{2n}(x, y, t) \\ u_z(x, y, \zeta, t) = a\zeta\theta_1(x, y) + \sum_{n=1}^q a\zeta(1 - \zeta^{2n})\theta_{2n+1}(x, y) \end{cases} \quad (8.1)$$

where  $p$  and  $q$  are the numbers of terms kept in the series and related to the total number of independent variables, i.e. DOFs, of a given theory. In the case of higher-order theories being developed, the traction-free boundary condition may be used in order to lower the total number of independent variables, i.e. DOFs, as was demonstrated in Sect. 7.2.

It can also be easily checked that the above form of the displacement field may also be obtained by Maclaurin series expansion of the appropriate relationships describing the symmetric behaviour in the case of SH-waves and Lamb waves, and given by Eq. (5.3) in Sect. 5.1 and Eq. (5.20) in Sect. 5.2. It is also clear that the appropriate truncation of the series in Eq. (8.1) may lead to numerous theories describing the symmetric behaviour of plates.

<sup>1</sup> In a sense that the in-plane displacement components and the transverse strain must remain even functions with respect to the  $z$  coordinate.

Based on the results presented in [1, 2] it should be emphasised that the total number of terms kept in the case of the in-plane displacement components  $u_x$  and  $u_y$  should be equal to the number of terms kept in the case of the out-of-plane displacement function  $u_z$ . This general recommendation helps to lower the modelling error, which otherwise tends to be increased in comparison to the case when  $p = q$  especially in the case of higher-order multi-mode theories.

In the Cartesian coordinate system  $(x, y, z)$  particular theories of the symmetric behaviour of plates can be associated with different forms of Maclaurin series expansions of each component of the displacement field  $u_x$ ,  $u_y$  and  $u_z$ , and presented as:

- *2-mode 2-D theory (classical)*<sup>2</sup>:

$$p = q = 0 \quad \text{and} \quad \theta_1(x, y, t) = 0$$

$$\downarrow$$

$$\begin{cases} u_x(x, y, \zeta, t) = \phi_0(x, y, t) \\ u_y(x, y, \zeta, t) = \psi_0(x, y, t) \\ u_z(x, y, \zeta, t) = 0 \end{cases} \quad (8.2)$$

for which the characteristic equation can be easily obtained as:

$$\left(k^2 - \frac{\omega^2}{\tilde{c}_p^2}\right) \left(k^2 - \frac{\omega^2}{c_s^2}\right) = 0 \quad (8.3)$$

which leads to the dispersion curves presented in Fig. 8.1 and where  $\tilde{c}_p$  is the phase velocity of P-waves under plane stress condition<sup>3</sup> related to the phase velocities of P-waves and S-waves in a 3-D elastic space by the following simple relationship:

$$\tilde{c}_p = 2c_s \sqrt{1 - \frac{c_s^2}{c_p^2}} \quad \text{or} \quad \tilde{c}_p = \sqrt{\frac{E}{(1 - \nu^2)\rho}} \quad (8.4)$$

<sup>2</sup> This theory is determined only by in-plane displacements due to the membrane type of loading. No symmetric transverse displacements are present regardless of the excitation type: static or dynamic and its frequency. For this reason its use should be limited to studies of static and low frequency dynamic problems rather than problems involving propagation of symmetric modes of Lamb waves.

<sup>3</sup> This condition requires vanishing of the stress vector  $\mathbf{T}$  across a particular plane, typically  $xy$  plane, which leads to vanishing of the stress components  $\sigma_{zz}$ ,  $\tau_{xz}$  and  $\tau_{yz}$ , i.e.  $\mathbf{T} = \boldsymbol{\sigma} \cdot [0, 0, 1]^T$  is equal to  $\mathbf{0}$ . This very often occurs in thin plates under static or low frequency dynamic loads. Thanks to this condition the analysis of the stress state within plates is reduced from 3-D to 2-D and considerably simplified.

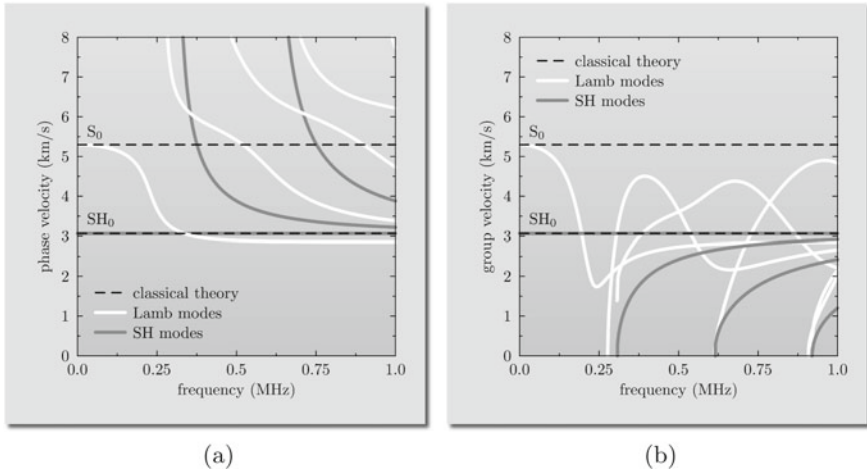


**Fig. 8.1** Dispersion curves for: **a** the phase velocity, **b** the group velocity, for symmetric modes of Lamb waves and SH-waves propagating in a 10 mm thick aluminium layer, according to the 2-mode 2-D theory (classical) of the symmetric behaviour of plates

- *Modified 2-mode 2-D theory:*

$$p = q = 0 \text{ and } \theta_1(x, y, t) = 0$$

↓

$$\begin{cases} u_x(x, y, \zeta, t) = \phi_0(x, y, t) \\ u_y(x, y, \zeta, t) = \psi_0(x, y, t) \\ u_z(x, y, \zeta, t) = 0 \end{cases} \quad (8.5)$$

with the additional condition for the rate of the transverse thickness change  $\dot{\epsilon}_{zz} = -\nu(\dot{\epsilon}_{xx} + \dot{\epsilon}_{yy})/2$  resulting from the Poisson effect and influencing the plate kinetic energy  $\mathcal{K}$  [3]:

$$\dot{u}_z(x, y, \zeta, t) = -\frac{\nu}{2} \left[ \frac{\partial \dot{\phi}_0(x, y, t)}{\partial x} + \frac{\partial \dot{\psi}_0(x, y, t)}{\partial y} \right] a\zeta \quad (8.6)$$

for which the characteristic equation can be easily obtained as:

$$\left( k^2 - \frac{\omega^2}{c^2} \right) \left( k^2 - \frac{\omega^2}{c_s^2} \right) = 0 \quad (8.7)$$

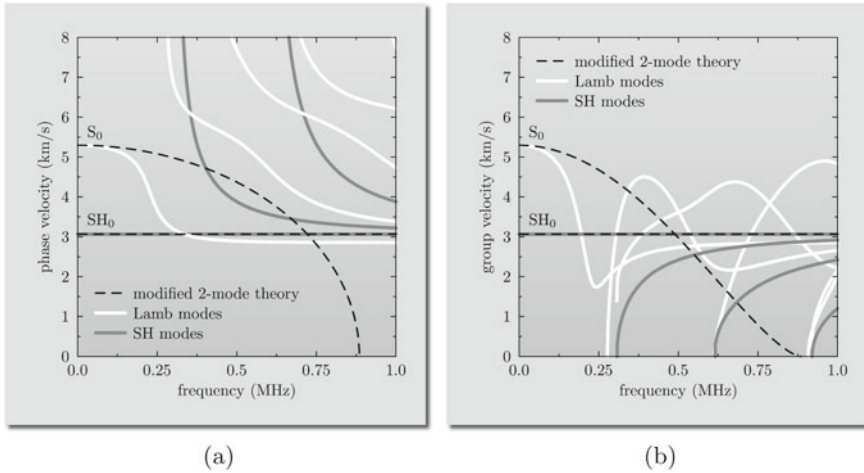


**Fig. 8.2** Dispersion curves for: **a** the phase velocity, **b** the group velocity, for symmetric modes of Lamb waves and SH-waves propagating in a 10 mm thick aluminium layer, according to the modified 2-mode 2-D theory of the symmetric behaviour of plates

which leads to the dispersion curves presented in Fig. 8.2, where now  $c$  is the phase velocity defined us:

$$c = \sqrt{\frac{E}{(1 + \beta^2)\rho}}, \quad \text{with } \beta = \frac{\nu}{2} \frac{ka}{\sqrt{3}} \quad (8.8)$$

- 3-mode 3-D theory [4]:

$$\begin{aligned}
 p = q = 0 \\
 \downarrow \\
 \begin{cases} u_x(x, y, \zeta, t) = \phi_0(x, y, t) \\ u_y(x, y, \zeta, t) = \psi_0(x, y, t) \\ u_z(x, y, \zeta, t) = a\zeta\theta_1(x, y, t) \end{cases} \quad (8.9)
 \end{aligned}$$

for which the characteristic equation is a 6th degree polynomial with respect to the wave number  $k$ . Its roots can be easily found numerically, which leads to the dispersion curves presented in Fig. 8.3. Based on [5] the additional assumption about the value of the shear correction factor  $\kappa = 0.83$  is also made in this case.

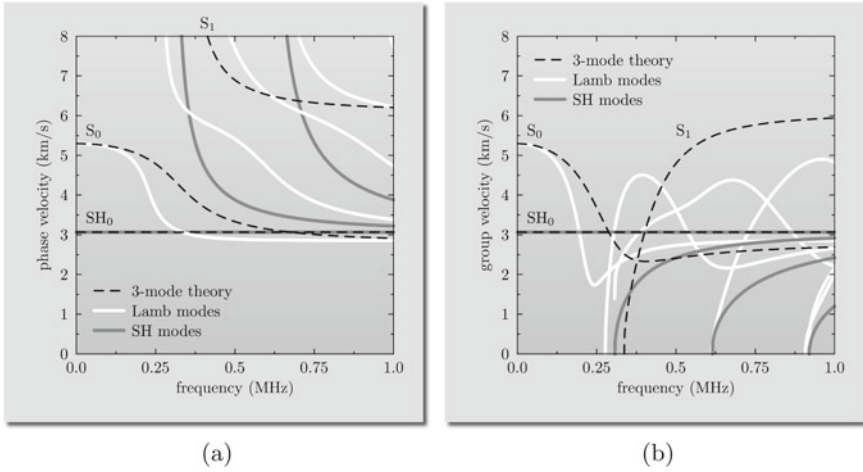


**Fig. 8.3** Dispersion curves for: **a** the phase velocity, **b** the group velocity, for symmetric modes of Lamb waves and SH-waves propagating in a 10 mm thick aluminium layer, according to the 3-mode 3-D theory of the symmetric behaviour of plates

- *Modified 3-mode 3-D theory* [4]:

$$\begin{aligned}
 & p = q = 0 \\
 & \quad \downarrow \\
 & \begin{cases} u_x(x, y, \zeta, t) = \phi_0(x, y, t) \\ u_y(x, y, \zeta, t) = \psi_0(x, y, t) \\ u_z(x, y, \zeta, t) = a\zeta\theta_1(x, y, t) \end{cases} \quad (8.10)
 \end{aligned}$$

for which the characteristic equation is also a 6th degree polynomial with respect to the wave number  $k$ . Its roots can be easily found numerically, which leads to the dispersion curves presented in Fig. 8.4. Based on [4] the additional assumption about the distribution of shear stresses is made using the correction function  $f(\zeta) = \alpha(1 - \zeta^2)$  with  $\alpha = 1.6\kappa$ , which is incorporated within the matrix of elastic coefficients at the positions corresponding to the stress components  $\tau_{xz}$  and  $\tau_{yz}$ .

- *Higher-order 3-mode 3-D theory* [6]:

$$\begin{aligned}
 & p = q = 1 \\
 & \quad \downarrow \\
 & \begin{cases} u_x(x, y, \zeta, t) = \phi_0(x, y, t) + (1 - \zeta^2)\phi_2(x, y, t) \\ u_y(x, y, \zeta, t) = \psi_0(x, y, t) + (1 - \zeta^2)\psi_2(x, y, t) \\ u_z(x, y, \zeta, t) = a\zeta\theta_1(x, y, t) + a\zeta(1 - \zeta^2)\theta_3(x, y, t) \end{cases} \quad (8.11)
 \end{aligned}$$

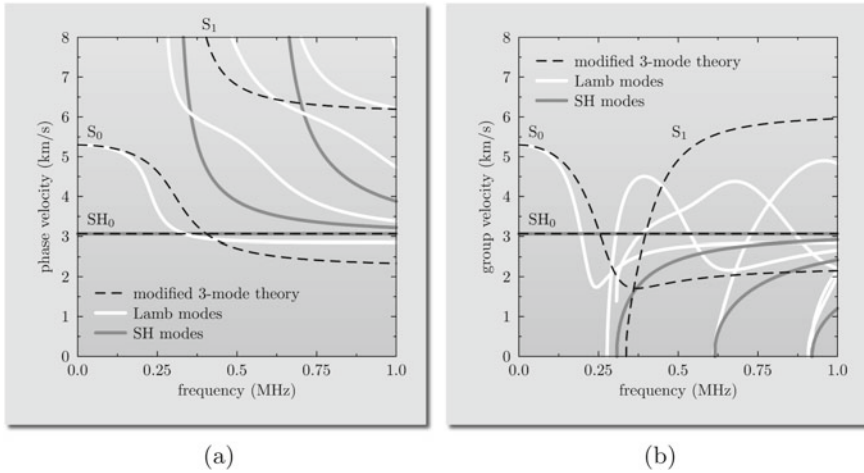


**Fig. 8.4** Dispersion curves for: **a** the phase velocity, **b** the group velocity, for symmetric modes of Lamb waves and SH-waves propagating in a 10 mm thick aluminium layer, according to the modified 3-mode 3-D theory of the symmetric behaviour of plates

for which the characteristic equation is a 10th degree polynomial with respect to the wave number  $k$ . Its roots can be easily found numerically, which leads to the dispersion curves presented in Fig. 8.5. The additional assumptions for  $\phi_2$ ,  $\psi_2$  and  $\theta_3$  are made resulting from the traction-free boundary conditions for the stress components  $\sigma_{zz}$ ,  $\tau_{xz}$  and  $\tau_{yz}$  leading to:

$$\left\{ \begin{array}{l} 2\phi_2(x, y, t) = a^2 \frac{\partial \theta_1(x, y, t)}{\partial x} \\ 2\psi_2(x, y, t) = a^2 \frac{\partial \theta_1(x, y, t)}{\partial y} \\ 2\theta_3(x, y, t) = \theta_1(x, y, t) \\ \quad + \frac{\lambda}{\lambda + 2\mu} \left[ \frac{\partial \phi_0(x, y, t)}{\partial x} + \frac{\partial \psi_0(x, y, t)}{\partial y} \right] \end{array} \right. \quad (8.12)$$

- 6-mode 3-D theory [7]:

$$\begin{array}{c} p = q = 1 \\ \downarrow \\ \left\{ \begin{array}{l} u_x(x, y, \zeta, t) = \phi_0(x, y, t) + (1 - \zeta^2)\phi_2(x, y, t) \\ u_y(x, y, \zeta, t) = \psi_0(x, y, t) + (1 - \zeta^2)\psi_2(x, y, t) \\ u_z(x, y, \zeta, t) = a\zeta\theta_1(x, y, t) + a\zeta(1 - \zeta^2)\theta_3(x, y, t) \end{array} \right. \quad (8.13) \end{array}$$



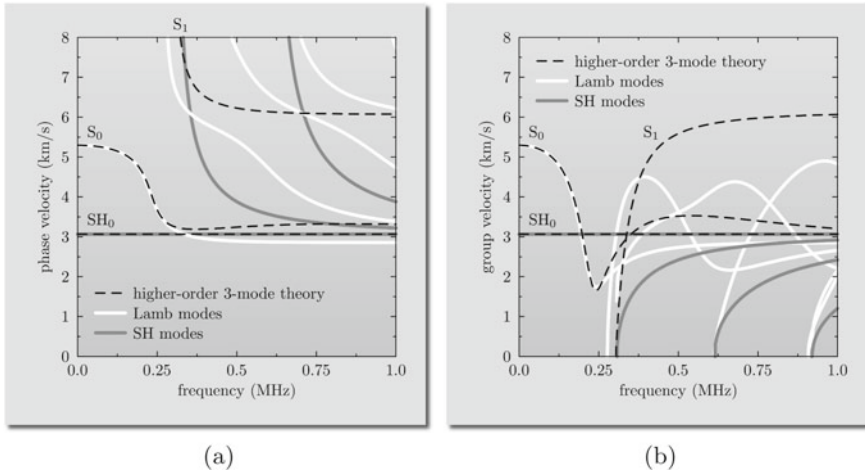


**Fig. 8.5** Dispersion curves for: **a** the phase velocity, **b** the group velocity, for symmetric modes of Lamb waves and SH-waves propagating in a 10 mm thick aluminium layer, according to the higher-order 3-mode 3-D theory of the symmetric behaviour of plates

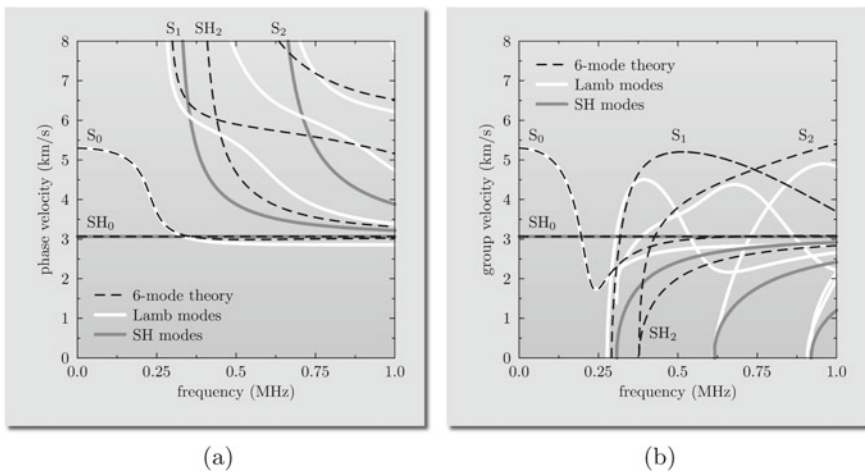


**Fig. 8.6** Dispersion curves for: **a** the phase velocity, **b** the group velocity, for symmetric modes of Lamb waves and SH-waves propagating in a 10 mm thick aluminium layer, according to the 6-mode 3-D theory of the symmetric behaviour of plates

for which the characteristic equation is a 12th degree polynomial with respect to the wave number  $k$ . Its roots can be easily found numerically, which leads to the dispersion curves presented in Fig. 8.6.

A very important aspect of each particular approximated theory presented above, which indicates its practical range of applicability, is the accuracy. There are many

methods and measures, which can be employed for the purpose of the evaluation of their accuracy [2], each of them characterised by different properties. The easiest and the most commonly used measure is the relative error, which was also used in the case of the calculated dispersion curves for the phase velocity, for all discussed theories. It is understood as the ratio of the error to the exact value predicted by the known analytical solution, while the error is the difference between the value of the phase velocity predicted by a given theory and the exact value.<sup>4</sup>

This relative error can be simply expressed as:

$$\delta(\omega) = \frac{c(\omega) - c_a(\omega)}{c_a(\omega)} \times 100\% \quad (8.14)$$

where  $c$  is the phase velocity obtained by the use of a given theory, while  $c_a$  is the corresponding value obtained from the analytical solution.

The results concerning the 6 theories of the symmetric behaviour of plates presented above are shown in Figs. 8.7, 8.8 and 8.9 as relative error curves<sup>5</sup> and a function of the cyclic frequency  $f$ . For clarity of presentation the frequency range is limited to 1 MHz, which in the case of a 10 mm thick aluminium layer is sufficient to incorporate a great number of modes of Lamb waves and SH-waves.

The results presented in Fig. 8.7 concern the 2-mode 2-D theory (classical) and the modified 2-mode 2-D theory. Since these 2-D theories neglect the out-of-plane component of the displacement field their application range turns out to be very limited. In practice it is driven by the accuracy of the fundamental symmetric mode of Lamb waves  $S_0$  and for this reason their application range should concentrate only on statics or low frequency dynamics. This is despite the fact that the prediction of the behaviour of the fundamental symmetric mode of SH-waves  $SH_0$  remains correct.

The enrichment of the 2-D theories with the additional modes, which in the case of the 3-mode 3-D theory and the modified 3-mode 3-D theory is the second symmetric mode  $S_1$ , improves the quality of the theories as well as their ranges of applicability. This is clearly seen in Fig. 8.8. As the result of this enrichment the 3-D theories become also suitable for problems involving mid frequency dynamics. In order to further extend this range of applicability and to improve theoretical predictions it is necessary to further enrich the theories. This can be achieved in two alternative ways. The first one assumes a simple process of adding extra modes of Lamb waves and SH-waves, preferably in such a manner that the corresponding Maclaurin series expansion of each displacement component includes the same number of terms, i.e. the same number of independent mid-plane functions. The second method additionally assumes the application of the traction-free boundary conditions in order to

---

<sup>4</sup> Very often in the literature the definition of the relative error uses the absolute value of the error instead of the plain error. In such a case an important piece of information, namely whether a given theory predicts values higher or lower than the exact solution, is lost. In order to preserve this information the plain error is used now instead of the absolute error.

<sup>5</sup> Hereinafter solid lines in all presented figures depicting changes in the relative error of the phase velocity as a function of the frequency correspond to the range of phase velocities not exceeding 8 km/s. Otherwise they are presented as dashed lines.

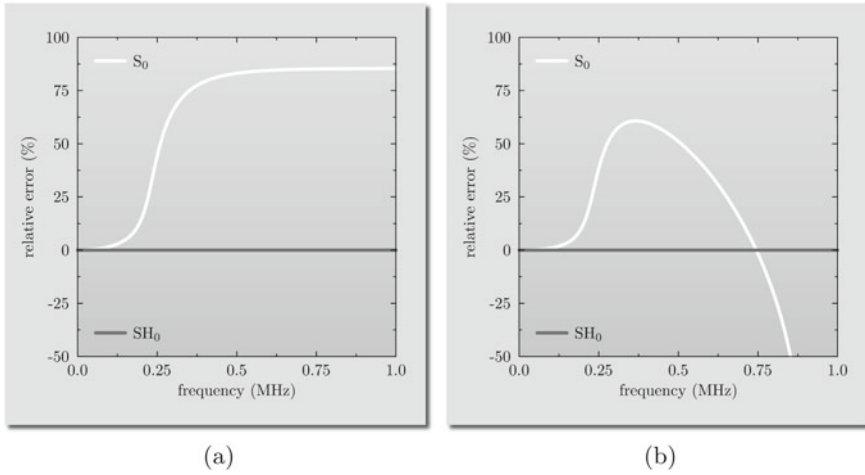


**Fig. 8.7** Relative error for: **a** the 2-mode 2-D theory (classical), **b** the modified 2-mode 2-D theory, of the symmetric behaviour of plates measured against the analytical solution for symmetric modes of Lamb waves and SH-waves propagating in a 10 mm thick aluminium layer

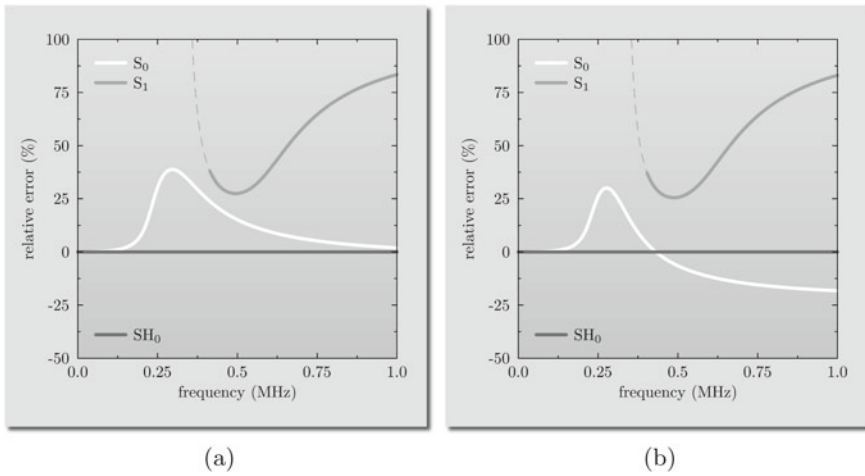


**Fig. 8.8** Relative error for: **a** the 3-mode 3-D theory, **b** the modified 3-mode 3-D theory, of the symmetric behaviour of plates measured against the analytical solution for symmetric modes of Lamb waves and SH-waves propagating in a 10 mm thick aluminium layer

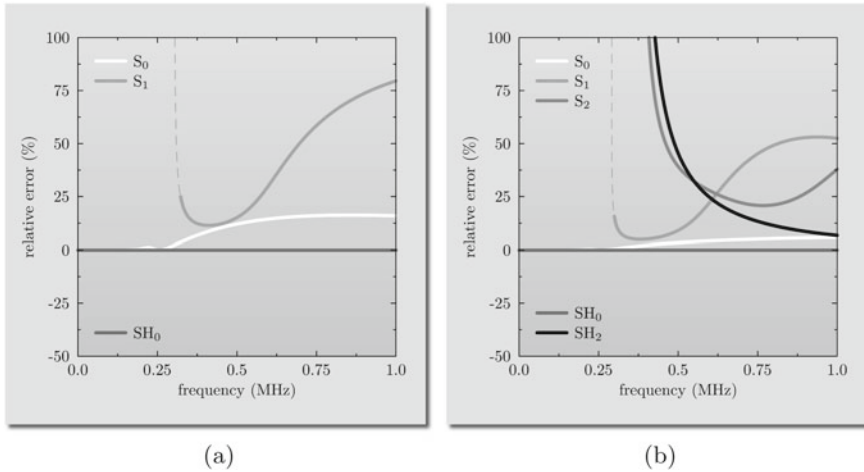


**Fig. 8.9** Relative error for **a** the higher-order 3-mode 3-D theory, **b** the 6-mode 3-D theory, of the symmetric behaviour of plates measured against the analytical solution for symmetric modes of Lamb waves and SH-waves propagating in a 10 mm thick aluminium layer

lower this increased number of independent mid-plane functions. The result of such an approach is presented in Fig. 8.9 in the case of the higher-order 3-mode 3-D theory and the 6-mode 3-D theory. It can be clearly seen that the applicability of these two 3-D theories is substantially increased in comparison with the remaining theories.

In practical applications concerning the analysis and investigation of the symmetric behaviour of plates it is the fundamental symmetric mode  $S_0$  that plays the most important role. For this reason it is much better to compare the studied theories, if the investigation of their accuracy is limited to this mode only, as well as the frequency range up to the first cut-off frequency  $f_{S_1}$ , as presented and summarised in Table 8.1. In the current case of a 10 mm aluminium plate the second symmetric mode  $S_1$  appears at the frequency  $f_{S_1}$  of 277.1 kHz.

It is evident from Fig. 8.10 that for the simplest 2-D and 3-D theories the fundamental symmetric mode  $S_0$  is characterised by the relative error of the phase velocity, which grows very rapidly with an increase in the frequency. This is the case for the 2-mode 2-D theory (classical), the modified 2-mode 2-D theory, the 3-mode 3-D theory as well as the modified 3-mode 3-D theory. For these theories the relative error reaches 5% at 151.2, 167.0, 183.0 and 189.0 kHz, respectively. However, this is not observed in the case of the higher-order 3-mode 3-D theory and the 6-mode 3-D theory, for which the maximum value of the modelling error within the frequency range of interest is never higher than 1.2% and 0.39%, respectively. Although at higher computational cost due to the increased number of independent variables, i.e. DOFs, it is recommended to use the latter or other multi-mode or higher-order multi-mode 3-D theories to ensure high accuracy of numerical predictions, especially where high frequency dynamic problems are investigated.

**Table 8.1** Statistical data on the relative modelling error associated with the phase velocity of the fundamental symmetric mode  $S_0$  propagating in a 10 mm thick aluminium layer in the frequency range up to the first cut-off frequency  $f_{S_1}$  of 277.1 kHz, for various theories of the symmetric behaviour of plates.

Theory	Extr. error (%)	Avg. error (%)	Std. deviation (%)
Classical 2-D	58.0	12.4	16.8
Modified 2-mode 2-D	50.1	10.3	14.6
3-mode 3-D	37.6	7.83	11.5
Modified 3-mode 3-D	30.1	6.57	9.72
Higher-order 3-mode 3-D	1.20	0.22	0.34
6-mode 3-D	0.39	0.08	0.11

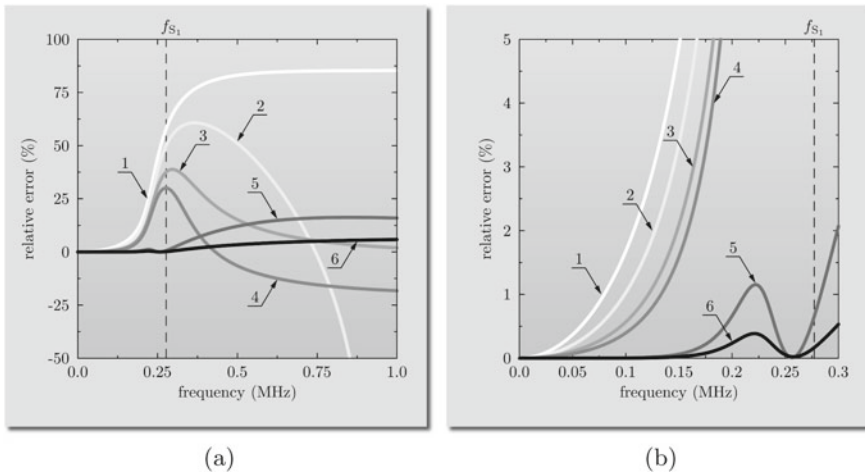


**Fig. 8.10** Relative error of the fundamental symmetric mode  $S_0$  propagating in a 10 mm thick aluminium layer: **a** full range, **b** magnified view, for various theories of the symmetric behaviour of plates (1—classical 2-D, 2—modified 2-mode 2-D, 3—3-mode 3-D, 4—modified 3-mode 3-D, 5—higher-order 3-mode 3-D, 6—6-mode 3-D)

## 8.2 Antisymmetric Behaviour of Plates

The general form of the displacement field related to the antisymmetric behaviour of plates also results from the same considerations as presented in the section related to the shell element,<sup>6</sup> and expressed by Eqs. (7.8). Due to the antisymmetric type of plate behaviour it is required that:

<sup>6</sup> In a sense that this time the in-plane displacements and the transverse strain must remain odd functions with respect to the  $z$  coordinate.

$$\begin{cases} u_x(x, y, \zeta, t) = a\zeta\phi_1(x, y, t) + \sum_{n=1}^p a\zeta(1 - \zeta^{2n})\phi_{2n+1}(x, y, t) \\ u_y(x, y, \zeta, t) = a\zeta\psi_1(x, y, t) + \sum_{n=1}^p a\zeta(1 - \zeta^{2n})\psi_{2n+1}(x, y, t) \\ u_z(x, y, \zeta, t) = \theta_0(x, y, t) + \sum_{k=1}^q (1 - \zeta^{2k})\theta_{2k}(x, y, t) \end{cases} \quad (8.15)$$

where as previously  $p$  and  $q$  are the numbers of terms kept in the series and related to the total number of independent variables, i.e. DOFs, of a given theory. In the same manner as before in the case of higher-order theories being developed the traction-free boundary condition may be used in order to lower the total number of independent variables, i.e. DOFs, as was demonstrated in Sect. 7.2.

It can also be easily checked that the above form of the displacement field may be obtained by Maclaurin series expansion of the appropriate relations describing the antisymmetric behaviour in the case of SH-waves and Lamb waves, and given by Eq. (5.3) in Sect. 5.1 and Eq. (5.21) in Sect. 5.2. Following the same approach as for the symmetric behaviour of plates already presented, it can be clearly seen that by the appropriate truncation of the series in Eq. (8.15) may lead to numerous theories describing the antisymmetric behaviour of plates.

Based on the results presented in [1, 2] it should be emphasised once more that it is recommended that the total number of terms kept in the case of the in-plane displacement components  $u_x$  and  $u_y$  is equal to the number of terms kept in the case of the out-of-plane displacement function  $u_z$ . This general rule helps to lower the modelling error, which otherwise would be increased in comparison to the case when  $p = q$ .

In the Cartesian coordinate system  $(x, y, z)$  particular theories of the antisymmetric behaviour of plates can be associated with different forms of Maclaurin series expansions of each component of the displacement field  $u_x$ ,  $u_y$  and  $u_z$ , and presented as:

- *Higher-order 1-mode 2-D theory (Kirchhoff-Love):*

$$\begin{aligned} p = q = 0 \\ \downarrow \\ \begin{cases} u_x(x, y, \zeta, t) = a\zeta\phi_1(x, y, t) \\ u_y(x, y, \zeta, t) = a\zeta\psi_1(x, y, t) \\ u_z(x, y, \zeta, t) = \theta_0(x, y, t) \end{cases} \end{aligned} \quad (8.16)$$

where thanks to the additional assumptions resulting from the traction-free boundary conditions for the shear stress components  $\tau_{xz}$  and  $\tau_{yz}$ , the mid-plane displacement functions  $\phi_1$  and  $\psi_1$  can be expressed as:

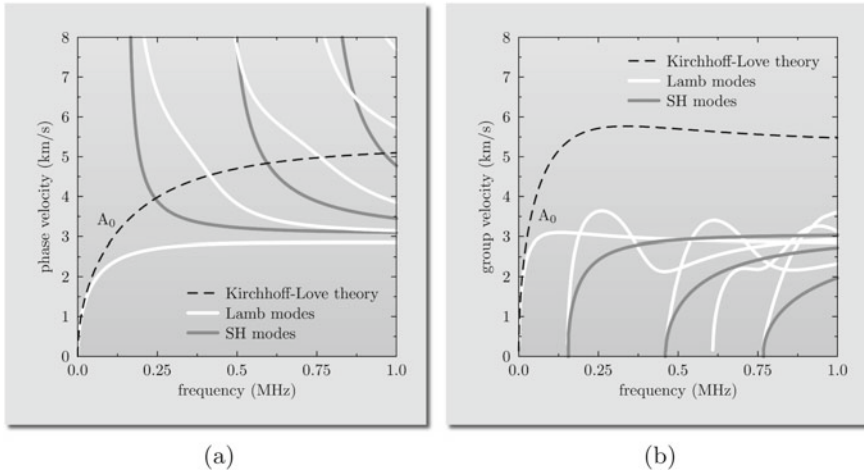


**Fig. 8.11** Dispersion curves for: **a** the phase velocity, **b** the group velocity, for antisymmetric modes of Lamb waves and SH-waves propagating in a 10 mm thick aluminium layer, according to the higher-order 1-mode 2-D theory (Kirchhoff-Love) of the antisymmetric behaviour of plates

$$\begin{cases} \phi_1(x, y, t) = -\frac{\partial\theta_0(x, y, t)}{\partial x} \\ \psi_1(x, y, t) = -\frac{\partial\theta_0(x, y, t)}{\partial y} \end{cases} \quad (8.17)$$

where the characteristic equation takes the following simple form:

$$h^2k^4 - (12 + h^2k^2)\frac{\omega^2}{c_p^2} = 0 \quad (8.18)$$

which leads to the dispersion curves presented in Fig. 8.11. The presence of the factor  $h^2k^2$  results from taking into account the higher-order terms of the transverse accelerations associated with the mid-plane functions  $\phi_1$  and  $\psi_1$ .

In the case of very thin plates these higher-order terms are usually neglected, which is equivalent to the assumption of  $h^2k^2 \approx 0$ , which leads to the characteristic equation in the form which is well-known from the literature [8]:

$$k = \pm \frac{\sqrt{\omega}}{\beta} \quad \text{or} \quad \omega = \beta^2 k^2, \quad \text{where} \quad \beta = \sqrt[4]{\frac{Eh^2}{12(1-\nu^2)\rho}} \quad (8.19)$$

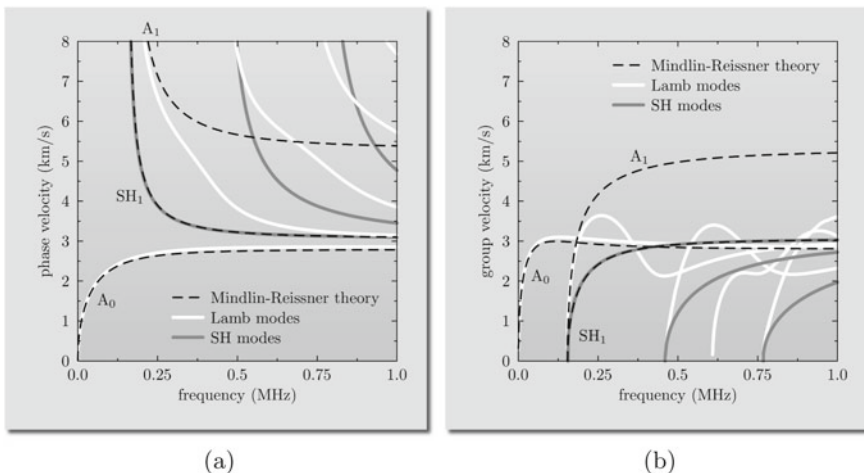


**Fig. 8.12** Dispersion curves for: **a** the phase velocity, **b** the group velocity, for antisymmetric modes of Lamb waves and SH-waves propagating in a 10 mm thick aluminium layer, according to the 3-mode 2-D theory (Mindlin-Reissner) of the antisymmetric behaviour of plates

- 3-mode 2-D theory (Mindlin-Reissner):

$$\begin{aligned}
 p &= q = 0 \\
 &\downarrow \\
 \begin{cases} u_x(x, y, \zeta, t) = a\zeta\phi_1(x, y, t) \\ u_y(x, y, \zeta, t) = a\zeta\psi_1(x, y, t) \\ u_z(x, y, \zeta, t) = \theta_0(x, y, t) \end{cases} & \quad (8.20)
 \end{aligned}$$

for which the characteristic equation is a 6th degree polynomial with respect of the wave number  $k$ . Its roots can be easily found numerically, which leads to the dispersion curves presented in Fig. 8.12. Based on [5] the additional assumption about the value of the shear correction factor  $\kappa = 0.83$  is also made in this case.

- Modified 3-mode 2-D theory [4]:

$$\begin{aligned}
 p &= q = 0 \\
 &\downarrow \\
 \begin{cases} u_x(x, y, \zeta, t) = a\zeta\phi_1(x, y, t) \\ u_y(x, y, \zeta, t) = a\zeta\psi_1(x, y, t) \\ u_z(x, y, \zeta, t) = \theta_0(x, y, t) \end{cases} & \quad (8.21)
 \end{aligned}$$



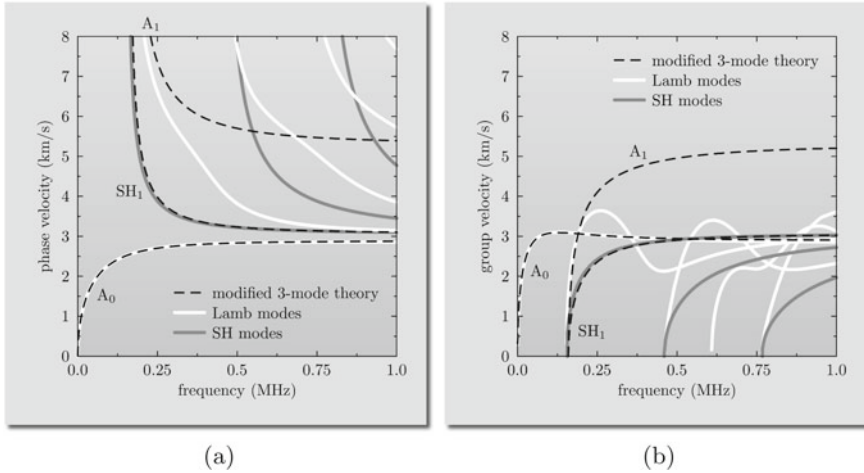


**Fig. 8.13** Dispersion curves for: **a** the phase velocity, **b** the group velocity, for antisymmetric modes of Lamb waves and SH-waves propagating in a 10 mm thick aluminium layer, according to the modified 3-mode 2-D theory of the antisymmetric behaviour of plates

for which the characteristic equation is also a 6th degree polynomial with respect of the wave number  $k$ . Its roots can be easily found numerically, which leads to the dispersion curves presented in Fig. 8.13. Based on [4, 5] the additional assumption about the distribution of shear stresses is made using the correction function  $f(\zeta) = \alpha(1 - \zeta^2)$  with  $\alpha = 1.6\kappa$ , which is incorporated within the matrix of elastic coefficients at the positions corresponding to the stress components  $\tau_{xz}$  and  $\tau_{yz}$ .

- Higher-order 3-mode 2-D theory (Reddy) [9]:

$$\begin{aligned}
 & p = 1, \quad q = 0 \\
 & \quad \downarrow \\
 & \begin{cases} u_x(x, y, \zeta, t) = a\zeta\phi_1(x, y, t) + a\zeta(1 - \zeta^2)\phi_3(x, y, t) \\ u_y(x, y, \zeta, t) = a\zeta\psi_1(x, y, t) + a\zeta(1 - \zeta^2)\psi_3(x, y, t) \\ u_z(x, y, \zeta, t) = \theta_0(x, y, t) \end{cases} \quad (8.22)
 \end{aligned}$$

for which the characteristic equation is now a 8th degree polynomial with respect of the wave number  $k$ . Its roots can be easily found numerically, which leads to the dispersion curves presented in Fig. 8.14. The additional assumptions for  $\phi_3$  and  $\psi_3$  are made, resulting from the traction-free boundary conditions for the stress components  $\tau_{xz}$  and  $\tau_{yz}$ , leading to:

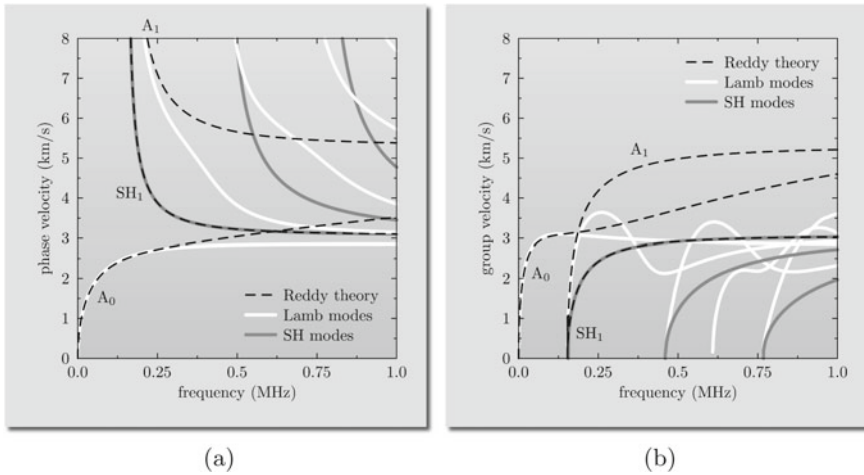


**Fig. 8.14** Dispersion curves for: **a** the phase velocity, **b** the group velocity, for antisymmetric modes of Lamb waves and SH-waves propagating in a 10 mm thick aluminium layer, according to the higher-order 3-mode 2-D theory (Reddy) of the antisymmetric behaviour of plates

$$\begin{cases} 2\phi_3(x, y, t) = \phi_1(x, y, t) + \frac{\partial\theta_0(x, y, t)}{\partial x} \\ 2\psi_3(x, y, t) = \psi_1(x, y, t) + \frac{\partial\theta_0(x, y, t)}{\partial y} \end{cases} \quad (8.23)$$

- Higher-order 3-mode 3-D theory [6]:

$$\begin{aligned} p = q = 1 \\ \downarrow \\ \begin{cases} u_x(x, y, \zeta, t) = a\zeta\phi_1(x, y, t) + a\zeta(1 - \zeta^2)\phi_3(x, y, t) \\ u_y(x, y, \zeta, t) = a\zeta\psi_1(x, y, t) + a\zeta(1 - \zeta^2)\psi_3(x, y, t) \\ u_z(x, y, \zeta, t) = \theta_0(x, y, t) + (1 - \zeta^2)\theta_2(x, y, t) \end{cases} \end{aligned} \quad (8.24)$$

for which the characteristic equation is also a 10th degree polynomial with respect of the wave number  $k$ . Its roots can be easily found numerically, which leads to the dispersion curves presented in Fig. 8.15. The additional assumptions for  $\phi_3$ ,  $\psi_3$  and  $\theta_2$  are made, resulting from the traction-free boundary conditions for the stress components  $\sigma_{zz}$ ,  $\tau_{xz}$  and  $\tau_{yz}$ , leading to:

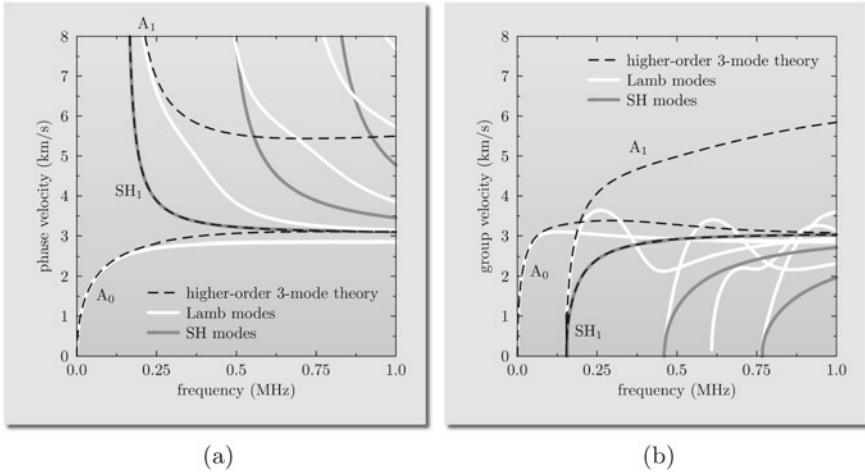


**Fig. 8.15** Dispersion curves for: **a** the phase velocity, **b** the group velocity, for antisymmetric modes of Lamb waves and SH-waves propagating in a 10 mm thick aluminium layer, according to the higher-order 3-mode 3-D theory of the antisymmetric behaviour of plates

$$\begin{cases} 2\phi_3(x, y, t) = \phi_1(x, y, t) + \frac{\partial\theta_0(x, y, t)}{\partial x} \\ 2\psi_3(x, y, t) = \psi_1(x, y, t) + \frac{\partial\theta_0(x, y, t)}{\partial y} \\ 2\theta_2(x, y, t) = a^2 \frac{\lambda}{\lambda + 2\mu} \left[ \frac{\partial\phi_1(x, y, t)}{\partial x} + \frac{\partial\psi_1(x, y, t)}{\partial y} \right] \end{cases} \quad (8.25)$$

• 6-mode 3-D theory [7]:

$$\begin{aligned} p = q = 1 \\ \downarrow \\ \begin{cases} u_x(x, y, \zeta, t) = a\zeta\phi_1(x, y, t) + a\zeta(1 - \zeta^2)\phi_3(x, y, t) \\ u_y(x, y, \zeta, t) = a\zeta\psi_1(x, y, t) + a\zeta(1 - \zeta^2)\psi_3(x, y, t) \\ u_z(x, y, \zeta, t) = \theta_0(x, y, t) + (1 - \zeta^2)\theta_2(x, y, t) \end{cases} \end{aligned} \quad (8.26)$$

for which the characteristic equation is a 12th degree polynomial with respect to the wave number  $k$ . Its roots can be easily found numerically, which leads to the dispersion curves presented in Fig. 8.16.

As shown in the case of the symmetric behaviour of plates, the same analysis of the relative error of the phase velocity for particular theories of the antisymmetric behaviour of plates presented above can be carried out here. The results concerning

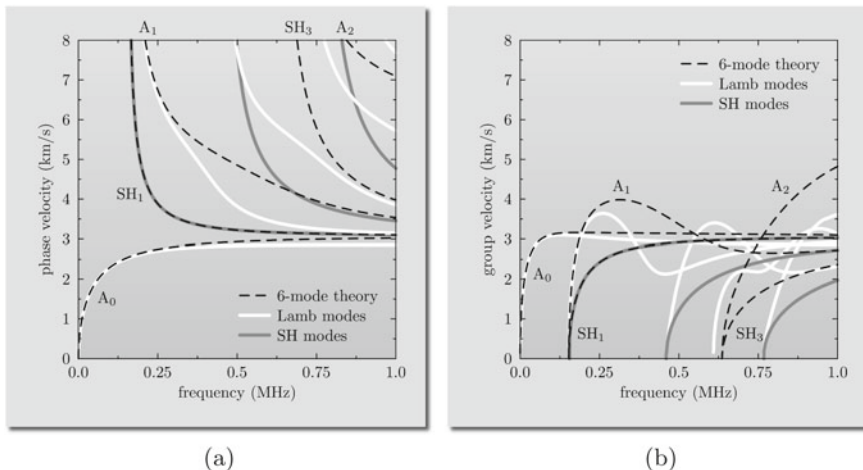


**Fig. 8.16** Dispersion curves for: **a** the phase velocity, **b** the group velocity, for antisymmetric modes of Lamb waves and SH-waves propagating in a 10 mm thick aluminium layer, according to the 6-mode 3-D theory of the antisymmetric behaviour of plates

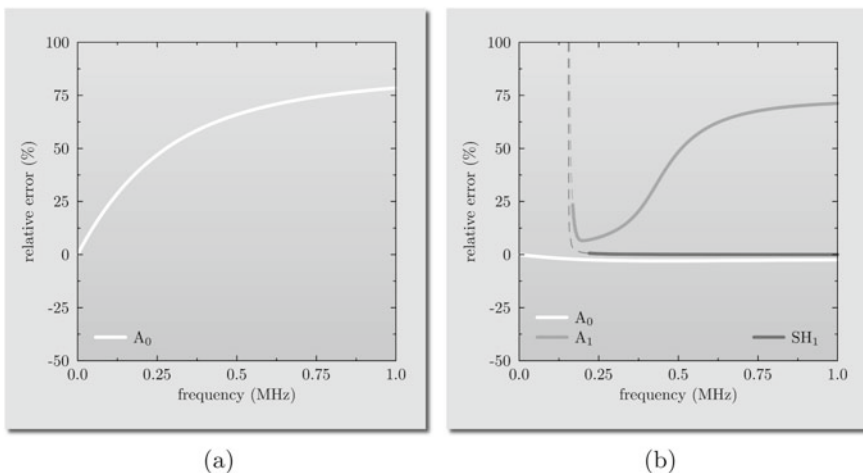


**Fig. 8.17** Relative error for: **a** the higher-order 1-mode 2-D theory (Kirchhoff-Love), **b** the 3-mode 2-D theory (Mindlin-Reissner), of the antisymmetric behaviour of plates measured against the analytical solution for antisymmetric modes of Lamb waves and SH-waves propagating in a 10 mm thick aluminium layer

the 6 theories of the antisymmetric behaviour of plates are given in Figs. 8.17, 8.18 and 8.19 as relative error curves and a function of the cyclic frequency  $f$ . As before for clarity of presentation the frequency range is limited to 1 MHz, which in the case of a 10 mm thick aluminium layer is sufficient to incorporate a great number of modes of Lamb waves and SH-waves.

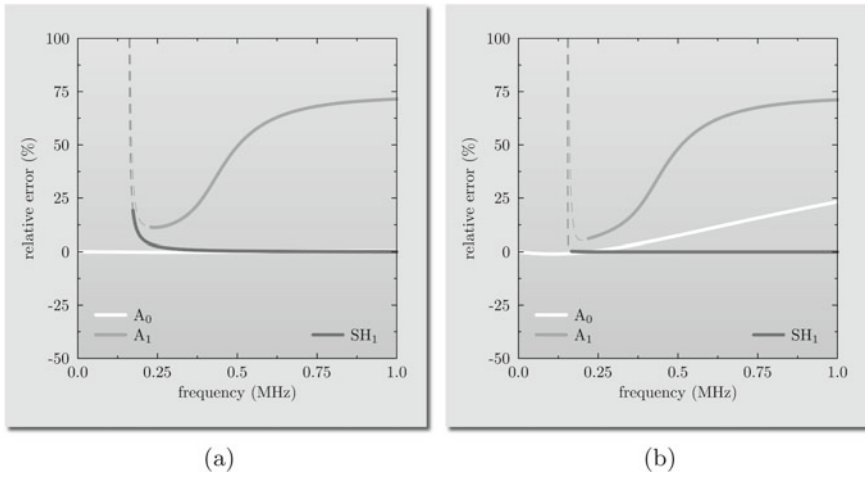


**Fig. 8.18** Relative error for: **a** the modified 3-mode 2-D theory, **b** the higher-order 3-mode 2-D theory (Reddy), of the antisymmetric behaviour of plates measured against the analytical solution for antisymmetric modes of Lamb waves and SH-waves propagating in a 10 mm thick aluminium layer

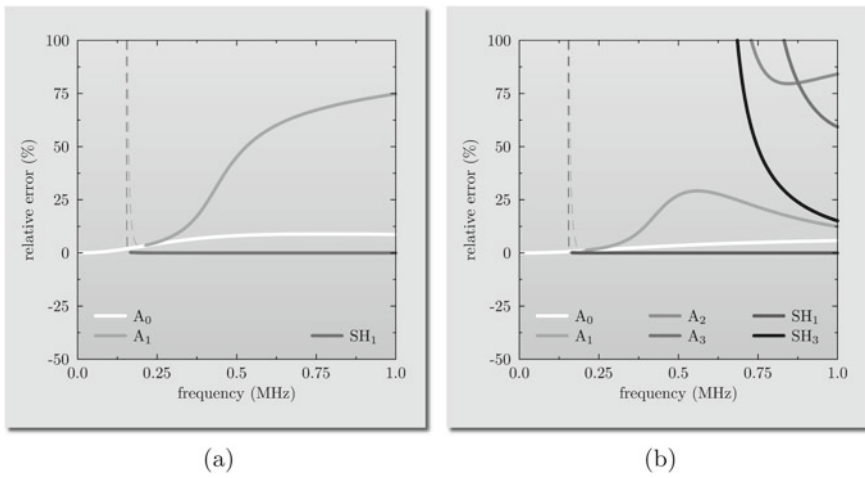


**Fig. 8.19** Relative error for: **a** the higher-order 3-mode 3-D theory, **b** the 6-mode 3-D theory, of the antisymmetric behaviour of plates measured against the analytical solution for antisymmetric modes of Lamb waves and SH-waves propagating in a 10 mm thick aluminium layer

The results presented in Fig. 8.17 concern the higher-order 1-mode 2-D theory (Kirchhoff-Love) and the 3-mode 3-D theory (Mindlin-Reissner). The first 2-D theory (Kirchhoff-Love) is entirely based on the out-of-plane displacement component and its derivatives, which limits its application range due to the rapidly growing modelling error. In this 2-D theory only the fundamental antisymmetric mode  $A_0$  is present. In the case of the second 2-D theory (Mindlin-Reissner) the situation is significantly improved by the enrichment of the theory by the second antisymmetric mode  $A_1$  as well as the second antisymmetric mode of SH-waves  $SH_1$ . The relative error for the fundamental antisymmetric mode  $A_0$  is relatively small within the entire frequency range of interest, however this is not the case for the remaining two modes. For this reason the 2-mode 2-D theory (Mindlin-Reissner) has a greater application range than the higher-order 1-mode 2-D theory (Kirchhoff-Love) and can be applied for problems involving mid frequency dynamics up to the frequencies corresponding to the second antisymmetric mode  $A_1$ , while the application range of the latter remains within the range of low frequency dynamics.

The results obtained in the case of the modified 3-mode 2-D theory and the higher-order 3-mode 2-D theory (Reddy) are presented in Fig. 8.18. It is clearly seen that the modification of the 3-mode 2-D theory (Mindlin-Reissner), by correction of the distribution of shear stresses, profoundly improves the predictions of this 2-D theory in the frequency range of interest only in the case of the fundamental antisymmetric mode  $A_0$ . The correction offered by the higher-order 3-mode 2-D theory (Reddy) has a more significant influence on the obtained results in the case of the remaining two modes, but this is at the cost of the loss of the accuracy in the case of the fundamental antisymmetric mode  $A_0$  within the frequency range above the cut-off frequency for the second antisymmetric mode  $A_1$ . It can be also observed that the appearance of the antisymmetric SH-mode  $SH_1$ , which is characterized by a small relative error at higher frequencies, results in an increase in the relative error associated with the fundamental antisymmetric mode  $A_0$  and the second antisymmetric mode  $A_1$  to unacceptable levels.

A further improvement of the 2-D theories, as observed in the case of the higher-order 3-mode 3-D theory and the 6-mode 3-D theory, has little effect on the relative errors. This is clearly seen in Fig. 8.19. As shown in the case of the symmetric behaviour of plates the enrichment process can be obtained by two alternative ways. The first is based on a simple process of adding extra modes, of Lamb waves and SH-waves, preferably in such a manner that the corresponding Maclaurin series expansion of each displacement component includes the same number of terms, i.e. the same number of independent mid-plane functions, as in the case of the 6-mode 3-D theory. The second method additionally takes advantage of the traction-free boundary conditions in order to lower this increased number of independent mid-plane functions, as in the case of the higher-order 3-mode 3-D theory. However, it can be seen that in the case of the antisymmetric behaviour of plates only the enrichment of the 3-D theory by additional modes, as observed for the 6-mode 3-D theory, results in a significant improvement of the predictions. Such an approach makes it suitable for problems involving moderately high frequency dynamics as well as propagation of elastic waves. This significantly increases the applicability of the

**Table 8.2** Statistical data on the relative modelling error associated with the phase velocity of the fundamental antisymmetric mode  $A_0$  propagating in a 10 mm thick aluminium layer in the frequency range up to the first cut-off frequency  $f_{A_1}$  of 153.4 kHz for various theories of the antisymmetric behaviour of plates.

Theory	Extr. error (%)	Avg. error (%)	Std. deviation (%)
Kirchhoff-Love 2-D	33.6	18.4	9.76
Mindlin-Reissner 2-D	-2.00	-1.11	0.59
Modified 3-mode 2-D	-0.09	0.03	0.04
Reddy 2-D	-0.98	-0.73	0.28
Higher-order 3-mode 3-D	1.96	0.68	0.60
6-mode 3-D	0.62	0.21	0.19

6-mode 3-D theory in comparison to the higher-order 3-mode 3-D theory, although at higher computational cost related to the increased number of independent mid-plane variables, i.e. DOFs.

As previously mentioned, in practical applications concerning the analysis and investigation of the antisymmetric behaviour of plates, it is the fundamental antisymmetric mode  $A_0$  that plays the most important role. For this reason it is much better to compare the investigated 2-D and 3-D theories, if the analysis of their accuracy is limited to this mode only, as well as within the frequency range up to the first cut-off frequency  $f_{A_1}$ , as presented and summarised in Table 8.2. In the current case of a 10 mm aluminium plate the second antisymmetric mode  $A_1$  appears at the frequency  $f_{A_1}$  of 153.4 Hz.

It is noticeable from Fig. 8.20 that for the simplest 2-D theory the fundamental antisymmetric mode  $A_0$  is characterised by the relative error of the phase velocity, which grows very rapidly with an increase in the frequency. This is the case for the higher-order 1-mode 2-D theory (Kirchhoff-Love). The observed behaviour changes significantly for the 3-mode 2-D theory (Mindlin-Reissner), the modified 3-mode 2-D theory as well as the higher-order 3-mode 2-D theory (Reddy), which are characterised by small negative errors within the frequency range of interest. For the higher-order 1-mode 2-D theory (Kirchhoff-Love) the relative error reaches 5% at 18.0 kHz, while for the 3-mode 2-D theories takes the extreme values of -2.00, -0.09 and -0.98%, respectively. It should be noted that these small values of the relative errors, smaller than in the case of the remaining 3-D theories, i.e. the higher-order 3-mode 3-D theory as well as the 6-mode 3-D theory, are unfortunately associated with higher values of the relative errors for the second antisymmetric mode  $A_1$  as well as the second antisymmetric mode of SH-waves  $SH_1$ .

For the 6-mode 3-D theory the modelling error within the frequency range up to the first cut-off frequency  $f_{A_1}$  stays below 0.62%. Although at higher computational cost due to the increased number of independent variables, i.e. DOFs, it is recommended to use the latter or other multi-mode or higher-order multi-mode 3-D theories to ensure high accuracy of numerical predictions, especially when high frequency dynamics is investigated.

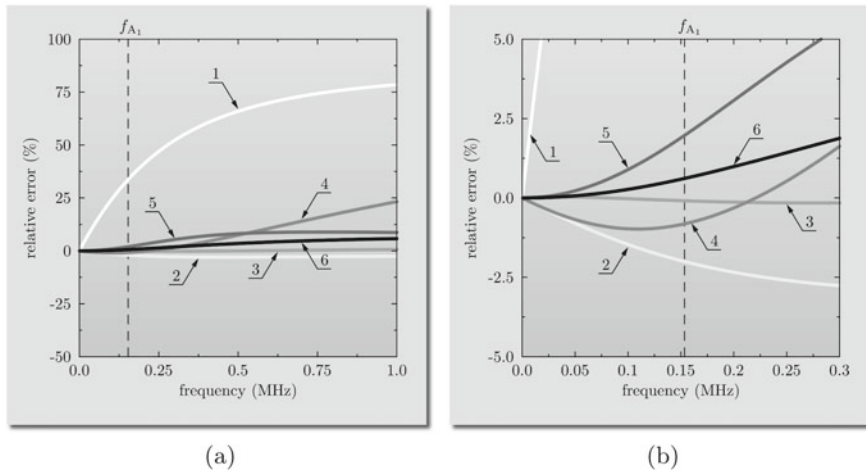


**Fig. 8.20** Relative error of the fundamental antisymmetric mode  $A_0$  propagating in a 10 mm thick aluminium layer: **a** full range, **b** magnified view, for various theories of the antisymmetric behaviour of plates (1—Kirchhoff-Love 2-D, 2—Mindlin-Reissner 2-D, 3—modified 3-mode 2-D, 4—Reddy 2-D, 5—higher-order 3-mode 3-D, 6—6-mode 3-D)

### 8.3 Coupled Behaviour of Shells

The mechanical behaviour associated with the phenomena of wave propagation in shell structural elements requires bonding of the in-plane and out-of-plane behaviour standard for 2-D plate structural elements. This requirement results from the inherent coupling of different types of wave modes leading to their conversion, which is observed in the case of shells, and which is a direct consequence of their geometrical complexity<sup>7</sup> typical for 3-D structures [10–12].

For this reason the displacement fields associated with the behaviour of shell structural elements should always take into account this phenomenon and allow the conversion of wave modes between each symmetric and each antisymmetric mode as a result of their interaction with the existing boundaries, having 3-D nature. Moreover, for the same reason not every two arbitrarily chosen plate theories of the in-plane and out-of-plane behaviour may be combined together to represent a complete<sup>8</sup> theory of shell mechanical behaviour, and than employed for the analysis of high frequency dynamics or wave propagation.

<sup>7</sup> Despite the fact that real shell structural elements very often represent complex 3-D structures, they may still be successfully investigated based on the theories used in the analysis of 2-D plate structural elements. This is possible thanks to the fact that the same approach can be used for shells based on the description of their behaviour at the mid-plane, in exactly the same manner as in the case of 2-D plates.

<sup>8</sup> Employing pairs of wave modes, symmetric and antisymmetric, to describe the investigated behaviour of shells.



This problem can be well illustrated in the case of the displacement field resulting from combining together the 2-mode 2-D theory (classical) of the in-plane behaviour of plates, described by Eq. (8.2), with the higher-order 1-mode 2-D theory (Kirchhoff-Love) of the out-of-plane behaviour of plates, described by Eq. (8.16). The resulting displacement field takes use of 3 fundamental wave modes, which are the symmetric and antisymmetric modes of Lamb waves  $S_0$  and  $A_0$  as well as the symmetric mode of SH-waves  $SH_0$ , as shown below:

$$\begin{cases} u_x(x, y, \zeta, t) = \boxed{\phi_0(x, y, t)} - a\zeta \frac{\partial \theta_0(x, y, t)}{\partial x} \\ u_y(x, y, \zeta, t) = \boxed{\psi_0(x, y, t)} - a\zeta \frac{\partial \theta_0(x, y, t)}{\partial y} \\ u_z(x, y, \zeta, t) = \theta_0(x, y, t) \end{cases} \quad (8.27)$$

where 2 boxed mid-plane functions  $\phi_0$  and  $\psi_0$  are associated with the presence of the fundamental symmetric wave modes  $S_0$  and  $SH_0$ , while the remaining mid-plane function  $\theta_0$  is associated with the presence of the fundamental antisymmetric wave mode  $A_0$ .

Despite the lower accuracy offered by the resulting 2-D theory, which was analysed in detail in the previous sections concerning the in-plane and out-of-plane behaviour of plate structural elements based on various plate theories, the shell theory under consideration not only prevents the existence of, but also the conversion of modes between symmetric and antisymmetric SH-modes, since the antisymmetric mode  $SH_1$  of SH-waves is not taken into account by this theory.

In order to take into account the conversion of particular pairs of wave modes resulting from their interaction due to geometrical coupling a proper approach in this respect should be based on the representation of particular displacement components using the same number of terms resulting from their Maclaurin series expansions. This general recommendation can be successfully fulfilled in the case of a simple 6-mode 3-D theory of shells presented below:

$$\begin{cases} u_x(x, y, \zeta, t) = \boxed{\phi_0(x, y, t)} + a\zeta \phi_1(x, y, t) \\ u_y(x, y, \zeta, t) = \boxed{\psi_0(x, y, t)} + a\zeta \psi_1(x, y, t) \\ u_z(x, y, \zeta, t) = \theta_0(x, y, t) + \boxed{a\zeta \theta_1(x, y, t)} \end{cases} \quad (8.28)$$

as well as in the case of the 12-mode theory given by Eq. (7.8) or the higher-order 6-mode 3-D theory given by Eqs. (7.11) and (7.12), both discussed in Sect. 7.2 in full detail. It can be easily seen that now 3 boxed mid-plane functions  $\phi_0$ ,  $\psi_0$  and  $\theta_1$  are associated with the presence of the symmetric wave modes  $S_0$ ,  $S_1$  and  $SH_0$ , while the remaining 3 mid-plane functions  $\theta_0$ ,  $\phi_1$  and  $\psi_1$  are associated with the presence of the antisymmetric wave modes  $A_0$ ,  $A_1$  and  $SH_1$ .

Displacement fields of shell structural elements based on such an approach can be considered as well-balanced, otherwise they are ill-balanced. This is despite the fact that the frequency content of typical signals associated with propagation of elastic waves typically remains within the range of frequencies well below the first cut-off frequency for the antisymmetric wave modes  $f_{A_1}$  and  $f_{SH_1}$  and for this reason concerns only 3 fundamental wave modes: the symmetric  $A_0$  and  $SH_0$  as well as the antisymmetric  $A_0$ .

It should be emphasised that in the case of shell structural elements conversion of wave modes may result not only from geometrical coupling due their complex 3-D geometry, but also from any types of discontinuities including boundaries, edges, structural faults or cracks, etc. This can be clearly seen in Fig. 8.21 in the case of a z-shape 10 mm thick aluminium profile, which represents a complex 3-D shell structural element.

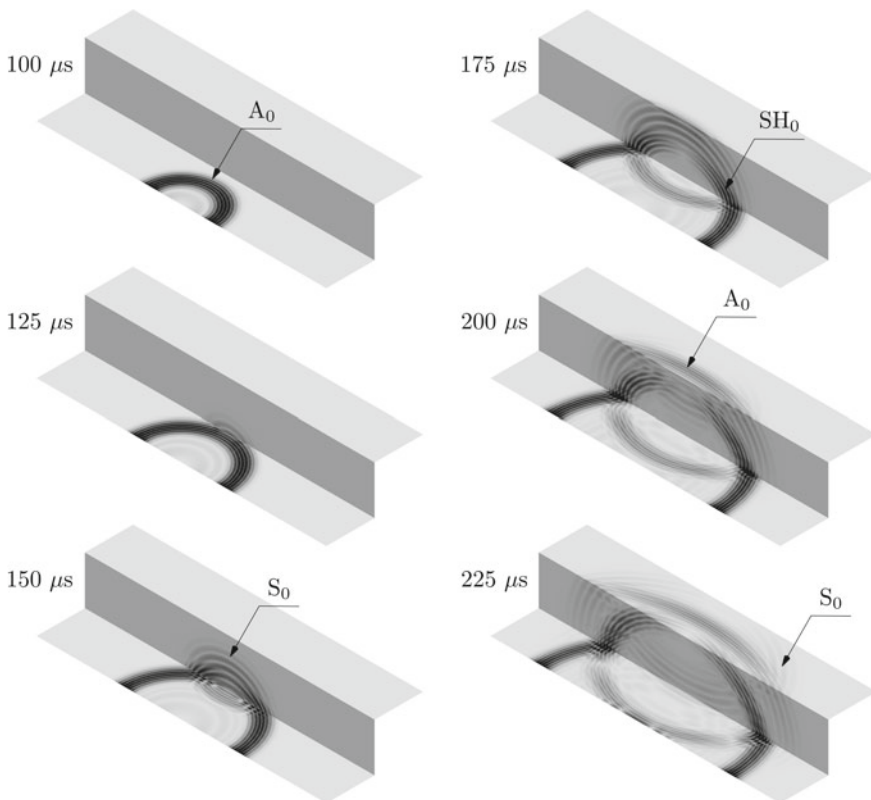


**Fig. 8.21** Conversion of wave modes propagating in a z-shape 10 mm thick aluminium profile in consecutive moments in time. Results of numerical computations by TD-SFEM according to the modified 6-mode 3-D theory of shells

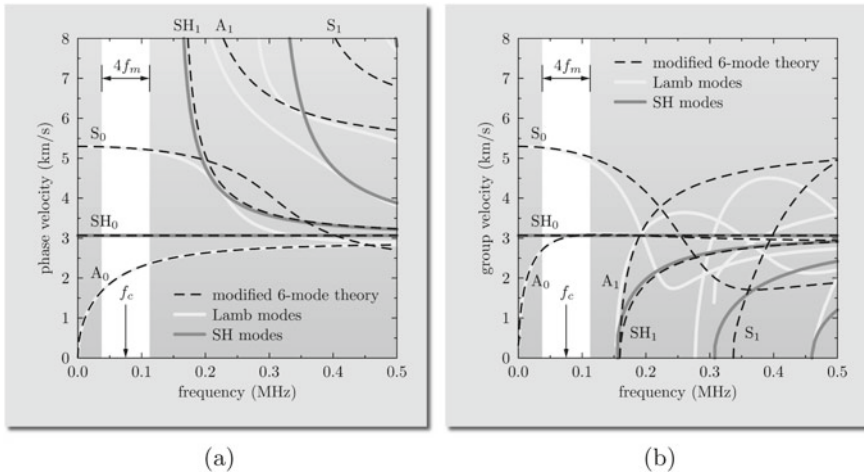


**Fig. 8.22** Dispersion curves for: **a** the phase velocity, **b** the group velocity, for modes of Lamb waves and SH-waves propagating in a 10 mm thick aluminium shell, according to the modified 6-mode 3-D theory of shells

In this case the central frequency of the excitation signal  $f_c$  was assumed as equal to 75 kHz, while the frequency of modulation  $f_m$  as equal to 18.75 kHz. Thus, the frequency content of the excitation covered frequencies from  $f_c - 2f_m = 37.5$  kHz up to  $f_c + 2f_m = 112.5$  kHz. The position of this frequency range against the dispersion curves for the phase velocity and the group velocity is illustrated in Fig. 8.22.

It can be clearly seen that within this frequency range only three fundamental modes exist: the symmetric  $S_0$  and  $SH_0$  as well as the antisymmetric  $A_0$ . As a result any conversion of modes that can take place for excitation signals from this frequency range is limited to three wave modes only. It can be also observed from Fig. 8.21 that the antisymmetric mode  $A_0$  of Lamb waves converts to the symmetric mode of Lamb waves  $S_0$  and vice versa, as well as that both these modes become a source of the symmetric mode of SH-waves  $SH_0$  while passing through structural discontinuities in the form of edges. At the same time it may be observed that the symmetric mode of SH-waves  $SH_0$  exhibits no conversion.

Another very important aspect of the analysis and investigation of shell structural elements is the way, in which their 3-D geometry is defined. Typically, there are three different coordinate systems, as presented in Fig. 8.23, which can be distinguished and used here:

- *Curvilinear/normalised coordinate system*  $(\xi, \eta, \zeta)$  is an orthogonal coordinate system, in which the 3-D geometry of a shell structural element is defined. This coordinate system may be local, in the case when it concerns a part of a shell structure such as is a single FE, or global, for the definition of shell structural elements such as pipes, domes, hemispheres, etc. The main advantage of the use

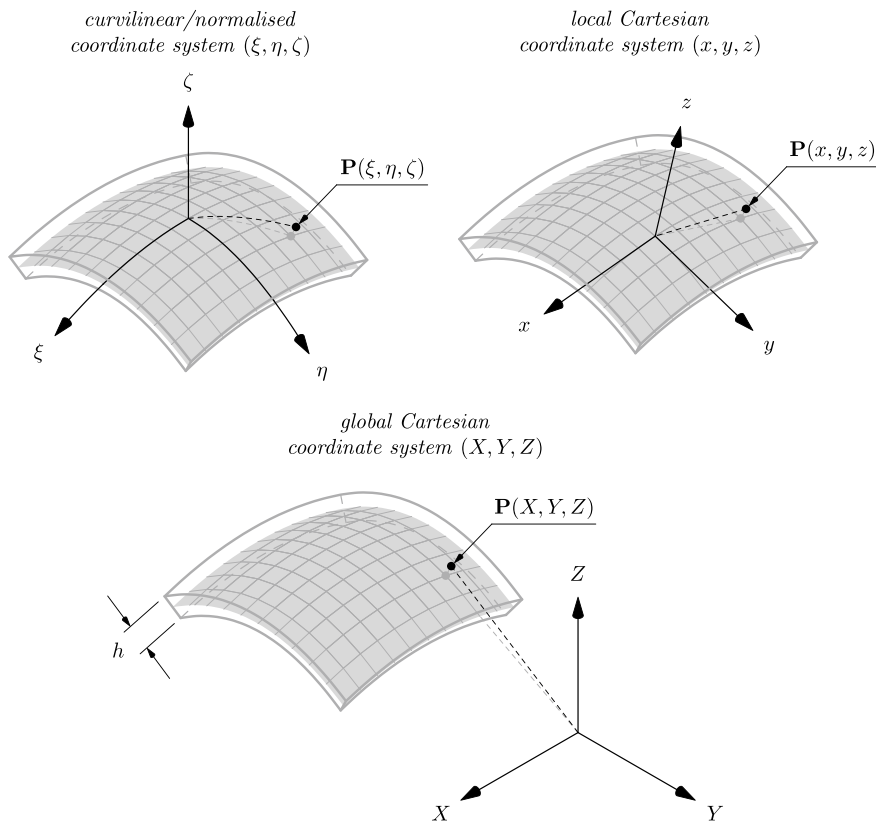


**Fig. 8.23** Different coordinate systems used in the analysis of a structural shell element

of the curvilinear coordinate system  $(\xi, \eta, \zeta)$  comes from the fact that for the definition of the 3-D geometry it uses the mid-plane defined quantities, i.e. defined in the  $\xi\eta$  plane, and the shell thickness. This effectively helps to reduce the dimensionality of the problem from 3-D to 2-D. In the curvilinear coordinate system shell structural elements are often represented by squares or rectangles of various dimensions.<sup>9</sup> Examples of curvilinear coordinate systems very often used in engineering and research practice can be the polar coordinate system in 2-D or the cylindrical coordinate system or the spherical coordinate system in 3-D.

<sup>9</sup> 1-D FEs are usually represented in FEM in the local curvilinear/normalised coordinates systems as sections of the non-dimensional length of 2, i.e.  $\xi \in \langle -1, +1 \rangle$ , 2-D plates and shell FEs as squares of the non-dimensional area of 4, i.e.  $\xi, \eta \in \langle -1, +1 \rangle$ , while 3-D FEs as cubes of the non-dimensional volume of 8, i.e.  $\xi, \eta, \zeta \in \langle -1, +1 \rangle$  [13].

- *Local Cartesian coordinate system*  $(x, y, z)$  is the Cartesian coordinate system defined locally, which can be associated with any point  $\mathbf{P}(x, y, z)$  located on the mid-plane representing the 3-D geometry of a shell structural element. It should be mentioned here that conventionally in FEM the orientation of the local Cartesian coordinate system  $(x, y, z)$  determines two mutually orthogonal directions tangential to the mid-plane  $x$  and  $y$  as well as one normal direction to the mid-plane  $z$ . Its use comes from the fact that the coupled in-plane and out-of-plane behaviour of shell structural elements is local in nature. A proper description of this feature requires an appropriate coordinate system, in which the values of local displacement, strain and stress components can be easily expressed and calculated. Moreover, in the case of plane shell structural elements (linear or plane elements in general) the local Cartesian coordinate system  $(x, y, z)$  is often interchangeably regarded and identified as the global Cartesian coordinate system  $(X, Y, Z)$ .
- *Global Cartesian coordinate system*  $(X, Y, Z)$  is also the Cartesian coordinate system, which is the absolute reference frame for other coordinate systems employed in the analysis of shell structural elements. This is the coordinate system, in which all requested information about the displacement, strain or stress fields are finally expressed and presented. It should be remembered, however, that depending on the types of problems and the 3-D nature of the geometry of shell structural elements also other coordinate systems are very frequently in use as global coordinate systems, instead of the Cartesian coordinate system. For example, in the case of spherical shells this can be the spherical coordinate system, while in the case of tubular shell structures the cylindrical coordinate system is used.

## References

1. A. Źak and M. Krawczuk. Assessment of rod behaviour theories used in spectral finite element modelling. *Journal of Sound and Vibration*, 329:2099–2113, 2010.
2. A. Źak and M. Krawczuk. Assessment of flexural beam behaviour theories used for dynamics and wave propagation problems. *Journal of Sound and Vibration*, 331:5715–5731, 2012.
3. A. E. Love. *A treatise on the mathematical theory of elasticity*. Cambridge: at the University Press, Cambridge, 1892.
4. A. Źak. A novel formulation of a spectral plate element for wave propagation in isotropic structures. *Finite Element in Analysis and Design*, 45:650–658, 2009.
5. N. Challamel and I. Elishakoff. A brief history of first-order shear-deformable beam and plate models. *Mechanics Research Communications*, 102:1–14, 2019.
6. A. Źak and M. Krawczuk. A higher order transversely deformable shell-type spectral finite element for dynamic analysis of isotropic structures. *Finite Elements in Analysis and Design*, 141:17–29, 2018.
7. W. Ostachowicz, P. Kudela, M. Krawczuk, and A. Źak. *Guided waves in structures for SHM. The time-domain spectral element method*. John Wiley & Sons Ltd., Singapore, 2012.
8. S. P. Timoshenko and S. Woinowsky-Krieger. *Theory of plates and shells*. McGraw-Hill Book Company, New York, 1959.
9. J. N. Reddy. A simple higher-order theory for laminated composite plates. *ASME Journal of Applied Mechanics*, 51:745–752, 1984.

10. J. D. Achenbach. *Wave propagation in elastic solids*. North-Holland Publishing Company, Amsterdam, 1973.
11. J. L. Rose. *Ultrasonic waves in solid media*. Cambridge University Press, Cambridge, 1999.
12. P. Wilcox. Modeling the excitation of Lamb and SH waves by point and line sources. *AIP Conference Proceedings*, 700:206–213, 2004.
13. O. C. Zienkiewicz. *The finite element method*. McGraw-Hill Book Company, London, 1989.

# Chapter 9

## Simplified Theories of 1-D Structural Elements



### 9.1 Longitudinal Behaviour of Rods

The general form of the displacement field associated with the longitudinal behaviour of rods can be expressed in an analogous manner to the in-plane behaviour of plates. In the cylindrical coordinate system  $(x, r, \theta)$  the displacement field takes the following form:

$$\begin{cases} u_x(x, \zeta, t) = \phi_0(x, t) + \sum_{n=1}^p (1 - \zeta^{2n})\phi_{2n}(x, t) \\ u_r(x, \zeta, t) = a\zeta\psi_1(x, t) + \sum_{n=1}^q a\zeta(1 - \zeta^{2n})\psi_{2n+1}(x, t) \end{cases} \quad (9.1)$$

with  $r = a\zeta$  and  $2a = d$ , where  $d$  denotes the diameter of the rod.

It should be emphasised that the form of the displacement field given by Eq. (9.1) fully conforms with the Maclaurin series expansion of the resulting form of the displacement field presented in Sect. 6.1 and expressed by Eqs. (6.11), (6.12) and (6.15).

As before  $p$  and  $q$  denote the numbers of terms kept in the series and related to the total number of independent variables, i.e. DOFs, of a given theory. Again, in order to minimise the modelling error it is recommended that the total number of terms kept in the case of the longitudinal displacement components  $u_x$  be equal to the number of terms kept in the case of the radial displacement component  $u_r$ . It should be also noted that now the independent variables, i.e. DOFs, are represented by the mid-axis displacement functions  $\phi_n$  and  $\psi_n$ .

In the cylindrical coordinate system  $(x, r, \theta)$  particular theories of the longitudinal behaviour of rods can be associated with different forms of Maclaurin series expansions of each component of the displacement fields  $u_x$  and  $u_r$ , and presented as:

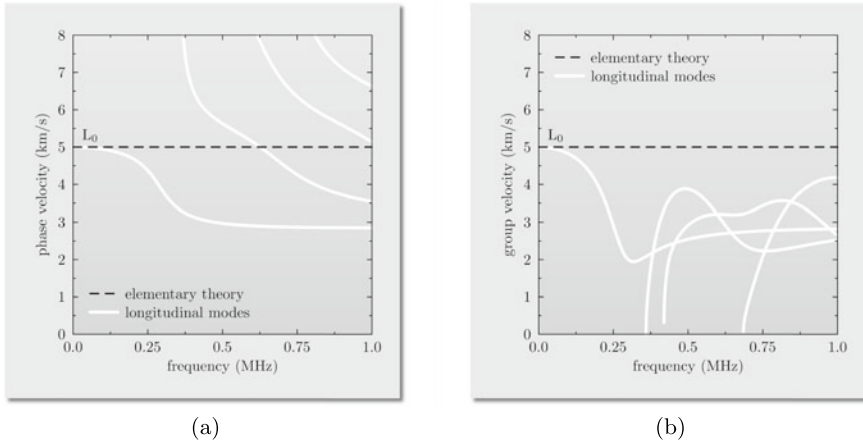


**Fig. 9.1** Dispersion curves for: **a** the phase velocity, **b** the group velocity, for longitudinal modes of elastic waves propagating in a 10 mm diameter aluminium bar, according to the 1-mode 1-D theory (elementary) of rods

- *1-mode 1-D theory (elementary):*

$$\begin{aligned}
 p = q = 0 \quad \text{and} \quad \psi_1(x, t) = 0 \\
 \downarrow \\
 u_x(x, \zeta, t) = \phi_0(x, t)
 \end{aligned}
 \tag{9.2}$$

for which the characteristic equation and its solution has the already known form of Eq. (2.47) or Eq. (2.49), which is formally presented below once more:

$$k^2 - \frac{\omega^2}{c_0^2} = 0
 \tag{9.3}$$

leading to the dispersion curves presented in Fig. 9.1, where  $c_0$  is the phase velocity of longitudinal waves related to the phase velocities of P-waves and S-waves in a 3-D elastic space by the following simple relationship:

$$c_0 = c_S \sqrt{\frac{3c_P^2 - 4c_S^2}{c_P^2 - c_S^2}} \quad \text{or} \quad c_0 = \sqrt{\frac{E}{\rho}}
 \tag{9.4}$$



- *Modified 1-mode 1-D theory (Love) [1]:*

$$\begin{aligned}
 p = q = 0 \quad \text{and} \quad \psi_1(x, t) = 0 \\
 \downarrow \\
 u_x(x, \zeta, t) = \phi_0(x, t)
 \end{aligned}
 \tag{9.5}$$

with the additional condition for the rate of the transverse thickness change  $\dot{\epsilon}_{rr} = -\nu\dot{\epsilon}_{xx}$  resulting from the Poisson effect and influencing the rod kinetic energy  $\mathcal{K}$  [1]:

$$\dot{u}_r(x, r, t) = -\nu \frac{\partial \dot{\phi}_0(x, t)}{\partial x} a \zeta
 \tag{9.6}$$

for which the characteristic equation can be easily obtained as:

$$k^2 - \frac{\omega^2}{c^2} = 0
 \tag{9.7}$$

leading to the dispersion curves presented in Fig. 9.2, where now  $c$  is the phase velocity defined as:

$$c = \sqrt{\frac{E}{(1 + \beta^2)\rho}}, \quad \text{with} \quad \beta = \frac{\nu}{2}ka
 \tag{9.8}$$

with  $2a = d$ , where  $d$  denotes the diameter of the rod.

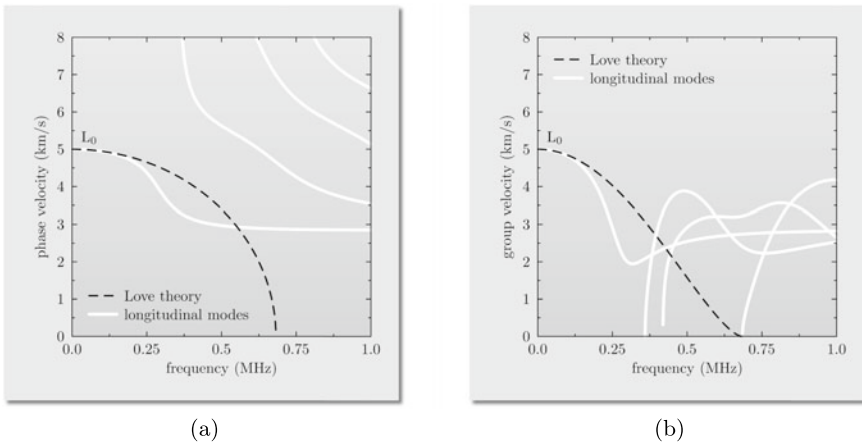


**Fig. 9.2** Dispersion curves for: **a** the phase velocity, **b** the group velocity, for longitudinal modes of elastic waves propagating in a 10 mm diameter aluminium bar, according to the modified 1-mode 1-D theory (Love) of rods

- 2-mode 2-D theory (Mindlin-Herrmann) [2]:

$$\begin{aligned}
 p = q = 0 \\
 \downarrow \\
 \begin{cases} u_x(x, \zeta, t) = \phi_0(x, t) \\ u_r(x, \zeta, t) = a\zeta\psi_1(x, t) \end{cases} \tag{9.9}
 \end{aligned}$$

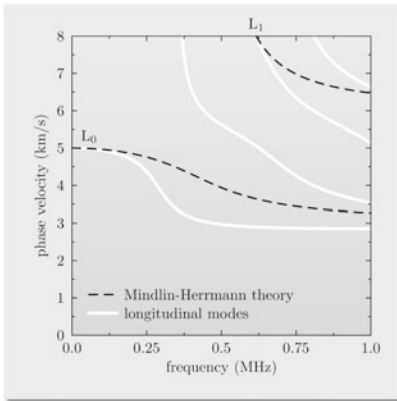
for which the characteristic equation is a 4th degree polynomial with respect to the wave number  $k$ :

$$\begin{aligned}
 k^2(24 + a^2k^2)c_P^2c_S^2 - (8 + a^2k^2)\omega^2c_P^2 + (8 - a^2k^2)\omega^2c_S^2 \\
 - 32k^2c_S^4 + a^2\omega^4 = 0 \tag{9.10}
 \end{aligned}$$

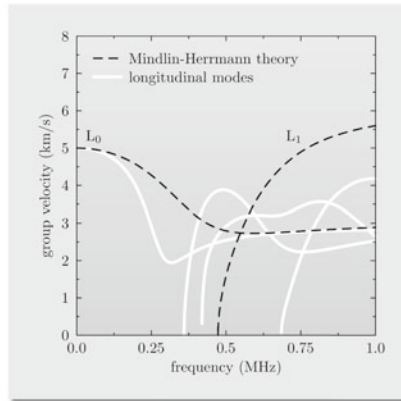
Its roots can be easily found numerically leading to the dispersion curves presented in Fig. 9.3.

- Higher-order 2-mode 2-D theory [3]:

$$\begin{aligned}
 p = q = 1 \\
 \downarrow \\
 \begin{cases} u_x(x, \zeta, t) = \phi_0(x, t) + (1 - \zeta^2)\phi_2(x, t) \\ u_r(x, \zeta, t) = a\zeta\psi_1(x, t) + a\zeta(1 - \zeta^2)\psi_3(x, t) \end{cases} \tag{9.11}
 \end{aligned}$$



(a)



(b)

**Fig. 9.3** Dispersion curves for: **a** the phase velocity, **b** the group velocity, for longitudinal modes of elastic waves propagating in a 10 mm diameter aluminium bar, according to the modified 2-mode 2-D theory (Mindlin-Herrmann) of rods

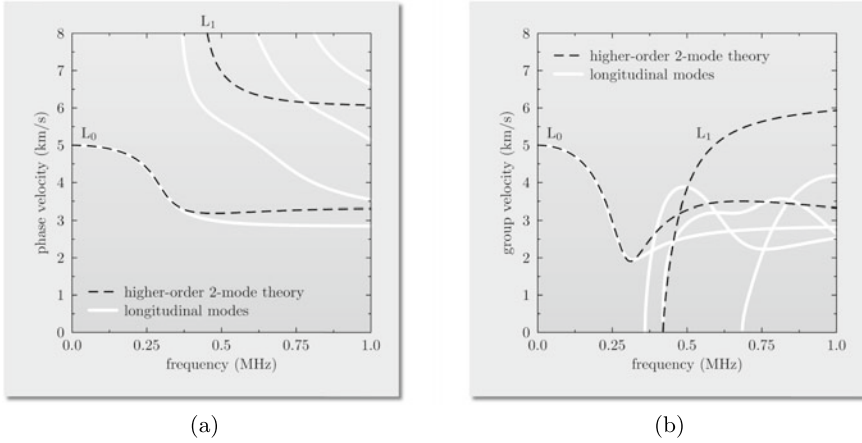


**Fig. 9.4** Dispersion curves for: **a** the phase velocity, **b** the group velocity, for longitudinal modes of elastic waves propagating in a 10 mm diameter aluminium bar, according to the higher-order 2-mode 2-D theory of rods

for which the characteristic equation is a 8th degree polynomial with respect to the wave number  $k$ . Its roots can be easily found numerically, which leads to the dispersion curves presented in Fig. 9.4. The additional assumptions for  $\phi_2$  and  $\psi_2$  are made resulting from the traction-free boundary conditions for the stress components  $\sigma_{rr}$  and  $\tau_{xr}$  leading to:

$$\begin{cases} 2\phi_2(x, t) = a^2 \frac{\partial \psi_1(x, t)}{\partial x} \\ 2\psi_3(x, t) = \frac{2(\lambda + \mu)}{\lambda + 2\mu} \psi_1(x, t) + \frac{\lambda}{\lambda + 2\mu} \frac{\partial \phi_0(x, t)}{dx} \end{cases} \quad (9.12)$$

- 4-mode 2-D theory [4]:

$$\begin{aligned} p = q = 1 \\ \downarrow \\ \begin{cases} u_x(x, \zeta, t) = \phi_0(x, t) + (1 - \zeta^2)\phi_2(x, t) \\ u_z(x, \zeta, t) = a\zeta\psi_1(x, t) + a\zeta(1 - \zeta^2)\psi_3(x, t) \end{cases} \end{aligned} \quad (9.13)$$

for which the characteristic equation also is a 8th degree polynomial with respect to the wave number  $k$ . Its roots can be easily found numerically, which leads to the dispersion curves presented in Fig. 9.5.

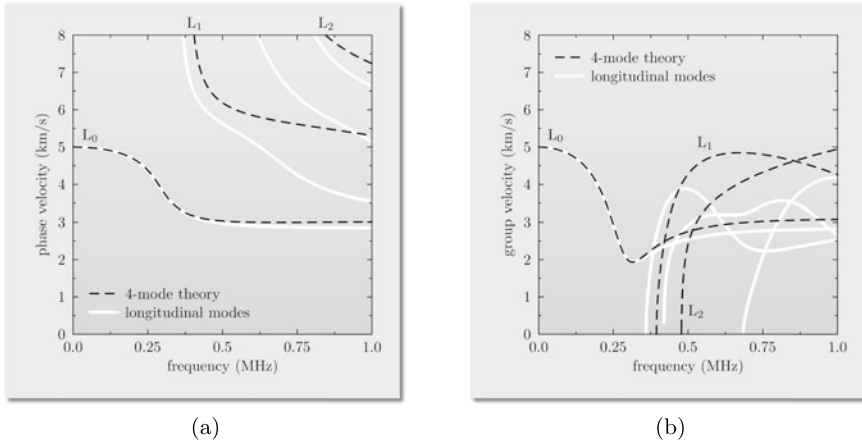


**Fig. 9.5** Dispersion curves for: **a** the phase velocity, **b** the group velocity, for longitudinal modes of elastic waves propagating in a 10 mm diameter aluminium bar, according to the 4-mode 2-D theory of rods

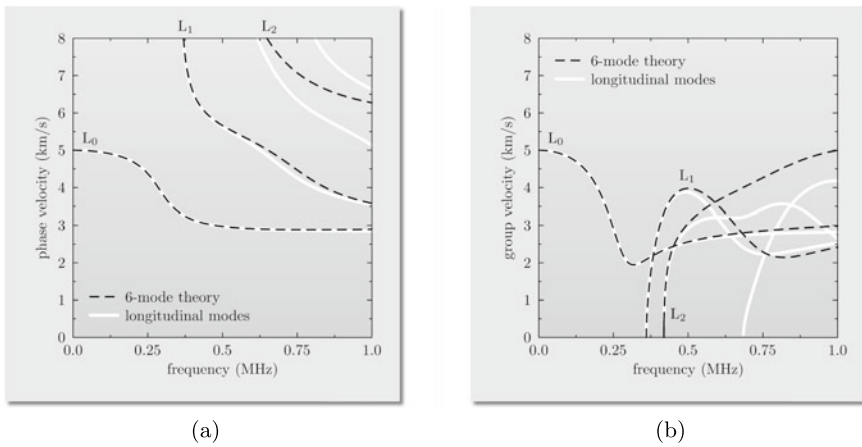


**Fig. 9.6** Dispersion curves for: **a** the phase velocity, **b** the group velocity, for longitudinal modes of elastic waves propagating in a 10 mm diameter aluminium bar, according to the 6-mode 2-D theory of rods

- 6-mode 2-D theory [5]:

$$\begin{aligned}
 & p = q = 2 \\
 & \quad \downarrow \\
 & \left\{ \begin{aligned} u_x(x, \zeta, t) &= \phi_0(x, t) + \sum_{n=1}^2 (1 - \zeta^{2n}) \phi_{2n}(x, t) \\ u_r(x, \zeta, t) &= a\zeta\psi_1(x, t) + \sum_{n=1}^2 a\zeta(1 - \zeta^{2n})\psi_{2n+1}(x, t) \end{aligned} \right. \quad (9.14)
 \end{aligned}$$

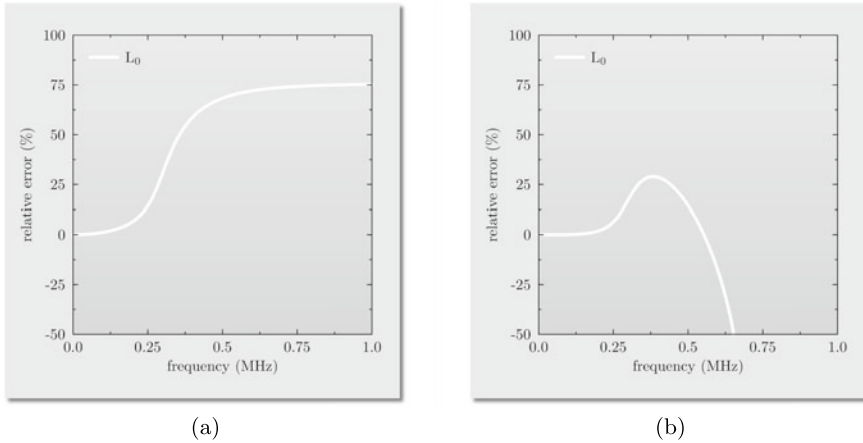
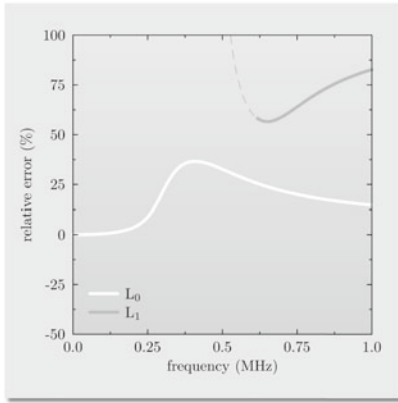


**Fig. 9.7** Relative error for: **a** the 1-mode 1-D theory (elementary), **b** the modified 1-mode 1-D theory (Love), of the longitudinal behaviour of rods measured against the analytical solution for longitudinal waves propagating in a 10 mm diameter aluminium bar

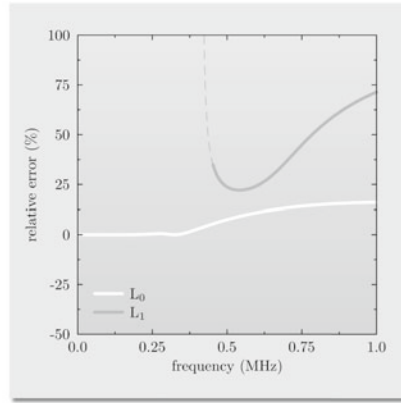
for which the characteristic equation also is a 12th degree polynomial with respect to the wave number  $k$ . Its roots can be easily found numerically, which leads to the dispersion curves presented in Fig. 9.6.

As previously, the same kind of analysis of the relative error of the phase velocity for particular 1-D and 2-D theories of the longitudinal behaviour of rods presented above was carried out here. The results concerning the 6 theories of the longitudinal behaviour of rods are presented in Figs. 9.7, 9.8 and 9.9 as relative error curves and a function of the cyclic frequency  $f$ . As before, for clarity of the presentation, the frequency range is limited to 1 MHz, which in the case of a 10 mm diameter aluminium bar is sufficient to incorporate 4 longitudinal modes.

The results shown in Fig. 9.7 concern the 1-mode 1-D theory (elementary) and the modified 1-mode 1-D theory (Love) of the longitudinal behaviour of rods. This is the simplest existing theory developed under a strong assumption of no transverse deformation during wave motion. This strong assumption significantly influences the accuracy of this 1-D theory, which obviously limits its application range due to the rapidly growing modelling error. In the case of the modified 1-mode 1-D theory (Love) the strong assumption of no transverse deformation is eased by taking into account the kinetic energy of the transverse wave motion due to the Poisson effect. Thanks to this the modelling error is initially smaller. For higher frequencies, however, predictions of this 1-D theory very fast diverge from the known analytical solution, as clearly seen in Fig. 9.7.

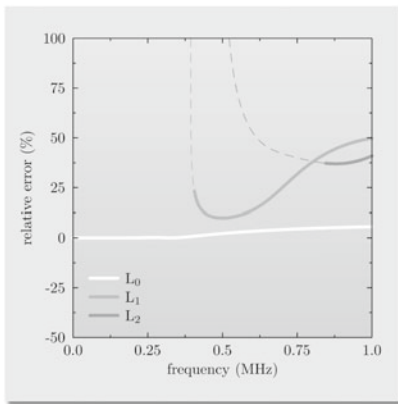


(a)

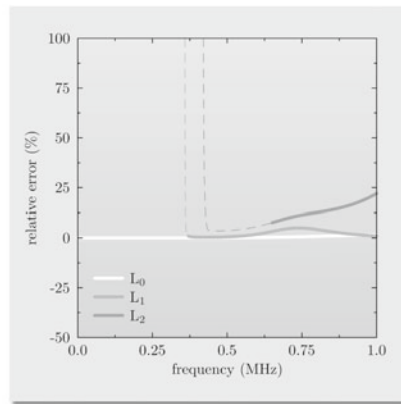


(b)

**Fig. 9.8** Relative error for: **a** the 2-mode 2-D theory (Mindlin-Herrmann), **b** the higher-order 2-mode 2-D theory, of the longitudinal behaviour of rods measured against the analytical solution for longitudinal waves propagating in a 10 mm diameter aluminium bar



(a)



(b)

**Fig. 9.9** Relative error for: **a** the 4-mode 2-D theory, **b** the 6-mode 2-D theory, of the longitudinal behaviour of rods measured against the analytical solution for longitudinal waves propagating in a 10 mm diameter aluminium bar

Quite surprisingly the enrichment of the 1-D theory by an extra mode, mode  $L_1$ , in the case of the 2-mode 2-D theory (Mindlin-Herrmann) has the opposite effect, as presented in Fig. 9.8. In this case the predictions of the enriched 2-D theory, based on the use of two modes of longitudinal waves, are initially worse in comparison with the predictions of the modified 1-mode 1-D theory (Love). At higher frequencies the situation slightly improves, but the level of modelling error remains unacceptable. This undesired behaviour can be improved, however, when the traction-free boundary

conditions are used enabling one to formulate the higher-order 2-mode 2-D theory. In this case the predictions of the fundamental mode  $L_0$  are then significantly improved. The prediction of the 2-D theory related to the behaviour of the second longitudinal mode  $L_1$ , however, is fairly poor. This is well illustrated in Fig. 9.8.

The low and mid frequency predictions can be further improved, in the frequency range up to the first cut-off frequency  $f_{L_1}$  of 359.5 kHz, when additional longitudinal modes are employed to further enrich the theories. This is clearly seen in Fig. 9.9 in the case of the 4-mode 2-D theory as well as the 6-mode 2-D theory. In both cases the predictions of the 2-D theories are significantly improved and for the 6-mode 2-D theory this improvement concerns the frequency range including the appearance of the second and third longitudinal modes  $L_1$  and  $L_2$ . This is despite the fact that both 2-D theories make no use of the traction-free boundary conditions. The multi-mode nature of the theories significantly increases their applicability making them suitable for problems involving moderately high frequency dynamics as well as propagation of elastic waves, yet at additional computational cost. This is related to the increased number of independent mid-axis displacement functions, i.e. DOFs, in comparison to other 1-D or 2-D theories under investigation.

As was mentioned before in the case of the symmetric and antisymmetric behaviour of plates, in practical applications concerning the analysis and investigation of the longitudinal behaviour of rods it is the fundamental longitudinal mode  $L_0$  that plays the most important role. For this reason it is much better to compare the investigated 1-D and 2-D theories, if the analysis of their accuracy is limited to this mode only, as well as within the frequency range up to the first cut-off frequency  $f_{L_1}$ , as presented and summarised in Table 9.1. In the current case of a 10 mm diameter aluminium bar the second longitudinal mode  $L_1$  appears at the frequency  $f_{L_1}$  of 359.5 Hz.

With no surprise it is clearly seen from Fig. 9.10 that for the simplest 1-mode 1-D and 2-D theories the fundamental longitudinal mode  $L_0$  is characterised by the relative error of the phase velocity, which grows very rapidly with an increase in the frequency. This is the case for the 1-mode 1-D theory (elementary), the modified

**Table 9.1** Statistical data on the relative modelling error associated with the phase velocity of the fundamental longitudinal mode  $L_0$  propagating in a 10 mm diameter aluminium bar in the frequency range up to the first cut-off frequency  $f_{L_1}$  of 359.5 kHz for various theories of the longitudinal behaviour of rods

Theory	Extr. error (%)	Avg. error (%)	Std. deviation (%)
Elementary 1-D	50.7	12.3	15.1
Love 1-D	28.1	6.22	8.88
Mindlin-Herrmann 2-D	34.0	8.02	10.5
Higher-order 2-mode 2-D	0.82	0.15	0.20
4-mode 2-D	0.21	0.05	0.07
6-mode 2-D	0.00	0.00	0.00

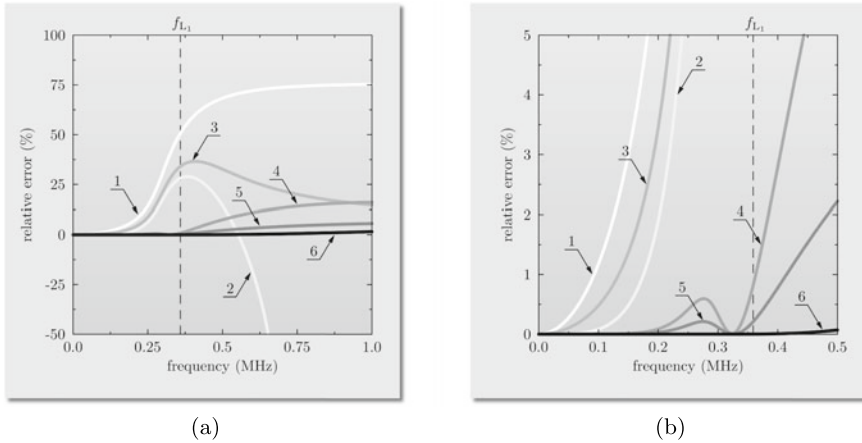


**Fig. 9.10** Relative error of the fundamental longitudinal mode  $L_0$  propagating in a 10 mm diameter aluminium bar: **a** full range, **b** magnified view, for various theories of the longitudinal behaviour of rods (1—elementary 1-D, 2—Love 1-D, 3—Mindlin-Herrman 2-D, 4—higher-order 2-modes 2-D, 5—4-mode 2-D, 6—6-mode 2-D)

1-mode 2-D theory (Love) as well as the 2-mode 2-D theory (Mindlin-Herrmann), which is characterised by a greater relative error than the modified 1-mode 1-D theory (Love). For these 3 theories the relative error reaches 5% at 182.0, 239.0 and 219.0 kHz, respectively. However, this is not observed in the case of the remaining 2-D theories: the higher-order 2-mode 2-D theory as well as the 4-mode 2-D theory and the 6-mode 2-D theory. For these theories the maximum value of the modelling error within the frequency range of interest is never higher than 0.85%. In the case of the higher-order 2-mode 2-D theory the relative error slowly increases and has a local maximum of 0.60% at 276.0 kHz. For higher frequencies, after an initial drop in its value, it further increases to reach 0.85%. For the 4-mode 2-D theory the relative error remains even smaller and after reaching its local maximum of 0.21% at 275.0 kHz the error decreases slightly to rise again to 0.21% at the cut-off frequency  $f_{L_1}$  of 359.5 kHz. The smallest values of the relative error are associated with the 6-mode 2-D theory, when the error within the whole range of interest is negligible.

As before the same recommendation can be made here, which confirms that although at higher computational cost due to the increased number of independent variables, i.e. DOFs, it is recommended to use the latter or other multi-mode or higher-order multi-mode 2-D theories to ensure high accuracy of numerical predictions, especially where high frequency dynamics is investigated.



## 9.2 Flexural Behaviour of Beams

The general form of the displacement field associated with the flexural behaviour of beams can be expressed in the cylindrical coordinate system  $(x, r, \theta)$  in the following way:

$$\begin{cases} u_x(x, \zeta, \theta, t) = \left[ a\zeta\phi_1(x, t) + \sum_{n=1}^p a\zeta(1 - \zeta^{2n})\phi_{2n+1}(x, t) \right] \cos \theta \\ u_r(x, \zeta, \theta, t) = \left[ \tilde{\psi}_0(x, t) + \sum_{n=1}^q (1 - \zeta^{2n})\psi_{2n}(x, t) \right] \cos \theta \\ u_\theta(x, \zeta, \theta, t) = \left[ \tilde{\theta}_0(x, t) + \sum_{n=1}^q (1 - \zeta^{2n})\theta_{2n}(x, t) \right] \sin \theta \end{cases} \quad (9.15)$$

where  $\tilde{\psi}_0$  and  $\tilde{\theta}_0$  are expressed as<sup>1</sup>:

$$\begin{cases} \tilde{\psi}_0(x, t) = \psi_0(x, t) - \sum_{n=1}^q \psi_{2n}(x, t) \\ \tilde{\theta}_0(x, t) = \theta_0(x, t) - \sum_{n=1}^q \theta_{2n}(x, t) \end{cases} \quad (9.16)$$

with  $r = a\zeta$  and  $2a = d$ , where  $d$  denotes the diameter of the beam.

Again, it should be noted that the form of the displacement field expressed by Eq. (9.15) fully conforms with the Maclaurin series expansion of the resulting form of the displacement field presented in Sect. 6.2 and expressed by Eqs. (6.28), (6.29) and (6.34).

In the same manner as before  $p$  and  $q$  denote the numbers of terms kept in the series and related to the total number of independent variables, i.e. DOFs, of a given theory. In order to minimise the modelling error it is recommended that the total number of terms kept in the case of the longitudinal displacement components  $u_x$  be equal to the number of terms kept in the case of the radial displacement component  $u_r$  and the angular displacement component  $u_\theta$ . As before it should be noted that the independent variables, i.e. DOFs, represent the mid-axis displacement functions  $\phi_n$ ,  $\psi_n$  and  $\theta_n$ .

In the cylindrical coordinate system  $(x, r, \theta)$  particular theories of the flexural behaviour of beams can be associated with different forms of Maclaurin series expansions of each component of the displacement fields  $u_x$ ,  $u_r$  and  $u_\theta$ , and presented as:

---

<sup>1</sup> The coupling between the mid-axis functions  $\tilde{\psi}_0$  and  $\tilde{\theta}_0$  results from the necessary condition for the vanishing of the displacement component  $u_z$  transverse to the bending plane, as well as the constant value of the displacement component  $u_y$  in the bending plane, when  $r \rightarrow 0$ . This condition leads to  $\psi_0 = \theta_0$ .

- Higher-order 1-mode 1-D theory (Euler-Bernoulli):

$$\begin{aligned}
 p &= q = 0 \\
 &\downarrow \\
 \begin{cases} u_x(x, \zeta, \theta, t) = a\zeta\phi_1(x, t) \cos \theta \\ u_r(x, \zeta, \theta, t) = \psi_0(x, t) \cos \theta \\ u_\theta(x, \zeta, \theta, t) = \psi_0(x, t) \sin \theta \end{cases} & \quad (9.17)
 \end{aligned}$$

where thanks to the additional assumption resulting from the traction-free boundary condition for the shear stress component  $\tau_{xr}$ , the mid-axis displacement functions  $\phi_1$  can be expressed as:

$$\phi_1(x, t) = -\frac{\partial\psi_0(x, t)}{\partial x} \quad (9.18)$$

where the characteristic equation takes the following simple form:

$$a^2k^4 - (4 + a^2k^2)\frac{\omega^2}{c_0^2} = 0 \quad (9.19)$$

leading to the dispersion curves presented in Fig. 9.11. The presence of the factor  $a^2k^2$  results from taking into account the higher-order terms of the transverse accelerations associated with the mid-axis function  $\phi_1$ . For very slender beams

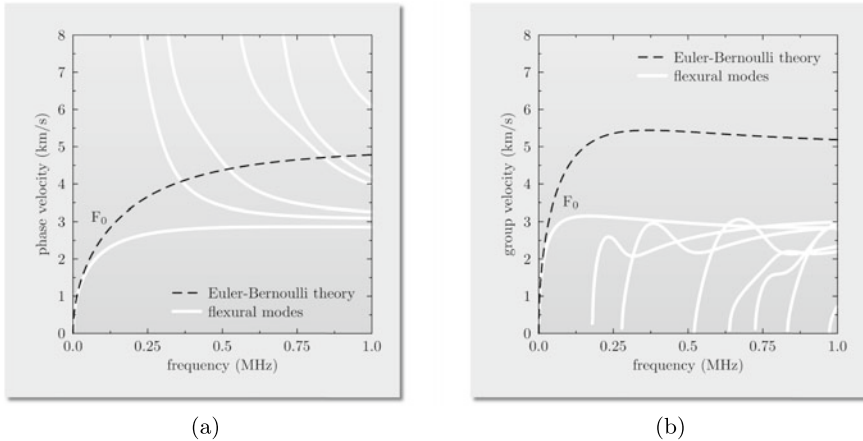


**Fig. 9.11** Dispersion curves for: **a** the phase velocity, **b** the group velocity, for flexural modes of elastic waves propagating in a 10 mm diameter aluminium bar, according to the higher-order 1-mode theory (Euler-Bernoulli) of beams

this higher-order term is usually neglected, which is equivalent to the assumption of  $a^2k^2 \approx 0$ , which leads to the characteristic equation in the form well-know from the literature [6].

- 2-mode 1-D theory (Timoshenko) [6]:

$$\begin{aligned}
 p &= q = 0 \\
 &\downarrow \\
 \begin{cases} u_x(x, \zeta, \theta, t) = a\zeta\phi_1(x, y, t) \cos \theta \\ u_r(x, \zeta, \theta, t) = \psi_0(x, y, t) \cos \theta \\ u_\theta(x, \zeta, \theta, t) = \psi_0(x, y, t) \sin \theta \end{cases} & \quad (9.20)
 \end{aligned}$$

where the characteristic equation takes the following simple form:

$$\left[ a^2k^4 - (4 + a^2k^2) \frac{\omega^2}{c_0^2} \right] \kappa\mu - \rho\omega^2 a^2 \left[ k^2 - \frac{\omega^2}{c_0^2} \right] = 0 \quad (9.21)$$

The roots of the characteristic equation can be easily found numerically, which leads to the dispersion curves presented in Fig. 9.12. Based on [7] the additional assumption about the value of the shear correction factor  $\kappa = 0.89$  is also made in this case.

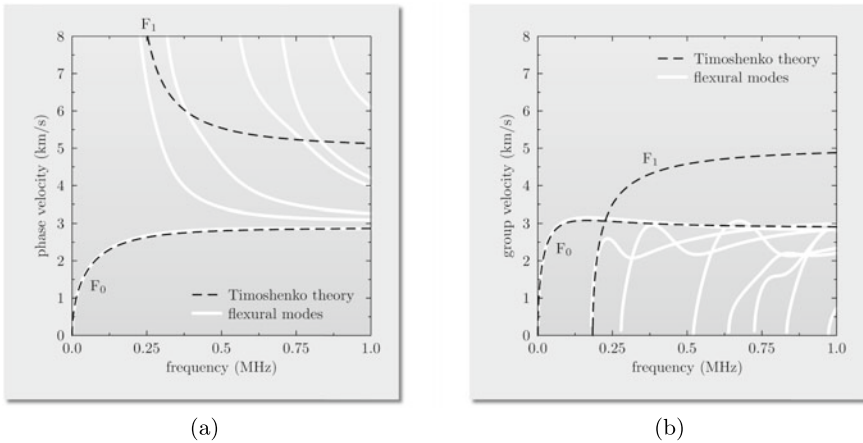


**Fig. 9.12** Dispersion curves for: **a** the phase velocity, **b** the group velocity, for flexural modes of elastic waves propagating in a 10 mm diameter aluminium bar, according to the 2-mode 1-D theory (Timoshenko) of beams

- *modified 2-mode 1-D theory*:

$$\begin{aligned}
 p &= q = 0 \\
 &\downarrow \\
 \begin{cases} u_x(x, \zeta, \theta, t) = a\zeta\phi_1(x, y, t) \cos \theta \\ u_r(x, \zeta, \theta, t) = \psi_0(x, y, t) \cos \theta \\ u_\theta(x, \zeta, \theta, t) = \psi_0(x, y, t) \sin \theta \end{cases} & \quad (9.22)
 \end{aligned}$$

for which the characteristic equation also is a 4th degree polynomial with respect to the wave number  $k$ . Its roots can be easily found numerically, which leads to the dispersion curves presented in Fig. 9.13. Based on [7, 8] the additional assumption about the distribution of the shear stresses is made using the correction function  $f(\zeta) = \alpha(1 - \zeta^2)$  with  $\alpha = 2.1\kappa$ , which is incorporated within the matrix of elastic coefficients at the positions corresponding to the stress components  $\tau_{xr}$  and  $\tau_{r\theta}$ .

- *Higher-order 2-mode 1-D theory (Reddy) [9]*:

$$\begin{aligned}
 p &= 1, \quad q = 0 \\
 &\downarrow \\
 \begin{cases} u_x(x, \zeta, \theta, t) = [a\zeta\phi_1(x, t) + a\zeta(1 - \zeta^2)\phi_3(x, t)] \cos \theta \\ u_r(x, \zeta, \theta, t) = \psi_0(x, t) \cos \theta \\ u_\theta(x, \zeta, \theta, t) = \psi_0(x, t) \sin \theta \end{cases} & \quad (9.23)
 \end{aligned}$$

where the additional assumptions for  $\phi_3$  is made, resulting from the traction-free boundary conditions for the stress components  $\tau_{xr}$ :

$$2\phi_3(x, t) = \phi_1(x, t) + \frac{\partial\psi_0(x, t)}{\partial x} \quad (9.24)$$

leading to the characteristic equation, which is now a 6th degree polynomial with respect to the wave number  $k$ . Its roots can be easily found numerically, which leads to the dispersion curves presented in Fig. 9.14.

- *Higher-order 2-mode 3-D theory [10]*:

$$\begin{aligned}
 p &= q = 1 \\
 &\downarrow \\
 \begin{cases} u_x(x, \zeta, \theta, t) = [a\zeta\phi_1(x, t) + a\zeta(1 - \zeta^2)\phi_3(x, t)] \cos \theta \\ u_r(x, \zeta, \theta, t) = [\tilde{\psi}_0(x, t) + (1 - \zeta^2)\psi_2(x, t)] \cos \theta \\ u_\theta(x, \zeta, \theta, t) = [\tilde{\theta}_0(x, t) + (1 - \zeta^2)\theta_2(x, t)] \sin \theta \end{cases} & \quad (9.25)
 \end{aligned}$$

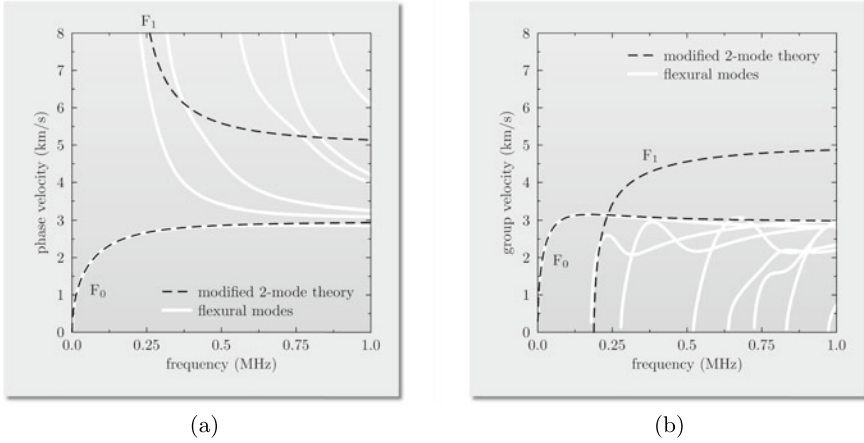


**Fig. 9.13** Dispersion curves for: **a** the phase velocity, **b** the group velocity, for flexural modes of elastic waves propagating in a 10 mm diameter aluminium bar, according to the modified 2-mode 1-D theory of beams

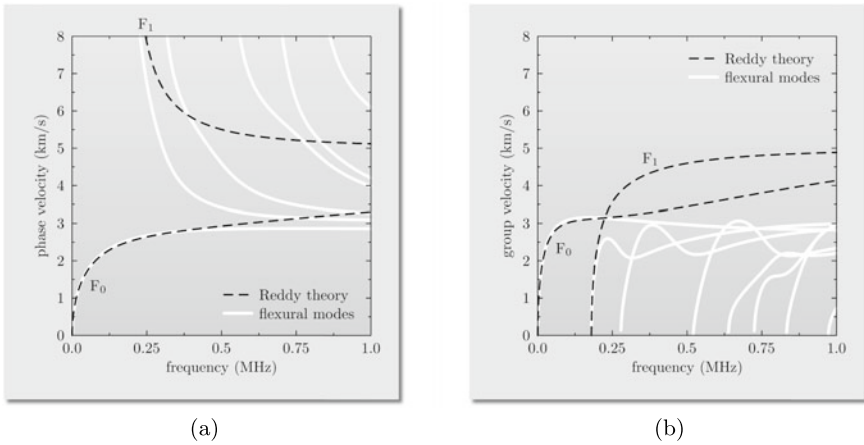


**Fig. 9.14** Dispersion curves for: **a** the phase velocity, **b** the group velocity, for flexural modes of elastic waves propagating in a 10 mm diameter aluminium bar, according to the higher-order 2-mode 1-D theory (Reddy) of beams

where  $\tilde{\psi}_0$  and  $\tilde{\theta}_0$  are expressed as:

$$\begin{cases} \tilde{\psi}_0(x, t) = \psi_0(x, t) - \psi_{2n}(x, t) \\ \tilde{\theta}_0(x, t) = \theta_0(x, t) - \theta_{2n}(x, t) \end{cases} \quad (9.26)$$

for which the characteristic equation is now a 10th degree polynomial with respect to the wave number  $k$ . Its roots can be easily found numerically, which leads to

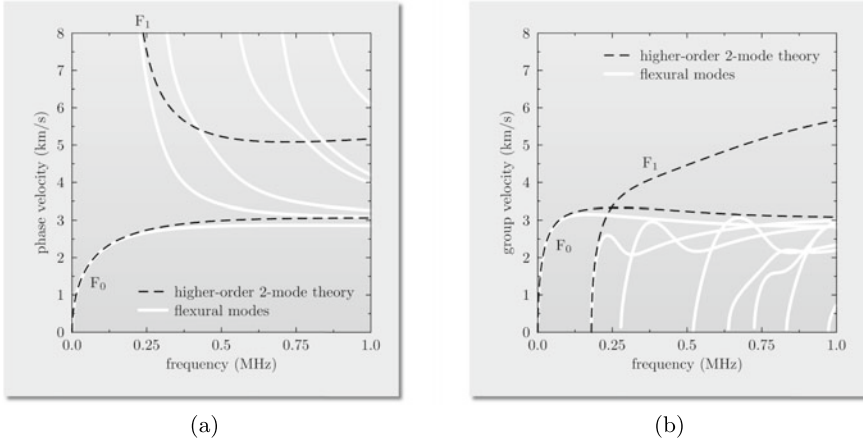


**Fig. 9.15** Dispersion curves for: **a** the phase velocity, **b** the group velocity, for flexural modes of elastic waves propagating in a 10 mm diameter aluminium bar, according to the higher-order 2-mode 3-D theory of beams

the dispersion curves presented in Fig. 9.15. The additional assumptions for  $\phi_3$ ,  $\psi_2$  and  $\theta_2$  are made, resulting from the traction-free boundary conditions for the stress components  $\sigma_{rr}$ ,  $\tau_{xr}$  and  $\tau_{r\theta}$ , leading to:

$$\begin{cases} 2\phi_3(x, t) = \phi_1(x, t) + \frac{\partial\psi_0(x, t)}{\partial x} - \frac{\partial\psi_2(x, t)}{\partial x} \\ 4\psi_2(x, t) = a^2 \frac{\lambda}{\lambda + \mu} \frac{\partial\phi_1(x, t)}{\partial x} \\ \theta_2(x, t) = -\psi_2(x, t) \end{cases} \quad (9.27)$$

- 5-mode 3-D theory [10]:

$$\begin{aligned} p = q = 1 \\ \downarrow \\ \begin{cases} u_x(x, \zeta, \theta, t) = [a\zeta\phi_1(x, t) + a\zeta(1 - \zeta^2)\phi_3(x, t)] \cos \theta \\ u_r(x, \zeta, \theta, t) = [\tilde{\psi}_0(x, t) + (1 - \zeta^2)\psi_2(x, t)] \cos \theta \\ u_\theta(x, \zeta, \theta, t) = [\tilde{\theta}_0(x, t) + (1 - \zeta^2)\theta_2(x, t)] \sin \theta \end{cases} \quad (9.28) \end{aligned}$$

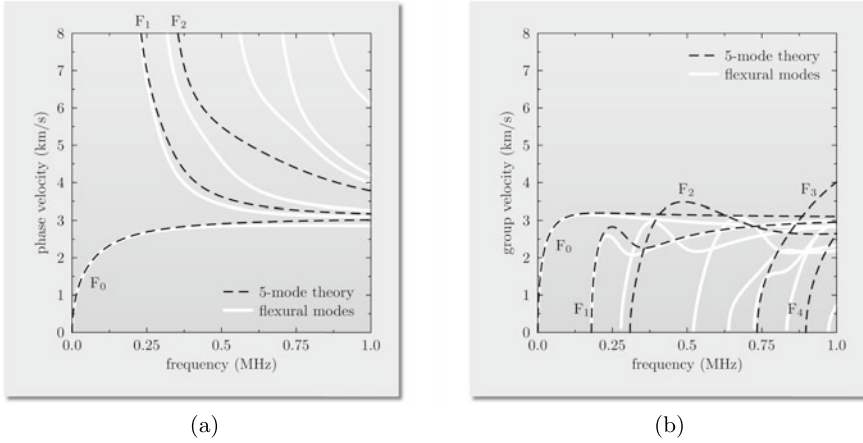


**Fig. 9.16** Dispersion curves for: **a** the phase velocity, **b** the group velocity, for flexural modes of elastic waves propagating in a 10 mm diameter aluminium bar, according to the 5-mode 3-D theory of beams

where  $\tilde{\psi}_0$  and  $\tilde{\theta}_0$  are expressed in the same manner as before:

$$\begin{cases} \tilde{\psi}_0(x, t) = \psi_0(x, t) - \psi_{2n}(x, t) \\ \tilde{\theta}_0(x, t) = \psi_0(x, t) - \theta_{2n}(x, t) \end{cases} \quad (9.29)$$

for which the characteristic equation is now a 10th degree polynomial with respect to the wave number  $k$ . Its roots can be easily found numerically, which leads to the dispersion curves presented in Fig. 9.16.

The same analysis of the relative error of the phase velocity for particular 1-D and 3-D theories of the flexural behaviour of beams presented above can be carried out. The results concerning the 6 theories of the flexural behaviour of beams are presented in Figs. 9.17, 9.18 and 9.19 as relative error curves and a function of the cyclic frequency  $f$ . For clarity of presentation the frequency range is limited to 1 MHz, which in the case of a 10 mm diameter aluminium bar is sufficient to incorporate as many as 6 flexural modes in the dispersion curves for the phase velocity and 8 flexural modes in the dispersion curves for the group velocity.

The results shown in Fig. 9.11 concern the higher-order 1-mode 1-D theory (Euler-Bernoulli) and the 2-mode 1-D theory (Timoshenko) of the flexural behaviour of beams. This is the simplest existing theory developed under a strong assumption of no shear deformation during wave motion. Again, this strong assumption significantly influences the accuracy of this 1-D theory, which obviously limits its application range to statics or low frequency dynamics due to the rapidly growing modelling error, while in the case of the 2-mode 1-D theory (Timoshenko) no assumptions are made except the one about adjusting the distribution of the shear stresses by the use of the so-called shear correction factor  $\kappa$ . Thanks to this simple adjustment

the modelling error for the fundamental flexural mode  $F_0$  is very small in the entire frequency range of interest. However, this is not the case for the second flexural mode  $F_1$  except near its cut-off frequency, as clearly seen in Fig. 9.17. As a result the 2-mode 1-D theory (Timoshenko) has its application range extended only to mid frequency dynamics for frequencies up to the second flexural mode  $F_1$ .

Quite surprisingly the correction of the distribution of the shear stresses by the use of the correction function  $f(\zeta) = \alpha(1 - \zeta^2)$ , with  $\alpha = 2.1\kappa$ , in the case of the modified 2-mode 1-D theory has a strong effect and significantly increases the accuracy of this theory at higher frequencies well below the appearance of the second flexural mode  $F_1$ , as shown in Fig. 9.18. However, this takes place only for the fundamental flexural mode  $F_0$  and as a result the modified 2-mode theory, similarly to the 2-mode 1-D theory (Timoshenko) appears as suitable only for problems involving mid frequency dynamics for frequencies up to the second flexural mode  $F_1$ .

The enrichment of the 1-D theory proposed by the higher-order 2-mode 1-D theory (Reddy) is based on the use of the traction-free boundary conditions for the distribution of the shear stresses only. However, this enrichment has no significant effect on the accuracy of the predictions offered by this 1-D theory in comparison with a much simpler 2-mode 1-D theory (Timoshenko), as presented in Fig. 9.18. The higher-order 2-mode 1-D theory slightly underestimates the values of the calculated phase velocities, but its accuracy stays relatively high for the fundamental flexural mode  $F_0$  up to the frequencies near the cut-off frequency of the second flexural mode  $F_1$ . As a consequence its application range stays similar to the 2-mode 1-D theory (Timoshenko).

This undesired behaviour is slightly improved in the case of the higher-order 2-mode 3-D theory, which makes use of all available traction-free boundary conditions,

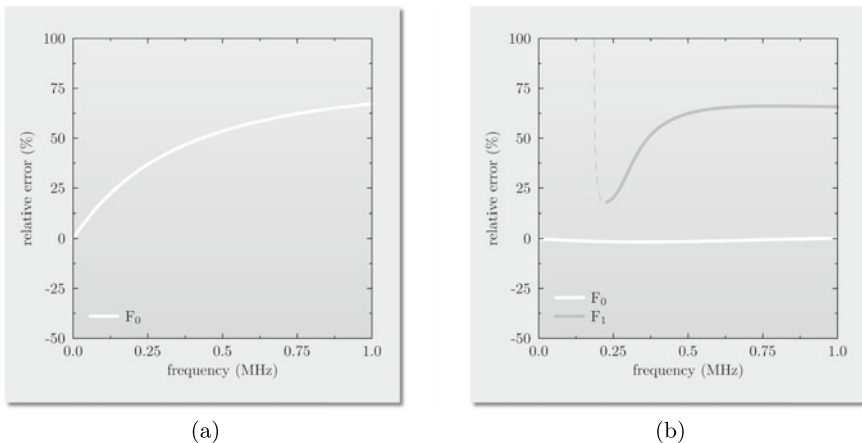


**Fig. 9.17** Relative error for: **a** the higher-order 1-mode 1-D theory (Euler-Bernoulli), **b** the 2-mode 1-D theory (Timoshenko), of the flexural behaviour of beams measured against the analytical solution for flexural waves propagating in a 10 mm diameter aluminium bar



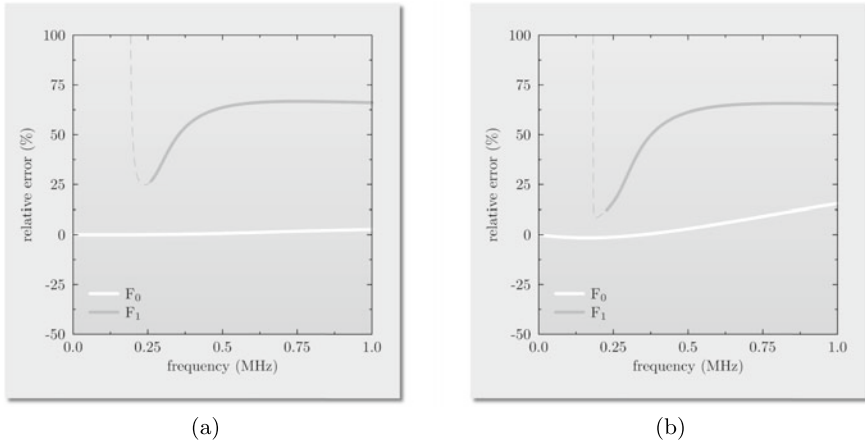


**Fig. 9.18** Relative error for: **a** the modified 2-mode 1-D theory, **b** the higher-order 2-mode 1-D theory (Reddy), of the flexural behaviour of beams measured against the analytical solution for flexural waves propagating in a 10 mm diameter aluminium bar

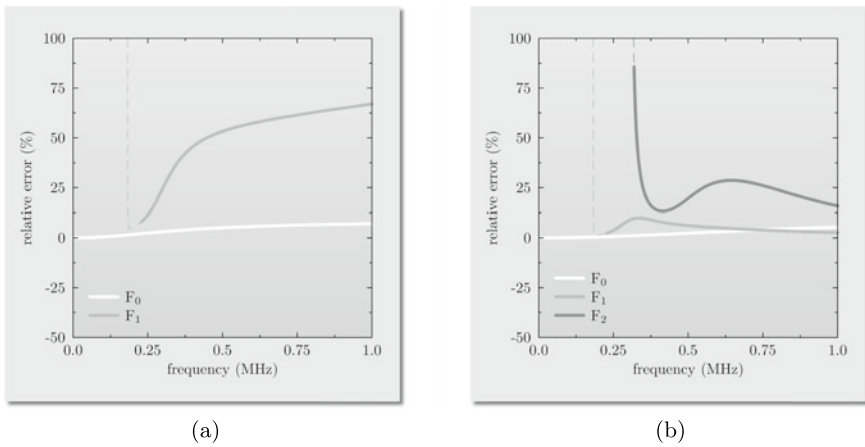


**Fig. 9.19** Relative error for: **a** the higher-order 2-mode 3-D theory, **b** the 5-mode 3-D theory, of the flexural behaviour of beams measured against the analytical solution for flexural waves propagating in a 10 mm diameter aluminium bar

as seen in Fig. 9.19. Despite this improvement the predictions offered by this 3-D theory are not significantly improved, especially for the frequencies near the cut-off frequency of the second flexural mode  $F_1$  and higher. For this reason also this 3-D theory has its application range limited to mid frequency dynamics up to the second flexural mode  $F_1$ .

It is interesting to note that the application of the traction-free boundary conditions in the case of 1-D and 3-D higher-order theories of the flexural behaviour of beams

has no significant effect on the quality and accuracy of the predictions concerning the second flexural mode  $F_1$ . This fact limits their application range just to the frequencies near the cut-off frequency of the second flexural mode  $F_1$ . As clearly seen from Fig. 9.19 presenting dispersion curves in the case of the 5-mode 3-D theory, only the enrichment of the 3-D theory by additional modes, not necessarily supported by the use of the traction-free boundary conditions, substantially enhances the applicability of the given theory.

In the case of the 5-mode 3-D theory this application range is enhanced well above the second flexural mode  $F_1$ , however the accuracy of the predictions offered by the theory in this frequency range are characterised by higher errors. It should be remembered that although the multi-mode nature of the 5-mode 3-D theory substantially increases its applicability making it suitable for problems involving moderately high frequency dynamics as well as propagation of elastic waves, yet at additional computational cost. This is related to the increased number of independent mid-axis displacement variables (degrees of freedom) in comparison to other 1-D and 3-D theories under investigation.

For the reasons discussed previously, in practical applications concerning the analysis and investigation of the flexural behaviour of beams it is the fundamental flexural mode  $F_0$  that plays the most important role. For this reason the investigated theories can be compared based on the analysis of their accuracy limited to this mode only, as well as within the frequency range up to the first cut-off frequency  $f_{F_1}$ , as presented and summarised in Table 9.2. In the current case of a 10 mm diameter aluminium bar the second longitudinal mode  $F_1$  appears at the frequency  $f_{F_1}$  of 179.7 Hz.

With no surprise it is clearly seen from Fig. 9.20 that for the simplest higher-order 1-mode 1-D theory (Euler-Bernoulli) the fundamental longitudinal mode  $F_0$  is characterised by the relative error of the phase velocity, which grows very rapidly with an increase in the frequency. For this 1-D theory the relative error reaches 5% at 23.0 kHz. However, this is not observed in the case of the second 1-D theory, which is the 2-mode 1-D theory (Timoshenko). In the case of this theory the relative

**Table 9.2** Statistical data on the relative modelling error associated with the phase velocity of the fundamental flexural mode  $F_0$  propagating in a 10 mm diameter aluminium bar in the frequency range up to the first cut-off frequency  $f_{F_1}$  of 179.7 kHz for various theories of the flexural behaviour of beams

Theory	Extr. error (%)	Avg. error (%)	Std. deviation (%)
Euler-Bernoulli 1-D	29.3	16.2	8.49
Timoshenko 1-D	-1.35	-0.77	0.40
Modified 2-mode 1-D	-0.01	0.00	0.04
Reddy 1-D	-1.53	-1.07	0.46
Higher-order 2-mode 3-D	1.46	0.53	0.45
5-mode 3-D	0.40	0.14	0.12

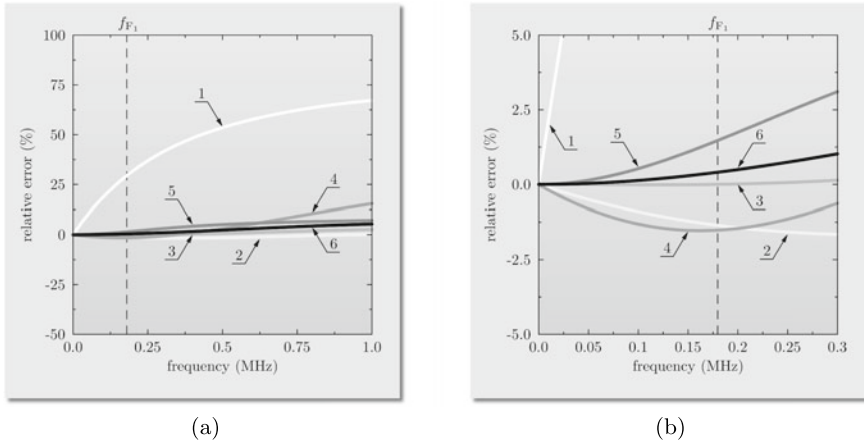


**Fig. 9.20** Relative error of the fundamental flexural mode  $F_0$  propagating in a 10 mm diameter aluminium bar: **a** full range, **b** magnified view, for various theories of the flexural behaviour of bars (1—Euler-Bernoulli 1-D, 2—Timoshenko 1-D, 3—modified 2-mode 1-D, 4—Reddy 1-D, 5—higher-order 2-mode 3-D, 6—5-mode 3-D)

error of the phase velocity stays small and negative and its extreme value never exceeds 5%, reaching only  $-1.35\%$ . This is not the case for the modified 2-mode 1-D theory, for which the relative error drops significantly and stays negligible, reaching only  $-0.01\%$  at the first cut-off frequency. The remaining 1-D and 3-D theories are characterised by small, but still higher values of the errors in comparison with the modified 2-mode 1-D theory in the frequency range of interest. In the case of the higher-order 2-mode 1-D theory (Reddy) the error also remains small and negative to take its extreme value of  $-1.53\%$  at 163 kHz. The situation is only slightly improved in the case of the higher-order 2-mode 3-D theory, for which the maximum value of the error also never exceeds 5%, never reaching 1.46% at the first cut-off frequency. Finally, even a smaller value of the relative error of the phase velocity is observed in the case of the richest theory based on 5 independent wave modes, i.e. 5 independent mid-axis variables, i.e. DOFs. For the 5-mode 3-D theory the maximum value of the relative error stays well below 5% for the frequencies up to the first cut-off frequency, reaching its maximum value of 0.4%.

The same recommendation can be made here, that although at higher computational cost due to the increased number of independent variables, i.e. DOFs, it is recommended to use the latter or other multi-mode or higher-order multi-mode 3-D theories to ensure high accuracy of numerical predictions, especially where high frequency dynamics or wave propagation problems are investigated.

### 9.3 Torsional Behaviour of Shafts

In the cylindrical coordinate system  $(x, r, \theta)$  the general form of the displacement field associated with the torsional behaviour of shafts may be expressed in the following way:

$$u_\theta(x, \zeta, t) = a\zeta\theta_1(x, t) + \sum_{n=1}^q a\zeta(1 - \zeta^{2n})\theta_{2n+1}(x, t) \quad (9.30)$$

with  $r = a\zeta$  and  $2a = d$ , where  $d$  denotes the diameter of the shaft.

The form of the displacement field given by Eq. (9.30) fully conforms with the Maclaurin series expansion of the resulting form of the displacement field presented in Sect. 6.3 and expressed by Eq. (6.4).

As before  $q$  is the number of terms kept in the series and related to the total number of independent variables, i.e. DOFs, of a given theory. It should be also noted that now the independent variables, i.e. DOFs, represent the mid-axis displacement functions  $\theta_n$ .

In the cylindrical coordinate system  $(x, r, \theta)$  particular theories of the torsional behaviour of shafts can be associated with different forms of Maclaurin series expansions of the sole non-zero component of the displacement field  $u_\theta$  and presented as:

- *1-mode 1-D theory:*

$$\begin{aligned} q &= 0 \\ &\downarrow \\ u_\theta(x, \zeta, t) &= a\zeta\theta_0(x, t) \end{aligned} \quad (9.31)$$

for which the characteristic equation and its solution has the already known form of Eq. (2.47). However, this time propagation of torsional waves is associated with the phase velocity of S-waves  $c_S$  rather than than the phase velocity of longitudinal waves  $c_0$ :

$$k^2 - \frac{\omega^2}{c_S^2} = 0 \quad (9.32)$$

which leads to the dispersion curves presented in Fig. 9.21.

- *2-mode 1-D theory:*

$$\begin{aligned} q &= 1 \\ &\downarrow \\ u_\theta(x, \zeta, t) &= a\zeta\theta_1(x, t) + a\zeta(1 - \zeta^2)\theta_3(x, t) \end{aligned} \quad (9.33)$$

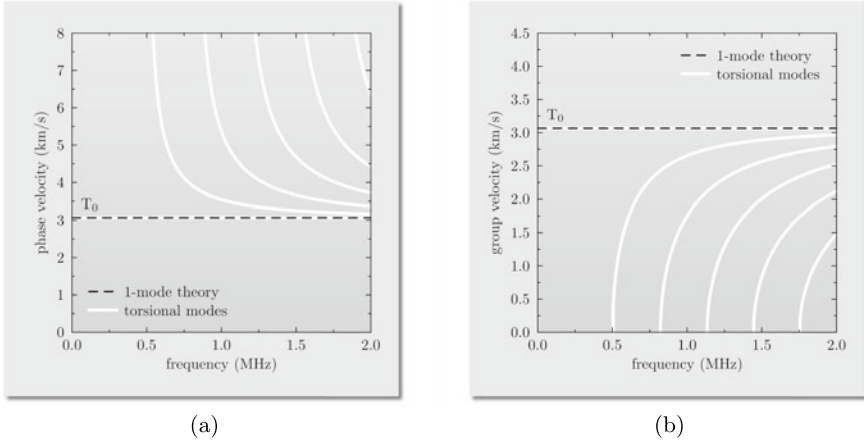


**Fig. 9.21** Dispersion curves for: **a** the phase velocity, **b** the group velocity, for torsional modes of elastic waves propagating in a 10 mm diameter aluminium bar, according to the 1-mode 1-D theory of shafts

where the characteristic equation takes the following simple form:

$$\left[ (48 + a^2k^2) - a^2 \frac{\omega^2}{c_s^2} \right] \left[ k^2 - \frac{\omega^2}{c_s^2} \right] = 0 \tag{9.34}$$

where solutions of the characteristic equation can be indicated:

$$c = c_s \quad \text{and} \quad c = c_s \sqrt{1 + \frac{48}{a^2k^2}} \tag{9.35}$$

leading to the dispersion curves presented in Fig. 9.22.

- Higher-order 2-mode 1-D theory:

$$\begin{aligned}
 & q = 2 \\
 & \quad \downarrow \\
 & u_\theta(x, \zeta, t) = a\zeta\theta_1(x, t) + \sum_{n=1}^2 a\zeta(1 - \zeta^{2n})\theta_{2n+1}(x, t)
 \end{aligned} \tag{9.36}$$

where the additional assumption for  $\theta_5$  is made, resulting from the traction-free boundary condition for the stress components  $\tau_{r\theta}$ , leading to:

$$2\theta_5(x, t) = -\theta_3(x, t) \tag{9.37}$$

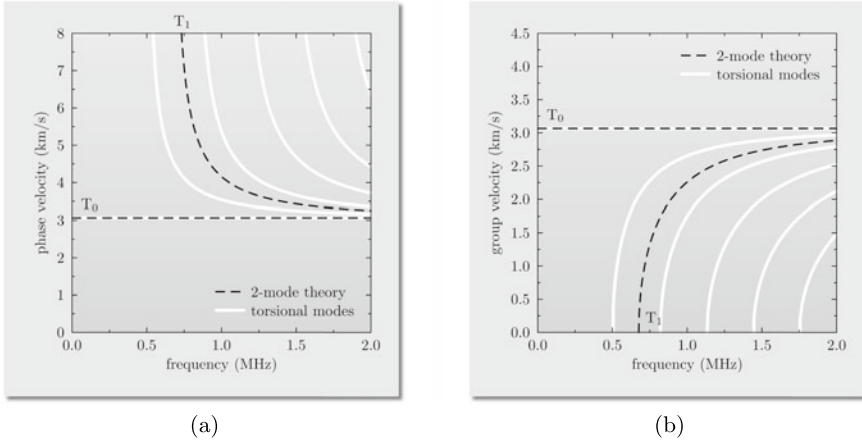


**Fig. 9.22** Dispersion curves for: **a** the phase velocity, **b** the group velocity, for torsional modes of elastic waves propagating in a 10 mm diameter aluminium bar, according to the 2-mode 1-D theory of shafts

where the characteristic equation takes the following simple form:

$$\left[ (192 + 7a^2k^2) - 7a^2\frac{\omega^2}{c_s^2} \right] \left[ k^2 - \frac{\omega^2}{c_s^2} \right] = 0 \tag{9.38}$$

where solutions of the characteristic equation can be indicated:

$$c = c_s \quad \text{and} \quad c = c_s \sqrt{1 + \frac{192}{7a^2k^2}} \tag{9.39}$$

leading to the dispersion curves presented in Fig. 9.23.

- *3-mode 1-D theory:*

$$\begin{aligned}
 q &= 2 \\
 &\downarrow \\
 u_\theta(x, \zeta, t) &= a\zeta\theta_1(x, t) + \sum_{n=1}^2 a\zeta(1 - \zeta^{2n})\theta_{2n+1}(x, t)
 \end{aligned} \tag{9.40}$$

where the characteristic equation is a 6th degree polynomial with respect to the wave number  $k$  and can be presented in the following form:

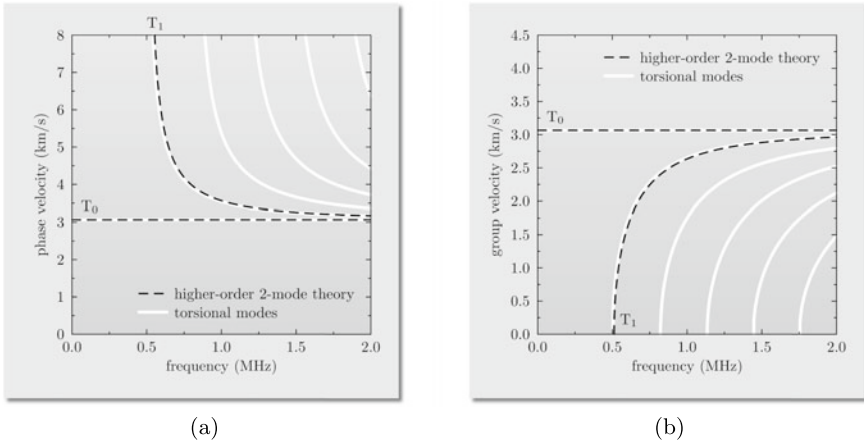


**Fig. 9.23** Dispersion curves for: **a** the phase velocity, **b** the group velocity, for torsional modes of elastic waves propagating in a 10 mm diameter aluminium bar, according to the higher-order 2-mode 1-D theory of shafts

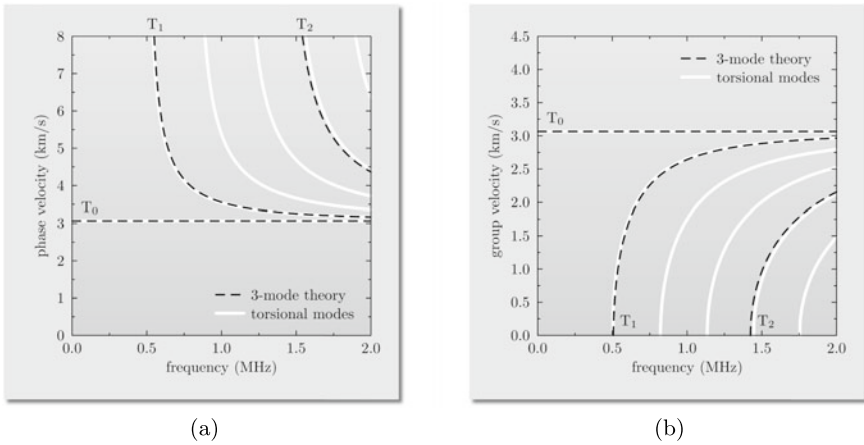


**Fig. 9.24** Dispersion curves for: **a** the phase velocity, **b** the group velocity, for torsional modes of elastic waves propagating in a 10 mm diameter aluminium bar, according to the 3-mode 1-D theory of shafts

$$\left[ (5750 + 240a^2k^2 + a^4k^4) - 2a^2 (120 + a^2k^2) \frac{\omega^2}{c_S^2} + a^4 \frac{\omega^4}{c_S^4} \right] \left[ k^2 - \frac{\omega^2}{c_S^2} \right] = 0 \tag{9.41}$$

Its roots can be easily found numerically, which leads to the dispersion curves presented in Fig. 9.24.

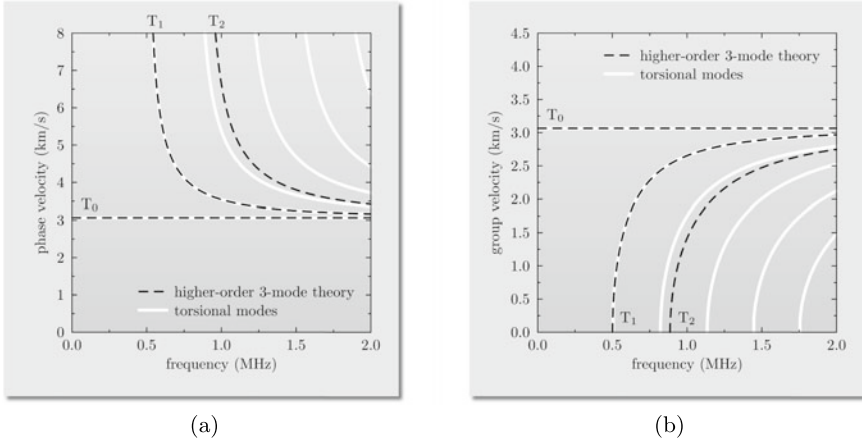


**Fig. 9.25** Dispersion curves for: **a** the phase velocity, **b** the group velocity, for torsional modes of elastic waves propagating in a 10 mm diameter aluminium bar, according to the higher-order 3-mode 1-D theory of shafts

- *Higher-order 3-mode 1-D theory:*

$$\begin{aligned}
 q &= 3 \\
 &\downarrow \\
 u_{\theta}(x, \zeta, t) &= a\zeta\theta_1(x, t) + \sum_{n=1}^3 a\zeta(1 - \zeta^{2n})\theta_{2n+1}(x, t)
 \end{aligned}
 \tag{9.42}$$

where the additional assumption for  $\theta_7$  is made, resulting from the traction-free boundary condition for the stress components  $\tau_{r\theta}$ , leading to:

$$3\theta_7(x, t) = -\theta_3(x, t) - 2\theta_5(x, t)
 \tag{9.43}$$

where the characteristic equation also is a 6th degree polynomial with respect to the wave number  $k$  and can be presented in the following form:

$$\begin{aligned}
 &\left[ (80640 + 4032a^2k^2 + 37a^4k^4) - 2a^2(2016 + 37a^2k^2) \frac{\omega^2}{c_s^2} \right. \\
 &\quad \left. + 37a^4 \frac{\omega^4}{c_s^4} \right] \left[ k^2 - \frac{\omega^2}{c_s^2} \right] = 0
 \end{aligned}
 \tag{9.44}$$

Its roots can be easily found numerically, which leads to the dispersion curves presented in Fig. 9.25.

- *4-mode 1-D theory:*



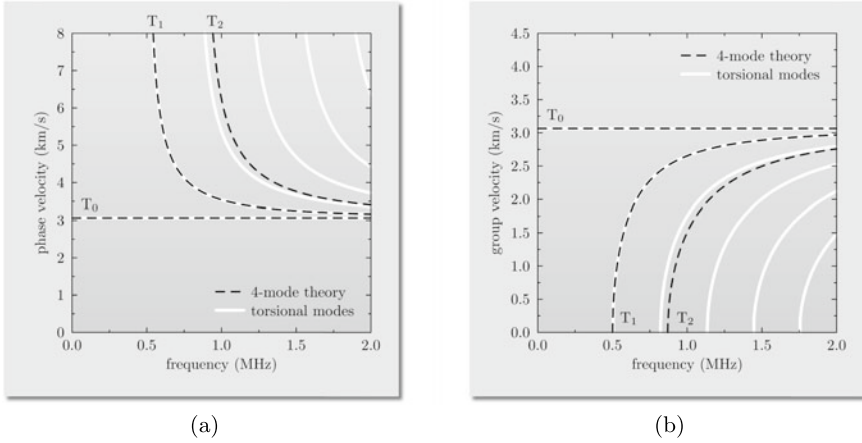


**Fig. 9.26** Dispersion curves for: **a** the phase velocity, **b** the group velocity, for torsional modes of elastic waves propagating in a 10 mm diameter aluminium bar, according to the 4-mode 1-D theory of shafts

$$\begin{aligned}
 & q = 3 \\
 & \quad \downarrow \\
 & u_\theta(x, \zeta, t) = a\zeta\theta_1(x, t) + \sum_{n=1}^4 a\zeta(1 - \zeta^{2n})\theta_{2n+1}(x, t)
 \end{aligned}
 \tag{9.45}$$

where the characteristic equation is a 8th degree polynomial with respect to the wave number  $k$ . Its roots can be easily found numerically, which leads to the dispersion curves presented in Fig. 9.26.

As previously, for the 1-D theories of the torsional behaviour of shafts presented above the analysis of their accuracy can be carried out based on the relative error of the phase velocity. The results concerning the 6 theories of the torsional behaviour of shafts are presented in Figs. 9.27, 9.28 and 9.29 as relative error curves and as a function of the cyclic frequency  $f$ . This time, however, due to the nature of the analysed torsional waves, an extended frequency range was used up to 2 MHz, which in the case of a 10 mm diameter aluminium bar was sufficient to incorporate as many as 6 torsional modes in the dispersion curves for the phase velocity and 6 torsional modes in the dispersion curves for the group velocity.

The results shown in Fig. 9.27 concern two theories, i.e. the 1-mode theory and the 2-mode theory of the torsional behaviour of shafts. These are the simplest theories developed. It is interesting to observe that since the dominant wave mode is the fundamental torsional mode  $T_0$ , which is non-dispersive, its representation even in the case of the 1-mode theory is exact with no errors associated. This type of behaviour is also observed in the case of the remaining theories, for which the representation of the fundamental torsional mode  $T_0$  is always exact. For this reason the analysis

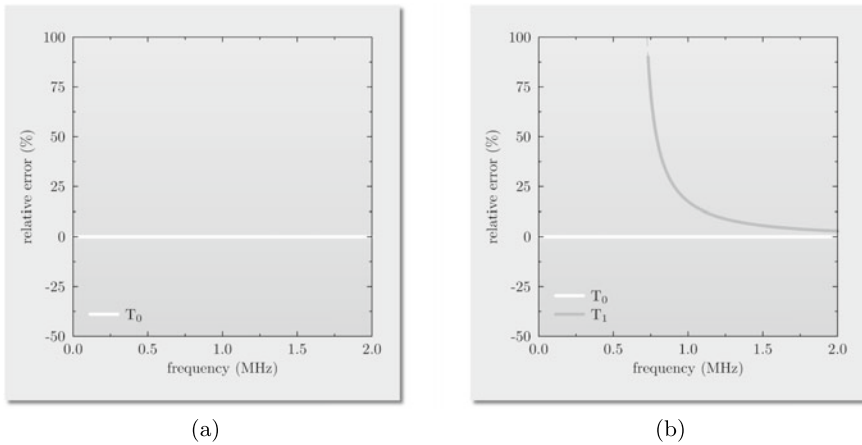


**Fig. 9.27** Relative error for: **a** the 1-mode 1-D theory, **b** the 2-mode 1-D theory, of the torsional behaviour of shafts measured against the analytical solution for torsional waves propagating in a 10 mm diameter aluminium bar

of the accuracy of the remaining multi-mode and higher-order multi-mode theories must focus on higher torsional wave modes.

It can be clearly seen in Fig. 9.27 that in the case of the 2-mode theory the relative error of the phase velocity related to the second torsional mode  $T_1$  stays at a relatively high level decreasing gradually towards higher frequencies. The application of the traction-free boundary condition in the case of the higher-order 2-mode theory has a great impact on the obtained results. The accuracy of the representation of the second torsional mode  $T_1$  for this theory is very similar to the representation offered by the 3-mode theory, as presented in Fig. 9.28.

A further improvement of the theories, as observed in the case of the higher-order 3-mode theory and the 4-mode theory, substantially lowers the relative error to very small values for lower torsional modes, as presented in Fig. 9.29. It should be said that at the same time the relative errors associated with the representation of higher modes remain significant.

At this place it should be emphasised that in contrast to the previously presented and investigated theories of the longitudinal behaviour of rods and flexural behaviour of beams, even the simplest theories of the torsional behaviour of shafts remain exact in the frequency range up to the first cut-off frequency  $f_{T_1}$ . For this reason their application range covers not only mid frequency dynamics, but also problems involving high frequency dynamics or wave propagation problems. At the same time, if the frequency range covers frequencies exceeding the first cut-off frequency  $f_{T_1}$  it is recommended as before to employ other multi-mode or higher-order multi-mode theories.

For the very same reason the detailed analysis of the accuracy of the multi-mode and higher-order multi-mode theories developed and presented above concerned the second torsional mode  $T_1$  rather than the fundamental torsional mode  $T_0$ . This

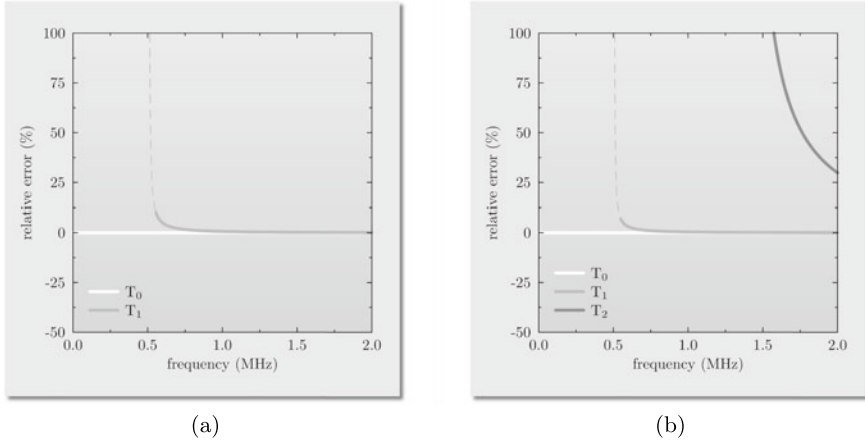


**Fig. 9.28** Relative error for: **a** the higher-order 2-mode 1-D theory, **b** the 3-mode 1-D theory, of the torsional behaviour of shafts measured against the analytical solution for torsional waves propagating in a 10 mm diameter aluminium bar

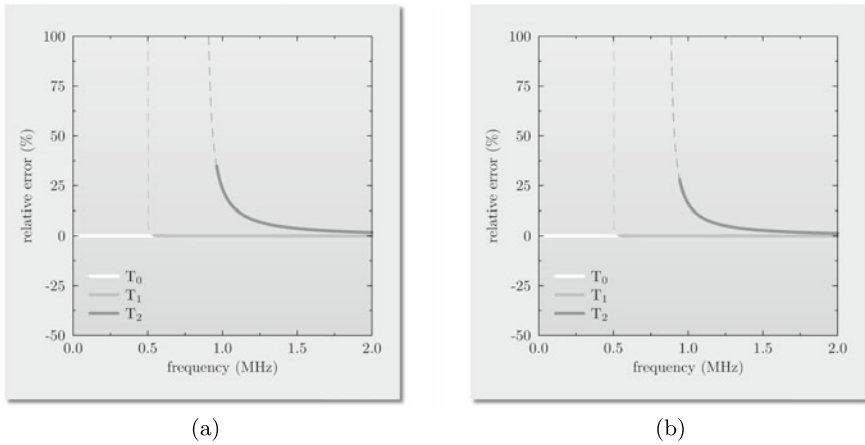


**Fig. 9.29** Relative error for: **a** the higher-order 3-mode 1-D theory, **b** the 4-mode 1-D theory, of the torsional behaviour of shafts measured against the analytical solution for torsional waves propagating in a 10 mm diameter aluminium bar

analysis was carried out in the range of frequencies starting from the first cut-off frequency  $f_{T_1}$  up to 1 MHz, as presented and summarised in Table 9.3. In the current case of a 10 mm diameter aluminium bar the second torsional mode  $T_1$  appears at the frequency  $f_{T_1}$  of 501.2 kHz.

Unsurprisingly, it is clearly seen from Fig. 9.30 that for the 2-mode 1-D theory the second torsional mode  $T_0$  is characterised by the relative error of the phase velocity, which is relatively high for the frequencies near the first cut-off frequency

**Table 9.3** Statistical data on the relative modelling error associated with the phase velocity of the second torsional mode  $T_1$  propagating in a 10 mm diameter aluminium bar, for phase velocities below 8 km/s in the frequency range up to 1 MHz, for various theories of the torsional behaviour of shafts

Theory	Extr. error (%)	Avg. error (%)	Std. deviation (%)
1-mode 1-D	–	–	–
2-mode 1-D	90.1	9.86	18.8
Higher-order 2-mode 1-D	10.4	1.01	1.73
3-mode 1-D	6.90	0.42	0.84
Higher-order 3-mode 1-D	0.19	0.02	0.03
4-mode 1-D	0.13	0.01	0.02

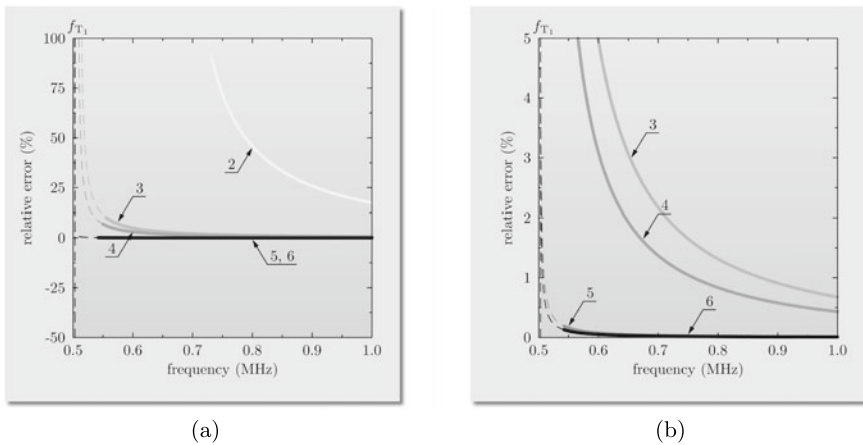


**Fig. 9.30** Relative error of the second torsional mode  $T_1$  propagating in a 10 mm diameter aluminium bar: **a** full range, **b** magnified view, for various theories of the flexural behaviour of bars (1—n/a, 2—2-mode 1-D, 3—higher-order 2-mode 1-D, 4—3-mode 1-D, 5—higher-order 3-mode 1-D, 6—4-mode 1-D)

$f_{T_1}$  reaching 90.1% (this value corresponds to the value of the phase velocity of 8 km/s) to decrease slowly to 17.4% at 1 MHz. This behaviour is significantly improved in the case of the higher-order 2-mode theory, for which the corresponding values of the relative error are 10.4 and 6.77%, while in the case of the 3-mode theory they further reduce to 6.90 and 4.30%, respectively.

Only in the cases of the higher-order 3-mode theory and the 4-mode theory the relative error in the frequency range of interest drops down significantly to a preferable level below 5%. For the higher-order 3-mode theory the relative error of the phase velocity near the first cut-off frequency  $f_{T_1}$  of 501.2 kHz is as small as 0.19% (this value corresponds to the value of the phase velocity of 8 km/s) to decrease to 0.01% at 1 MHz. For the 4-mode theory the corresponding values of the relative error are 0.13% and 0.01%, respectively.

Based on the obtained results the same recommendation can be made here, that although at higher computational cost due to the increased number of independent variables, i.e. DOFs, it is recommended to use the latter or other multi-mode or higher-order multi-mode 1-D theories to ensure high accuracy of numerical predictions, especially where high frequency dynamics or wave propagation problems are investigated.

## References

1. A. E. Love. *A treatise on the mathematical theory of elasticity*. Cambridge: at the University Press, Cambridge, 1892.
2. R. D. Mindlin and G. Herrmann. A one dimensional theory of compressional waves in an elastic rod. *Proceedings of the First U.S. National Congress on Applied Mechanics, Chicago, Illinois*, 1:187–191, 11-16 June 1951.
3. A. Źak and M. Krawczuk. Assessment of rod behaviour theories used in spectral finite element modelling. *Journal of Sound and Vibration*, 329:2099–2113, 2010.
4. S. P. Anderson. Higher-order rod approximations for the propagation of longitudinal stress waves in elastic bars. *Journal of Sound and Vibration*, 290:290–308, 2006.
5. A. Źak, M. Krawczuk, G. Redlarski, Ł. Doliński, and S. Koziel. A three-dimensional periodic beam for vibroacoustic isolation purposes. *Mechanical Systems and Signal Processing*, 130:524–544, 2019.
6. S. P. Timoshenko and S. Woinowsky-Krieger. *Theory of plates and shells*. McGraw-Hill Book Company, New York, 1959.
7. G. R. Cowper. The shear coefficient in Timoshenko's beam theory. *ASME Journal of Applied Mechanics*, 33:335–340, 1966.
8. A. Źak. A novel formulation of a spectral plate element for wave propagation in isotropic structures. *Finite Element in Analysis and Design*, 45:650–658, 2009.
9. J. N. Reddy. A simple higher-order theory for laminated composite plates. *ASME Journal of Applied Mechanics*, 51:745–752, 1984.
10. A. Źak and M. Krawczuk. Assessment of flexural beam behaviour theories used for dynamics and wave propagation problems. *Journal of Sound and Vibration*, 331:5715–5731, 2012.

# Chapter 10

## FEM Essentials



### 10.1 What Is FEM?

The Finite Element Method (FEM) is a modern computational technique originally developed for solving partial differential equations. Due to its unquestionable power and robustness [1–3], nowadays FEM is considered to be the most popular numerical tool employed to solve various complex engineering and scientific problems. An example can be the results concerning normal modes of an aluminium periodic vibration isolator presented in Fig. 10.1.

As already mentioned in Chap. 1 a precise date of birth of FEM does not exist. The method itself takes a lot from early works of many great scientists and researchers. On the foundations laid by such great names as: Bernoulli, Euler, Lagrange, Legendre, Gauss, Cauchy and many more, who by many are considered as the pioneers of the calculus of variations, as well as contemporary works of Rayleigh, Ritz and Galerkin, who should also be mentioned here, solid frames for the current success of FEM have been established. These works were true milestones in the development of something, which in the 1960s and 1970s, the beginning of the era of modern computers, took finally the shape of FEM. This, however, would not happen without a great input of numerous scientists and researchers forming a long list of names including: Hrennikoff [4, 5], Courant [6, 7], Argyris [8, 9], Zienkiewicz [10, 11], Ciarlet [12, 13], Gallagher [14, 15], Babuška [16, 17], Oden [18] and many more (Fig. 10.1).

As previously stated FEM is a numerical tool, which is used to solve partial differential equations. Because of its weak (integral) formulation the method is more flexible in finding such solutions than the traditionally used strong (differential) formulation. This can be easily explained in the case of the problem of propagation of longitudinal waves in a 1-D elastic rod discussed in Sect. 2.3.1.

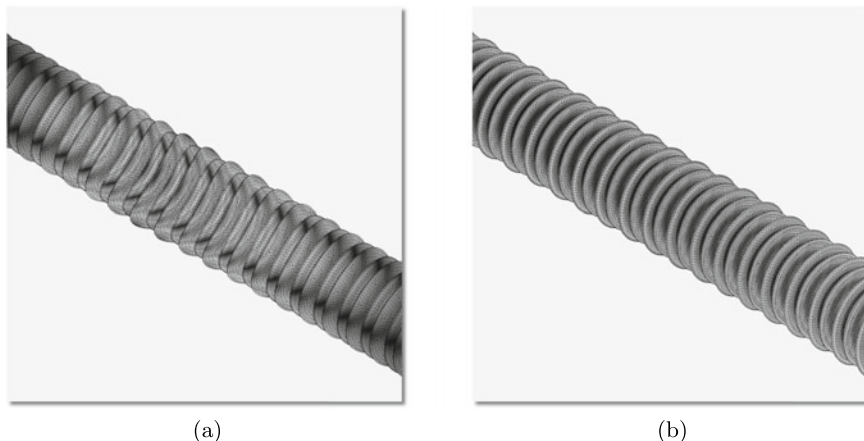


**Fig. 10.1** Normal modes of an aluminium periodic vibration isolator belonging to: **a** the 180th frequency of natural vibrations at 15.8 kHz, **b** the 181th frequency of natural vibrations at 25.5 kHz, modelled by more than 1,200,000 FEs. Results of numerical computations by FEM

## 10.2 Weak Formulation

A good starting point leading to the weak formulation of the 1-D wave equation, presented in Sect. 2.3.1 and given by Eq. (2.15), can be its already known form. However, in the current case the 1-D wave equation is additionally supplemented with an externally acting force  $f(x, t)$  (expressed in newtons per metres), as presented below:

$$ES \frac{\partial^2 u(x, t)}{\partial x^2} - \rho S \frac{\partial^2 u(x, t)}{\partial t^2} + f(x, t) = 0 \quad (10.1)$$

where the physical meaning of particular symbols and quantities remains the same.

For regions of interest having finite dimensions this wave equation is typically supplemented with certain boundary and initial conditions for the unknown solution function  $u(x, t)$ , which allow one to search for some specific solutions. These boundary conditions may be conveniently assumed to have the following forms:

$$u(0, t) = u(L, t) = 0 \quad \text{or} \quad \frac{\partial u(0, t)}{\partial x} = \frac{\partial u(L, t)}{\partial x} = 0 \quad (10.2)$$

where  $L$  is the length of the rod and  $T$  denotes a certain time interval within which these solutions are sought.

At this point it is noteworthy that the unknown solution function  $u(x, t)$  must satisfy the 1-D wave equation within the whole region of interest, i.e. for all  $x \in (0, L)$  and for all  $t \in (0, T)$ . In order to do this the function  $u(x, t)$  must be continuous and

differentiable up to the second derivative<sup>1</sup> with respect to the spatial coordinate  $x$  and the time  $t$ . Moreover, its derivatives must exist in the whole region of interest, so the unknown solution function  $u(x, t)$  must be of class  $C^2$  at least.

It can be said that the strong requirements placed on the function  $u(x, t)$  resulting from the order of the differential equation under consideration, i.e. the wave equation in the form of Eq. (10.1), presents a *strong formulation* of the problem of propagation of longitudinal waves in a 1-D elastic rod.

However, this strong formulation can be relaxed by the use of a certain weight (test) function  $w(x, t)$ , which satisfies the same boundary and initial conditions as the unknown solution function  $u(x, t)$ . This can be presented in the following integral form:

$$\int_0^L w(x, t) \left[ ES \frac{\partial^2 u(x, t)}{\partial x^2} - \rho S \frac{\partial^2 u(x, t)}{\partial t^2} + f(x, t) \right] dx = 0 \quad (10.3)$$

At this point, with no loss of generality, it may be assumed that the weight (test) function is the unknown solution function  $u(x, t)$  itself. Furthermore, the integration by parts of the first component of the wave equation leads to the following relationship:

$$\begin{aligned} \int_0^L u(x, t) \frac{\partial^2 u(x, t)}{\partial x^2} dx &= \int_0^L u(x, t) d \left[ \frac{\partial u(x, t)}{\partial x} \right] \\ &= \underbrace{u(x, t) \frac{\partial u(x, t)}{\partial x} \Big|_0^L}_{=0 \text{ due to b.c.}} - \int_0^L \frac{\partial u(x, t)}{\partial x} \frac{\partial u(x, t)}{\partial x} dx \end{aligned} \quad (10.4)$$

which allows one to express the integral form of the wave equation as:

$$\begin{aligned} ES \int_0^L \frac{\partial u(x, t)}{\partial x} \frac{\partial u(x, t)}{\partial x} dx + \rho S \int_0^L u(x, t) \frac{\partial^2 u(x, t)}{\partial t^2} dx \\ - \int_0^L u(x, t) f(x, t) dx = 0 \end{aligned} \quad (10.5)$$

It can be easily seen that the strong requirements originally placed on the unknown solution function  $u(x, t)$  are weakened, as now it is sufficient for this function  $u(x, t)$  to be of class  $C^1$  with respect to the spatial coordinate  $x$ . For this reason the

---

<sup>1</sup> Mathematically, a function is of class  $C^n$  in its domain, if its first  $n$  derivatives exist and remain continuous. Additionally, a function is of class  $C^\infty$ , if its derivatives of any order exist and remain continuous. Such a function is called smooth.



formulation of the wave equation given by Eq. (10.5) presents a *weak formulation* of the problem of propagation of longitudinal waves in a 1-D elastic rod. This weak form of the wave equation can be further transformed to equations of motion describing the dynamic behaviour of the rod under investigation, when some additional assumption concerning the unknown solution function  $u(x, t)$  are made.

### 10.3 Equations of Motion

In FEM there are some specific rules regarding the methods used to approximate the unknown solution function  $u(x, t)$ . This is done not only to simplify the resulting weak formulation of the original wave equation, but first of all to guarantee the correctness of obtained solutions. As a consequence it is assumed that within the region of interest, i.e. for all  $x \in (0, L)$ , the function  $u(x, t)$  can be approximated by a finite sum of certain test functions as:

$$u(x, t) \cong \sum_{n=1}^p N_n(x)q_n \quad (10.6)$$

where  $N_n(x)$  are so-called 1-D *shape functions*,  $q_n$  are nodal displacements dependent on time  $t$ , while  $p$  denotes the number of nodes distributed over the length  $L$  of the rod.

The unknown solution function  $u(x, t)$  can also be presented using matrix notation [19], in a manner typical for FEM:

$$u(x, t) \cong \sum_{n=1}^p N_n(x)q_n = \mathbf{N}(x)\mathbf{q}_e, \quad \mathbf{q}_e = [q_1, q_2, \dots, q_p]^T \quad (10.7)$$

where now  $\mathbf{N}(x)$  is a *matrix of 1-D shape functions* and  $\mathbf{q}_e$  is a vector of nodal displacements of a certain FE  $e$ , now represented by the entire rod under investigation. Thanks to this, the spatial and time differentiation can be expressed as follows:

$$\begin{cases} \frac{\partial u(x, t)}{\partial x} \cong \mathbf{N}'(x)\mathbf{q}_e, & \frac{\partial^2 u(x, t)}{\partial x^2} \cong \mathbf{N}''(x)\mathbf{q}_e, \dots \\ \frac{\partial u(x, t)}{\partial t} \cong \mathbf{N}(x)\dot{\mathbf{q}}_e, & \frac{\partial^2 u(x, t)}{\partial t^2} \cong \mathbf{N}(x)\ddot{\mathbf{q}}_e, \dots \end{cases} \quad (10.8)$$

where the symbols  $(\bullet')$  and  $(\bullet'')$  denote the first and the second derivatives with respect to the spatial coordinate  $x$ , while the symbols  $\dot{\mathbf{q}}_e$  and  $\ddot{\mathbf{q}}_e$  denote vectors of nodal velocities and accelerations.

At this point it is important to mention that the matrix notation used in FEM requires that all necessary differentiations in Eq. (10.5) are performed in the following manner:

$$\left\{ \begin{array}{l} \frac{\partial u(x, t)}{\partial x} \frac{\partial u(x, t)}{\partial x} \cong [\mathbf{N}'(x)\mathbf{q}_e]^\top [\mathbf{N}'(x)\mathbf{q}_e] \\ \quad = \mathbf{q}_e^\top \mathbf{N}'(x)^\top \mathbf{N}'(x) \mathbf{q}_e \\ u(x, t) \frac{\partial^2 u(x, t)}{\partial t^2} \cong [\mathbf{N}(x)\mathbf{q}_e]^\top [\mathbf{N}(x)\ddot{\mathbf{q}}_e] \\ \quad = \mathbf{q}_e^\top \mathbf{N}(x)^\top \mathbf{N}(x) \ddot{\mathbf{q}}_e \end{array} \right. \quad (10.9)$$

As a result of this particular components of the weak form of the wave equation, given by Eq. (10.5), may be transformed and presented as:

$$ES \int_0^L \frac{\partial u(x, t)}{\partial x} \frac{\partial u(x, t)}{\partial x} dx \cong \mathbf{q}_e^\top \underbrace{\left[ ES \int_0^L \mathbf{N}'(x)^\top \mathbf{N}'(x) dx \right]}_{=\mathbf{K}_e} \mathbf{q}_e \quad (10.10)$$

$$\rho S \int_0^L u(x, t) \frac{\partial^2 u(x, t)}{\partial t^2} dx \cong \mathbf{q}_e^\top \underbrace{\left[ \rho S \int_0^L \mathbf{N}(x)^\top \mathbf{N}(x) dx \right]}_{=\mathbf{M}_e} \ddot{\mathbf{q}}_e \quad (10.11)$$

$$\int_0^L u(x, t) f(x, t) dx \cong \mathbf{q}_e^\top \underbrace{\left[ \int_0^L \mathbf{N}(x)^\top f(x, t) dx \right]}_{=\mathbf{F}_e} \quad (10.12)$$

where following the notation typical for FEM the symbols  $\mathbf{K}_e$ ,  $\mathbf{M}_e$  and  $\mathbf{F}_e$  denote the elemental characteristic stiffness and inertia matrices as well as the elemental vector of external forces (expressed in newtons), respectively [19–22]. Moreover, in the current case they concern the entire rod, which may be thought of as represented by one FE only.

Finally, substitution of Eqs. (10.10), (10.11) and (10.12) into the wave equation expressed by Eq. (10.5) leads to a matrix equation:

$$\mathbf{q}_e^\top \mathbf{M}_e \ddot{\mathbf{q}}_e + \mathbf{q}_e^\top \mathbf{K}_e \mathbf{q}_e - \mathbf{q}_e^\top \mathbf{F}_e = \mathbf{0} \quad (10.13)$$

which after grouping of appropriate terms takes the form:

$$\mathbf{q}_e^\top (\mathbf{M}_e \ddot{\mathbf{q}}_e + \mathbf{K}_e \mathbf{q}_e - \mathbf{F}_e) = \mathbf{0} \quad (10.14)$$

The result obtained represents a system of linear differential equations, which is satisfied only if the expression within the brackets is satisfied, which leads to the following equation:

$$\mathbf{M}_e \ddot{\mathbf{q}}_e + \mathbf{K}_e \mathbf{q}_e = \mathbf{F}_e \quad (10.15)$$

representing 1-D *equations of motion* corresponding to the original wave equation, which were obtained thanks to the representation of the unknown solution function  $u(x, t)$  by a set of 1-D shape functions  $N_n(x)$ . Consequently, these equations of motion *are satisfied in a discrete sense* only for a set of  $p$  points  $q_p$ , which represent so-called *nodes* of the FE  $e$ .

It is noteworthy that in the current case under consideration only one DOF associated per node is assumed, i.e. the longitudinal displacement component. Thus, the number of DOFs of the entire numerical model of the rod must be equal to the total number of nodes in this model. However, this may be different in a general case, where the number of DOFs in a single node can be greater than one including, for example, other displacement components, their derivatives, etc. Then, the number of DOFs of the entire numerical FEM discrete model is equal to the total number of nodes of this model multiplied by the number of DOFs in a single node.

It should be mentioned here that sometimes the obtained 1-D equations of motion should be supplemented with a dissipation component  $\mathbf{C}_e \dot{\mathbf{q}}_e$ , where  $\mathbf{C}_e$  is the elemental characteristic damping matrix. This matrix is usually expressed as a linear combination of the inertia and stiffness matrices, i.e.  $\mathbf{C}_e = \alpha \mathbf{M}_e + \beta \mathbf{K}_e$ , where  $\alpha$  and  $\beta$  are certain constants [23].

## 10.4 Shape Functions

In the case of 1-D FEs, as can be viewed the rod under investigation, it is typical for FEM to assume as shape functions polynomials of certain degrees, usually equal to  $r = p - 1$  with  $p$  denoting the number of nodes  $q_n$  within a single FE, where  $n = 1, 2, \dots, p$ . Higher degrees of approximation polynomials can be obtained in special cases, which take advantage of some additional conditions regarding shape functions [24] or the smoothness of strain/stress fields, etc. [24–26]. Candidates for shape functions should be chosen carefully, as they must satisfy certain conditions in order to guarantee the correctness of the obtained results as well as the convergence of these results with an increase in the number of nodes and/or DOFs of numerical models. The requirements concerning the properties of the approximation shape functions can be summarised as follows [19]:

- Shape functions should be chosen so that they allow one to achieve no strains in the case of displacement fields compatible with no strains. This can be translated as the ability of the shape functions to reproduce the vanishing of their first derivatives under appropriate nodal conditions.
- Shape functions should be chosen so that they allow one to achieve constant strains in the case of displacement fields compatible with constant strains. This can be translated as the ability of the shape functions to reproduce constant values of their first derivatives under appropriate nodal conditions.

- Shape functions should be chosen so that they allow one to achieve finite strains, even though these strains can be discontinuous between adjacent FEs. This can be translated as the ability of the shape functions to reproduce the unknown solution function as a piecewise smooth function of class  $C^0$  at least.

In order to make shape functions independent of the rod length  $L$  a simple transformation can be used. In the case of the rod under consideration it takes the following simple form:

$$\xi = \frac{2x}{L} - 1, \quad x \in \langle 0, L \rangle \quad (10.16)$$

which transforms<sup>2</sup> the region of interest from  $x \in \langle 0, L \rangle$  to a new region  $\xi \in \langle -1, +1 \rangle$  and 1-D shape functions  $N_n(x)$  to new shape functions  $N_n(\xi)$ . Thanks to such an approach 1-D shape functions can be easily obtained, tabulated and manipulated by modern computation packages [27, 28] as having a universal definition.

Polynomials used for shape functions can be characterised by different distributions of their nodes  $q_n$ . These distributions can influence their approximation properties, thus influencing numerical properties of FEs built based on their application [29].

In general, distributions of nodes within FEs can be equidistant or non-equidistant. The non-equidistant distributions of nodes within FEs take advantage of zeros of specialised polynomials, namely Chebyshev polynomials of the first kind or Lobatto polynomials [20]. The use of these kinds of polynomials leads to the so-called *spectral convergence*, typical for Fourier series, which guarantees that computational errors decrease very fast, or even exponentially [30], with an increase in the degree of approximation polynomials  $r$ . Additionally, their use helps to avoid so-called *Runge's phenomenon*, which leads to undesired oscillations of solutions near the edges of investigation regions in the case of higher degrees of approximation polynomials based on equidistant node distributions.

In each these cases the coordinates of the nodes of appropriate approximation polynomials can be calculated based on simple formulae.

- For equidistant node distributions the coordinates  $\xi_n$  of nodes of 1-D shape functions being approximation polynomials of degree  $r = p - 1$  are obtained as:

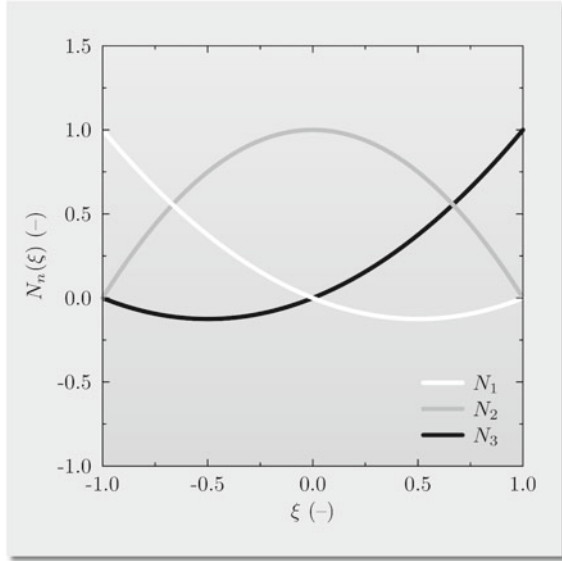
$$\xi_n = \frac{2(n-1)}{p-1} - 1, \quad n = 1, 2, \dots, p \quad (10.17)$$

The equidistant node distributions are typical for the classical FEM, where the degrees of approximation polynomials  $r$  are usually equal to 1, 2 or vary rarely 3. Shape functions for the equidistant distribution of nodes and the degree of approximation polynomials  $r = 2$  are shown in Fig. 10.2.

---

<sup>2</sup> This is equivalent to the transformation of shape functions to the local curvilinear/normalised coordinates system.

**Fig. 10.2** Shape functions for equidistant node distribution, for approximation polynomials of degree  $r = 2$



- For non-equidistant node distributions based on the zeros of Chebyshev polynomials of the first kind, or simply Chebyshev nodes, the coordinates  $\xi_n$  of nodes of 1-D shape functions being approximation polynomials of degree  $r = p - 1$  can be obtained as:

$$\xi_n = -\cos\left[\frac{\pi(n-1)}{p-1}\right], \quad n = 1, 2, \dots, p \quad (10.18)$$

The non-equidistant node distributions based on Chebyshev nodes are typical for specialised FEM approaches as is TD-SFEM, when the degrees of approximation polynomials  $r$  is usually equal 5, but can be as high as 10. Shape functions for the non-equidistant distribution of nodes based on Chebyshev nodes and degree of approximation polynomials  $r = 5$  are shown in Fig. 10.3. It should be noted that for  $r = 1$  and  $r = 2$  the obtained coordinates  $\xi_n$  are the same as for the equidistant node distribution.

- For non-equidistant node distributions based on the zeros of Lobatto polynomials, or simply Lobatto nodes, the coordinates  $\xi_n$  of nodes of 1-D shape functions being approximation polynomials of degree  $r = p - 1$  can be obtained from the following formula:

$$L_p^c(\xi) = (1 - \xi^2) \frac{dP_{p-1}(\xi)}{d\xi} = 0 \rightarrow \xi_n, \quad n = 1, 2, \dots, p \quad (10.19)$$

where  $P_{p-1}(\xi)$  is the Legendre polynomial of degree  $p - 1$ , while  $L_p^c(\xi)$  is the complete Lobatto polynomial of degree  $p$ .

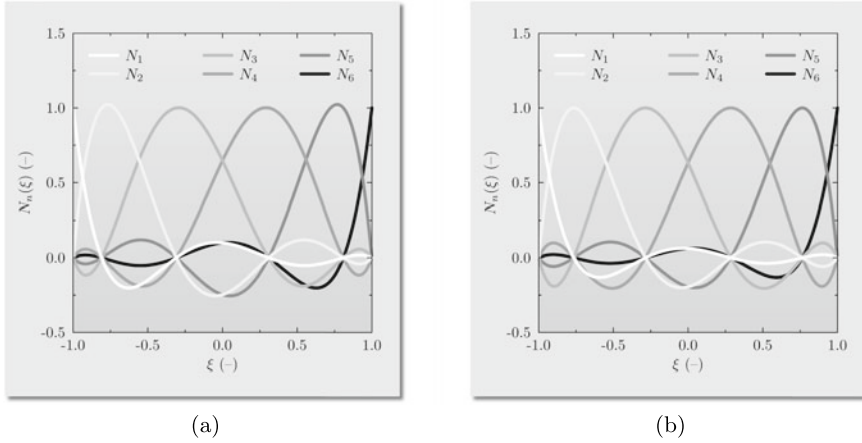


**Fig. 10.3** Shape functions for non-equidistant node distributions based on: **a** Chebyshev nodes, **b** Lobatto nodes, for degree of approximation polynomials  $r = 5$

The non-equidistant node distributions based on Lobatto nodes are also typical for specialised FEM approaches as is TD-SFEM, when the degrees of approximation polynomials  $r$  is usually equal 5, but can be as high as 10. Shape functions for the non-equidistant distribution of nodes based on Lobatto nodes and degree of approximation polynomials  $r = 5$  are shown in Fig. 10.3. It should be noted that for  $r = 1$  and  $r = 2$  the obtained coordinates  $\xi_n$  are the same as in the case of the equidistant node distribution.

The knowledge of the node distribution allows one to evaluate 1-D shape functions  $N_n(\xi)$ , being polynomials of  $r = p - 1$  degree, by the use of a simple relationship:

$$N_n(\xi_m) = \sum_{n=1}^p a_{n-1} \xi_m^{n-1} = \delta_{mn}, \quad m, n = 1, 2, \dots, p \quad (10.20)$$

where  $\delta_{mn}$  is the already known Kronecker delta. This leads to a set of  $p$  linear equations for unknown coefficients  $a_n$ . Such a system can be easily solved to obtain desired shape functions  $N_n(\xi)$  for all  $p$  nodes of a single FE. Alternatively, the very well-known Lagrange formula [31] can be used for a given set of nodes in order to establish the shape functions  $N_n(\xi)$ . It should be emphasised that in the literature there are numerous other definitions of shape functions, such as those based on the use of Hermite polynomials [19], splines [24], orthogonal trigonometric polynomials [30] or other specialised approaches using wavelets [32], etc.

It can be shown [19] that 1-D shape functions, based on the definition given by Eq. (10.20), have very important properties, which can be expressed by the following two simple identities:

$$\begin{cases} \sum_{n=1}^p N_n(\xi) = 1 \\ \sum_{n=1}^p \frac{dN_n(\xi)}{d\xi} = 0 \end{cases} \quad (10.21)$$

which often are very useful in FEM since corresponding identities also hold in 2-D and 3-D cases.<sup>3</sup>

## 10.5 Numerical Integration

Despite the fact that the use of modern computation packages [27, 28] allows one to perform many computations required by FEM analytically with no practical limitations, the effective use of this computational method is strongly based on numerical integration [19]. In order to obtain the elemental characteristic stiffness  $\mathbf{K}_e$ , inertia  $\mathbf{M}_e$  and other matrices as well as vectors required by FEM certain integrals must be computed numerically.

In the case of the rod under consideration 1-D integrals of the following type must be calculated repeatedly:

$$\int_0^L f(x) dx = \dots \quad (10.22)$$

Since the above integral is defined in the global coordinate system ( $x$ ), its value is always dependent on the length of the rod  $L$ , which can vary. This makes the direct computation of this integral not universal. In a more general case its repeated evaluation can be not only tedious, but also time consuming. For this reason it is much more effective to transform the integral given by Eq. (10.22) to the local normalised coordinate system ( $\xi$ ) by the use of Eq. (10.16) to obtain:

$$\int_0^L f(x) dx = \int_{-1}^{+1} f(\xi) \det \mathbf{J}_e d\xi \quad (10.23)$$

where  $\det \mathbf{J}_e$  denotes the determinant of the Jacobi matrix  $\mathbf{J}_e$ , which is related to the transformation of the region of interest  $x \in (0, L)$  to  $\xi \in (-1, +1)$  and which determinant can be evaluated from the following simple relationships in the case of the rod under consideration:

---

<sup>3</sup> This is because in 2-D and 3-D cases shape functions are obtained by appropriate multiplications of corresponding 1-D shape functions. Consequently, in the case of 2-D shape functions it can be formally written that  $N_l(x, y) = N_i(x)N_j(y)$ , while in the case of 3-D shape functions that  $N_m(x, y, z) = N_i(x)N_j(y)N_k(z)$ , where indexes  $i, j, k$  and  $l, m$  take values dependent on the chosen degrees of approximation polynomials.

$$\mathbf{J}_e = \frac{dx}{d\xi} \rightarrow x = \frac{L}{2}(\xi + 1) \rightarrow \det \mathbf{J}_e = \frac{L}{2} \quad (10.24)$$

With no loss of accuracy the integrals given by Eq. (10.23) can be conveniently replaced by appropriate summation as long as the integrated function  $f(\xi)$  can be represented by polynomials of certain degree  $r$ . This summation must be carried out for a required number of sampling points in order to guarantee the exactness of such a replacement [31]:

$$\int_{-1}^{+1} f(\xi) \det \mathbf{J}_e d\xi = \sum_{n=1}^p w_n f(a_n) \det \mathbf{J}_e \quad (10.25)$$

where both the weights  $w_n$  and the so-called abscissas  $a_n$  are dependent on the degree of approximation polynomials.

The representation of an integral by the appropriate sum presented above is called *quadrature*.<sup>4</sup> It can be checked [31] that the Gaussian quadrature based on  $p$  integration points is exact for polynomials of degrees up to  $r = 2p - 1$  [31]. This is a universal quadrature used in FEM and its specialised clones. At the same time the Lobatto quadrature based on  $p$  integration points, also known as the Gauss-Lobatto-Legendre quadrature (GLL), is exact for polynomials of degrees up to  $r = 2p - 3$  [31], and is typically used in combination with the non-equidistant node distributions based on Lobatto nodes. In both these cases the weights  $w_n$  and the abscissas  $a_n$  can be easily calculated from the following formulae:

- for the Gaussian quadrature:

$$\begin{cases} P_p(a_n) = 0 \rightarrow a_n \\ w_n = \frac{2}{(1 - a_n^2) \frac{dP_{p-1}(a_n)}{d\xi}} \end{cases}, \quad n = 1, 2, \dots, p \quad (10.26)$$

- for the Lobatto quadrature:

$$\begin{cases} (1 - a_n^2) \frac{dP_{p-1}(a_n)}{d\xi} = 0 \rightarrow a_n \\ w_n = \frac{2}{p(p-1)P_p^2(a_n)} \end{cases}, \quad n = 1, 2, \dots, p \quad (10.27)$$

However, it should be emphasised here that when used together with the Lobatto nodes the Lobatto quadrature leads to a very important numerical property, which is called discrete orthogonality since:

---

<sup>4</sup> The term quadrature reflects understanding of the process of the determination of the area of figures by ancient Greek mathematicians, who tried to solve it geometrically by the construction of squares of the corresponding areas.



$$\int_{-1}^{+1} L_m^c(\xi)L_n^c(\xi)d\xi = \sum_{i=1}^p w_i L_m^c(a_i) \sum_{j=1}^q w_j L_n^c(a_j) = \delta_{mn} \quad (10.28)$$

which is very willingly employed in TD-SFEM, as it leads to the diagonal or semi-diagonal forms of the elemental characteristic inertia matrix  $\mathbf{M}_e$ . This is a very desirable feature of the GLL quadrature, which significantly simplifies numerical computations [33] in the case of dynamic or wave propagation problems.

## 10.6 Division into FEs

In FEM the computational region of interest can be conveniently divided into sub-regions taking advantage of the property of definite integrals, which allows one to split the integration interval into a finite number of sub-intervals. As a consequence, in the case of the 1-D rod under investigation having the length  $L$ , it can be formally written that:

$$\int_0^L f(x)dx = \sum_{e=1}^m \int_{L_{e-1}}^{L_e} f(x)dx \quad (10.29)$$

where  $m$  denotes the number of sub-intervals, which can also be thought of as representing finite elements (FEs). They can be of the same or different lengths,<sup>5</sup> where  $L_0 < L_1 < \dots < L_m$  with  $L_0 = 0$  and  $L_m = L$ .

The use of Eq. (10.23) allows one to transform the integral (10.29) from the global coordinate system ( $x$ ) to the local normalised coordinate system ( $\xi$ ) to obtain:

$$\int_0^L f(x)dx = \sum_{e=1}^m \int_{-1}^{+1} f(\xi) \det \mathbf{J}_e d\xi \quad (10.30)$$

where appropriate determinants of the Jacobi matrix  $\mathbf{J}_e$  [19] are:

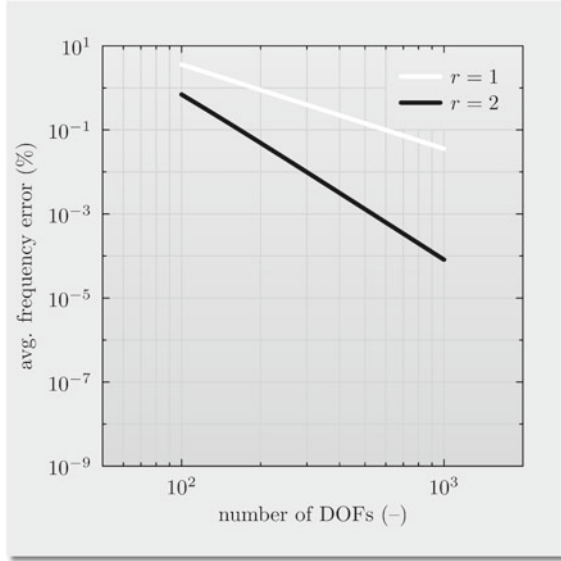
$$\det \mathbf{J}_e = \frac{L_{e-1} - L_e}{2}, \quad e = 1, 2, \dots, m \quad (10.31)$$

It is noteworthy that thanks to Eq. (10.6) the unknown function  $f(x)$  in Eq. (10.30) is expressed by  $m$  sets of shape functions  $N_n(\xi)$  of the degree of approximation polynomials  $r = p - 1$ , which are spanned over  $(p - 1)m + 1$ , or simply  $rm + 1$ , nodes rather than a single set spanned over  $p$  nodes, since it can be written that:

---

<sup>5</sup> For problems concerning high frequency dynamics or wave propagation it is usually required that FEs are uniformly distributed in space in order to minimise so-called numerical anisotropy.

**Fig. 10.4** Results of numerical computations by FEM. An average frequency error for equidistant node distributions, for different degrees of approximation polynomials, as a function of the number of DOFs of numerical models. Results according to the 1-mode 1-D theory (elementary) of the longitudinal behaviour of rods for the first 30 frequencies of free vibrations of a 10 mm diameter, 2 m long aluminium bar of free ends



$$\sum_{e=1}^m \int_{-1}^{+1} f(\xi) \det \mathbf{J}_e d\xi = \sum_{e=1}^m \sum_{n=1}^p \int_{-1}^{+1} N_n(\xi) \det \mathbf{J}_e d\xi q_{r(e-1)+n} \tag{10.32}$$

$$= \sum_{e=1}^m \sum_{n=1}^p w_n N_n(a_n) \det \mathbf{J}_e q_{r(e-1)+n}$$

As a consequence each division into sub-intervals increases the number of nodes, thus the accuracy of obtained solutions also increases and converges to the exact solution [19]. This process is clearly visible in Figs. 10.4 and 10.5 in the case of the average frequency error calculated for the 30 first frequencies of free vibrations of the rod under consideration, calculated according to Eq. (2.68), when the error is expressed as a function of the number of DOFs<sup>6</sup> of rod numerical models.

The use of Eq. (10.30) allows one to express the characteristic stiffness matrix  $\mathbf{K}$  and the characteristic inertial matrix  $\mathbf{M}$  as well as the vector of external forces  $\mathbf{F}$  as follows:

$$\mathbf{K} = \sum_{e=1}^m \mathbf{K}_e, \quad \mathbf{M} = \sum_{e=1}^m \mathbf{M}_e, \quad \mathbf{F} = \sum_{e=1}^m \mathbf{F}_e \tag{10.33}$$

where now their meaning is slightly changed. The characteristic stiffness matrix  $\mathbf{K}$  and the characteristic inertial matrix  $\mathbf{M}$ , as well as the vector of external forces  $\mathbf{F}$ ,

<sup>6</sup> In the current case only one DOF is associated with one node. As a consequence within each sub-region/finite element out of  $m$  such sub-regions/finite elements there are  $p = r + 1$  local/elemental DOFs, while within the whole region of interest there are  $(p - 1)m + 1$  or  $rm + 1$  global/total DOFs.

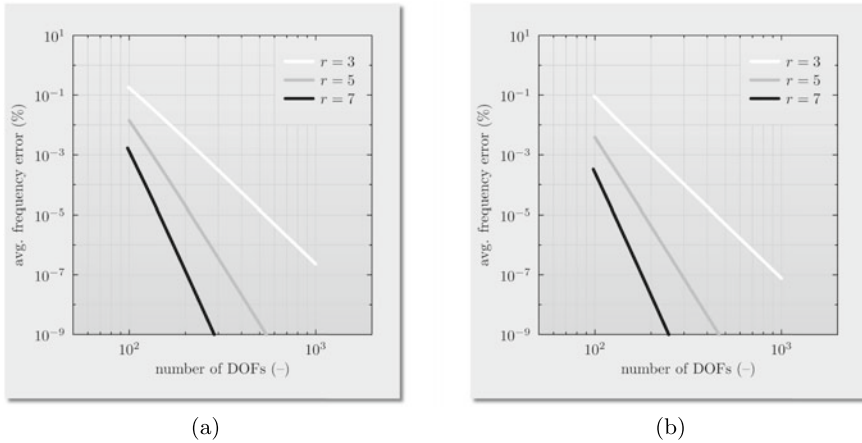


**Fig. 10.5** Results of numerical computations by TD-SFEM. An average frequency error for non-equidistant node distributions for: **a** Chebyshev nodes, **b** Lobatto nodes, for different degrees of approximation polynomials, as a function of the number of DOFs of numerical models. Results according to the 1-mode 1-D theory (elementary) of the longitudinal behaviour of rods for the first 30 frequencies of free vibrations of a 10 mm diameter, 2 m long aluminium bar of free ends

now have a global nature as they collect local/elemental shares resulting from the division of the rod into smaller sub-regions/elements. Thus, the symbols  $\mathbf{K}_e$ ,  $\mathbf{M}_e$  and  $\mathbf{F}_e$  denote the elemental characteristic stiffness and inertia matrices and the elemental vector of external forces, respectively.

Following FEM notation [19–21] general formulae for computation of the elemental characteristic stiffness matrix  $\mathbf{K}_e$ , the elemental characteristic inertia matrix  $\mathbf{M}_e$  and the vector of external forces  $\mathbf{F}_e$  can be expressed as:

$$\left\{ \begin{array}{l} \mathbf{K}_e = \iiint_{V_e} \mathbf{B}^T \mathbf{D}_e \mathbf{B} dV_e \\ \mathbf{M}_e = \iiint_{V_e} \mathbf{N}^T \rho_e \mathbf{N} dV_e \\ \mathbf{F}_e = \iiint_{V_e} \mathbf{N}^T f(x, y, z, t) dV_e \end{array} \right. , \quad e = 1, 2, \dots, m \quad (10.34)$$

where  $V_e$  denotes the volume of a particular sub-region/finite element.

At this point it should be stressed that the elegant form of summation present in Eq. (10.33) is not trivial in FEM [19–21] as it concerns two different node numbering systems: local/elemental and global, as shown in Fig. 10.6. As a result of this the summation process, known in FEM as the aggregation or assembling process, has been the subject of research for many years as it has profound consequences for numerical properties of the global characteristic matrices. Optimisation of their band

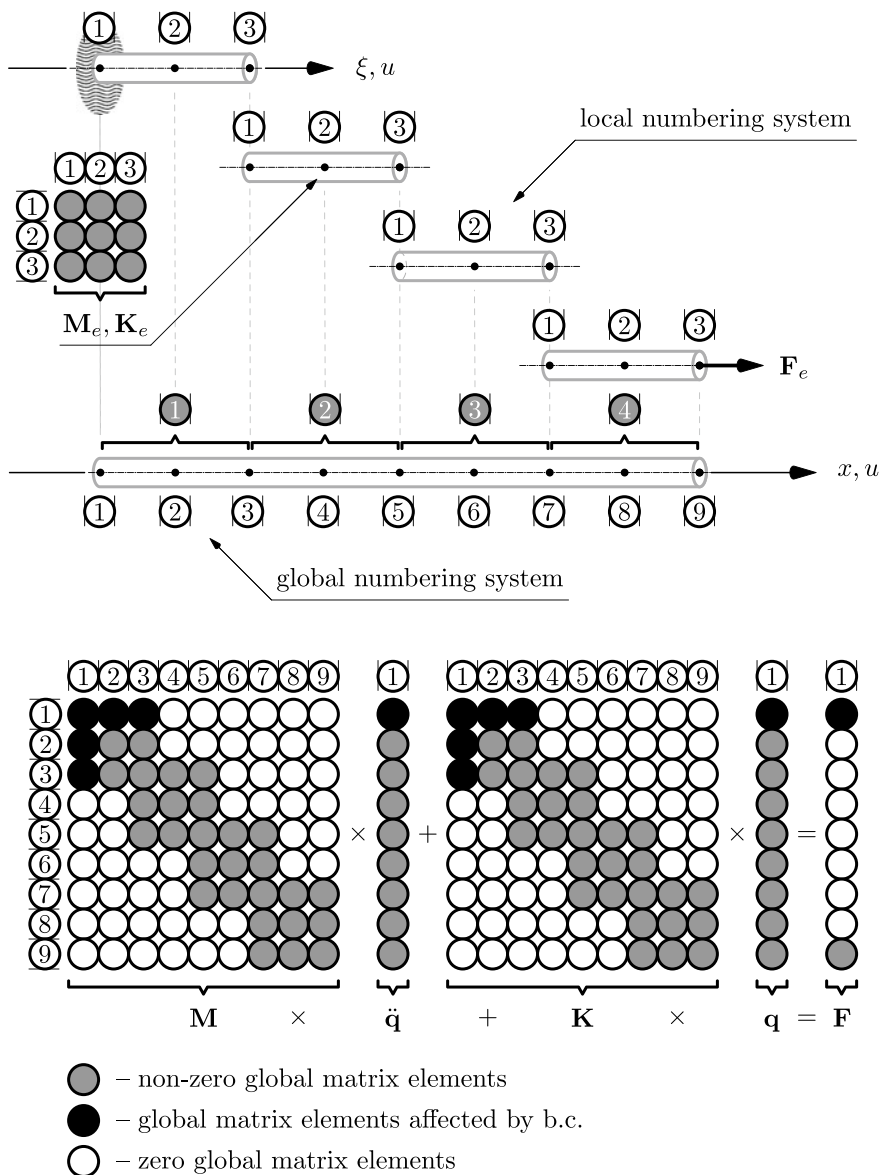


**Fig. 10.6** A concept of the discretisation and the assembling process in FEM in the case of a numerical model of 1-D bar consisting of 4 rod FEs, for degree of approximation polynomials  $r = 2$

properties resulting from the local/elemental and global numbering has a significant influence on the effectiveness and accuracy of all FEM computations. However, nowadays it has a much smaller impact as the majority of FEM packages as well as modern computation packages [27, 28] allow one to work on sparse/indexed matrices—see Appendix E.

It should also be noted here that the symbol  $\mathbf{B}$  in Eq. (10.34) denotes the matrix of the linear relationships<sup>7</sup> between strains and displacements:

$$\boldsymbol{\epsilon} = \mathbf{B}\mathbf{q}_e, \quad \boldsymbol{\epsilon} = [\epsilon_{xx}, \epsilon_{yy}, \epsilon_{zz}, \gamma_{yz}, \gamma_{zx}, \gamma_{xy}]^T \quad (10.35)$$

where the symbol  $\boldsymbol{\epsilon}$  denotes in FEM the vector of strains.<sup>8</sup> Additionally, the matrix  $\mathbf{B}$  can be expressed as:

$$\mathbf{B} = \Gamma\mathbf{N}, \quad \Gamma = \begin{bmatrix} \frac{\partial}{\partial x} & 0 & 0 & 0 & \frac{\partial}{\partial z} & \frac{\partial}{\partial y} \\ 0 & \frac{\partial}{\partial y} & 0 & \frac{\partial}{\partial z} & 0 & \frac{\partial}{\partial x} \\ 0 & 0 & \frac{\partial}{\partial z} & \frac{\partial}{\partial y} & \frac{\partial}{\partial x} & 0 \end{bmatrix}^T \quad (10.36)$$

where  $\Gamma$  is the matrix operator of linear differentiation, which in the case of 1-D rod under investigation is simply  $\Gamma = \frac{d}{dx}$  and  $\mathbf{B}(x) = \mathbf{N}'(x)$ .

The matrix  $\mathbf{D}_e$  is the matrix of linear relationships between the stress vector  $\boldsymbol{\sigma}$  and the strain vector  $\boldsymbol{\epsilon}$ :

$$\boldsymbol{\sigma} = \mathbf{D}_e\boldsymbol{\epsilon}, \quad \boldsymbol{\sigma} = [\sigma_{xx}, \sigma_{yy}, \sigma_{zz}, \tau_{yz}, \tau_{zx}, \tau_{xy}]^T \quad (10.37)$$

where the form of the matrix  $\mathbf{D}_e$  depends not only the dimension of a problem under consideration: 1-D, 2-D or 3-D, but also the type of elastic material—see Appendix B.

## 10.7 Solving Equations of Motion

Solving equations of motion takes a central position in all problems involving wave propagation in structural elements analysed by FEM. As a very important aspect of numerical investigations, appropriate solving of equations of motion remained the subject of intensive research for decades. The use of numerical solution procedures enabled researchers and scientists to investigate problems, which until the emerge of numerical solution techniques, were unreachable. This included various problems

<sup>7</sup> In general, the relationship between strains and displacements can be non-linear. Then a different definition of the matrix  $\mathbf{B}$  is used, as presented in [20], for example.

<sup>8</sup> Certainly, in other coordinate systems than the Cartesian coordinate system the strain vector  $\boldsymbol{\epsilon}$  has components of different physical meaning. The same also applies to the stress vector  $\boldsymbol{\sigma}$ .

of wave propagation not only in the case of the presence of geometrical or material non-linear behaviour, but also problems involving structural elements of complex geometries.

Numerous solution procedures were developed to solve equations of motion in the past including the methods of: central differences [34], leapfrog [35],  $\beta$ -Newmark [36],  $\theta$ -Wilson [37] as well as many other specialised methods developed and employed for exclusive use by numerous commercial FEM packages [38]. However, two of them are of special importance and interest. The first one is the explicit method of central difference and the second is the implicit  $\beta$ -Newmark method, also known in the literature as the Newmark method or the  $\beta$ -method.

At this point it should be remembered that in general solution schemes can be explicit or implicit ones. Explicit solution schemes are those that are based on the assumption that the current state of structural dynamics can be fully described by the knowledge of its past state, whereas implicit solution schemes ignore this assumption. Instead, they assume that the current state of structural dynamic results from its past and present states, which leads to the necessity of solving of some specific equations.

The central difference scheme is one of many schemes employed by the finite difference method (FDM), which is a numerical technique used for solving partial differential equations by the use of the differential operators. It is interesting to note that as such the method was already known to Euler and further developed by Runge.<sup>9</sup>

Now, a good starting point can be provided by the equations of motion, expressed by Eq. (10.15), written for discrete moments in time  $t$ . Moreover, this time these equations are formulated at the level of the global characteristic matrices and supplemented by a dissipation term expressed by the global damping matrix  $\mathbf{C}$ , presented below in a slightly modified form:

$$\mathbf{M}\ddot{\mathbf{q}}_t + \mathbf{C}\dot{\mathbf{q}}_t + \mathbf{K}\mathbf{q}_t = \mathbf{F}_t \quad (10.38)$$

where discrete dependence on time  $t$  is explicitly noted for the vectors of nodal accelerations  $\ddot{\mathbf{q}}_t$ , velocities  $\dot{\mathbf{q}}_t$  and displacements  $\mathbf{q}_t$  as well as forces  $\mathbf{F}_t$ .

In the central difference method the vector of nodal acceleration  $\ddot{\mathbf{q}}_t$  and the vector of nodal velocities  $\dot{\mathbf{q}}_t$  are approximated by the well-known finite difference central stencils [39]:

$$\begin{cases} \dot{\mathbf{q}}_t = \frac{\mathbf{q}_{t+\Delta t} - \mathbf{q}_{t-\Delta t}}{2\Delta t} + O(\Delta t^2) \\ \ddot{\mathbf{q}}_t = \frac{\mathbf{q}_{t+\Delta t} - 2\mathbf{q}_t + \mathbf{q}_{t-\Delta t}}{\Delta t^2} + O(\Delta t^2) \end{cases} \quad (10.39)$$

where  $\Delta t$  denotes a time step resulting from the discretisation of the time interval of analysis  $T$  into a number of equidistant moments in time, for which a numerical

---

<sup>9</sup> Carl David Tolmé Runge (1856–1927) was a German scientist, a professor of mathematics at the University of Hanover. His indisputable input in mathematics, especially numerical computations, include the famous Runge-Kutta method used nowadays for solving partial differential equations numerically. Apart from mathematics his scientific interests also included physics and spectroscopy.

solution to the equations of motion is sought, while the truncation error  $O(\Delta t^2)$  is proportional to the square of the time step  $\Delta t$ .

Substitution of Eq. (10.39) into the equations of motion, given by Eq. (10.38), leads to the following relationships:

$$\begin{cases} \left(\frac{\mathbf{M}}{\Delta t^2} + \frac{\mathbf{C}}{2\Delta t}\right) \mathbf{q}_{t+\Delta t} \cong \mathbf{R}_t \\ \mathbf{R}_t = \mathbf{F}_t - \left(\mathbf{K} - \frac{2\mathbf{M}}{\Delta t^2}\right) \mathbf{q}_t - \left(\frac{\mathbf{M}}{\Delta t^2} - \frac{\mathbf{C}}{2\Delta t}\right) \mathbf{q}_{t-\Delta t} \end{cases} \quad (10.40)$$

which can be easily expressed in the form of an algorithm presented below in Table 10.1 and where  $\mathbf{R}_t$  represents the vector of effective loads.

**Table 10.1** The algorithm for solution of equations of motion by the explicit method of central differences for the consistent forms of the global inertia matrix  $\mathbf{M}$  and the global damping matrix  $\mathbf{C}$

	Preliminary operations
1.	Assembling the characteristic matrices: stiffness $\mathbf{K}$ , damping $\mathbf{C}$ and inertia $\mathbf{M}$
2.	Initialisation of the vectors of nodal: displacements $\mathbf{q}_0$ , velocities $\dot{\mathbf{q}}_0$ and accelerations $\ddot{\mathbf{q}}_0$
3.	Selection of the time step $\Delta t$ as resulting from time discretisation
4.	Computation of auxiliary coefficients $a_0 = \frac{1}{\Delta t^2}$ , $a_1 = \frac{1}{2\Delta t}$ , $a_2 = 2a_0$ , $a_3 = \frac{1}{a_2}$
5.	Determination (if necessary) of the vector of nodal displacements $\mathbf{q}_{-\Delta t}$ as $\mathbf{q}_{-\Delta t} = \mathbf{q}_0 - \dot{\mathbf{q}}_0\Delta t + a_3\ddot{\mathbf{q}}_0$
6.	Computation of the global effective inertia matrix $\tilde{\mathbf{M}}$ as $\tilde{\mathbf{M}} = a_0\mathbf{M} + a_1\mathbf{C}$
7.	Triangularisation of the global effective inertia matrix $\tilde{\mathbf{M}}$ from $\tilde{\mathbf{M}} = \mathbf{LDL}^T$
<i>Computations on a typical time step <math>\Delta t</math></i>	
8.	Computation of the vector of effective nodal loads $\mathbf{R}_t$ as $\mathbf{R}_t = \mathbf{F}_t - (\mathbf{K} - a_2\mathbf{M})\mathbf{q}_t - (a_0\mathbf{M} - a_1\mathbf{C})\mathbf{q}_{t-\Delta t}$
9.	Solving a system of linear algebraic equations to find the vector of nodal displacements $\mathbf{q}_{t+\Delta t}$ from $\mathbf{LDL}^T\mathbf{q}_{t+\Delta t} = \mathbf{R}_t$
10.	Computation (if necessary) of the vectors of nodal velocities $\dot{\mathbf{q}}_t$ and accelerations $\ddot{\mathbf{q}}_t$ as $\dot{\mathbf{q}}_t = a_1(\mathbf{q}_{t+\Delta t} - \mathbf{q}_{t-\Delta t})$ $\ddot{\mathbf{q}}_t = a_0(\mathbf{q}_{t+\Delta t} - 2\mathbf{q}_t + \mathbf{q}_{t-\Delta t})$

**Table 10.2** The algorithm for solution of equations of motion by the implicit  $\beta$ -Newmark method for the consistent forms of the global inertia matrix  $\mathbf{M}$  and the global damping matrix  $\mathbf{C}$ 

Preliminary operations	
1.	Assembling the characteristic matrices: stiffness $\mathbf{K}$ , damping $\mathbf{C}$ and inertia $\mathbf{M}$
2.	Initialisation of the vectors of nodal: displacements $\mathbf{q}_0$ , velocities $\dot{\mathbf{q}}_0$ and accelerations $\ddot{\mathbf{q}}_0$
3.	Selection of the time step $\Delta t$ as resulting from time discretisation
4.	Computation of auxiliary coefficients $a_0 = \frac{1}{\beta\Delta t^2}$ , $a_1 = \frac{1}{\beta\Delta t}$ , $a_2 = \frac{1}{2\beta} - 1$ , $a_3 = \frac{\alpha}{\beta\Delta t}$ $a_4 = \frac{\alpha}{\beta} - 1$ , $a_5 = \left(\frac{\alpha}{2\beta} - 1\right)\Delta t$ , $a_6 = (1 - \alpha)\Delta t$ , $a_7 = \alpha\Delta t$
5.	Computation of the global effective stiffness matrix $\tilde{\mathbf{K}}$ as $\tilde{\mathbf{K}} = \mathbf{K} + a_0\mathbf{M} + a_1\mathbf{C}$
6.	Triangularisation of the global effective stiffness matrix $\tilde{\mathbf{K}}$ from $\tilde{\mathbf{K}} = \mathbf{LDL}^T$
<i>Computations on a typical time step <math>\Delta t</math></i>	
7.	Computation of the vector of effective nodal loads $\mathbf{R}_{t+\Delta t}$ as $\mathbf{R}_{t+\Delta t} = \mathbf{F}_{t+\Delta t} + \mathbf{M}(a_0\mathbf{q}_t + a_1\dot{\mathbf{q}}_t + a_2\ddot{\mathbf{q}}_t)$ $+ \mathbf{C}(a_3\mathbf{q}_t + a_4\dot{\mathbf{q}}_t + a_5\ddot{\mathbf{q}}_t)$
8.	Solving a system of linear algebraic equations to find the vector of nodal displacements $\mathbf{q}_{t+\Delta t}$ from $\mathbf{LDL}^T\mathbf{q}_{t+\Delta t} = \mathbf{R}_{t+\Delta t}$
9.	Computation of the vectors of nodal velocities $\dot{\mathbf{q}}_{t+\Delta t}$ and accelerations $\ddot{\mathbf{q}}_{t+\Delta t}$ as $\dot{\mathbf{q}}_{t+\Delta t} = \dot{\mathbf{q}}_t + a_6\ddot{\mathbf{q}}_t + a_7\ddot{\mathbf{q}}_{t+\Delta t}$ $\ddot{\mathbf{q}}_{t+\Delta t} = a_0(\mathbf{q}_{t+\Delta t} - \mathbf{q}_{t-\Delta t}) - a_1\dot{\mathbf{q}}_t - a_2\ddot{\mathbf{q}}_t$

It is clear that in the case of diagonal<sup>10</sup> forms of the global inertia matrix  $\mathbf{M}$  and the global damping matrix  $\mathbf{C}$  the algorithm presented in Table 10.1 can be significantly simplified, which usually takes place for FEs whose definition is based on Lobatto nodes.

Such an approach allows one to significantly decrease the time of computations or alternatively to improve the accuracy of these computations at a relatively low cost for an increased number of FEs. However, it should be emphasised that the explicit method of central differences is conditionally stable and appropriate time discretisation is of great importance.

It can be easily checked in the literature [19] that the critical time step  $\Delta t$  in the case of the method of central difference is  $\Delta t \leq 2/\omega_{max}$  in order to guarantee its stability, where  $\omega_{max}$  is the maximum angular frequency associated with a given

<sup>10</sup> Typically, the form of the characteristic inertia matrix  $\mathbf{M}$  can be consistent (all or nearly all elements are non-zero) or diagonal/lumped (only diagonal elements are non-zero). It results from the assumed type of numerical integration: the Gauss quadrature leads to its consistent form, while the Lobatto quadrature to its diagonal form, or additional requirements, which make it necessary to diagonalise the characteristic inertia matrix  $\mathbf{M}$  through the process called lumping, well known in FEM.



numerical model/spatial discretisation. This condition is very difficult to satisfy, so in computational practice much larger time steps are used.

Because numerical errors tend to build up on each time step very slowly and the truncation error  $O(\Delta t^2)$  is proportional to the square of the time step, these features allows one to use the method of central difference effectively for various time dependent problems. Its higher-order modifications offer even greater accuracy at similar computational costs [40] and can be used in the case where such accuracy is required.

In the case when the time interval of the analysis  $T$  is great, which could lead to unreasonably small time steps  $\Delta t$  in order to obtain numerical solutions, the method of central differences can be replaced by a method much more effective in that respect, developed by Newmark [36], the algorithm of which is presented in Table 10.2. The  $\beta$ -Newmark method is based on a simple assumption that changes in the vectors of nodal displacements  $\mathbf{q}_{t+\Delta t}$  and velocities  $\dot{\mathbf{q}}_{t+\Delta t}$  over a single time step  $\Delta t$  depend simultaneously on the vectors of nodal accelerations at the beginning  $\ddot{\mathbf{q}}_t$  and end  $\ddot{\mathbf{q}}_{t+\Delta t}$  of this time step, which can be expressed as:

$$\begin{cases} \dot{\mathbf{q}}_{t+\Delta t} = \dot{\mathbf{q}}_t + (1 - \alpha)\ddot{\mathbf{q}}_t \Delta t + \alpha\ddot{\mathbf{q}}_{t+\Delta t} \Delta t \\ \mathbf{q}_{t+\Delta t} = \mathbf{q}_t + \dot{\mathbf{q}}_t \Delta t + \left(\frac{1}{2} - \beta\right)\ddot{\mathbf{q}}_t \Delta t^2 + \beta\ddot{\mathbf{q}}_{t+\Delta t} \Delta t^2 \end{cases} \quad (10.41)$$

where  $\alpha$  and  $\beta$  are certain parameters, which indicate what the proportions of this dependence are.

The values of the parameters  $\alpha$  and  $\beta$  are of great importance for the quality and accuracy of the result of numerical computations obtained by the use of the  $\beta$ -Newmark method [20]. In computational practice the value of the  $\alpha$  parameter is usually taken as  $\alpha = 1/2$ , while in the case of the  $\beta$  parameter as  $\beta = 1/4$ , which guarantee unconditional stability of the method. If the value of the  $\alpha$  parameter is greater than  $1/2$ , i.e.  $\alpha > 1/2$ , some artificial damping is introduced, which sometimes may have positive effects on the quality of numerical results. On the other hand, when  $\alpha = 1/2$  and  $\beta = 0$  the implicit  $\beta$ -Newmark method becomes the explicit method of central differences. In general, for  $\beta = 1/4$  the average constant value of acceleration over a single time step  $\Delta t$  is obtained, for  $\beta = 1/6$  the change in acceleration is linear, while for  $\beta = 1/8$  it is stepped.

At this point it should be strongly emphasised that apart from the time discretisation process there is the process of space discretisation, which is also of great importance, especially where high accuracies are expected and high frequency dynamics and/or wave propagation problems are investigated. There is a strong correlation between the space and time discretisation in the case of time dependent problems. Depending on the type of excitation and its frequency content as well as application domain different rules are reported in the literature [41], which suggest that the number of nodal distances per wavelength in the case of the classical FEM can be as small as 4 or 5 [42] or as great as 18 [43].

## References

1. F. Moser, L. J. Jacobs, and J. Qu. Modeling elastic wave propagation in waveguides with the finite element method. *NDT&E International*, 32:225–234, 1999.
2. T. Belytschko, R. Gracie, and G. Ventura. A review of extended/generalized finite element methods for material modelling. *Modelling and Simulation in Materials Science and Engineering*, 17:1–24, 2009.
3. M. Mirta and S. Gopalakrishnan. Guided wave based structural health monitoring: A review. *Smart Materials and Structures*, 25:1–27, 2016.
4. A. Hrennikoff. Solution of problems of elasticity by the framework method. *Journal of Applied Mechanics*, 8:169–175, 1941.
5. A. Hrennikoff. Framework method and its technique for solving plane stress problems. *International Association for Bridge and Structural Engineering Publications*, 9:217–248, 1949.
6. R. Courant. *On a method for the solution of boundary-value problems*. in: Theodore von Kármán Anniversary Volume. University of Michigan, 1941.
7. R. Courant. Variational methods for the solution of problems of equilibrium and vibrations. *Bulletin of the American Mathematical Society*, 49:1–23, 1943.
8. J. H. Argyris and D. W. Scharpf. Finite elements in time and space. *Nuclear Engineering and Design*, 10:456–464, 1969.
9. J. H. Argyris, H. Balmer, J. S. Doltsinis, P. C. Dunne, M. Haase, M. Kleiber, G. A. Melejannakis, H. P. Mlejnek, M. Müller, and D. W. Scharpf. Finite element method – natural approach. *Computer Methods in Applied Mechanics and Engineering*, 17:1–106, 1979.
10. O. C. Zienkiewicz, D. W. Kelly, and P. Bettess. Reduced integration technique in general analysis of plates and shells. *International Journal for Numerical Methods in Engineering*, 3:275–290, 1971.
11. O. C. Zienkiewicz, D. W. Kelly, and P. Bettess. Coupling of finite element method and boundary solution procedures. *International Journal for Numerical Methods in Engineering*, 11:355–375, 1977.
12. P. G. Ciarlet and C. Wagschal. Multipoint Taylor formulas and applications to the finite element method. *Numerische Mathematik*, 17:84–100, 1971.
13. P. G. Ciarlet and P. A. Raviart. General Lagrange and Hermite interpolation in  $R^n$  with applications to finite element methods. *Archive for Rational Mechanics and Analysis*, 46:178–198, 1972.
14. R. H. Gallagher and R. H. Mallett. Efficient solution processes for finite element analysis of transient heat conduction. *Journal of Heat Transfer*, 93:257–263, 1971.
15. R. H. Gallagher. The finite element method in shell stability analysis. *Computers & Structures*, 3:543–557, 1973.
16. I. Babuška and M. Suri. Locking effects in the finite element approximation of elasticity problems. *Numerische Mathematik*, 62:439–463, 1992.
17. I. Babuška, J. R. Whiteman, and T. Strouboulis. *Finite elements: An introduction to the method of error estimation*. Oxford University Press, Oxford, 2011.
18. J. T. Oden and J. N. Reddy. *An introduction to the mathematical theory of finite elements*. Wiley, New York, 1976.
19. O. C. Zienkiewicz. *The finite element method*. McGraw-Hill Book Company, London, 1989.
20. W. Ostachowicz, P. Kudela, M. Krawczuk, and A. Żak. *Guided waves in structures for SHM. The time-domain spectral element method*. John Wiley & Sons Ltd., Singapore, 2012.
21. S. S. Rao. *The finite element method in engineering*. Pergamon Press, Oxford, 1981.
22. F. Ihlenburg. *Finite element analysis of acoustic scattering*. Springer, New York, 1998.
23. J. Przemieniecki. *Finite element structural analysis*. AIAA, Reston, 2009.
24. A. Żak and W. Waszkowiak. A spline-based FE approach to modelling of high frequency dynamics of 1-d structures. *Computers & Mathematics with Applications*, 104:14–33, 2021.
25. M. Krawczuk, W. Ostachowicz, and A. Żak. Modal analysis of cracked, unidirectional composite beam. *Composites Part B: Engineering*, 28:641–650, 1997.

26. M. Krawczuk, W. Ostachowicz, and A. Żak. Dynamics of cracked composite material structures. *Computational Mechanics*, 20:79–83, 1997.
27. <http://www.mathworks.com>.
28. <http://www.wolfram.com>.
29. A. Żak and M. Krawczuk. Certain numerical issues of wave propagation modelling in rods by the Spectral Finite Element Method. *Finite Elements in Analysis and Design*, 47:1036–1046, 2011.
30. J. P. Boyd. *Chebyshev and Fourier spectral methods*. Dover Publications, Inc., New York, 2000.
31. A. Ralston and P. Rabinowitz. *A first course in numerical analysis*. Dover Publications, Inc., New York, 2001.
32. X. Chen, S. Yang, J. Ma, and Z. He. The construction of wavelet finite element and its application. *Finite Elements in Analysis and Design*, 40:541–554, 2004.
33. D. Komatitsch and J. Tromp. Introduction to the spectral element method for three-dimensional seismic wave propagation. *Geophysical Journal International*, 139:806–822, 1999.
34. R. C. Swanson and E. Turkel. On central-difference and upwind schemes. *Journal of Computational Physics*, 101:292–306, 1992.
35. P. Hut, J. Makino, and S. McMillan. Building a better leapfrog. *Astrophysical Journal*, 443:L93–L96, 1995.
36. N. M. Newmark. A method for computation for structural dynamics. *Journal of the Engineering Mechanics Division*, 85:67–94, 1959.
37. E. L. Wilson and R. W. Clough. Dynamic response by step-by-step matrix analysis. *Laboratório Nacional de Engenharia Civil, Lisbon–Portugal: Symposium on the Use of Computers in Civil Engineering*, 1:1–14, 1-5 October 1962.
38. T. Belytschko. A survey of numerical methods and computer programs for dynamic structural analysis. *Nuclear Engineering and Design*, 37:23–34, 1976.
39. B. Fornberg. Generation of finite difference formulas on arbitrarily spaced grids. *Mathematics of Computation*, 51:699–706, 1988.
40. A. Asmus and R. Lammering. Actual time integration methods for elastic wave propagation analysis. *Proceedings in Applied Mathematics and Mechanics*, 14:857–858, 2014.
41. N. M. Papadakis and G. E. Stavroulakis. Effect of mesh size for modeling impulse responses of acoustic spaces via Finite Element Method in Time Domain. *Euronoise 2018 Proceedings*, 1:323–329, 2018.
42. T. Łodygowski and W. Sumelka. Limitations in application of finite element method in acoustic numerical simulation. *Journal of Theoretical and Applied Mechanics*, 44:849–865, 2006.
43. G. L. Wojcik, D. K. Vaughan, J. Mould Jr., F. A. Leon, Q. D. Quian, and M. A. Lutz. Laser alignment modeling using rigorous numerical simulations. *SPIE Proceedings: Optical/Laser Microlithography IV*, 1463:292–303, 1991.

# Chapter 11

## Waves in Unbounded Structures



### 11.1 Infinite Versus Finite

Despite their infinite dimensions propagation of elastic waves in unbounded engineering structures can be successfully analysed by the use of FEM [1]. This can be achieved by numerous computational techniques, which can be employed for this purpose and which are able to mimic the properties of unbounded structures. The primary and main feature of these techniques is their ability to simulate the process of diffusion of propagating waves, which allows the wave energy to be transferred from the region of interest out to infinity with no reflections, conforming with *the Sommerfeld radiation condition* [2].

It should be noted that many engineering structures may be considered as unbounded. A good example of such structures represent railways, shown in Fig. 11.1, since their longitudinal dimension can be considered as many, many times greater than the remaining transverse dimensions. The same applies to various pipeline systems or truss structures known from their use in bridges. In each of these cases, however, the analysis of wave propagation by the use of FEs demands a special approach, as it must take into account a very specific behaviour of elastic waves propagating within these structures, which comes from their freedom to diffuse with no reflections.

This is a very strong requirement, which makes such analysis computationally demanding, especially if a so-called direct approach is used, when local responses of infinite structures are simply approximated by local responses calculated for enlarged FE models, but still in the finite space [4–6]. This approach can be understood as the use of FEM in the case of an appropriately selected large sections of the original unbounded structures, which can be assumed as a good representation of the required part of the structures under consideration. This simple approach can be correct as long as the wave propagation analysis is carried out for a period of time, which guarantees no reflections of propagating waves from existing boundaries,

**Fig. 11.1** Railways are a good example of engineering structures, which can be regarded as unbounded for propagation of elastic waves [3]



which could influence local responses of interest. Unfortunately, very often such an approach requires impractically large numerical models consisting of many FEs in order to comprise with the process of space discretisation, which additionally must conform with the requirement of providing the sufficient number of nodal distances per wavelength due to scale factors, as mentioned previously in Sect. 10.7. However, there are other solutions to this problem known and reported in the literature.

## 11.2 Treatment of Unwanted Boundary Reflections

In general, there exists three general approaches in FEM,<sup>1</sup> which can be successfully employed for treating unwanted boundary reflections in order to mimic the properties of unbounded structures.

The first and the most intuitive approach is the application of specially modified FEs with their shape functions defined over infinite regions. This can be computationally considered as extending some of their boundaries to infinity, which in fact makes them infinite elements [10–12]. This approach comes useful and effective in solving various static and dynamics problems, however, its direct use for problems related to propagation of elastic waves in elements of structures becomes difficult and ineffective. This is because in this formulation the characteristic matrices appear as wave number dependent, which makes this approach impractical in the case of the analysis of propagation of wave packets, since they represent non-monochromatic signals composed of many harmonic components.

---

<sup>1</sup> The boundary integral method, also known as the Boundary Element Method (BEM), is a close FEM cousin, which was also successfully employed for solving problems related to wave propagation in unbounded media [7–9].

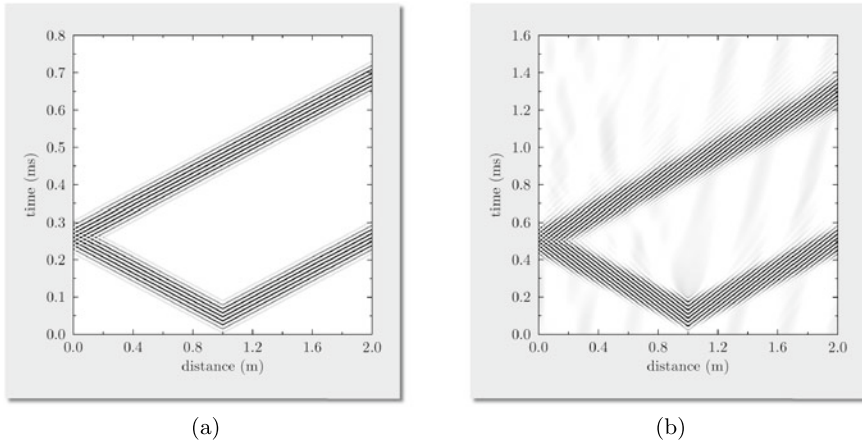


**Fig. 11.2** Wave propagation patterns for: **a** the longitudinal displacement component  $u_x$  for the 1-mode 1-D theory (elementary) of rods, **b** for the radial displacement component  $u_r$ , for the 2-mode 1-D theory (Timoshenko) of beams, obtained for a 10mm diameter semi-infinite aluminium bar. Results of numerical computations by FD-SFEM with NRBCs at infinity modelled by throw-off FEs

The second and very interesting solution to this problem is a formulation, in which a similar approach is used, but taking advantage of the discrete Fourier transform [13–15], which transforms the space and time domains into the wave number<sup>2</sup> and frequency domains. The application of a computationally effective discrete fast Fourier transform (FFT) combined with a new class of boundary FEs, so-called throw-off elements, mimicking the existence of structural boundaries at infinity, makes this FE approach, better known in the literature as FD-SFEM, very powerful and effective. Despite its unquestionable advantages FD-SFEM turns out to be limited to simple 1-D or 2-D geometries as well as simple 1-D or 2-D theories of the dynamic behaviour of structural elements [16–18], as presented in Fig. 11.2.

The third and very effective approach is the application of so-called non-reflective boundary conditions (NRBCs) as a numerical technique, in which some extra variables are used in order to obtain structural responses conforming with *the Sommerfeld radiation condition* [2], for these structural boundaries, which extend to infinity [19–21]. Although this approach can be combined with the classical FEM, it requires some modifications to the standard FEM solution procedures, in which the original equations of motion are supplemented with an additional integral term depending on the assumed properties of the non-reflective boundaries. For this reason its practical use stays limited to rather specific cases and as such in time the approach gave way to a new method, known as the absorbing layer method.

<sup>2</sup> In physics the resulting space of the Fourier transform of a spatial function is often called the reciprocal space or just  $k$ -space.

The fourth approach, the absorbing layer method, in fact represents two numerical techniques, these being: the perfectly matched layer (PML) and the absorbing layer with increasing damping (ALID), which can be much better integrated with FEM than those previously mentioned.

The concept of PML is based on the assumption that within PML the space coordinates and their derivatives have a new definition, according to which they become frequency dependent [22]. In the case of the coordinate  $x$  being transformed within PML to a new coordinate  $\xi$  it can be formally written that:

$$x = \xi + i\alpha(\xi) \quad \text{with} \quad \alpha(\xi) = \frac{1}{\omega} \int_0^{\xi} \beta(\eta) d\eta \quad (11.1)$$

where the derivative with respect to the coordinate  $x$  can be now expressed as:

$$\frac{\partial}{\partial x} = \frac{\partial}{\partial \xi} \frac{\partial \xi}{\partial x} = \frac{\partial}{\partial \xi} \left[ 1 + \frac{i h(\xi)}{\omega} \right]^{-1} \quad (11.2)$$

where  $\alpha(\xi)$  and  $\beta(\xi)$  represent certain unknown smooth functions having the following properties:

$$\alpha(0) = \beta(0) = 0, \quad \text{and} \quad \alpha(1) = \beta(1) = 1 \quad (11.3)$$

where  $\xi = 0$  corresponds to PML-structure interface, while  $\xi = 1$  to the full depth of the layer, which functions are responsible for wave attenuation within PML for wave numbers  $k > 0$  and space coordinates  $\xi > 0$ .

It can be easily noted that according to such a definition a monochromatic wave  $Ae^{i(kx - \omega t)}$  propagating in the positive direction of the  $x$  axis is attenuated after entering PML since the following relationship is satisfied within the layer:

$$\begin{aligned} Ae^{i(kx - \omega t)} &= Ae^{ikx} e^{-i\omega t} = Ae^{ik[\xi + i\alpha(\xi)]} e^{-i\omega t} \\ &= Ae^{ik\xi} e^{-k\alpha(\xi)} e^{-i\omega t} = e^{-k\alpha(\xi)} Ae^{i(k\xi - \omega t)} \end{aligned} \quad (11.4)$$

as long as the attenuation function  $\alpha(\xi)$  is positive.

The application of PML extends to various problems related to: electromagnetism [23–25], seismology [26–28], acoustics [29–31] as well as the propagation of elastic waves [32–34]. Although it is reported in the literature that the use of PML offers better computational properties and higher accuracy in terms of damping properties than the use of ALID, its full integration with the classical FEM approach becomes cumbersome. This is due to the inherent property of PML, which lies in the frequency dependence of the attenuation function  $\alpha(\xi)$ , which results in the necessity to seek for solutions using implicit solvers in the frequency domain rather than in the time domain [22].

Contrary to PML the use of ALID is very flexible in this respect and free of such additional requirements. The concept of ALID, which can be dated to early 1980s, is based on a simple assumption that the absorbing properties of ALID result purely from the damping properties of the medium, which is assumed to increase with the depth of the layer [35]. This is explained in detail in the next Sect. 11.3.

### 11.3 Absorbing Layer with Increasing Damping

Because of its definition the use of ALID can be much easier integrated with FEM [22] including numerous FEM packages available commercially.

In the case of FEM the damping properties of ALID can be easily expressed by the characteristic global damping matrix  $\mathbf{C}$ , which typically are represented as a linear combination of the characteristic global inertia matrix  $\mathbf{M}$  and the global stiffness matrix  $\mathbf{K}$  as:

$$\mathbf{C} = \alpha(x)\mathbf{M} + \beta(x)\mathbf{K} \quad (11.5)$$

where  $\alpha(x)$  and  $\beta(x)$  represents unknown smooth attenuation functions having the following properties:

$$\alpha(0) = \beta(0) = 0, \quad \text{and} \quad \alpha(L) = \beta(L) = 1 \quad (11.6)$$

with  $L$  denoting the depth of ALID.

As before a monochromatic wave  $\mathbf{q}(t) = \hat{\mathbf{q}} e^{i(kx - \omega t)}$  propagating in the positive direction of the  $x$  axis, resulting from the monochromatic excitation  $\mathbf{F}(t) = \hat{\mathbf{F}} e^{i(kx - \omega t)}$ , can be assumed. Thanks to this the equations of motion presented below:

$$\mathbf{M}\ddot{\mathbf{q}}(t) + \mathbf{C}\dot{\mathbf{q}}(t) + \mathbf{K}\mathbf{q}(t) = \mathbf{F}(t) \quad (11.7)$$

where the well-known relationships are employed:

$$\dot{\mathbf{q}}(t) = -i\omega\hat{\mathbf{q}} e^{i(kx - \omega t)}, \quad \ddot{\mathbf{q}}(t) = -\omega^2\hat{\mathbf{q}} e^{i(kx - \omega t)} \quad (11.8)$$

can be expressed as the equations of equilibrium in the frequency domain, since they have to be satisfied for a given angular frequency  $\omega$  independently of time  $t$ :

$$-\omega^2\mathbf{M}\hat{\mathbf{q}} - i\omega\mathbf{C}\hat{\mathbf{q}} + \mathbf{K}\hat{\mathbf{q}} = \hat{\mathbf{F}} \quad (11.9)$$

Now, the resulting equilibrium equations, expressed by Eq. (11.9) in the frequency domain, can be modified by taking advantage of the assumed form of the characteristic global damping matrix  $\mathbf{C}$ , given by Eq. (11.5). Thanks to this it can be written that:

$$-\left[1 + \frac{i\alpha(x)}{\omega}\right]\omega^2\mathbf{M}\hat{\mathbf{q}} + [1 - i\omega\beta(x)]\mathbf{K}\hat{\mathbf{q}} = \hat{\mathbf{F}} \quad (11.10)$$



It can be immediately noted that within ALID the material density  $\rho$  as well as material Young's modulus  $E$  may be interpreted as frequency dependent since:

$$\rho(\omega) = \rho \left[ 1 + \frac{i\alpha(x)}{\omega} \right], \quad E(\omega) = E[1 - i\omega\beta(x)] \quad (11.11)$$

Finally, taking into account the fact that the wave number  $k$  associated with the given monochromatic wave, being proportional to the square root of the material density  $\rho$  and inversely proportional to Young's modulus  $E$ , can also be expressed as frequency dependent [1]:

$$k(\omega) \propto \omega \sqrt{\frac{\rho(\omega)}{E(\omega)}} = \omega \sqrt{\frac{\rho}{E} \sqrt{a(x) + ib(x)}} \rightarrow k_{1,2} = \pm(k' + ik'') \quad (11.12)$$

where  $\pm k'$  and  $\pm k''$  denote the real and imaginary parts of the roots  $k_{1,2}$  and where:

$$a(x) = \frac{1 - \alpha(x)\beta(x)}{1 + \omega^2\beta^2(x)}, \quad b(x) = \frac{\alpha(x) + \omega^2\beta(x)}{\omega[1 + \omega^2\beta^2(x)]} \quad (11.13)$$

A careful examination of these roots allows one to check that the first root  $k_1$  has its real and imaginary parts  $k'$  and  $k''$  always positive, while the second root  $k_2 = -k_1$  always negative.<sup>3</sup> For this reason the second root can be disregarded as a consequence of the assumed direction of wave propagation within ALID in the positive direction of the  $x$  axis.

As a final step the variation of the unknown smooth attenuation functions  $\alpha(x)$  and  $\beta(x)$  must be selected in order to obtain desired properties of ALID. According to [1, 22, 36] the most desirable form for these functions are power expressions, which can be assumed as:

$$\alpha(x) = \alpha x^p, \quad \beta(x) = \beta x^q, \quad \text{with } p, q > 0 \quad (11.14)$$

where  $\alpha$  and  $\beta$  are certain constants.

It should be emphasised that the constant value of  $\alpha$  and  $\beta$  leads to the frequency dependence of the attenuation according to Eq. (11.9), which is not always desirable. In order to make the attenuation properties of ALID frequency independent it is sufficient to assume that:

$$\alpha(x) = \omega \alpha x^p, \quad \beta(x) = \frac{\beta x^q}{\omega}, \quad \text{with } p, q > 0 \quad (11.15)$$

---

<sup>3</sup> It can be observed that formally it can be assumed that  $k' + ik'' = \pm\sqrt{(a+ib)^2} = \sqrt{a^2 - b^2 + 2iab}$ , with the real and imaginary parts  $a$  and  $b$  being positive, i.e.  $a, b > 0$ . Thus, it can be further observed that the principal root of the equation  $z^2 - k^2 = 0$ , equal to  $k' + ik'' = a + ib$  must have its real and imaginary parts also positive, even if the real part of the expression under the square remains negative, i.e. even if  $a^2 - b^2 < 0$ .

which allows one to express the characteristic global damping matrix  $\mathbf{C}$  in the following form:

$$\mathbf{C} = \omega \alpha x^p \mathbf{M} + \frac{\beta x^q}{\omega} \mathbf{K} \tag{11.16}$$

As a consequence of this also the equations of equilibrium in the frequency domain are modified and can be presented as:

$$- [1 + i \alpha x^p] \omega^2 \mathbf{M} \hat{\mathbf{q}} + [1 - i \beta x^q] \mathbf{K} \hat{\mathbf{q}} = \hat{\mathbf{F}} \tag{11.17}$$

It turns out that in computational practice not only the values of the constants  $\alpha$  and  $\beta$ , but also the exponents  $p$  and  $q$  are very important. The depth of ALID is also a crucial parameter, which has a great influence on the overall effectiveness of the attenuation properties of ALID. Each time the depth of ALID should be precisely defined based on the knowledge about the excitation type and its frequency content, which on the other hand is closely correlated with the total number of modes, which can possibly participate in the calculated dynamic responses and wave motion [1, 22]. The effectiveness of ALID in the case of non-dispersive and dispersive waves is illustrated in Fig. 11.3.

For majority of cases related to the analysis in the time domain, however, a slightly modified definition of ALID comes as very useful:

$$\mathbf{C} = 10^p (\xi L)^p \left( \omega_c \mathbf{M} + \frac{\mathbf{K}}{\omega_c} \right), \quad p = 3, 4, \quad \omega_c = 2\pi f_c \tag{11.18}$$

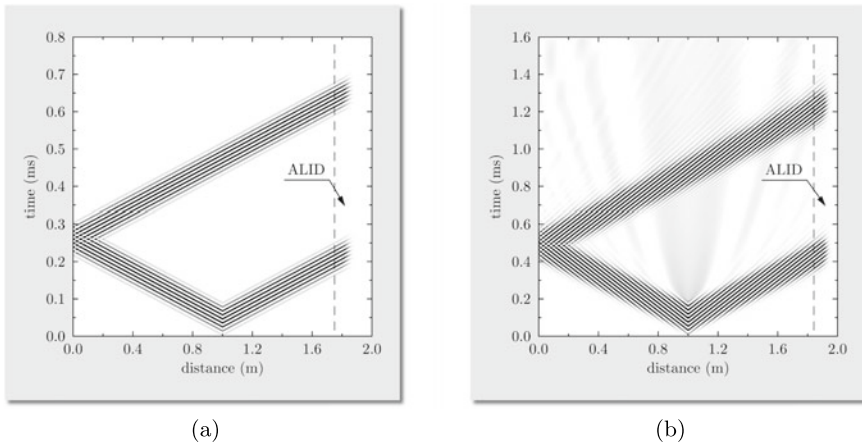


**Fig. 11.3** Wave propagation patterns for: **a** the longitudinal displacement component  $u_x$  for the 1-mode 1-D theory (elementary) of rods, **b** for the radial displacement component  $u_r$  for the 2-mode 1-D theory (Timoshenko) of beams, obtained for a 10 mm diameter semi-infinite aluminium bar. Results of numerical computations by TD-SFEM with NRBCs at infinity modelled by ALID

where now the depth of ALID  $L$  is expressed in terms of a multiple of  $n$  of a certain wavelength  $\lambda$ , i.e.  $L = n\lambda$ , while  $f_c$  denotes the carrier frequency associated with typical excitation signals having the form of a wave packet and characterised by the modulation frequency  $f_m$ .

Typically, the wavelength  $\lambda$  should be taken as associated with the longest wavelength in the frequency content of the excitation signal out of all modes available.<sup>4</sup> Bearing in mind that this content can be estimated with various precision, in the majority of cases it is sufficient to assume that the range of frequencies starting from  $f_c - 2f_m$  to  $f_c + 2f_m$  is taken for satisfactory accuracy<sup>5</sup> or alternatively starting from  $f_c - 4f_m$  to  $f_c + 4f_m$  for better results, as discussed in Sect. 2.5. In the same manner it is recommended that the multiple of  $n$  is taken as at least equal to 4, while for better results it can be increased up to 6 or even to 8. This is in slight contrast to the recommendations made in [1], when a much safer approach was used leading to unnecessary large depths of ALID and therefore large numerical models.

Finally, it should be said that the use of ALID together with the explicit method of central differences, or other explicit time integration schemes, strongly affects the stability of the scheme and reduces the useful time increment  $\Delta t$  due to very large values of damping introduced [22]. Out of two damping sources, one being proportional to the characteristic global inertia matrix  $\mathbf{M}$  and the second to the characteristic global stiffness matrix  $\mathbf{K}$ , the latter has a much more profound effect on the stability of the scheme, which leads to impractical small time steps. This can be easily avoided if this damping source is omitted. In the case of the damping proportional to the characteristic global inertia matrix  $\mathbf{M}$  this problem is not present. Moreover, it can be added that in order to take full advantage of the explicit solution method the characteristic global inertia matrix  $\mathbf{M}$  can be diagonalised or, when TD-SFEM is exploited, it may take full advantage of its existing diagonal or semi-diagonal form. The problem described above is not present, however, if the implicit  $\beta$ -Newmark method is used or other implicit methods.

At this point it is noteworthy that the concept of ALID has been extended to the reduced stiffness method (RSM) as reported in the literature [36]. Since only the damping source proportional to the characteristic global stiffness inertia matrix  $\mathbf{M}$  can be used directly, due to resulting stability problems of the explicit time integration schemes, in RSM the frequency dependence of Young's modulus from Eq. (11.11) is incorporated directly into the characteristic global stiffness matrix  $\mathbf{K}$  instead. Such an approach leads to an improved performance and effectiveness of the damping layer in comparison with ALID. However, this is achieved at additional computational cost.

---

<sup>4</sup> For this reason the use of ALID should be limited in the case of low frequency excitations, as the longest wavelength requirement may lead to impractical large depths of the layer comparable to or even larger than the characteristic length of the structure under investigation.

<sup>5</sup> This means the damping levels of approximately 40, 70 or 80 dB for displacement components, their velocities or accelerations, respectively.

## References

1. A. Žak, M. Krawczuk, Ł. Skarbek, and M. Palacz. Numerical analysis of elastic wave propagation in unbounded structures. *Finite Elements in Analysis and Design*, 90:1–10, 2014.
2. A. Sommerfeld. *Partial differential equations in physics*. Academic Press, New York, 1949.
3. <https://pixabay.com/pl/photos/torow-podroz-szyny-tory-kolejowe-3703349>, 2018. Visited on 09/12/2023.
4. L. A. Yang, W. Powrie, and J. A. Priest. Dynamic stress analysis of a ballasted railway track bed during train passage. *Journal of Geotechnical and Geoenvironmental Engineering*, 135:605–707, 2009.
5. H. Yu, Y. Yuan, Z. Qiao, Y. Gu, Z. Yang, and X. Li. Seismic analysis of a long tunnel based on multi-scale method. *Engineering Structures*, 49:572–587, 2013.
6. P. Li and E. X. Song. Three-dimensional numerical analysis for the longitudinal seismic response of tunnels under asynchronous wave input. *Computers and Geotechnics*, 63:229–243, 2015.
7. A. J. Burton and G. F. Miller. The application of integral equation methods to the numerical solution of some exterior boundary-value problems. *Proceedings of the Royal Society. Series A*, 323:201–210, 1971.
8. D. S. Jones. Integral equations for the exterior acoustic problems. *The Quarterly Journal of Mechanics and Applied Mathematics*, 27:129–141, 1973.
9. S. Amini and S. M. Kirkup. Solution of Helmholtz equation in the exterior domain by elementary boundary integral methods. *Journal of Computational Physics*, 118:208–221, 1995.
10. P. Battess. Infinite elements. *International Journal for Numerical Methods in Engineering*, 11:53–64, 1977.
11. P. Battess and O. C. Zienkiewicz. Diffraction and refraction of surface waves using finite and infinite elements. *International Journal for Numerical Methods in Engineering*, 11:1271–1290, 1977.
12. K. Gerdes. A summary of infinite element formulations for exterior Helmholtz problems. *Computer Methods in Applied Mechanics and Engineering*, 164:95–105, 1998.
13. J. F. Doyle. *Wave propagation in structures*. Springer-Verlag, Inc., New York, 1997.
14. S. A. Rizzi and J. F. Doyle. A spectral element approach to wave motion in layered solids. *Journal of Vibration and Acoustics*, 114:569–577, 1992.
15. S. Gopalakrishnan and J. F. Doyle. Spectral super-elements for wave-propagation in structures with local nonuniformities. *Computer Methods in Applied Mechanics and Engineering*, 121:79–90, 1995.
16. M. Krawczuk, M. Palacz, and W. Ostachowicz. The dynamics analysis of a cracked timoshenko beam by the spectral element method. *Journal of Sound and Vibration*, 5:1139–1153, 2003.
17. M. Krawczuk, M. Palacz, and W. Ostachowicz. Wave propagation in plane structures for crack detection. *Finite Elements in Analysis and Design*, 40:991–1004, 2004.
18. M. Palacz, M. Krawczuk, and A. Žak. Spectral element methods for damage detection and condition monitoring. *Advances in Asset Management and Condition Monitoring. Part of the SIST Book Series*, 166:549–558, 2020.
19. D. Givoli. Non-reflecting boundary conditions. *Journal of Computational Physics*, 94:1–29, 1991.
20. I. Harari and T. J. R. Hughes. Galerkin/least-squares finite element methods for the reduced wave equation with non-reflecting boundary conditions in unbounded domains. *Computer Methods in Applied Mechanics and Engineering*, 98:411–454, 1992.
21. D. Givoli. Higher-order local non-reflecting boundary conditions: A review. *Wave Motion*, 39:319–326, 2004.
22. M. B. Drozd. *Efficient finite element modelling of ultrasound waves in elastic media (Ph.D. Thesis)*. Imperial College of Science and Technology and Medicine, University of London, 2008.
23. J. P. Berenger. A perfectly matched layer for the absorption of electromagnetic waves. *Journal of Computational Physics*, 114:185–200, 1994.

24. R. Mittra. A new look at the perfectly matched layer (PML) concept for the reflectionless absorption of electromagnetic waves. *IEEE Microwave and Guided Wave Letters*, 5:84–86, 1995.
25. J. P. Berenger. Three-dimensional perfectly matched layer for the absorption of electromagnetic waves. *Journal of Computational Physics*, 127:363–379, 1996.
26. D. Komatitsch and J. Tromp. A perfectly matched layer absorbing boundary condition for the second-order seismic wave equation. *Geophysical Journal International*, 154:146–153, 2003.
27. D. Komatitsch and R. Martin. An unsplit convolutional perfectly matched layer improved at grazing incidence for the seismic wave equation. *Geophysics*, 75:SM155–SM167, 2007.
28. J. Kristek, P. Moczo, and M. Galis. A brief summary of some PML formulations and discretizations for the velocity-stress equation of seismic motion. *Studia Geophysica et Geodaetica*, 53:459–474, 2009.
29. Q. H. Liu and J. Tao. The perfectly matched layer for acoustic waves in absorptive media. *Journal of the Acoustical Society of America*, 102:2072–2082, 1997.
30. Q. Qi and T. L. Geers. Evaluation of the perfectly matched layer for computational acoustics. *Journal of Computational Physics*, 139:166–183, 1998.
31. A. Bermúdez, L. Hervella-Nieto, A. Prieto, and R. Rodríguez. An optimal perfectly matched layer with unbounded absorbing function for time-harmonic acoustic scattering problems. *Journal of Computational Physics*, 223:469–488, 2007.
32. F. D. Hastings, J. B. Schneider, and S. L. Broschat. Application of the perfectly matched layer (PML) absorbing boundary conditions to elastic wave propagation. *Journal of Acoustical Society of America*, 100:3061–3069, 1996.
33. K. C. Meza-Fajardo and A. S. Papageorgiou. A nonconvolutional, split-field, perfectly matched layer for wave propagation in isotropic and anisotropic elastic media: Stability analysis. *Bulletin of the Seismological Society of America*, 98:1811–1836, 2008.
34. U. Basu. Explicit finite element perfectly matched layer for transient three-dimensional elastic waves. *International Journal for Numerical Methods in Engineering*, 77:151–176, 2009.
35. M. Israeli and S. A. Orszag. Approximation of radiation boundary conditions. *Journal of Computational Physics*, 41:115–134, 1981.
36. J. R. Pettit, A. Walker, P. Cawley, and Lowe M. J. S. A stiffness reduction method for efficient absorption of waves at boundaries for use in commercial Finite Element codes. *Ultrasonics*, 54:1868–1879, 2014.

# Chapter 12

## Numerical Case Studies



### 12.1 Wave Propagation in a Stepped Bar

#### 12.1.1 Problem Definition

As the first numerical example, wave propagation in an infinite stepped bar of the circular cross-section is considered. It is assumed that only longitudinal elastic waves can propagate within the bar. It is also assumed that the bar is made out of aluminium having the already known material properties: Young's modulus  $E$  of 67.5 GPa, Poisson's ratio  $\nu$  of 0.33 and material density  $\rho$  of 2700 kg/m<sup>3</sup>, also summarised in Table 4.2 in Sect. 4.2. The geometry of the bar under investigation is presented in Fig. 12.1.

A finite section of the bar, having length  $L_1$  of 600 mm, is of particular interest. This section is indicated by points  $P_1$  and  $P_2$  as the points where dynamic responses of the bar are examined. The excitation signal is applied as a longitudinally acting force at point  $P_1$ , having the amplitude of 1 N and the form of 5 sine pulses at the carrier frequency  $f_c$  of 166.7 kHz, modulated by the Hann window, i.e. the frequency of modulation  $f_m = f_c/m$  being equal to 33.3 kHz, where  $m = 5$ . The total calculation time  $T$  covers 300  $\mu$ s and is divided into 6,000 equal time steps. The excitation signal is presented in Fig. 12.2 in the time and frequency domains, for the initial 100  $\mu$ s of its duration in the time domain and the frequency range up to 500 kHz in the frequency domain.

As clearly seen from Fig. 12.2b the excitation signal is broad in the frequency domain covering frequencies from the range starting at  $f_1 = 100.0$  kHz up to  $f_2 = 233.3$  kHz, where  $f_{1,2} = f_c \mp 2f_m$ . It should be recalled that within this frequency range 97% of the signal energy is stored, as discussed earlier in Sect. 2.5.

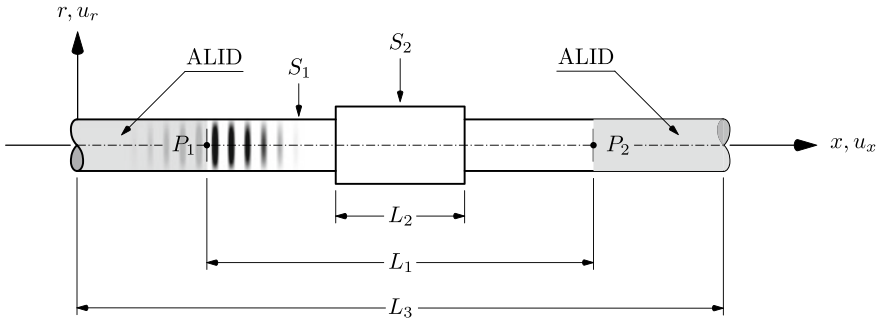


**Fig. 12.1** Geometry of an infinite stepped aluminium bar with NRCBs at infinity modelled by ALID

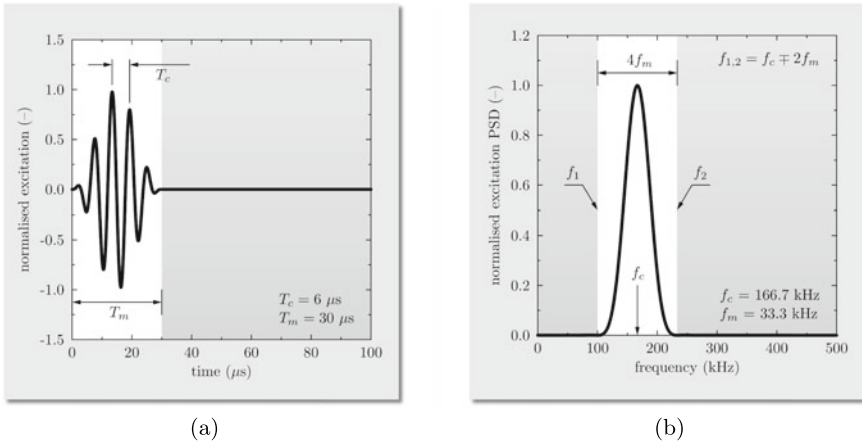


**Fig. 12.2** Normalised excitation signal in: **a** the time domain, **b** in the frequency domain

The stepped bar under consideration can be characterised by two different cross-sectional areas, as clearly seen in Fig. 12.1. The cross-sectional area of the bar is  $S_1 = \pi R_1^2$  over its entire length except a short section having length  $L_3$  of 200 mm, where the cross-sectional area is increased to  $S_2 = \pi R_2^2$ . The assumed values of the radii  $R_1$  and  $R_2$  are 5 and 7 mm, respectively.

### 12.1.2 Dispersion Curves and Theory Selection

For modes of longitudinal waves propagating within the bar, the wide range of excited frequencies must be compared with the analytical dispersion curves already known from Sect. 6.1, in order to select the most appropriate theory of longitudinal behaviour of rods, which next can be employed for numerical computations.

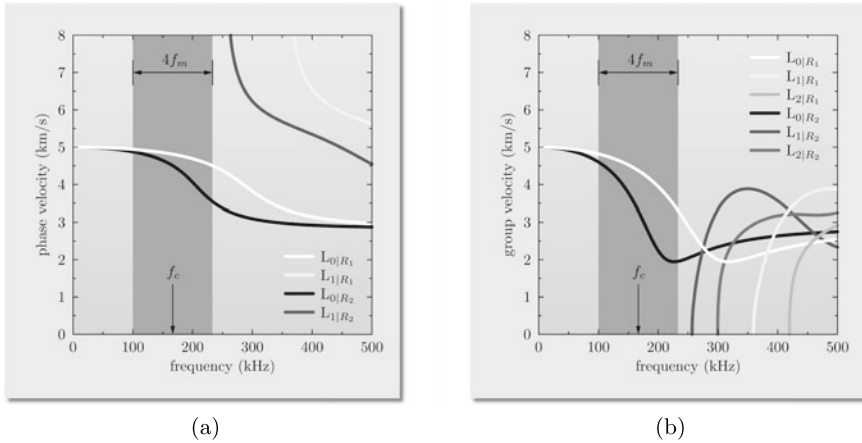


**Fig. 12.3** Dispersion curves for: **a** the phase velocity, **b** the group velocity, for modes of longitudinal waves  $L_n$  ( $n = 0, 1, 2$ ) corresponding to both cross-sectional areas of an infinite stepped aluminium bar, according to the analytical solution

It is clear from Figs. 12.1 and 12.2 that excited elastic longitudinal waves cover different ranges of wave velocities for each cross-sectional area of the bar. According to the analytical solutions presented in Sect. 6.1, in the case of the cross-sectional area  $S_1$  this range covers phase velocities from 4.94 km/s at  $f_1 = 100.0$  kHz down to 4.51 km/s at  $f_2 = 233.3$  kHz, while in the case of the cross-sectional area  $S_2$ , phase velocities from 4.88 km/s at  $f_1 = 100.0$  kHz down to 3.55 km/s at  $f_2 = 233.3$  kHz, respectively.

In a similar manner to the case of the cross-sectional area  $S_1$  the same range of frequencies covers group velocities from 4.82 km/s at  $f_1 = 100.0$  kHz up to 3.31 km/s at  $f_2 = 233.3$  kHz, while in the case of the cross-sectional area  $S_2$ , group velocities from 4.01 km/s at  $f_1 = 100.0$  kHz up to 1.96 km/s at  $f_2 = 233.3$  kHz, respectively. This is clearly illustrated in Fig. 12.3.

As clearly seen from Fig. 12.3 the longitudinal waves propagating in 1-D elastic space, which is the infinite stepped aluminium bar under consideration, are characterised by *very strong dispersion*,<sup>1</sup> i.e.  $-8.7\%$  of the relative change in the phase velocity and  $-31\%$  in the group velocity in the case of the cross-sectional area  $S_1$ , as well as  $-27\%$  of the relative change in the phase velocity and  $-51\%$  in the group velocity in the case of the cross-sectional area  $S_2$ . This dispersion directly results from the Pochhammer characteristic equation and the broad range of excited frequencies. Moreover, it practically concerns the fundamental longitudinal mode  $L_0$ ,

<sup>1</sup> It is convenient to assume wave signals as characterised by dispersion of various strengths: very small, small, moderate, strong and very strong. These strengths correspond to absolute levels of the relative change in their phase or group velocities over a given frequency range, i.e. less than 1% for very small, up to 5% for small, up to 10% for moderate, up to 20% for strong and above 30% for very strong dispersion.



which is denoted as  $L_{0|R_1}$  in the case of the cross-sectional area  $S_1$  and as  $L_{0|R_2}$  in the case of the cross-sectional area  $S_2$ . A similar notation is used for higher longitudinal modes  $L_1$  and  $L_2$ .

Moreover, it was clearly indicated in Fig. 9.10 from Sect. 9.1 that in the case of very strong dispersion, multi-mode or higher-order multi-mode theories of the longitudinal behaviour of rods prove to be more useful due to small relative modelling errors, as also summarised in Table 9.1. It is seen that in the current case the upper frequency limit of the excitation signal never exceeds the frequency corresponding to the first cut-off frequency  $f_{L_1|R_1}$  of 359.4 kHz in the case of the cross-sectional area  $S_1$  and  $f_{L_1|R_2}$  of 256.7 kHz in the case of the cross-sectional area  $S_2$ . For this reason it is decided to employ *the higher-order 2-mode 2-D theory of rod behaviour* for the purpose of numerical modelling. This theory can be characterised by relatively simple definition of its displacement field and a great accuracy in the frequency range of interest. It should be emphasised here that the values of the cut-off frequencies based on analytical dispersion curves are always lower than the corresponding values obtained as based on simplified theories, providing a kind of safe margin in modelling.

The phase velocity dispersion curves obtained for the selected theory, for modes of longitudinal waves  $L_{0|R_1}$  and  $L_{1|R_1}$  as well as  $L_{0|R_2}$  and  $L_{1|R_2}$ , corresponding to both cross-sectional areas  $S_1$  and  $S_2$  of the bar under consideration, are presented in Fig. 12.4.

Indeed, it can be checked that within the range of excited frequencies the dispersion curves for the fundamental mode of longitudinal waves  $L_0$ , corresponding to both cross-sectional areas of the bar, obtained for the selected higher-order 2-mode 2-D theory of the longitudinal behaviour of rods, agree very well with the analytical solutions obtained based on the Pochhammer characteristic equation. In the case of

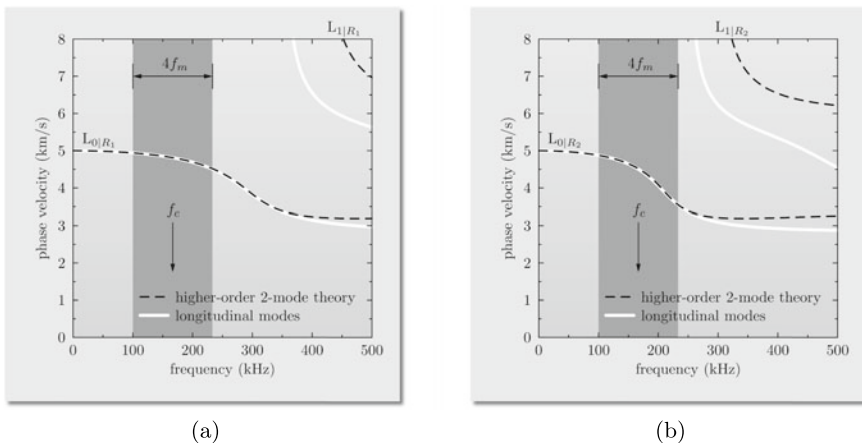


**Fig. 12.4** Dispersion curves for the phase velocity for modes of longitudinal waves  $L_0$  and  $L_1$ , corresponding to: **a** the cross-sectional area  $S_1$ , **b** the cross-sectional area  $S_2$ , of an infinite stepped aluminum bar, according to the higher-order 2-mode 2-D theory of the longitudinal behaviour of rods

the cross-sectional area  $S_1$  the extreme value of the relative modelling error associated with the phase velocity is negligible, since its value is equal to 0.26%, while its average value to 0.06%. In the case of the cross-sectional area  $S_2$  the extreme value of the relative modelling error is higher, but still very small, and is equal to 0.60%, while its average value to 0.22%.

In order to mimic the infinite length of the bar the technique of ALID is used, discussed in detail in Sect. 11.3. As a consequence of this the numerical model must be extended<sup>2</sup> accordingly in order to incorporate the presence of two damping layers, one at each end of the bar, as presented in Fig. 12.1. The depths of the layers must be defined as resulting not only from the frequency content of the excitation signal, but also as depending on the applied theory.

### 12.1.3 ALID Parameters and Numerical Discretisation

It is noteworthy that the knowledge of the range of excited frequencies can be used not only in order to select the most appropriate theory of the longitudinal behaviour of rods, or to establish the depth of ALID, but also to establish the requirements for the bar discretisation conforming with the minimal number of nodal distances per wavelength. The dispersion curves for the wavelength for modes of longitudinal waves corresponding to both cross-sectional areas of the bar, according to the higher-order 2-mode theory of the longitudinal behaviour of rods, are presented in Fig. 12.5.

It can be clearly seen from Fig. 12.5 that in the case of the cross-sectional area  $S_1$  the extreme wavelengths for the selected excitation signal and its frequency content are  $\lambda_{1|R_1} = 49.4$  mm at the frequency  $f_1 = 100.0$  kHz and  $\lambda_{2|R_1} = 19.4$  m at the frequency  $f_2 = 233.3$  kHz. In a similar manner in the case of the cross-sectional area  $S_2$  the corresponding wavelengths are  $\lambda_{1|R_2} = 48.8$  mm at the frequency  $f_1 = 100.0$  kHz and  $\lambda_{1|R_2} = 15.2$  m at the frequency of  $f_2 = 233.3$  kHz. Since the presence of ALID solely concerns the cross-sectional area  $S_1$  the depth of each damping layer should be selected as a multiple of  $\lambda_{1|R_1} = 49.4$  mm, so the assumed depth of ALID is  $L = 4\lambda_{1|R_1} \approx 200$  mm, with  $p = 3$ . For this reason the total length of the bar under consideration is increased by  $2L$  from  $L_2 = 600$  mm to  $L_3 = 1000$  mm.

It also is evident from Fig. 12.5 that the cut-off frequencies  $f_{L_1|R_1}$  and  $f_{L_1|R_2}$  corresponding to the current higher-order 2-D theory of the longitudinal behaviour of rods are greater than those corresponding to the analytical solution based on the Pochhammer characteristic equation. In the case of the cross-sectional area  $S_1$  this value is equal to 419.3 kHz, while in the case of the cross-sectional area  $S_2$  it is equal to 299.5 kHz.

At this point it should be strongly emphasised that any changes in the excitation frequency  $f_c$  or the modulation frequency  $f_m$  must involve corresponding modifi-

<sup>2</sup> In order to mimic the behaviour of an infinite bar by the direct approach the enlarged FE model should be approximately 3 times greater to guarantee no reflections from the external boundaries within the assumed time window.

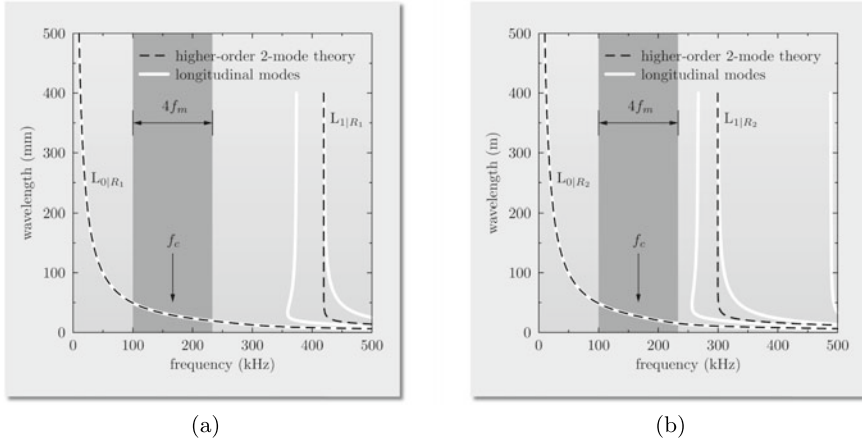


**Fig. 12.5** Dispersion curves for the wavelength for modes of longitudinal waves  $L_0$  and  $L_1$ , corresponding to: **a** the cross-sectional area  $S_1$ , **b** the cross-sectional area  $S_2$ , of an infinite stepped aluminium bar, according to the higher-order 2-mode 2-D theory of the longitudinal behaviour of rods

cations to the depth of ALID in order to guarantee its optimal damping properties. Based on the established parameters of ALID and the requirements for rod discretisation a numerical model of the stepped bar under investigation can be finally built. For the purpose of the current analysis it is decided to use TD-SFEM and 6-node rod SFEs based on Chebyshev nodes [1], as discussed in Sect. 10.4.

The knowledge of the corresponding shortest wavelengths obtained from Fig. 12.5 allows one to state that in the case of the cross-sectional area  $S_1$  the requirement of 5 nodal distances per wavelength is satisfied only for the lengths of SFEs equal<sup>3</sup> to or shorter than the wavelength  $\lambda_{2|R_1} = 19.4$  mm, while in the case of the cross-sectional area  $S_2$  for the lengths of SFEs equal to or shorter than the wavelength  $\lambda_{2|R_2} = 15.2$  mm. Since it is decided to divide the bar into 500 rod SFEs of equal lengths, with the resulting length  $l$  of a single rod SFE equal to 2 mm, the number of nodal distances per wavelength secured by such a discretisation level can be estimated as approximately equal to 48 nodal distances in the case of the cross-sectional area  $S_1$  and 38 nodal distances in the case of the cross-sectional area  $S_2$ , respectively. The resulting number of the discrete numerical model DOFs is 5,002.

### 12.1.4 Numerical Computations and Result Discussion

For numerical computations carried out the implicit  $\beta$ -Newmark method is used, as discussed in Sect. 10.7, for the recommended values of the parameters  $\alpha$  and  $\beta$

<sup>3</sup> It is because for 6-node SFEs there are always 4 nodal distances between their first and last nodes.

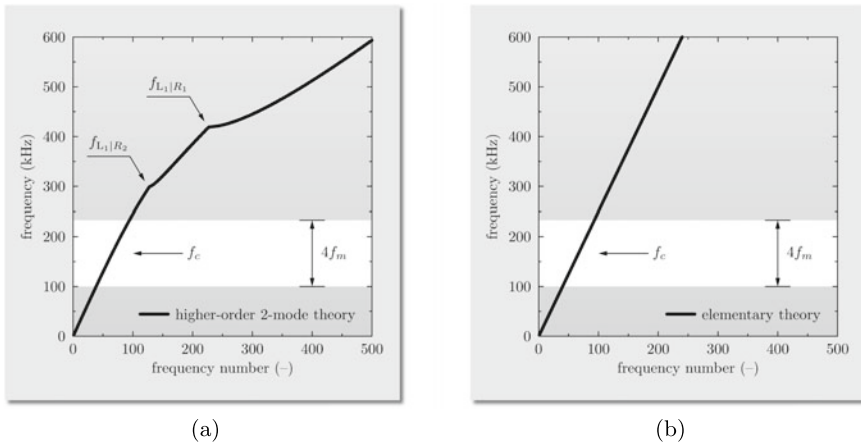


**Fig. 12.6** Spectra of frequencies of free vibrations for modes of longitudinal waves, corresponding to: **a** the higher-order 2-mode 2-D theory, **b** the 1-mode 1-D (elementary) theory, of the longitudinal behaviour of rods, obtained for an infinite stepped aluminium bar. Results of numerical computations by TD-SFEM with NRBCs at infinity modelled by ALID

equal to  $1/2$  and  $1/4$ , respectively. However, prior to the solution of the equations of motion the spectrum of frequencies of free vibrations of the bar under investigation is examined to confirm the correctness of the assumed parameters of the discrete numerical model of the bar, as presented in Fig. 12.6.

It should be noted that in this step the discrete numerical model of the bar must take into account the contributions to the characteristic global inertia matrix  $\mathbf{M}$  and the global stiffness matrix  $\mathbf{K}$  resulting from the presence of both damping layers. For the sake of comparison this spectrum is accompanied by the spectrum of frequencies of free vibrations of the same bar, however, obtained in the case of the 1-mode 1-D theory (elementary) of rods. The remaining features and parameters of the discrete numerical model of the bar remain the same.

It can be seen from Fig. 12.6 that the obtained spectrum of frequencies of free vibrations correlates very well with the dispersion curves for the phase velocity, previously presented in Fig. 12.4. At the same time the computational effort related to finding the frequencies of free vibrations, preferably a finite number of them, is much smaller than that corresponding to the process of establishing all dispersion curves from the Pochhammer characteristic equation.

As a final element of the examination of the discrete numerical model the analysis of the performance of ALID is examined, since the use of ALID is directly responsible for the correctness and accuracy of calculated dynamic responses and generally for appropriate mimicking of the infinite dimensions of the bar [2]. The damping properties of ALID are tested in the case of a simplified geometry of the bar under the assumption of the constant cross-sectional area of the bar of  $S_1$  along its entire length. In such a manner the only reflections, which potentially can be present in the

**Table 12.1** Statistical data on the relative amplitude damping associated with the ALID performance for the 1-mode 1-D (elementary) and the higher-order 2-mode 2-D theory of longitudinal behaviour of rods

Theory	Component	Disp. (dB)	Vel. (dB)	Acc. (dB)
Elementary 1-D	Longitudinal	42.69	60.32	83.25
Higher-order 2-mode 2-D	Longitudinal	38.52	70.15	82.56
	Radial	74.11	105.9	118.5

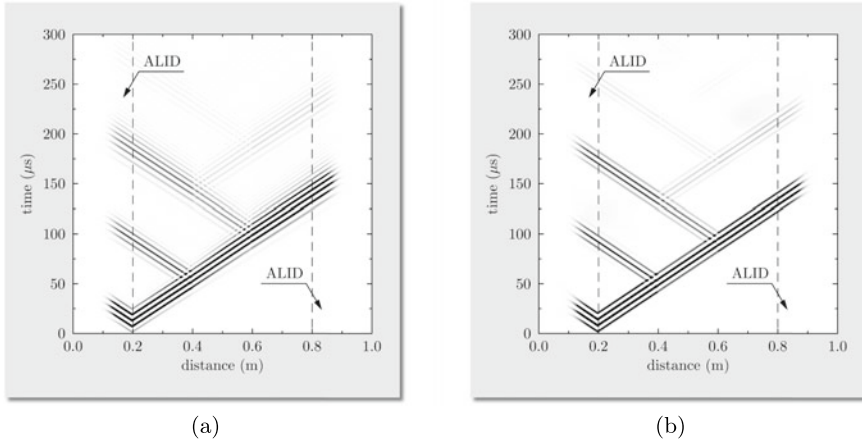


**Fig. 12.7** Wave propagation patterns for the longitudinal acceleration component  $\ddot{u}_x$  for: **a** the higher-order 2-mode 2-D theory, **b** the 1-mode 1-D (elementary) theory, of the longitudinal behaviour of rods, obtained for an infinite stepped aluminium bar. Results of numerical computations by TD-SFEM with NRBCs at infinity modelled by ALID

calculated dynamic responses are those related to the improper performance of ALID. The obtained results for the assumed form of the excitation signal are summarised in Table 12.1.

Knowledge of the established parameters of the discrete numerical model of the bar under consideration allows one to compute its dynamic responses. They are presented as wave propagation patterns for the longitudinal acceleration component  $\ddot{u}_x$  in Fig. 12.7 and compared with similar results obtained in the case of the 1-mode 1-D theory (elementary) of the longitudinal behaviour of rods.<sup>4</sup> It is also evident from Fig. 12.7 that the wave propagation patterns exhibit regions, when propagating elastic waves interact with the structural discontinuity present, very clearly revealing the part of the bar of the increased cross-sectional area. This concerns both discrete

<sup>4</sup> In the case of the higher-order 2-mode 2-D theory of the longitudinal behaviour of rods the longitudinal displacement component  $u_x$ , or its time derivatives, can be compared with that of the 1-mode 1-D (elementary) theory only on the upper surface of the bar, i.e. for  $\zeta = 1$ . Note that no such relationship exists for the radial displacement component  $u_r$ .

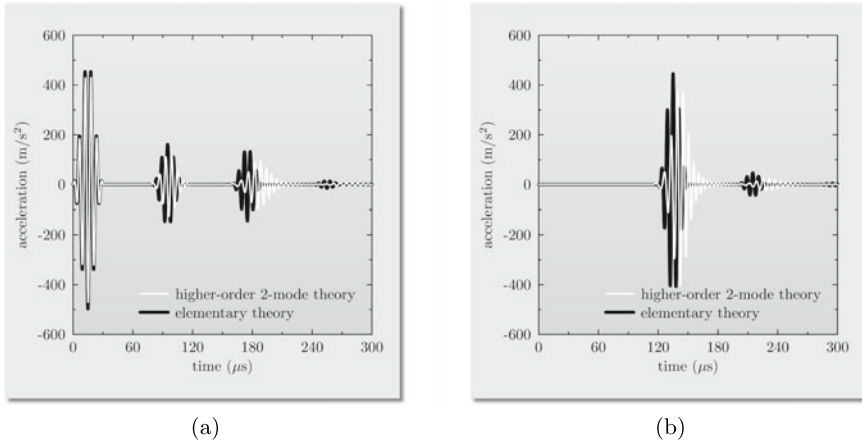


**Fig. 12.8** Dynamic responses for the longitudinal acceleration component  $\ddot{u}_x$  taken at: **a** point  $P_1$ , **b** point  $P_2$ , of an infinite stepped aluminium bar modelled according to the 1-mode 1-D (elementary) and the higher-order 2-mode 2-D theory of the longitudinal behaviour of rods. Results of numerical computations by TD-SFEM with NRBCs at infinity modelled by ALID

numerical models of the bar. Despite the fact that qualitatively the obtained results are similar, certain obvious differences can be indicated.

It can be stated that the observed differences result from the dispersive nature of the longitudinal waves, which is the direct consequence of the analytical solutions arising from the Pochhammer characteristic equation as well as the frequency content of the excitation signal. Obviously, this feature cannot be mimicked by the 1-mode 1-D (elementary) theory of the longitudinal behaviour of rods, since in the case of this theory the phase and the group velocities remain independent of the frequency as well as the cross-sectional area of the bar. In other words the 1-mode 1-D (elementary) theory is non-dispersive.

The difference between the results obtained based on both discrete numerical models of the bar becomes more apparent and even more strongly emphasised when the dynamic responses obtained are compared at points  $P_1$  and  $P_2$ , as presented in Fig. 12.8, for the longitudinal acceleration component  $\ddot{u}_x$ .

Now, it is evident from Figs. 12.7 and 12.8 that this difference builds up in time and distance, which for elongated structural elements may lead to significant discrepancies. Such behaviour may be important for problems related to detection of any structural discontinuities, such as the stepped change in the bar cross-sectional area. For this reason the use of the 1-mode 1-D (elementary) theory for problems involving propagation of elastic waves should practically be limited only to quantitative numerical tests before more appropriate multi-mode or higher-order multi-mode theories are applied.

## 12.2 Wave Propagation in a Strip with a Side Cut-Out

### 12.2.1 Problem Definition

In the second numerical example a similar configuration to the previously analysed infinite stepped aluminium bar with NRBC is considered. This time, however, the object of the analysis is an infinite strip with a side cut-out. The geometry of the strip is presented in Fig. 12.9.

It is assumed that as well as flexural waves, also shear horizontal waves can propagate within the strip. It is assumed that the strip is made out of the same material as previously, which is aluminium of the already known material properties: Young's modulus  $E$  of 67.5 GPa, Poisson's ratio  $\nu$  of 0.33 and material density of  $2700 \text{ kg/m}^3$ , as summarised in Table 4.2 in Sect. 4.2.

As before a finite section of the strip, having length  $L_1$  of 900 mm, width  $B_1$  of 300 mm and thickness  $h$  of 10 mm, is of particular interest. This section is indicated by points  $P_1$  and  $P_2$  as the points where dynamic responses of the strip are examined. The excitation signal is applied at point  $P_1$  as a transversely acting bending force leading to the generation of antisymmetric SH-waves and antisymmetric Lamb waves. The excitation signal is assumed to have the amplitude of 1 N and the form of 12 sine pulses at the carrier frequency  $f_c$  of 60 kHz, modulated by the Hann window, i.e. the frequency of modulation  $f_m = f_c/m$  being equal to 5 kHz, where  $m = 12$ . The total calculation time  $T$  covers  $800 \mu\text{s}$  and is divided into 6400 equal time steps. The

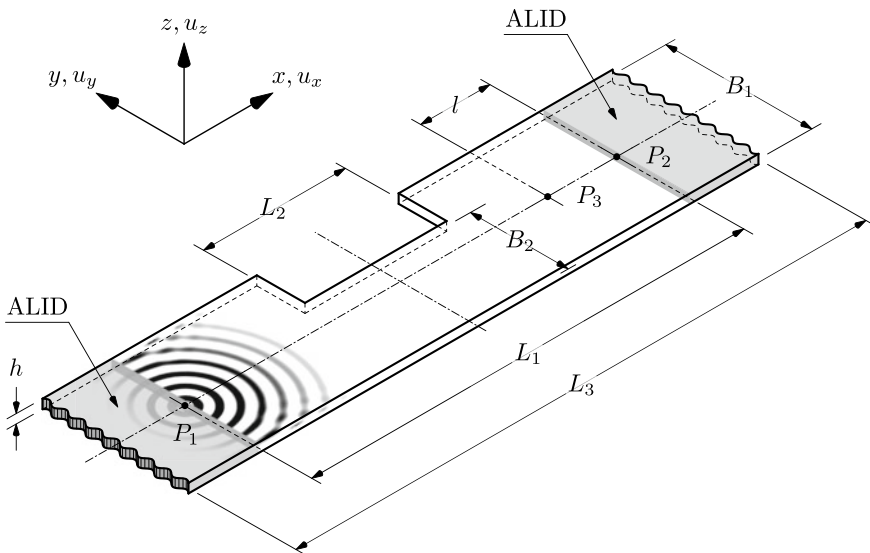


**Fig. 12.9** Geometry of an infinite aluminium strip with a side cut-out, with NRCBs at infinity modelled by ALID

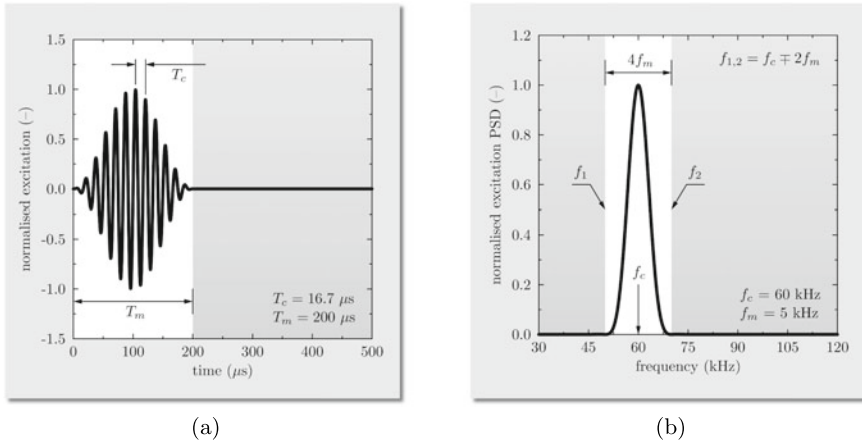


**Fig. 12.10** Normalised excitation signal in: **a** the time domain, **b** in the frequency domain

excitation signal is presented in Fig. 12.10 in the time and frequency domains, for the initial 500  $\mu\text{s}$  of its duration in the time domain and the frequency range from 30 kHz up to 120 kHz in the frequency domain.

It is evident from Fig. 12.10b that this time the excitation signal is narrow in the frequency domain covering frequencies from within the range from  $f_1 = 50 \text{ kHz}$  up to  $f_2 = 70 \text{ kHz}$ , where as before  $f_{1,2} = f_c \mp 2f_m$ . It should be recalled that within this frequency range 97% of the signal energy is stored, as discussed earlier in Sect. 2.5.

From Fig. 12.9 it can be seen that the strip under consideration can be characterised by a stepped change in its width, which is reduced from one side from the initial width  $B_1$  of 300 mm to  $B_2$  of 200 mm, i.e. by the cut-out of depth equal to 100 mm extending over the distance  $L_2$  of 300 mm. Additionally, point  $P_3$ , located at the distance  $l$  of 150 mm from point  $P_2$  indicates the position of an additional mass of 5 g. It is noteworthy that the additional mass of 5 g is equivalent to less than 0.1% of the total mass of the strip. The additional mass is assumed to be placed on the upper surface of the strip.

### 12.2.2 Dispersion Curves and Theory Selection

In a similar manner to before the range of excited frequencies must be compared with the analytical dispersion curves already known from Sects. 5.1 and 5.2, for the antisymmetric modes of SH-waves and the Lamb waves propagating within the strip, in order to select the most appropriate theory of antisymmetric behaviour of plates, which next can be employed for numerical computations.



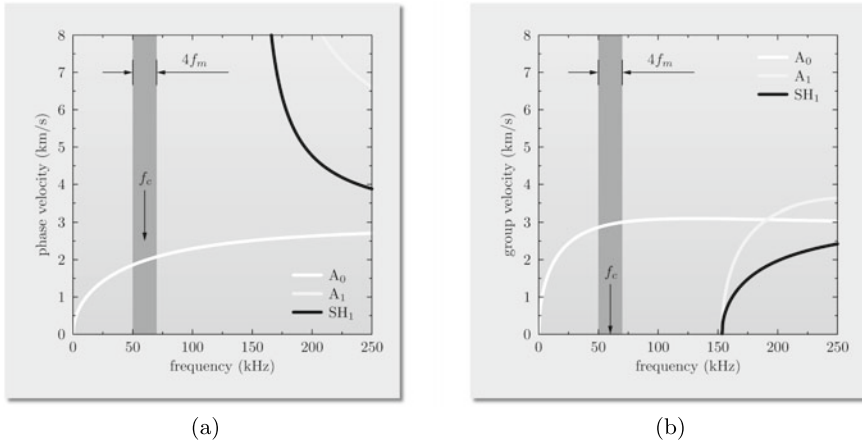


**Fig. 12.11** Dispersion curves for: **a** the phase velocity, **b** the group velocity, for antisymmetric modes of Lamb waves and SH-waves:  $A_0$ ,  $A_1$  and  $SH_1$  propagating in a 10 mm thick aluminium strip with a side cut-out, according to the analytical solutions

From Figs. 12.9 and 12.10 it is clear that due to the assumed form of the excitation signal the excited waves within the strip practically concern the fundamental antisymmetric mode of Lamb waves  $A_0$ , while the other antisymmetric modes of SH-waves and Lamb waves are absent. According to the analytical solutions presented in Sect. 5.2 the excited phase velocities for the fundamental antisymmetric mode of Lamb waves  $A_0$  cover the range from 1.86 km/s at  $f_1 = 50$  kHz up to 2.08 km/s at  $f_2 = 70$  kHz, while in the case of the group velocities from 2.87 km/s at  $f_1 = 50$  kHz up to 3.01 km/s at  $f_2 = 70$  kHz.

Based on Fig. 12.11 it can be concluded that the waves propagating as the fundamental antisymmetric mode of Lamb waves  $A_0$  in 2-D elastic space, which is the infinite aluminium strip under investigation with a side cut-out, are characterised by a moderate dispersion, i.e. 12% of the relative change in the phase velocity and 5% in the group velocity. This is a direct consequence of the characteristic equation for antisymmetric modes of Lamb waves. This, together with the considerations from Sect. 8.2 and the results presented in Fig. 8.20 allow one to state that simple multi-mode theories of the antisymmetric behaviour of plates appears sufficient for modelling purposes, as summarised in Table 8.2.

It is seen that in the current case the upper frequency limit of the excitation signal is placed well below the frequency corresponding to the first cut-off frequency for the first antisymmetric mode of SH-waves and Lamb waves  $A_1$  and  $SH_1$ ,  $f_{A_1|SH_1}$  of 153.4 kHz. For this reason it is decided to employ the modified 3-mode 2-D theory of antisymmetric behaviour of plates. This theory is characterised by a simple definition of its displacement field combined with the greatest accuracy in the frequency range of interest out of the theories discussed in Sect. 8.2. As before it should be emphasised that the values of the cut-off frequencies provided by analytical dispersion curves

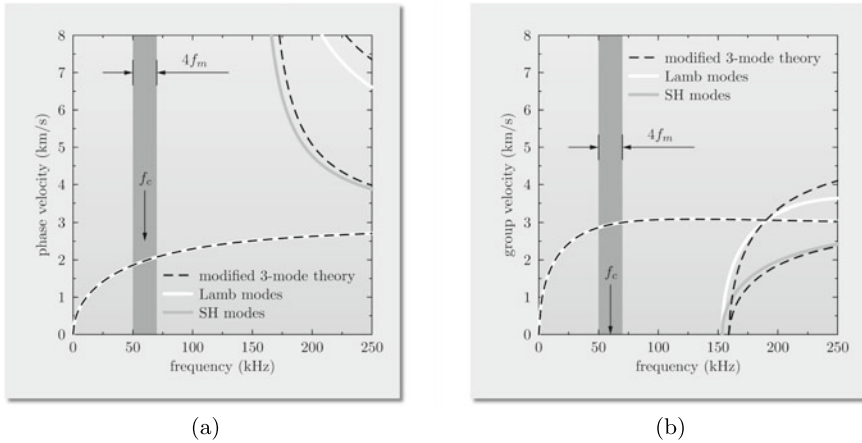


**Fig. 12.12** Dispersion curves for: **a** the phase velocity, **b** the group velocity, for antisymmetric modes of Lamb waves and SH-waves propagating in a 10 mm thick infinite aluminium strip with a side cut-out, according to the modified 3-mode 2-D theory of the antisymmetric behaviour of plates

are always lower than the values obtained from simplified theories, thus providing a kind of safe margin in modelling.

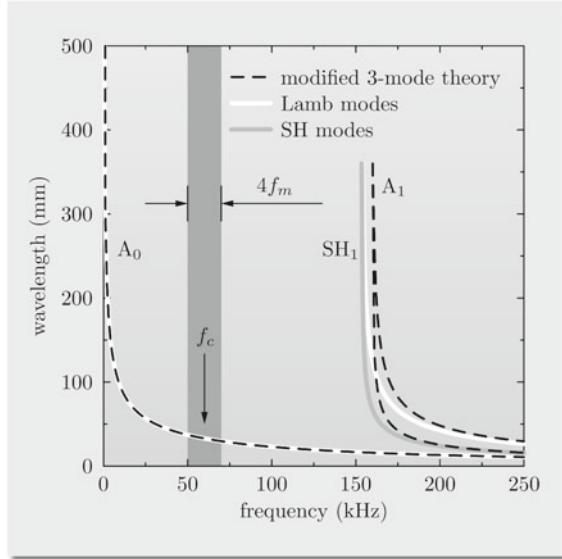
The phase and group velocity dispersion curves obtained for this theory, for antisymmetric modes of Lamb waves and SH-waves, are presented in Fig. 12.12. It can be clearly seen Fig. 12.12 that within the range of excited frequencies the dispersion curve for the fundamental antisymmetric mode of Lamb waves  $A_0$ , obtained for the selected modified 3-mode 2-D theory of the antisymmetric behaviour of plates, agrees very well with the analytical solution obtained based on the characteristic equation.

The results presented in Fig. 12.12 allow one to easily assess the values of the modelling error. In the case of the fundamental antisymmetric mode of Lamb waves  $A_0$  it can be checked that the extreme value of the modelling error associated with the phase velocity is negligible with its value equal to 0.03% and its average value to 0.02%. In a similar manner the extreme value of the modelling error associated with the group velocity is equal to  $-0.10\%$  and its average value to  $-0.06\%$ .

### 12.2.3 ALID Parameters and Numerical Discretisation

In order to model the infinite length of the strip the same method is employed in the current case as in the case of the infinite stepped aluminium bar, which is the technique of ALID, discussed in detail in Sect. 11.3. As before a consequence of the use of ALID is that the numerical model of the strip must be extended accordingly to incorporate the presence of two damping layers, one at each end of the strip, as

**Fig. 12.13** Dispersion curves for the wavelength for modes of Lamb waves and SH-waves of a 10 mm thick infinite aluminium strip with a side cut-out, according to the modified 3-mode 2-D theory of the antisymmetric behaviour of plates



presented in Fig. 12.9. The depths of the layers must be defined as resulting not only from the frequency content of the excitation signal, but also as depending on the applied theory.

Again, it can be stated that the knowledge of the range of the excited frequencies can be used not only to select the most appropriate theory of the antisymmetric behaviour of plates or to establish the depth of ALID, but also to establish the requirements for the strip discretisation conforming with the minimal number of nodal distances per wavelength. The dispersion curves for the wavelength for modes of Lamb waves and SH-waves, according to the modified 3-mode 2-D theory of the antisymmetric behaviour of plates, are presented in Fig. 12.13.

It can be clearly seen from Fig. 12.13 that the extreme wavelengths for the selected excitation signal and its frequency content are  $\lambda_1 = 37.1$  mm at the frequency  $f_1 = 50$  kHz and  $\lambda_2 = 29.7$  mm at the frequency  $f_2 = 70$  kHz. Since the presence of ALID solely concerns the fundamental antisymmetric mode of Lamb waves  $A_0$  the depth of each damping layer should be selected as a multiple of  $\lambda_1 = 37.1$  mm, so the assumed depth of ALID is  $L = 4\lambda_1 \approx 150$  mm, with  $p = 3$ . For this reason the total length of the strip under consideration is increased by  $2L$  from  $L_2 = 900$  mm to  $L_3 = 1200$  mm.

Yet again it should be strongly emphasised that any changes in the excitation frequency  $f_c$  or the modulation frequency  $f_m$  must involve corresponding modifications to the depth of ALID in order to guarantee its optimal damping properties. Based on the established parameters of ALID and the requirements for plate discretisation a numerical model of the strip under investigation with a side cut-out can be finally

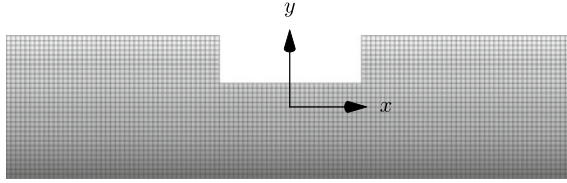


**Fig. 12.14** The mesh of plate SFEs, according to the modified 3-mode 2-D theory of the antisymmetric behaviour of plates, used for numerical computations, consisting of 3,300 SFEs and 249,903 DOFs

built. For the purpose of the current analysis it is decided to use TD-SFEM and 36-node plate SFEs based on Lobatto nodes [1], as discussed in Sect. 10.4.

The knowledge of the corresponding shortest wavelengths obtained from Fig. 12.13 allows one to state, in a similar manner as in the case of the stepped aluminium bar, that the requirement of 5 nodal distances per wavelength is satisfied only for the characteristic dimensions of FEs equal to or shorter than the wavelength  $\lambda_2 = 29.7$  mm. Thus, it is decided to divide the strip into 3,300 plate SFEs, i.e. 120 SFEs along its length axis and 30 SFEs along its width, excluding 300 SFEs resulting from the presence of the cut-out. The mesh of SFEs resulting from the discretisation process is presented in Fig. 12.14. All SFEs represent squares of equal dimensions of 10 by 10 mm. Since the characteristic dimension of a single plate SFE is 10 mm, the number of nodal distances per wavelength secured by such a discretisation level can be estimated as approximately equal to 15 nodal distances per shortest wavelength. The resulting number of DOFs of the discrete numerical model is 249,903.

### 12.2.4 Numerical Computations and Result Discussion

For numerical computations carried out the explicit method of central differences is used, as discussed in Sect. 10.7. The use of the explicit method of central differences enables one to take full advantage of the diagonal form of the resulting global inertia matrix  $\mathbf{M}$ . It is noteworthy that in the current case however, the spectrum of frequencies of free vibrations of the strip is not examined due to the 2-D nature of the strip and, resulting from this, couplings of normal modes, which significantly complicate such an analysis in comparison with a 1-D case. For the very same reason also the performance of ALID is not tested. This performance can only be estimated based on the methodology presented before and concerning the results obtained in the case of the 1-D infinite stepped aluminium bar.

The knowledge of the established parameters of the discrete numerical model of the strip under consideration allows one to compute its dynamic responses. They are presented in Fig. 12.15 as wave propagation patterns at selected moments in time for the transverse acceleration component  $\ddot{u}_z$ . It can be expected that the interaction of propagating waves with a structural discontinuity in the form of the additional

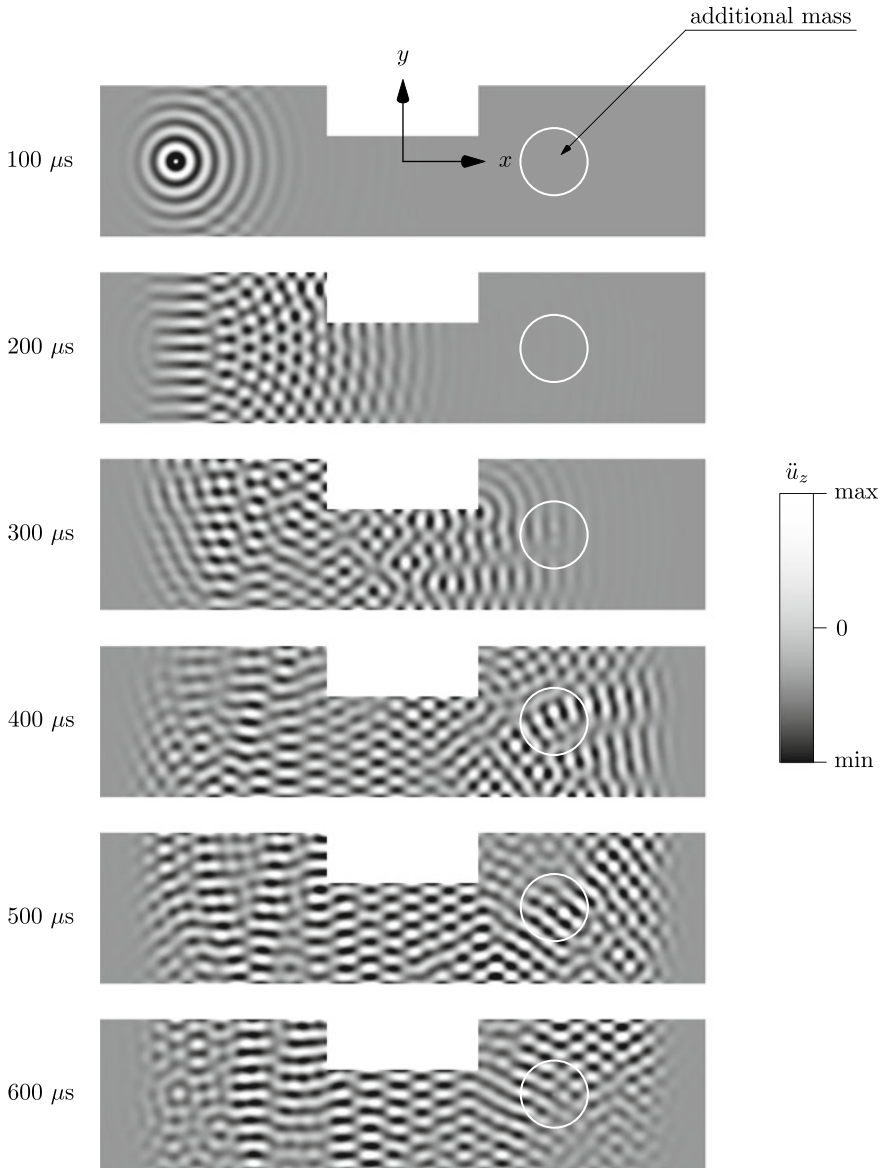


**Fig. 12.15** Wave propagation patterns for the transverse acceleration component  $\ddot{u}_z$  according to the modified 3-mode 2-D theory of the antisymmetric behaviour of plates, obtained for a 10 mm thick infinite aluminium strip with a side cut-out. Results of numerical computations by TD-SFEM with NRBCs at infinity modelled by ALID

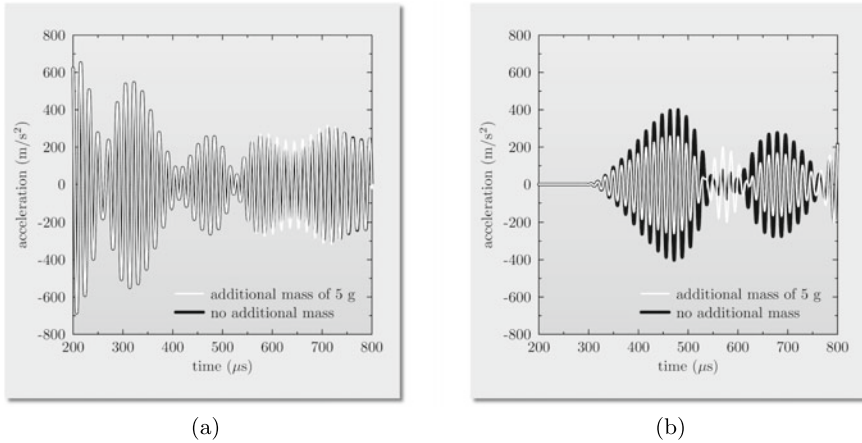


**Fig. 12.16** Dynamic responses for the transverse acceleration component  $\ddot{u}_x$  taken at: **a** point  $P_1$ , **b** point  $P_2$ , of an infinite aluminium strip with a side cut-out modelled according to the modified 3-mode 2-D theory of the antisymmetric behaviour of plates. Results of numerical computations by TD-SFEM with NRBCs at infinity modelled by ALID

mass should influence the observed patterns in such a way that the location of the additional mass is clearly revealed. However, from the results presented in Fig. 12.15 this is not evident.

The reason for such behaviour may seem to lay in too small sensitivity of the propagating waves to structural damage/discontinuity. This sensitivity may be estimated as proportional to the shortest wavelength out of all wavelengths constituent in the propagating waves and resulting from the assumed form of the excitation signal, which in the current case is  $\lambda_2 = 29.7$  mm. However, this is not applicable to damage/discontinuity represented by a point mass. Alternatively, the problem may also be related to too complicated wave propagation patterns, which are very difficult to interpret due to multiple reflections and/or possible mode conversion. This problem is very well illustrated by Fig. 12.16 where the obtained dynamic responses are compared at points  $P_1$  and  $P_2$ . It should be stressed that since the dynamic responses obtained at point  $P_1$  are initially dominated by the excitation, it is decided to exclude the time window corresponding to the duration of excitation, which is equal to the modulation time  $T_m$  of 200  $\mu$ s.

It can be seen from Fig. 12.16 that within the time signals corresponding to points  $P_1$  and  $P_2$  there is no clear evidence of any reflections resulting from the presence of the additional mass, which on the other hand is the effect of signal reflections from lateral structural boundaries. Despite the fact that the signals obtained for the case when the additional mass is present or not must be different, it is impossible to extract directly from them any useful information about the location of the additional mass.

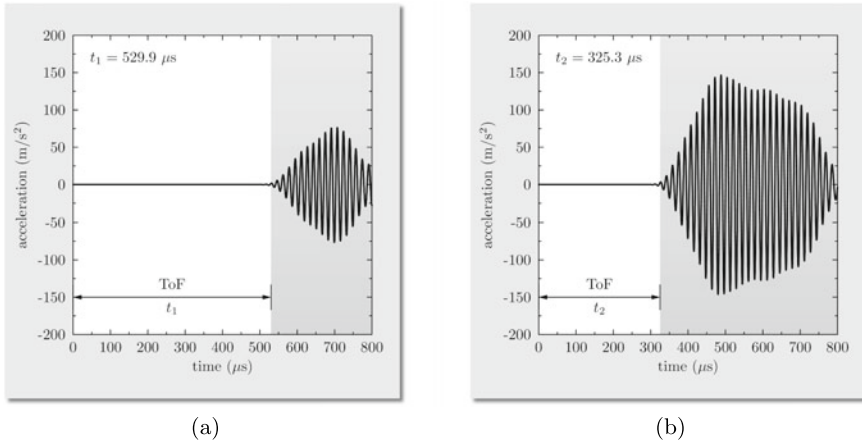


**Fig. 12.17** Differential signals for the transverse acceleration component  $\ddot{u}_x$  taken at: **a** point  $P_1$ , **b** point  $P_2$ , of an infinite aluminium strip with a side cut-out modelled according to the modified 3-mode 2-D theory of the antisymmetric behaviour of plates. Results of numerical computations by TD-SFEM with NRBCs at infinity modelled by ALID

This adverse situation is not significantly improved when differential signals<sup>5</sup> are examined, as shown in Fig. 12.17. It is clear that the amplitudes of the differential signals corresponding to points  $P_1$  and  $P_2$  are smaller than those of the original signals, which may present an additional problem for small signal-to-noise ratios. For this reason the estimation of the times of flight (ToF), in the current case, indicated as  $t_1$  and  $t_2$  in Fig. 12.17 based on which the location of the additional mass can be identified [1, 3], may be difficult and/or not precise due to the inherent dispersion of propagating wave signals. For this reason both ToFs are estimated assuming the signal threshold equal to 2% of its maximum value. In general, the poor sensitivity may be improved either by an increase in the carrier frequency  $f_c$  or alternatively by the use of more specialised damage indicators.

It can be checked that in the current case the distance  $l$  can be easily calculated from the following simple relationships:

$$\begin{cases} 2|P_1 P_2| = c_{g|f_2} t_1 \\ |P_1 P_3| = c_{g|f_2} t_2 \\ l = |P_1 P_2| - |P_1 P_3| \end{cases} \rightarrow l = c_{g|f_2} \left( t_2 - \frac{t_1}{2} \right) \quad (12.1)$$

which lead to the result of 182.3 mm, which is not too close to the assumed value of the distance  $l$  equal to 150 mm, giving the relative error of 21.5%.

<sup>5</sup> A differential signal is understood here as a signal resulting from the difference between the signal obtained at a given point for the current but unknown state of a structure, and some reference signal obtained at the same point, but for a well-defined state of the structure.

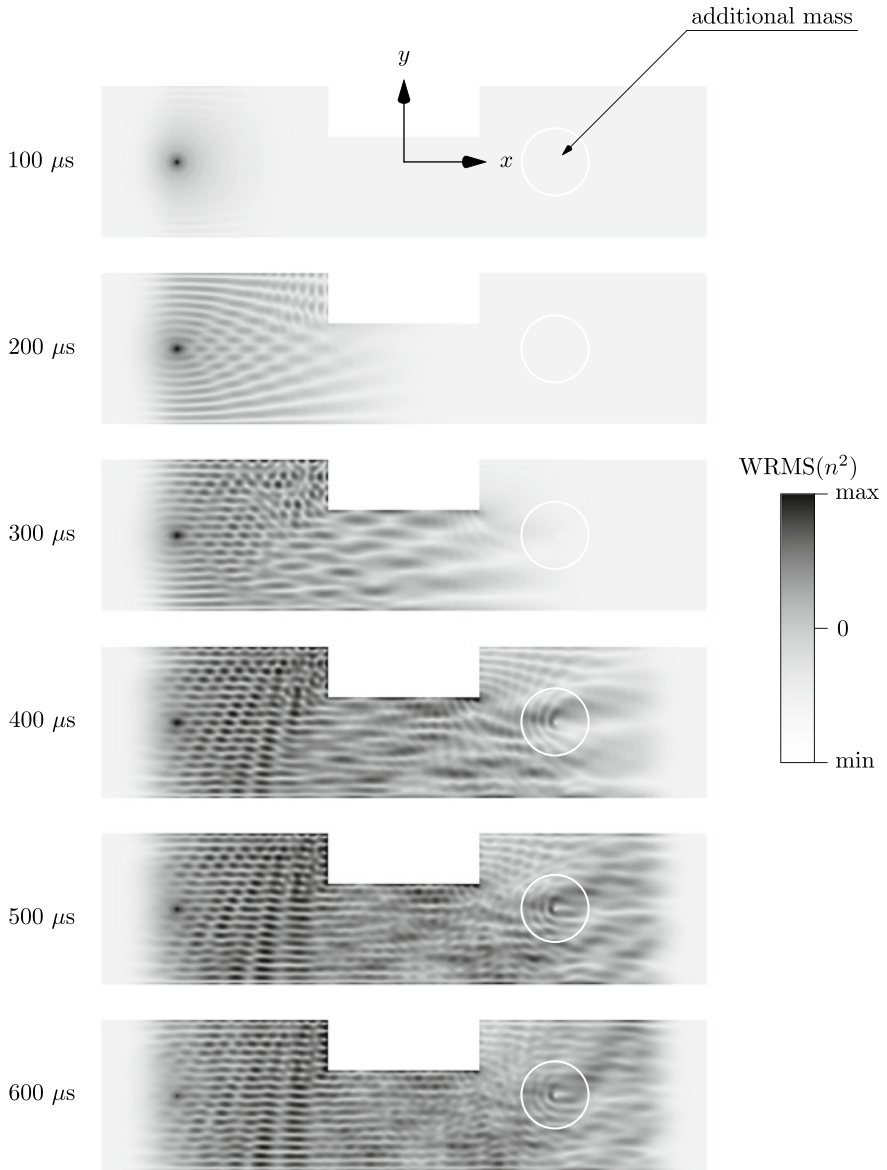


**Fig. 12.18**  $WRMS(n^2)$  patterns for the transverse acceleration component  $\ddot{u}_z$  according to the modified 3-mode 2-D theory of the antisymmetric behaviour of plates, obtained for a 10 mm thick infinite aluminium strip with a side cut-out. Results of numerical computations by TD-SFEM with NRBCs at infinity modelled by ALID



Of many damage indicators that can be possibly built and used, those which are based on the observation of the propagation of energy within a structure, rather than the observation of pure wave propagation patterns, seem particularly attractive. Typically a cumulative kinetic energy indicator or the root mean square (RMS) of measured time signals can be used for that purpose [1, 4]. It is noteworthy that damage indicators based on modified RMS, such as is a weighted root mean square (WRMS) for example, provide an increased sensitivity even in the case of damage of small magnitudes located at large distances from signal sources.<sup>6</sup> The use of such an improved damage indicator in the form of  $\text{WRMS}(n^2)$  is demonstrated in Fig. 12.18.

Thanks to this the location of the additional mass within the strip under consideration with a side cut-out becomes clearly visible as soon as the excited waves reach point  $P_2$ , that is after initial 400  $\mu\text{s}$ . In subsequent moments in time the obtained RMS patterns only become sharpened and amplified, which allows one to shorten the time of numerical analysis significantly. In the current case, according to results presented in Fig. 12.18, with no loss of accuracy the total calculation time  $T$  can be reduced by half from the initial 800 to 400  $\mu\text{s}$  and from 6,400 equal time steps to 3,200.

It should be emphasised that for excitation signals broader in the frequency domain, which may lead to the propagation of other antisymmetric modes of SH-waves and Lamb waves than the fundamental  $A_0$  mode of Lamb waves, other theories of antisymmetric behaviour of plates should be used, preferably multi-mode or higher-order multi-mode 3-D theories.

## 12.3 Wave Propagation in a Flanged Pipe with a Circumferential Crack

### 12.3.1 Problem Definition

The last numerical example concerns wave propagation in the most complex configuration, which is represented by an infinite flanged pipe section with a small circumferential crack.

As before, thanks to the application on NRBC only a finite section of the structure can be investigated. Its geometry is presented in Fig. 12.19. It is assumed that the flanged pipe section under consideration is made out of aluminium of the same material properties as before: Young's modulus  $E$  of 67.5 GPa, Poisson's ratio  $\nu$  of 0.33 and material density of 2700  $\text{kg/m}^3$ , as summarised in Table 4.2 in Sect. 4.2.

---

<sup>6</sup> For a discrete sequence  $u_1, u_2, \dots, u_n$  of  $n$  numbers a weighted RMS can be simply defined as  $\text{WRMS}(w_n) = \sqrt{w_1 u_1^2 + w_2 u_2^2 + \dots + w_n u_n^2} / \sqrt{w_1 + w_2 + \dots + w_n}$ , where  $w_n$  denote certain weights. In the case of  $\text{WRMS}(1)$  the weights are assumed as  $w_n = 1$  and  $\text{WRMS}(1) \equiv \text{RMS}$ , while in the case of  $\text{WRMS}(n^2)$  the weights are assumed as  $w_n = n^2$ , thus  $\text{WRMS}(n^2) = \sqrt{u_1^2 + 4u_2^2 + \dots + n^2 u_n^2} / \sqrt{1 + 4 + \dots + n^2}$ .

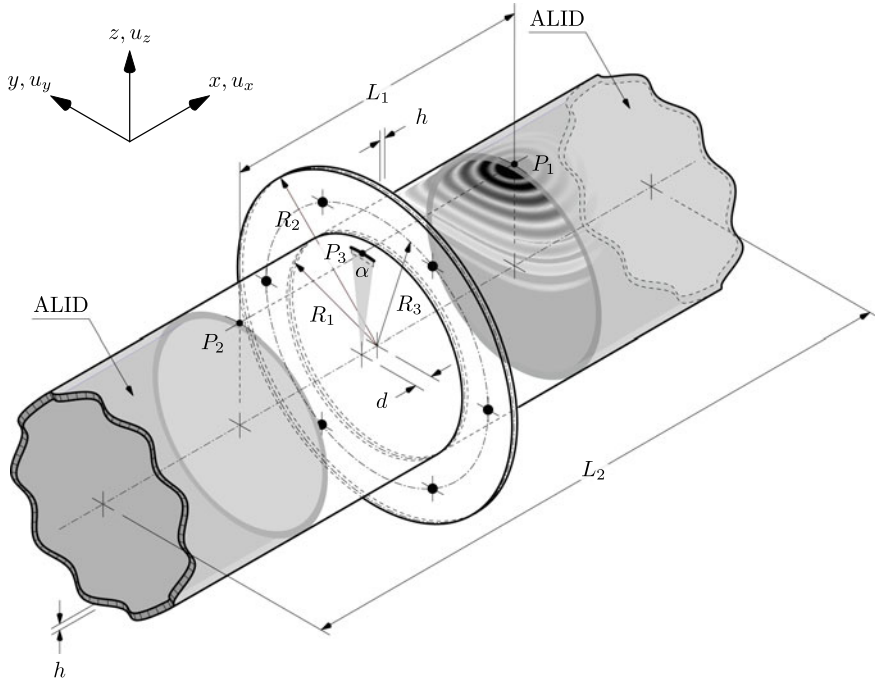


**Fig. 12.19** Geometry of an aluminium flanged pipe section with a circumferential crack, with NRCBs at infinity modelled by ALID

The finite section of the pipe, having length  $L_1$  of 500 mm, outer radius  $R_1$  of 150 mm and thickness  $h$  of 10 mm, is of special interest. In the middle of this section a flange is located, having an outer radius  $R_2$  of 250 mm and the same thickness  $h$  of 10 mm. On the flange face 6 evenly spaced M12 bolt sets are placed at a radius  $R_3$  of 200 mm, represented by additional masses of 50 g each. Additionally, it is assumed that a small open circumferential crack, with its centre at point  $P_3$  located at a distance  $d$  of 17 mm from the flange centre, is spanned over the angle  $\alpha$  of  $12^\circ$ , which corresponds to its surface length of 31 mm. The crack is also assumed as open and a through-thickness crack.

The flanged pipe section of interest is indicated by points  $P_1$  and  $P_2$ , which are the points where dynamic responses are examined. The excitation signal is applied at point  $P_1$  either as a transversely acting bending force leading to the generation of antisymmetric waves (antisymmetric excitation) or a transversely acting pair of tensile or compressive forces leading to the generation of symmetric waves (symmetric excitation), as discussed in [5]. It has the amplitude of 1 N and the form of 11 sine pulses of the carrier frequency  $f_c$  of 110 kHz, modulated by the Hann window, i.e. the frequency of modulation  $f_m = f_c/m$  being equal to 10 kHz, where  $m = 11$ . As previously, the total calculation time  $T$  covers 800  $\mu$ s and is divided into 6400 equal time steps.

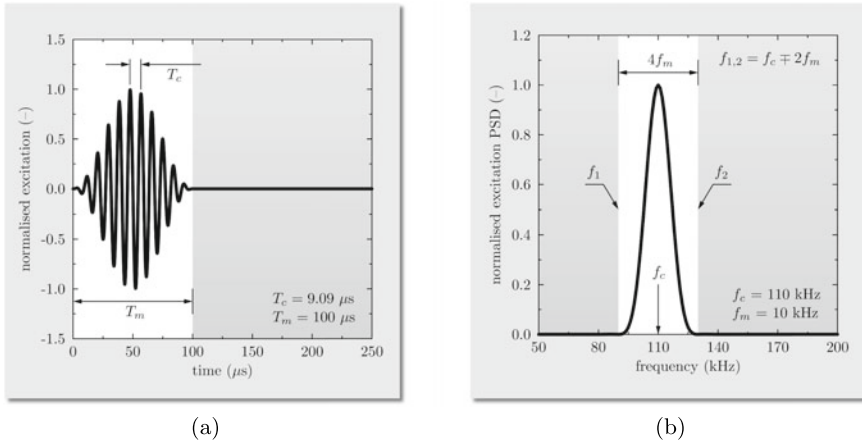


**Fig. 12.20** Normalised excitation signal in: **a** the time domain, **b** the frequency domain

The excitation signal is presented in Fig. 12.20 in the time and frequency domains, for the initial 250  $\mu s$  of its duration in the time domain and the frequency range from 50 kHz up to 200 kHz in the frequency domain.

### 12.3.2 Dispersion Curves and Theory Selection

In the current case, due to the geometry of the section under consideration as well as two excitation modes, the process of the theory selection must concern both symmetric and antisymmetric modes, which can propagate. As before the range of excited frequencies must be compared with the analytical dispersion curves already known from Sects. 5.1 and 5.2. This time, however, this process concerns the symmetric and antisymmetric modes of SH-waves and the Lamb waves, which can propagate within the structure, in order to select the most appropriate theories of symmetric and antisymmetric behaviour of plates/shells, which next can be employed for numerical computations.

From Figs. 12.20 and 12.21 it is evident that due to the assumed form of the excitation signal the excited waves within the section only concern three fundamental modes: the fundamental symmetric mode of Lamb waves  $S_0$ , the fundamental antisymmetric mode of Lamb waves  $A_0$  as well as the fundamental symmetric mode of SH-waves  $SH_0$ , while the remaining symmetric and antisymmetric modes of SH-waves and Lamb waves are absent.

According to the analytical solutions presented in Sect. 5.2 the excited phase velocities for the fundamental symmetric mode of Lamb waves  $S_0$  cover the range from 5.23 km/s at  $f_1 = 90 \text{ kHz}$  down to 5.13 km/s at  $f_2 = 130 \text{ kHz}$ , for the fundamental antisymmetric mode of Lamb waves  $A_0$  from 2.23 km/s at  $f_1 = 90 \text{ kHz}$  up to

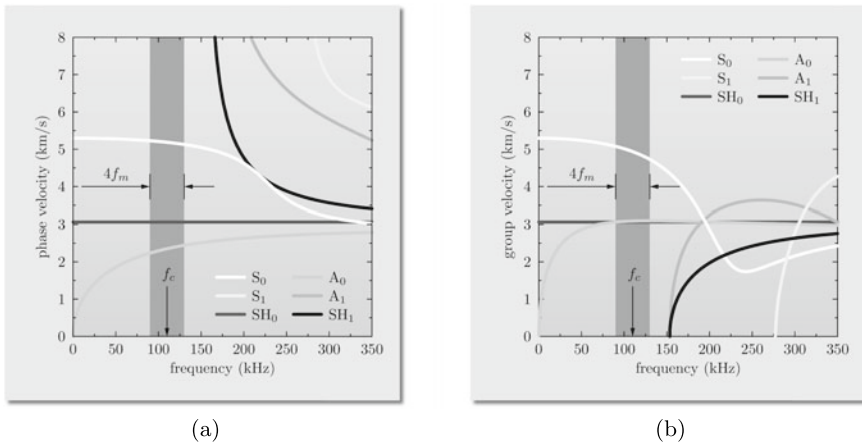


**Fig. 12.21** Dispersion curves for: **a** the phase velocity, **b** the group velocity, for symmetric and antisymmetric modes of Lamb waves and SH-waves:  $S_0$ ,  $S_1$ ,  $A_0$ ,  $A_1$ ,  $SH_0$  and  $SH_1$  propagating in a 10mm thick aluminium flanged pipe section with a circumferential crack, according to the analytical solutions

2.44 km/s at  $f_2 = 130$  kHz, while for the fundamental symmetric mode of SH-waves  $SH_0$ , which is non-dispersive, it is constant and equal to 3.07 km/s for all frequencies. In the case of the group velocities the obtained values are different and for the fundamental symmetric mode of Lamb waves  $S_0$  cover the range from 5.08 km/s at  $f_1 = 90$  kHz down to 4.73 km/s at  $f_2 = 130$  kHz, for the fundamental antisymmetric mode of Lamb waves  $A_0$  from 3.07 km/s at  $f_1 = 90$  kHz up to 3.10 km/s at  $f_2 = 130$  kHz.

Based on Fig. 12.21 it can be concluded that the waves propagating as the fundamental modes in 2-D elastic space, which is the infinite flanged pipe section under investigation with a circumferential crack, are characterised by *moderate dispersion*, i.e.  $-1.9\%$  of the relative change in the phase velocity and  $-6.9\%$  in the group velocity in the case of the fundamental symmetric mode of Lamb waves  $S_0$  and  $9.4\%$  of the relative change in the phase velocity and  $1.0\%$  in the group velocity in the case of the fundamental antisymmetric mode of Lamb waves  $A_0$ . This is a direct consequence of the characteristic equations for the symmetric and antisymmetric modes of Lamb waves and SH-waves. This, together with the considerations from Sects. 8.1 and 8.2, as well as the results presented in Fig. 8.20, allows one to state that simple multi-mode theories of the symmetric and antisymmetric behaviour of plates appear sufficient for modelling purposes, as summarised in Tables 8.1 and 8.2.

In the same manner as before it can be noted that in the current case the upper frequency limit of the excitation signal is placed below the frequency corresponding to the first cut-off frequency for the first antisymmetric mode of SH-waves and Lamb waves,  $A_1$  and  $SH_1$ ,  $f_{A_1|SH_1}$  of 153.4 kHz. Based on the same reasoning as in the case of the previous numerical example, discussed in Sect. 12.2, it is decided to employ *the modified 6-mode 3-D theory of shells*. Of the simple theories discussed in Sects. 8.1

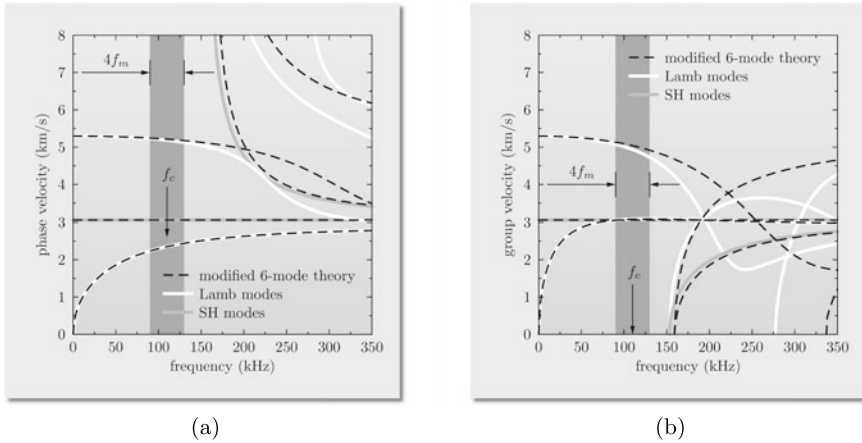


**Fig. 12.22** Dispersion curves for: **a** the phase velocity, **b** the group velocity, for symmetric and antisymmetric modes of Lamb waves and SH-waves propagating in a 10 mm thick infinite aluminium flanged pipe section with a circumferential crack, according to the modified 6-mode 3-D theory of shells

and 8.2, the current theory, being a simple combination of the modified 3-mode theories of the symmetric and antisymmetric behaviour of plates, is characterised by a simple definition of its displacement field combined with a great accuracy in the frequency range of interest. As previously it should be emphasised that the values of the cut-off frequencies provided by analytical dispersion curves are always lower than the values obtained from simplified theories, thus providing a kind of safe margin in modelling.

The phase and group velocity dispersion curves obtained for the modified 6-mode theory of shells, for symmetric and antisymmetric modes of Lamb waves and SH-waves, are presented in Fig. 12.22. It can be clearly seen in Fig. 12.22 that within the range of excited frequencies the dispersion curves for the fundamental symmetric mode of Lamb waves  $S_0$ , the fundamental antisymmetric mode of Lamb waves  $A_0$  and the fundamental symmetric mode of SH-waves  $SH_0$ , obtained for the selected modified 6-mode 3-D theory of shells, agree very well with the analytical dispersion curves obtained based on the corresponding characteristic equations.

It should be emphasised that based on the results presented in Fig. 12.22 the extreme values of the modelling errors can be easily assessed. In the case of the fundamental symmetric mode of Lamb waves  $S_0$  the relative error associated with the phase velocity is very small with its value equal to 0.92% and its average value to 0.55%, while in the case of the fundamental antisymmetric mode of Lamb waves  $A_0$  is negligible with its value equal to  $-0.06\%$  and its average value equal to  $-0.04\%$ . In the same manner the extreme values of the modelling errors associated with the group velocity are examined. As a result it can be stated that in the case of the fundamental symmetric mode of Lamb waves  $S_0$  the relative error associated with the group velocity is small with its value equal to 3.92% and its average value equal to

2.21%, while in the case of the fundamental antisymmetric mode of Lamb waves  $A_0$  is negligible with its value equal to  $-0.26\%$  and its average value equal to  $-0.21\%$ .

The modelling errors associated with the fundamental symmetric mode of SH-waves  $SH_0$  is neglected in this analysis, since this wave mode is non-dispersive and as a consequence it fully conforms with the analytical dispersion curves obtained for the phase and group velocities.

### 12.3.3 ALID Parameters and Numerical Discretisation

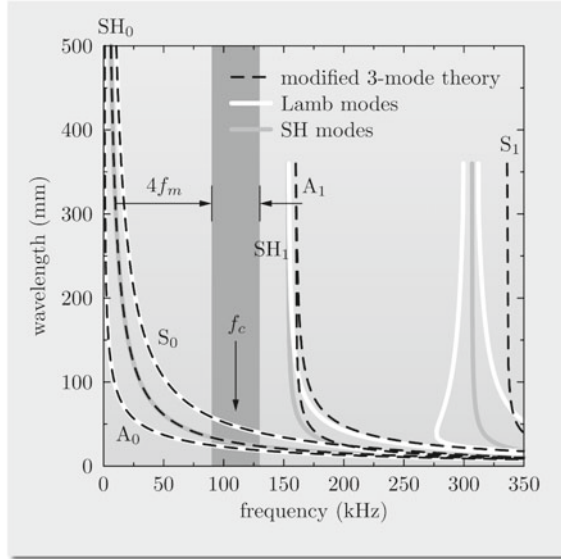
In order to model the infinite length of the flanged pipe section the same method is employed in the current case as in the case of the infinite aluminium strip, which is the technique of ALID, discussed in detail in Sect. 11.3. In the same manner as before it can be said that as a consequence of the use of ALID the numerical model of the pipe section must be extended accordingly to incorporate the presence of two damping layers, one at each end of the pipe section, as presented in Fig. 12.19. The depths of the layers must be defined as resulting not only from the frequency content of the excitation signal, but also as depending on the applied theory.

Once again, it can be stated that the knowledge of the range of the excited frequencies can be used not only to select the most appropriate theory of the shell behaviour or to establish the depth of ALID, but also to establish the requirements for the flanged pipe section discretisation conforming with the minimal number of nodal distances per wavelength. The dispersion curves for the wavelength for modes of Lamb waves and SH-waves, according to the modified 6-mode 3-D theory of shells, are presented in Fig. 12.23.

It can be clearly seen from Fig. 12.23 that the extreme wavelengths for the selected excitation signal and its frequency content must differ depending on the wave mode under consideration, since three fundamental modes of Lamb waves and SH-waves are present there. In the case of the fundamental symmetric mode of Lamb waves  $S_0$  the corresponding values of the extreme wavelengths are the greatest and equal to  $\lambda_{1|S_0} = 58.4$  mm at the frequency  $f_1 = 90$  kHz and  $\lambda_{2|S_0} = 39.8$  mm at the frequency  $f_2 = 130$  kHz. In the case of the fundamental antisymmetric mode of Lamb waves  $A_0$  the corresponding values of the extreme wavelengths are the smallest and equal to  $\lambda_{1|A_0} = 24.8$  mm at the frequency  $f_1 = 90$  kHz and  $\lambda_{2|A_0} = 18.8$  mm at the frequency  $f_2 = 130$  kHz. Consequently, in the case of the fundamental symmetric mode of SH-waves  $SH_0$  the extreme wavelengths take intermediate values equal to  $\lambda_{1|SH_0} = 34.1$  mm at the frequency  $f_1 = 90$  kHz and  $\lambda_{2|SH_0} = 23.6$  mm at the frequency  $f_2 = 130$  kHz.

Since the depth of ALID must be defined using the knowledge about the longest wavelength in the frequency content of the excitation signal out of all modes available, it can be stated that in the current case this must be done based on the values related to the fundamental symmetric mode of Lamb waves  $S_0$ . As before the depth of each damping layer is taken as a multiple of  $\lambda_{1|S_0} = 58.3$  mm, so the assumed depth of ALID is  $L = 4\lambda_1 \approx 234$  mm, with  $p = 3$ . For this reason the total length of

**Fig. 12.23** Dispersion curves for the wavelength for modes of Lamb waves and SH-waves of a 10 mm thick infinite aluminium flanged pipe section with a circumferential crack, according to the modified 6-mode 3-D theory of shells



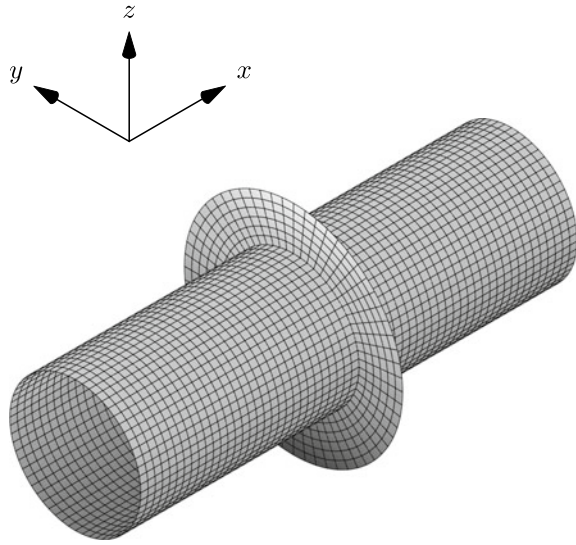
the flanged pipe section under consideration must be increased by at least  $2L$  from  $L_1 = 500$  mm to  $L_2 = 968$  mm, which value is additionally increased to  $L_2 = 1000$  mm in order to simplify the discretisation process.

It should be emphasised here that any changes in the excitation frequency  $f_c$  or the modulation frequency  $f_m$  must involve corresponding modifications to the depth of ALID in order to guarantee its optimal damping properties. Based on the established parameters of ALID and the requirements for shell discretisation a numerical model of the flanged pipe section under investigation with a circumferential crack can be finally built. For the purpose of the current analysis it is decided to use TD-SFEM and 36-node shell SFEs based on Lobatto nodes [1], as discussed in Sect. 8.3.

The knowledge of the corresponding shortest wavelengths obtained from Fig. 12.23 allows one to state, in a similar manner as in both previous numerical cases, that the requirement of 4 nodal distances per wavelength is satisfied only for the lengths of SFEs equal to, or shorter than, the wavelength  $\lambda_{2|A_0} = 18.8$  mm.

Thus, it is decided to divide the strip into 3,960 shell SFEs, i.e. 60 SFEs along its length axis and 60 SFEs along its circumference, plus 360 SFEs used for modelling the flange, as presented in Fig. 12.24. As a result of the discretisation process the characteristic dimension of each SFE can be estimated as 16.6 mm, thus the number of nodal distances per wavelength secured by such a discretisation level can be estimated as approximately equal to 6 nodal distances per shortest wavelength. The resulting number of DOFs of the discrete numerical model is 595,854.

**Fig. 12.24** The mesh of shell SFEs, according to the modified 6-mode 3-D theory of shells, used for numerical computations, consisting of 3,960 SFEs and 595,854 DOFs



### 12.3.4 Numerical Computations and Result Discussion

For numerical computations carried out the explicit method of central differences, as discussed in Sect. 10.7, is employed exactly in the same manner as in the case of the infinite aluminium strip with a side cut-off. The use of the explicit method of central differences enables one to take advantage of the diagonal form of the resulting global inertia matrix  $\mathbf{M}$ . However, it should be strongly emphasised here that in the case of the flanged pipe section under investigation the geometrical couplings resulting from non-flat geometry lead to certain off-diagonal elements in the global inertia matrix  $\mathbf{M}$ . Their magnitudes, being inversely proportional to the local radius of curvature, remain very small in comparison with the diagonal elements of this matrix and for this reason all off-diagonal elements in the global inertial matrix  $\mathbf{M}$  are neglected.

The spectrum of frequencies of free vibrations of the flanged pipe section is also not examined due to the 3-D nature of the section and resulting couplings of normal modes, which significantly complicate, or simply prevent, such an analysis in comparison with 1-D cases. For the very same reason also the performance of ALID is not tested. However, this performance can be estimated based on the methodology presented before and concerning the results obtained in the case of the 1-D infinite stepped aluminium bar.

The knowledge of the established parameters of the discrete numerical model of the flanged pipe section under consideration allows one to compute its dynamic responses. They are presented in Figs. 12.25 and 12.26 as wave propagation patterns at selected moments in time for the amplitudes of the resulting acceleration components  $AMP^2 = \ddot{u}_x^2 + \ddot{u}_y^2 + \ddot{u}_z^2$ , for both types of excitation. It can be expected that the interaction of propagating waves with structural discontinuities in the form of



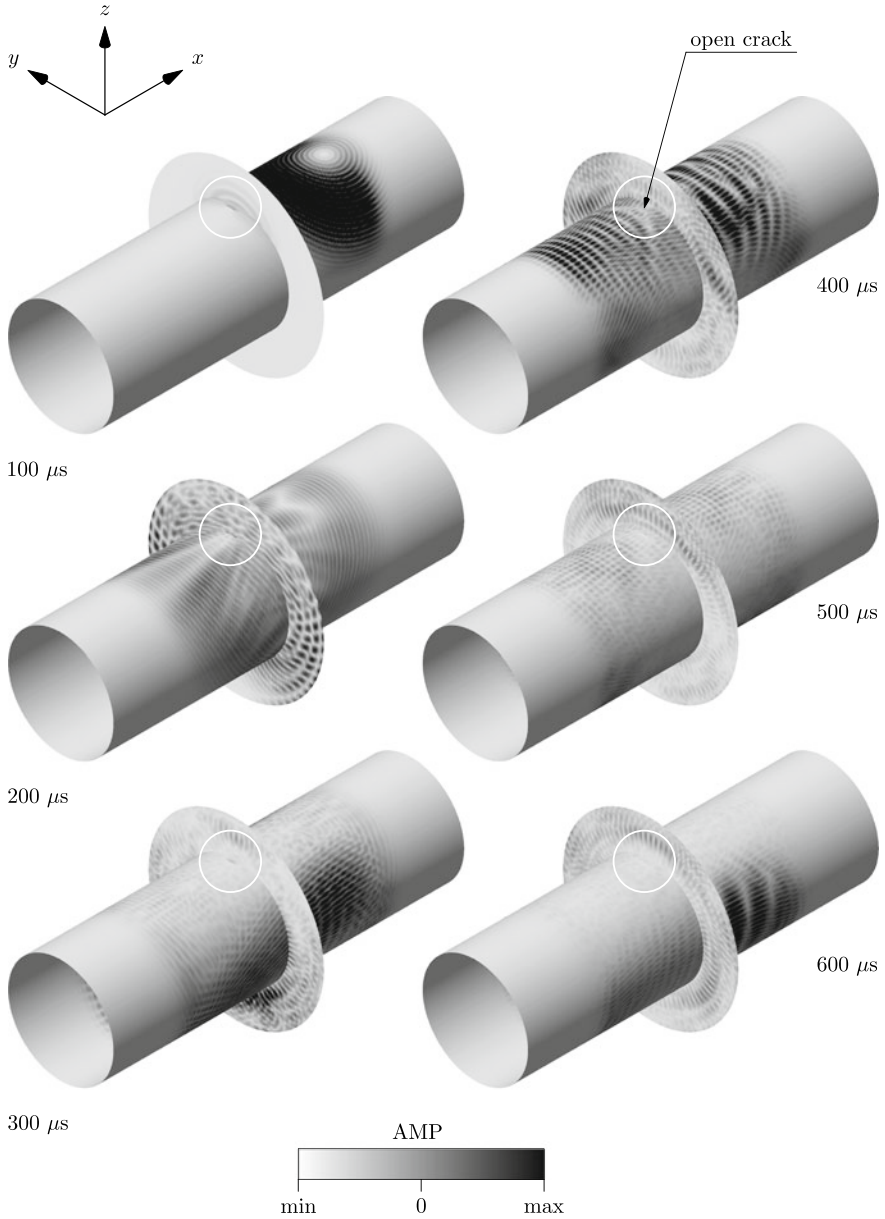


**Fig. 12.25** Wave propagation patterns for the amplitude of the resulting acceleration component AMP according to the modified 6-mode 3-D theory of shells, obtained for an aluminium flanged pipe section with a circumferential crack in the case of antisymmetric excitation. Results of numerical computations by TD-SFEM with NRBCs at infinity modelled by ALID

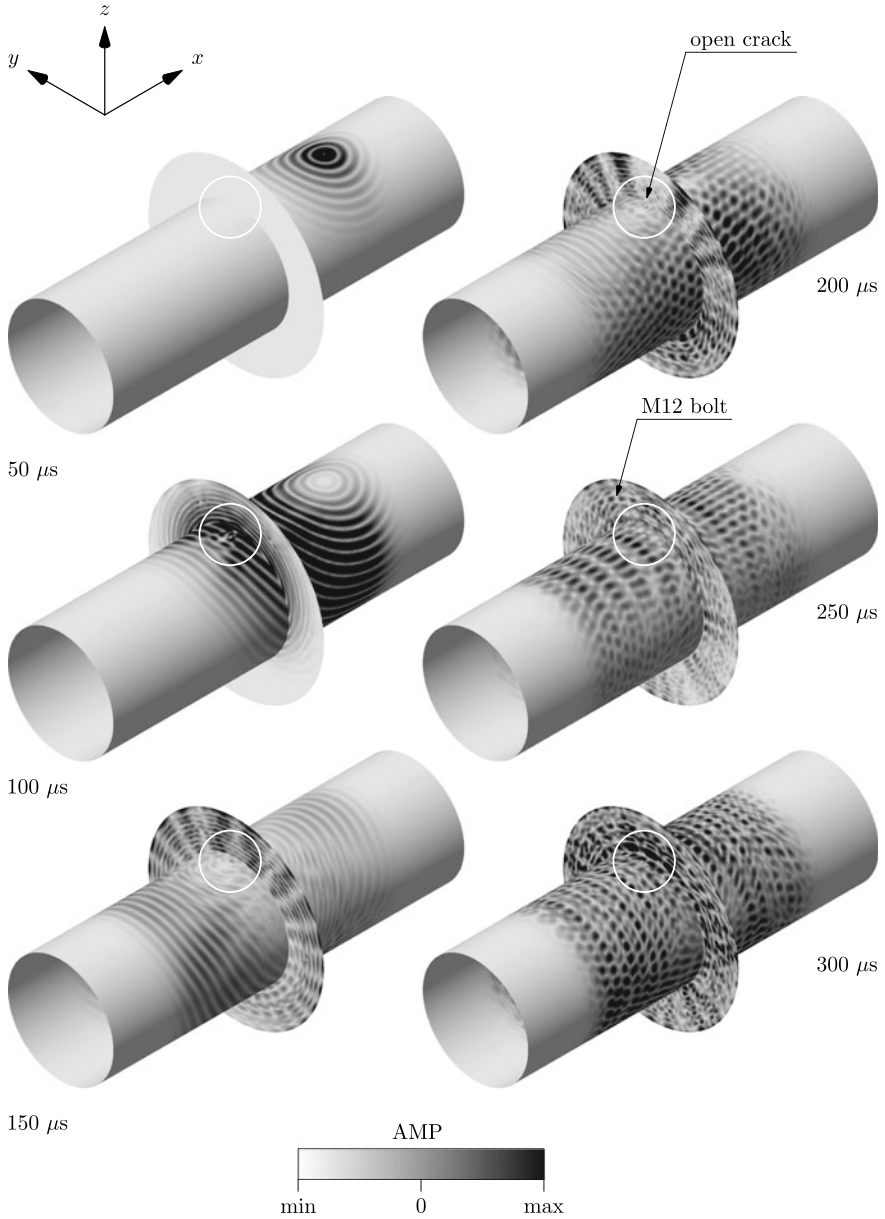


**Fig. 12.26** Wave propagation patterns for the amplitude of the resulting acceleration component AMP according to the modified 6-mode 3-D theory of shells, obtained for an aluminium flanged pipe section with a circumferential crack in the case of the symmetric excitation. Results of numerical computations by TD-SFEM with NRBCs at infinity modelled by ALID

the crack and bolts should influence the observed patterns in such a way that their locations are revealed. However, from the results presented in Figs. 12.25 and 12.26 this is not evident.

The reason for such behaviour may seem to lie in too small sensitivity of the propagating waves to structural damage/discontinuity. This sensitivity may be estimated as proportional to the shortest wavelength out of all wavelengths constituent in the propagating waves and resulting from the assumed form of the excitation signal, but it also depends on the type of excitation [1, 6, 7]. In the case of antisymmetric excitation the shortest wavelengths is  $\lambda_{2|A_0} = 18.8$  mm, while in the case of symmetric excitation it is  $\lambda_{2|S_0} = 39.8$  mm. Despite the fact of mode conversion between symmetric and antisymmetric modes at the flange position the response of the pipe section is dominated by the type of excitation. For this reason, at least in the case of the antisymmetric excitation, since the crack length of 31 mm is grater than the shortest wavelength, the location of the crack should be clearly revealed. However, this is not visible in either case of excitation except the early stage of development of wave propagation patterns, as seen in Fig. 12.25 at 200  $\mu$ s and Fig. 12.26 at 100  $\mu$ s. Alternatively, the problem may also be related to too complicated wave propagation patterns, which are very difficult to interpret due to multiple reflections and/or possible mode conversion. This problem is very well illustrated by Figs. 12.27 and 12.28, for both types of excitation, where the obtained dynamic responses are compared at points  $P_1$  and  $P_2$ . As previously it should be pointed out that the dynamic responses obtained at point  $P_1$  are initially dominated by the excitation. For this reason it is decided to exclude the time window corresponding to the time of excitation, which is equal to the modulation time  $T_m$  of 100  $\mu$ s.

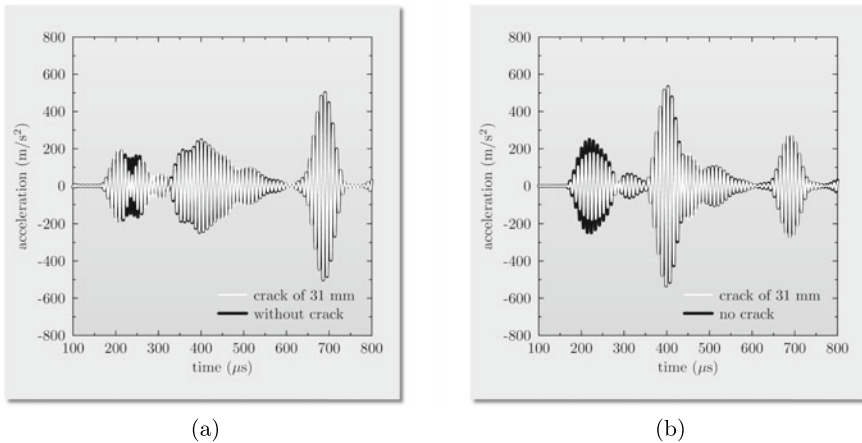


**Fig. 12.27** Dynamic responses for the transverse acceleration component  $\ddot{u}_x$  taken at: **a** point  $P_1$ , **b** point  $P_2$ , of an aluminium flanged pipe section with a circumferential crack in the case of the antisymmetric excitation, according to the modified 6-mode 3-D theory of shells. Results of numerical computations by TD-SFEM with NRBCs at infinity modelled by ALID

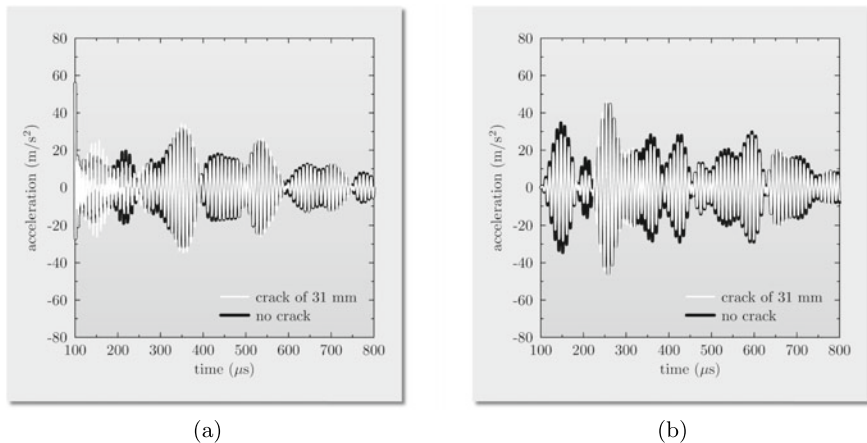


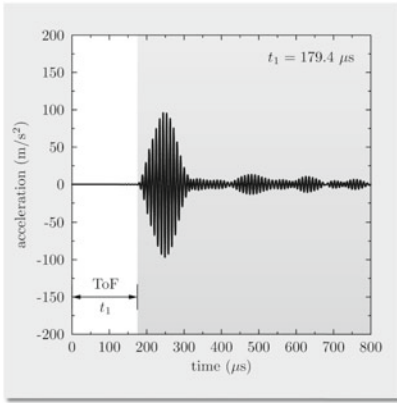
**Fig. 12.28** Dynamic responses for the transverse acceleration component  $\ddot{u}_x$  taken at: **a** point  $P_1$ , **b** point  $P_2$ , of an aluminium flanged pipe section with a circumferential crack in the case of the symmetric excitation, according to the modified 6-mode 3-D theory of shells. Results of numerical computations by TD-SFEM with NRBCs at infinity modelled by ALID

It can be seen from Figs. 12.27 and 12.28 that within the time signals corresponding to points  $P_1$  and  $P_2$  there is no clear evidence of any reflections resulting from the presence of the crack, which on the other hand is the effect of signal reflections/conversion at the flange position. Despite the fact that the signals obtained for the cases when the crack is present or not must be different, it is impossible to directly extract from them any useful information about the location of the crack.

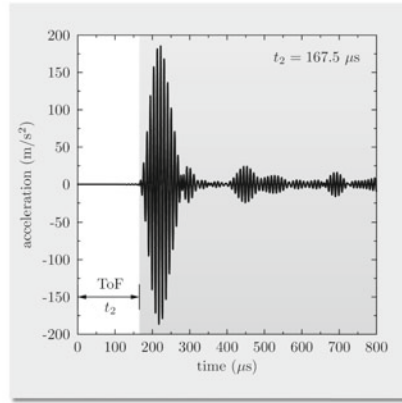
This adverse situation is not significantly improved when differential signals are examined, as shown in Figs. 12.29 and 12.30, for the same two types of excitation. It is clear that the amplitudes of the differential signals corresponding to points  $P_1$  and  $P_2$  are smaller than those of the original signals, which may present a problem for small signal-to-noise ratios. For this reason the estimation of the times of flight (ToF), in the current case indicated as  $t_1$  and  $t_2$  in Figs. 12.29 and 12.30, based on which the location of the additional mass can be evaluated [1, 3], is difficult and/or not precise due to the inherent dispersion of propagating wave signals. Both ToFs are estimated assuming the same signal threshold equal to 2% of its maximum value. In the same manner as before the poor sensitivity may be improved either by an increase in the carrier frequency  $f_c$  or alternatively by the use of more specialised damage indicators.

It can be checked that in the current case the distance  $d$  can be easily calculated from the following simple relationships:

$$\begin{cases} 2|P_1 P_3| = c_{g|f_2} t_1 \\ |P_1 P_2| = c_{g|f_2} t_2 \\ 2d = 2|P_1 P_3| - |P_1 P_2| \end{cases} \rightarrow d = c_{g|f_2} \left( \frac{t_1 - t_2}{2} \right) \quad (12.2)$$

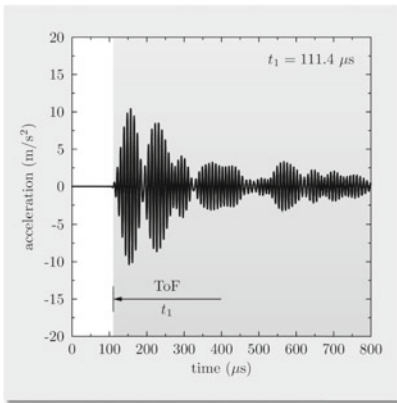


(a)

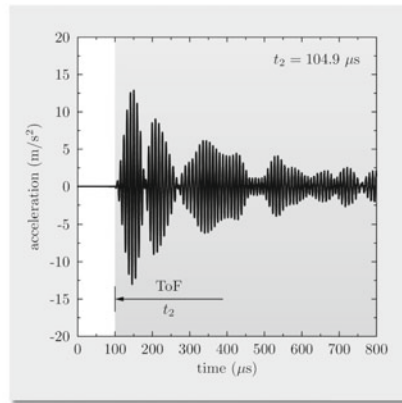


(b)

**Fig. 12.29** Differential signals for the transverse acceleration component  $\ddot{u}_x$  taken at: **a** point  $P_1$ , **b** point  $P_2$ , of an aluminium flanged pipe section with a circumferential crack in the case of the antisymmetric excitation, according to the modified 6-mode 3-D theory of shells. Results of numerical computations by TD-SFEM with NRBCs at infinity modelled by ALID



(a)



(b)

**Fig. 12.30** Differential signals for the transverse acceleration component  $\ddot{u}_x$  taken at: **a** point  $P_1$ , **b** point  $P_2$ , of an aluminium flanged pipe section with a circumferential crack in the case of the symmetric excitation, according to the modified 6-mode 3-D theory of shells. Results of numerical computations by TD-SFEM with NRBCs at infinity modelled by ALID

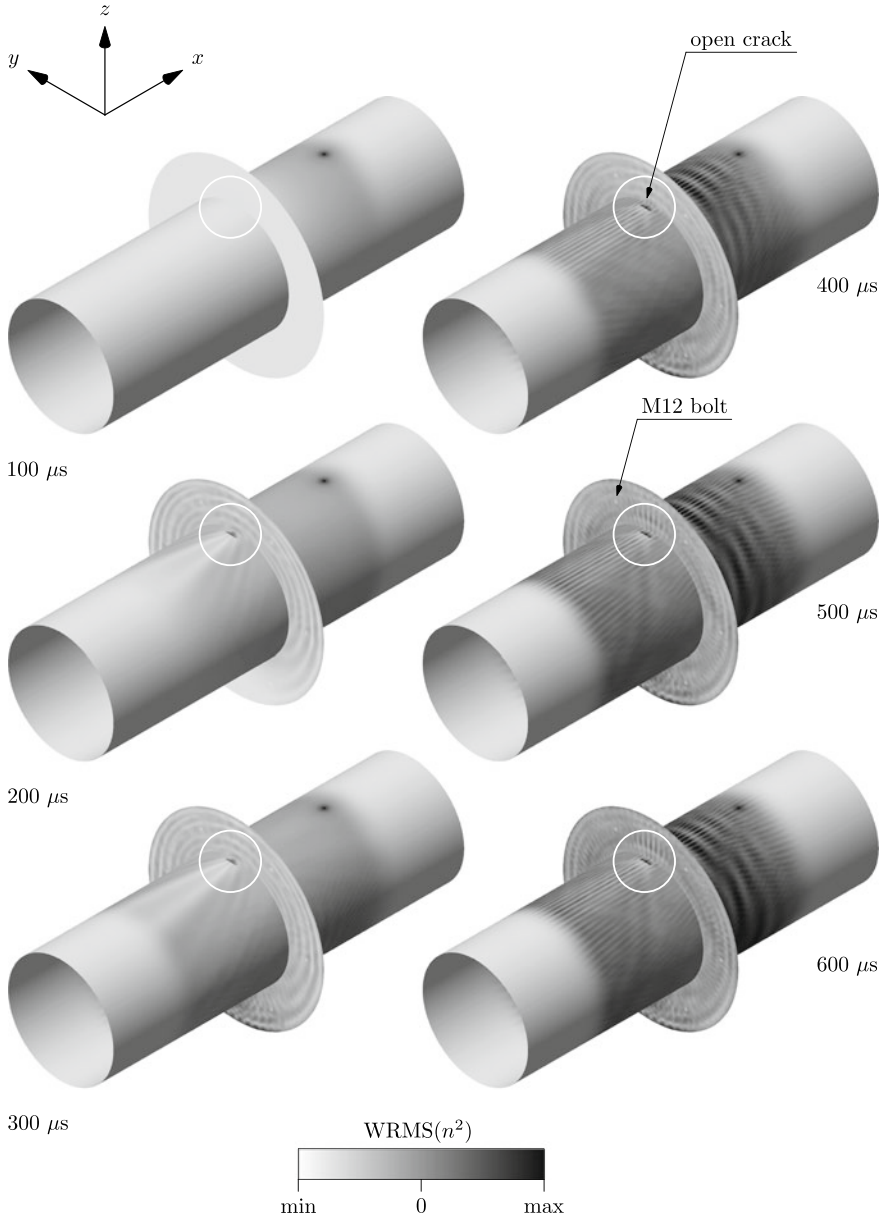


**Fig. 12.31** WRMS ( $n^2$ ) patterns for the amplitude of the resulting acceleration component AMP according to the modified 6-mode 3-D theory of shells, obtained for an aluminium flanged pipe section with a circumferential crack in the case of the antisymmetric excitation. Results of numerical computations by TD-SFEM with NRBCs at infinity modelled by ALID

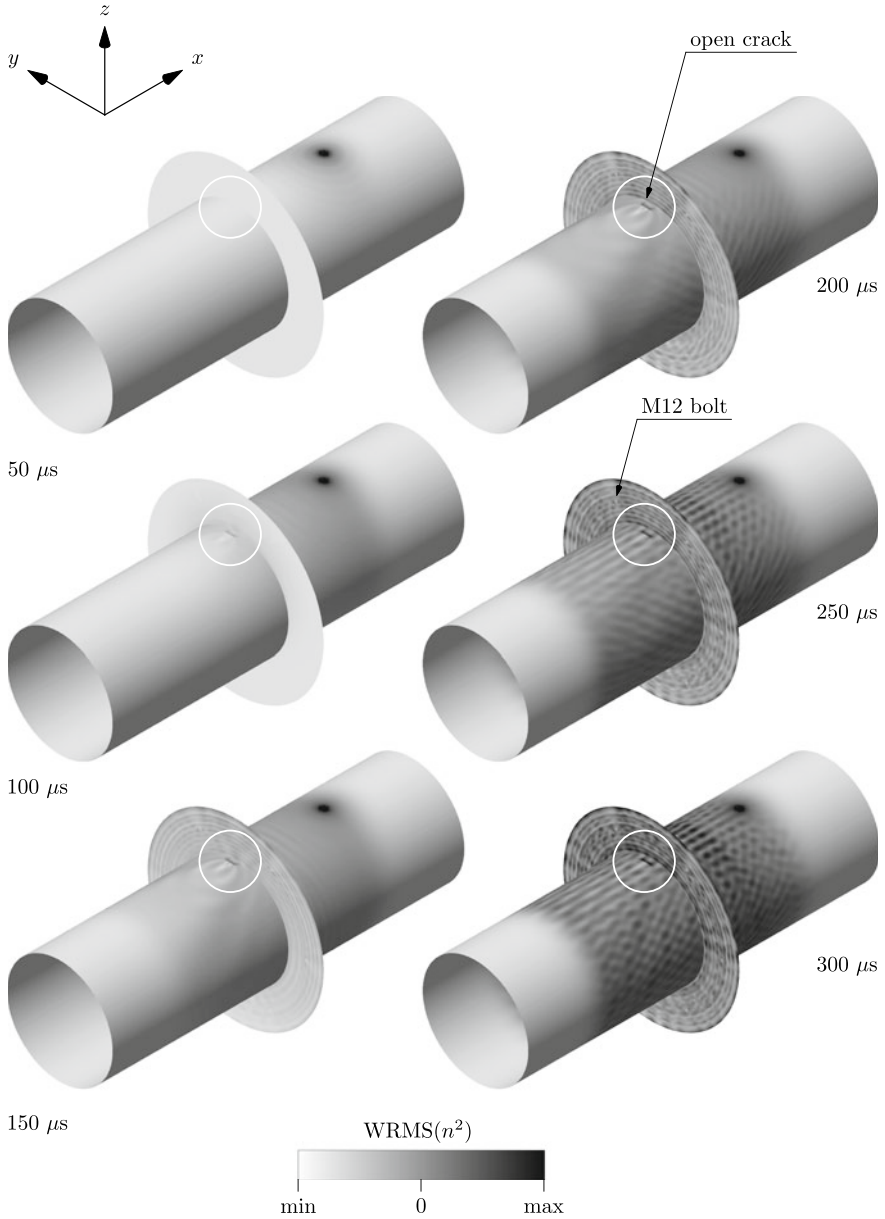


**Fig. 12.32** WRMS ( $n^2$ ) patterns for the amplitude of the resulting acceleration component AMP according to the modified 6-mode 3-D theory of shells, obtained for an aluminium flanged pipe section with a circumferential crack in the case of the symmetric excitation. Results of numerical computations by TD-SFEM with NRBCs at infinity modelled by ALID

which lead to the result of 18.5 mm in the case of antisymmetric excitation and of 16.0 mm in the case of symmetric excitation. The obtained results stay close to the assumed value of the distance  $d$  equal to 17 mm with the relative error of 8.5% and  $-5.5\%$ , respectively.

In the very same manner as before, in order to precisely pinpoint the location of the crack, the damage indicator in the form of  $WRMS(n^2)$  is employed as presented in Figs. 12.31 and 12.32. Thanks to this the location of the crack within the flanged pipe section under consideration with a circumferential crack becomes easily visible as soon as the excited waves reach point  $P_2$ , that is well before the initial 400  $\mu\text{s}$ . At the same time the locations of the bolts are also revealed.

It can be also noted that the interaction of propagating waves with the crack leads to more prominent patterns revealing the crack location in the case of the antisymmetric excitation than in the case of the symmetric excitation. The behaviour observed is explained based on the same analysis of the characteristic wavelengths associated with both types of excitations already given. Consequently, in the case of the symmetric excitation these wavelengths are much greater due to the greater values of the phase and group velocities associated with the fundamental symmetric mode of Lamb waves  $S_0$ , as clearly seen from Fig. 12.23. Thus, the resulting sensitivity to damage is smaller than in the case of the antisymmetric excitation.

As before, it can be observed that in consecutive moments in time the obtained RMS patterns only become sharpened and amplified, which allows one to shorten the time of numerical analysis significantly. In the current case, according to results presented in Figs. 12.31 and 12.32, with no loss of accuracy the total calculation time  $T$  can be reduced by half from the initial 800 to 400  $\mu\text{s}$  and from 6,400 equal time steps to 3,200.

It should be emphasised that for excitation signals broader in the frequency domain, which may lead to the propagation of other symmetric or antisymmetric modes of Lamb waves and SH-waves than the fundamental modes  $S_0$ ,  $A_0$  and  $SH_0$  mode other theories of shell behaviour should be used, preferably multi-mode or higher-order multi-mode 3-D theories.

## References

1. W. Ostachowicz, P. Kudela, M. Krawczuk, and A. Żak. *Guided waves in structures for SHM. The time-domain spectral element method*. John Wiley & Sons Ltd., Singapore, 2012.
2. A. Żak, M. Krawczuk, Ł. Skarbek, and M. Palacz. Numerical analysis of elastic wave propagation in unbounded structures. *Finite Elements in Analysis and Design*, 90:1–10, 2014.
3. W. Ostachowicz, M. Krawczuk, A. Żak, and P. Kudela. Damage detection strategies in elements of structures by the elastic wave propagation method. *Computer Assisted Mechanics and Engineering Sciences*, 13:109–204, 2006.
4. A. Żak, M. Radziński, M. Krawczuk, and W. Ostachowicz. Damage detection strategies based on propagation of guided elastic waves. *Smart Materials and Structures*, 21:1–18, 2012.
5. A. Żak. A novel formulation of a spectral plate element for wave propagation in isotropic structures. *Finite Element in Analysis and Design*, 45:650–658, 2009.



6. V. Giurgiutiu. *Structural health monitoring of aerospace composites*. Academic Press, Oxford, 2016.
7. J. L. Rose. *Ultrasonic waves in solid media*. Cambridge University Press, Cambridge, 1999.

# Chapter 13

## Periodic Properties of FE Discrete Numerical Models



### 13.1 Bloch's Theorem

Bloch's<sup>1</sup> theorem is one of the most fundamental theorems in solid-state physics, which allows one to study the properties and the behaviour of periodic structures. It should be said that now its application fields lay far beyond solid-state physics and concern not only the investigations of crystal lattices, but also the design and development of metamaterials and even further, to study the numerical properties of computational models. The close resemblance of these application fields is well illustrated by Fig. 13.1.

The essence of Bloch's theorem is the statement that the solution to the Schrödinger<sup>2</sup> wave equation  $\psi$  in the case of periodic potentials takes a special form and can be represented as a plane harmonic wave  $e^{i\mathbf{k}\cdot\mathbf{r}}$  modulated by a certain periodic function  $u$ , which expresses the properties of the potentials. This can be formally written in the following manner:

$$\psi(\mathbf{r}) = e^{i\mathbf{k}\cdot\mathbf{r}}u(\mathbf{r}) \quad (13.1)$$

---

<sup>1</sup> Felix Bloch (1905–1983) was a Swiss born American physicist whose works mainly concerned solid-state physics: ferromagnetism and nuclear magnetic resonance. For his input in this field he was awarded the Nobel Prize in Physics in 1952. His theoretical works concerned the application of the Schrödinger equation for studies of the behaviour of electrons in crystal lattices and led to the formulation of the theorem known today as Bloch's theorem.

<sup>2</sup> Erwin Rudolf Josef Alexander Schrödinger (1887–1961) was an Austrian theoretical physicist, naturalised in Ireland in 1948, who formulated one of the most important and fundamental equations of the solid-state physics, which is known nowadays as the Schrödinger equation. For his theoretical works on quantum mechanics he was awarded the Nobel Prize in Physics in 1933. His broad scientific interests concerned also statistical mechanics, thermodynamics, electrodynamics, general relativity and many more.

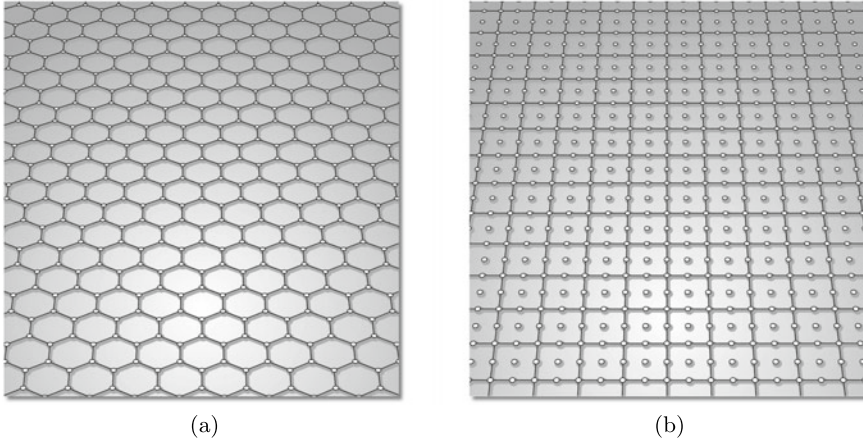


**Fig. 13.1** A schematic representation of periodic structures: **a** a 2-D lattice of carbon atoms in graphene formed out of hexagonal cells, **b** a 2-D mesh of FEs formed out of 9-node square FEs

where  $\mathbf{r} = [x, y, z]^T$  denotes the position vector in a 3-D space, the symbol  $\mathbf{k} = [k_x, k_y, k_z]^T$  denotes the vector of wave numbers, while  $i$  is the imaginary unit, i.e.  $i^2 = -1$ .

Despite its general applicability to problems in 3-D space Bloch's theorem is much easier to follow in a 1-D case. For this purpose it is assumed that longitudinal harmonic waves propagate within a 1-D periodic medium, which can be described by two different wave propagation phase velocities  $c_1$  and  $c_2$ . In order to further simplify the analysis it is also assumed that the wave behaviour can be fully described by the 1-D wave equation for longitudinal waves, given by Eq. (2.15), which in the realm of FEM is equivalent to the 1-mode 1-D theory (elementary) of rods, given by Eq. (9.2).

Formally, Bloch's theorem in a 1-D case can be presented in the following way:

$$\psi(x) = e^{ikx}u(x) \quad (13.2)$$

where  $k$  is the wave number. As a consequence, for periodically spaced cells of length  $a$  the following relation must be satisfied at the cell level:

$$\psi(x + a) = e^{ik(x+a)}u(x + a) = e^{ika}e^{ikx}u(x) = e^{ika}\psi(x) \quad (13.3)$$

since the modulation function  $u$  is periodic, i.e.  $u(x + a) = u(x)$ .

It is noteworthy that although Bloch's theorem is formulated for infinite media it can also be applied to study the behaviour of finite structures, such as, for example, structures composed of a large number of cells<sup>3</sup> periodically arranged in space. This

<sup>3</sup> In practice the properties of periodic structures are well exhibited for the number of cells as small as 100. However, for real structures of finite dimensions composed of a smaller number of cells

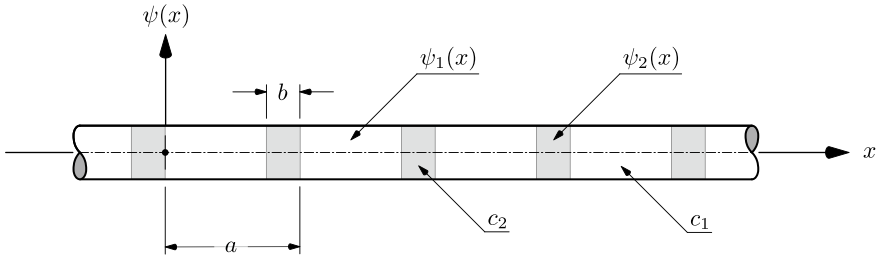


**Fig. 13.2** A schematic representation of a 1-D periodic medium characterised by two different phase velocities  $c_1$  and  $c_2$  of propagating waves

can be easily achieved by a simple assumption of periodic/cyclic boundary conditions for the function  $\psi$ , i.e. when  $\psi(x + aN) = \psi(x)$ , where  $N$  is the total number of cells.

Consequently, the 1-D periodic medium under consideration can be well described by a sequence of  $N$  cells of length  $a$ , where within each cell the phase velocity of propagating waves is equal to  $c_1$  over the distance  $(a - b)$  and to  $c_2$  over the distance  $b$ , as presented in Fig. 13.2 [1].

Next, the periodic/cyclic boundary conditions  $\psi(x + aN) = \psi(x)$  can be combined with Eq. (13.3) in order to obtain the relationship, which must be satisfied at the sequence level:

$$\psi(x + aN) = e^{ikaN} \psi(x) = \psi(x) \quad \rightarrow \quad e^{ikaN} = 1 \quad (13.4)$$

which leads to the relationship for the wave number  $k$ :

$$e^{ikaN} = 1 \quad \rightarrow \quad k_n = \frac{2\pi n}{aN}, \quad n = 0, \pm 1, \pm 2, \dots, \pm N/2 \quad (13.5)$$

where  $k_n$  takes only  $N/2 + 1$  different values<sup>4</sup> in order to represent waves travelling in the negative and positive directions of the  $x$  axis.

It can be checked that in the 1-D periodic medium both Bloch's waves  $\psi_1$  and  $\psi_2$ , representing the solutions to the wave equation within a single cell of length  $a$ , can be expressed as:

$$\begin{cases} \psi_1(x) = A_1 e^{ik_1 x} + A_2 e^{-ik_1 x}, & 0 \leq x \leq a - b \\ \psi_2(x) = B_1 e^{ik_2 x} + B_2 e^{-ik_2 x}, & a - b \leq x \leq a \end{cases} \quad (13.6)$$

---

reaching only 40 or 50 cells such properties can also be found, although in such cases they may be influenced by structural boundary conditions.

<sup>4</sup> Note that  $n = 0$  is the value of the wave number  $k_n \rightarrow 0$  corresponding to the wavelength  $\lambda_n \rightarrow \infty$  or alternatively to a constant wave field.

while thanks to the use of Eq. (13.3) both periodic waves  $u_1$  and  $u_2$  have the following form:

$$\begin{cases} u_1(x) = A_1 e^{i(\hat{k}_1 - k_n)x} + A_2 e^{-i(\hat{k}_1 + k_n)x}, & 0 \leq x \leq a - b \\ u_2(x) = B_1 e^{i(\hat{k}_2 - k_n)x} + B_2 e^{-i(\hat{k}_2 + k_n)x}, & a - b \leq x \leq a \end{cases} \quad (13.7)$$

where  $A_1$ ,  $A_2$ ,  $B_1$  and  $B_2$  are certain unknown constants, while  $\omega$  is the common angular frequency for both harmonic waves  $\psi_1$  and  $\psi_2$  such that:

$$\omega = \hat{k}_1 c_1 = \hat{k}_2 c_2 \quad (13.8)$$

The use of the continuity conditions for the Bloch's waves  $\psi_1$  and  $\psi_2$  and their spatial derivatives, as well as for the periodic waves  $u_1$  and  $u_2$ , which can be written as:

$$\begin{cases} \psi_1|_{0^+} = \psi_2|_{0^-}, \quad \frac{d\psi_1}{dx}|_{0^+} = \frac{d\psi_2}{dx}|_{0^-} \\ u_1|_{a-b} = u_2|_b, \quad \frac{du_1}{dx}|_{a-b} = \frac{du_2}{dx}|_b \end{cases} \quad (13.9)$$

leads to a set of four homogeneous equations for the unknown constants  $A_1$ ,  $A_2$ ,  $B_1$  and  $B_2$ . A non-trivial solution to this set can be obtained only if its determinant vanishes, i.e. when the following equation is satisfied:

$$\begin{aligned} \cos[\hat{k}_1(a - b)] \cos \hat{k}_2 b - \frac{\hat{k}_1^2 + \hat{k}_2^2}{2\hat{k}_1\hat{k}_2} \sin[\hat{k}_1(a - b)] \sin \hat{k}_2 b \\ = \cos k_n a, \quad n = 0, \pm 1, \pm 2, \dots, \pm N/2 \end{aligned} \quad (13.10)$$

which equation represents the characteristic solution to the wave propagation problem in the 1-D periodic medium characterised by two different wave propagation phase velocities.

It should be pointed out that the characteristic Eq. (13.10) is dependent on the angular frequency  $\omega$  through the wave numbers  $k_1$  and  $k_2$ . It can be easily solved numerically, with the angular frequency  $\omega$  treated as a parameter. Based of the form of the characteristic equation it can be stated that that the phenomenon of wave propagation in a 1-D periodic medium described by two different phase velocities  $c_1$  and  $c_2$  is dispersive. An interesting feature of the characteristic equation is also the fact that it has real solutions only if the absolute value of its left-hand side stays below 1. Also for this reason the resulting dispersion curve becomes discontinuous.

Consequently, the characteristic Eq. (13.10) predicts the presence of certain frequency bands, so-called *frequency band gaps*,<sup>5</sup> within which no harmonic waves can propagate within the 1-D periodic medium under consideration. This is well illustrated by Fig. 13.3 in the case of a 1-D periodic medium modelled by  $N = 200$  cells

<sup>5</sup> In the literature frequency band gaps are very often referred to as stop bands.

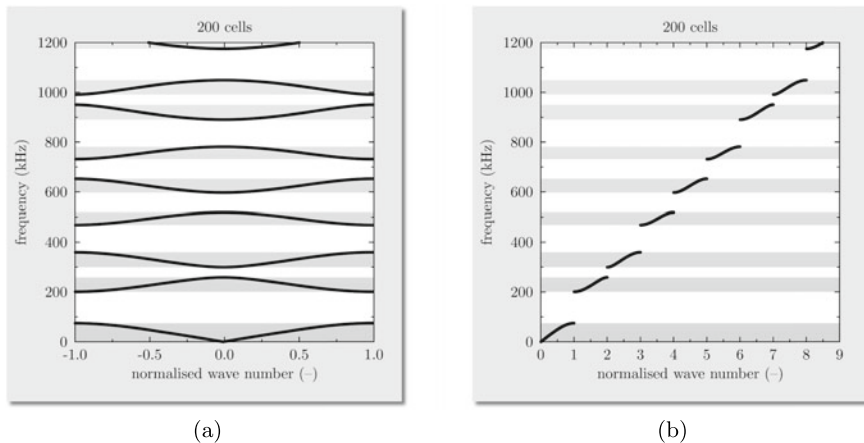


**Fig. 13.3** Spectra of frequencies of free vibrations for the fundamental mode of longitudinal waves  $L_0$  propagating in a 1-D periodic medium characterised by two different phase velocities  $c_1$  and  $c_2$  of propagating waves: **a** in the reduced zone, **b** in the extended zone. Results of numerical computations obtained by the use of Bloch's theorem for 200 cells,  $c_1 = 5$  km/s,  $c_2 = 1$  km/s,  $a = 10$  mm,  $b = 2$  mm

of length  $a = 10$  mm. In this case it is assumed that the phase velocity  $c_1$  is equal to 5 km/s over the distance  $(a - b)$  and drops to 1 km/s over the distance  $b = 2$  mm.

Similar results can be obtained by the use of TD-SFEM, as presented in Fig. 13.4, for the same 1-D periodic medium but modelled by 1000 SFEs. For the purpose of numerical computations 6-node SFEs based on Chebyshev nodes, as discussed in Sect. 10.4, according to the 1-mode 1-D theory (elementary) of rods are employed. Periodic/cyclic boundary conditions are used in this case. This time, however, the obtained results are shown as a function of the frequency number  $n$  rather than the wave number  $k_n$  in order to emphasise their periodic nature and the model periodicity. Then, it is interesting to observe that the frequency band gaps  $FG_j (j = 1, 2, \dots)$ , shown in Fig. 13.4, regularly appear for frequency numbers  $n$  being multiplies of the total number of cells  $N = 200$ . This feature of periodic structures can be exploited to assess the dynamic properties of discrete numerical models built by the use of FEM or its clones, which is very important in the case of wave propagation problems.<sup>6</sup>

It can be also seen from the results presented in Fig. 13.4 that in the regime of higher frequencies or for higher frequency numbers  $n$ , i.e. for  $n > 800$ , the relative frequency error increases rapidly. Moreover, its changes have a clearly periodic nature, indicating periodic properties of the discrete numerical model of the 1-D periodic medium under consideration, which have an as yet unknown origin and which gradually become more apparent. It will turn out that the source of this unknown periodicity, in the case of the numerical model of the medium, based on the appli-

<sup>6</sup> Note that the ends of the calculated frequency spectra as well as the edges of existing frequency band gaps indicate points where  $d\omega/dk \rightarrow 0$ . On the other hand when  $d\omega/dk \rightarrow 0$  then  $c_g \rightarrow 0$ .

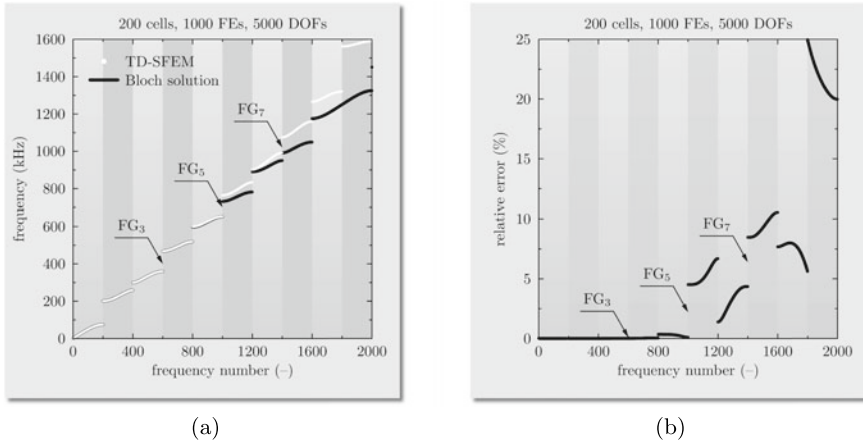


**Fig. 13.4** Spectra of: **a** frequencies of free vibrations, **b** relative frequency errors, for the fundamental mode of longitudinal waves  $L_0$  propagating in a 1-D periodic medium characterised by two different phase velocities  $c_1$  and  $c_2$  of propagating waves: **a** in the reduced zone, **b** in the extended zone. Results of numerical computations by TD-SFEM according to the 1-mode 1-D theory (elementary) of rods versus results of numerical computations by Bloch’s theorem for 200 cells,  $c_1 = 5$  km/s,  $c_2 = 1$  km/s,  $a = 10$  mm,  $b = 2$  mm

cation of FEM or its clones, comes from the discontinuity of the strain/stress fields between adjacent FEs, as discussed in detail in the next sections.

It should be mentioned that Eq. (13.10) can be simplified in the case of a 1-D periodic medium characterised by a single wave velocity  $c_1$  and the discontinuity of its properties between adjacent cells. This can be obtained under the following assumption:  $b \rightarrow 0$  and  $k_2 \rightarrow 0$ , for  $k_2 b = \text{const}$ . Then a new characteristic equation takes a simpler form:

$$\cos \hat{k}_1 a + A \frac{\sin \hat{k}_1 a}{\hat{k}_1 a} = \cos k_n a, \quad n = 0, \pm 1, \pm 2, \dots, \pm N/2 \quad (13.11)$$

where  $A$  represents a constant expressing the intensity of the discontinuity.

It can be immediately noted that if  $A = 0$  the characteristic Eq. (13.11) reduces itself to the very well-known characteristic equation, which is obtained in the case of a non-periodic 1-D elastic rod for periodic/cyclic boundary conditions.

### 13.2 Bloch Reduction

The Bloch reduction technique is a numerical implementation of Bloch’s theorem, which enables one to practically apply Bloch’s theorem especially in the case of FEM. The Bloch reduction technique allows one to investigate the dynamic properties of

the entire periodic structure from the level of its single cell, as presented in Fig. 13.5, which may also be represented by a single FE [2].

A starting point of the analysis by the Bloch reduction technique is the eigenvalue problem, which arises from the already-known form of the equations of motion, given by Eq. (11.9), which under specific conditions of no damping and no external forces acting reduces itself to the well-known eigenvalue problem.<sup>7</sup>

In the case of the 1-mode 1-D theory (elementary) of rods considered in previous Sect. 13.1 the eigenvalue problem can be expressed as follows:

$$(\mathbf{K} - \omega^2 \mathbf{M}) \cdot \mathbf{q} = \mathbf{0} \quad (13.12)$$

which has solutions represented by a finite number of pairs  $(\omega_j, \mathbf{q}_j)$ , where  $j = 1, 2, \dots, m$ . As before the symbols  $\mathbf{M}$  and  $\mathbf{K}$  denote the characteristic global inertia and stiffness matrices of a single cell.

In the pair  $(\omega_j, \mathbf{q}_j)$   $\omega_j$  denotes the  $j$ -th angular frequency of free vibrations and  $\mathbf{q}_j$  is the corresponding  $j$ -th mode (vector) of free vibrations, where  $m$  is equal to the total number of nodes, i.e. DOFs, of a discrete numerical model of one single cell only,<sup>8</sup> as presented in Fig. 13.5.

In the case of a single cell the displacements within the vector of nodal displacements  $\mathbf{q}$  may be conveniently divided as belonging to the internal nodes  $\mathbf{q}_a$  or the boundary nodes  $\mathbf{q}_b$ . Following the concept a 1-D periodic medium presented in Fig. 13.5 it can be formally written that:

$$\begin{aligned} \mathbf{q} &= [q_1, q_2, \dots, q_{m-1}, q_m]^\top \\ &\quad \swarrow \qquad \searrow \\ \mathbf{q}_a &= [q_2, q_3, \dots, q_{m-1}]^\top, \quad \mathbf{q}_b = [q_1, q_m]^\top \end{aligned} \quad (13.13)$$

At this point the application of the cyclic/periodic boundary conditions for the boundary nodes  $\mathbf{q}_b$  leads to the following relationship:

$$q_m = q_1 e^{ik_n a}, \quad k_n = \frac{2\pi n}{aN}, \quad n = 0, \pm 1, \pm 2, \dots, \pm N/2 \quad (13.14)$$

which consequently allows one to create the reduced vector of nodal displacements  $\mathbf{q}_r(n)$  expressed as:

$$\mathbf{q} = \mathbf{A}(n) \cdot \mathbf{q}_r(n) \quad (13.15)$$

<sup>7</sup> The eigenvalue problem belongs to a very important group of problems in structural dynamics. This is because structural dynamic responses are always built up from eigenmodes/modes of free vibrations, whose number and amplitudes depend on the frequency content of the excitation signal [3].

<sup>8</sup> This is because in the current case there is only one DOF per node. Also for this reason the total number of nodes is equal to the total number of DOFs. In a more general case the number of DOFs per node can be greater than one.



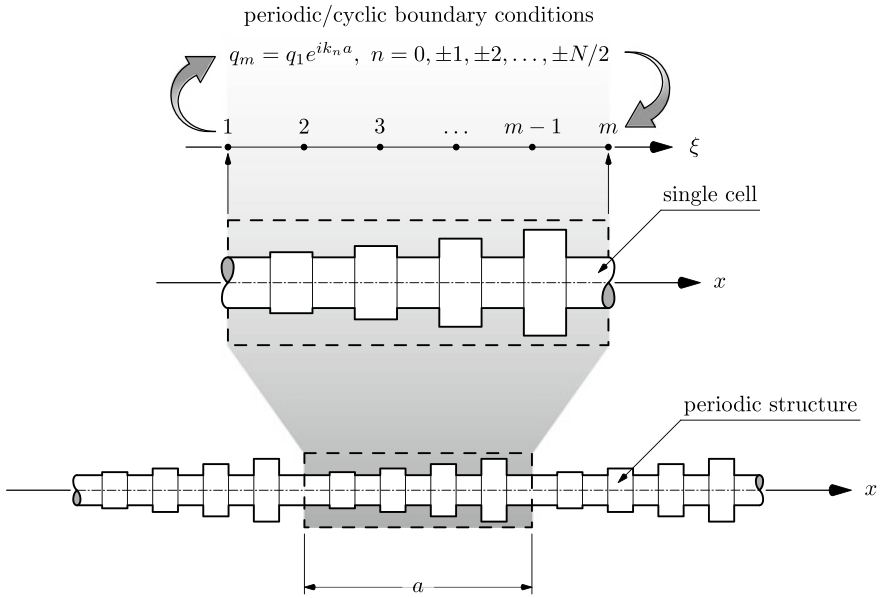


**Fig. 13.5** A concept of the Bloch reduction technique in the case of a 1-D periodic medium modelled by FEM

where the rectangular matrix  $\mathbf{A}(n)$  of size  $m \times (m - 1)$  is defined as follows:

$$\begin{cases} A_{j,j} = 1, & j = 1, 2, \dots, m - 1 \\ A_{j,1} = e^{ik_n a}, & j = m \end{cases} \quad (13.16)$$

As a consequence a modified eigenvalue problem can be formulated:

$$[\mathbf{K}_r(n) - \omega^2 \mathbf{M}_r(n)] \cdot \mathbf{q}_r(n) = \mathbf{0} \quad (13.17)$$

where  $\mathbf{M}_r(n)$  and  $\mathbf{K}_r(n)$  denote the reduced characteristic global inertia and stiffness matrices of a single cell expressed as:

$$\begin{cases} \mathbf{M}_r(n) = \mathbf{A}(n)^T \cdot \mathbf{M} \cdot \mathbf{A}(n) \\ \mathbf{K}_r(n) = \mathbf{A}(n)^T \cdot \mathbf{K} \cdot \mathbf{A}(n) \end{cases} \quad (13.18)$$

Finally, repeated solutions to the reduced eigenvalue problem (13.17) lead to the frequency spectrum of free vibrations of the 1-D periodic medium modelled by FEM, which is obtained from the level of its single cell.

It should be strongly emphasised that such a general procedure as the one described above, after necessary modifications, may be successfully applied for other types of

1-D, 2-D or even 3-D periodic structures. Then, the Bloch reduction technique must take into account all available boundary nodes as well as corresponding nodal DOFs.

### 13.3 Numerical Dispersion

Depending on the degree of approximation polynomials discrete numerical models produced by FEM or its clones may exhibit some undesired numerical dispersion, which has its origin in certain periodic properties resulting from the applied modelling techniques [1]. As discussed in Sect. 10.4 it is not required for the shape functions employed by FEM or its clones to guarantee the continuity of strain/stress fields between adjacent FEs in order to guarantee the convergence of obtained numerical solutions. Consequently, certain discontinuities of these fields always exist, even though they can be minimised by increasing the degree of approximation polynomials  $r$ . For problems that require fine spatial discretisation the resulting meshes of FEs gradually build up properties typical of periodic structures with their inherent feature, which is the presence of frequency band gaps. However, the frequency band gaps tend to manifest themselves strongly at high frequencies in the upper parts of the available frequency spectra.

Typically, in FEM it is sufficient to assume that the shape functions employed lead to solutions of class  $C^0$  only. Such an approach works very well in the case of various static or low frequency dynamic problems, where the presence of frequency band gaps in the frequency spectrum remain unnoticed. However, in the case of high frequency dynamics or wave propagation problems this approach may lead to completely wrong or falsified results even for relatively rich discrete numerical models of many DOFs.

Here, the Bloch reduction technique comes as a very useful tool, which can be applied in order to investigate the properties of built discrete numerical models and to search for undesired numerical dispersion in the spatial domain as well as the presence of frequency band gaps. Yet again a good starting point for such an analysis is the 1-D wave equation for longitudinal waves, given by Eq. (2.15), which in the realm of FEM is equivalent to the 1-mode 1-D theory (elementary) of rods, given by Eq. (9.2). As shown in Sect. 2.5 the solutions to the 1-D wave equations are non-dispersive longitudinal waves with the corresponding dispersion curves for the phase and group velocities presented in Sect. 9.1.

It can be demonstrated that for various degrees of approximation polynomials  $r$  a similar characteristic equation can be obtained to that given by Eq. (13.11), which can be presented in a general form as:

$$\prod_{j=1}^{2r} \frac{\hat{k}_1 a - \alpha_j}{\hat{k}_1 a - \beta_j} = \frac{\cos k_n a}{(-1)^r (r+1)}, \quad n = 0, \pm 1, \pm 2, \dots, \pm N/2 \quad (13.19)$$

**Table 13.1** Roots  $\alpha_j$  and  $\beta_j$ , where  $j = 1, 2, \dots, 2r$ , from the characteristic equation (13.19), for selected degrees of approximation polynomials  $r$

Degree $r$	Roots $\alpha_j$	Roots $\beta_j$
1	$\alpha_1 = 1.732, \alpha_2 = -\alpha_1$	$\beta_1 = 2.449i, \beta_2 = \bar{\beta}_1$
2	$\alpha_1 = 1.577, \alpha_2 = -\alpha_1$	$\beta_1 = 1.935 + 3.427i, \beta_2 = \bar{\beta}_1$
	$\alpha_3 = 5.673, \alpha_4 = -\alpha_3$	$\beta_3 = -\beta_1, \beta_4 = -\bar{\beta}_1$
3	$\alpha_1 = 1.571, \alpha_2 = -\alpha_1$	$\beta_1 = 5.088i, \beta_2 = \bar{\beta}_1$
	$\alpha_3 = 4.836, \alpha_4 = -\alpha_3$	$\beta_3 = 3.817 + 4.078i, \beta_4 = \bar{\beta}_3$
	$\alpha_5 = 10.45, \alpha_6 = -\alpha_5$	$\beta_5 = -\beta_3, \beta_6 = -\bar{\beta}_3$
4	$\alpha_1 = 1.571, \alpha_2 = -\alpha_1$	$\beta_1 = 1.848 + 6.228i, \beta_2 = \bar{\beta}_1$
	$\alpha_3 = 4.725, \alpha_4 = -\alpha_3$	$\beta_3 = -\beta_1, \beta_4 = -\bar{\beta}_1$
	$\alpha_5 = 8.331, \alpha_6 = -\alpha_5$	$\beta_5 = 5.691 + 4.584i, \beta_6 = \bar{\beta}_5$
	$\alpha_7 = 16.30, \alpha_8 = -\alpha_7$	$\beta_7 = -\beta_5, \beta_8 = -\bar{\beta}_5$
5	$\alpha_1 = 1.571, \alpha_2 = -\alpha_1$	$\beta_1 = 7.734i, \beta_2 = \bar{\beta}_1$
	$\alpha_3 = 4.713, \alpha_4 = -\alpha_3$	$\beta_3 = 3.675 + 7.127i, \beta_4 = \bar{\beta}_3$
	$\alpha_5 = 7.939, \alpha_6 = -\alpha_4$	$\beta_5 = -\beta_3, \beta_6 = -\bar{\beta}_3$
	$\alpha_7 = 12.17, \alpha_8 = -\alpha_4$	$\beta_7 = 7.567 + 5.007i, \beta_8 = \bar{\beta}_7$
	$\alpha_9 = 23.36, \alpha_{10} = -\alpha_4$	$\beta_9 = -\beta_7, \beta_{10} = -\bar{\beta}_7$

where  $\alpha_j$  and  $\beta_j$ , with  $j = 1, 2, \dots, 2r$ , represent roots of certain Lagrange polynomials of  $\hat{k}_1 a$  and degree  $2r$ , which can be easily obtained by the application of the Bloch reduction technique and some mathematical simplifications and manipulations. For selected degrees of approximation polynomials  $r$  the roots  $\alpha_j$  and  $\beta_j$  are shown in Table 13.1.

It should be emphasised that the very existence of the characteristic equation in the form given by Eq. (13.19) confirms the periodic nature of the investigated discrete numerical models built by the use of FEM or its clones and based on the 1-mode 1-D theory (elementary) of rods. Similar characteristic equations can also be obtained for other multi-mode and higher-order multi-mode theories in the case of 1-D, 2-D or 3-D structural elements.

The characteristic equations for various degrees of approximation polynomials  $r$ , resulting from Eq. (13.19) and evaluated based on the data from Table 13.1, can be easily solved numerically. The results of such solutions are presented in Fig. 13.6 as appropriate spectra of frequencies of free vibrations and in Fig. 13.7 as corresponding dispersion curves for the phase velocity.

Indeed, the results presented in Fig. 13.6 confirm a strong link between the number of frequency band gaps, denoted as  $FG_j (j = 1, 2, \dots, r - 1)$ , observable in the frequency spectra and the degree of approximation polynomials  $r$ . Independently of the dimensionality of the problem under consideration the periodicity of a discrete numerical model can be understood as the number of identical cells or FEs per unit length. It can be observed that frequency band gaps tend to appear at the frequency numbers being multiples of the model periodicity. If the model periodicity is equal

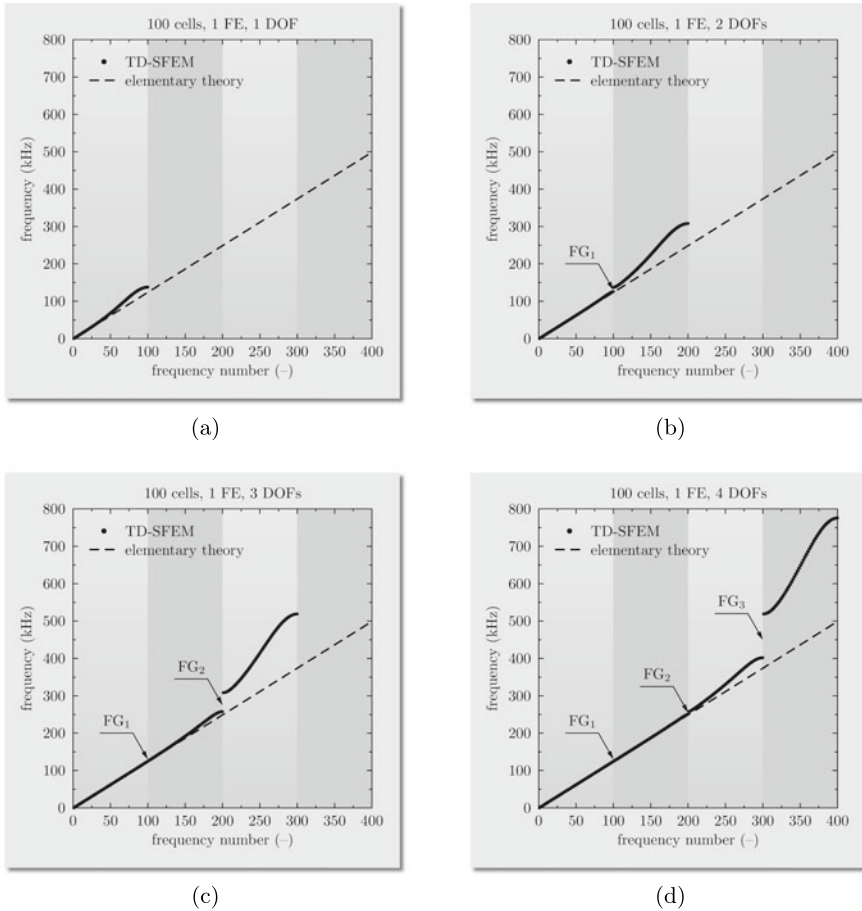


**Fig. 13.6** Spectra of frequencies of free vibrations for the fundamental mode of longitudinal waves  $L_0$  propagating a 1-D non-periodic medium for selected degrees of approximation polynomials: **a**  $r = 1$ , **b**  $r = 2$ , **c**  $r = 3$ , **d**  $r = 4$ . Results of numerical computations by FEM/TD-SFEM according to the 1-mode 1-D theory (elementary) of rods, obtained by the use of the Bloch reduction technique for 100 cells  $c_1 = 5$  km/s,  $a = 20$  mm

to 100, as in the case of results presented in Fig. 13.6, then frequency band gaps build at multiples of the model periodicity, i.e. every 100 frequencies of free vibrations, with an increase in the degree of approximation polynomials  $r$ .

Moreover, it should also be observed that the frequency band gaps of lower indexes tend to fade with an increase of the degree of approximation polynomials  $r$  and gradually become unrecognisable based on the analysis of the frequencies of free vibrations or dispersion curves for the phase velocity, as seen in the case of the frequency band gap  $FG_1$  from Table 13.2.

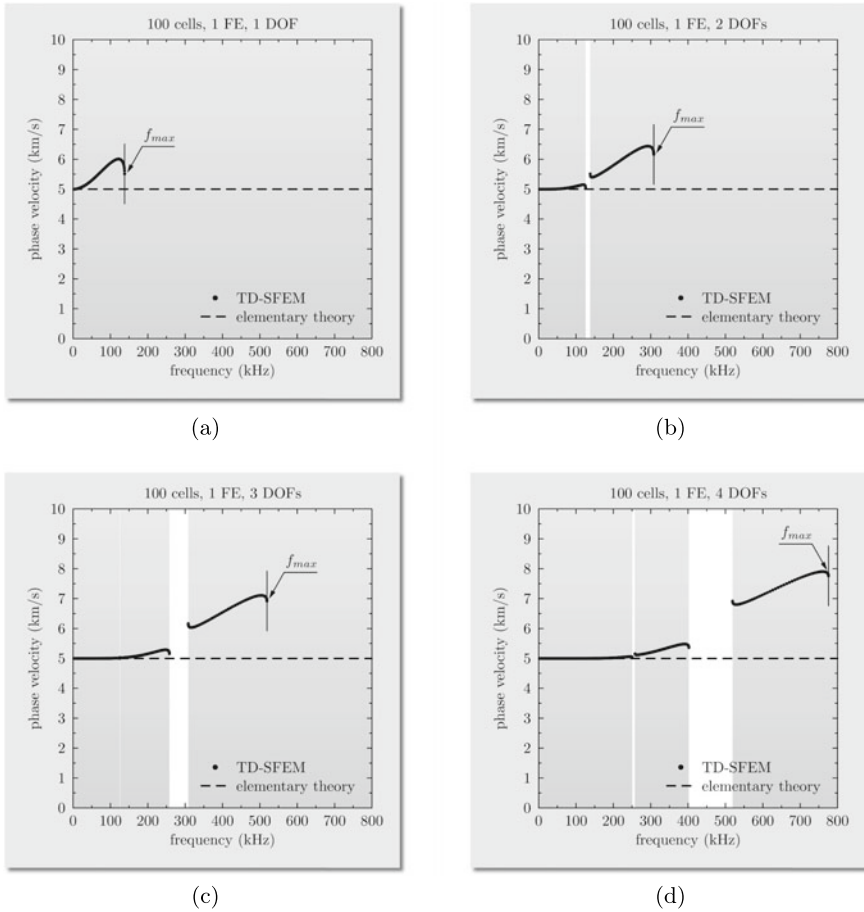


**Fig. 13.7** Dispersion curves for the phase velocity for the fundamental mode of longitudinal waves  $L_0$  propagating in a 1-D non-periodic medium for selected degrees of approximation polynomials: **a**  $r = 1$ , **b**  $r = 2$ , **c**  $r = 3$ , **d**  $r = 4$ . Results of numerical computations by FEM/TD-SFEM according to the 1-mode 1-D theory (elementary) of the longitudinal behaviour of rods, obtained by the use of the Bloch reduction technique for 100 cells,  $c_1 = 5$  km/s,  $a = 20$  mm

As already mentioned the presence of frequency band gaps has a great impact on dispersion curves. The dispersion curves obtained numerically for the phase velocity  $c_p$  tend to diverge from the analytical ones at the ends of frequency spectra as well as exhibit discontinuities/jumps at the edges of frequency band gaps with an increase in the frequency, as shown in Fig. 13.7. In this case it can be easily checked for  $r = 1$  that the characteristic equation obtained based on Eq. (13.19) can be presented as:

$$\frac{\hat{k}_1^2 a^2 - \alpha_1^2}{\hat{k}_1^2 a^2 - \beta_1^2} = \frac{\cos k_n a}{(-2)}, \quad n = 0, \pm 1, \pm 2, \dots, \pm N/2 \quad (13.20)$$

**Table 13.2** Statistical data on the influence of the degree of approximation polynomials  $r$  on the number and positions of frequency band gaps in the case of discrete numerical models of a 1-D non-periodic medium. Results of numerical computations by FEM/TD-SFEM according to the 1-mode 1-D theory (elementary) of the longitudinal behaviour of rods, obtained by the use of the Bloch reduction technique for 100 cells,  $c_1 = 5$  km/s,  $a = 20$  mm

Degree $r$	FG <sub>1</sub> (kHz)	FG <sub>2</sub> (kHz)	FG <sub>3</sub> (kHz)	FG <sub>4</sub> (kHz)
2	125.8 ... 137.8	–	–	–
3	125.0 ... 125.8	257.9 ... 308.2	–	–
4	125.0 ... 125.0	250.9 ... 257.9	402.1 ... 519.0	–
5	125.0 ... 125.0	250.1 ... 250.9	380.0 ... 402.1	563.4 ... 775.9

which, after noting that  $\omega = \hat{k}_1 c_1$ , can be easily simplified and transformed to the following form:

$$\omega^2 = \frac{c_1^2}{a^2} \cdot \frac{2\alpha_1^2 + \beta_1^2 \cos k_n a}{2 + \cos k_n a}, \quad n = 0, \pm 1, \pm 2, \dots, \pm N/2 \quad (13.21)$$

leading to the relationship for the phase velocity  $c_p$  given by:

$$c_p = \frac{\omega}{k} = \frac{c_1}{k_n a} \cdot \sqrt{\frac{2\alpha_1^2 + \beta_1^2 \cos k_n a}{2 + \cos k_n a}}, \quad n = 0, \pm 1, \pm 2, \dots, \pm N/2 \quad (13.22)$$

Remembering that at the end of calculated frequency spectra  $k_n \rightarrow \pm\pi/a$  and  $\cos k_n a \rightarrow -1$  the corresponding phase velocity  $c_p$  is:

$$c_p = \pm \sqrt{2\alpha_1^2 - \beta_1^2} \cdot \frac{c_1}{\pi} = \pm 12 \cdot \frac{c_1}{\pi} \cong \pm 1.10 \cdot c_1, \quad \text{for } k_n = \pm\pi/a \quad (13.23)$$

The dispersion curves obtained numerically for the group velocity  $c_g$  tend to zero at the ends of frequency spectra as well as the edges of frequency band gaps, as shown in Fig. 13.8. In this case by the use of Eq. 13.21 it can be found, after differentiation with respect to the wave number  $k$  and necessary simplifications that:

$$\omega d\omega = \frac{c_1^2}{a} \cdot \frac{(\alpha_1^2 - \beta_1^2) \sin k_n a}{(2 + \cos k_n a)^2} dk, \quad n = 0, \pm 1, \pm 2, \dots, \pm N/2 \quad (13.24)$$

which leads directly to the relationship for the group velocity  $c_g$  expressed as:

$$c_g = \frac{d\omega}{dk} = \frac{c_1^2}{\omega a} \cdot \frac{(\alpha_1^2 - \beta_1^2) \sin k_n a}{(2 + \cos k_n a)^2}, \quad n = 0, \pm 1, \pm 2, \dots, \pm N/2 \quad (13.25)$$

Again, noting that at the end of calculated frequency spectra  $k_n \rightarrow \pm\pi/a$  and  $\sin k_n a \rightarrow 0$  the corresponding phase velocity  $c_g$  is zero:

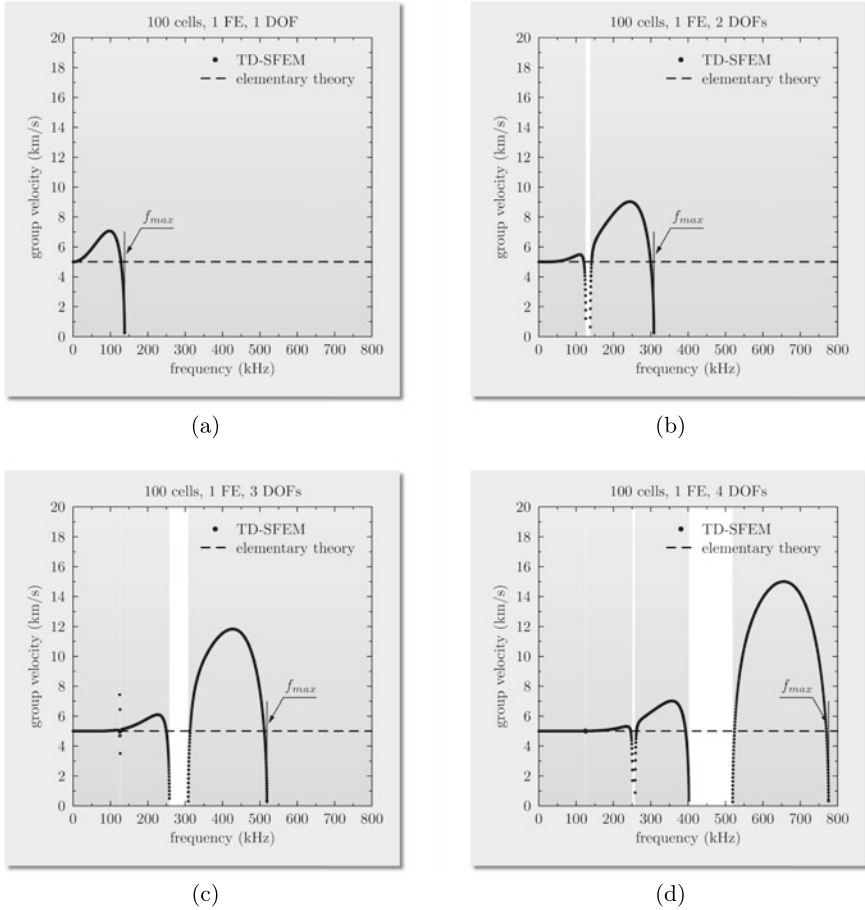


**Fig. 13.8** Dispersion curves for the group velocity for the fundamental mode of longitudinal waves  $L_0$  propagating in a 1-D non-periodic medium for selected degrees of approximation polynomials: **a**  $r = 1$ , **b**  $r = 2$ , **c**  $r = 3$ , **d**  $r = 4$ . Results of numerical computations by FEM/TD-SFEM according to the 1-mode 1-D theory (elementary) of the longitudinal behaviour of rods, obtained by the use of the Bloch reduction technique for 100 cells,  $c_1 = 5$  km/s,  $a = 20$  mm

$$c_g = 0, \text{ for } k_n = \pm\pi/a \tag{13.26}$$

Indeed, the results obtained confirm that the presence of frequency band gaps in the investigated spectra of frequencies of free vibrations has a strong impact on the usability of discrete numerical models in spite of the broadness of these spectra. Moreover, the presence of the frequency band gaps resulting from the periodicity of discrete numerical models, governed by the characteristic Eq. (13.19), leads to additional spatial numerical dispersion. This is well illustrated by Figs. 13.7 and 13.8, from which it can be seen that the obtained frequency spectra of free vibrations are

**Table 13.3** Statistical data on the influence of the degree of approximation polynomials  $r$  on the spatial numerical dispersion in the case of discrete numerical models of a 1-D non-periodic medium. Results of numerical computations by FEM/TD-SFEM according to the 1-mode 1-D theory (elementary) of rods, obtained by the use of the Bloch reduction technique for 100 cells,  $c_1 = 5 \text{ km/s}$ ,  $a = 20 \text{ mm}$

Degree $r$	Mode	1% disp. (kHz)	5% disp. (kHz)	$f_{max}$ (kHz)
1	L <sub>0</sub>	<20.21 (14.7%)	<47.42 (34.4%)	137.8
2	L <sub>0</sub>	<83.37 (27.1%)	<125.8 (40.8%)	308.2
3	L <sub>0</sub>	<125.0 (24.1%)	<231.2 (44.5%)	519.0
4	L <sub>0</sub>	<234.8 (30.3%)	<318.1 (40.1%)	775.9
5	L <sub>0</sub>	<313.2 (28.9%)	<380.0 (35.1%)	1081.6

In brackets the percentage of the entire frequency spectrum is indicated

characterised by clear numerical dispersion, even though the employed 1-mode 1-D theory (elementary) of rods is entirely non-dispersive.

The source of this additional dispersion is solely due to the periodicity of discrete numerical models built. It is noteworthy that the usable part of the available frequency spectra for the analysis of high frequency dynamics as well as wave propagation problems, offered by the discrete numerical models of the rod, are therefore defined and limited by the presence of the first significant<sup>9</sup> frequency band gap.

In the case of the degree of approximation polynomials  $r = 2$  or  $r = 3$  this is the first frequency band gap  $FG_1$ , while in the case of the degree of approximation polynomials  $r = 4$  this is the second frequency band gap  $FG_2$  since the first frequency band gap  $FG_1$  is undetectable. For this reason the usable part of the frequency spectra must also be dependent on the degree of approximation polynomials. This is summarised by the results given in Table 13.3.

But not only this, since the additional numerical dispersion due to the periodicity of the discrete numerical models under investigation should be minimised as an undesired numerical feature. Following the definition of the degrees of dispersion from Sect. 12.1, for very small dispersion below 1% only very small parts of available spectra of frequencies of free vibrations remain available for the analysis of high frequency dynamics as well as wave propagation problems, these being: 14.7, 27.1, 24.1 and 30.3% for the degrees of approximation polynomials  $r$  equal to 1, 2, 3 or 4, respectively. For small dispersion below 5% the corresponding values are: 34.4, 27.1, 24.1 and 33.5%. However, it should be noted that in these cases the obtained values are limited by the presence of neighbouring frequency band gaps, except the case of the linear approximation polynomials for  $r = 1$ , as also seen from Fig. 13.7.

<sup>9</sup> It is understood as the frequency band gap, which can be identified either based on the analysis of the frequencies of free vibrations or dispersion curves for the phase velocity.



### 13.4 Numerical Anisotropy

Numerical anisotropy can be viewed as a property of discrete numerical models in 2-D or 3-D, being a direct consequence of numerical dispersion. Its presence may also be understood as resulting from the fact that for a finite number of nodes in 2-D or 3-D it is topologically impossible to provide the same number of nodal distances per wavelength in every direction, even in the case of very fine spatial discretisation typical for high frequency dynamics or wave propagation problems solved by FEM. Similarly to the numerical dispersion also the numerical anisotropy can be investigated and studied by the use of the Bloch reduction technique.

For the purpose of such investigation an isotropic plate of infinite dimensions and constant thickness  $h$  is considered, which represents a 2-D elastic medium, as presented in Fig. 13.9. The plate is modelled as a uniform 2-D lattice/mesh of  $N \times N$  square cells/plate FEs characterised by the edge length  $a$ . The Mindlin-Reissner theory of plates is used, which in the realm of FEM corresponds to the 3-mode 2-D theory from Sect. 8.2. Thanks to the application of the Bloch reduction technique, periodic properties of discrete numerical models of the plate can be easily revealed and assessed from the level of a single cell/FE, for example, in the context of the future wave propagation analysis.

It should be recalled that the 3-mode 2-D (Mindlin-Reissner) theory of the anti-symmetric behaviour of plates is based on the use of three independent modes of elastic waves, as discussed in Sect. 8.2, which can propagate within the plate as:  $A_0$ ,  $A_1$  and  $SH_1$ . These modes are not only dispersive, but also have fully 2-D nature, which means that they can freely propagate in all available directions of the  $xy$  plane. In such a case the application of the Bloch reduction technique becomes significantly more difficult and complicated in comparison with 1-D cases.

The process of the analysis can be simplified greatly thanks to the use of the concepts known from crystallography, since the arrangements of crystal lattices in many aspects resemble uniform meshes of FEs. In the analysis of crystal lattices typically wave vectors of the reciprocal space<sup>10</sup> are used in order to describe their properties, which also indicate the directions of wave propagation within the lattices.

The same concept is employed here, where three non-dimensional wave vectors of the reciprocal space  $\tilde{k}_n^{[10]}$ ,  $\tilde{k}_n^{[01]}$  and  $\tilde{k}_n^{[11]}$  are used and where the following relationships hold:

$$\begin{cases} \tilde{k}_n^{[10]} = \tilde{k}_n^{[01]} = \tilde{k}_n^{[11]} = \frac{2n}{N}, & n = 0, \pm 1, \pm 2, \dots, \pm N/2 \\ k_n^{[10]} = k_n^{[01]} = \left(\frac{\pi}{a}\right) \tilde{k}_n^{[10]}, & k_n^{[11]} = \left(\frac{\pi}{\sqrt{2}a}\right) \tilde{k}_n^{[11]} \end{cases} \quad (13.27)$$

<sup>10</sup> The reciprocal space is a mathematical concept of space representing the Fourier transform of a physical lattice, which is also referred to as the  $k$ -space or the wave vector space. Consequently, spatial properties of the lattice are expressed in terms of wave numbers.

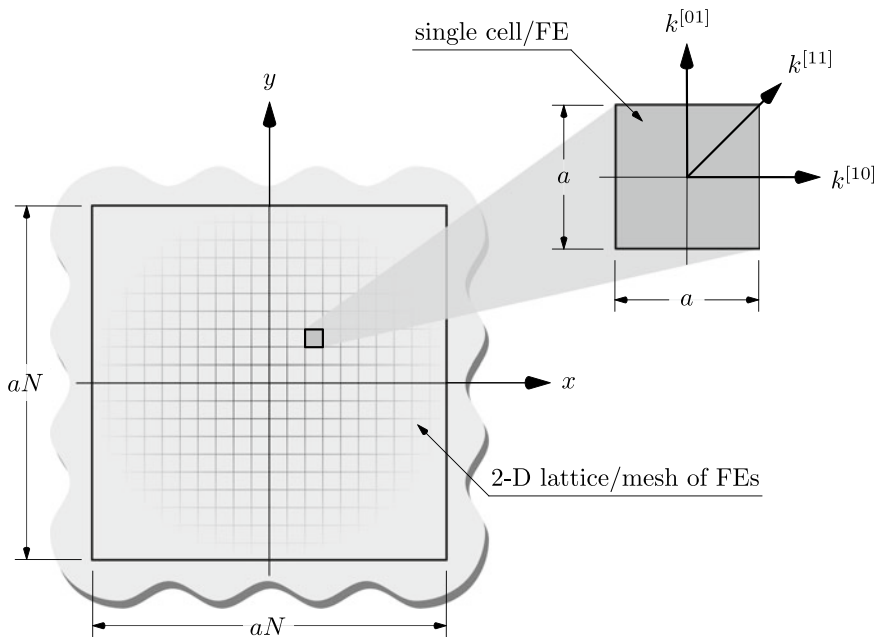


**Fig. 13.9** An isotropic plate of infinite dimensions modelled as a uniform mesh of plate FEs, representing a 2-D non-periodic medium

with  $N$  denoting the number of cells along the  $x$  and  $y$  axes. The superscript [10] is a Miller<sup>11</sup> index denoting the direction corresponding to the  $x$  axis of a cell/FE, [01] is a Miller index denoting the direction corresponding to the  $y$  axis of a cell/FE, while the superscript [11] is a Miller index denoting the direction corresponding to the cell/FE diagonal.

The results of the application of the Bloch reduction technique in the case of the isotropic plate under consideration are shown in Fig. 13.10. In this example two different degrees of approximation polynomials are examined, i.e.  $r = 2$  and FEM, and  $r = 5$  and TD-SFEM for Chebyshev nodes. The computations carried out concerned also two different 2-D lattices, which consist of  $126 \times 126 = 15,876$  cells and  $50 \times 50 = 2,500$  cells, in order to lead to similar densities of calculated frequency spectra of 190,512 and 187,500 frequencies of free vibrations,<sup>12</sup> respectively.

Again, thanks to the Bloch reduction technique the entire spectra of frequencies of free vibrations of the plate can be determined based on repeated solutions to the reduced eigenvalue problem, expressed by Eq. (13.17), by the use of a single cell/FE. As shown in Fig. 13.10 the obtained spectra are complex and difficult to

<sup>11</sup> William Hallowens Miller (1801–1880) was a Welsh mineralogist. In 1839 he introduced a notation system used in crystallography until today, which helps to identify different lattice planes in crystals. The system is known as Miller indices.

<sup>12</sup> These numbers take into account the periodic/cyclic boundary conditions.

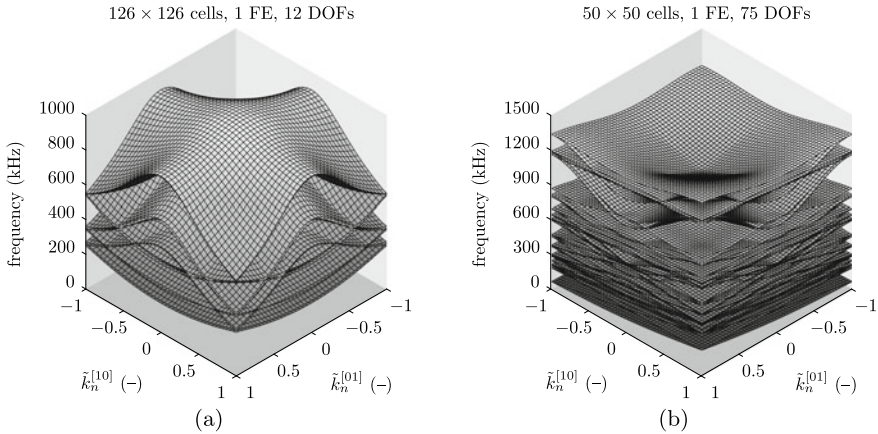


**Fig. 13.10** Spectra of frequencies of free vibrations for antisymmetric modes of elastic waves propagating in a 10 mm thick non-periodic medium, for degrees of approximation polynomials: **a**  $r = 2$  and FEM, **b**  $r = 4$  and TD-SFEM. Results of numerical computations for the reduced zone, according to the 3-mode 2-D theory (Mindlin-Reissner) theory of the antisymmetric behaviour of plates, obtained by the use of the Bloch reduction technique for a uniform lattice of: **a**  $126 \times 126$  cells and  $a = 7.94$  mm, **b**  $50 \times 50$  cells and  $a = 20$  mm,  $c_{P3pt} = 6.09$  km/s,  $c_{S3pt} = 3.07$  km/s

study. Their 3-D nature and complexity make the process of the identification of particular frequency band gaps and their mode association practically impossible. At the same time it is noteworthy that the density of the spectra are directly dependent on the number of independent wave modes and the square of the degree of approximation polynomials  $r$  employed in the analysis. On the other hand, this is directly related to the resulting number of DOFs of the discrete numerical models employed. These factors are the reasons why the direct analysis of the 3-D spectra obtained should be simplified.

It should be pointed out that the analysis of the frequency band gaps in the spectra of frequencies of free vibrations of the plate, presented in Fig. 13.10, becomes somehow easier, if the analysis takes place for particular directions, which are usually associated with the wave vectors of the reciprocal space  $k^{[10]}$  and  $k^{[11]}$ , as presented in Figs. 13.11 and 13.12.

Additionally, the results of numerical computations obtained and presented in Figs. 13.11 and 13.12, as related to the reduced zone [4] are tainted by the results associated with other directions than [10] and [11]. For this reason they should be further processed: unfolded to recover the whole range of the variation of the wave vectors  $k^{[10]}$  and  $k^{[11]}$ , as well as filtered out to fully reveal the periodic nature of the discrete numerical models of the plate. In such a manner appropriate frequencies of free vibrations of the plate from the entire frequency spectrum can be checked and examined, and next associated with appropriate wave modes. The result of these two operations are presented in Figs. 13.13 and 13.14 as dispersion curves for the phase velocity.

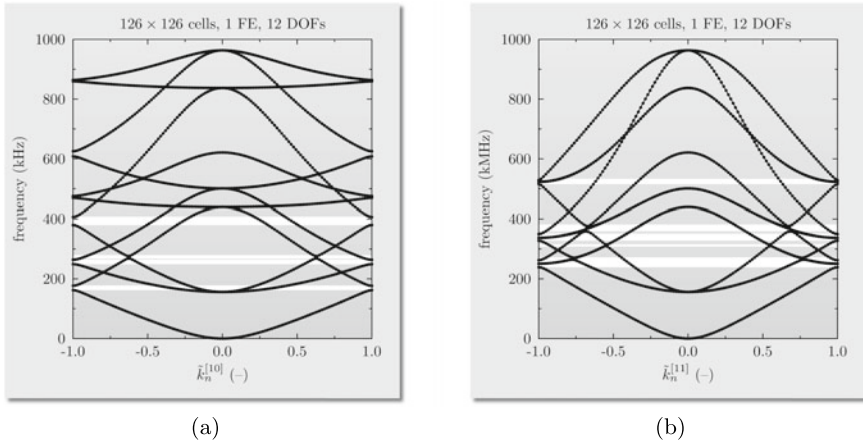


**Fig. 13.11** Spectra of frequencies of free vibrations for antisymmetric modes of elastic waves propagating in a 10 mm thick non-periodic medium as a function of non-dimensional wave vectors of the reciprocal space: **a**  $\tilde{k}_n^{[10]}$ , **b**  $\tilde{k}_n^{[11]}$ . Results of numerical computations in the reduced zone, for the degree of approximation polynomials  $r = 2$  and FEM, according to the 3-mode 2-D theory (Mindlin-Reissner) of the antisymmetric behaviour of plates, obtained by the use of the Bloch reduction technique for a uniform lattice of  $126 \times 126$  cells,  $c_{P3pt} = 6.09$  km/s,  $c_{S3pt} = 3.07$  km/s,  $a = 7.94$  mm

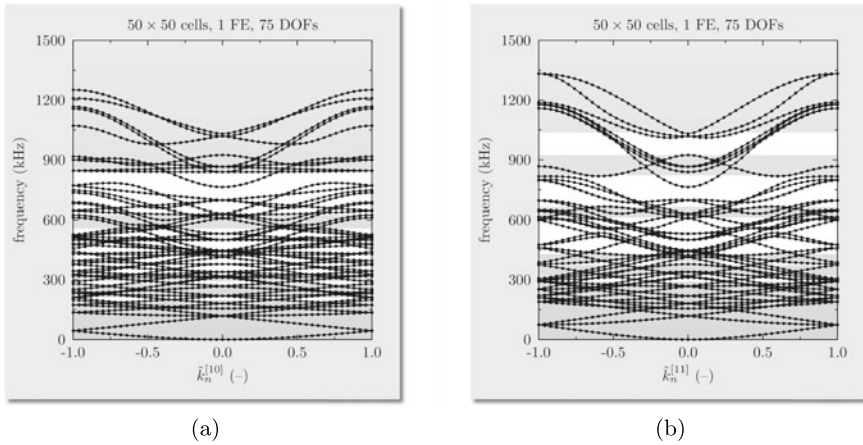


**Fig. 13.12** Spectra of frequencies of free vibrations for antisymmetric modes of elastic waves propagating in a 10 mm thick non-periodic medium as a function of non-dimensional wave vectors of the reciprocal space: **a**  $\tilde{k}_n^{[10]}$ , **b**  $\tilde{k}_n^{[11]}$ . Results of numerical computations in the reduced zone, for the degree of approximation polynomials  $r = 5$  and TD-SFEM for Chebyshev nodes, according to the 3-mode 2-D theory (Mindlin-Reissner) of the antisymmetric behaviour of plates, obtained by the use of the Bloch reduction technique for a uniform lattice of  $50 \times 50$  cells,  $c_{P3pt} = 6.09$  km/s,  $c_{S3pt} = 3.07$  km/s,  $a = 20$  mm

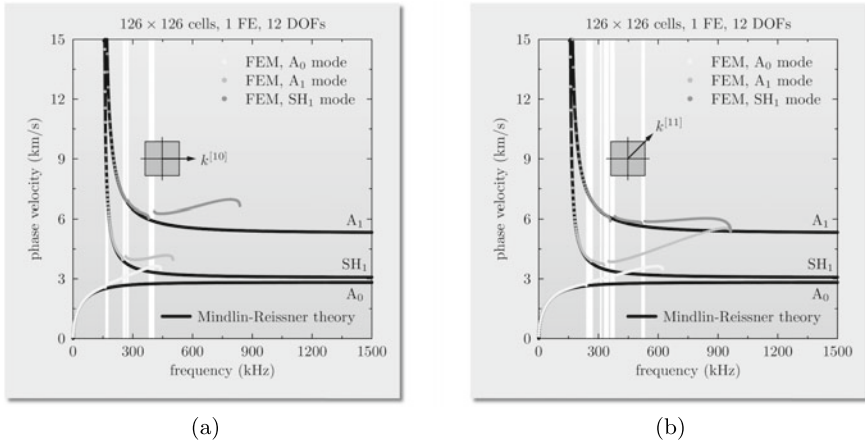


**Fig. 13.13** Dispersion curves for the phase velocity for antisymmetric modes of elastic waves propagating in a 10 mm thick non-periodic medium in the directions of non-dimensional wave vectors of the reciprocal space: **a**  $\tilde{k}_n^{[10]}$ , **b**  $\tilde{k}_n^{[11]}$ . Results of numerical computations in the reduced zone, for the degree of approximation polynomials  $r = 2$  and FEM, according to the 3-mode 2-D theory (Mindlin-Reissner) theory of the antisymmetric behaviour of plates, obtained by the use of the Bloch reduction technique for a uniform lattice of  $126 \times 126$  cells,  $c_{P3pt} = 6.09$  km/s,  $c_{S3pt} = 3.07$  km/s,  $a = 7.94$  mm

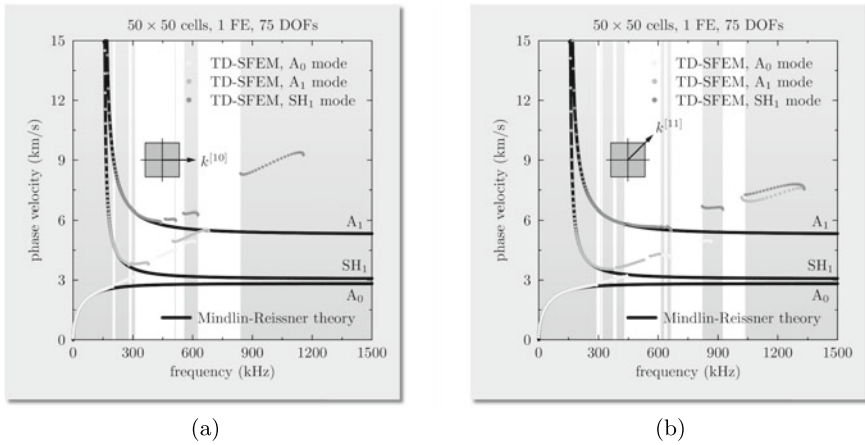


**Fig. 13.14** Dispersion curves for the phase velocity for antisymmetric modes of elastic waves propagating in a 10 mm thick non-periodic medium in the directions of non-dimensional wave vectors of the reciprocal space: **a**  $\tilde{k}_n^{[10]}$ , **b**  $\tilde{k}_n^{[11]}$ . Results of numerical computations in the reduced zone, for the degree of approximation polynomials  $r = 5$  and TD-SFEM for Chebyshev nodes, according to the 3-mode 2-D theory (Mindlin-Reissner) theory of the antisymmetric behaviour of plates, obtained by the use of the Bloch reduction technique for a uniform lattice of  $50 \times 50$  cells,  $c_{P3pt} = 6.09$  km/s,  $c_{S3pt} = 3.07$  km/s,  $a = 20$  mm

**Table 13.4** Statistical data on the influence of the degree of approximation polynomials  $r$  on the position of the frequency band gap  $FG_1$  and the frequency spectrum availability in the case of discrete numerical models of a 10 mm thick non-periodic medium. Results of numerical computations according to the 3-mode 2-D theory (Mindlin-Reissner) theory of the antisymmetric behaviour of plates, obtained by the use of the Bloch reduction technique for the uniform lattices of:  $126 \times 126$  cells for FEM and  $50 \times 50$  cells for TD-SFEM and Chebyshev nodes,  $c_{P3pt} = 6.09$  km/s,  $c_{S3pt} = 3.07$  km/s,  $a = 20$  mm

FEM approach	Mode	Direction	$FG_1$ (kHz)	$f_{max}$ (kHz)	% spectr. (%)
FEM, $r = 2$	$A_0$	[10]	162.2 ... 177.6	439.3	<36.9
FEM, $r = 2$	$A_0$	[11]	238.9 ... 263.6	621.2	<38.5
TD-SFEM, $r = 5$	$A_0$	[10]	198.8 ... 210.8	612.5	<32.5
TD-SFEM, $r = 5$	$A_0$	[11]	290.6 ... 309.5	867.2	<33.5

The results presented in Figs. 13.13 and 13.14 clearly confirm the existence of numerical anisotropy. Consequently, the usable parts of the frequency spectra for numerical computations, due to the presence of the frequency band gaps, are effectively reduced to the frequencies corresponding to the beginnings of the first frequency band gaps, which are different for the directions [10] and [11]. The remaining parts of the frequency spectra are not usable and practically inaccessible for simulation purposes due to the presence of multiple frequency band gaps and their potential influence on calculated dynamic responses. This is also indicated in Table 13.4.

It can also be noted that the positions of these frequency band gaps are not fixed in the frequency spectra under investigation, but they depend on the direction of the observation, different in the direction [10] and [11]. This is due to the obvious differences in nodal densities of the discrete numerical models in these two directions, as indicated by Eq. 13.27. Consequently, it is noteworthy that sole different nodal densities in various directions, resulting in differences of computational properties of the same discrete numerical model in these directions, are sufficient to fulfil very well the definition of numerical anisotropy.

From these results it can be also seen that in the case of numerical computations concerning FEM and the degree of approximation polynomials  $r = 2$  the first frequency band gap concerns the fundamental antisymmetric mode  $A_0$  is located between 162.2 kHz and 177.6 kHz for the direction [10] and between 238.9 kHz and 263.6 kHz for the direction [11]. As a consequence the usable parts of the frequency spectra for these modes, are reduced to not more than 36.9% and 38.5%, respectively. In the case of numerical computations concerning TD-SFEM for Chebyshev nodes and the degree of approximation polynomials  $r = 5$  the corresponding values are not significantly higher as the first frequency band gap is located between 198.2 kHz and 210.8 kHz for the direction [10] and between 290.6 kHz and 309.5 kHz for the direction [11]. Despite the fact that the use of TD-SFEM enables one to access higher frequencies, this time the usable parts of the frequency spectra are reduced to

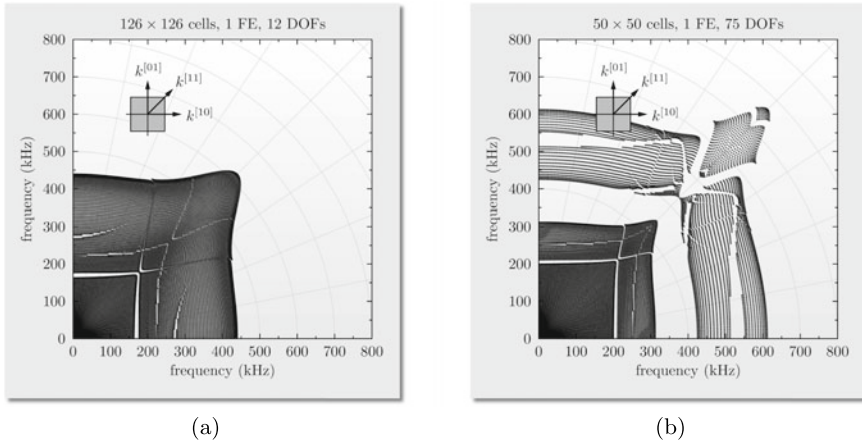


**Fig. 13.15** Directional maps of frequencies of free vibrations for the fundamental antisymmetric mode of Lamb waves  $A_0$  of elastic waves propagating in a 10 mm thick non-periodic medium, for degrees of approximation polynomials: **a**  $r = 2$  and FEM, **b**  $r = 4$  and TD-SFEM. Results of numerical computations for the reduced zone, according to the 3-mode 2-D theory (Mindlin-Reissner) of the antisymmetric behaviour of plates, obtained by the use of the Bloch reduction technique for a uniform lattice of: **a**  $126 \times 126$  cells and  $a = 7.94$  mm, **b**  $50 \times 50$  cells and  $a = 50$  mm,  $c_{P3pt} = 6.09$  km/s,  $c_{S3pt} = 3.07$  km/s

not more than 32.5% and 33.5%, as summarised in Table 13.4. It is noteworthy that the obtained values are significantly smaller when they are related to the frequencies of free vibrations corresponding to the entire calculated spectrum. Then the usable parts of the frequency spectra drop to: 19.4 and 24.8% for FEM, 17.2 and 21.8% for TD-SFEM, respectively.

Obviously, the direction of the observation is an important factor. However, the results given by Figs. 13.13 and 13.14 provide no information about such influence except the two directions [10] and [11]. This information can be extracted from the spectra of frequencies of free vibrations of the plate, presented in Fig. 13.10, however they require advanced mathematical manipulations and/or the use of artificial intelligence (AI) algorithms. The information obtained in this manner can be directly associated with a corresponding wave modes to form 2-D directional maps, which fully reveal the directional nature of the periodicity of discrete numerical models of the plate. Since the usable part of the spectrum of the calculated frequencies of free vibrations of the plate is practically limited by the presence of the first frequency band gap  $FG_1$  for the fundamental antisymmetric mode of Lamb waves  $A_0$ , in order to assess the extents of numerical anisotropy of the discrete numerical model of the plate it is sufficient to base on the maps corresponding to this mode only. Such maps are shown in Fig. 13.15.

## References

1. A. Żak, M. Krawczuk, and M. Palacz. Periodic properties of 1-D FE discrete models in high frequency dynamics. *Smart Materials and Structures*, 21016:1–15, 2016.
2. A. Żak, M. Krawczuk, M. Palacz, Ł. Doliński, and W. Waszkowiak. High frequency dynamics of an isotropic Timoshenko periodic beam by the use of time-domain spectral finite element method. *Journal of Sound and Vibration*, 409:318–335, 2017.
3. A. Żak and W. Waszkowiak. A spline-based FE approach to modelling of high frequency dynamics of 1-d structures. *Computers & Mathematics with Applications*, 104:14–33, 2021.
4. L. Brillouin. *Wave propagation in periodic structures, electric filters and crystal lattices*. Dover Publications, Inc., New York, 1946.



# Chapter 14

## Spline-Based FEM Approach



### 14.1 Some General Considerations

Numerical dispersion in 1-D cases as well as numerical anisotropy in 2-D and 3-D cases, but most of all the presence of frequency band gaps in the calculated spectra of the frequencies of free vibrations, are the primary reasons for the development of a new FEM approach, which could help to minimise their negative influence on the computational properties of discrete numerical models, which were discussed in previous sections. Since the presence and the impact of these features on calculated dynamic responses in FEM or its clones are directly linked to the properties of the shape functions employed, a search for a new FEM approach should start just from introducing new shape functions.

The shape functions traditionally used in FEM and its specialised clones such as TD-SFEM represent smooth approximation polynomials, but lead to solutions of class  $C^0$  only. Typically, the shape functions are based on equidistant node distributions or zeros of Chebyshev or Lobatto polynomials for non-equidistant node distributions, as discussed in Sect. 10.4. The  $C^0$  class of solution continuity results from the discontinuities of the strain/stress fields between adjacent FEs, which consequently leads to the presence of frequency band gaps, as discussed in Sect. 13.1. For this reason it is expected that an increase in the class of solution continuity from  $C^0$  to  $C^1$  or  $C^2$ , or even higher, may result in a significant improvement in the computational properties of FEM discrete numerical models. This can be achieved by the use of such shape functions, which by their very definition provide the continuity of the strain/stress fields between adjacent FEs. Good candidates here are splines,<sup>1</sup> as they offer continuous and smooth solutions at relatively low computational costs.

---

<sup>1</sup> The word *spline* is commonly attributed to Isaac Jacob Schoenberg (1903–1990), who was a Romania born American mathematician of Jewish origins, and who used this term for the first time in his work from 1946 to describe smooth, piecewise approximation polynomials.

**Table 14.1** The influence of the degree of approximation polynomials  $r$  and the class of solution continuity  $c$  on the number of frequency band gaps  $d$ , where  $d = r - c - 1$ , within the calculated spectra of frequencies of free vibrations, in the case of 1-D shape functions employed by 1-mode 1-D theories

Type of approach	Approx. polynomials	$r$	$c$	$d$
Classical FEM	Lagrange [1–3] for equidistant nodes within FEs	1	0	0
		2	0	1
		3	0	2
		...	...	...
TD-SFEM	Chebyshev/Lobatto [1, 3, 4] for non-equidistant nodes within FEs	3	0	2
		4	0	3
		5	0	4
		...	...	...
Specialised FEM	Hermite [5–7] for 2-node FEs	3	1	1
		5	2	2
		7	3	3
		...	...	...
spFEM	Spline [1, 8–10] for 2-node FEs	1	0	0
		2	1	0
		3	2	0
		...	...	...

Consequently, a FEM approach employing splines for shape functions can be named as the Spline-based Finite Element Method (spFEM).

It is interesting to note that in the case of 1-D shape functions employed by 1-mode theories, as discussed in Sect. 13.1, there is a close link between the number of frequency band gaps observed in the calculated spectra of frequencies of free vibrations, noted as  $d$ , and the degree of approximation polynomials  $r$  employed for shape functions, and the class of solution continuity  $c$ , since  $d = r - c - 1$  as shown in [1]. This is clearly illustrated by Table 14.1.

From Table 14.1 it can be seen that in the case of FEM the number of frequency band gaps  $d$  in the calculated spectra is equal to 0 only for the linear shape functions, i.e., when the degree of approximation polynomials  $r$  is equal to 1, since the class of solution continuity  $c$  is equal to 0. For this reason it is expected that similar results can be obtained for higher degrees of approximation polynomials  $r$  as long as the class of solution continuity  $c$  is one smaller from the degree  $r$ , i.e., when the class of solution continuity  $c = r - 1$ . Such a condition can be easily satisfied in the case of spFEM, which is based on the use of piecewise shape functions represented by splines, as shown below.

At this point it should be emphasised that a special type of splines known as B-splines [11–13], or Non-uniform Rational B-splines (NURBS), are already well-

established and frequently used for numerical computations for the same kinds of problems as the classical FEM. Despite their unquestionable advantages NURBS do not belong to FEM approaches, since they are based on so-called *patches* rather than typical FEs, which in FEM are well localised in space. Additionally, NURBS use a concept different from elemental nodes, which is based on discretisation points within so-called *knot vectors*. Such discretisation points may also stay outside computational domains [14–16], which makes the computation process more complex and difficult. The lack of the features typical to FEM makes NURBS rather difficult to directly adopt or combine with FEM as, for example in the case of damage modelling techniques well developed in FEM [17] or modelling of structural joints [18], etc.

## 14.2 1-D Spline-Based Shape Functions

1-D spline-based piecewise shape functions can be easily derived by using standard FEM procedures for this purpose [1, 2, 4, 19]. Since the class of solution continuity  $c$  is assumed to be one smaller than their degree  $r$ , derivation of spline-based piecewise elemental shape functions requires the use of some internal nodes. This is in contrast to Hermite approximation polynomials, which are solely based on edge nodes of FEs, and which are characterised, in general, by higher degrees  $r$  of approximation polynomials for the same nodal quantities as spline-based approximation polynomials.

A family of 1-D spline-based piecewise shape functions can be easily built in the local normalised coordinate system ( $\xi$ ) by assuming that a 2-node FE of length  $a$  is divided into a number of  $r$  sections of equal lengths,<sup>2</sup> where  $r$  denotes the degree of approximation polynomials. These  $r - 1$  sections are defined by internal nodes  $\xi_n$  with  $n = 1, 2, \dots, r - 1$  and indicate so-called stitching points, where continuity conditions for all nodal quantities must be satisfied. Detailed information about the methodology for obtaining 1-D spline-based piecewise shape functions can be found in [1].

Following this methodology and by taking into account the definition of shape functions from Sect. 10.3 and given by Eq. (10.7), the variation of an unknown solution function  $u(x, t)$  over the length  $a$  of the element under consideration can be expressed by 1-D spline-based piecewise shape functions, for particular degrees  $r$  of approximation polynomials,<sup>3</sup> in the following manner:

- *Linear shape functions* ( $r = 1, c = 0$ ):

$$u(x, t) \cong \mathbf{N}(\xi(x))\mathbf{q}_e, \quad \mathbf{q}_e = [q_1, q_2]^T \quad (14.1)$$

<sup>2</sup> This is not a fixed requirement, as other divisions are also allowed.

<sup>3</sup> Although the current study is limited to linear, quadratic and cubic shape functions, shape functions of higher degrees can also be easily obtained by the use of modern mathematical packages suitable for such computations [20, 21].

where the vector of nodal displacements  $\mathbf{q}_e$  has only one DOF per node represented by two displacements:  $q_1, q_2$ . No internal nodes/stitching points are required.

In the local normalised coordinate system ( $\xi$ ) the matrix of piecewise shape functions  $\mathbf{N}(\xi)$  takes the following form:

$$\mathbf{N}(\xi) = [N_1(\xi), N_2(\xi)] \quad (14.2)$$

where:

$$N_1(\xi) = +\frac{1}{2} - \frac{1}{2}\xi, \quad \xi \in \langle -1, +1 \rangle \quad (14.3)$$

$$N_2(\xi) = +\frac{1}{2} + \frac{1}{2}\xi, \quad \xi \in \langle -1, +1 \rangle$$

- *Quadratic shape functions* ( $r = 2, c = 1$ ):

$$u(x, t) \cong \mathbf{N}(\xi(x))\mathbf{q}_e, \quad \mathbf{q}_e = [q_1, q'_1, q_2, q'_2]^T \quad (14.4)$$

where the vector of nodal displacements  $\mathbf{q}_e$  has two DOFs per node represented by two displacements:  $q_1, q_2$  and their first space derivatives with respect to  $x$ :  $q'_1, q'_2$ . In this case the element is divided into two sections and one internal node/stitching point at  $\xi_1 = 0$  is required.

In the local normalised coordinate system ( $\xi$ ) the matrix of piecewise shape functions  $\mathbf{N}(\xi)$  takes the following form:

$$\mathbf{N}(\xi) = [N_1(\xi), N_2(\xi), N_3(\xi), N_4(\xi)] \quad (14.5)$$

where:

$$N_1(\xi) = \begin{cases} +\frac{1}{2} - \xi - \frac{1}{2}\xi^2, & \xi \in \langle -1, 0 \rangle \\ +\frac{1}{2} - \xi + \frac{1}{2}\xi^2, & \xi \in \langle 0, +1 \rangle \end{cases}$$

$$\frac{N_2(\xi)}{a} = \begin{cases} +\frac{1}{8} - \frac{1}{4}\xi - \frac{3}{8}\xi^2, & \xi \in \langle -1, 0 \rangle \\ +\frac{1}{8} - \frac{1}{4}\xi + \frac{3}{8}\xi^2, & \xi \in \langle 0, +1 \rangle \end{cases} \quad (14.6)$$

$$N_3(\xi) = \begin{cases} +\frac{1}{2} + \xi + \frac{1}{2}\xi^2, & \xi \in \langle -1, 0 \rangle \\ +\frac{1}{2} + \xi - \frac{1}{2}\xi^2, & \xi \in \langle 0, +1 \rangle \end{cases}$$

$$\frac{N_4(\xi)}{a} = \begin{cases} -\frac{1}{8} - \frac{1}{4}\xi - \frac{1}{8}\xi^2, & \xi \in \langle -1, 0 \rangle \\ -\frac{1}{8} - \frac{1}{4}\xi + \frac{3}{8}\xi^2, & \xi \in \langle 0, +1 \rangle \end{cases}$$

- *Cubic shape functions* ( $r = 3, c = 2$ ):

$$u(x, t) \cong \mathbf{N}(\xi(x))\mathbf{q}_e, \quad \mathbf{q}_e = [q_1, q'_1, q''_1, q_2, q'_2, q''_2]^T \quad (14.7)$$

where the vector of nodal displacements  $\mathbf{q}_e$  has three DOFs per node represented by two displacements:  $q_1, q_2$  and their first and second space derivatives with respect to  $x$ :  $q'_1, q'_2$  and  $q''_1, q''_2$ . In this case the element is divided into three sections and two internal node/stitching point at  $\xi_{1,2} = \pm 1/3$  are required.

In the local normalised coordinate system ( $\xi$ ) the matrix of piecewise shape functions  $\mathbf{N}(\xi)$  takes the following form:

$$\mathbf{N}(\xi) = [N_1(\xi), N_2(\xi), N_3(\xi), N_4(\xi), N_5(\xi), N_6(\xi)] \quad (14.8)$$

where:

$$\begin{aligned} N_1(\xi) &= \begin{cases} +\frac{7}{16} - \frac{27}{16}\xi - \frac{27}{16}\xi^2 - \frac{9}{16}\xi^3, & \xi \in \langle -1, -\frac{1}{3} \rangle \\ +\frac{1}{2} - \frac{9}{8}\xi + \frac{9}{8}\xi^3, & \xi \in \langle -\frac{1}{3}, +\frac{1}{3} \rangle \\ +\frac{9}{16} - \frac{27}{16}\xi + \frac{27}{16}\xi^2 - \frac{9}{16}\xi^3, & \xi \in \langle +\frac{1}{3}, +1 \rangle \end{cases} \\ \frac{N_2(\xi)}{a} &= \begin{cases} +\frac{1}{8} - \frac{5}{8}\xi - \frac{9}{8}\xi^2 - \frac{3}{8}\xi^3, & \xi \in \langle -1, -\frac{1}{3} \rangle \\ +\frac{23}{144} - \frac{5}{16}\xi - \frac{3}{16}\xi^2 + \frac{9}{16}\xi^3, & \xi \in \langle -\frac{1}{3}, +\frac{1}{3} \rangle \\ +\frac{3}{16} - \frac{9}{16}\xi + \frac{9}{16}\xi^2 - \frac{3}{16}\xi^3, & \xi \in \langle +\frac{1}{3}, +1 \rangle \end{cases} \\ \frac{N_3(\xi)}{a^2} &= \begin{cases} +\frac{1}{96} - \frac{3}{32}\xi - \frac{7}{32}\xi^2 - \frac{11}{96}\xi^3, & \xi \in \langle -1, -\frac{1}{3} \rangle \\ +\frac{5}{288} - \frac{1}{32}\xi - \frac{1}{32}\xi^2 + \frac{7}{96}\xi^3, & \xi \in \langle -\frac{1}{3}, +\frac{1}{3} \rangle \\ +\frac{1}{48} - \frac{1}{16}\xi + \frac{1}{16}\xi^2 - \frac{1}{48}\xi^3, & \xi \in \langle +\frac{1}{3}, +1 \rangle \end{cases} \\ N_4(\xi) &= \begin{cases} +\frac{9}{16} + \frac{27}{16}\xi + \frac{27}{16}\xi^2 + \frac{9}{16}\xi^3, & \xi \in \langle -1, -\frac{1}{3} \rangle \\ +\frac{1}{2} + \frac{9}{8}\xi - \frac{9}{8}\xi^3, & \xi \in \langle -\frac{1}{3}, +\frac{1}{3} \rangle \\ +\frac{7}{16} + \frac{27}{16}\xi - \frac{27}{16}\xi^2 + \frac{9}{16}\xi^3, & \xi \in \langle +\frac{1}{3}, +1 \rangle \end{cases} \\ \frac{N_5(\xi)}{a} &= \begin{cases} -\frac{3}{16} - \frac{9}{16}\xi - \frac{9}{16}\xi^2 - \frac{3}{16}\xi^3, & \xi \in \langle -1, -\frac{1}{3} \rangle \\ -\frac{23}{144} - \frac{5}{16}\xi + \frac{3}{16}\xi^2 + \frac{9}{16}\xi^3, & \xi \in \langle -\frac{1}{3}, +\frac{1}{3} \rangle \\ -\frac{1}{8} - \frac{5}{8}\xi + \frac{9}{8}\xi^2 - \frac{3}{8}\xi^3, & \xi \in \langle +\frac{1}{3}, +1 \rangle \end{cases} \\ \frac{N_6(\xi)}{a^2} &= \begin{cases} +\frac{1}{48} + \frac{1}{16}\xi + \frac{1}{16}\xi^2 + \frac{1}{48}\xi^3, & \xi \in \langle -1, -\frac{1}{3} \rangle \\ +\frac{5}{288} + \frac{1}{32}\xi - \frac{1}{32}\xi^2 - \frac{7}{96}\xi^3, & \xi \in \langle -\frac{1}{3}, +\frac{1}{3} \rangle \\ +\frac{1}{96} + \frac{3}{32}\xi + \frac{7}{32}\xi^2 + \frac{11}{96}\xi^3, & \xi \in \langle +\frac{1}{3}, +1 \rangle \end{cases} \end{aligned} \quad (14.9)$$

It can be easily noticed based on Eqs. (14.3), (14.6) and (14.9) that an increase in the degree of approximation polynomials  $r$  requires the incorporation of additional nodal DOFs in the form of higher order space derivatives in order to obtain corresponding spline-based piecewise shape functions. These higher order derivatives may

be thought of as corresponding to higher order corrections to the unknown function  $u(x, t)$  and may be effectively included in the case of the degrees of approximation polynomials  $r$  higher than 3.

Despite that such a procedure can be easily carried out, from a practical point of view it is sufficient to limit oneself to quadratic or cubic spline-based piecewise shape functions for computational purposes. This is due to an increased complexity of the notation/definition of such FEs, especially in 2-D or 3-D cases, which is not fully compensated by an increase in the computational accuracy. 1-D spline-based piecewise shape functions obtained by the use of Eqs. (14.3), (14.6) and (14.9) are presented in Fig. 14.1 together with a quartic case, which is not discussed here, all in the case of a 2-node FE of length  $a = 2\text{ m}$ .

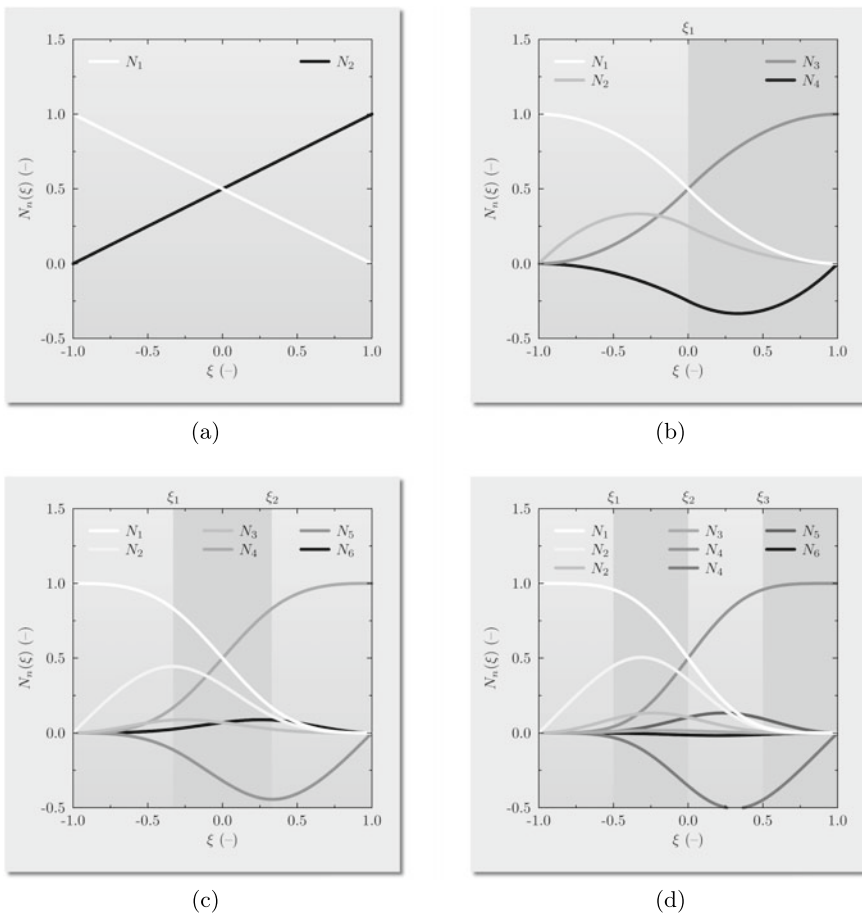
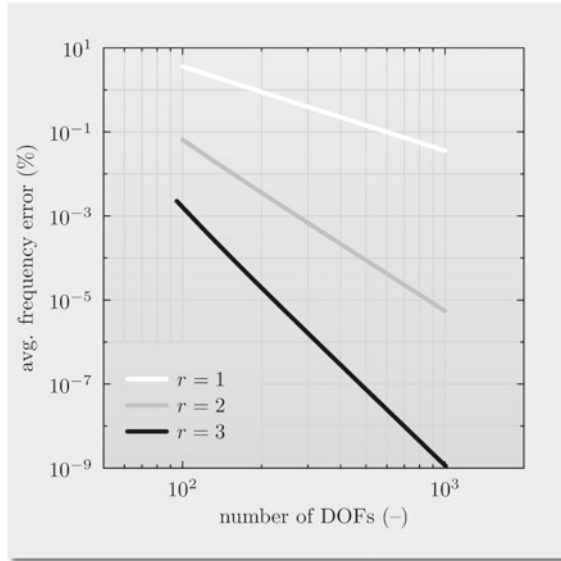


**Fig. 14.1** 1-D spline-based piecewise shape functions for various degrees of approximation polynomials: **a** linear  $r = 1$ , **b** quadratic  $r = 2$ , **c** cubic  $r = 3$ , **d** quartic  $r = 4$ , in the local normalised coordinate system  $(\xi)$ , obtained in the case of a 2-node FE,  $a = 2\text{ m}$

**Fig. 14.2** Results of numerical computations by spFEM. An average frequency error for 1-D spline-based piecewise shape functions of various degrees of approximation polynomials, as a function of the number of DOFs of numerical models. Results according to the 1-mode 1-D theory (elementary) of the longitudinal behaviour of rods for the first 30 frequencies of free vibrations of a 10 mm diameter, 2 m long aluminium bar with free ends



It is noteworthy that 1-D spline-based piecewise shape functions are characterised by excellent convergence of computational results in comparison with the classical FEM and comparable with TD-SFEM, as shown in Figs. 10.4 and 10.5 from Sect. 10.6. This is well illustrated by the results presented in Fig. 14.2 in the case of linear ( $r = 1$ ), quadratic ( $r = 2$ ) and cubic ( $r = 3$ ) approximation polynomials used for 1-D spline based piecewise shape functions.

Bearing in mind that spFEM employs for shape functions approximation polynomials of similar degrees as FEM, but much lower than TD-SFEM, spFEM appears to be a very good computational alternative to FEM and TD-SFEM from the point of view of computational accuracy. However, it should be strongly emphasised here that the convergence is not the only feature of spFEM, which should be taken into account. It is shown and discussed in the following section that the application of spFEM eliminates frequency band gaps from calculated spectra of frequencies of free vibrations, which has a great impact on the computational properties of discrete numerical models and which fully manifests in the case of dynamic responses as well as wave propagation problems.

### 14.3 Wave Propagation Problems by spFEM

The computational problems analysed in this section make a direct reference to previously considered computational issues. This time however, they are tackled by the use of spFEM in order to emphasise the computational robustness and advantages of this FEM approach.

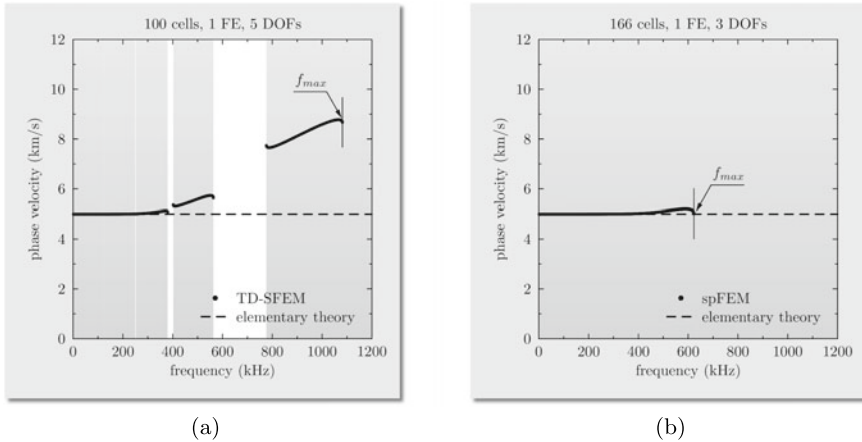


**Fig. 14.3** Dispersion curves for the phase velocity for the fundamental mode of longitudinal waves  $L_0$  propagating in a 1-D non-periodic bar for selected degrees of approximation polynomials: **a**  $r = 5$  and TD-SFEM, **b**  $r = 3$  and spFEM. Results of numerical computations by TD-SFEM/spFEM according to the 1-mode 1-D theory (elementary) of the longitudinal behaviour of rods, obtained by the use of the Bloch reduction technique for: **a** 100 cells,  $a = 20$  mm and TD-SFEM, **b** 166 cells,  $a = 12$  mm and spFEM, and  $c_1 = 5$  km/s

At first a 40 mm diameter, 2 m long aluminium bar with free ends is considered, for which the phase velocity of the fundamental mode of longitudinal waves  $L_0$  is  $c_1 = 5$  km/s. However, prior to any analysis concerning propagation of longitudinal waves the dispersion curves for the phase velocity for the  $L_0$  mode should be investigated.

The effects of such analysis are presented in Fig. 14.3, where the dispersion curves obtained in the case of TD-SFEM and the degree of approximation polynomials  $r = 5$  are contrasted with similar curves obtained in the case of spFEM and the degree of approximation polynomials  $r = 3$ . They result from the application of the Bloch reduction technique leading to the frequency spectra of free vibrations of similar densities.

For these computations 100 cells of length  $a = 20$  mm is used for TD-SFEM, while in the case of spFEM it is 166 cells of length  $a = 12$  mm. This translates to 500 frequencies of free vibrations for TD-SFEM and 498 for spFEM, respectively. In both these cases the same 1-mode 1-D theory (elementary) of the longitudinal behaviour of rods is employed.

It is evident from Fig. 14.3 that the dispersion curve obtained in the case of spFEM, contrary to the case of TD-SFEM, is continuous and free of any frequency band gaps. In the case of spFEM undesired spatial numerical dispersion is on a much smaller level than in the case of TD-SFEM, as presented in Table 14.2, and never exceeds 5%. This is clear evidence of the superiority of spFEM over TD-SFEM in that respect.

The dispersion curves obtained for TD-SFEM and spFEM, presented in Fig. 14.3, have a strong impact on calculated dynamic responses of the bar in the form of



**Table 14.2** Statistical data on the spatial numerical dispersion in the case of two discrete numerical models of a 1-D non-periodic medium. Results of numerical computations by spFEM/TD-SFEM according to the 1-mode 1-D theory (elementary) of the longitudinal behaviour of rods, obtained by the use of the Bloch reduction technique for: **a** 100 cells,  $a = 20$  mm and TD-SFEM, **b** 166 cells,  $a = 12$  mm and spFEM, and  $c_1 = 5$  km/s

FEM approach	Mode	1% disp. (kHz)	5% disp. (kHz)	$f_{max}$ (kHz)
TD-SFEM, $r = 5$	$L_0$	<313.2 (28.9%)	<380.0 (35.1%)	1081.6
spFEM, $r = 3$	$L_0$	<446.9 (71.7%)	<622.9 (100%)	622.9

In brackets the percentage of the frequency spectrum associated with a given mode is indicated

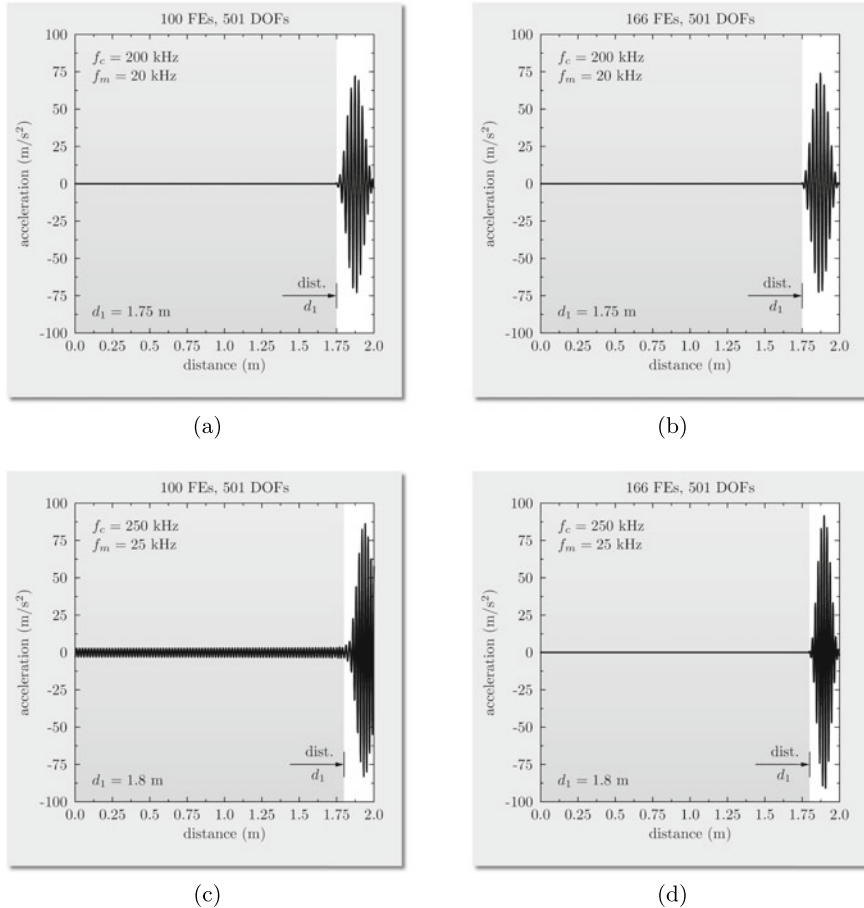


**Fig. 14.4** Response patterns for the longitudinal acceleration component  $\ddot{u}_x$  of the fundamental mode of longitudinal waves  $L_0$  propagating in a 1-D non-periodic bar for selected degrees of approximation polynomials: **a, c**  $r = 5$  and TD-SFEM, **b, d**  $r = 3$  and spFEM. Results of numerical computations by TD-SFEM/spFEM according to the 1-mode 1-D theory (elementary) of the longitudinal behaviour of rods for a 40 mm diameter, 2 m long aluminium bar of free ends

wave propagation patterns, as shown in Fig. 14.4. For this analysis the implicit  $\beta$ -Newmark method is used, as discussed in Sect. 10.7, for the recommended values of the parameters  $\alpha$  and  $\beta$  equal to 1/2 and 1/4, respectively. The total calculation time  $T$  covers 400  $\mu$ s and is divided into 8,000 equal time steps. The excitation signal is applied as a longitudinally acting force at the left hand, free end of the bar, having the amplitude of 1 N and the form of 10 sine pulses at the carrier frequency  $f_c$  of 200 or 250 kHz, modulated by the Hann window, i.e., with the frequency of modulation  $f_m = f_c/m$  equal to 20 or 25 kHz, where  $m = 10$ . The total calculation time  $T$  is chosen in such a manner that the resulting wave packet travelling along the bar should reach the right hand free end of the bar. The expected position of the wave packet, calculated based on the dispersion curves presented in Fig. 9.1 in Sect. 9.1, is indicated by a white box. It should be emphasised that any deviation in this respect is a clear indication of the quality of the discrete numerical model of the bar employed for this numerical simulation.

It can be seen from Fig. 14.4 that both discrete numerical models, based on the use of TD-SFEM and spFEM, perform well in the case of the excitation signal characterised by the lower carrier frequency  $f_c = 200$  kHz, for which the frequency content covers frequencies from  $f_c - 2f_m = 160$  kHz up to  $f_c + 2f_m = 240$  kHz. However, a slight increase in the carrier frequency to  $f_c = 250$  kHz results in a sudden change in the calculated dynamic responses for TD-SFEM. In this case, however, the frequency content covers higher frequencies from  $f_c - 2f_m = 200$  kHz up to  $f_c + 2f_m = 300$  kHz, which just in the case of TD-SFEM leads to a strong influence of the frequency band gap  $FG_2$  with its central frequency matching the central frequency of the excitation signal, as presented in Table 13.2 from Sect. 13.3. This is despite a relatively small width of the frequency gap  $FG_2$ , which is of only 0.8 kHz. Consequently, the calculated dynamic responses exhibit not only some additional spatial numerical dispersion, manifested by an increased speed of the wave packet, but also the behaviour typical of periodic structures, when a signal gets trapped within the structure leading to observable oscillations along the whole length of the bar. This is not the case for spFEM, where no such influence can be detected.

Additionally, it can easily be checked, based on the dispersion curves presented in Fig. 14.3, that in the case of TD-SFEM the assumed excitation signals of the central frequency  $f_c$  equal to 200 and 250 kHz conform well with the requirement of 4 nodal distances per wavelength [22–24]. In the case of spFEM, however, this requirement is changed to 4 nodal DOFs per wavelength,<sup>4</sup> which is also satisfied.

Next, a similar analysis is performed in the case of the 2-mode 1-D theory (Timoshenko) of the flexural behaviour of beams. This analysis is carried out in exactly the same two steps, however, due to the 2-mode nature of the applied theory it concerns 1000 frequencies of free vibrations for TD-SFEM and 996 for spFEM, respectively.

It can be seen from Fig. 14.5 that the dispersion curves obtained in the case of spFEM, in the same manner as before and contrary to TD-SFEM, are continuous and

---

<sup>4</sup> This is due to the fact that in spFEM, contrary to the classical FEM or TD-SFEM, 1-D FEs use higher order nodal DOFs and always have only two nodes.

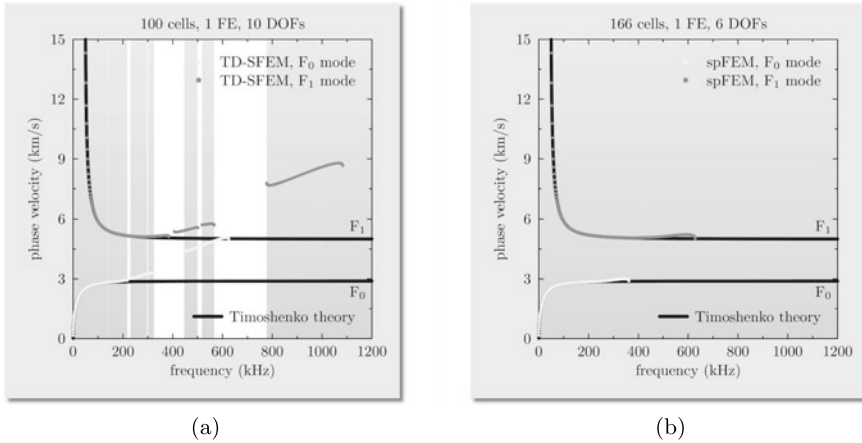


**Fig. 14.5** Dispersion curves for the phase velocity for flexural modes of elastic waves propagating in a 1-D non-periodic bar for selected degrees of approximation polynomials: **a**  $r = 5$  and TD-SFEM, **b**  $r = 3$  and spFEM. Results of numerical computations by TD-SFEM/spFEM according to the 2-mode 1-D theory (Timoshenko) of the flexural behaviour of beams, obtained by the use of the Bloch reduction technique for: **a** 100 cells,  $a = 20$  mm and TD-SFEM, **b** 166 cells,  $a = 12$  mm and spFEM,  $c_{P3pt} = 6.09$  km/s,  $c_{S3pt} = 3.07$  km/s

**Table 14.3** Statistical data on the spatial numerical dispersion in the case of two discrete numerical models of a 1-D non-periodic medium. Results of numerical computations by spFEM/TD-SFEM according to the 2-mode 1-D theory (Timoshenko) of the flexural behaviour of beam, obtained by the use of the Bloch reduction technique for: **a** 100 cells,  $a = 20$  mm and TD-SFEM, **b** 166 cells,  $a = 12$  mm and spFEM, and  $c_{P3pt} = 6.09$  km/s,  $c_{S3pt} = 3.07$  km/s

FEM approach	Mode	1% disp. (kHz)	5% disp. (kHz)	$f_{max}$ (kHz)
TD-SFEM, $r = 5$	F <sub>0</sub>	<176.7 (28.3%)	<217.4 (34.8%)	625.2
	F <sub>1</sub>	<315.5 (29.1%)	<384.2 (35.5%)	1082.6
spFEM, $r = 3$	F <sub>0</sub>	<256.3 (70.8%)	<362.2 (100%)	362.2
	F <sub>1</sub>	<452.8 (72.1%)	<628.3 (100%)	628.3

In brackets the percentage of the frequency spectrum associated with a given mode is indicated

free of any frequency band gaps. In the case of spFEM undesired spatial numerical dispersion is also on a much smaller level than in the case of TD-SFEM, as presented in Table 14.3.

It is noteworthy that in the case of TD-SFEM the undesired spatial numerical dispersion is entirely driven by the presence of frequency band gaps, i.e., FG<sub>2</sub> (217.4 kHz ... 230.1 kHz) for the fundamental flexural mode F<sub>0</sub> as well as FG<sub>3</sub> (296.6 kHz ... 300.4 kHz) for the second flexural mode F<sub>1</sub>, rather than the finite size of the frequency spectrum. The absence of frequency band gaps in the calculated spectrum in the case of spFEM once more indicates its superiority over TD-SFEM, especially that for spFEM the undesired spatial numerical dispersion never exceeds 5%. It should be emphasised that in computational practice the first significant frequency band gap

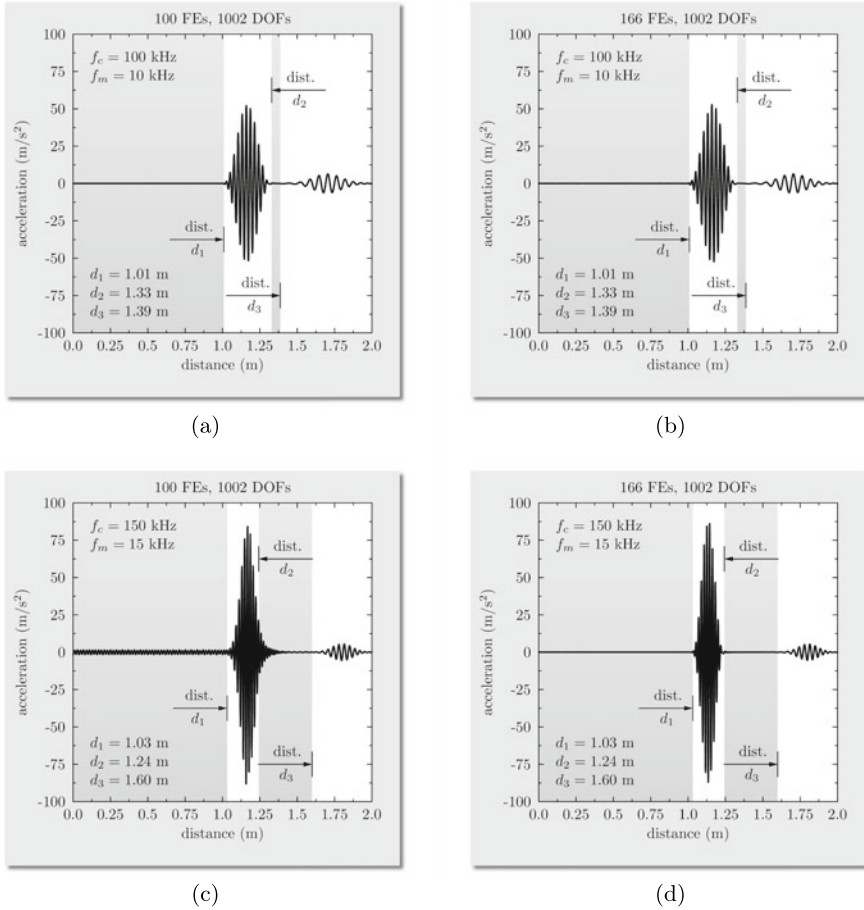


**Fig. 14.6** Response patterns for the radial acceleration component  $\ddot{u}_r$  of flexural waves propagating in a 1-D non-periodic bar for selected degrees of approximation polynomials: **a, c**  $r = 5$  and TD-SFEM, **b, d**  $r = 3$  and spFEM. Results of numerical computations by TD-SFEM/spFEM according to the 2-mode 1-D theory (Timoshenko) of the flexural behaviour of beams for a 40 mm diameter, 2 m long aluminium bar of free ends

is the one which effectively limits the available spectrum for numerical simulations. In the case of TD-SFEM this is  $FG_1$  (217.4 kHz ... 230.1 kHz) for the fundamental flexural mode  $F_0$ .

The dispersion curves obtained for TD-SFEM and spFEM, presented in Fig. 14.5, due to the 2-mode nature of the applied theory, have even a stronger impact on calculated wave propagation patterns of the bar, as shown in Fig. 14.6. Also in this analysis the implicit  $\beta$ -Newmark method is used, as discussed in Sect. 10.7, for the recommended values of the parameters  $\alpha$  and  $\beta$  equal to 1/2 and 1/4, respectively.

The phase velocity dispersion curve as well as the group velocity dispersion curve for the 2-mode 1-D theory (Timoshenko) of the flexural behaviour of beams, as presented in Fig. 9.12 from Sect. 9.2, indicate a strong frequency dependence on associated velocities. Consequently, the total calculation time  $T$  covers 430 or 414  $\mu\text{s}$  and is divided into 8,000 equal time steps. The excitation signal is applied as a transversely acting force at the left hand, free end of the bar, having the amplitude of 1 N and the form of 10 sine pulses at the carrier frequency  $f_c$  of 100 or 150 kHz, modulated by the Hann window, i.e., with the frequency of modulation  $f_m = f_c/m$  equal to 10 or 15 kHz, where  $m = 10$ . The total calculation time  $T$  is chosen in such a manner that the faster wave packet, due to the excitation of both modes  $F_0$  and  $F_1$ , travelling along the bar should reach the right hand, free end of the bar. The expected positions of both wave packets, calculated based on the dispersion curves presented in Fig. 9.12 from Sect. 9.2, are indicated by white boxes. As before it should be emphasised that any deviation in this respect is a clear indication of the quality of the discrete numerical model of the bar employed for this numerical simulation.

It can be seen from Fig. 14.6 that both discrete numerical models, based on the use of TD-SFEM and spFEM, perform well in the case of the excitation signal characterised by the lower carrier frequency  $f_c = 100$  kHz, for which the frequency content covers frequencies from  $f_c - 2f_m = 80$  kHz up to  $f_c + 2f_m = 120$  kHz. However, an increase in the carrier frequency to  $f_c = 150$  kHz results in a significant change in the calculated dynamic responses for TD-SFEM. In this case the frequency content covers higher frequencies from  $f_c - 2f_m = 120$  kHz up to  $f_c + 2f_m = 180$  kHz, which in the case of TD-SFEM leads to a subtle influence on the frequency band gap  $FG_1$  (141.1 kHz ... 141.6 kHz) for mode  $F_0$ , having its central frequency very close to the central frequency of the excitation signal. This influence is observable despite a relatively small width of the frequency gap  $FG_1$ , which is of only 0.5 kHz.

As a consequence and in the same manner as observed in the case of longitudinal waves, the calculated dynamic responses exhibit not only some additional spatial numerical dispersion manifesting by an increased speed of both wave packets, but also the behaviour typical of periodic structures, when a signal gets trapped within the structure leading to observable oscillations along the whole length of the bar. This is not the case for spFEM, where no such influence can be detected.

Also in this case, it can easily be checked based on the dispersion curves presented in Fig. 14.5 that in the case of TD-SFEM the assumed excitation signals of the central frequency  $f_c$  equal to 100 or 150 kHz conforms well with the requirement of 4 nodal distances per wavelength, while in the case of spFEM with the requirement of 4 nodal DOFs per wavelength [22–24].

Finally, the analysis carried out concerns a 2-D structure, which is a 10 mm thick,  $1\text{ m} \times 1\text{ m}$  aluminium plate with free edges. The application of the 3-mode 2-D theory (Mindlin-Reissner) of the antisymmetric behaviour of plates for wave propagation purposes, as before is preceded by the analysis of the dispersion curves for the antisymmetric modes  $A_0$ ,  $A_1$  and  $SH_1$  employed by this theory.

The dispersion curves obtained in the case of TD-SFEM and the degree of approximation polynomials  $r = 5$  are already presented in Fig. 13.14 from Sect. 13.4. Similar curves obtained in the case of spFEM and the degree of approximation polynomials

$r = 3$  are presented in Fig. 14.7. The Bloch reduction technique is used for that purpose aiming again for the frequency spectra of free vibrations of similar densities. In order to achieve this a uniform lattice of  $82 \times 82$  cells of length  $a = 12.2$  mm is used. It is clear from the results presented in Fig. 14.7 that the dispersion curves are free of any frequency band gaps in the entire spectrum available. Also the level of undesired spatial numerical dispersion is on a much lower level than in the case of TD-SFEM, which is summarised by Table 14.4.

Once more special attention should be paid to the fact that in computational practice the percentage values from Table 14.4 could be also related to the maximum frequency from the available spectrum of free vibrations, which to some extent gives more adequate information about the discrete numerical model in use. In the current case under consideration these percentage values could be approximately lowered by half. Additionally, the spectra of free vibrations obtained by spFEM, with no frequency band gaps, enable one to use excitation signals of the frequency content reaching at least twice or three times higher frequencies in comparison with TD-SFEM.

The high quality of the results obtained by the use of spFEM, already presented in Fig. 14.7, is also confirmed by the same type of a 2-D directional map of frequencies of free vibrations, presented in Fig. 14.8, in order to assist the previously obtained 2-D directional maps presented in Fig. 13.15 from Sect. 13.4. Since the presented map is free of any frequency band gaps in the case of spFEM, in contrast to TD-SFEM, the usable part of the spectrum of the calculated frequencies of free vibrations of the plate is practically limited by the presence and magnitude of undesired spatial numerical anisotropy for the fundamental antisymmetric mode of Lamb waves  $A_0$ , as summarised in Table 14.3. As before in order to assess the extent of this numerical anisotropy of the discrete numerical model of the plate it is sufficient to use as basis the map corresponding to the fundamental antisymmetric mode of Lamb waves  $A_0$  only.

The observation made until this point concerning numerical properties of three FEM approaches, i.e., the classical FEM, TD-SFEM and spFEM are best illustrated by the results of numerical computations concerning propagation of elastic waves within the plate under consideration presented in Fig. 14.9.

For this purpose the explicit  $\beta$ -Newmark method is used, as discussed in Sect. 10.7, for the recommended values of the parameters  $\alpha$  and  $\beta$  equal to  $1/2$  and  $1/4$ , respectively. Moreover, in order to ensure that discrete numerical models of similar number of DOFs are used, the already tested uniform meshes of the plate are employed:  $126 \times 126$  FEs and 192,027 DOFs for FEM,  $50 \times 50$  FEs and 189,003 DOFs for TD-SFEM,  $82 \times 82$  FEs and 186,003 DOFs for spFEM. The obtained numbers result directly from the degrees of approximation polynomials used by these FEM approaches, which are:  $r = 2$  for FEM,  $r = 5$  for TD-SFEM and  $r = 3$  for spFEM.

This time the total calculation time  $T$  covers 500  $\mu$ s and is divided into 6,000 equal time steps. The excitation signal is applied as a transversely force acting at the plate centre, having the amplitude of 1 N and the form of 10 sine pulses at the carrier frequency  $f_c$  equal to 70, 120 or 165 kHz, modulated by the Hann window, i.e., with the frequency of modulation  $f_m = f_c/m$  equal to 5.83, 10.0 or 13.75 kHz, where

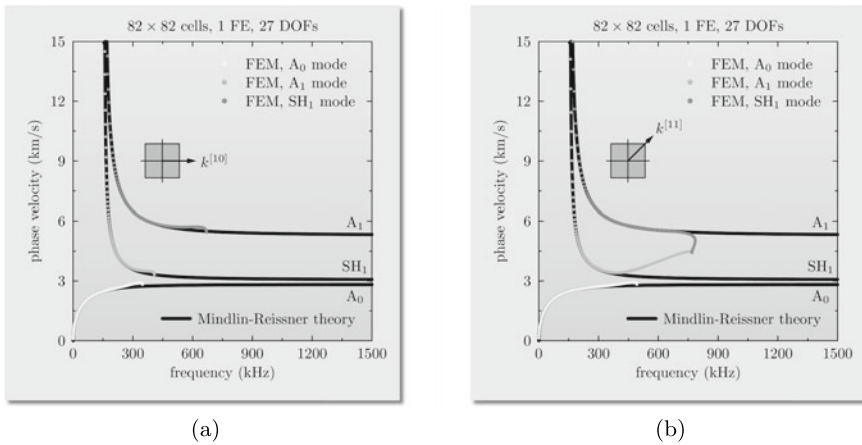


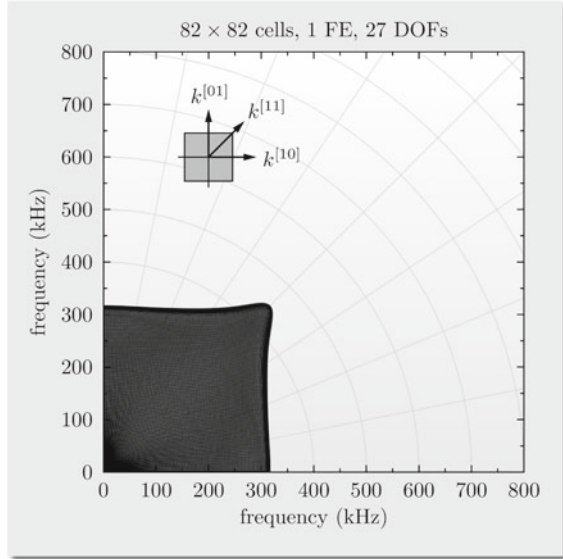
**Fig. 14.7** Dispersion curves for the phase velocity for antisymmetric modes of elastic waves propagating in a 10 mm thick non-periodic medium in the directions of non-dimensional wave vectors of the reciprocal space: **a**  $\tilde{k}_n^{[10]}$ , **b**  $\tilde{k}_n^{[11]}$ . Results of numerical computations in the reduced zone, for the degree of approximation polynomials  $r = 3$  and spFEM, according to the 3-mode 2-D theory (Mindlin–Reissner) theory of the antisymmetric behaviour of plates, obtained by the use of the Bloch reduction technique for a uniform lattice of  $82 \times 82$  cells,  $c_{P3pt} = 6.09$  km/s,  $c_{S3pt} = 3.07$  km/s,  $a = 12.2$  mm

**Table 14.4** Statistical data on the spatial numerical dispersion in the case of two discrete numerical models of a 2-D non-periodic medium. Results of numerical computations by TD-SFEM/spFEM according to the 2-mode 2-D theory (Mindlin-Reissner) of the antisymmetric behaviour of plates, obtained by the use of the Bloch reduction technique for a uniform lattice of: **a**  $50 \times 50$  cells,  $a = 20$  mm and TD-SFEM, **b**  $82 \times 82$  cells,  $a = 12$  mm and spFEM, and  $c_{P3pt} = 6.09$  km/s,  $c_{S3pt} = 3.07$  km/s

FEM approach	Mode	Direct.	1% disp. (kHz)	5% disp. (kHz)	$f_{max}$ (kHz)
TD-SFEM, $r = 5$	A <sub>0</sub>	[10]	150.2 (24.5%)	198.8 (32.5%)	612.5
		[11]	229.5 (26.5%)	290.6 (33.5%)	867.2
	A <sub>1</sub>	[10]	244.8 (35.9%)	280.4 (41.2%)	681.2
		[11]	294.1 (22.1%)	374.1 (28.1%)	1333.1
spFEM, $r = 3$	A <sub>0</sub>	[10]	219.6 (63.1%)	290.8 (83.5%)	348.1
		[11]	334.5 (68.0%)	447.4 (90.1%)	492.2
	A <sub>1</sub>	[10]	311.1 (76.2%)	408.3 (100%)	408.3
		[11]	359.3 (46.7%)	434.1 (56.4%)	769.2
SH <sub>1</sub>	[10]	509.0 (75.9%)	670.3 (100%)	670.3	
	[11]	734.9 (93.6%)	779.7 (99.3%)	785.2	

In brackets the percentage of the frequency spectrum associated with a given mode is indicated

**Fig. 14.8** Directional map of frequencies of free vibrations for the fundamental antisymmetric mode of Lamb waves  $A_0$  of elastic waves propagating in a 10 mm thick non-periodic medium, for the degree of approximation polynomials  $r = 3$  and spFEM. Results of numerical computations for the reduced zone, according to the 3-mode 2-D theory (Mindlin-Reissner) of the antisymmetric behaviour of plates, obtained by the use of the Bloch reduction technique for a uniform lattice of  $82 \times 82$  cells and  $a = 12.2$  mm,  $c_{P3pt} = 6.09$  km/s,  $c_{S3pt} = 3.07$  km/s



$m = 10$ . The total calculation time  $T$  is chosen in such a manner that the resulting wave packet travelling within the plate should at least reach any of the free edges of the plate.

The values of the carrier frequency  $f_c$  are carefully selected, so the periodic nature of discrete numerical models of the plate can be fully revealed. This is possible since in the case of FEM the first frequency band gap  $FG_1$  (162.2 kHz ... 177.7 kHz) is centrally located within the range of excited frequencies for the carrier frequency of the excitation  $f_c = 165$  kHz, while in the case of TD-SFEM the first frequency band gap  $FG_1$  (198.8 kHz ... 210 kHz) is located on its edge, all in the direction of the wave vector of reciprocal space  $k^{[10]}$ , as presented in Table 13.4 in Sect. 13.4. For lower values of the carrier frequencies, i.e., 70 and 120 kHz, the periodic nature of the discrete numerical model of the plate should stay hidden, except some influence of numerical anisotropy can be revealed depending on the properties of discrete numerical models used.

It is evident from the results presented in Fig. 14.9 that an increase in the carrier frequency  $f_c$  leads to an increasing influence of the periodic nature of the discrete numerical models of the plate, for both FEM and TD-SFEM. In the case of FEM clear numerical dispersion is observed yet for the carrier frequency  $f_c$  of 120 kHz, while in the case of TD-SFEM this becomes observable for the carrier frequency  $f_c$  of 165 kHz. This higher excitation frequency leads to strong numerical dispersion in the case of FEM, which is a clear indication of the influence of a frequency band gap within the range of excited frequencies. However, in the case of spFEM no such behaviour is observed, except some small numerical dispersion, which can be noticed for the higher excitation frequency  $f_c$  of 165 kHz. Once more the superior behaviour



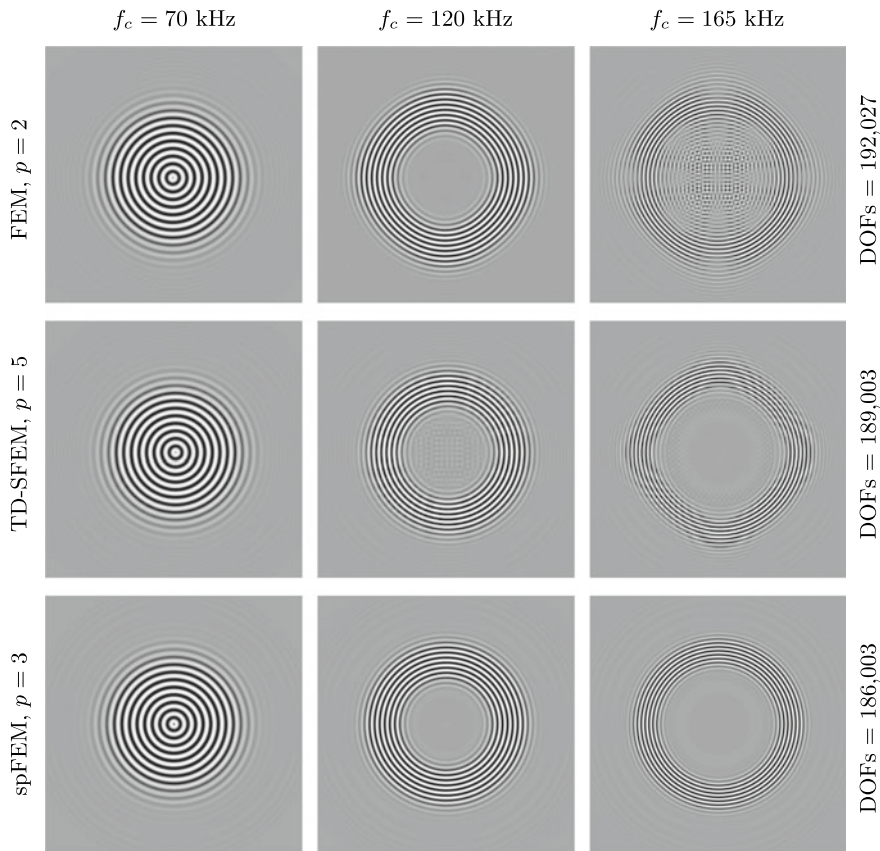


**Fig. 14.9** Wave propagation patterns for transverse acceleration component  $\ddot{u}_z$  for the fundamental antisymmetric mode of Lamb waves  $A_0$  of elastic waves propagating in a 2-D non-periodic plate, for various modelling approaches: (top) FEM, (middle) TD-SFEM and (bottom) spFEM and various excitation frequencies: (left) 70 kHz, (centre) 120 kHz, (right) 165 kHz, for similar number of DOFs of discrete numerical models. Results of numerical computations according to the 3-mode 2-D theory (Mindlin-Reissner) of the antisymmetric behaviour of plates for a 10 mm thick non-periodic  $1 \text{ m} \times 1 \text{ m}$  aluminium plate with free edges

of spFEM over both FEM and TD-SFEM, in the case of analysis of wave propagation patterns, is clearly confirmed.

Finally, also in this case it can easily be checked, based on the dispersion curves presented in Fig. 14.9 as well as in Figs. 13.13 and 13.14 from Sect. 13.4, that in the case of the classical FEM and TD-SFEM the assumed excitation signals of the central frequency  $f_c$  equal to 70, 120 and 165 kHz conforms well with the requirement of 4 nodal distances per wavelength, while in the case of spFEM with the requirement of 4 nodal DOFs per wavelength [22–24].

## References

1. A. Źak and W. Waszkowiak. A spline-based FE approach to modelling of high frequency dynamics of 1-d structures. *Computers & Mathematics with Applications*, 104:14–33, 2021.
2. O. C. Zienkiewicz, D. W. Kelly, and P. Bettess. Reduced integration technique in general analysis of plates and shells. *International Journal for Numerical Methods in Engineering*, 3:275–290, 1971.
3. A. Źak and M. Krawczuk. Certain numerical issues of wave propagation modelling in rods by the Spectral Finite Element Method. *Finite Elements in Analysis and Design*, 47:1036–1046, 2011.
4. W. Ostachowicz, P. Kudela, M. Krawczuk, and A. Źak. *Guided waves in structures for SHM. The time-domain spectral element method*. John Wiley & Sons Ltd., Singapore, 2012.
5. A. Ralston and P. Rabinowitz. *A first course in numerical analysis*. Dover Publications, Inc., New York, 2001.
6. P. G. Ciarlet and P. A. Raviart. General Lagrange and Hermite interpolation in  $R^n$  with applications to finite element methods. *Archive for Rational Mechanics and Analysis*, 46:178–198, 1972.
7. V. Ruas. Hermite finite elements for second order boundary value problems with sharp gradient discontinuities. *Journal of Computational and Applied Mathematics*, 246:234–242, 2013.
8. P. M. Prenter. *Splines and variational methods*. Dover Publications, Inc., New York, 1975.
9. C. de Boor. *A practical guide to splines*. Springer-Verlag New York Inc., New York, 1978.
10. Z. Kosma. On a special type of cubic splines. *Bulletin de l'Académie Polonaise des Sciences. Série des Sciences Techniques*, 26:373–382, 1978.
11. D. F. Rogers. *An introduction to NURBS: With historical perspective*. Morgan Kaufmann Publishers, San Francisco, 2000.
12. T. J. R. Hughes, J. A. Cottrell, and Y. Bazilevs. Isogeometric analysis: CAD, finite elements, NURBS, exact geometry and mesh refinement. *Computer Methods in Applied Mechanics and Engineering*, 194:4135–4195, 2005.
13. J. A. Cottrell, T. J. R. Hughes, and Y. Bazilevs. *Isogeometric analysis: Toward integration of CAD and FEA*. John Wiley & Sons Ltd., Singapore, 2009.
14. K. Höllig, U. Reif, and J. Wipper. Weighted extended B-spline approximation of Dirichlet problems. *SIAM Journal on Numerical Analysis*, 39:442–462, 2001.
15. L. Shen, Z. Liu, and J. H. Wu. B-spline finite element method based on node moving adaptive refinement strategy. *Finite Elements in Analysis and Design*, 91:84–94, 2014.
16. A. Chakraborty and B. V. R. Kumar. Weighted extended B-spline finite element analysis of a coupled system of general elliptic equations. *International Journal of Advances in Engineering Sciences and Applied Mathematics*, 10:34–40, 2018.
17. W. Ostachowicz and M. Krawczuk. Modeling for detection of degraded zones in metallic and composite structures. in: *Encyclopedia of Structural Health Monitoring*, John Wiley & Sons Ltd., Chichester:851–866, 2009.
18. A. A. Shabana, A. M. Hamed, A.-N. A. Mohamed, P. Jayakumar, and M. D. Letherwood. Limitations of B-spline geometry in the finite element/multibody system analysis. in: *Proceedings of the 8th International Conference on Multibody Systems, Nonlinear Dynamics, and Control, Parts A and B*, 4:861–871, 2011.
19. S. S. Rao. *The finite element method in engineering*. Pergamon Press, Oxford, 1981.
20. <http://www.mathworks.com>.
21. <http://www.wolfram.com>.
22. N. M. Papadakis and G. E. Stavroulakis. Effect of mesh size for modeling impulse responses of acoustic spaces via Finite Element Method in Time Domain. *Euronoise 2018 Proceedings*, 1:323–329, 2018.
23. T. Łodygowski and W. Sumelka. Limitations in application of finite element method in acoustic numerical simulation. *Journal of Theoretical and Applied Mechanics*, 44:849–865, 2006.
24. G. L. Wojcik, D. K. Vaughan, J. Mould Jr., F. A. Leon, Q. D. Quian, and M. A. Lutz. Laser alignment modeling using rigorous numerical simulations. *SPIE Proceedings: Optical/Laser Microlithography IV*, 1463:292–303, 1991.

# Afterword

*Think it over, think it under—Winnie-the-Pooh*

Despite the fact that this book is intended as a textbook for undergraduate, postgraduate as well as doctoral students, it is far from being complete. In a way it leaves readers enough space for their own study and research, but on the other hand it provides all information that is needed to start this process. In all necessary places it refers readers not only to the most recent scientific literature, but also to the most important and influential historical positions. However, it is a very difficult, if not an impossible task to fit and squeeze all available historical as well as contemporary information from such broad scientific disciplines as: physics, acoustics, mathematics and additionally computational techniques such as is FEM, into a finite number of pages.

In view of this, while looking on the content of the book, for the benefit of its readers, it is perhaps at this stage much more important to point out what is missing in this book rather than to state what is included.

The historical background, for the reasons already mentioned, had to be limited to the most important aspects of the developments in the scientific disciplines most relevant to the subject of the book and is intended by the author to present a kind of sequence of historical factors, discoveries and milestones leading to the current state of knowledge. Perhaps more inquisitive readers will find this kind of information placed in the book as inspirational and sufficient to start their own investigations in this respect.

The theoretical considerations included in the book are focused on the most important and typical aspects of acoustics and wave propagation. The necessary mathematical background is offered to readers to support these considerations. But yet again, the vast range of existing aspects of modern acoustics and associated wave propagation problems, remains far beyond what was possible to include in the book. For this reason the book is focused on linear problems in elastic solids only. However, this somehow narrowed scope offers readers an insight into and understanding of the

associated phenomena to the extent which allows them to start to conduct their own research in these fields.

Due to the sheer number of more or less advanced textbooks on FEM available, the relevant section of the book dealing with FEM modelling also had to be limited. For this reason it is focused on the linear displacement FEM approach concerning isotropic media only, but places particular emphasis on those problems of FEM modelling which are new or not too well recognised in the available literature. This concerns the process of building simplified as well as higher-order multi-mode FEM models of typical structural elements and their subsequent assessment, especially in the context of wave propagation analysis. Based on the information provided more inquisitive readers may easily apply the methodology presented in the book to other types of problems typically solved by FEM, which are not covered in the book.

However, it is noteworthy that two very important aspects of numerical analysis of the problems associated with the propagation of elastic waves in engineering structures, carried out by the use of FEM, are investigated in the book to some greater depth. The first of them concerns the wave propagation phenomena in unbounded/infinite engineering structures by FEM, while the second concerns periodic properties of FE discrete numerical models, which are used for this purpose. In that context some basic theoretical background on periodic structures is also offered to readers not familiar with this subject. This original part of the book is meant by the author as offering readers deeper understanding of important issues related to FEM modelling and analysis, which can be easily moved onto and adopted for new types of scientific or engineering problems tackled by FEM.

Finally, a concept of spFEM is explained and introduced as a new type of FEM approach offering computational properties, which are not accessible in the case of classical FEs. This further original aspect of the book, still under development, is presented to readers in a very accessible and easy to follow form, but supported by a number of simple and demonstrative case studies. Nevertheless, it is also meant to encourage more inquisitive readers to start their own investigations in this respect to the benefit of the field and whole research community.

At this point the author of this book would also like to gratefully acknowledge the support for his research provided by the Centre of Informatics Tricity Academic Supercomputer & Network (CI TASK). All results presented in this book have been obtained by the use of the software available at CI TASK.

## Appendix A

### Material Constants

**Anisotropic materials**<sup>1</sup> have no planes of material symmetry. Typical examples of anisotropic materials include: wood, most crystals or short-fibre reinforced composites. The number of independent material coefficients in the stiffness tensor  $\mathbf{C}$  is 21. They have to be established through as many as 21 independent experimental tests [1].

In the case anisotropic materials the stiffness tensor  $\mathbf{C}$  takes the following form:

$$\mathbf{C} = \begin{bmatrix} C_{11} & C_{12} & C_{13} & C_{14} & C_{15} & C_{16} \\ & C_{22} & C_{23} & C_{24} & C_{25} & C_{26} \\ & & C_{33} & C_{34} & C_{35} & C_{36} \\ & & & C_{44} & C_{45} & C_{46} \\ & & & & C_{55} & C_{56} \\ \text{symm.} & & & & & C_{66} \end{bmatrix} \quad (\text{A.1})$$

At this place it is noteworthy that the stiffness tensor  $\mathbf{C}$ , as defined by Eq. (3.47) from Sect. 3.3, fully corresponds to the matrix  $\mathbf{D}_e$  of linear relationships between the stress vector  $\boldsymbol{\sigma}$  and the strain vector  $\boldsymbol{\epsilon}$ , as defined by Eq. (10.37) from Sect. 10.6, which can be written as:

$$\mathbf{C} = \mathbf{D}_e \quad (\text{A.2})$$

**Orthotropic materials**, also known as **orthogonally anisotropic materials**, have three orthogonal planes of material symmetry. Typical examples of orthotropic materials include: wood, rolled metals, certain crystals or single layers of long-fibre reinforced composites. The number of independent material coefficients in the stiffness tensor  $\mathbf{C}$  is 9. They can be established through 6 independent experimental tests [2].

---

<sup>1</sup> The term *anisotropy* comes for Greek (*an*—not, *isos*—the same, *trópos*—a turn, way, manner or style) and means not the same or different for the direction or rotation. Its opposite is isotropy.

In the case orthotropic materials the stiffness tensor  $\mathbf{C}$  takes the following form:

$$\mathbf{C} = \begin{bmatrix} C_{11} & C_{12} & C_{13} & 0 & 0 & 0 \\ & C_{22} & C_{23} & 0 & 0 & 0 \\ & & C_{33} & 0 & 0 & 0 \\ & & & C_{44} & 0 & 0 \\ & & & & C_{55} & 0 \\ \text{symm.} & & & & & C_{66} \end{bmatrix} \quad (\text{A.3})$$

**Transversely isotropic materials** have an infinite number of planes of material symmetry and exhibit isotropy in one direction, which is normal to the plane of isotropy. Typical examples of transversely isotropic materials include: unidirectional long-fibre reinforced composites, stratified soils and rocks as well as bones. The number of independent material coefficients in the stress tensor  $\mathbf{C}$  is 5. They have to be established through 5 independent experimental tests [3].

In the case transversely isotropic materials the stiffness tensor  $\mathbf{C}$  takes the following form:

$$\mathbf{C} = \begin{bmatrix} C_{11} & C_{12} & C_{23} & 0 & 0 & 0 \\ & C_{22} & C_{23} & 0 & 0 & 0 \\ & & C_{22} & 0 & 0 & 0 \\ & & & \hat{C} & 0 & 0 \\ & & & & C_{66} & 0 \\ \text{symm.} & & & & & C_{66} \end{bmatrix} \quad (\text{A.4})$$

where  $\hat{C} = (C_{11} - C_{12})/2$ .

**Isotropic material** have an infinite number of planes of material symmetry. Typical examples of isotropic materials include: glass, plastics, metals and their alloys. The number of independent material coefficients in the stress tensor  $\mathbf{C}$  is 2. They can be established through 2 simple and independent experimental tests [3].

In the case isotropic materials the stiffness tensor  $\mathbf{C}$  takes the following form:

$$\mathbf{C} = \begin{bmatrix} C_{11} & C_{12} & C_{12} & 0 & 0 & 0 \\ & C_{11} & C_{12} & 0 & 0 & 0 \\ & & C_{11} & 0 & 0 & 0 \\ & & & \hat{C} & 0 & 0 \\ & & & & \hat{C} & 0 \\ \text{symm.} & & & & & \hat{C} \end{bmatrix} \quad (\text{A.5})$$

where as before  $\hat{C} = (C_{11} - C_{12})/2$ .

In engineering practice the material coefficients within the stress tensor  $\mathbf{C}$  can be expressed either by Lamé parameters or more preferably by engineering constants describing material properties in various directions [4]. For this purpose it is convenient to use the subscripts 1, 2 and 3 as a reference to the principal directions of material symmetries, which coincide with the  $x$ ,  $y$  and  $z$  axes, respectively.

In the case of **orthotropic material** the material coefficients in the stiffness tensor **C** can be expressed by the following relationships:

$$\begin{cases} C_{11} = \frac{1 - \nu_{23}\nu_{32}}{\Delta E_{22}E_{33}}, & C_{12} = \frac{\nu_{21} + \nu_{23}\nu_{31}}{\Delta E_{22}E_{33}} = \frac{\nu_{12} + \nu_{13}\nu_{32}}{\Delta E_{11}E_{33}} \\ C_{13} = \frac{\nu_{31} + \nu_{21}\nu_{32}}{\Delta E_{22}E_{33}} = \frac{\nu_{13} + \nu_{12}\nu_{23}}{\Delta E_{11}E_{22}}, & C_{22} = \frac{1 - \nu_{13}\nu_{31}}{\Delta E_{11}E_{33}} \\ C_{23} = \frac{\nu_{32} + \nu_{12}\nu_{31}}{\Delta E_{11}E_{33}} = \frac{\nu_{23} + \nu_{13}\nu_{21}}{\Delta E_{11}E_{22}}, & C_{33} = \frac{1 - \nu_{12}\nu_{21}}{\Delta E_{11}E_{22}} \\ C_{44} = G_{23}, & C_{55} = G_{31}, \quad C_{66} = G_{12} \end{cases} \quad (\text{A.6})$$

where the factor  $\Delta$  is defined as:

$$\Delta = \frac{1 - \nu_{12}\nu_{21} - \nu_{13}\nu_{31} - \nu_{23}\nu_{32} - 2\nu_{12}\nu_{23}\nu_{31}}{E_{11}E_{22}E_{33}} \quad (\text{A.7})$$

since due to the symmetry of the stress tensor **C** it can be found that:

$$\frac{\nu_{12}}{E_{11}} = \frac{\nu_{21}}{E_{22}}, \quad \frac{\nu_{13}}{E_{11}} = \frac{\nu_{31}}{E_{33}}, \quad \frac{\nu_{23}}{E_{22}} = \frac{\nu_{32}}{E_{33}} \quad (\text{A.8})$$

In the case of **transversely isotropic material** the number of material coefficients in the stiffness tensor **C** is reduced since:

$$E_{33} \rightarrow E_{22}, \quad \nu_{13} \rightarrow \nu_{12}, \quad \nu_{31} \rightarrow \nu_{21}, \quad \nu_{32} \rightarrow \nu_{23}, \quad G_{31} \rightarrow G_{12} \quad (\text{A.9})$$

Finally, in the case of **isotropic material** the number of material coefficients in the stiffness tensor **C** is further reduced since:

$$E_{22} \rightarrow E_{11} \rightarrow E, \quad \nu_{23} \rightarrow \nu_{12} \rightarrow \nu, \quad G_{23} \rightarrow G_{12} \rightarrow G \quad (\text{A.10})$$

The values of material coefficients in the stiffness tensor **C**, for various types of materials mentioned above, can be defined by many ways. They can be obtained experimentally or established based on the results available in the literature. In the case of unidirectional composite materials or laminates they can be calculated by the use of well-known formulae [2–4].

Additionally, material coefficients in the stiffness tensor **C**, describing the elastic properties of the material in 3-D, may take into account various stress or strain conditions, which lead to the reduction of its dimension in the case of 2-D or 1-D problems. This takes place under such conditions as: plane stress or plane strain, pure bending, tension or torsion [5–7], also exploited in this book.

# Appendix B

## Solving for $c(\omega)$

In many places throughout this book in order to obtain dispersion curves it is necessary to solve characteristic equations  $f(k) = 0$  for a specific cyclic frequency  $\omega$  as a parameter. This process can be formally written as:

$$\text{for given } \omega \rightarrow f(k) = 0 \rightarrow k \rightarrow c(\omega) = \frac{\omega}{k} \tag{B.1}$$

which leads directly to the phase velocity  $c(\omega)$ .

The characteristic equation  $f(k) = 0$  can be also thought of as representing a certain complex function  $f(z)$  of a complex variable  $z = x + iy$ . This function has complex roots and they can be found numerically. There are numerous numerical methods available in the literature, which allow one to find them. The method used in this book is a simple approach, which is based on the very well-known method of bisection [8]. The use of such a simple method leads to a very fast and good estimation of the sought roots, which next can be precisely pinned down by the use of the Newton-Raphson method or similar methods, which in general are characterised by much faster convergence than the method of bisection.

However, one must remember that finding roots of a complex function  $f(z)$  of a complex variable  $z = x + iy$  can be a difficult task of its own. In order to simply this task the function  $f(z)$  can be represented as a sum of its real and imaginary parts, expressed by certain functions  $u(z)$  and  $v(z)$ , but treated as functions of  $x$  and  $y$  variables instead:

$$\begin{aligned} f(z) &= f(x + iy) = \text{Re}[f(z)] + i\text{Im}[f(z)] \\ &= u(z) + iv(z) = u(x, y) + iv(x, y) \end{aligned} \tag{B.2}$$

Moreover, it can be noticed that the roots of the function  $f(z)$  must simultaneously be the roots of the functions  $u(z)$  and  $v(z)$  and vice versa. This property can be exploited to construct a new real-valued function  $F(x, y)$ , which has the same roots as the original complex function  $f(z)$ :



$$F(x_0, y_0) = 0 \rightarrow f(z_0) = 0, \text{ where } z_0 = x_0 + iy_0 \quad (\text{B.3})$$

Consequently, many real-valued functions  $F(x, y)$  can be used here [9]. In order to simplify computational operations and avoid dealing with very high positive and negative numbers, for the results presented in this book a real-valued function  $F(x, y)$  in the following form was employed:

$$F(x, y) = \frac{\text{sgn}[u(x, y) + v(x, y)]}{2} + \frac{\text{sgn}[u(x, y) - v(x, y)]}{2} \quad (\text{B.4})$$

where  $\text{sgn}$  is the sign function. It can be also checked that as a result  $F(x, y) \in (-1, 1)$  and particular roots of the new function  $F(x, y)$  on  $xy$  plane can be easily located by the use of the bisection method. The absolute accuracy of the obtained values of the phase velocity  $c(\omega)$  by the use of the proposed approach can easily reach  $10^{-5}$  m/s.

# Appendix C

## Coordinate Systems

Very often the equations of motion, given by Eq. (3.4) from Sect. 3.1, must be analysed in coordinate systems other than the Cartesian coordinate system  $(x, y, z)$ . In all such cases it is necessary to express the nabla operator of differentiation  $\nabla$  associated with calculations of:

- the gradient  $\nabla f \equiv \text{grad } f$ ,
- the divergence  $\nabla \cdot \mathbf{f} \equiv \text{div } \mathbf{f}$ ,
- the curl (rotor)  $\nabla \times \mathbf{f} \equiv \text{curl } \mathbf{f}$ ,

in such coordinate systems [10].

Since three coordinate systems are typically used in engineering practice, i.e. the Cartesian coordinate system  $(x, y, z)$ , the cylindrical coordinate system  $(x, r, \theta)$  as well as the spherical coordinate system  $(r, \theta, \vartheta)$ , the corresponding formulae for calculations of the gradient, divergence and curl become very important.

In the case of **the Cartesian coordinate system**  $(x, y, z)$ :

- **the gradient** of a scalar function  $f(x, y, z)$  is:

$$\nabla f(x, y, z) = \mathbf{g}(x, y, z) \tag{C.1}$$

where  $\mathbf{g}(x, y, z)$  is a vector function such that:

$$g_x = \frac{\partial f}{\partial x}, \quad g_y = \frac{\partial f}{\partial y}, \quad g_z = \frac{\partial f}{\partial z} \tag{C.2}$$

- **the divergence** of a vector function  $\mathbf{g}(x, y, z)$  is:

$$\nabla \cdot \mathbf{g}(x, y, z) = \nabla \cdot [g_x, g_y, g_z] = f(x, y, z) \tag{C.3}$$

where  $f(x, y, z)$  is a scalar function such that:

$$f(x, y, z) = \frac{\partial g_x}{\partial x} + \frac{\partial g_y}{\partial y} + \frac{\partial g_z}{\partial z} \quad (\text{C.4})$$

- **the curl** of a vector function  $\mathbf{g}(x, y, z)$  is:

$$\nabla \times \mathbf{g}(x, y, z) = \nabla \times [g_x, g_y, g_z] = \mathbf{h}(x, y, z) \quad (\text{C.5})$$

where  $\mathbf{h}(x, y, z)$  is a vector function such that:

$$h_x = \frac{\partial f_z}{\partial y} - \frac{\partial f_y}{\partial z}, \quad h_y = \frac{\partial f_x}{\partial z} - \frac{\partial f_z}{\partial x}, \quad h_z = \frac{\partial f_y}{\partial x} - \frac{\partial f_x}{\partial y} \quad (\text{C.6})$$

In the case of **the cylindrical coordinate system**  $(x, r, \theta)$ :

- **the gradient** of a scalar function  $f(x, r, \theta)$  is:

$$\nabla f(x, r, \theta) = \mathbf{g}(x, r, \theta) \quad (\text{C.7})$$

where  $\mathbf{g}(x, r, \theta)$  is a vector function such that:

$$g_x = \frac{\partial f}{\partial x}, \quad g_r = \frac{\partial f}{\partial r}, \quad g_\theta = \frac{1}{r} \frac{\partial f}{\partial \theta} \quad (\text{C.8})$$

- **the divergence** of a vector function  $\mathbf{g}$  is:

$$\nabla \cdot \mathbf{g}(x, r, \theta) = \nabla \cdot [g_x, g_r, g_\theta] = f(x, r, \theta) \quad (\text{C.9})$$

where  $f(x, r, \theta)$  is a scalar function such that:

$$f(x, r, \theta) = \frac{\partial f_x}{\partial x} + \frac{1}{r} \frac{\partial (r f_r)}{\partial r} + \frac{1}{r} \frac{\partial f_\theta}{\partial \theta} \quad (\text{C.10})$$

- **the curl** of a vector function  $\mathbf{g}(x, r, \theta)$  is:

$$\nabla \times \mathbf{g}(x, r, \theta) = \nabla \times [g_x, g_r, g_\theta] = \mathbf{h}(x, r, \theta) \quad (\text{C.11})$$

where  $\mathbf{h}(x, r, \theta)$  is a vector function such that:

$$\begin{cases} h_x = \frac{1}{r} \frac{\partial (r g_\theta)}{\partial r} - \frac{1}{r} \frac{\partial g_r}{\partial \theta} \\ h_r = \frac{1}{r} \frac{\partial g_x}{\partial \theta} - \frac{\partial g_\theta}{\partial x} \\ h_\theta = \frac{\partial g_r}{\partial x} - \frac{\partial g_x}{\partial r} \end{cases} \quad (\text{C.12})$$

In the case of **the spherical coordinate system**  $(r, \theta, \vartheta)$ :

- **gradient** of a scalar function  $f(r, \theta, \vartheta)$  is:

$$\nabla f(r, \theta, \vartheta) = \mathbf{g}(r, \theta, \vartheta) \quad (\text{C.13})$$

where  $\mathbf{g}(r, \theta, \vartheta)$  is a vector function such that:

$$g_r = \frac{\partial f}{\partial r}, \quad g_\theta = \frac{1}{r} \frac{\partial f}{\partial \theta}, \quad g_\vartheta = \frac{1}{r \sin \theta} \frac{\partial f}{\partial \vartheta} \quad (\text{C.14})$$

- **divergence** of a vector function  $\mathbf{g}(r, \theta, \vartheta)$  is:

$$\nabla \cdot \mathbf{g}(r, \theta, \vartheta) = \nabla \cdot [g_r, g_\theta, g_\vartheta] = f(r, \theta, \vartheta) \quad (\text{C.15})$$

where  $f(r, \theta, \vartheta)$  is a scalar function such that:

$$f(r, \theta, \vartheta) = \frac{1}{r^2} \frac{\partial(r^2 g_r)}{\partial r} + \frac{1}{r \sin \theta} \frac{\partial(g_\theta \sin \theta)}{\partial \theta} + \frac{1}{r \sin \theta} \frac{\partial g_\vartheta}{\partial \vartheta} \quad (\text{C.16})$$

- **curl** of a vector function  $\mathbf{g}(r, \theta, \vartheta)$  is:

$$\nabla \times \mathbf{g}(r, \theta, \vartheta) = \nabla \times [g_r, g_\theta, g_\vartheta] = \mathbf{h}(r, \theta, \vartheta) \quad (\text{C.17})$$

where  $\mathbf{h}(r, \theta, \vartheta)$  is a vector function such that:

$$\begin{cases} h_x = \frac{1}{r \sin \theta} \frac{\partial(g_\vartheta \sin \theta)}{\partial \theta} - \frac{1}{r \sin \theta} \frac{\partial g_\theta}{\partial \vartheta} \\ h_y = \frac{1}{r \sin \theta} \frac{\partial g_r}{\partial \vartheta} - \frac{1}{r} \frac{\partial(r g_\vartheta)}{\partial r} \\ h_z = \frac{1}{r} \frac{\partial(r g_\theta)}{\partial r} - \frac{1}{r} \frac{\partial g_r}{\partial \theta} \end{cases} \quad (\text{C.18})$$

Additionally, the following calculations rules [10] involving the nabla operator of differentiation  $\nabla$  may come as useful:

$$\begin{cases} \nabla \cdot (\nabla f) = \nabla^2 f \\ \nabla \times (\nabla f) = \mathbf{0} \\ \nabla \cdot (\nabla \times \mathbf{h}) = 0 \\ \nabla \times (\nabla \times \mathbf{h}) = \nabla(\nabla \cdot \mathbf{h}) - \nabla^2 \mathbf{h} \\ \nabla^2(f \cdot g) = f \nabla^2 g + 2(\nabla f) \cdot (\nabla g) + g \nabla^2 f \end{cases} \quad (\text{C.19})$$

as they are fully independent of the choice of the coordinate system.

The first of them represents the so-called Laplace operator (Laplacian), also noted as  $\Delta$ , which plays an important role in engineering sciences [6, 11–14]. The Laplace operator can be expressed in the three coordinate systems under consideration [10] in the following manner:

$$\begin{aligned}
 \Delta f = \nabla^2 f &= \underbrace{\frac{\partial^2 f}{\partial x^2} + \frac{\partial^2 f}{\partial y^2} + \frac{\partial^2 f}{\partial z^2}}_{f=f(x,y,z)} \\
 &= \underbrace{\frac{\partial^2 f}{\partial x^2} + \frac{\partial^2 f}{\partial r^2} + \frac{1}{r} \frac{\partial f}{\partial r} + \frac{1}{r^2} \frac{\partial^2 f}{\partial \theta^2}}_{f=f(x,r,\theta)} \tag{C.20} \\
 &= \underbrace{\frac{\partial^2 f}{\partial r^2} + \frac{2}{r} \frac{\partial f}{\partial r} + \frac{1}{r^2 \sin \theta} \frac{\partial}{\partial \theta} \left( \sin \theta \frac{\partial f}{\partial \theta} \right) + \frac{1}{r^2 \sin^2 \theta} \frac{\partial^2 f}{\partial \vartheta^2}}_{f=f(r,\theta,\vartheta)}
 \end{aligned}$$

# Appendix D

## Transformation of Mid-plane Displacement Fields

Very often it is necessary to transform the resulting form of the Maclaurin series expansion of a particular displacement components of the 3-D displacement field. Thanks to this transformation as well as the application of the traction-free boundary conditions higher-order theories can be built and formulated with a relative ease [15]. On the other hand, without the transformation the application of the traction-free boundary conditions leads to systems of partial differential equations, which very often cannot be solved analytically.

It is show in Sect. 7.2 that in the case of the 3-D displacement field, the Maclaurin series expansion of the displacement component  $u_x$  of this field, in the direction of the  $z$  axis, has the form of Eq. (7.2), which for  $m = 5$  can be presented in an expanded form as:

$$u_x(x, y, z, t) = \phi_0(x, y, t) + z\phi_1(x, y, t) + z^2\phi_2(x, y, t) + z^3\phi_3(x, y, t) + z^4\phi_4(x, y, t) + z^5\phi_5(x, y, t) \tag{D.1}$$

where the expansion error  $O(z^6)$  is omitted for the simplicity of notation.

This equation is a starting point for a mid-plane representation of the displacement component  $u_x$  of the initial 3-D displacement field, which can be presented as follows:

$$u_x(x, y, \zeta, t) = \phi_0(x, y, t) + a\zeta\phi_1(x, y, t) + a^2\zeta^2\phi_2(x, y, t) + a^3\zeta^3\phi_3(x, y, t) + a^4\zeta^4\phi_4(x, y, t) + a^5\zeta^5\phi_5(x, y, t) \tag{D.2}$$

where a new variable  $\zeta$  is introduced with  $z = a\zeta$ , where  $2h = a$ , such that if  $z \in \langle -a, +a \rangle$  then  $\zeta \in \langle -1, +1 \rangle$ .

A simple supplementation of the above equation by a number of *zero* terms leads to:

$$\begin{aligned}
u_x(x, y, \zeta, t) &= \phi_0(x, y, t) + a\zeta\phi_1(x, y, t) \\
&\quad + a^2\zeta^2\phi_2(x, y, t) + \underbrace{[\phi_2(x, y, t) - \phi_2(x, y, t)]}_{=0}a^2 \\
&\quad + a^3\zeta^3\phi_3(x, y, t) + \underbrace{[\phi_3(x, y, t) - \phi_3(x, y, t)]}_{=0}a^3\zeta \\
&\quad + a^4\zeta^4\phi_4(x, y, t) + \underbrace{[\phi_4(x, y, t) - \phi_4(x, y, t)]}_{=0}a^4 \\
&\quad + a^5\zeta^5\phi_5(x, y, t) + \underbrace{[\phi_5(x, y, t) - \phi_5(x, y, t)]}_{=0}a^5\zeta
\end{aligned} \tag{D.3}$$

which can be rearranged to form the following equation:

$$\begin{aligned}
u_x(x, y, \zeta, t) &= [\phi_0(x, y, t) + a^2\phi_2(x, y, t) + a^4\phi_4(x, y, t)] \\
&\quad - (1 - \zeta^2)\underbrace{a^2\phi_2(x, y, t)}_{=-\bar{\phi}_2(x, y, t)} - (1 - \zeta^4)\underbrace{a^4\phi_4(x, y, t)}_{=-\bar{\phi}_4(x, y, t)} \\
&\quad + a\zeta[\phi_1(x, y, t) + a^3\phi_3(x, y, t) + a^5\phi_5(x, y, t)] \\
&\quad - a\zeta(1 - \zeta^2)\underbrace{a^3\phi_3(x, y, t)}_{=-\bar{\phi}_3(x, y, t)} - a\zeta(1 - \zeta^4)\underbrace{a^5\phi_5(x, y, t)}_{=-\bar{\phi}_5(x, y, t)}
\end{aligned} \tag{D.4}$$

Next, a set of new variables  $\bar{\phi}_n = -a^n\phi_n$  ( $n = 2, 3, 4, 5$ ) can be introduced as shown above, which allows one to rewrite the above equation in a modified form as:

$$\begin{aligned}
u_x(x, y, \zeta, t) &= \underbrace{[\phi_0(x, y, t) - \bar{\phi}_2(x, y, t) - \bar{\phi}_4(x, y, t)]}_{=\bar{\phi}_0(x, y, t)} \\
&\quad + (1 - \zeta^2)\bar{\phi}_2(x, y, t) + (1 - \zeta^4)\bar{\phi}_4(x, y, t) \\
&\quad + a\zeta \underbrace{[\phi_1(x, y, t) - \bar{\phi}_3(x, y, t) - \bar{\phi}_5(x, y, t)]}_{=\bar{\phi}_1(x, y, t)} \\
&\quad + a\zeta(1 - \zeta^2)\bar{\phi}_3(x, y, t) + a\zeta(1 - \zeta^4)\bar{\phi}_5(x, y, t)
\end{aligned} \tag{D.5}$$

Finally, introduction of two new variables  $\bar{\phi}_0 = \phi_0 - \bar{\phi}_2 - \bar{\phi}_4$  as well as  $\bar{\phi}_1 = \phi_1 - \bar{\phi}_3 - \bar{\phi}_5$  leads to the mid-plane representation of the displacement component  $u_x$  of the 3-D displacement field in a desired form:

$$\begin{aligned}
u_x(x, y, \zeta, t) &= \bar{\phi}_0(x, y, t) + a\zeta\bar{\phi}_1(x, y, t) + (1 - \zeta^2)\bar{\phi}_2(x, y, t) \\
&\quad + \bar{\phi}_3(x, y, t) + (1 - \zeta^4)\bar{\phi}_4(x, y, t) + a\zeta(1 - \zeta^4)\bar{\phi}_5(x, y, t)
\end{aligned} \tag{D.6}$$

The above simple methodology can be successfully applied to the remaining displacements components  $u_y$  and  $u_z$ , which helps to transform the initial form of the displacement field to a new form, which allows one to take full advantage of the traction-free boundary condition for building higher-order theories, as it occurs in many places throughout this book.



## Appendix E

# FEM Aggregation/Assembly in MATLAB

The aggregation/assembly process is a core operation for FEM. There is no fixed methodology, which can be applied for that purpose, as such a methodology may be dependent not only on the dimensionality of the problem under investigation 1-D, 2-D or 3-D, the dimensionality of the elemental matrices of FEs in use, but also such factors as the adopted nodal numbering convention, etc. For these reasons the methodology presented below should be considered only as one example out of many possibilities.

In the case of 1-D problems concerning the use of 3-node FEs, defined according to the 1-mode 1-D theory (elementary) of the longitudinal behaviour of rods, the elemental characteristic stiffness and inertia matrices  $k_e$  and  $m_e$  may be presented in the following forms as appropriate MATLAB codes:

```
————— MATLAB code for the elemental stiffness matrix —————  
function ke = stiffness_matrix(e,l,s)  
  
% ke - elemental stiffness matrix, e - material Young's modulus  
% l - element length, s - element cross-sectional area  
  
ke = zeros(3,3);  
  
ke(1,1) = 7*e*s/6/l;  
ke(2,2) = 8*e*s/3/l;  
ke(3,3) = 7*e*s/6/l;  
  
ke(1,2) = -8*e*s/3/l;  
ke(1,3) = e*s/3/l;  
ke(2,3) = -8*e*s/3/l;  
  
ke = ke + transpose(ke);
```

————— MATLAB code for the elemental inertia matrix —————

```
function ke = inertia_matrix(rho,l,s)

% me - elemental inertia matrix, rho - material density
% l - element length, s - element cross-sectional area

me = zeros(3,3);

me(1,1) = rho*l*s/15;
me(2,2) = 4*rho*l*s/15;
me(3,3) = rho*l*s/15;

me(1,2) = rho*l*s/15;
me(1,3) = -rho*l*s/30;
me(2,3) = rho*l*s/15;

me = me + transpose(me);
```

while the corresponding part of a MATLAB code responsible for the aggregation/assembly process of FEs may be presented as follows:

————— MATLAB code for the aggregation/assembly process of FEs —————

```
% kg - global stiffness matrix, mg - global inertia matrix
% me - elemental stiffness matrix, me - elemental inertia matrix
% iout - auxiliary matrix, elements - matrix of node numbers
% fen - number of FEs, dof - number of DOFs

kg = sparse(dof,dof);
mg = sparse(dof,dof);

ke = stiffness_matrix(e,l,s);
me = inertia_matrix(rho,l,s);

for n = 1:fen
    iout = dofs(elements,n,dof);
    kg = kg + transpose(iout)*ke*iout;
    mg = mg + transpose(iout)*me*iout;
end
```

where  $kg$  and  $mg$  are the global stiffness and inertia matrices. The symbol  $fen$  denotes the total number of FEs employed in a discrete numerical model, the symbol  $dof$  its total number of DOFs, while the symbol  $elements$  denotes a matrix of node numbers, which size depends on the total number of FEs used in the discrete numerical model as well as the number of nodes of a single FE. The aggregation/assembly loop may be thought of as stretching/distributing elements of the elemental characteristic matrices onto the global characteristic matrices by a simple mathematical operation/manipulation.

In the case of a discrete numerical model consisting of 10 FEs, being 3-node rod FEs, the matrix of node numbers may have the following form:

```

— Matrix of node numbers for a 10 FE assembly of 3-node FEs —
elements =

    01 02 03
    03 04 05
    05 06 07
    07 08 09
    09 10 11
    11 12 13
    13 14 15
    15 16 17
    17 18 19
    19 20 21

```

A key element of the transformation mentioned above is the `dofs` function. This function is responsible for appropriate distribution of particular elements of the elemental characteristic stiffness and inertia matrices  $k_e$  and  $m_e$  into the global characteristic stiffness and inertia matrices, which is fully based on the assumed numbering convention encoded in the matrix `elements`.

For the 3-node FEs used in this example, having 1 DOF per node, as are FEs employed in the case the 3-mode 1-D theory (elementary) of the longitudinal behaviour of rods, the function `dofs` may have the following simple form:

```

— MATLAB code for the transformation from local-to-global DOFs —
function iout = dofs(elements,n,dof)

% iout - auxiliary matrix, elements - matrix of node numbers
% n - number of current FE, dof - number of DOFs

iout = sparse(3,dof);

for j = 1:3
    iout(j,elements(n,j)-1) = 1;
end

```

where the dimensionality of the auxiliary matrix `iout` is dependent on the total number of FEs `fen` in the discrete numerical model, or in a more general case dependent on the resulting form this number the total number DOFs of this model `dof`, as well as on the total number of DOFs within a single FE. On the other hand, the latter one is dependent on the total number of nodes within a FE and the number of DOFs per each node. In the current example of the 3-node FEs, combined with the 1-mode 1-D theory (elementary) of the longitudinal behaviour of rods, the

number of nodes within a single FE is 3, while the number of DOFs per each node is 1, i.e. the resulting number is also 3. It should be strongly emphasised that the aggregation/assembly methodology presented above is also fully applicable in the case of 2-D or 3-D problems involving any types of FEs.

## References

1. C. Lamuta. Elastic constants determination of anisotropic materials by depth-sensing indentation. *Springer Nature Applied Sciences*, 1263:1–13, 2019.
2. J. R. Vinson and Sierakowski R. L. *The behaviour of structures composed of composite materials*. Springer, Dordrecht, 2008.
3. O. O. Ochoa and J. N. Reddy. *Finite Element Analysis of Composite Laminates*. Kluwer Academic Publishers, Dordrecht, 1992.
4. G. C. Sih and Chen E. P. *Mechanics of Fractures: Cracks in composite materials*. Martinus Nijhoff Publishers, Hague, 1981.
5. W. Ostachowicz, P. Kudela, M. Krawczuk, and A. Żak. *Guided waves in structures for SHM. The time-domain spectral element method*. John Wiley & Sons Ltd., Singapore, 2012.
6. O. C. Zienkiewicz. *The finite element method*. McGraw-Hill Book Company, London, 1989.
7. S. S. Rao. *The finite element method in engineering*. Pergamon Press, Oxford, 1981.
8. A. Ralston and P. Rabinowitz. *A first course in numerical analysis*. Dover Publications, Inc., New York, 2001.
9. J. F. Doyle. *Wave propagation in structures*. Springer-Verlag, Inc., New York, 1997.
10. J. M. Massalski and J. Studnicki. *Legal units of measurements and physical constants (in Polish)*. Polish Scientific Publishers (PWN), Warsaw, 1988.
11. P. G. Ciarlet and R. Glowinski. Dual iterative techniques for solving a finite element approximation of the biharmonic equation. *Computer Methods in Applied Mathematics and Engineering*, 5:277–295, 1975.
12. J. D. Achenbach. *Wave propagation in elastic solids*. North-Holland Publishing Company, Amsterdam, 1973.
13. J. L. Rose. *Ultrasonic waves in solid media*. Cambridge University Press, Cambridge, 1999.
14. S. P. Timoshenko and S. Woinowsky-Krieger. *Theory of plates and shells*. McGraw-Hill Book Company, New York, 1959.
15. A. Żak and M. Krawczuk. Assessment of rod behaviour theories used in spectral finite element modelling. *Journal of Sound and Vibration*, 329:2099–2113, 2010.